Gaussian Wave Propagation in Alternating Positive and Negative Coupling Waveguide Arrays

Keivan Mahmoud Aghdami and Fatemeh Mokhtari
Physics Department, Payame Noor University, Tehran 19395-4697, Iran

Abstract— We numerically simulate propagation of a Gaussian beam passing through an array of alternating positive and negative coupling waveguides for different inclination beam angle, in presence and absence of nonlinear term. Major differences are seen in comparison with the constant coupled waveguides analogous.

1. INTRODUCTION

The study of linear and nonlinear phenomena in coupled waveguide arrays as an evidence of discrete indexed optical medium has attracted a lot of attention over the past decade and is investigated in one and two dimensions [1]. The coupling in waveguide lattices is due to light electric field leakage and is mathematically defined as a specific overlap integral between the linear modes of adjacent waveguides. So far the sign of coupling parameter has been considered positive (DC-coupling) in most of the works in this area, where the portion of electric field penetrate to first adjacent neighbours are in phase with itself. More recently, negative coupling has also been proposed [2], which is physically equivalent to an additional phase shift of π caused by the coupling. A one-dimensional array of parallel and adjacent waveguides that are located in the air or inside a different D-electric environment can be studied as such systems. Fig. 1 depicts such a periodic waveguide array arrangement. All waveguide elements are identical and equally spaced from each other.

In this article, propagation of a Gaussian beam in arrays of waveguides with alternating positive and negative coupling (AC-coupling), in the absence and in presence of nonlinear phenomenon is studied numerically and compared to homogenous positive coupling case [3]. Here Gaussian beam evolution is simulated while propagate along waveguides and its route is investigated by several initial phase difference of waveguides which is caused by input beam tilt angle.

2. THEORETICAL MODEL

Behaviour of light is described by one-dimensional discrete nonlinear Schrodinger equation with alternating positive and negative coupling (AC) for array of N waveguides as [2].

$$i\frac{dE_n}{dz} + \beta\, E_n + (-1)^n\, \kappa\, (E_{n-1} - E_{n+1}) + \gamma\, |E_n|^2\, E_n = 0 \tag{1}$$

where the field amplitude in nth waveguide is E_n, β is propagation constant at individual waveguide and $(-1)^n\kappa$ is alternative coupling coefficient between $n-1$ and nth guide. z is the propagation coordinate and the fourth term illustrates nonlinear Kerr phenomenon in which γ is proportional to the Kerr nonlinear coefficient. As so defined, the coupling coefficient switches between positive and negative signs periodically across the waveguide arrays. In all of the calculations, the constant parameters are as follows: $\kappa = 109\,\mathrm{m}^{-1}$, $\lambda = 633\,\mathrm{nm}$, $d = 8.5\,\mu\mathrm{m}$.

3. SIMULATION

In order to solve Equation (1) numerically, and simulate the light's behavior while passing through the wave guides, Relax method has been applied. In this method, after dividing Equation (1)

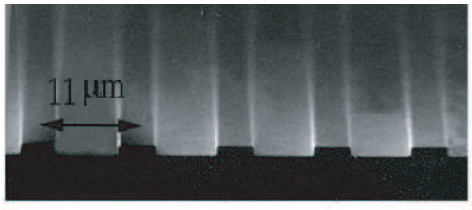

Figure 1: The schema of array of wave guides.

into N coupled equations, with access to early quantities of the field, the equation is integrated using Runge-Kutta method. In this article, light's behavior in the process of propagation in the environment is studied in two different situations: in the absence of nonlinear Kerr phenomenon and in its presence.

3.1. In the Absence of Nonlinear Kerr Phenomenon ($\gamma = 0$):

Light propagation through 6 cm long, 41 AC-coupled guide is simulated in Figs. 2(a) and 2(b) for initial phase difference $\varphi = 0$ and $\varphi = \pi/2$ respectively, correspond to the input beam tilt angle $t = 0$ and $t = 1.1°$ for $L = 8.5\,\mu m$ separation of adjacent guides. Just in initial steps for $\varphi = 0$ (Fig. 2(a)), diffraction dynamic leads to the splitting of the Gaussian beam into two parts with opposite lateral group velocities. Intensity between two forwarding peaks descents to zero level when it propagates more along the guides. Unlike in Fig. 2(b) for $\varphi = \pi/2$ beam almost keeps its concentration, except a small deep in center, but intensity gets high and low value in adjacent waveguides alternatively as it propagates. This picture is clearer in Fig. 3 which compares output beam profile for $\varphi = \pi/2$ (line) and $\varphi = 3\pi/2$ (dot) and reveals displacement of maxima/minima of intensity. Taking $\varphi = \pi$ between adjacent guide at entrance facet, shows the same behavior as $\varphi = 0$.

Comparing the plots to which had been obtained in literature for DC-coupling [5] shows significant differences. AC and DC–coupling for vertical ($\varphi = 0$) and oblique incidence ($\varphi = \pi/2$) are plotted in Fig. 4 and Fig. 5 respectively. In DC-coupling the beam broadens and keeps its Gaussian shape at the center in $\varphi = 0$ while it almost is un-broaden with a lateral displacement for $\varphi = \pi/2$ which has known as discrete soliton. $\varphi = 3\pi/2$ has the same shape as $\varphi = \pi/2$ in DC-coupling but with a mirror image respect to the axis of input beam.

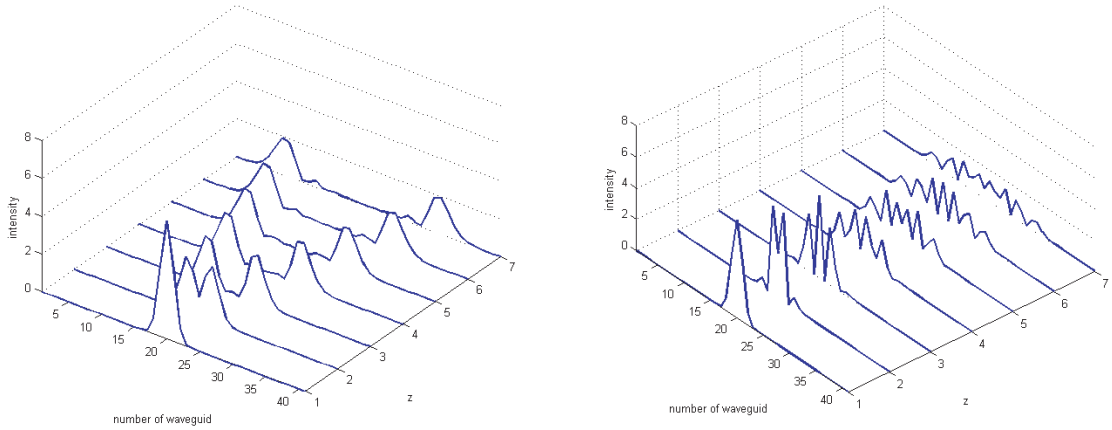

Figure 2: Evolution of a Gaussian beam in an AC coupling waveguides in (a) $\varphi = 0$ and (b) $\varphi = \pi/2$ initial phase difference.

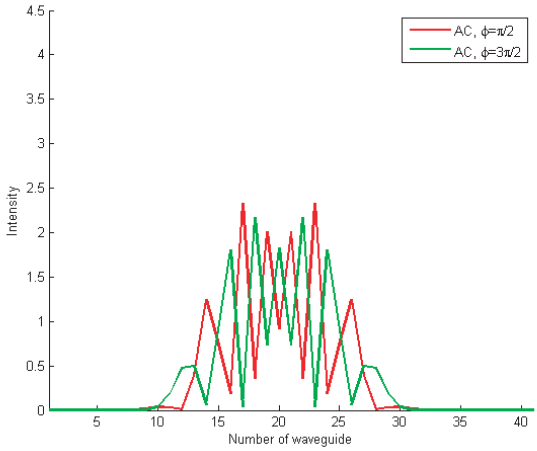

Figure 3: Output beam profile for $\varphi = \pi/2$ (line) and $\varphi = 3\pi/2$ (dot) for AC-coupling.

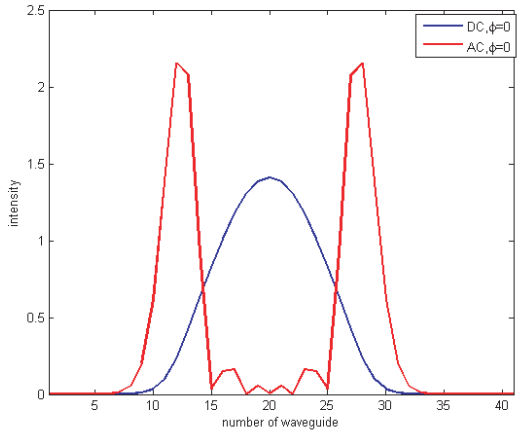

Figure 4: Output beam profile for $\varphi = 0$ in AC-coupling (line) and DC-coupling (dot).

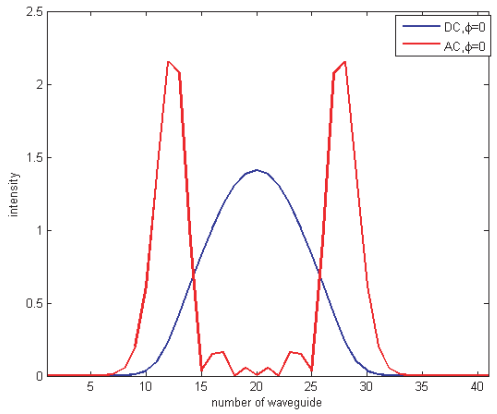

Figure 5: Output beam profile for $\varphi = \pi/2$ in AC-coupling (line) and DC-coupling (dot).

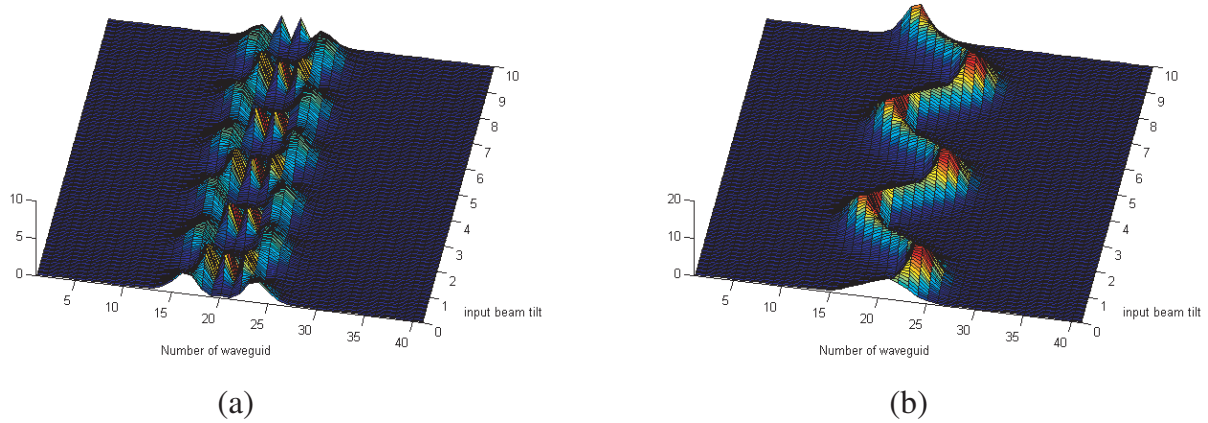

Figure 6: Outgoing energy distribution vs. Input beam tilt angle for (a) AC and (b) DC coupling.

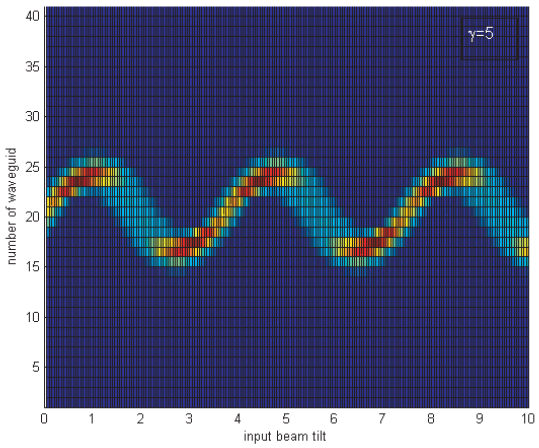

Figure 7: Outgoing energy distribution vs. Input beam tilt angle for DC coupling for $\gamma = 5$.

A periodic change in outgoing intensity distribution is seen by a continuous change in tilt angle (Fig. 6(a)). Energy flows along two transversally symmetric channels when exposure is vertical and this frequently happens in $\varphi = m\pi$ $(m = 0, 1, 2, \ldots)$, while intensity tends to concentrate at

centre in $\varphi = m\pi/2$. Difference is significant in comparison to the analogous plot for DC coupling in Fig. 6(b) [3].

3.2. In the Presence of Nonlinear Kerr Phenomenon ($\gamma \neq 0$):

Any sizable change has not observed in AC-coupling at any beam incidence angle when the Kerr nonlinearity is considered even for sufficiently large value of γ. While the incidence tilt angle for the maximum beam concentration shifts toward $\varphi = m\pi$ in DC-coupling when γ increases (Fig. 7) [3].

4. CONCLUSION

Refraction and propagation of light in a discrete system with periodic refractive index is completely different with homogeneous medium and they strongly depend on the phase difference between adjacent waveguides. In this paper, we investigate a waveguide array model with alternating positive and negative couplings between adjacent waveguides driven by a Gaussian beam in absence and presence of Kerr nonlinearity and we compared to the system with constant coupling for different beam incidence angle to entrance facet.

REFERENCES

1. Lederer, F., G. I. Stegeman, D. N. Christodoulides, G. M. Assanto, and Y. Silberberg, "Discrete solitons in optics," *Phys. Rep.*, Vol. 463, 1–126, 2008.
2. Nikolaos, K. E., Z. Peng, C. Zhigang, N. C. Demetrios, E. R. Christian, and K. Detlef, "Wave propagation in waveguide arrays with alternating positive and negative couplings," *Phy Rev. A*, Vol. 81, 053817, 2010.
3. Aghdami, K. M., A. Gharaati, and F. Mokhtari, "Control of self-focusing and self-defocusing in the waveguides array," *Jap. J. Appl. Phys.*, Vol. 50, 05FG06, 2011.
4. Iwanow, R., D. A. Arrioja, D. N. Christoulides, and G. I. Stegeman, "Discrete talbot effect in waveguide arrays," *Phys. Rev. Lett.*, Vol. 95, 053902, 2005.
5. Lederer, F., et al., "Discrete solitons in optics," *Phys. Rep.*, Vol. 463, 1–126, 2008.

Surface and Non-surface Gap Solitons at the Junction of Two Periodic Lattices with Phase Mismatch

K. Mahmoud Aghdami and S. Alidust
Physics Department, Payame Noor University, Tehran 19395-4697, Iran

Abstract— In this paper, we investigate propagation of gap solitons at between two similar lattices, imprinted defocusing media, that one has a phase difference respect to another at the interference. Surface and non-surface solitons appears in gaps of Floquet-Bloch spectrum because of nonlinearity. We also deal with energy flow and localization of energy at right and left of interface.

1. INTRODUCTION

Interface between different physical media, age of materials like crystals and some others stats that system has a defect can support a special class of localized waves known as surface waves. Nonlinear response of materials makes possible dynamic control of surface localization. This ability has generated great interest in the study of nonlinear surface waves in different fields of physics and most extensively in optics. Such localize surface modes also exist in periodic lattices with defect in their structures The combination of periodicity and nonlinearity allows one to overcome both of these limitations due to the ability of periodic structures to dramatically modify beam diffraction. This leads to a wealth of different types of modes localized at and near the surface [1]. So surface gap modes with nonlinear response are identified as Surface Gap Solitons. Linear photonic band-gap structures, such as photonic crystal fibers (PCFs), with a high-contrast refractive index modulation have attracted broad interest during the past decade [1–5]. On the other hand, a single interface between periodic and uniform media can guide light both in the focusing and defocusing cases [6–12]. Lattice surface solitons are either associated with the semi-infinite photonic gap induced by total internal reflection [6, 7] or with finite photonic gaps induced by Bragg reflections [8–15]. The latter includes surface gap solitons at defocusing lattice interfaces [10, 11], and hybrid mixed-gap states at the interface of different lattices [12]. The surface of a semi-infinite defocusing lattice also supports kink solitons [13]. Formation of optical domain walls is possible in quadratic nonlinear waveguide arrays [16]. In self-defocusing materials the existence of surface gap solitons at the interface between uniform and periodic media was also recently predicted theoretically [8, 16]. In this case, light localization occurs inside the photonic band gap in the form of staggered surface modes [8]. This enables one to extend the analogy with the localized electronic Tamm states into the nonlinear regime, so the surface gap solitons can be termed as nonlinear Tamm states.

In this paper, we consider to light propagation at interface between two similar lattices that one has a lattice phase difference respect to another at the interference. We stress that the localized mode considered in this paper is truncated. This introduces specific features into properties of solitons considered here and is allowed to discuss the concept of surface states. Such periodic systems can fabricated by etching waveguide arrays on top of a substrate [17], or they might be induced optically by an interference pattern in a photorefractive crystal using vectorial interactions [18].

2. THE MODEL

In the case of defocusing media this system is described by the nonlinear Schrodinger equation for dimensionless amplitude of the light field q [19]:

$$i\frac{\partial q}{\partial z} = -\frac{1}{2}\frac{\partial^2 q}{\partial x^2} - q\left|q\right|^2 - pR\left(x\right) \tag{1}$$

Here $R(x)$ is refractive index profile and given by $R_{left}\left(x\right) = \cos^2\left(\Omega x\right)$ at $x \leq 0$, and $R_{right}\left(x\right) = \cos^2\left(\Omega x + \phi\right)$ at $x > 0$, also as mentioned above R respect to induced periodicity of refractive index of a photorefractive crystal with period frequency Ω. ϕ is phase difference between two lattices and p is linear lattice depth. We assume that the depth of refractive index modulation is small compared with the unperturbed refractive index and is of the order of the nonlinear contribution. Notice that

Equation (1) admits several conserved quantities including the energy flow U, the Hamiltonian H:

$$\begin{aligned} U &= \int_{-\infty}^{\infty} |q|^2 \, dx \\ H &= \frac{1}{2} \int_{-\infty}^{\infty} \left(|q_x|^2 - |q|^4 \right) dxdx \end{aligned} \tag{2}$$

3. FLOQUET-BLOCH SPECTRUM

To understand the basic properties of surface gap solitons, it is needful to consider the Floquet-Bloch spectrum of the linear infinite lattice and to found band gap structure. Band gap structures that are formed in Photonic Crystal because of periodicity of medium and according to Bloch theorem led to existence of nonlocalized mode in the case of on-axis propagation. In this case propagation just is along the period direction Also in the case of off-axis propagation, in Photonic Crystals with defect, if wave vector has a non-zeros component at non periodic direction, localized modes exist as defect modes in gaps of band gap [20].

To determine band structure we consider a periodic lattice with $R(x) = \cos^2(\Omega x)$ for $-\infty < x < \infty$, and act like Photonic Crystal with defect in the case of off-axis propagation. So we search solution of the linear version of Equation (1) in the form $q(x,z) = w(x) \exp(ikx + ibz)$, k is Bloch wave vector and b is real propagation constant in z direction. $w(x) = w(x + 2\pi/\Omega)$ is the complex periodic function. Substitution of the light field in such form yields the eigenvalue problem:

$$bw = \frac{1}{2} \left(\frac{d^2 w}{dx^2} + 2ik \frac{dw}{dx} - k^2 w \right) + pRw \tag{3}$$

To solve this equation we use numerically method and find Floquet-Bloch spectrum $b(p,k)$. According to Finite Difference method, we develop Equation (3) to N finite differential equation:

$$bw_j = \frac{1}{2} \left(\frac{w_{j-1} - 2w_j + w_{j+1}}{\Delta x^2} + 2ik \frac{w_{j-1} - w_{j+1}}{\Delta x} - k^2 w_j \right) + pR_j w_j \qquad x = j \cdot \Delta x, \quad j = 1 \ldots N \tag{4}$$

Eigenvalue of this coefficient matrix forms Floquet-Bloch spectrum $b(p,k)$ as shown in Fig. 1.

Inside the transmission bands (gray regions) Equation (1) admits periodic Bloch wave solutions, while in the gaps (white regions) periodic waves do not exist. The Floquet-Bloch spectrum possesses single semi-infinite gap and infinite number of finite gaps. When the nonlinearity of medium take in to account, similar to photonic crystal with defect, localized modes or solitons appear as defect modes inside the gaps.

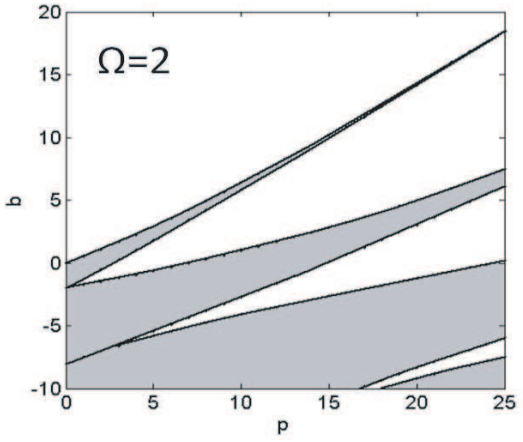

Figure 1: Band-gap structure of periodic lattice $\Omega = 2$. Bands are marked with gray color; gaps are shown in white.

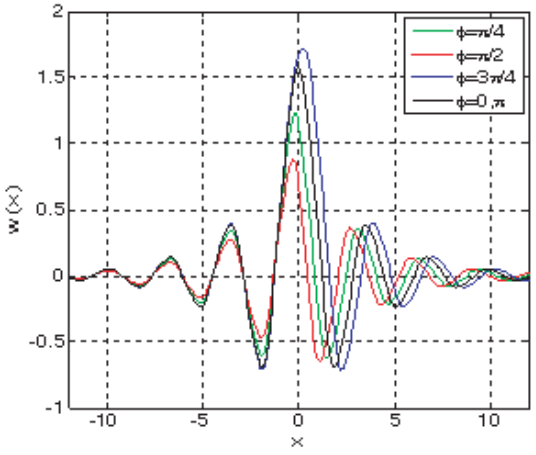

Figure 2: Fundamental modes for $p = 3$, $b = -0.8$, $\Omega = 2$.

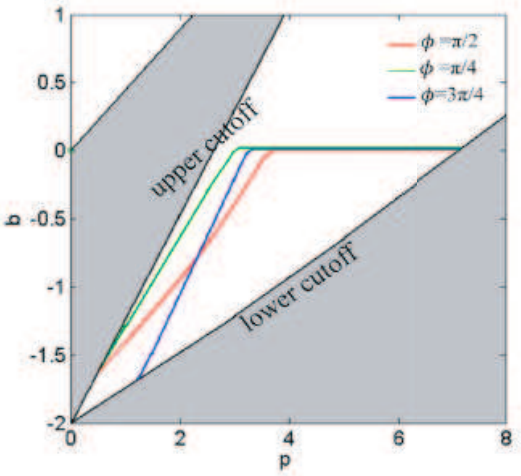

Figure 3: Existence region of solitons for different values of ϕ ($p = 3,\ \Omega = 2$).

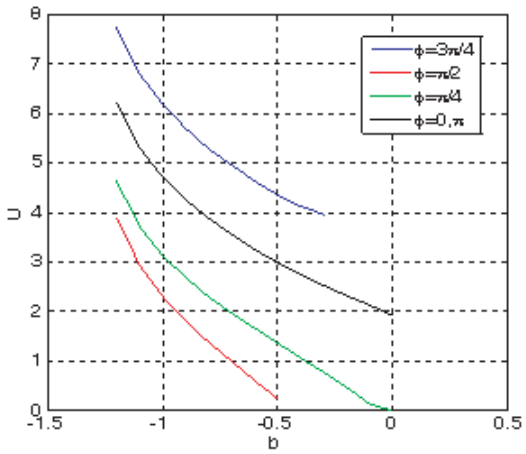

Figure 4: Energy flow vs. propagation constant ($p = 3,\ \Omega = 2$).

4. STATIONARY SOLUTIONS

We search for stationary solutions in the form of $q(x) = w(x)\exp(ibz)$, where $w(x)$ is real function. Substitution of the light field in such form in to Equation (1) yields a nonlinear differential equation:

$$\frac{d^2w}{dx^2} - 2bw - 2w^3 + 2pRw = 0 \tag{5}$$

This equation is solved numerically using Newton-Raphson method. Fundamental soliton modes of different values for ϕ have a sharp pick at the interface and unsymmetrical decaying oscillating wings in the lattices (Fig. 2) For $\phi = 0$ and $\phi = \pi$ the lattice is not truncated and localized non-surface mode exist because of nonlinearity which changes refractive index locally and acts as a defect in lattice. The solution for $\phi \neq 0$ and π is considered as surface soliton which appears in truncated domain. It should be pointed out again that the truncated lattice considered here are different from one complete lattice. In complete lattice we need to defect for localization of modes, but here localization exist, so can also obtained for $\phi = 0, \pi$.

In the case of defocusing nonlinearity the simplest gap solitons can be found in the first finite gap. Fig. 3 shows existence regions of surface soliton inside first finite gap for different values of lattice phase mismatch, ϕ. Localized non-surface mode exist in whole gap with negative values of b for non-truncated lattice ($\phi \neq 0$ and π) while this domain shrinks for truncated one as indicated in Fig. 3 for three different values of ϕ. The localization of nonlinear modes depends on the value of b inside the existence region $b_{low} \leq b \leq b_{upp}$. Modes are well localized at the middle of the existence region, and their wings decay rapidly inside the lattices. When b approaches the lower cutoff, b_{low} the mode wings strongly penetrate into the bulk of the lattice and the energy flow carried by the mode grows (Fig. 4). The lower cutoff coincides with the lower gap edge, and it is independent of the ϕ values while the upper one is depend on ϕ.

Also localization of energy at right and left of interface and distribution of amplitude (or energy) for $\phi \neq 0, \pi$ is different at right and left (Fig. 2). In truncated lattice ($\phi \neq 0$ and π) distribution of amplitude at left is affected by right lattice, so distribution of amplitude in this case is different from distribution of amplitude for $\phi = 0, \pi$.

5. CONCLUSION

We investigate the localized surface and non-surface modes at interference of two identical periodic lattices with phase mismatch. Existence domain inside in gap of Floquet-Bragg spectrum is found and energy flows and field localization are compared for difference values of phase mismatch.

REFERENCES

1. Kivshar, Yu. S., F. Zhang, and S. Takeno, *Physica (Amsterdam)*, Vol. D113, 248, 1998.

2. Hart, S. D., G. R. Maskaly, B. Temelkuran, P. H. Prideaux, J. D. Joannopoulos, and Y. Fink, *Science*, Vol. 296, 510, 2002.
3. Russell, P., *Science*, Vol. 299, 358, 2003.
4. Knight, J. C., *Nature*, Vol. 424, 847, 2003.
5. Knight, J. C. and D. V. Skryabin, *Opt. Express*, Vol. 15, 15365, 2007.
6. Makris, K. G., S. Suntsov, D. N. Christodoulides, G. I. Stegeman, and A. Hache, *Opt. Lett.*, Vol. 30, 2466, 2005.
7. Suntsov, S., et al., *Phys. Rev. Lett.*, Vol. 96, 063901, 2006.
8. Kartashov, Y. V., V. A. Vysloukh, and L. Torner, *Phys. Rev. Lett.*, Vol. 96, 073901, 2006.
9. Molina, M. I., R. A. Vicencio, and Y. S. Kivshar, *Opt. Lett.*, Vol. 31, 1693, 2006.
10. Smirnov, E., M. Stepic, C. E. Rüter, D. Kip, and V. Shandarov, *Opt. Lett.*, Vol. 31, 2338, 2006.
11. Rosberg, C. R., et al., *Phys. Rev. Lett.*, Vol. 97, 083901, 2006.
12. Makris, K. G., J. Hudock, D. N. Christodoulides, G. I. Stegeman, O. Manela, and M. Segev, *Opt. Lett.*, Vol. 31, 2774, 2006.
13. Kartashov, Y. V., V. A. Vysloukh, and L. Torner, *Opt. Express*, Vol. 14, 12365, 2006.
14. Kominis, Y., A. Papadopoulos, and K. Hizanidis, *Opt. Express*, Vol. 15, 10041, 2007.
15. Kominis, Y. and K. Hizanidis, *Opt. Lett.*, Vol. 31, 2888, 2006.
16. Makris, K. G., et al., *Opt. Lett.*, Vol. 30, 2466, 2005.
17. Mandelik, D., et al., *Phys. Rev. Lett.*, Vol. 92, 093904, 2004.
18. Fleischer, J. W., et al., *Phys. Rev. Lett.*, Vol. 90, 023902, 2003; *Nature*, Vol. 422, 147, London, 2003.
19. Ye, F., Y. V. Kartashov, V. A. Vysloukh, and L. Torner, *Opt. Lett.*, Vol. 33, 1288, 2008.
20. Joannopoulos, J. D., *Photonic Crystal, Molding the Flow of Light*, 2nd Edition, Princeton University Press, New Jersey, 2006.

A New Practicable GLLH EM Invisible Cloak without Exceeding Light Speed Wave

Jianhua Li[1, 2], **Ganquan Xie**[1, 2], **Lee Xie**[1], **Feng Xie**[1], **and Hao Zhou**[2]

[1]GL Geophysical Laboratory, USA
[2]Hunan GL, Supercomputational Science Center, China

Abstract— In this paper, we propose a new GLLH EM invisible cloak class without exceeding light speed. The GLLH cloak material in this paper is different from our paper ArXiv 1050.3999. The refractive index of the GLLH cloak material, $n(r)$, is large than one or equal to one. Our GLLH EM cloak is created by GL EM Cloak modeling and inversion with searching in a class of the function of $a_{m,n}\log^n(b_{m,n}/h)h^m$, $h = r-R_1$. The GLLH cloaks in this paper have finite speed and have no exceed light speed physical difficulty. The GLLH EM Cloaks can be practicable by using conventional optical materials Radial GLLH EM invisible cloak modeling, inversion and electromagnetic integral equation for cloak are proposed in our recent ArXiv paper. The properties of our GLLH EM cloak are presented in this paper. The novel EM wave propagation and front branching in the GLLH Cloak by GL EM modeling are presented in this paper. The EM wave front propagation in GLLH Cloak is behind of the front in free space. At time steps 118 dt, in the GLLH Cloak, the wave front is curved as a crescent like and propagates slower than the light in free space. At the time step 119 dt, the EM wave inside of the GL EM cloak propagates slower than light speed, moreover, its two crescent front peaks intersect at a front branching point. At the front branching point, the front is split to two fronts. The novel front branching and crescent like wave propagation are displayed in figures in this paper. All copyright and patent of the GLLH EM Cloaks and GL modeling and inversion methods are reserved by authors in GL Geophysical Laboratory.

1. INTRODUCTION

In May 21, 2010, we published paper ArXiv 1050.3999v1, In the paper, we proposed a GLLH electromagnetic (EM) invisible cloak with novel front branching and without exceed light speed violation [1]. In July 2, 2011, we published paper ArXiv submitted0276008 [6], we proposed a new GL invisible cloak without exceeding light speed wave. In this paper, we propose a new GLLH invisible cloak without exceeding light speed. The new GLLH Cloak material in this paper and GL EM cloak in ArXiv submitted0276008 are different from the ArXiv 1050.3999. The refractive index of the new GLLH Cloak material in this paper, $n(r)$, is large than one or equal to one. Moreover, in our paper in ArXiv submitted0276008 [6] The radial dielectric and permeability of GL EM cloak are large than one. Our GLLH EM Cloak is created from our observation in 2001 in [2] and by GL EM Cloak modeling [3, 8, 11, 16–18] and inversion [5] with searching in a class of function of $a_{m,n}\log^n(b_{m,n}/h)h^m$, $h = r - R_1$. The GLLH Cloaks in this paper have finite speed and overcome exceeding light speed physical difficulty. Pendry cloak [4] has strong exceeding light speed difficulty. The GLLH EM Cloaks can be practicable by using conventional optical materials. Radial GL EM invisible cloak modeling, inversion and electromagnetic integral equation for cloak are proposed in our paper [6]. The properties of our GLLH EM Cloak and are presented in this paper. They are proved by GL modeling simulation. The novel EM wave propagation and front branching in the GLLH Cloak by GL EM modeling are presented in this paper. The EM wave front propagation in cloak is behind of the front in free space. At time steps 118 dt, in the GLLH Cloak, the wave front is curved as a crescent like and propagates slower than the light in free space. At the time step 1119 dt, the EM wave inside of the GL EM cloak propagates slower than light speed, moreover, its two crescent front peaks intersect at a front branching point. At the front branching point, the front is split to two fronts. The novel front branching and crescent like wave propagation are displayed in figures in this paper. By comparison, the electric wave E_z propagation through GLLH Cloak in Figure 13 and through Ps cloak [4] in Figure 14 at 84 step time. It is obvious that the GLLH EM Cloak has no exceeding light speed difficulty, the Ps cloak [4] has the infinite speed difficulty. Compare the electric wave propagation through Ps cloak [4] in Figure 16 and through GLLH EM Cloak in Figure 15 at 94 step time. It is obvious that the GLLH EM Cloak has no exceeding light speed difficulty, the Ps cloak [4] has the strong exceeding light speed difficulty.

A paper with same research goal and object of our paper is published in same net journal ArXiv. In May 1, 2011 and in June 20, 2011, Professor Ulf Leonhardt et al. published their paper

ArXir 1105.0164v3 titled "invisibility Cloaking without superluminal propagation" [7]. In [7]. Ulf Leonhardt referred almost all recent cloak publish papers, include Pendry cloak and Ulf cloak, and wrote that "However, the realisation of electromagnetic cloaking suffers from a practical and a fundamental problem."

Professor Ulf Leonhardt did cite our paper "ArXiv 1050.3999v1" as his reference [35], and wrote that "the preprint [35] proposes a different method for cloaking without superluminal propagation."

We had observed double layer cloak phenomena in 2001 [2]. There exist two approaches to study new cloak physics, one is the conventional theoretical and experimental physical methods, other is theoretical and computational physical methods. conventional physicist only use computation as physical simulation to follow and verify physical phenomena. Real computational physicist research and develop new computational physics modeling and inversion and use them as new tools and experiments to find, discover and study new physical phenomena. No scattering inversion is complete different from (or little) scattering inversion. No scattering idea cloak is totally different from the approximate cloak. Because complete cloak does not disturb the exterior EM field. In contrast, almost physical measurement instruments to measure exterior scattering are the electromagnetic devices. The experiment for complete cloaking should be very expensive and very difficult. The computational physical modeling and inversion are very important. Therefore, we developed GL no scattering EM modeling [3, 8, 16, 17] and inversion [5] to discover the GLLH Cloak without exceeding light speed. The GL method is totally different from Finite Element method (FEM) [10, 28] and finite difference method (FD), also is different from Born approximation [14]. In the GL method [3] and GILD method [9], the artificial boundary and absorption condition are no necessary and removed. The GL method does not need to solve big matrix equation and is a full parallel algorithm. FEM and FD method have difficulties to solve high frequency wave equation. However, FEM's numerical error estimation form [21, 22, 25] and number theory estimation form [22–24] can be used as research class [1] in GLLH EM Cloaking inversion [5]. In computational physics, the numerical observation is important, the double layer cloak had been numerically observed in 2001 [2], 3D FEM superconvergence had been numerically observed in 1973 [10, 21, 22].

Our GLLH Cloak class [1], GL Invisivle Cloak [6] and GL method [3, 5, 16, 17, 68] to study cloak that are different from Ulf cloak [7, 19] and other Pendry cloak [4]. Most cloak are created based on coordinate transforms. Paper [26, 27] presented the analysis for Pendry cloak [4]. In this paper, we propose a new GLLH EM invisible cloak without exceeding light speed which is created based on the GL EM computational physical modeling and inversion. New radial EM integral equation and GL EM method for radial EM wave are proposed in our recent paper in ArXiv.

The description order of this paper is as follows: A new GLLH EM invisible cloak materials without exceeding light speed are proposed in Section 2. GLLH Cloak properties are presented in Section 3. In Section 4, by using GL EM modeling, we simulate full electromagnetic wave propagation through GLLH Cloak and has no exceeding light speed propagation. The conclusion is presented in Section 5.

2. A NEW GL EM INVISIBLE CLOAK CLASS

2.1. The Maxwell Equation

The Maxwell equation with anisotropic parameters is presented here as follows:

$$\begin{aligned} \nabla \times E &= -\bar{\mu}\frac{\partial H}{\partial t}, \\ \nabla \cdot B &= 0, \\ \nabla \times H &= \bar{\sigma}E + \bar{\varepsilon}\frac{\partial E}{\partial t} + J, \\ \nabla \cdot D &= \rho, \end{aligned} \tag{1}$$

$$\begin{aligned} B &= \bar{\mu}H, \\ D &= \bar{\varepsilon}E, \end{aligned} \tag{2}$$

where E is the electric field, H is the magnetic field, B is the magnetic flux field, D is the electric displacement field, $\bar{\varepsilon}$ is the anisotropic dielectric diagonal matrix tensor, $\bar{\mu}$ is the magnetic permeability diagonal matrix tensor, in the free space, $\bar{\varepsilon} = I\varepsilon_0$ and $\bar{\mu} = I\mu_0$, ε_0 is the basic dielectric parameter, μ_0 is basic permeability, $\bar{\sigma}$ is the anisotropic electric conductivity diagonal matrix, in free space, $\bar{\sigma} = 0$, we consider $\bar{\sigma} = 0$ in this paper.

2.2. GLLH EM Cloak without Exceeding Light Speed Wave

In this paper, we propose a new class of GLLH Cloak without exceeding light speed which is used as outer layer in our GL double layer cloak [8]. The inner cloak of our GL double layer cloak does no exceed light speed in [8, 16–18]. In paper [13, 17], we proved that there exist no Maxwell EM field can be excited by the source inside of the concealment, if the concealment is free space and cloaked by a single layer cloak. Therefore the double layer cloak is necessary for a normal EM environmental concealment. For overcoming the exceeding light speed difficulty, in this section, we propose a GLLH invisible cloak for outer layer of our double layer cloak [8]. In the concentric spherical annular $R_1 \le r \le R_2$ cloaking device, we propose an GLLH Cloaking material which consist of the anisotropic dielectric diagonal matrix tensor $\bar{\varepsilon}$ and permeability $\bar{\mu}$ diagonal matrix tensor as follows:

$$\bar{\varepsilon} = \operatorname{diag}(\varepsilon_r, \varepsilon_\theta, \varepsilon_\phi)\,\varepsilon_0 \tag{3}$$

$$\bar{\mu} = \operatorname{diag}(\mu_r, \mu_\theta, \mu_\phi)\,\mu_0 \tag{4}$$

where ε_0 is the basic dielectric parameter in free space, ε_r is the relative dielectric in r direction, ε_θ is the relative dielectric in θ direction, ε_ϕ is the relative dielectric in ϕ direction, similar explanation descriptions are for basic permeability μ_0 and for relative permeability parameters $\mu_r, \mu_\theta, \mu_\phi$. From the GL EM modeling [3] and inversion [5], we obtain a new class form of the GLLH EM invisible cloak without exceeding light speed.

2.3. New GLLH EM Cloak

In this section, we propose a new GLLH EM invisibility cloak as follows.

$$\begin{aligned}\varepsilon_r &= \mu_r \\ &= \frac{1}{1+4R_2+2R_2^2}\left(\frac{2R_2^2(R_2-R_1)}{R_1R_2}+\frac{2+6R_2}{\log\left(e^{\frac{1}{R_2}}\frac{r(R_2-R_1)}{R_2(r-R_1)}\right)}\frac{r-R_1}{rR_1R_2}-\frac{1+2R_2}{\log^2\left(e^{\frac{1}{R_2}}\frac{r(R_2-R_1)}{R_2(r-R_1)}\right)}\frac{r-R_1}{rR_1R_2^2}\right)\end{aligned} \tag{5}$$

and

$$\varepsilon_\theta = \frac{1}{2}\frac{R_1\sqrt{R_2}}{r(r-R_1)}\frac{1}{\log^{\frac{3}{2}}\left(\frac{r(R_2-R_1)}{R_2(r-R_1)}e^{\frac{1}{R_2}}\right)}+\frac{1}{2}\frac{R_1}{\sqrt{R_2}r(r-R_1)}\frac{1}{\log^{\frac{5}{2}}\left(\frac{r(R_2-R_1)}{R_2(r-R_1)}e^{\frac{1}{R_2}}\right)}, \tag{6}$$

3. PROPERTIES OF GL INVISIBLE CLOAK

In previous section, we proposed the new GLLH Cloak (5) and (6) of the EM invisible cloak without exceeding light speed wave. The GLLH Cloak properties are presented in this section,

Property1 : Assume that the GL EM relative cloak material $\varepsilon_r(r)$ and $\mu_r(r)$ are defined by (5) in the cloak, $\varepsilon_r(r) = 1$ and $\mu_r(r) = 1$ in the free space and concealment, and additional condition,

$$R_1(1 + R_2) = R_2, \tag{7}$$

then the relative radial dielectric parameter $\varepsilon_r(r)$ and magnetic permeability $\mu_r(r)$ are continuous in domain $r > R_1$, in particular, cross $r = R_2$, we have

$$\varepsilon_r(R_2) = \mu_r(R_2) = 1. \tag{8}$$

Property2 : Assume that the EM relative transverse dielectric $\varepsilon_\theta(r)$, $\varepsilon_\phi(r)$ and permeability $\mu_\theta(r)$, $\mu_\phi(r)$ materials are defined by (6) in the GLLH Cloak, $\varepsilon_\theta(r) = \varepsilon_\phi(r) = 1$ and $\mu_\theta(r) = \mu_\phi(r) = 1$ in the free space and concealment, and if assumption (7) is satisfied, then

$$\varepsilon_\theta(R_2) = \mu_\theta(R_2) = \varepsilon_\phi(R_2) = \mu_\phi(R_2) = 1, \tag{9}$$

the relative transverse dielectric parameter $\varepsilon_\theta(r), \varepsilon_\phi(r)$ and magnetic permeability $\mu_\theta(r), \mu_\phi(r)$ are continuous in domain $r > R_1$, in particular, cross outer boundary $r = R_2$.

Property3 : Assume that the GL EM relative radial dielectric material $\varepsilon_r(r)$ and permeability $\mu_r(r)$ are defined by (5) in the cloak, the relative transverse dielectric parameter $\varepsilon_\theta(r)$, $\varepsilon_\phi(r)$ and magnetic permeability $\mu_\theta(r)$, $\mu_\phi(r)$ are defined by (6) in the cloak, if there is the additional assumption (7), there exist EM wave $E(r, \theta, \phi)$ and $H(r, \theta, \phi)$ satisfy the Maxwell Equation (1), moreover, the grading $\nabla E(r, \theta, \phi)$ and $\nabla H(r, \theta, \phi)$ are continuous in the domain $r > R_1$, in particular, the

exterior EM wave $E(r,\theta,\phi)$, $H(r,\theta,\phi)$ and their grading $\nabla E(r,\theta,\phi)$ and $\nabla H(r,\theta,\phi)$ are continuous when the they propagate from outside of cloak into the inside of the cloak cross the outer boundary $r = R_2$. Therefore, there is no scattering wave from the cloak to disturb the exterior EM wave.

Property4 : Assume that the GL EM relative radial dielectric material$\varepsilon_r(r)$ and permeability $\mu_r(r)$ are defined by (5) in the cloak, the relative transverse dielectric parameter $\varepsilon_\theta(r)$, $\varepsilon_\phi(r)$ and magnetic permeability $\mu_\theta(r)$, $\mu_\phi(r)$ are defined by (6) in the cloak, if there is the additional assumption (7), then the EM wave propagation $E(r,\theta,\phi)$ and $H(r,\theta,\phi)$ can not penetrate into the concealment.

Property5 : Assume that the GL EM relative radial dielectric material $\varepsilon_r(r)$ and permeability $\mu_r(r)$ are defined by (5) in the cloak, the relative transverse dielectric parameter $\varepsilon_\theta(r)$, $\varepsilon_\phi(r)$ and magnetic permeability $\mu_\theta(r)$, $\mu_\phi(r)$ are defined by (6) in the cloak, if there is the additional assumption (7), we have the refractive index

$$N(r) = \sqrt{\varepsilon_r(r)\mu_\theta(r)} = \sqrt{\varepsilon_\theta(r)\mu_r(r)} \geq 1, \tag{10}$$

in the all cloak domain

$$R_1 \leq r \leq R_2. \tag{11}$$

Property6 : Assume that the GL EM relative cloak material $\varepsilon_r(r)$ and $\mu_r(r)$ are defined by (5) in the cloak, the EM relative transverse dielectric $\varepsilon_\theta(r)$, $\varepsilon_\phi(r)$ and permeability $\mu_\theta(r)$, $\mu_\phi(r)$ materials are defined by (6) in the GLLH Cloak, if there is the additional assumption (7) is satisfied. When the source and receiver are located outside of cloak, then

$$\begin{aligned}
&\omega^2 \int_{R_1}^{R_2} r'^4(\mu_r\varepsilon_{\theta,b}\mu_{r,b} - \mu_{r,b}\varepsilon_\theta\mu_r)G_{l,b}h_l dr' - l(l+1)\int_{R_1}^{R_2} r'^2(\mu_r - \mu_{r,b})G_{l,b}h_l dr' \\
&- \int_{R_1}^{R_2}\left(\frac{1}{\mu_{\theta,b}} - \frac{1}{\mu_\theta}\right)\frac{\partial}{\partial r'}\left(r'^2\mu_r h_l\right)\frac{\partial}{\partial r'}\left(r'^2\mu_{r,b}G_{l,b}\right)dr' = 0,
\end{aligned} \tag{12}$$

i.e., there is no scattering wave from the GLLH EM Cloak to disturb the incident EM wave in the free space

$$h_l(r) = h_{l,b} \tag{13}$$

when the source is located outside of cloak, and the receiver is located inside of the concealment then

$$\begin{aligned}
&r^2\mu_{r,b}h_{l,b} + \omega^2 \int_{R_1}^{R_2} r'^4(\mu_r\varepsilon_{\theta,b}\mu_{r,b} - \mu_{r,b}\varepsilon_\theta\mu_r)G_{l,b}h_l dr' - l(l+1)\int_{R_1}^{R_2} r'^2(\mu_r - \mu_{r,b})G_{l,b}h_l dr' \\
&- \int_{R_1}^{R_2}\left(\frac{1}{\mu_{\theta,b}} - \frac{1}{\mu_\theta}\right)\frac{\partial}{\partial r'}\left(r'^2\mu_r h_l\right)\frac{\partial}{\partial r'}\left(r'^2\mu_{r,b}G_{l,b}\right)dr' = 0,
\end{aligned} \tag{14}$$

i.e., the exterior EM wave can not propagate penetrate into the concealment, the concealment is invisible room, inside of the concealment,

$$h_l = 0. \tag{15}$$

Therefore GLLH EM Cloak is complete cloak,

The refractive index $N > 1$ in the whole GLLH EM Cloak. Therefore GLLH EM Cloak is practicable complete cloak without exceeding light speed wave through it.

4. FULL ELECTROMAGNETIC WAVE PROPAGATION THROUGH GLLH CLOAK AND HAS NO EXCEEDING LIGHT SPEED PROPAGATION

In this section, using the GL EM modeling method, we simulate full electromagnetic wave propagation through GLLH Cloak by (5)–(6) and has no exceeding light speed propagation.

Let $E_{z,b}$ denote the background electric intensity plane wave at source plane $x = x_s$, $x = -0.83$, in the left side outside of the cloak in free space.

$$E_{z,b}(x, x_s, t) = \delta(x - x_s)\delta(t). \tag{16}$$

The electric plane wave is denoted by vertical red line through red S in the figures in this paper. In Figure 1, at time step 38 dt, Figure 2, at time step 48 dt, Figure 3, at time step 58 dt, Figure 4, at time step 68 dt, Figure 5, at time step 78 dt, Figure 6, at time step 88 dt, the electric wave E_z inside of the GLLH EM Cloak $R_1 \leq r \leq R_2$, $R_1 = 0.2491$ m, $R_2 = 0.47$ m, propagates slower than light speed. In Figure 7, at time step 98 dt, Figure 8, at time step 108 dt, Figure 8, at time step 118 dt, electric wave E_z inside of the GLLH EM Cloak $R_1 \leq r \leq R_2$ propagates slower than light speed. The E_z wave front successively form novel CRESCENT curve front.

In Figure 9, at time step 120 dt, electric wave E_z inside of the GLLH EM Cloak $R_1 \leq r \leq R_2$ propagates slower than light speed. The upside and downside parts of curved CRESCENT electric wave front are intersected at a branching point. These branching points form a 2D subsurface which depends on the source location. The vertical red dashing line cross red S denotes the incident electric plane wave $E_{z,b}$ which is located in the left of the cloak. The front branching point is located in

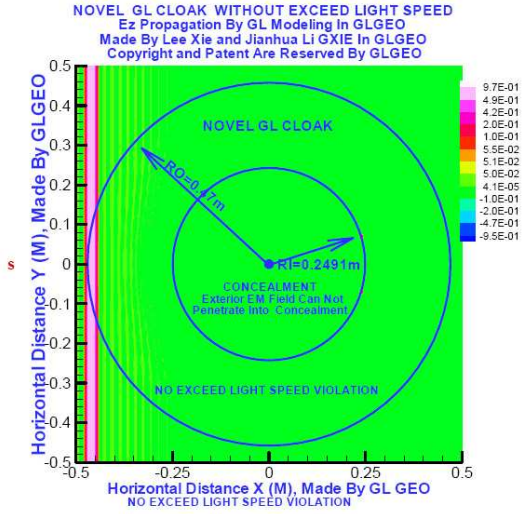

Figure 1: (color online) Electric wave E_z propagation at time step 38 dt.

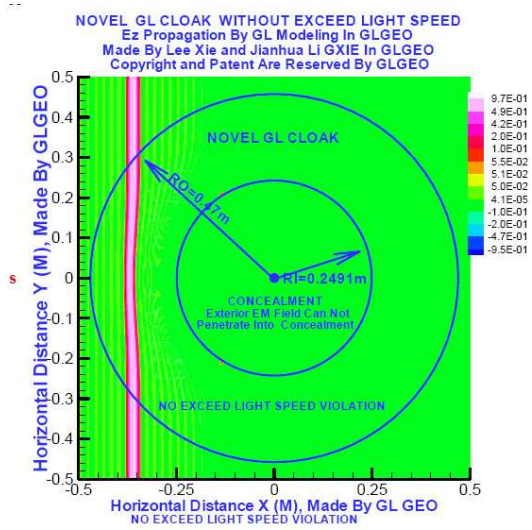

Figure 2: (color online) Electric wave E_z propagation at time step 48 dt.

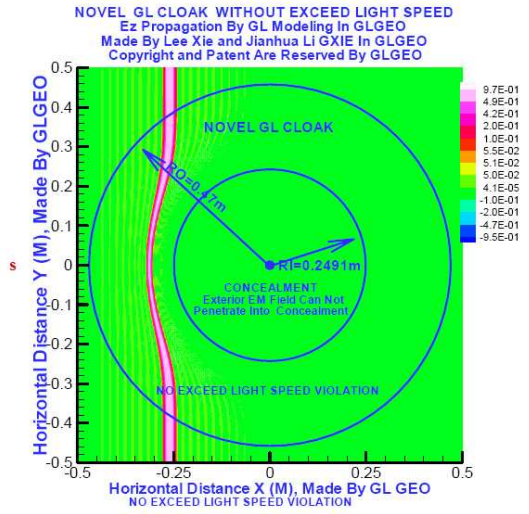

Figure 3: (color online) Electric wave E_z propagation at time step 58 dt.

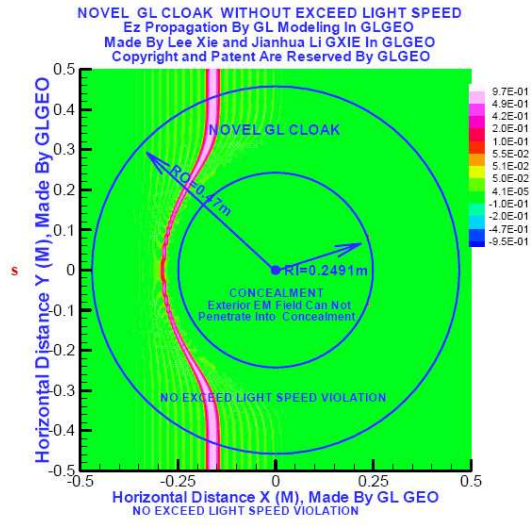

Figure 4: (color online) Electric wave E_z propagation at time step 68 dt.

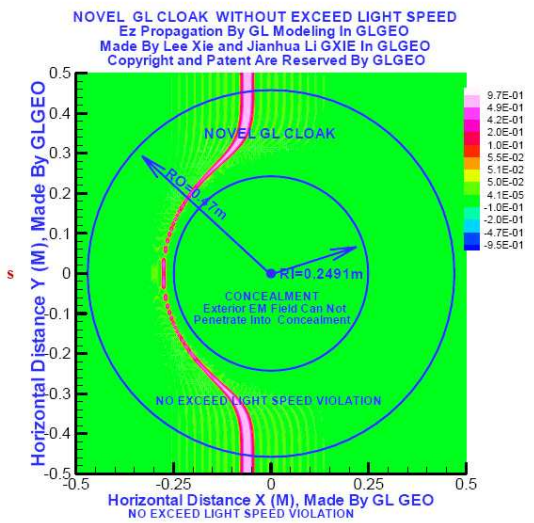

Figure 5: (color online) Electric wave E_z propagation at time step 78 dt.

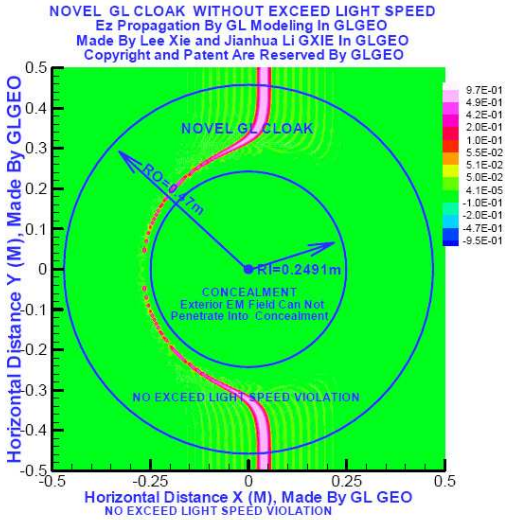

Figure 6: (color online) Electric wave E_z propagation at time step 88 dt.

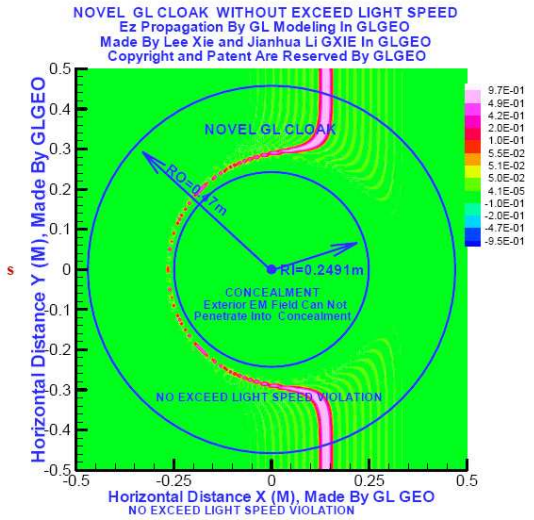

Figure 7: (color online) Electric wave E_z propagation at time step 88 dt.

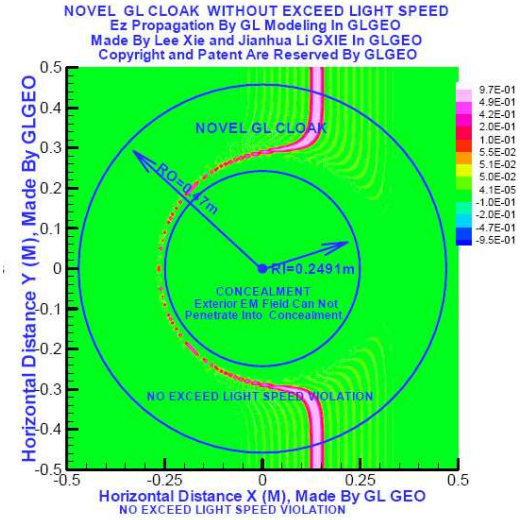

Figure 8: (color online) Electric wave E_z propagation at time step 108 dt.

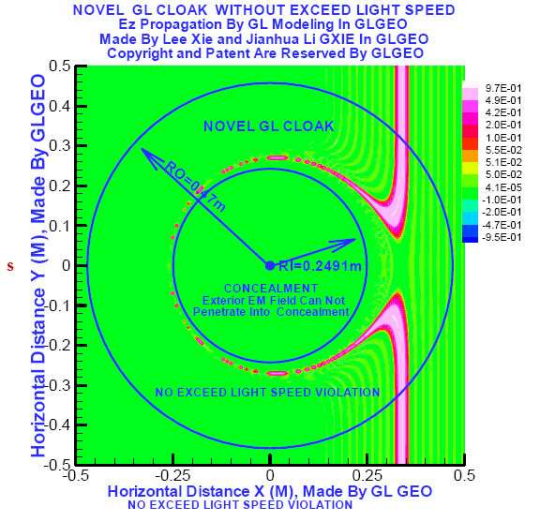

Figure 9: (color online) Electric wave E_z propagation at time step 118 dt.

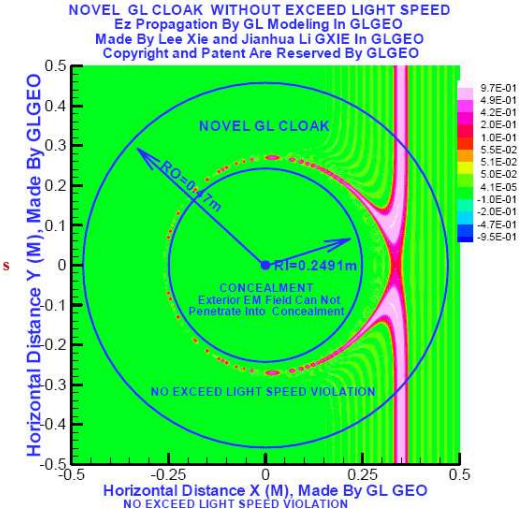

Figure 10: (color online) Electric wave E_z propagation at time step 119 dt.

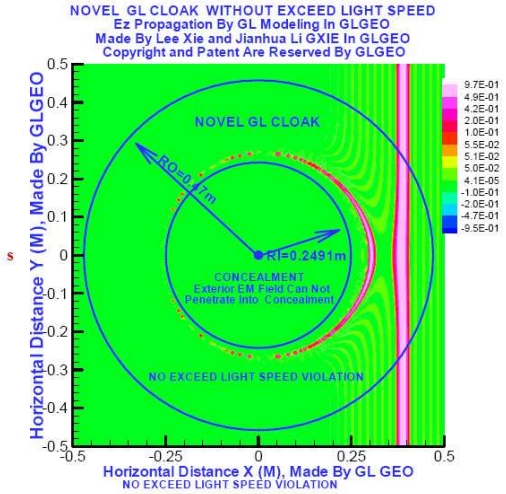

Figure 11: (color online) Electric wave E_z propagation at time step 123 dt.

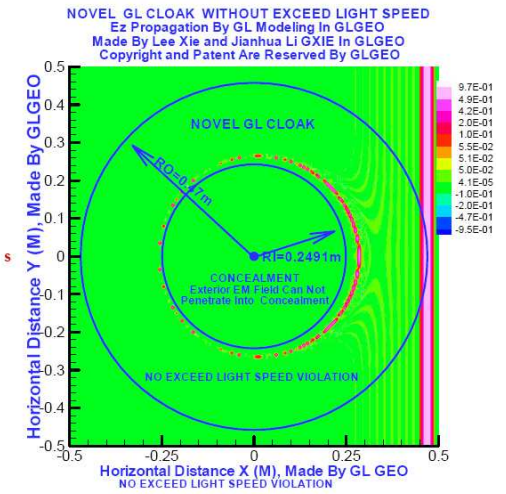

Figure 12: (color online) Electric wave E_z propagation at time step 131 dt.

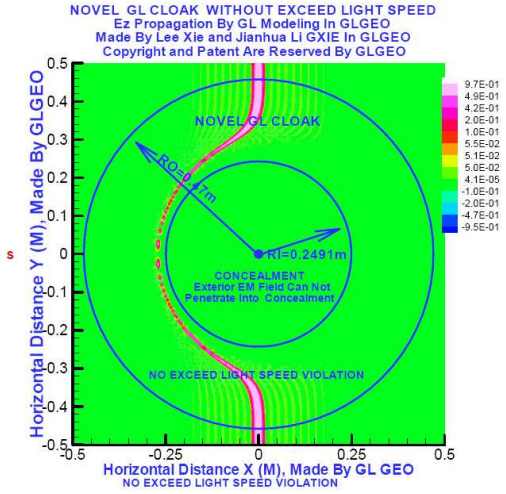

Figure 13: (color online) At time step 84 dt, electric wave E_z propagation through GL cloak without exceeding light speed.

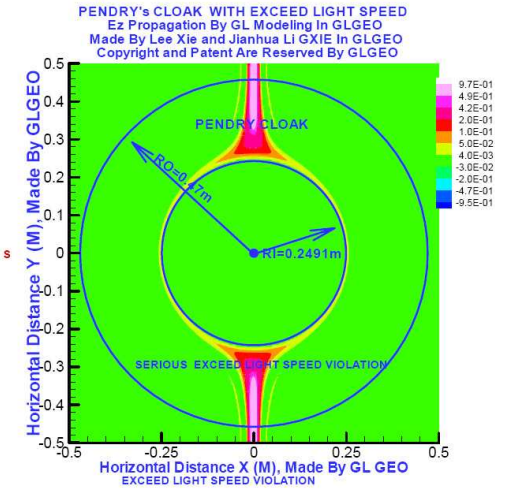

Figure 14: (color online) At time step 84 dt, electric wave E_z propagation through Ps cloak with infinite speed.

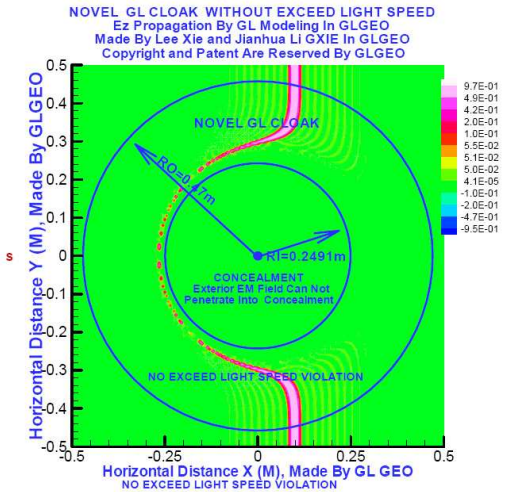

Figure 15: (color online) At time step 94 dt, electric wave E_z propagation through GL cloak without exceeding light speed wave.

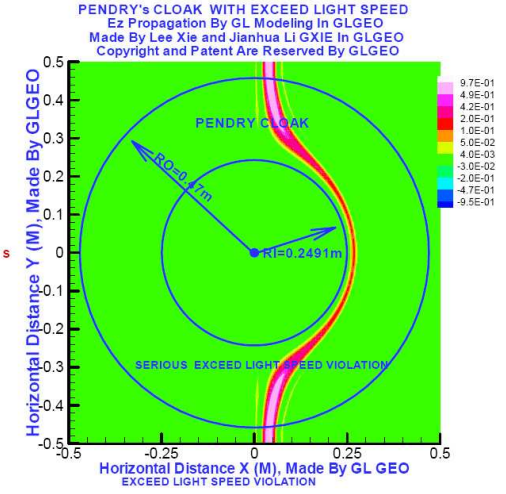

Figure 16: (color online) At time step 94 dt, electric wave E_z propagation through Ps cloak with strong exceeding light speed.

right of the concealment. The Figure 10 shows that at time step 123 dt, E_z electric wave front is split to two wave fronts, The outgoing front propagates forward to left and going to outer boundary $r = R_2$. The attractive front propagates and shrinks to the inner boundary. The two wave front propagate slower than light speed. The Figure 11 shows that at time step 128 dt, outgoing front propagates continuously forward to outer boundary $r = R_2$. The attractive front rapidly decay propagates to the inner boundary. The two wave front propagate slower than light speed. In Figure 12, at time step 131 dt, the outgoing front of the electric wave E_z propagates on the outer boundary $r = R_2$, the attracting front rapid decay to zero and closes to the inner boundary of the cloak, $r = R_1$.

5. CONCLUSION

By the GLLH invisible cloak class properties in Section 3 and full EM propagation through the GLLH EM cloak, our GLLH EM invisible cloak without exceeding light speed that is verified. Compare the electric wave E_z propagation through GLLH cloak in Figure 13 and through Ps cloak in Figure 14 at 84 step time. It is obvious that the GLLH EM cloak has no exceeding light speed difficulty, the Ps cloak has the infinite speed difficulty. Compare the electric wave propagation through Ps cloak in Figure 16 and through GLLH EM cloak in Figure 15 at 94 step time. It is obvious that the GL EM cloak has no exceeding light speed difficulty, the Ps cloak has the exceeding light speed difficulty.

ACKNOWLEDGMENT

We wish to acknowledge the support of the GL Geophysical Laboratory and thank the GLGEO Laboratory to approve the paper publication. Authors thank to Professor P. D. Lax for his concern and encouragements Authors thank to Professor Michael Oristaglio, Professor Lin Qun, Senior Engeering Zhaogui Cai, Professor Yuesheng Li for his encouragments.

REFERENCES

1. Xie, G., J. Li, L. Xie, and F. Xie, arXiv:1005.3999.
2. Li, J., G. Xie, C. Lin, and J. Liu, "2.5 dimensional GILD electromagnetic modeling and application," *SEG, Expanded Abstracts*, Vol. 21, No. 1, 692–695, 2002, http://www.segdl.org/journals/doc/SEGLIBhome/dci/searchDCI.jsp.
3. Xie, G., F. Xie, L. Xie, and J. Li, "New GL method and its advantages for resolving historical diffculties," *Progress In Electromagnetics Research*, Vol. 63, 141–152, 2006.
4. Pendry, J. B., D. Schurig, and D. R. Smith, "Controlling electromagnetic field," *Science Express*, Vol. 312, 1780, 2006.
5. Xie, G., J. Li, L. Xie, and F. Xie, "GL metro carlo EM inversion," *Journal of Electromagnetic Waves and Applications*, Vol. 20, No. 14, 1991–2000, 2006.
6. Xie, G., J. H. Li, L. Xie, and F. Xie, "New GL invisible cloak without exceeding light speed wave," *Physics Optics*, arXiv:1107.0858v1, Jul. 5, 2009.
7. Perczel, J., T. Tyc, and U. Leonhardt, arXiv:1105.0164.
8. Xie, G., J. H. Li, F. Xie, and L. Xie, "A double layer electromagnetic cloak and GL EM modeling," *Physics Optics*, arXiv:0907.0858v1, Jul. 5, 2009.
9. Xie, G., J. H. Li, E. Majer, D. Zuo, and M. Oristaglio, "3-D electromagnetic modeling and nonlinear inversion," *Geophysics*, Vol. 65, No. 3, 804–822, 2000.
10. Xie, G., "Three dimensional finite element method for solving the Elastic problem," *Mathematical Practice and Knowledge*, Vol. 1, No. 1, 28–41, 1975.
11. Xie, F. and L. Xie, "New computational mirage," *Progress In Electromagnetics Research Symposium*, 296, Hangzhou, Aug. 22–26, 2005.
12. Xie, G., J. H. Li, F. Xie, and L. Xie, "An electromagnetic GL double layered cloak," *Physics Optics*, arXiv:0904.3168v1, Apr. 21, 2009.
13. Xie, G., J. H. Li, L. Xie, and F. Xie, "No Maxwell electromagnetic wavefield excited inside cloaked concealment," *Physics Optics*, arXiv:0904.3040v1, Apr. 20, 2009.
14. Hohmann, G. W., "Three dimensional induced polarization and electromagnetic modeling," *Geophysics*, Vol. 40, 309–324, 1975.
15. Xie, G., J. H. Li, L. Xie, and F. Xie, "A GL double layer cloak in broad frequency band and reciprocal law," *Physics Optics*, arXiv:1002.4249v1, Feb. 23, 2010.

16. Xie, G., J. Li, F. Xie, and L. Xie, "Global and local field EM modeling and novel GL double layered electromagnetic cloaks," *PIERS Proceedings*, 335–343, Moscow, Russia, Aug. 18–22, 2009.
17. Li, J., G. Xie, L. Xie, and F. Xie, "No Maxwell electromagnetic wavefield excited inside cloaked concealment and broadband GL cloaks," *PIERS Proceedings*, 66–72, Moscow, Russia, Aug. 18–22, 2009.
18. Xie, G., J. Li, F. Xie, and L. Xie, "A novel GL double layer electromagnetic cloaks in broad frequency band and reciprocal law," *PIERS Proceedings*, 623–630, Xi'an, China, Mar. 22–26, 2010.
19. Leonhardt, U. and T. Tyc., "Broadband invisibility by non-euclidean cloaking," *Science*, Vol. 323, 110, 2009.
20. Brandts, J. and M. Krizek, "History and futures of superconvergence in three dimensional finite element method," *Mathematical Sciences and Applications*, Vol. 15, 24–35, 2001.
21. Krizek, M., "Superconvergence phenomena on three dimenional meshes," *International Journal of Numerical Analysis and Modeling*, Vol. 2, No. 1, 43, 56, 2005.
22. Tao, T. and B. Green, "The primes contain arbitrarily long arithmetic progressions," ArXiv [Math0404188v6], Vol. 23, Sept. 2007.
23. Chen, J. R., "On the representation of a large even integer as the sum of a prime and a product of at most two primes," *Sci. Sinica*, Vol. 16, 157–176, 1973.
24. Wang, Y., "On the representation of large even integer as a sum of a product of at most 3 primes and a product of at most 4 primes," *Acts Mathernatica Sinica*, Vol. 6, No. 3, 500–513, 1956.
25. Lin, Q. and N. N. Yan, *The Construction and Analysis of High Effective Finite Element Methods*, Hebei University Press Ltd., 1996.
26. Chen, H., B. Wu, B. Zhang, and A. Kong, *PRL*, Vol. 99, 063903, 2007.
27. Zhang, B., H. Chen, B. I. Wu, and J. Kong, *PRL*, Vol. 100, 063904, 2008.
28. Feng, K., "Difference scheme based on the variational principle," *Applied Mathematical and Computational Mathematics*, Vol. 4, No. 1, 238–262, 1996.

The Momentum of Photon May Explain the Measurement's Paradox in the Subatomic World

Antonio Puccini
Department of Neurophysiology, Order of Malta, Naples, Italy

Abstract— As we know particles of the subatomic world, that is quantum objects (QOs), do not have defined properties until we observe them making a Measurement (M). Before the M the QO is *delocalized*, it is potentially detectable in one of the points of its *wave volume*. We can just presume approximately their structure and behaviour, but we have not certitude. According to Quantum Mechanics before the M it is not possible to tell if it is a particle or a wave.

In order to make a M of a QO, we need to illuminate it, however, as we learn from Quantum Mechanics, we change, against our will, the subatomic system we are trying to measure. As Feynman reminds us, to observe electrons, we need a light because the light rebounding on electrons make them visible, but the light affects electron behaviour. When light is sent on an electron, it makes the electron vibrate thus behaving in a different manner. Therefore, the photons (Ps) are indispensable to carry out a M.

As we know also the P has a its own *momentum (p)*, according to the formula: $p = h/\lambda$, where h is Planck's constant and λ is the wavelength of the considered P. In the case of a medium visible P its p is: $p = 6.625 \cdot 10^{-27}\,[\mathrm{erg \cdot s}]/5 \cdot 10^{-5}\,[\mathrm{cm}]$, that is:

$$p = 1.325 \cdot 10^{-22}\,[\mathrm{g \cdot cm/s}]$$

Our calculations show that a P of the optic band hits an electron with a *momentum*, a *dynamic-mass*, bigger than the mass of the electron itself. This may explain why the M induces the well-known changes on the observed QO and may contribute to solve the enigma of the *M's Paradox*.

1. INTRODUCTION

In 1924 Louis de Broglie suggested, without experimental data, to give particles the same property as waves. He gave each particle a its own wave length depending only on the *momentum* of the particle itself. Any particle with a *momentum* p seems to be something periodic, oscillating as a wave, with a universal relation between the wave length of the particle, indicated by λ, and modulus p of its *momentum*. In this way we have the formula:

$$\lambda = h/p \tag{1}$$

where h is Planck's constant. The question, wave or particle, can be solved with the Quantum Mechanics (QM) leaving to the particles — rather, to *quantum objects* (QO) — a *wave function* (WF) of their own, indicated with ψ, which describes correctly both their wave and particle character. The WF is a *mathematical function* which depends on time (t) and on the position (x) of the particle it is referred to. According to the QM, "we are not able to say that a quantum system, before being observed, has well defined properties, since we cannot know them" [1]. The QM tells us that the wave or particle aspects are not at all outlined: the *square of the modulus* of the, $|\psi|^2$, has to be interpreted as the *density of probability* to find the particle, its *quantum state*, in one of the several possible positions:

$$\|\psi\| = \int_E^3 |\psi(x)|^2 dx^1 \wedge dx^2 \wedge dx^3 \tag{2}$$

That is "the integral of $|\psi^2|$ on all the space gives the total probability to find the particle in a place of the 3-dimensional physical space, with coordinates x^1, x^2, x^3" [2].

2. DISCUSSION

Let's examine as in the mathematical formalism of QM a M of a quantum system must be represented: a 'measurable quantity' of a quantum system is represented by a certain kind of operator **Q**, called *observable*. Examples of *observables* are the 'dynamic variables': i.e., the *momentum (p)*

and the *position* (x) of the particle we wish to examine. The theory requires that an *observable* **Q** is represented by a *linear operator* **L**, so that its action in Hilbert space (**HS**) is to make a linear transformation of **HS**. According to the rules of QM the result of a M, related to an *operator* (**Q**, is always one of the two *self states*: this is the *jump* of the *quantum state*, indicated as WF *collapse* (WFC). "Whatever the state before the M, it *jumps* in one of the **Q** *self states*, as soon as the state (that is the particles in exam) is measured. After the M the state gets a definite value for the *observable* **Q**, precisely the *self value* q" [3]. When the *observable* **Q** is measured on the state $|\psi|$, the rule is that the *probability* tells us that the state *jumps* from $|\psi|$ to one of the **Q** *self states*: $|\varphi\rangle$, for example. The *jump* of the WF, or WFC, induced by any kind of M, is represented as follows:

$$|\langle\psi|\phi\rangle| \tag{3}$$

This is not true, of course, for the macroscopic world. As Miller reminds us "if we want to make a M, as to detect the position of a falling ball, we have to see or photograph, that is we need to *light* it up. In order to do so we have to hit it with light beams, that is with a number of photons (Ps): however the hit Ps do not modify the trajectory of the ball, nor its velocity. Thus, both the *position* and the speed or *momentum* of the ball can be determined at the same time, with all the precision and accuracy we wish.

Let's see what would happen if the ball was a single electron. According to QM the falling electron can be in any position, since its WF is *diffused* throughout the space (the ball, instead, is localised since the beginning). It doesn't have any sense to wonder where the electron is, until a M is carried out, i.e., taking a picture of it: in this case we need to light it up, at least with a light quantum, which becomes part of the M system. The interaction of the single light quantum (1P) with the electron, localises it in that moment" [3], at the same time we have induced a particular phenomenon of the QM: the WFC. The contact of a single P with the electron in exam can collapse its *quantum state*, its WF.

Well, the interaction between the M system (that is also a single light quantum) and the examined physical system (the electron) induces the **R** process: that is the *reduction* of the electron WF (which was *diffuse*, till a moment before the M), so now it tends to converge to a certain, well defined, region of the space. That is "among all the possible positions which the electron WF can occupy, as a *diffused* wave in all the space, the M process chooses one. Thus, with the M, the *quantum state* of the electron is transformed from being potentially in any position to being in a well defined position. The Uncertainty Principle tells us that the cost of this localization is an enormous *uncertainty* about the *momentum* of the electron" [3].

What kind of mechanism can be concealed behind the observation, behind the M, behind this kind of interactions? No one knows. Miller states "both Schrodinger equation and the other QM fundamental equations remain mute!" [3]. However, what seems important is that "the WF does not evolve along with Schrodinger equation, after the M" [4]. It really seems that when the particle is not disturbed, that is when any M is carried out, it stays in its natural state: it *lives*, as a QO. Thus it occupies a volume, it is *spread* in the space which is allowed to it (it is *delocalized*), and it is represented by *superimposed quantum state*: it tends to behave as a wave. This is the *phase of linear evolution* **U**, described by Schrodinger equation. Whereas, when we carry out the M, the QO, its WF, concentrates in a well specific point in space appearing as a corpuscle.

What happened is that with the M, with the light (necessary to see the particle), it took place a *reduction* of the *state vectors*, that is the WFC of the electron. This is the crucial point: the use of the electromagnetic radiation (EMR), results in a modification of the *quantum state* of the particle observed, since it undergoes, under the action of the EMR, the *jump*, the *collapse* of its WF, as represented in Eq. (3). "It is clear that the WF is something more *real* than a simple *probability wave*" [2]. Physicists wondered what was the role of the observer in the M process of a physical system. Bohr suggested that it does not exist any reality independent by the M apparatus: it is not possible to trace a clear separation between the behaviour of the observed particle and the instrument of M. A physical theory can describe physical phenomenon only if it includes an experimental content, the observation, the M, which make these phenomena show (though there are modified).

What is particularly relevant is that to carry out a M, to observe anything in the universe, any macroscopic object or particle, it is necessary to use an EMR, having a wave length shorter or equal to the diameter of the object to be observed. Hence, the smaller the object or particle to be examined, the smaller has to be the wave length of the EMR used, thus bigger its energy. Thus if we want to detect, observe, *measure* an electron, we need to point on it an EMR with a short wave

length. However in this case we hit it so deviate and modify its trajectory. Indeed, the QM teaches us that the observation of the microscopic world, the M, modify the physical system we want to examine.

It seems that the main character in this enigma(the M's Paradox) is the EMR. Why? The main reason is that in order to observe, to see, or make a M, we need to use the EMR. Only using the EMR we can acquire the information about the state and the property of the objects of the subatomic world. The EMR, the Ps are the *wire* which allow us to get the M of the particle we are interested in. As long as the P is concerned, Fermi reminds us "the P too, as other particles, has a its own *momentum (p)*, through which transfers its energy to the hit particle" [5]. Feynman states: each P has a has a energy and a *momentum (p)*. This p is represented in the formula:

$$p = h/\lambda \tag{4}$$

where h (the Planck's constant) is equal to $6.625 \cdot 10^{-27}$ [erg·s], and λ is the wave length of the considered P [6]. The mean wave length of a P in the optical band corresponds to $5 \cdot 10^{-5}$ [cm] and its p is:

$$p = 6.625 \cdot 10^{-27}\,[\mathrm{erg} \cdot \mathrm{s}]/5 \cdot 10^{-5}\,[\mathrm{cm}] \tag{5}$$

Since $1\,\mathrm{erg} = \mathrm{g{\cdot}cm^2/s^2}$, we have:

$$p = 6.625 \cdot 10^{-27}\,[\mathrm{g} \cdot \ \mathrm{cm^2/s}]/5 \cdot 10^{-5}\,[\mathrm{cm}] \tag{6}$$

That is:

$$p = 1.325 \cdot 10^{-22}\,[\mathrm{g} \cdot \mathrm{cm/s}] \tag{7}$$

3. CONCLUSION

What can we infer? When we wish to carry out a M of a QO we need to illuminate it, but then we modify the physical system we are examining. The electron, for instance, does not remain indifferent to the light. To this purpose Feynman said: "To observe electrons, we need a light because the light rebounding on electrons make them visible. Nevertheless the light affects the result because the result of light on is different from that of light off. We can say that the light affects electron behaviour. The electrons are very sensitive. When light is sent on an electron, it makes the electron vibrate so that the electron because of light, behaves in a different manner" [7]. If we consider that an electron weighs $9.1 \cdot 10^{-28}$ [g], what we get from our calculations is that a single luminous P hits the electron with an *impact force* of a million times bigger than the mass of the electron itself: it expresses the *work-force* of a P when interacting with another particle, thus transferring to it its energy, its p [5].

Thus, every time a M is carried out (using the EMR), the observed QO undergoes a *probabilistic reduction of the state vector*, indicated as Reduction Process, or **R** Process. With the **R** Process the *state vector*, represented by $|\psi\rangle$, *jumps* to another stated vector, let's say $|\varphi\rangle$, which represents one out of two or more *orthogonal* alternative possibilities: the other can be $|q\rangle$, $|X\rangle$, etc., which depend on the kind of observation, the kind of M carried out. The M, thus, produces a big changes on the physical properties of the observed particle, as well as on its morphological configuration. Which mean do we use to carry out a M? A EMR with a short wave length. Our calculations show that the EMR is not evanescent, ethereal, inconsistent, but it produces a mechanical action, a "*push effect*" [8]: the so called *radioactive pressure of the light*, which induces the WFC of the measured QO.

It seems that only through a mechanical effect induced by the EMR we can try to reveal the mystery of the Measurement Paradox.

REFERENCES

1. Zeilinger, A., *Einsteins Schleier: Die neve Welt der Quantenohysik*, Vol. 18, Verlag C. H., Bech H. G., Einaudi Ed. (To), Munchen, 2005.
2. Penrose, R., *The Road to Reality*, 516–518, 533–544, 520, 786, 477, 499, RCS Ed., Milano, 2005.
3. Miller, A. I., "Erotism, estetica and Schrodinger wave equation," *It Must be Beautiful: Great Equations of Moderne Science*, 186–187, Il Saggiatore Ed., Milano, Granta Publ., London, 2005.

4. Penrose, R., "La riscoperta della gravità. L'eaquazione di Einstein della relatività generale," *It Must be Beautiful: Great Equations of Moderne Science*, 293, Il Saggiatore Ed., Milano, Granta Publ., London, 2005.
5. Fermi, E., *Atomi Nuclei Particelle*, Boringhieri Ed. (To), Vol. 24, 2009.
6. Feynman, R. P., *Lectures on Physics*, Vol. 3, 16-7, 21-1, California Institute of Technology, Zanichelli Ed., Bologna, 2001.
7. Feynman, R., *The Character of Physical Law*, 158–159, Bollati Boringhieri Ed., Torino, British Broadcasting Corporation, London, 1971.
8. Puccini, A., "About the zero mass of the photon," *Progress In Electromagnetics Research*, Vol. 55,117–146, 2005.

Ship Detection by Synthetic Aperture Radar with Ground-based Maritime Radar with AIS

Eun-Sung Won and Kazuo Ouchi
Department of Computer Science, School of Electrical and Computer Engineering
National Defense Academy, 1-10-20 Hashirimizu, Yokosuka, Kanagawa 239-8686, Japan

Abstract— MLCC (Multi-Look Cross-Correlation) is a useful technique to extract the images of ships embedded in sea clutter from SAR (Synthetic Aperture Radar) data [1, 2]. However, the previous MLCC has a difficulty of detecting small ships since SNR (Signal-to-Noise Ratio) is not high enough. Therefore, we developed a new Improved MLCC (IMLCC) to increase SNR to extract small boats. Although the LMLCC method increased SNR, there still remained some highly correlated noises in the coherence images caused by strong radar backscatter from sea surface. In order to improve the IMLCC algorithm further, we propose a new method of applying Lognormal-CFAR (Constant False Alarm Rate) to IMLCC coherence images. The results using ALOS-PALSAR (Advanced Land Observing Satellite-Phased Array L-band SAR) data showed substantial improvement in SNR and detection rate.

1. INTRODUCTION

In recent years, ship detection by synthetic aperture radar (SAR) has attracted much attention for monitoring traffic, fishing activity, and increasing illegal maritime crimes, and substantial number of experimental and theoretical studies have been reported.

Since the launch of Advanced Land Observing Satellite (ALOS) in 2006, we have been developing a ship detection system using PALSAR on board of ALOS. One of the algorithms we focused on is the multi-look cross-correlation technique (MLCC), yielding improvement in detection accuracy [3, 4]. However, the previous MLCC could not detect small ships very well since SNR and the detection rate are also not high enough. Therefore, to increase the SNR and detection rate of MLCC, we propose, in this paper, a method of IMLCC and Lognormal-CFAR.

We conducted experiments in Tokyo Bay in order to develop an integrated ship detection and identification system with SAR, ground-based maritime radar with auto identification system (AIS). In this paper, we will report out result of ship detection experiment in the Tokyo Bay using PALSAR data.

2. SAR AND METEOROLOGICAL DATA

The data we used in the experiments are ALOS-PALSAR FBS 34.3 data (Fine Beam Single mode at off-nadir angle 34.3 degrees) acquired at 01:10–01:20 (UT) on the 18th December 2008 and 16th January 2009. The spatial resolution cells are 4.1 m in azimuth direction and 7.2 m in range direction. Fig. 1 shows the test site in the white square and the ground-based radar site from which visual observation was also made. According to the meteorological data obtained at a station close to the experimental site, the sea was calm with significant wave height 0.26 m and 0.27 m, and wind speed 2.0 m/s and 2.0 m/s at the time of PALSAR observation in 2008 and 2009 respectively.

3. THEORY OF IMPROVED MLCC

The MLCC and IMLCC is defined as

$$C = \frac{\langle A_1 A_2 \rangle}{\langle A_1 \rangle \langle A_2 \rangle} - 1 \tag{1}$$

where A_j is the look j image amplitude, and the angular brackets indicate taking an ensemble average.

$$C_{improved}(i,j) = \sum_{m=0}^{M-1} \sum_{n=0}^{N-1} A(m,n) \cdot B(m+i, n+j)^* \tag{2}$$

where M and N are window size, $A(m,n)$ and $B(m+i, n+j)$ are the look-1 and look-2 amplitude images respectively and $*$ indicates taking complex conjugate.

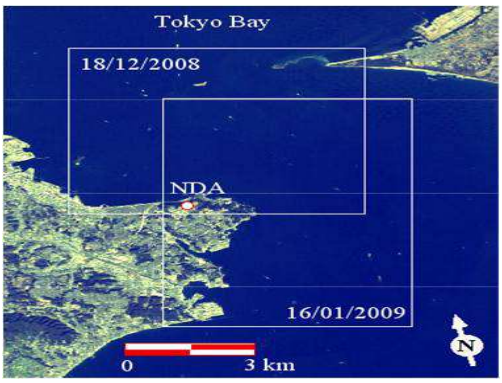

Figure 1. AVNIR-2 image indication the test areas by white squares. The different test area in the 2008 and 2009 data are due to different visual observation sites. The X-band radar (AIS) is located at NDA.

Table 1. Average Peak to Background Noise Ratio (PBNR) in dB unit for the images of ships shown in Fig. 2 and the numbers inside the brackets show the number of detected ships.

No	Amplitude image	MLCC coherence image	Improved MLCC coherence image
2008	1.38 (23)	1.48 (23)	4.50 (33)
2009	3.15 (11)	3.20 (10)	4.13 (18)

Because the center frequencies of sub-apertures are separated in such a way that the subapertures do not overlap, the speckle patterns arising from background ocean surface are not correlated between looks. While the deterministic images of ships have strong inter-look correlation. In the conventional MLCC algorithm, the cross- correlation value is taken from the center of the cross-correlation function within a moving window. However, if the ships are moving, the images are produced at different positions in the sub-images. This is indeed the basis of velocity vector estimation of moving targets [5]. For ship detection, however, the peak value of the inter-look cross-correlation is different from the center of the axis of the window because the image positions of moving ships are different between looks. Thus, to optimize the MLCC algorithm, the maximum cross-correlation value is sought within the window as in Equation (2). This is IMLCC.

Table 1 shows the Peak to Background Noise Ratio (PBNR) in dB unit for the images of ships present in the test site in 2008 and 2009. The average PBNRs over all detected ship image in both the 2008 and 2009 data were 2.27 dB, 2.34 dB, and 4.32 dB in amplitude image, MLCC coherence image, and IMLCC coherence image respectively. The total of 37 and 20 ships corresponding to the 2008 and 2009 data respectively were confirmed by AVNIR-2, AIS, and visual observation using video camera, which were considered as the true number of ships.

Figure 2 shows that the numbers of detected ships were 23, 23 and 33 by the amplitude, MLCC and IMLCC respectively in 2008. In 2009, the corresponding numbers were 11, 10 and 18. The white circles correspond to the ships without AIS and their signals, whose positions were confirmed by the AVNIR-2 images and visual observation from ground by a video camera. The white triangles indicate the ships without AIS signals, located outside the video camera sight, but detected by the AVNIR-2. From these results, our report shows that the IMLCC performed best, followed by MLCC and amplitude-based methods.

4. APPLICATION TO PALSAR DATA WITH LOGNORMAL CFAR

The study about ship detection can now be advanced a step further to extract appropriate threshold. For this purpose, we adopted constant false alarm rate (CFAR) theory to the IMLCC coherence images. In order to apply CFAR to the coherence image from IMLCC, it is necessary to find a best fitted Probability Density Function (PDF). In this study, we considered 4 distribution models including Lognormal, Gamma, Weibull and Rayleigh distribution. After a best fitted distribution is confirmed, the next step is to determine parameters for estimated PDF by Maximum Likelihood Estimation (MLE) and calculating a threshold value by numerical integration. In this step, we used moving window whose size is 100×100 within the entire IMLCC coherence image and the

threshold value T is derived from

$$1 - FAR = \int_0^T f(H)dH \tag{3}$$

where f is the PDF, H means pixel value of moving window and FAR is the false alarm rate. We set a FAR value as 1.0E-04. In this step, when a certain threshold value is less than the mean pixel value of the whole image, we set a value of moving window to zero. For this reason, we detected ships very effectively and it was able to remove noise.

Figure 3 shows the PDF which fits best to the coherence images in 2008 (left) and 2009 (right) data. The best fit was Lognormal distribution (location parameter: 1.12, −1.14 and scale parameter: 0.27, 0.19), followed by gamma distribution (shape parameter: 13.31, 25.6 and scale parameter: 0.24, 0.12),Weibull distribution (order parameter: 3.55,0.35 and shape parameter: 3.54, 4.56) and Rayleigh distribution (shape parameter: 2.36, 0.23). The first and second numbers in the brackets mean the data in 2008 and 2009 respectively.

Figure 4 shows the results of Lognormal CFAR. The detection rate for the images of ships present in the test site decreased from 94% in IMLCC to 83% in Lognormal CFAR but PBNR improved from 4.31 dB in IMLCC to 6.27 dB in Lognormal CFAR respectively.

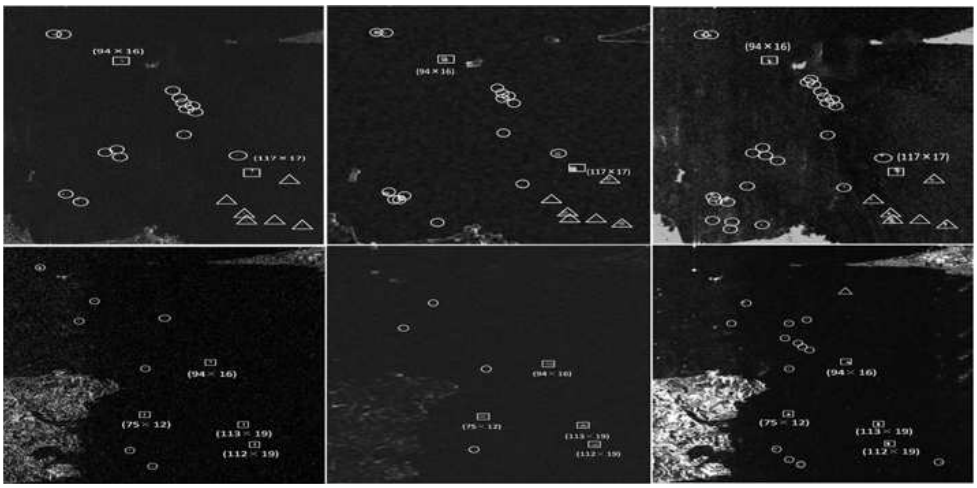

Figure 2. Amplitude image (left), MLCC coherence image (middle) and Improved MLCC coherence image (right). The upper and lower rows correspond respectively to the 2008 and 2009 data. The range and azimuth directions are from right to left and top to bottom respectively.

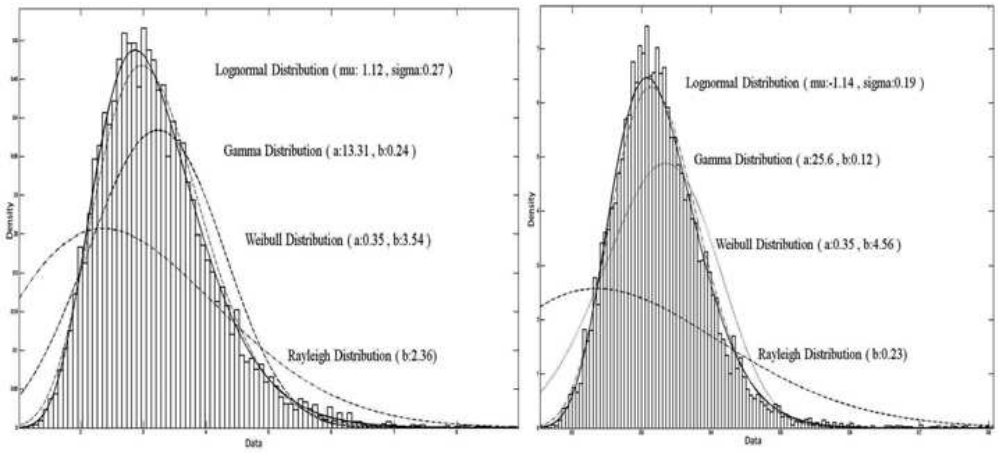

Figure 3. PDF of Improved MLCC coherence images. The left is the result of 2008 data. (range pixels: 1401 to 1500 and azimuth pixels: 3301 : 3400), and the right is result of 2009 data. (range pixels: 1501 to 1600 and azimuth pixels: 1601 : 1700).

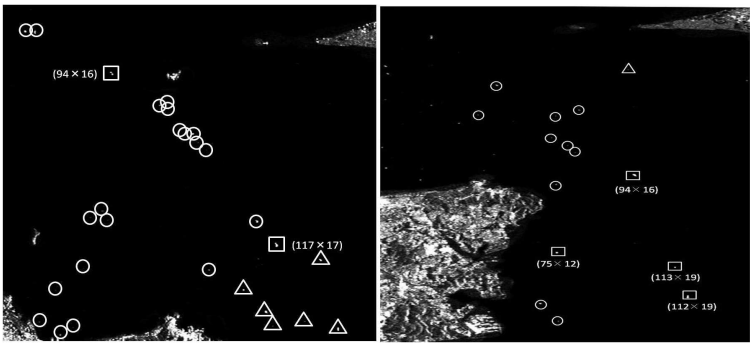

Figure 4. Results of Lognormal CFAR (left: 2008 and right: 2009). The whole area of this images are computed by Lognormal CFAR and the land areas are masked using Improved MLCC coherence image.

5. CONCLUSION

A technique of MLCC is known to be able to extract the images of ships embedded in clutter by thresholding coherence images produced by cross-correlating sub-aperture SAR images. The basic idea is the strong inter-look correlation of deterministic targets such as ships, and weak correlation of surrounding noise. One of the problems of this method is that it has a difficulty of detecting small sips since SNR is not high enough. In the present study, we proposed a new simple algorithm of IMLCC to increase SNR and extract small boats, and also proposed Lognormal CAR to determine an appropriate threshold value for IMLCC coherence images. We tested the proposed method of IMLCC and Lognormal-CFAR using ALOS-PALSAR data containing small boats of sizes comparable with the SAR resolution cells. The results showed that substantial improvements were made by Improved MLCC and Lognormal-CFAR in both the PBNR and detection rate in comparison with amplitude images. The project is still in progress, and currently, we are analyzing other sets of PALSAR, RADARSAT-2, and also TerraSAR-X data over the same test site with simultaneous ground truth data. The results will be reported in the near future.

ACKNOWLEDGMENT

This work was supported by the Sasakawa Scientific Research Grant from the Japan Science Society.

REFERENCES

1. Arnesen, T. N. and R. B. Olsen, "Literature review on vessel detection," FFI/RAPPORT-2004/02619, Forsvarets Forskningsinstitutt, Norwegian Defence Research Establishment, Kjeller, Norway, 2004.
2. Ouchi, K., S. Tamaki, H. Yaguchi, and M. Iehara, "Ship detection based on coherence images derived from cross-correlation of multilook SAR images," *IEEE Trans. Geosci. Remote Sens. Lett.*, Vol. 1, No. 3, 184–187, 2004.
3. Hwang, S.-I. and K. Ouchi, "On a novel approach using MLCC and CFAR for the improvement of ship detection by synthetic aperture radar," *IEEE Geosci. Remote Sens. Lett.*, Vol. 7, No. 2, 391–395, 2010.
4. Ouchi, K., S. Tamaki, H. Yaguchi, and M. Iehara, "Ship detection based on coherence images derived from cross-correlation of multilook SAR images," *IEEE Trans. Geosci. Remote Sens. Lett.*, Vol. 1, 184–187, 2004.
5. Ouchi, K., S. Maedoi, and H. Mitsuyasu, "Determination of ocean wave propagation direction by split-look processing using JERS-1 SAR data," *IEEE Trans. Geosci. Remote Sens.*, Vol. 37, 849–855, 1999.

On the SAR Image Classification by Rotation of the Covarience Matrix in the Four-component Scattering Power Decomposition

Mitsunobu Sugimoto and Kazuo Ouchi
Department of Computer Science, School of Electrical and Computer Engineering
National Defense Academy, 1-10-20 Hashirimizu, Yokosuka, Kanagawa 239-8686, Japan

Abstract— A modification is applied to the four-component scattering power decomposition based on covariance matrix. The concept of rotation is applied to covariance matrices and the effect of rotation on the four-component scattering power decomposition has been studied. With our approach, man-made structures can be distinguished from other areas more effectively. Our result shows that the rotation of the covariance matrix in the four-component scattering power decomposition contributes to better understanding and interpretation of POLSAR data.

1. INTRODUCTION

As more and more synthetic aperture radar (SAR) systems utilize polarimetric information recently, polarimetric SAR (POLSAR) are also becoming active in research. While conventional SAR systems handle only single polarimetric information, data acquired through POLSAR systems contain fully polarimetric information, that is HH, HV, VH and VV. H and V mean horizontal and vertical respectively, and the first letter represents transmitted signal and the second letter represents received signal.

The four-component scattering power decomposition [1–4] is an improved method of previously devised three-component decomposition [5]. Using the four-component scattering power decomposition, fully polarimetric data can be decomposed into four power categories: surface scattering power, double-bounce scattering power, volume scattering power, and helix scattering power. The four-component scattering power decomposition is a powerful tool to analyse data acquired through POLSAR systems and is one of the most successful methods to analyze fully polarimetric data.

According to [3], among all the scattering components, double-bounce scattering occurs when the transmitted signal is reflected by ground/sea surfaces and man-made structures (or natural targets such as tree trunks). However, if the man-made structures are not parallel or diagonal to SAR platforms, double-bounce scattering becomes weak and other scattering components become dominant. In such areas, volume scattering often becomes major reflected component. Thus, output results from the decomposition are sometimes confusing because volume scattering comes from both forested areas and urban areas. This makes the classification of man-made structure from other areas difficult. From our commonsense point of view, these two types of areas have quite different characteristics against each other. Therefore, it would be better if these areas are separated more clearly.

To overcome this problem, the concept of rotation in the four-component scattering power decomposition have been proposed. The idea of rotating scattering matrices is recently proposed by Yamaguchi et al. [6]. They applied rotation to coherency matrices so that cross-polarization (i.e., HV and VH) components which are closely related to volume scattering are minimized. We expanded this idea to the rotation of covariance matrices and compared results between the original four-component scattering power decomposition and improved methods using rotated coherence matrices and rotated covariance matrix respectively.

2. ROTATION OF COVARIANCE MATRIX

The covariance matrix is given by

$$\langle [\, C \,] \rangle = \begin{bmatrix} \langle |S_{HH}|^2 \rangle & \langle \sqrt{2} S_{HH} S_{HV}^* \rangle & \langle S_{HH} S_{VV}^* \rangle \\ \langle \sqrt{2} S_{HV} S_{HH}^* \rangle & \langle 2 |S_{HV}|^2 \rangle & \langle \sqrt{2} S_{HV} S_{VV}^* \rangle \\ \langle S_{VV} S_{HH}^* \rangle & \langle \sqrt{2} S_{VV} S_{HV}^* \rangle & \langle |S_{VV}|^2 \rangle \end{bmatrix} \tag{1}$$

where S_{HH}, S_{HV}, S_{VH} and S_{VV} denote complex numbers, $\langle\rangle$ denotes the ensemble average of an arbitrary window size, and * denotes complex conjugate. The covariance matrix after rotation can

be expressed using a unitary rotation matrix [3] as

$$[\,C(\theta)\,] = [\,U_\theta\,]\,[\,C\,]\,[\,U_\theta\,]^T \tag{2}$$

$$[U_\theta] = \begin{bmatrix} \cos^2\theta & \sqrt{2}\sin\theta\cos\theta & \sin^2\theta \\ -\sqrt{2}\sin\theta\cos\theta & \cos 2\theta & \sqrt{2}\sin\theta\cos\theta \\ \sin^2\theta & -\sqrt{2}\sin\theta\cos\theta & \cos^2\theta \end{bmatrix} \tag{3}$$

where θ denotes a rotation angle. The elements of the rotated covariance matrix are expressed as follows:

$$[\,C(\theta)\,] = \begin{bmatrix} C_{11}(\theta) & C_{12}(\theta) & C_{13}(\theta) \\ C_{21}(\theta) & C_{22}(\theta) & C_{23}(\theta) \\ C_{31}(\theta) & C_{32}(\theta) & C_{33}(\theta) \end{bmatrix}. \tag{4}$$

The chosen angle is the one which minimizes $C_{22}(\theta)$ because it is equivalent to suppress volume scattering as much as possible.

3. THE FOUR-COMPONENT SCATTERING POWER DECOMPOSITION ALGORITHM ON ROTATED COVARIANCE MATRIX

First, the helix scattering component can be derived from

$$P_c = \sqrt{2}\,|\,\mathrm{Im}\,(C_{12}(\theta) - C_{32}(\theta))\,|. \tag{5}$$

Next, the choice of the volume scattering covariance matrix [2] is based on the value of

$$10\log\,[\,C_{33}(\theta)\,/\,C_{11}(\theta)\,]. \tag{6}$$

If (6) $< -2\,\mathrm{dB}$,

$$P_v = \frac{15}{4}\,C_{22}(\theta) - \frac{15}{8}P_c \tag{7}$$

$$A = C_{11}(\theta) - 2\,C_{22}(\theta) + \frac{3}{4}P_c \tag{8}$$

$$B = C_{33}(\theta) - \frac{3}{4}\,C_{22}(\theta) + \frac{1}{8}P_c, \tag{9}$$

else if (6) $> 2\,\mathrm{dB}$,

$$P_v = \frac{15}{4}\,C_{22}(\theta) - \frac{15}{8}P_c \tag{10}$$

$$A = C_{33}(\theta) - \frac{3}{4}\,C_{22}(\theta) + \frac{1}{8}P_c \tag{11}$$

$$B = C_{11}(\theta) - 2\,C_{22}(\theta) + \frac{3}{4}P_c, \tag{12}$$

else,

$$P_v = 4\,C_{22}(\theta) - 2P_c \tag{13}$$

$$A = C_{11}(\theta) - \frac{3}{2}\,C_{22}(\theta) + \frac{1}{2}P_c \tag{14}$$

$$B = C_{33}(\theta) - \frac{3}{2}\,C_{22}(\theta) + \frac{1}{2}P_c, \tag{15}$$

where A and B are temporal variables. If $P_v < 0$ in (7), (10) and (13), P_c is substituted by 0. This means the output becomes three-component scattering power decomposition. Total power can be described as

$$TP = C_{11}(\theta) + C_{22}(\theta) + C_{33}(\theta). \tag{16}$$

Once P_c and P_v are obtained, P_s and P_d can be determined by the remaining power $(TP - P_c - P_v)$. If $P_v + P_c > TP$, the algorithm ends as two-component scattering power decomposition:

$P_v = TP - P_c$, $P_s = P_d = 0$. The branch condition C_0 can be defined in terms of the covariance matrix elements as

$$C_0 = C_{13}(\theta) - \frac{1}{2}\, C_{22}(\theta) + \frac{1}{2} P_c. \tag{17}$$

If $\mathrm{Re}(C_0) > 0$,

$$\alpha = -1, \quad f_d = \frac{AB - |\, C_0\,|^2}{A + B + 2\,\mathrm{Re}(C_0)}, \quad f_s = B - f_d, \quad \beta = \frac{C_0 + f_d}{f_s}, \tag{18}$$

else,

$$\beta = 1, \quad f_s = \frac{AB - |\, C_0\,|^2}{A + B - 2\,\mathrm{Re}(C_0)}, \quad f_d = A - f_s, \quad \alpha = \frac{C_0^* - f_s}{f_d}. \tag{19}$$

Finally, the remaining scattering components can be calculated as follows:

$$P_s = f_s(1 + |\beta|^2), \quad P_d = f_d(1 + |\alpha|^2). \tag{20}$$

As a result, all of the four scattering components have been determined. If P_s or P_d becomes negative, it is substituted by zero and the other is determined by $TP - P_c - P_v$. It should also be noted that all of the four scattering components can directly be obtained from the covariance matrix elements.

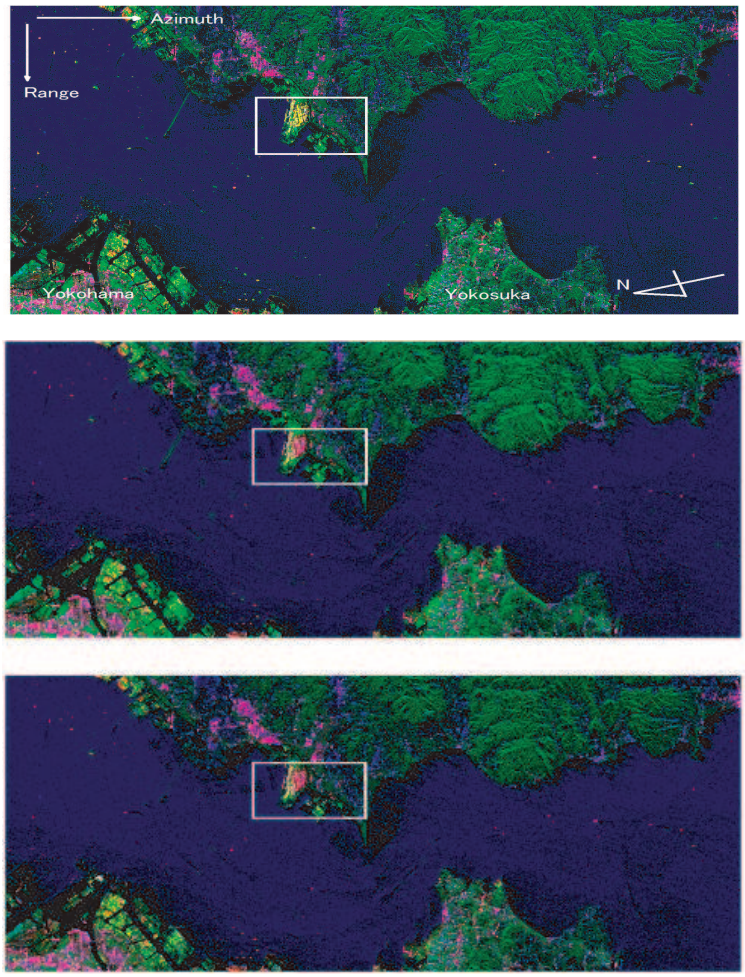

Figure 1: ALOS-PALSAR decomposition images of Tokyo Bay, Japan. (a) Four-component scattering power decomposition (helix component excluded). (b) Decomposition using rotated coherency matrices. (c) Decomposition using rotated covariance matrices. The red, green, and blue colors represent double-bounce, volume, and surface scattering components respectively.

4. DECOMPOSED RESULT

This section shows the results of the algorithm applied to SAR data. The Quad-Pol data used here were acquired by the Advanced Land Observation Satellite-Phased Array L-band SAR (ALOS-PALSAR) on November 24, 2008 (ALPSRP150972900-P1.1). Fig. 1 shows decomposed images of Tokyo Bay, Japan. From the top to bottom, the decomposition image from conventional four-component scattering power decomposition, the decomposition image using rotated coherency matrices and the decomposition image using rotated covariance matrices are shown respectively. The red, green, and blue colors represent double-bounce, volume, and surface scattering components respectively. The effect of the size of the moving window (i.e., ensemble average) has also been analyzed. As expected, if the size is too small, the result is too noisy and classification does not work very well. On the other hand, if the size is too large, the output becomes rougher and fine details are lost. An appropriate window size varies depending on situations. Therefore, when the decomposition is performed, this should be taken into consideration. At this time, the ensemble average window size chosen here is 2 pixels in range direction, and 18 pixels in azimuth direction.

Table 1 indicates relative contribution of double-bounce scattering, volume scattering and surface scattering to total power in the area surrounded by the white rectangle in Fig. 1. In either rotated scattering matrix, volume scattering is suppressed and the proportion of double-bounce scattering becomes larger. As a result, parts of the rectangular area turn to red, which implies man-made structures. The algorithm with rotation of covariance matrix shows a stronger inhibitory effect on volume scattering. Contribution from helix scattering is omitted here because it is so small compared with the other three scattering components. Some may notice that the sum of three contribution exceeds 100%. This comes from the process of substituting negative power to zero in the four-component scattering power decomposition algorithm.

Some areas surrounded by the rectangle in Fig. 1 are classified as yellow in the top image, but are classified as red in the middle and bottom images, increasing likelihood of being recognized as man-made structures. Fig. 2 is an enlarged Google Map image corresponding to the rectangular area in Fig. 1. The red areas in the middle and bottom images in Fig. 1 can be identified as industrialized bay areas in Fig. 2. In addition, a number of dots scattered on the sea surface is considered to be ships. More dots are classified as red in the middle and bottom images than in the top image. This helps to classify them not as rocks or tiny islands on the sea but as ships with more certainty.

Figure 2: The Google Map image of the region surrounded by the white rectangles in Fig. 1.

Table 1: Relative contribution to total power in the rectangle region in Fig. 1.

method	P_d	P_v	P_s
Four-component scattering power decomposition	26.56%	43.26%	29.42%
Decomposition with rotation of coherency matrix	40.54%	28.93%	32.42%
Decomposition with rotation of covariance matrix	42.53%	19.84%	34.40%

5. CONCLUSION

In this study, the idea of rotation of scattering matrix is extended to covariance matrix. At this time, the rotation of covariance matrix outperformed the rotation of coherency matrix. We chose appropriate rotation angles for the purpose of suppressing the volume scattering and was able to get better results than the related studies. This algorithm can contribute to the improvement of classification accuracy of man-made structures and vessels, and to better understanding and interpretation of POLSAR data. The difference between the rotation of coherency matrix and covariance matrix, and the implication will be examined in the near future.

REFERENCES

1. Yajima, Y., Y. Yamaguchi, R. Sato, H. Yamada, and W.-M. Boerner, "POLSAR image analysis of wetlands using a modified four-component scattering power decomposition," *IEEE Trans. Geosci. Remote Sens.*, Vol. 46, No. 6, 1667–1673, Jun. 2008.
2. Yamaguchi, Y., T. Moriyama, M. Ishido, and H. Yamada, "Four-component scattering model for polarimetric SAR image decomposition," *IEEE Trans. Geosci. Remote Sens.*, Vol. 43, No. 8, 1699–1706, Aug. 2005.
3. Yamaguchi, Y., *Radar Polarimetry From Basics to Applications,* 182 Pages, IEICE, Tokyo, Japan, 2007 (in Japanese).
4. Lee, J. S. and E. Pottier, *Polarimetric Radar Imaging From Basics to Applications,* FL, CRC Press, Boca Raton, 2009.
5. Freeman, A. and S. Durden, "A three-component scattering model for polarimetric SAR data," *IEEE Trans. Geosci. Remote Sens.,* Vol. 36, No. 3, 963–973, May 1998.
6. Yamaguchi, Y., A. Sato, W.-M. Boerner, R. Sato, and H. Yamada, "Four-component scattering power decomposition with rotation of coherency matrix," *IEEE Trans. Geosci. Remote Sens.*, to be published.

Detection and Evaluation of Building Damages in Earthquake from VHR Optical and SAR Images Using Multiple Mutual Information Techniques

Tian-Lin Wang and Ya-Qiu Jin
Key Laboratory of Wave Scattering and Remote Sensing Information (MoE)
Fudan University, Shanghai 200433, China

Abstract— How to make data/information fusion using all-weather and all-time SAR (synthetic aperture radar) technology with other optical/IR images is of great important for remote sensing applications. In this paper, a fusion approach using very high resolution (VHR) pre-event optical image and post-event SAR image is presented for detection and evaluation of building damages after earthquake. Some SAR images of the building objects are first numerically simulated using the mapping and projection algorithm (MPA) based on the parameters extracted from the optical image. These images are employed for similarity analysis with real SAR image of the building objects using multiple mutual information (M-MI), i.e., normalized MI (NMI), gradient MI (GMI) and regional MI (RMI). Based on the similarity results of the mean, maximum and height deviation of M-MI, the building damages can be detected and evaluated under the situations of collapsed, subsided or deformed.

As an example, the optical images of Ikonos and Geo-Eye of pre-event and post-event, respectively, and SAR images of Cosmo-Skymed and Radarsat-2 of post-event during Haiti earthquake 2000 are applied in the M-MI approach and analysis.

1. INTRODUCTION

Very high resolution (VHR) optical image is usually applied to visually monitoring natural disaster occurrence. However, the post-event VHR optical image has not been always available under some serious situations, such as bad weather or difficult geographic conditions. High-resolution and all-weather all-time SAR technology can provide reliable and high quality images. It's feasible to making fusion of VHR pre-event optical and post-event SAR images for accurate evaluation of earthquake losses [1, 2].

Mutual information (MI) has been applied to registration of medical images, e.g., X-ray projection and CT images [3], and later remote sensing images [4, 5]. Different extensions, i.e., normalized MI (NMI) [6], gradient MI (GMI) [7] and regional MI (RMI) [8] have been developed.

In this study, an approach of multiple mutual information (M-MI), combining NMI, GMI and RMI, is proposed for detection and evaluation of building damages after earthquake from the fusion of VHR pre-event optical image and post-event SAR images. The building objects are first selected and parameterized from the pre-event optical image. The mapping and projection algorithm (MPA) [9] is employed to simulate some SAR images of those building objects under different damage situations. Then, M-MI is applied for registration and matching of the simulated and post-event real SAR images of the building objects. The M-MI results, i.e., the mean, maximum and height deviation (HD), can detect and classify the damage situations of the building objects.

As an example, the pre-event Ikonos optical image, the post-event Radarsat-2 and Cosmo-Skymed SAR images for 2010 Haiti earthquake are applied to the M-MI experiment. The results are then validated by the post-event Geo-Eye optical image.

2. METHODOLOGY

Scatterings from volumetric building objects recorded in a SAR image are mainly governed by the processes i.e., of layover, double-bounce, and shadows [10]. The scattering feature of the building is mainly determined by the building height and aspect angles etc. If the building shape is simplified as a rectangular object, the layover, double bounce and shadow regions demonstrated in SAR image can be clearly identified. If these regions of two images, pre-even and post event, are found significantly different in terms of the similarity, i.e., MI analysis, it indicates the building changes or damages in the post-event image.

As shown in Fig. 1, M-MI methodology consists of 6 steps: 1) the parameters extraction of the building geometry and SAR configuration; 2) SAR image simulation of the building objects

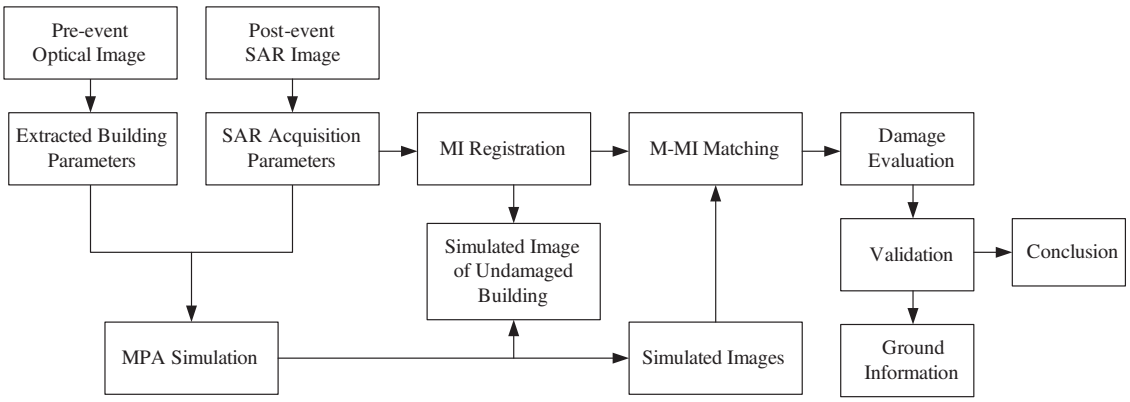

Figure 1: The methodology of building damage detection and evaluation from VHR optical and SAR images.

using MPA [9]; 3) MI registration of simulated and real SAR image of the undamaged buildings; 4) Matching process using M-MI; 5) Detection and evaluation of damaged buildings; 6) Validation with ground truth data, as available.

The length l and width w of a building can be directly estimated from optical image. The height h is calculated as $h = s \cdot \tan\theta_s$ from the shadow s and sun elevation angle θ_s. The roof angle α is used to describe the flat-roof or gable-roof buildings. The parameters of SAR configuration includes the azimuth resolution δ_a, the range resolution δ_r, the incident angle θ and included angle η, which is the angle between the azimuth angles of optical and SAR observations. The aspect angle ϕ is defined as the angle between the length of building and azimuth direction of optical sensor. The corresponding aspect angle φ in SAR image is calculated as $\varphi = \phi - \eta$. The size of image scene enclosing the building object is defined as follows

$$M = [(|\ell \times \cos\varphi| + |w \times \sin\varphi|) \times (1+t)/\delta_a] \quad (1)$$

$$N = [(|\ell \times \sin\varphi| + |w \times \cos\varphi|) \times (1+t)/\delta_r] \quad (2)$$

where t is a parameter of the image scene to enclose the building object including its shadows and $t = 1$. Thus, the parameters for SAR image simulation are described as $P = \{\ell, w, h, \alpha, \delta_a, \delta_r, \theta, \varphi, M, N\}$.

Mapping and projection algorithm (MPA) is employed for SAR image simulation of various buildings, non-damaged or damaged. The MPA incorporates the polarimetric single, double, and triple scattering, attenuation, shadowing, and coherent speckle using the Mueller matrix solution [9]. The registration of real and simulated building images is carried out by MI calculation. The geometric and radiometric differences in multi-modal images won't affect the registration result [5]. The MI registration is carried out by

$$m = \max\{\mathrm{MI}[\bar{\mathbf{X}}_R(\vec{t}), \bar{\mathbf{X}}_S]\} \quad (3)$$

where $\vec{t} = (dx, dy)$ denotes translation vector when MI takes the maximum, corresponding to best registration.

Then, the building height is specifically defined for MPA simulation to determine whether the building is damaged or not. The maximum of MI indicates that the simulated image is very similar to the real one as its height is approximately equal to the real value. Three parameters of M-MI results, i.e., the mean value, the maximum and the height deviation (HD) are applied for damage evaluation. The HD is calculated as $\mathrm{HD} = |h_{\mathrm{mat}} - h_{\mathrm{real}}| / h_{\mathrm{real}}$, where h_{mat} is the height as MI reaches the maximum. The definition of M-MI is given in next section.

3. M-MI ALGORITHM

The Shannon entropy of a random event with n probabilities as $p_1, p_2, \ldots, p_n$ is defined as

$$H = \sum_{i=1}^{n} p_i \log \frac{1}{p_i} = -\sum_{i=1}^{n} p_i \log p_i \quad (4)$$

Mutual information (MI) [3] is defined as

$$\mathrm{MI}(\bar{\mathbf{X}}_R, \bar{\mathbf{X}}_S) = H(\bar{\mathbf{X}}_R) + H(\bar{\mathbf{X}}_S) - H(\bar{\mathbf{X}}_R, \bar{\mathbf{X}}_S) \quad (5)$$

where the joint entropy is calculated from the joint histogram of the registered images as

$$H(\bar{\mathbf{X}}_R, \bar{\mathbf{X}}_S) = -\sum_{r,s} p_{RS}(r,s) \log_2 p_{RS}(r,s) \tag{6}$$

Normalized mutual information (NMI) [6] is calculated as

$$\mathrm{NMI}(\bar{\mathbf{X}}_R, \bar{\mathbf{X}}_S) = \frac{2\mathrm{MI}(\bar{\mathbf{X}}_R, \bar{\mathbf{X}}_S)}{H(\bar{\mathbf{X}}_R) + H(\bar{\mathbf{X}}_S)} \tag{7}$$

To reduce the overlapping effect, the gradient term taking account of both the magnitude and orientation of the gradients is considered. The gradient vectors $\nabla\mathbf{r}(\sigma)$ and $\nabla\mathbf{s}(\sigma)$ of two pixels $\mathbf{r} = [x, y, r]$ and $\mathbf{s} = [x, y, s]$ are calculated by convolving the image with the first derivatives of a Gaussian kernel scale σ [7]. The angle between gradient vectors are calculated as $\alpha_{\mathbf{r},\mathbf{s}}(\sigma) = \arccos\{[\nabla\mathbf{r}(\sigma) \cdot \nabla\mathbf{s}(\sigma)]/[|\nabla\mathbf{r}(\sigma)| \cdot |\nabla\mathbf{s}(\sigma)|]\}$.

GMI is finally defined as NMI with the gradient function of (7) as

$$\mathrm{GMI}(\bar{\mathbf{X}}_R, \bar{\mathbf{X}}_S) = G(\bar{\mathbf{X}}_R, \bar{\mathbf{X}}_S) \times \ \mathrm{NMI}(\bar{\mathbf{X}}_R, \bar{\mathbf{X}}_S) \tag{8}$$

where the gradient term is written as $G(\bar{\mathbf{X}}_R, \bar{\mathbf{X}}_S) = \sum w[\alpha_{\mathbf{r},\mathbf{s}}(\sigma)] \cdot \min[|\nabla\mathbf{r}(\sigma)|, |\nabla\mathbf{s}(\sigma)|]$ and the weighting function is set as $w[\alpha_{\mathbf{r},\mathbf{s}}(\sigma)] = \{\cos[2\alpha_{\mathbf{r},\mathbf{s}}(\sigma)] + 1\}/2$, for gradients with the same or opposite directions are favored.

Regional MI (RMI) takes account of spatial correlation of the corresponding pixels in neighborhood regions [8]. Using a square radius R to include those neighborhoods pixels around the pixel in both images, X_R and X_S, a vector $\mathbf{L}$ with $L = 2(2R+1)^2$-dimension is formed. Thus $K = (M - 2R) \times (N - 2R)$ L-dimension vectors will form a $L \times K$ matrix as $\bar{\mathbf{D}} = [\mathbf{L}_1, \ldots, \mathbf{L}_K]$. The covariance matrix of $\bar{\mathbf{D}}$ is calculated as $\bar{\mathbf{C}} = (\bar{\mathbf{D}}_0 \cdot \bar{\mathbf{D}}_0^{\mathrm{T}})/K$ and $\bar{\mathbf{D}}_0 = \bar{\mathbf{D}} - (\sum_{i=1}^{K} \mathbf{L}_i)/K$. The RMI is calculated as [8]

$$\mathrm{RMI} = H_g(\bar{\mathbf{C}}_R) + H_g(\bar{\mathbf{C}}_S) - H_g(\bar{\mathbf{C}}) \tag{9}$$

where $\bar{\mathbf{C}}$ is a $L \times L$-dimensional matrix, the matrix $\bar{\mathbf{C}}_R$ on the top left corner with $(L/2) \times (L/2)$-dimension corresponds to $\bar{\mathbf{X}}_R$, and the matrix $\bar{\mathbf{C}}_S$ with $(L/2) \times (L/2)$-dimension at the bottom right corner is due to $\bar{\mathbf{X}}_S$.

Three types of the building damage, i.e., collapsed, subsided, and deformed, are simulated. The MI of the undamaged building has a large mean and reaches the maximum around the height h_{real} with small HD. But the MI of the collapsed building shows much smaller mean and the maximum because the changes of the size and shape cause much different scattering. The subsided building shows small mean, and its HD is much larger as the regions of layover, double bounce and shadow might become narrow. Its large HD can be used to identify the subsidence. The MI of deformed building might give a moderate value with a small HD because the deformation is in varies forms. However, the image features, such as layover, double bounce, shadow etc., are certainly changed and produce the different MI from the undamaged one.

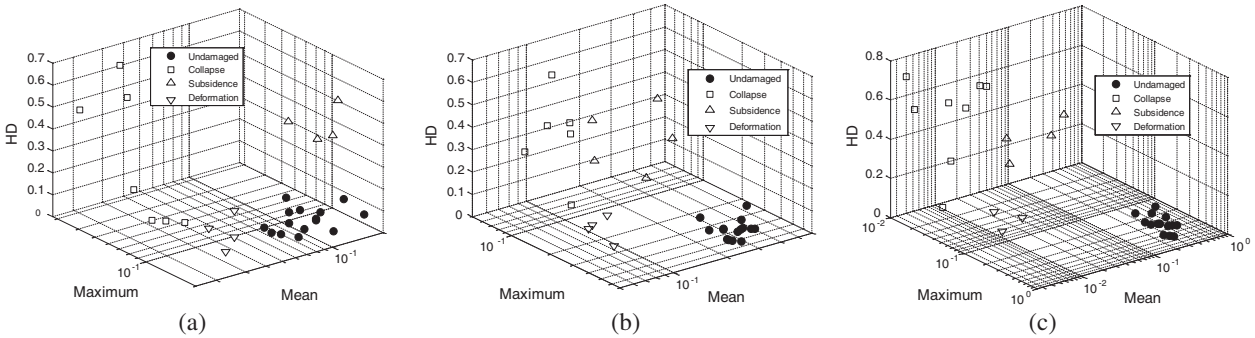

Figure 2: Buildings classifications, (a) Cosmo-NMI, (b) Cosmo-GMI, (c) Cosmo-RMI.

4. EXPERIMENTAL RESULTS

In the example of Haiti earthquake on January 12, 2010, the pre-event Ikonos optical image on September 9, 2008, the post-event GeoEye optical image on January 13, 2010, the post-event images of COSMO-SkyMed SAR on January 14, 2010 and Radarsat-2 SAR on January 16, 2010 over Port-au-Prince are collected. Total 30 buildings with large size, different aspect angles and roof angles are selected for M-MI analysis.

Using the MPA, 25 images for each selected building object under damage situations are first simulated. After registration of MI, the M-MI algorithms are applied for calculating the mean, maximum and HD between simulated and real SAR images. The results from Cosmo-Skymed SAR image are given in Fig. 2. It can be found that the undamaged and damaged buildings can be well classified based on M-MI.

5. CONCLUSION

Using pre-event optical image and post-event SAR image, the M-MI approach is presented for detection and evaluation of building damages after earthquake. Three parameters of M-MI, i.e., the mean, maximum and height deviation, can be synthesized for the detection and evaluation of undamaged, collapsed, subsided or deformed. It is believed that fully polarimetric SAR images and automatic algorithm for the building extraction can be further developed for the M-MI approach.

Recently, the same approach to analysis of the ALOS and TerraSAR image data in Japan earthquake and tsunami on March 11, 2011 are being processed.

ACKNOWLEDGMENT

This work was supported in part by the National Science Foundation of China 60971091 and 41071219, and Guanxi 2011GXNSFD018001.

REFERENCES

1. Brunner, D., G. Lemoine, and L. Bruzzone, "Earthquake damage assessment of buildings using VHR optical and SAR imagery," *IEEE Trans. Geosci. Remote Sens.*, Vol. 48, No. 5, 2403–2420, May 2010.
2. Chini, M., N. Pierdicca, and W. J. Emery, "Exploiting SAR and VHR optical images to quantify damage caused by the 2003 Bam earthquake," *IEEE Trans. Geosci. Remote Sens.*, Vol. 47, No. 1, 145–152, Jan. 2009.
3. Pluim, J. P. W., J. B. A. Maintz, and M. A. Viergever, "Mutual-information-based registration of medical images: a survey," *IEEE Trans. Medical Imaging*, Vol. 22, No. 8, 986–1004, Aug. 2003.
4. Chen, H., P. K. Varshney, and M. K. Arora, "Performance of mutual information similarity measure for registration of multitemporal remote sensing images," *IEEE Trans. Geosci. Remote Sens.*, Vol. 41, No. 11, 2445–2454, Nov. 2003.
5. Suri, S. and P. Reinartz, "Mutual-information-based registration of TerraSAR-X and Ikonos imagery in urban areas," *IEEE Trans. Geosci. Remote Sens.*, Vol. 48, No. 2, 939–949, Feb. 2010.
6. Saerndal, C., "A comparative study of association measures," *Psychometrika*, Vol. 39, No. 2, 165–187, Jun. 1974.
7. Pluim, J. P. W., J. B. A. Maintz, and M. A. Viergever, "Image registration by maximization of combined mutual information and gradient information," *IEEE Trans. Medical Imaging*, Vol. 19, No. 8, 809–814, Aug. 2000.
8. Russakoff, D. B., C. Tomasi, T. Rohlfing, and C. R. Maturer, "Image similarity using mutual information of regions," *Computer Vision-ECCV*, Vol. 3023, 596–607, 2004.
9. Xu, F. and Y.-Q. Jin, "Imaging simulation of polarimetric SAR for a comprehensive terrain scene using the mapping and projection algorithm," *IEEE Trans. Geosci. Remote Sens.*, Vol. 44, No. 11, 3219–3234, Nov. 2006.
10. Brunner, D., G. Lemoine, L. Bruzzone, and H. Greidanus, "Building height retrieval from VHR SAR imagery based on an iterative simulation and matching technique," *IEEE Trans. Geosci. Remote Sens.*, Vol. 48, No. 3, 1487–1504, Mar. 2010.

The Phenomenon of Positive Magnetoimpedance in $La_{0.75}Sr_{0.25}MnO_3$ PLD Film

Yifei Wang, **Hua Liu**, **and Jifan Hu**
School of Physics, State Key Laboratory for Crystal Materials
Shandong University, Jinan 250100, China

Abstract— In the present work, $La_{0.75}Sr_{0.25}MnO_3$ polycrystalline film was grown on Si (1 0 0) substrate by pulsed laser deposition. Negative magnetoimpedance $\Delta Z/Z_0 = -2.64\%$ was obtained under a low field of 500 Oe for the film with an 800°C annealing. For the film with a liquid nitrogen treatment after an 800°C annealing, a positive magnetoimpedance occurs at 10 MHz. The peak value of $\Delta Z/Z_0$ is 48.1% under 200 Oe. We suggested that the negative magnetoimpedance for the film with 800°C annealing is connected with a decrease of permeability induced by DC low fields, whereas the positive magnetoimpedance for the film with liquid-nitrogen treatment was connected with an increase of permeability with field, due to the existence of transverse anisotropy developed in the film during the liquid-nitrogen treatment process. With Machado-Rezende model on magnetic domain motion, we calculated the field dependence of transverse susceptibility χ. When a transverse anisotropy field H_A exists, the transverse susceptibility χ should have a peak at a field $H = H_A$.

1. INTRODUCTION

The manganese oxides $La_{1-x}A_xMnO_3$ (A = Ca, Ba, Sr and Pb) have attracted much attention due to their colossal DC magnetoresistance (CMR) effect [1, 2]. The CMR is very strong near Curie temperature. However, the magnetoresistance value of $La_{1-x}A_xMnO_3$ only reaches about 3% at room temperature under the magnetic fields of about 1 T [3]. The magnetoimpedance effects at radio frequencies have also been observed in $La_{1-x}A_xMnO_3$ manganites [4–11]. For metallic $La_{1-x}A_xMnO_3$, the magnetoimpedance strongly depends upon the transverse permeability change. Similar giant magnetoimpedance effect has been found in soft magnetic amorphous or nanocrystalline ribbons [12–16]. Few studies on magnetoimpedance of manganite film have been performed. Stanescu et al. investigated the ac transport behavior and ac magnetoresistance $\Delta R/R_0$ for $La_{0.7}Sr_{0.3}MnO_3$ polycrystalline films [17]. They found that magnetoresistance effect still exists up to 1 GHz. In the present work, the magnetoimpedance of the $La_{0.75}Sr_{0.25}MnO_3$ polycrystalline film are investigated at room temperature. Four-terminal method was used to measure the ac impedance of the film. Ac magnetoresistance of $\Delta R/R_0 = -4.63\%$, and magnetoimpedance $\Delta Z/Z_0 = -2.64\%$ were observed for the film with an 800°C annealing. Moreover, a positive giant magnetoimpedance (GMI) with a peak phenomenon in curves of $\Delta Z/Z_0 - H$ were observed for the film with liquid-nitrogen treatment after 800°C annealing, and the value of positive GMI could rich 48.1% at 10 MHz under an applied field of 200 Oe.

2. EXPERIMENTS

The $La_{0.75}Sr_{0.25}MnO_3$ thin film was grown on silicon (1 0 0) substrate by pulsed laser deposition. The depositing temperature was kept at 300°C while the depositing pressure was kept at 2.0×10^{-4} Pa. The laser energy was kept at about 10 J/cm^2, and the depositing time was 1 hour. The deposited thin film was then annealed at 800°C for 1 hour in air. X-ray diffraction study showed that film annealed at 800°C was polycrystalline. A nitrogen treatment was performed using a liquid nitrogen trap. The measurements of the magnetoimpedance were carried out with a four-terminal method using an impedance analyzer. Both 800°C annealed film and nitrogen treated film was measured with the applied DC magnetic field up to 500 Oe at room temperature.

3. RESULTS AND DISCUSSION

Figure 1 shows the AC frequency dependence of the resistance, reactance and impedance of the 800°C annealed $La_{0.75}Sr_{0.25}MnO_3$ polycrystalline film at frequency ranges $f \geqslant 5$ MHz at room temperature. The AC resistance, reactance and impedance increases with increasing AC current frequencies. Stanescu et al. investigated the $La_{0.7}Sr_{0.3}MnO_3$ polycrystalline film prepared by pulsed injection metal-organic chemical vapor deposition (MOCVD) on Si (0 0 1) substrate [17]. They found a sharp decrease of the resistance and of the magnitude of the reactance when increasing

the frequency from 100 kHz to 1 GHz, and explained it with a parallel resistive-capacitive-(RC) element, where the resistive contributions comes from the inner grains and the capacitive contributions comes from the grain boundaries. However, in our experiments, we found the 800°C annealed $La_{0.75}Sr_{0.25}MnO_3$ polycrystalline film showing simplex metallic conductivity at high frequency ranges $f \geqslant 5$ MHz at room temperature. This discrepancy may be caused by different film qualities.

Figure 2 shows the AC magnetoresistance $\Delta R/R_0$, magnetoreactance $\Delta X/X_0$ and magnetoimpedance $\Delta Z/Z_0$ of the 800°C annealed $La_{0.75}Sr_{0.25}MnO_3$ polycrystalline film at 10 MHz at room temperature. The AC resistance, reactance and impedance drop with an increase of applied DC field. The negative magnetoimpedance is connected with the large permeability change induced by DC magnetic fields. The transverse permeability could be affected by the applied DC field, and change the impedance of the $La_{0.75}Sr_{0.25}MnO_3$ polycrystalline film via penetration depth. The value of $\Delta X/X_0$ is about -0.43%, and $\Delta Z/Z_0$ is about -2.64%, and the value of AC magnetoresistance $\Delta R/R_0$ is -4.63% under an applied field of 500 Oe, which is more sensitive than the DC CMR effect at low fields. However, it is still not large enough for application.

Figure 3 shows the DC field dependence of magnetoimpedance $\Delta Z/Z_0$ for liquid-nitrogen treated $La_{0.75}Sr_{0.25}MnO_3$ polycrystalline film at 10 MHz at room temperature. With an increase of DC field, there is a peak phenomenon in curves of $\Delta Z/Z_0 - H$. Such peak phenomenon has been observed in giant magnetoimpedance in soft magnetic amorphous CoFeSiB wires/films [12], which is due to the transverse/circular magnetic anisotropy. Below transverse anisotropy field H_A, there

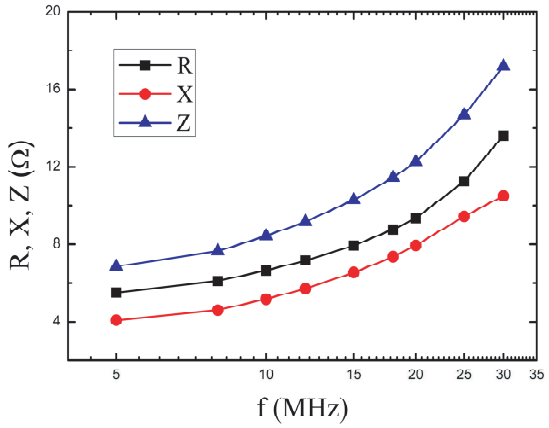

Figure 1: The AC frequency dependence of the resistance, reactance and impedance of the 800°C annealed $La_{0.75}Sr_{0.25}MnO_3$ polycrystalline film at frequency ranges $f \geqslant 5$ MHz at room temperature.

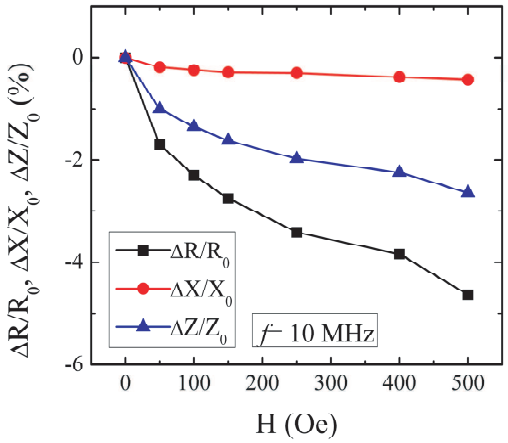

Figure 2: The AC magnetoresistance $\Delta R/R_0$, magnetoreactance $\Delta X/X_0$, and magnetoimpedance $\Delta Z/Z_0$ of the 800°C annealed $La_{0.75}Sr_{0.25}MnO_3$ polycrystalline film at 10 MHz at room temperature.

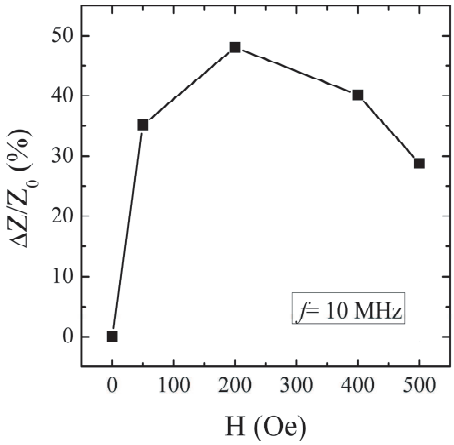

Figure 3: The DC field dependence of magnetoimpedance $\Delta Z/Z_0$ for nitrogen treated $La_{0.75}Sr_{0.25}MnO_3$ polycrystalline film at 10 MHz at room temperature.

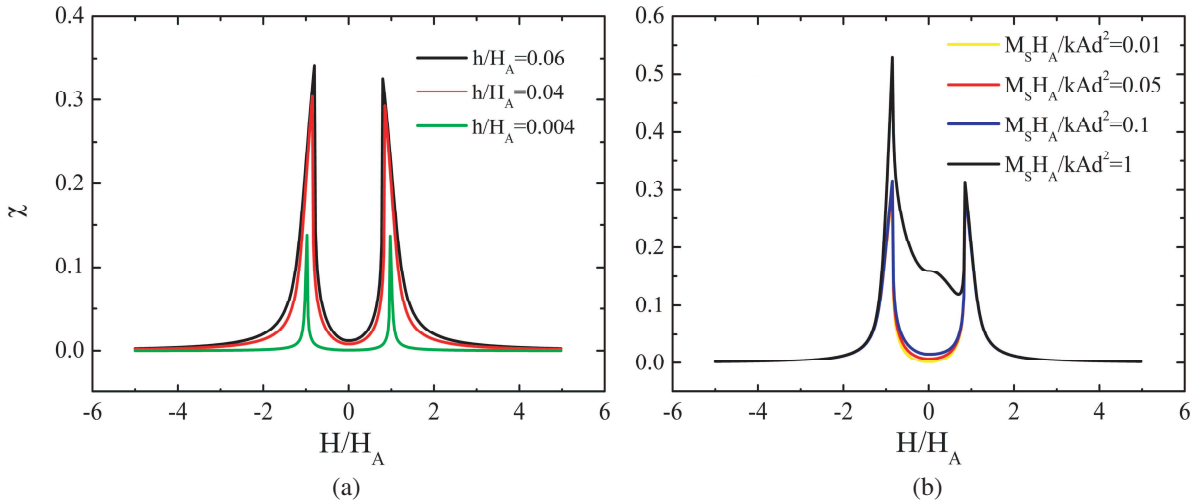

Figure 4: The field dependence of transverse susceptibility χ with different parameters: (a) $h/H_A = 0.06$, 0.04, 0.004; $M_S H_A/kAd^2 = 0.05$, (b) $M_S H_A/kAd^2 = 0.01$, 0.05, 0.1, 1; $h/H_A = 0.04$.

is an enhancement of permeability μ, leading to the increase of impedance. Similarly, the peak phenomena in liquid-nitrogen treated $La_{0.75}Sr_{0.25}MnO_3$ film may be connected with the transverse anisotropy developed in the liquid-nitrogen treatment process. The thermal expansion coefficients for $La_{0.75}Sr_{0.25}MnO_3$ film and Si (1 0 0) substrate are different. The liquid-nitrogen treatment could lead to a large strain at the interface between the film and substrate. The value of $\Delta Z/Z_0$ for $La_{0.75}Sr_{0.25}MnO_3$ film is 48.1% under an applied DC field of 200 Oe, which is much larger than the value of DC CMR effects. Such large magnetoimpedance may be potential for some applications such as magnetic sensors.

With Machado-Rezende model on magnetic domain motion [18], we calculated the field dependence of transverse susceptibility χ with different parameters, and results are shown in Fig. 4. Fig. 4(a) shows the influence of h/H_A on the ratio H/H_A dependence of transverse susceptibility χ. The value of h/H_A was chosen as 0.06, 0.04 and 0.004, value of $M_S H_A/kAd^2$ was chosen as 0.05. Here h is the transverse field created by the current, H is the dc magnetic field, $H_A = 2K/M_S$ is the anisotropy field of ribbon or film, K, M_s are anisotropy constant and saturation magnetization of film, k is the mean wall stiffness and A is the wall area per unit volume. One can see from Fig. 4(a) that the transverse susceptibility χ undergoes a peak at $H = H_A$. The transverse susceptibility χ increases with an increase of h/H_A from 0.004 to 0.06. Fig. 4(b) shows the influence of $M_S H_A/kAd^2$ on the ratio H/H_A dependence of transverse susceptibility χ, here h/H_A is chosen as 0.04. For low values of $M_S H_A/kAd^2 = 0.01$, 0.05, and 0.1, transverse susceptibility χ increases with an increase of H. There are little differences among three $\chi - H/H_A$ curves with $M_S H_A/kAd^2 = 0.01$, 0.05, and 0.1. However, for $M_S H_A/kAd^2 = 1$, with an increase of H/H_A, there is a decrease of χ at low field at first, then undergoes a peak at $H = H_A$, and finally drops again. Anyway, when a transverse anisotropy field H_A exists, transverse susceptibility χ should have a peak at $H = H_A$.

4. CONCLUSIONS

In the present work, $La_{0.75}Sr_{0.25}MnO_3$ polycrystalline film was deposited on Si (1 0 0) substrate. An ac magnetoresistance of $\Delta R/R_0 = -4.63\%$, and magnetoimpedance $\Delta Z/Z_0 = -2.64\%$ were obtained for the 800°C annealed film. After a liquid-nitrogen treatment, the $La_{0.75}Sr_{0.25}MnO_3$ film showed a positive magnetoimpedance effect. Peak phenomenon is observed, and a giant magnetoimpedance of 48.1% could be obtained under 200 Oe, showing sensitive response to low fields. In addition to CMR effects, the GMI effect in the $La_{0.75}Sr_{0.25}MnO_3$ polycrystalline film on Si substrate after liquid nitrogen treatment might have potential applications.

ACKNOWLEDGMENT

This work was supported by National Natural Science Foundation of China (Nos. 50872074 and 50872069).

REFERENCES

1. Von Helmolt, R., J. Wecker, B. Holzapfel, L. Schultz, and K. Samwer, "Giant negative magnetoresistance in perovskitelike $La_{2/3}Ba_{1/3}MnO_x$ ferromagnetic films," *Phys. Rev. Lett.*, Vol. 71, No. 14, 2331–2333, 1993.
2. Jin, S., T. H. Tiefel, M. McCormack, R. A. Fastnacht, R. Ramesh, and L. H. Chen, "Thousandfold change in resistivity in magnetoresistive La-Ca-Mn-O films," *Science*, Vol. 264, No. 5157, 413–415, 1994.
3. Coey, J. M. D, "Powder magnetoresistance (invited)," *J. Appl. Phys.*, Vol. 85, No. 8, 5576–5581, 1999.
4. Hu, J. and H. Qin, "Magnetoimpedance effect in $La_{0.67}Ba_{0.33}MnO_3$ under low dc magnetic fields," *Solid State Commun.*, Vol. 116, 159–162, 2000.
5. Hu, J. and H. Qin, "Magnetoimpedance effect in $La_{0.7}Sr_{0.3}MnO_3$," *J. Magn. Magn. Mater.*, Vol. 234, 419–422, 2001.
6. Belevtsev, B. I., A. Y. Kirichenko, N. T. Cherpak, G. V. Golubnichaya, I. G. Maximchuk, E. Y. Beliayev, A. S. Panfilov, and J. Fink-Finowicki, "Giant magnetic-field changes in radio-frequency absorption in $La_{0.67}Sr_{0.33}MnO_3$ near the Curie temperature," *J. Magn. Magn. Mater.*, Vol. 281, 97–104, 2004.
7. Nadeem, M., M. J. Akhtar, and A. Y. Khan, "Effects of low frequency near metal-insulator transition temperatures on polycrystalline $La_{0.65}Ca_{0.35}Mn_{1-y}FeyO_3$ (where y = 0.05–0.10) ceramic oxides," *Solid State Commun.*, Vol. 134, 431–436, 2005.
8. Ghatak, S. K., B. Kaviraj, and T. K. Dey, "Giant magnetoimpedance in Ag-doped $La_{0.7}Sr_{0.3}MnO_3$," *J. Appl. Phys.*, Vol. 101, 023910–023915, 2007.
9. Dutta, P., P. Dey, and T. K. Nath, "Effect of nanometric grain size on room temperature magnetoimpedance, magnetoresistance, and magnetic properties of $La_{0.7}Sr_{0.3}MnO_3$ nanoparticles," *J. Appl. Phys.*, Vol. 102, 073906–073903, 2007.
10. Qin, H., J. Hu, B. Li, Y. Hao, J. Chen, and M. Jiang, "Magnetoimpedance in $La_{0.67}Pb_{0.33}MnO_3$ manganite prepared by sol-gel method," *J. Magn. Magn. Mater.*, Vol. 320, 2770–2773, 2008.
11. Rebello, A. and R. Mahendiran, "Influence of length and measurement geometry on magnetoimpedance in $La_{0.7}Sr_{0.3}MnO_3$," *Appl. Phys. Lett.*, Vol. 96, 032502, 2010.
12. Panina, L. V., K. Mohri, T. Uchiyama, M. Noda, and K. Bushida, "Giant magneto-impedance in Co-rich amorphous wires and films," *J. Appl. Phys.,* Vol. 31, No. 2, 6198–6207, 1994.
13. Beach, R. S. and A. E. Berkowitz, "Giant magnetic field dependent impedance of amorphous FeCoSiB wire," *Appl. Phys. Lett.*, Vol. 64, 3652–3654, 1994.
14. Velázquez, J., M. Vázquez, D.-X. Chen, and A. Hernando, "Giant magnetoimpedance in nonmagnetostrictive amorphous wires," *Phys. Rev. B*, Vol. 50, No. 22, 16737–16740, 1994.
15. Knobel, M. and K. R. Pirota, "Giant magnetoimpedance: Concepts and recent progress," *J. Magn. Magn. Mater.*, Vol. 242–245, 33–40, 2002.
16. Phan, M. H. and H. X. Peng, "Giant magnetoimpedance materials: Fundamentals and applications," *Prog. Mater. Sci.*, Vol. 53, 323–420, 2008.
17. Stanescu, D. and P. Xavier, "Evidence of the magnetoimpedance effect up to microwave frequencies in polycrystalline $La_{0.7}Sr_{0.3}MnO_3$ films," *J. Appl. Phys.*, Vol. 102, 073707, 2006.
18. Machado, F. L. A. and S. M. Rezende, "A theoretical model for the giant magnetoimpedance in ribbons of amorphous soft-ferromagnetic alloys," *J. Appl. Phys.*, Vol. 79, 6558–6560, 1996.

Magnetoimpedance in Perovskite $La_{0.7}Sr_{0.3}MnO_3$ Ceramics

Hua Liu, **Qingfang Huang**, **and Jifan Hu**
State Key Laboratory for Crystal Materials, School of Physics
Shandong University, Jinan 250100, China

Abstract— The $La_{0.7}Sr_{0.3}MnO_3$ manganite prepared by sintering method exhibits a giant magnetoimpedance (GMI). Its AC magnetoresistance $\Delta R/R_0$ could reach -9.53%, magnetoimpedance $\Delta Z/Z$ is -3.05% at 200 kHz under a low field of 1.8 kOe at room temperature, which is more sensitive than its dc colossal magnetoresistance. With an increase of ac frequency, there is a maximum of the GMI effects. To investigate the intrinsic origin of the GMI effect, electrodynamics theory was used to simulate the frequency dependence of magnetoimpedance effect. The influences of frequency, permeability and sample thickness upon the effect of giant magnetoimpedance were investigated.

1. INTRODUCTION

Perovskite manganites $La_{1-x}A_xMnO_3$ (A = Ca, Ba, Sr and Pb) have attracted great attention due to the colossal magnetoresistance (CMR) [1]. However, a large field of several teslas is needed to obtain CMR. On the other hand, $La_{1-x}A_xMnO_3$ based manganites also exhibit giant magnetoimpedance in radio frequencies ($\sim$ MHz) at very low fields [2–4]. The GMI effect has also been found in soft magnetic ribbons and wires [5, 6]. The resistivities of manganites are much larger than those of metallic ribbons and wires. In contrast, the permeability values of the former are much smaller than those of the later. In the present work, the GMI effect of LaSrMnO sintered ceramics was investigated. To investigate the origin of the GMI effect in LaSrMnO manganite, we also simulated the frequency dependence of magnetoimpedance effect with electrodynamics model.

2. EXPERIMENTS

The $La_{0.7}Sr_{0.3}MnO_3$ ceramics was prepared by the conventional solid state sintering method. The magnetoimpedance behavior at room temperature for $La_{0.7}Sr_{0.3}MnO_3$ sintered ceramics was measured using an impedance analyzer (HP4294A), where the amplitude of the ac currents was 20 mA. The sample was connected to the analyzer with the accessory test lead with four coaxial cables. The longitudinal magnetoimpedance measurement was performed, where both ac currents and dc magnetic fields were applied along the sample length.

3. RESULTS AND DISCUSSION

Figure 1 shows frequency dependence of resistance R, reactance X and impedance Z for $La_{0.7}Sr_{0.3}MnO_3$ ceramics at 300 K for the 2.5 mm sample. The impedance as well as the resistance and reactance increase with increase in AC frequency above a frequency of 100 kHz, mainly due to skin effect of metal phase occurred in the $La_{0.7}Sr_{0.3}MnO_3$ manganite at room temperature below its Curie temperature. Fig. 2 shows the field dependence of ac magnetoresistance $\Delta R/R_0$, magnetoreactance $\Delta X/X_0$ and magnetoimpedance $\Delta Z/Z_0$ at 2 MHz for $La_{0.7}Sr_{0.3}MnO_3$ sintered sample at room temperature. The values of $\Delta R/R_0$, $\Delta X/X_0$ and $\Delta Z/Z_0$ are negative. The R, X and Z all decrease with the increase of the field. The curves $\Delta X/X_0$ vs. H and Z/Z_0 vs. H almost coincides. Values of $\Delta X/X_0$ and $\Delta Z/Z_0$ are much smaller than those of $\Delta R/R_0$. The thicker sample ($D = 2.5$ mm) has larger $\Delta R/R_0$, $\Delta X/X_0$ and $\Delta Z/Z_0$ than the thinner one ($D = 1.5$ mm), where D is the sample thickness.

The frequency dependence of magnetoimpedance $\Delta Z/Z_0$, magnetoresistance $\Delta R/R_0$ and magnetoreactance $\Delta X/X_0$ under $H = 1800$ Oe at room temperature for $La_{0.7}Sr_{0.3}MnO_3$ sintered sample ($D = 2.5$ mm) were measured, and results were shown in Fig. 3. The value of $\Delta R/R_0$ is about -0.79% at a low frequency of 100 kHz. With increasing frequency, the $\Delta R/R_0$ increases at first, experiences its maximum $(\Delta R/R_0)_{\max}$ of -9.53% at 2 MHz, and finally drops again. The magnetoimpedance $\Delta Z/Z_0$ has a similar trend as the magnetoreactance $\Delta X/X_0$. The maximum value of $\Delta Z/Z_0 = -3.05\%$ occurs at 200 kHz.

The complex impedance $Z = R + iX$ of a metallic flake with thickness $D = 2d$, width l and length L, when an AC current flows through the flake along the length direction, can be expressed as [7]

$$Z = R_{DC} ikd \coth(ikd) \tag{1}$$

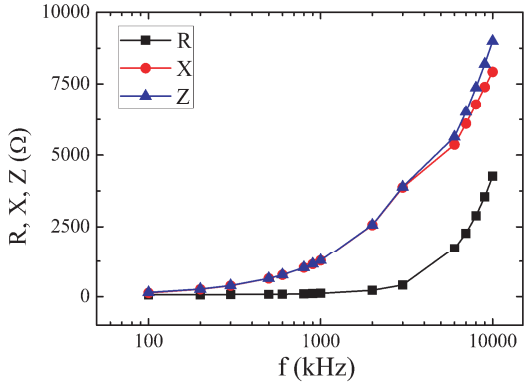

Figure 1: The frequency dependence of resistance R, reactance X and impedance Z for $La_{0.7}Sr_{0.3}MnO_3$ ceramics.

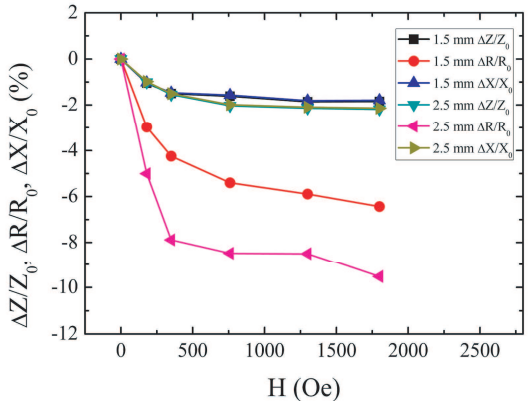

Figure 2: The field dependence of ac magnetoresistance $\Delta R/R_0$, magnetoreactance $\Delta X/X_0$ and magnetoimpedance $\Delta Z/Z_0$ for $La_{0.7}Sr_{0.3}MnO_3$ ceramics with different thickness.

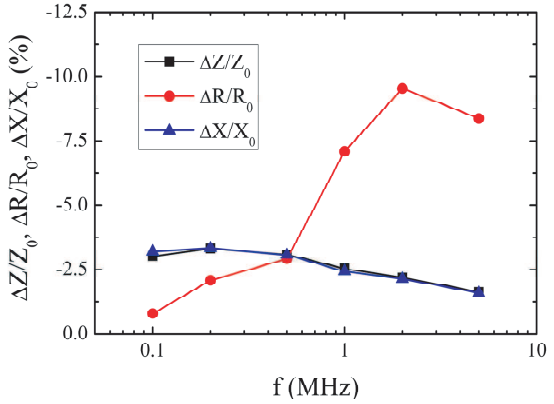

Figure 3: The frequency dependence of magnetoimpedance $\Delta Z/Z_0$, magnetoresistance $\Delta R/R_0$ and magneto- reactance $\Delta X/X_0$ under $H = 1800$ Oe at room temperature for $La_{0.7}Sr_{0.3}MnO_3$.

with

$$k = \frac{1+i}{\delta} \tag{2}$$

where

$$R_{DC} = \frac{L\rho}{2dl} \tag{3}$$

is DC resistance of the flake, δ is the penetration depth

$$\delta = \sqrt{\frac{2\rho}{\mu_0 \mu \omega}} \tag{4}$$

The complex permeability can be expressed as [8]

$$\mu = \frac{\mu_i}{1+(\frac{\omega}{\omega_r})^2} + i\frac{\mu_i(\frac{\omega}{\omega_r})}{1+(\frac{\omega}{\omega_r})^2} \tag{5}$$

The application of magnetic field could induce the changes of permeability μ and relaxation frequency ω_r [9]. Fig. 4(a) shows the frequency dependence of $\Delta Z/Z_0$ with decrease of permeability μ, where we chose $\rho = 10^{-4}\,\Omega\cdot$m, $D = 2d = 2.5$ mm, $\mu_i(0) = 30$ [10], $\omega_r(0) = 2\times10^7$ Hz for $H = 0$, $\mu_i(H_1) = 20$, $\omega_r(H_1) = 2\times10^7$ Hz for a field H_1. The negative giant magnetoimpedance could be observed. However, the values of $\Delta Z/Z_0$, $\Delta R/R_0$ and $\Delta X/X_0$ coincide at high frequencies, which is consistent with the experimental results (see Fig. 3). Fig. 4(b) shows the frequency dependence of $\Delta Z/Z_0$ with decrease of permeability μ, where we chose $\mu_i(0) = 30$, $\omega_r(0) = 2\times10^7$ Hz for

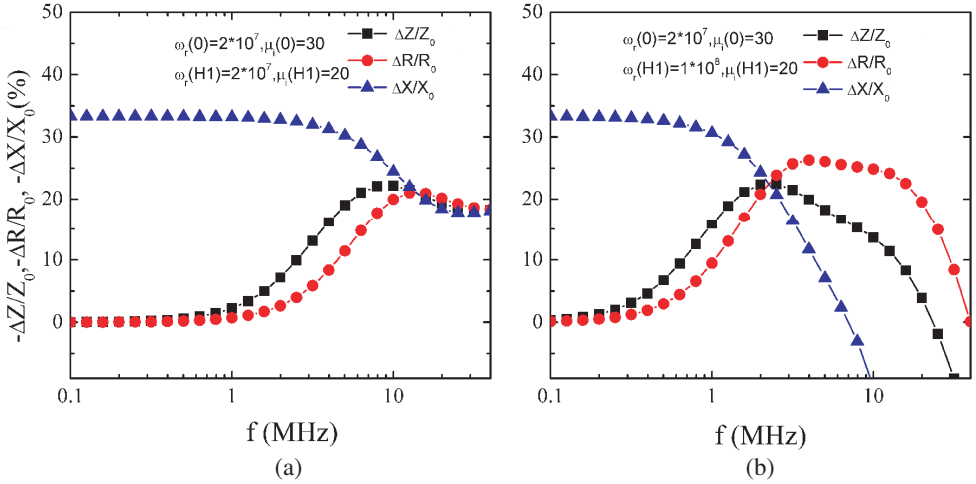

Figure 4: The simulation on the frequency dependence of $\Delta R/R_0$, $\Delta X/X_0$ and $\Delta Z/Z_0$ with $\rho = 10^{-4}\,\Omega\cdot$m, $D = 2.5$ mm and (a) $\mu_i(0) = 30$, $\omega_r(0) = 2\times10^7$ Hz for $H = 0$, $\mu_i(H_1) = 20$, $\omega_r(H_1) = 2\times10^7$ Hz for a field H_1; (b) $\mu_i(0) = 30$, $\omega_r(0) = 2\times10^7$ Hz for $H = 0$, $\mu_i(H_1) = 20$, $\omega_r(H_1) = 1\times10^8$ Hz for a field H_1.

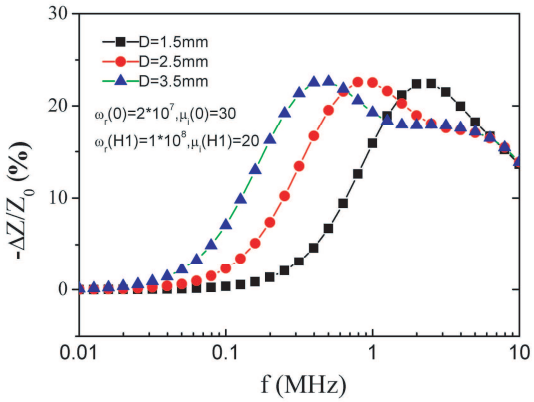

Figure 5: The simulation for thickness dependence of $\Delta Z/Z_0$ with $\rho = 10^{-4}\,\Omega\cdot$m, $D = 1.5$, 2.5 and 3.5 mm, $\mu_i(0) = 30$, $\omega_r(0) = 2\times10^7$ Hz for $H = 0$, $\mu_i(H_1) = 20$, $\omega_r(H_1) = 1\times10^8$ Hz for a field H_1.

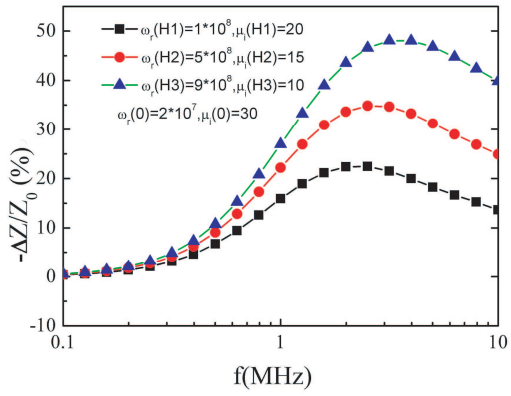

Figure 6: The frequency dependence of $\Delta Z/Z_0$ with different initial permeability μ_i and relaxation frequency ω_r.

$H = 0$, $\mu_i(H_1) = 20$, $\omega_r(H_1) = 1\times10^8$ Hz for a field H_1. Results indicated that with decrease of μ_i and an increase of ω_r, the nonzero $\Delta Z/Z_0$ could be obtained. The $\Delta Z/Z_0$ shows a maximum at a certain frequency. The $\Delta X/X_0$ drops with an increase of frequency. $\Delta R/R_0$, $\Delta X/X_0$ and $\Delta Z/Z_0$ intersects each other, similar to the experimental results. However, the calculated $\Delta R/R_0$ has a much lower maximum than that of the experimental results. It has been also found that both variations of permeability μ and relaxation frequency ω_r should be considered in simulation of GMI effect for amorphous CoFeSiB ribbons [9].

We also simulated the thickness dependence of $\Delta Z/Z_0$, and results are shown in Fig. 5, where we chose $\rho = 10^{-4}\,\Omega\cdot$m, $D = 1.5$, 2.5 and 3.5 mm, $\mu_i(0) = 30$, $\omega_r(0) = 2\times10^7$ Hz for $H = 0$, $\mu_i(H_1) = 20$, $\omega_r(H_1) = 1\times10^8$ Hz for a field H_1. With an increase of thickness, the maximum of $\Delta Z/Z_0$ shifts to lower frequency. The skin effect is greater for thicker sample. Fig. 6 shows the simulation on the frequency dependence of $\Delta Z/Z_0$, where we chose $\rho = 10^{-4}\,\Omega\cdot$m, $D = 2.5$ mm, $\mu_i(0) = 30$ [10], $\omega_r(0) = 2\times10^7$ Hz for $H = 0$, $\mu_i(H_1) = 20, \omega_r(H_1) = 1\times10^8$ Hz for a field H_1, $\mu_i(H_2) = 15$, $\omega_r(H_2) = 5\times10^8$ Hz for H_2, and $\mu_i(H_3) = 10$, $\omega_r(H_3) = 9\times10^8$ Hz for H_3. Fig. 6 represents the effect of GMI with different fields.

4. CONCLUSIONS

The $La_{0.7}Sr_{0.3}MnO_3$ manganite prepared by sintering method exhibits a giant magnetoimpedance. Our simulation based on the electrodynamics theory and magnetic domain model shows that the

magnetoimpedance is connected mainly with the change of permeability, via the penetration depth when a field is applied. In fact, both variations of permeability μ and relaxation frequency ω_r should be considered in simulation of GMI effect.

ACKNOWLEDGMENT

This work is supported by National Natural Science Foundation of China (Grant Nos. 50872074, 50872069 and 51072103).

REFERENCES

1. Von Helmolt, R., J. Wecker, B. Holzapfel, L. Schultz, and K. Samwer, "Giant negative magnetoresistance in perovskitelike $La_{2/3}Ba_{1/3}MnO_x$ ferromagnetic films," *Phys. Rev. Lett.*, Vol. 71, No. 14, 2331–2333, 1993.
2. Hu, J. F. and H. W. Qin, "Magnetoimpedance effect in $La_{0.67}Ba_{0.33}MnO_3$ under low dc magnetic fields," *Solid State Commun.*, Vol. 116, No. 2893, 159–162, 2000.
3. Hu, J. F. and H. W. Qin, "Magnetoimpedance effect in $La_{0.7}Sr_{0.3}MnO_3$," *J. Magn. Magn. Mater.*, Vol. 234, No. 3, 419–422, 2000.
4. Qin, H. W., J. F. Hu, J. Chen, Y. Z. Wang, and Z. X. Wang, "Giant magnetoimpedance and colossal magnetoresistance in $La_{0.75}Sr_{0.25}MnO_3$ at room temperature," *J. Appl. Phys.*, Vol. 91, No. 12, 10003–10006, 2002.
5. Jin, S., T. H. Tiefel, M. McCormack, R. A. Fastnacht, R. Ramesh, and L. H. Chen, "Thousandfold change in resistivity in magnetoresistive La-Ca-Mn-O films," *Science*, Vol. 264, No. 5157, 413–415, 1994.
6. Beach, R. S. and A. E. Berkowitz, "Giant magnetic field dependent impedance of amorphous FeCoSiB wire," *Appl. Phys. Lett.*, Vol. 64, No. 26, 3652–3654, 1994.
7. Panina, L. V., K.Mohri, K. Bushida, and M. Noda, " Giant magneto-impedance and magneto-inductive effects in amorphous alloys," *J. Appl. Phys.*, Vol. 76, No. 10, 6198–6203, 1994.
8. Wan, D. F. and X. L. Ma, *Magnetic Physics*, Electronic Press, Beijing, 1999.
9. Hu, J. F., H. W. Qin, T. Han, and J. Chen, "Giant magnetoimpedance in $(Co_{0.85}Fe_{0.06}Nb_{0.02}Ni_{0.07})_{75}Si_{10}B_{15}$ amorphous ribbon," *Mater. Trans.*, Vol. 45, No. 3, 812–817, 2004.
10. Hu, J. F., H. W. Qin, Y. F. Li, and B. Wang, "Giant magnetoimpedance and permeability change in $La_{2/3}Sr_{1/3}MnO_3$ manganite under low fields," *J. Magn. Magn. Mater.*, Vol. 322, No. 21, 3245–3249, 2010.

Investigation of the Electrical Properties of BCN-codoped TiO_2 Thin Film Using Impedance Spectroscopy

Ling Zhang, Yongfang Zhang, Liangguo Yan, and Fang He
School of Resources and Environment, University of Jinan, Jinan 250022, China

Abstract— Titanium dioxide has attracted much attention in the past decades. When it was doped by some elements, such as C, N, P, S and B, the conductibility will be obviously changed. In this work, the BCN-doped TiO_2 with nanostructured-film was fabricated by co-deposit method. The structure was studied by X-ray diffraction measurement. The microstructure was observed by XPS. The investigation of ac impedance spectra for BCN-doped TiO_2 thin film was performed. The grain resistance, resistance of grain boundary, and the capacitance in the thin film were determined from impedance technique.

1. INTRODUCTION

Recently, much progress has been achieved in the field of visible-light-active TiO_2 by incorporation of various dopants into its lattice. Especially the doping of nonmetal, such as nitrogen, fluorine, chlorine, sulfur, boron and carbon [1–5]. Some studies have been reported that doping of nonmetal showed dramatic improvement over undoped TiO_2 in its optical absorption and photocatalytic activity under visible light. Asahi et al. theoretically calculated the band structure of the N-doped TiO_2 and concluded that the visible light sensitivity was due to the narrowing of the band gap by mixing the N_2p and O_2p states [2, 6, 7]. An additional contribution to the impedance arises from the larger scale microstructural elements, such as grain boundaries and remote electrical contacts. From the analysis of impedance data, relaxation processes at the tip-surface junction, grain boundaries, and electrodes can be differentiated according to characteristic time constants [8, 9]. Combination of this analysis with spatially resolved impedance imaging yields frequency, bias, and position-dependent information on microscopic transport properties. In this paper, the BCN-doped TiO_2 with nanostructured-film was fabricated by co-deposit method.The structure was studied by X-ray diffraction measurement. The microstructure was observed by XPS. The investigation of ac impedance spectra for BCN-doped TiO_2 thin film was performed. The resistance and impedance value in deferent frequency for the thin film were determined from impedance technique.

2. SECTION 1

2.1. Experimental Procedure

The preparation of TiOBCN includes the use of the precursors $Ti(OH)_4$ and BCN, and subsequent calcination. Detailed procedures are described below.

The $Ti(OH)_4$ was prepared by precipitation as described below. The 0.005 mol $TiCl_4$ solution was cooled down $-10°$C below in ice water. Then, 28 mL of H_2O_2 solution (30%) was dropped under constant stirring to obtain a transparent, complex compound. Next, a strong NH_3-H_2O aqueous solution (25%) was added dropwise into the transparent yellow precursors resulting in a pH of 10. The transparent yellow precursors were heated to 50°C under constant stirring to a obtain yellow precipitate, which was then filtered, thoroughly washed with distilled water and dried overnight at 70°C. Finally, the prepared $Ti(OH)_4$ was calcined at 400°C for 4 h to yield TiO_2. Graphite BCN powder was synthesized by high temperature anneals. The resulting $Ti(OH)_4$ and BCN were mixed thoroughly at a mass ratio 10 : 1. This mixture was then calcined at 400° for 4 h for the synthesis of TiOBCN, then added some binder to the TiOBCN power formed film.

2.2. Results and Discussion

The crystalline phases of the prepared samples were measured by X-ray diffraction (XRD) using a Rigaku D/Max III. V X-ray diffrac-tometer with Cu Kα radiation (1.5406 Å) at 40 kV and 40 mA and a secondary graphite monochromator. Measurements were recorded in steps of 0.025°, with a count time of 2 s in the 2θ range of 20°–70°. Fig. 1 shows XRD patterns of the synthesized TiOBCN, and the precursor materials of BCN. We can see that BCN has graphite-like turbostatic structures. The pattern exhibited (002) diffraction characterized as an interlayer spacing, and a (100) diffraction, which coincides with the reported diffraction data for BCN. These data imply that crystalline BCN has been formed, while the TiOBCN is in the amorphous phase.

Figure 2 shows the XPS spectra for C1s, N1s and B1s for BCN-TiO_2. The C1s spectrum revealed the presence of a strong peak at 284.6 eV and a weak peak at 288.5 eV which can be ascribed to elemental carbon (285 eV) located within the tetrahedral and octahedral interstices existing within the anatase crystal, and the carbonate species adsorbed on the surface (288 eV). In addition, a peak around 281.5 eV is suggested to result from carbon substituting oxygen atoms a Ti-C bond, In our work, the mainly form of the carbon incorporated in the TiO_2 matrix was present as elemental carbon,with only a small amount of carbonate species in the interstices within the anatase crystal and little amount on the surface.

Figure 3 shows the impedance spectroscopy result of TiOBCN thin film at room temperature. Here, as the frequency from 10 MHz to 110 MHz, the overall impedance of the thin film for TiOBCN

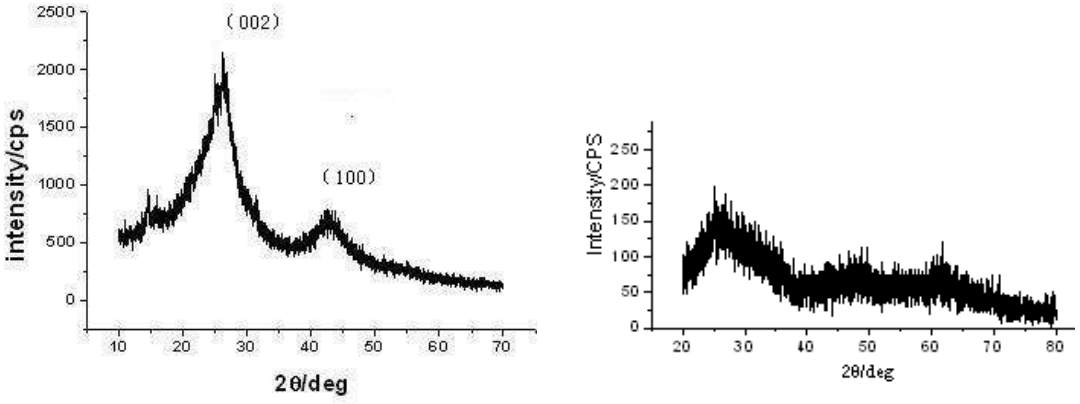

Figure 1: XRD patterns of the BCN (L) and TiOBCN (R).

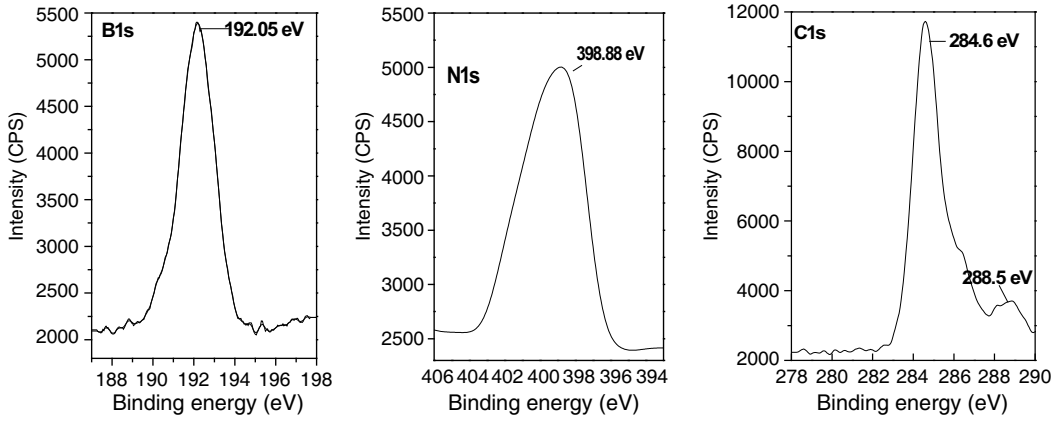

Figure 2: The XPS spectra for C1s, N1s and B1s for BCN-TiO_2.

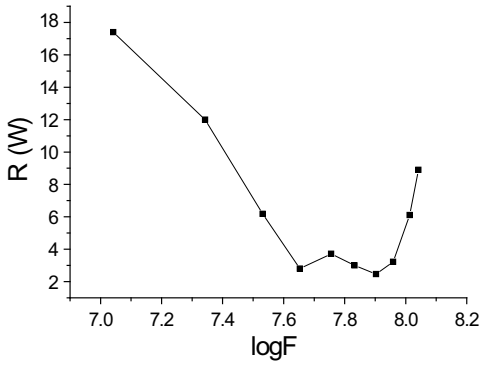

Figure 3: The impedance result of TiOBCN thin film.

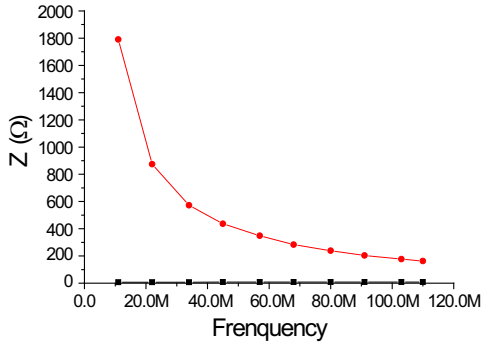

Figure 4: The resistance of TiOBCN thin film.

decreases. Fig. 4 is the resistance of TiOBCN thin film in deferent frequency. It shows that with the frequency increases, the resistance decreases first, then increases again.

3. CONCLUSIONS

The BCN-doped TiO_2 with amorphous phase and nanostructured-film was fabricated by co-deposit method. The XPS spectra shows that C1s spectrum revealed the presence of a strong peak at 284.6 eV and a weak peak at 288.5 eV; and the peak around 281.5 eV is formed a Ti-C bond; and B is in B^{x+}. With the frequency from 10 MHz to 110 MHz, the overall impedance of the thin film for TiOBCN decreases. And the resistance of TiOBCN decreases first, then increases again.

ACKNOWLEDGMENT

The work was financially supported by the Shangdong Natural Science Foundation (ZR2010BL002).

REFERENCES

1. Fujishima, A., T. N. Rao, D. A. Tryk, and J. Photochem, *Photobiol. C*, Vol. 1, 1–21, 2000.
2. Asahi, R., T. Morikawa, T. Ohwaki, K. Aoki, and Y. Taga, *Science*, Vol. 293, 269–271, 2001.
3. Sato, S., R. Nakamura, and S. Abe, *Appl. Catal. A*, Vol. 284, 131–137, 2005.
4. Rehman, S., R. Ullah, A. M. Butt, and N. D. Gohar, *J. Haza. Mater.*, Vol. 170, 560–569, 2009.
5. Ohno, T., M. Akiyoshi, T. Umebayashi, K. Asai, T. Mitsui, and M. Matsamura, *Appl. Catal. A*, Vol. 265, 115–121, 2004.
6. Ohno, T., T. Tsubota, Y. Nakamura, and K. Sayama, *Appl. Catal. A*, Vol. 288, 74, 2005.
7. Somekawa, S., Y. Kusumoto, M. Ikeda, B. Ahmmad, and Y. Horie, *Catal. Commun.*, Vol. 9, 437, 2008.
8. Jiang, S. P., J. G. Love, and S. P. S. Badwal, *Key Eng. Mater.*, Vol. 81, 125–126, 1997.
9. Macdonald, J. R. and W. B. Johnson, *Impedance Spectroscopy: Emphasizing Solid Materials and Systems*, edited by J. R. Macdonald, Wiley, New York, 1987.

Method of Measuring the Range from the UWB Borehole Logging Tool to the Oil-water Contact

M. I. Epov[1], **V. L. Mironov**[2], **and K. V. Muzalevskiy**[2]

[1]Trofimuk Institute of Petroleum Geology and Geophysics, SB, RAS, Russia
[2]Kirensky Institute of Physics, SB, RAS, Reshetnev Siberian State Aerospace University, Russia

Abstract— In this paper, a method was worked out to determine the distance from the borehole, horizontally drilled through oil stratum, to the oil-water contact (OWC), using the mathematical model [1] for an ultra-wideband electromagnetic pulse borehole radar (BHR). We simulated pulse shape voltages at the outputs of receiving antennas spaced along the borehole to determined their specific delay times relative to the pulse driver of the transmitting antenna. There was proposed the simple formula to calculate the distance from BHR to the OWC using this delay times. This formula was tasted with the use of the delay times simulated and measured. For simulation, the values of complex dielectric permittivity of the oil saturated rock and water saturated rock were assigned the refractive mixing dielectric model substantiated in [2]. The proposed method was experimentally tested using a laboratory prototype model of the BHR with the pulse duration 2 ns and a specific laboratory set up to physically simulate the oil-water contact environment. Having not used any a priori information about permittivity values for both the oil and water saturated rocks, the error of the distance determined proved to be of 2.3%.

1. INTRODUCTION

Geosteering electromagnetic logging tools are widely used for well placement technology [4]. Well placement technology helps optimize horizontal well position in order to minimize construction cost and risk. In order to develop methods for the detection of oil reservoir interfaces we made a laboratory instrument of borehole radar. The borehole radar considered operates nanosecond pulses using one transmitting and receiving dipole antennas with resistive elements. The borehole radar math model developed takes into account the processes of emitting and receiving by the finite size antennas taking into account impact of a sonde housing alongside with the contribution of the wave field reflected at the bed boundary. To model a voltage at the output of the receiving antenna, a method of auxiliary sources (MAS) [1] is applied. This model can also be developed using the method of moment (MoM). But as shown in [3], the MoM is more time-consuming as compared with the MAS. We generalized [1] the MAS to make it applicable to time domain analysis of the pulse waveforms propagating through a frequency dispersive medium. Based on the proposed version of MAS, the pulse shape distortion and pulse power attenuation were numerically simulated and analyzed. Especially, the reflection of pulse from the oil-water contact was studied, using the refractive mixing dielectric model [2] for the complex dielectric constants of both the media present in the oil-gas collector and the drilling mud present in a borehole.

2. PROBLEM DEFINITION

A chart of borehole logging tool used for numerical modeling is shown in Fig. 1. Both the transmitting and receiving Hertz dipoles antennas had perfectly conducting surface. The length and diameter of the antennas were equal of $l = 0.034$ m and 0.0066 m accordingly. For modeling used the pulse shape from the generator ("Trim Company", Russia) feeding the transmitting antenna at the input gap of 0.004 m in width. It's time shape and spectrum are shown in Fig. 2. The output impedance of pulse generator was assigned to be $R_L = 50$ Ohm. As seen from Fig. 2, the pulse has duration of about 0.3 ns, and its central frequency is of 2.5 GHz, while the lower and upper frequencies of the spectrum calculated at the level of 0.5 are equal to 0.8 and 4.4 GHz, respectively.

A receiving antenna is located at the distances of z_i from the transmitting one. Numerical model take into account the connecting oscilloscope and receiving antenna with coaxial cable having impedance of 50 Ohm. To ensure electrical insulation, both antennas were placed in a infinite dielectric tube with diameter of 0.01 m on Fig. 1 it's depicted as "borehole". The antennas are located in oil-saturated rock at a height d above the OWC. The oil-saturated rock was modeled as a mixture of sand (85%), brine (6%) and air (9%) where percentages denote volumetric content. The water-saturated bed is located under a planar OWC. The complex dielectric constant of brine

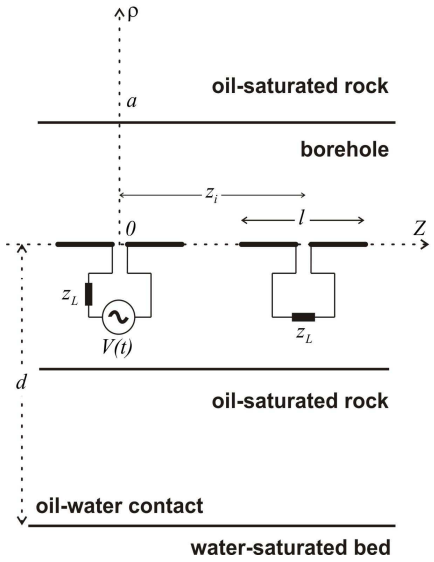

Figure 1: Logging tool in a borehole placed above the OWC.

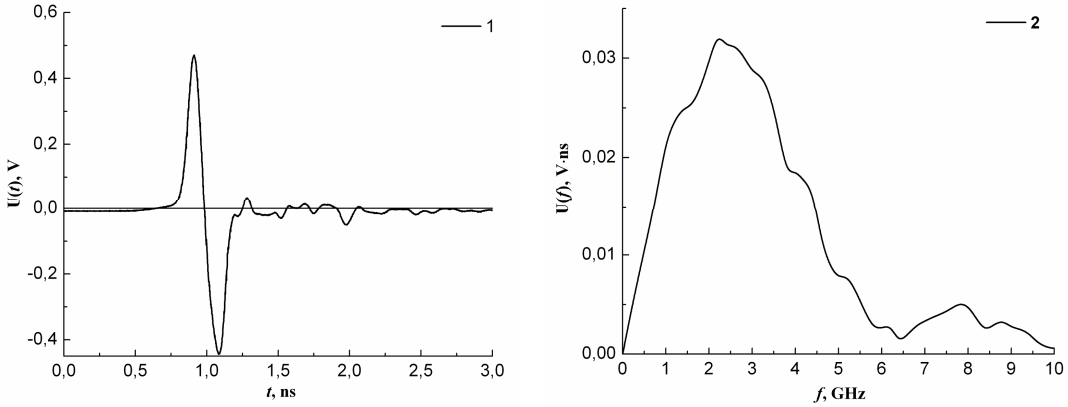

Figure 2: Pulse voltage (1) and its spectrum (2) as measured at the output of the pulse generator.

was calculated using the formulas given in [2] and the well-known *Debye* relaxation equation. The mineralization of solution in the water-saturated bed was assigned to be 17 g/cm^3. The dielectric constants of sand and air were assigned 2.9 and 1, respectively [2]. The temperature in the oil collector was taken to be of 22°C.

Further, based on the experiment, we show that proposed in [1] method of modeling borehole logging tool can be used to predict the shape pulse and time delay of pulses reflected from OWC.

3. MODEL VALIDATION WITH EXPERIMENT

A theoretical model to calculate the pulse voltage at the output of receiving antenna was developed with the use of the MAS. First, applying the technique proposed in [1], the Green function for the layered medium shown in Fig. 1 was found, taking into account boundaries of the housing cylinder and OWC interface. Second, there was set up an ensemble of auxiliary dipole sources located along the axis of the two Hertz dipole antennas. The total field exited by the auxiliary sources was calculated, and the boundary condition was implemented on the surfaces of the Hertz dipole antennas to yield a system of algebraic equations. Third, this system was numerically solved to provide for the unknown amplitudes of auxiliary sources. Given this amplitudes and the Green function found earlier, we calculated voltage at the output of the receiving antenna.

On the other hand, the output voltage was measured with the use of a transmitter/receiver set (see Fig. 1) placed in a tank filled with the layer of oil-saturated medium covered by a metal sheet. The thickness of the layer was equal to 0.44 m. The spacing between the antennas, z_i, changed from 0.23 m to 0.5 m. To ensure electrical insulation, both antennas were placed in a polyvinyl chloride (PVC) tube with diameter of 0.01 m. To register pulse signals we used a stroboscopic oscilloscope

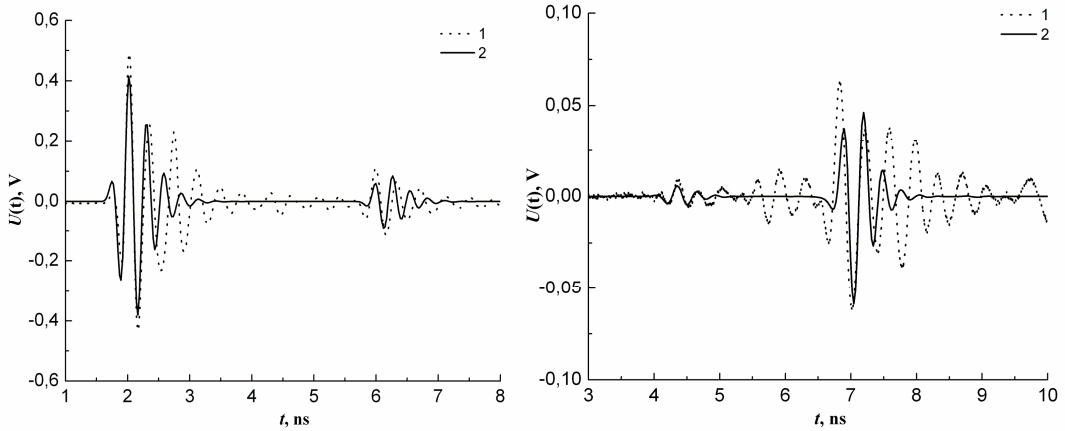

Figure 3: Pulse shape at the output of the receiving antenna at a distance (a) $z = 0.23\,\mathrm{m}$ and (b) $z = 0.5\,\mathrm{m}$ from a transmitting antenna. The solid and dot lines corresponds to the calculated and measured values.

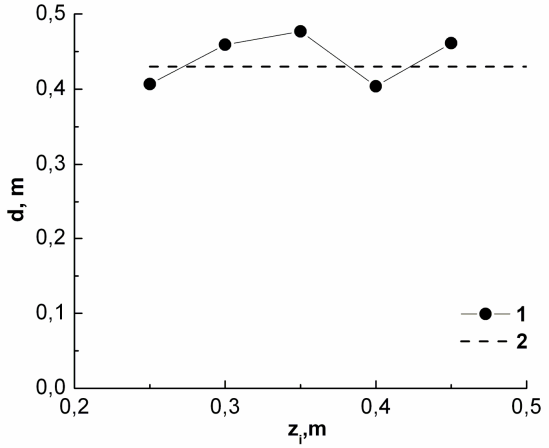

Figure 4: The distance to the OWC. 1 — calculated by formula (2), 2 — measured by ruler.

having a frequency band of 0 to 20 GHz. Pulse shapes at the output of the receiving antenna, both calculated and measured, with spacing being equal to $z = 0.23\,\mathrm{m}$ and $z = 0.5\,\mathrm{m}$, are shown in Fig. 3.

The most left pulses correspond to the pulse wave propagating directly along the antennas axis. While the right set of pulses are generated by the wave reflected from the OWC. In general, the results presented in Fig. 3 prove for the calculated and measured pulse shapes and arrival times to be in good agreement with each other. Some additional oscillations observed for the measured pulses could be attributed to the reflections from the bottom and side walls of the tank, which were not taken into account in the theoretical model.

4. METHOD OF MEASURING THE DISTANCE TO THE OIL-WATER CONTACT

The optical path lengths, L_i, and L_{i+1} of the reflected waves for two positions of the receiving antenna can be expressed as

$$L_i = \sqrt{4d^2 + z_i^2} = V_p\, T_{a,i}, \quad L_{i+1} = \sqrt{4d^2 + z_{i+1}^2} = V_p\, T_{a,i+1} \tag{1}$$

where $T_{a,i}$, $T_{a,i+1}$ — delay times of the pulses generated in the receiving antennas, when these are located in two positions, z_i and z_{i+1}, V_p — pulse velocity. Having measured the values $T_{a,i}$, $T_{a,i+1}$, z_i, z_{i+1}, we can resolve the system of two Equation (1) with regard to the distance d from the

transmitter/receiver set to the OWC, coming up with the following equation:

$$d_i = \frac{1}{2}\sqrt{\frac{z_{i+1}^2 T_{a,i}^2 - T_{a,i+1}^2 z_i^2}{T_{a,i+1}^2 - T_{a,i}^2}}, \tag{2}$$

subscript i designate the positions of antenna spaced from each other by the increment $z_i + 1 - z_i$. We measured the delay times using a point of maximum for the signal envelope in the range $0.23\,\mathrm{m} < z_i < 0.5\,\mathrm{m}$ with the increment of 5 cm and calculated the distance to the OWC with formula (2). The results of these estimations are shown in Fig. 4 The average for the distance over all measurements was equal to $d = 0.44\,\mathrm{m}$ (see Fig. 4). While the true distance was equal to $d = 0.43 \pm 0.01\,\mathrm{m}$. With these data available, we calculated the error for the distance measured with the borehole radar to be of 2.3%. What is most important to notice is the fact that the method proposed does not need any information about the velocity of pulse propagation in the oil-saturated medium.

5. CONCLUSIONS

The theoretical model of a borehole radar [1, 2] created by the authors using the method of discrete sources to calculate the shape and time delay of the pulse reflected from the oil-water contact has been proved experimentally. There was proposed and validated a method to determine the distance from the borehole radar to the oil-water contact. This method allows to determine the distance from a borehole radar to the oil-water contact with a relative error of 2.3% not needing any a priori information about the dielectric properties of the oil-saturated medium. The results of this study may initiate further studies of borehole radar applications for detecting the oil-water contact when drilling through the oil-saturated layers in oil mining industries.

ACKNOWLEDGMENT

This research was supported by the Siberian Branch of the Russian Academy of Sciences under Project No. 10.4.6, under interdisciplinary Project No. 6 and partly by Project No. 6650-8766 (FASIE foundation).

REFERENCES

1. Epov, M. I., V. L. Mironov, K. V. Muzalevskiy, and I. N. Yeltsov, "UWB electromagnetic borehole logging tool," *Proceedings of IGARSS*, 3565–3567, Honolulu, USA, July 2010.
2. Epov, M. I., V. L. Mironov, S. A. Komarov, and K. V. Muzalevsky, "Nanosecond electromagnetic sounding of a fluid-saturated layered formation," *Russian Geology and Geophysics*, Vol. 48, No. 12, 1054–1060, 2007.
3. Avdikos, G. K. and H. T. Anastassiu, "Antennas Computational cost estimations and comparisons for three methods of applied electromagnetics (MoM, MAS, MMAS)," *IEEE Propagation Magazine*, Vol. 47, No. 1, 121–129, 2005.

UWB Borehole Logging Tool to Explore the Electrical and Structural Properties of Near-wellbore Fluid-filled Areas

M. I. Epov[1], **V. L. Mironov**[2], **K. V. Muzalevskiy**[2], **and I. N. Yeltsov**[1]

[1]Trofimuk Institute of Petroleum Geology and Geophysics SB RAS, the Russian Federation
[2]Kirensky Institute of Physics, SB RAS
Reshetnev Siberian State Aerospace University, the Russian Federation

Abstract— In this paper, we studied the feasibility for the UWB Borehole Electromagnetic Logging Tool (BELT) considered in [1] to be applied for detecting the size of the zone of penetration of mud filtrate in the native rock of oil and gas reservoir and measuring the dielectric spectra of this zone. To this end there were studied the amplitude ratio and phase difference for the sounding pulse spectrum at the output of receiving antennas, spaced along the borehole, as a function of range of the flushed zone and enclosing rock. Such computer simulations were carried out to cover a number of realistic radial profiles for the petrophysical properties of the near-wellbore area. In this case, the radial profiles of respective complex dielectric constant were calculated on the basis of the dielectric model substantiated in [2], provided the temperature, salinity of brine water, and the petrophysical parameters of the near-wellbore area are known. There was studied relationship between the amplitude ratio and phase difference of the spectrum components of sounding pulses, on the one hand, and the petrophysical parameters of the near-wellbore area, on the other hand. The complex dielectric spectra in the near-wellbore area were shown to be retrieved with the use of the BELT proposed.

1. INTRODUCTION

Currently, there is a search for new technologies suitable to explore the electrical and structural properties of a spatially inhomogeneous near-wellbore area running through the fluid-filled rock [3]. Petrophysical interpretation of the data attained with these technologies allows to derive the oil saturation fraction, porosity, permeability, and fluid mobility of oil in the fluid-filled rock. At present, some technologies of this kind, which employ the electromagnetic sounding at frequencies from 1 kHz to several tens of MHz, are widely used in the oil mining industries [4]. Also, a wave dielectric method was used to determine the apparent values of the permittivity of oil bearing rocks in the frequency range from 40 to 60 MHz [5]. According to this method, the phase difference of the electromagnetic field measured at two spaced points on the axis of the logging tool is proportional to the apparent permittivity of enclosing rock. Based on this approach, an electromagnetic logging technique was analyzed in [6, 7]. The authors proposed a borehole radar which can be used for retrieving conductivity and relative permittivity of medium in the frequency range from 60 to 90 MHz. In this paper, we studied a broadband BELT, which operates in the frequency range from 0.01 to 0.6 GHz. For such an instrument the feasibility was shown to detect the spatial distribution of permittivity in the medium surrounding the borehole. This problem was solved for both the longitudinal and radial permittivity variations, with regard to the borehole axis. When studying the radial distribution, we suggest for the longitudinal scale of variations of the oil-saturated rock permittivity to be much larger then the length of the BELT.

2. UWB BOREHOLE ELECTROMAGNETIC LOGGING TOOL

UWB Borehole Electromagnetic Logging Tool consists of one transmitting and two receiving antennas as shown in Fig. 1. The transmitting and receiving antennas are perfectly conducting cylindrical dipoles, each having the length and radius of $l = 0.8$ m and 0.048 m, respectively. The receiving antennas are located at the distances of $z_1 = 1.5$ m and $z_2 = 2.5$ m from the transmitting one. The latter is connected to a pulse voltage generator with 50 Ohm coaxial cable. The gap between the antenna arms was equal to 0.01 m. Pulse voltage shape at the output of the generator attenuated by 67.2 dB and its spectrum are shown in Fig. 2. This generator is manufactured by Fid Technique Company (The Russian Federation). Transmitting and receiving antennas were placed in a separate downhole sonde housing in a form of dielectric cylinder having relative permittivity of $\varepsilon_{\mathrm{BELT}} = 14$, with its diameter being of 0.108 m. The BELT is immersed in drilling fluid filling a borehole, which diameter was assigned to be $2r_1 = 0.16$ m. The drilling fluid was composed of brine, sand, clay, and crud oil, with their volumetric contents being of 90%, 1%, 8% and 1%, respectively. The borehole

is surrounded by a flushed zone ($r_1 \leq r \leq r_2$) and the oil-bearing native bed ($r_2 \leq r$). The flushed zone and native bed were assigned as mixtures consisting of 1) sand (65%), clay (12%), oil (9,4%), brine (13,6%) and 2) oil (16,3%), brine (6,7%), respectively [1], where percentages denote volumetric content. The mineralization of brines present in the borehole, flushed zone, and native bed were assigned to be 5 g/l, 14.6 g/l and 17.4 g/l, respectively. The temperature in the oil collector was taken to be of 58°C. Complex dielectric constant of oil-bearing rock was calculated using the refractive index mixing model [2]. We used the three-dimensional finite-difference time domain (FDTD) algorithm [8] to simulate the borehole radar volatages at the outputs of the two receiving antennas.

The transmitting antenna emits a broadband electromagnetic pulse wave that propagates along the axis oz, partially penetrating into the enclosing oil-bearing rock. We suggest that this wave is a beam sea that propagates at the velocity corresponding to the enclosing oil-bearing rock. This assumption was taken as a basis for the method to retrieve permittivity of the media surrounding the borehole. According to this approach, the spectra of phase difference $\Delta\varphi(\omega)$ and amplitude ratio $U_{21}(\omega)$ of the voltages measured at the outputs of two receiving antennas situated at the distances z_1, z_2 can be linked to the apparent dielectric constant with following expressions:

$$\Delta\varphi(\omega) = \frac{\omega}{c} n(\omega)\Delta l, \tag{1}$$

$$\ln U_{21}(\omega) = -\frac{\omega}{c}\kappa(\omega)\Delta l, \tag{2}$$

In formulas (1) and (2), $\Delta l = z_2 - z_1$, and $n(\omega)$, $\kappa(\omega)$ are the refractive index and normalized attenuation coefficient relating to the enclosing oil-bearing rock, ω is angular frequency, c — velocity of light in the vacuum.

To evaluate formulas (1), (2), we will further simulate the values $\Delta\varphi(\omega)$ and $U_{1,2}$ for some specific structures of the borehole space media considered in Sections 3 and 4.

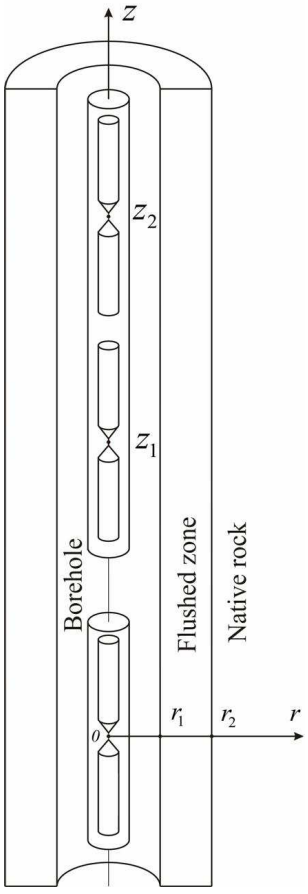

Figure 1: BELT in cylindrical layered rock: borehole-flushed zone-native bed.

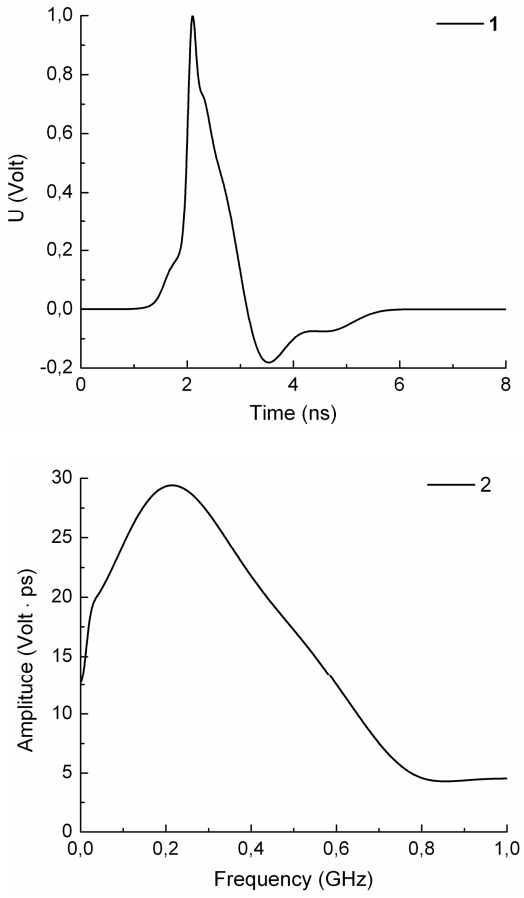

Figure 2: Pulse voltage (1) and its spectrum (2) as measured at the output of the pulse generator.

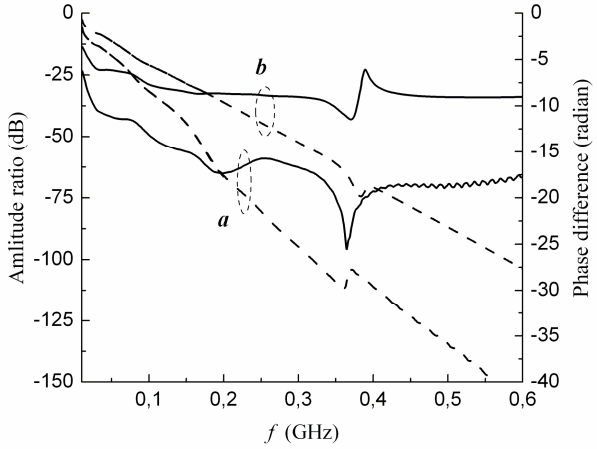

Figure 3: Spectra of amplitude ratio and the phase difference. (a) flushed zone medium, (b) native rock medium.

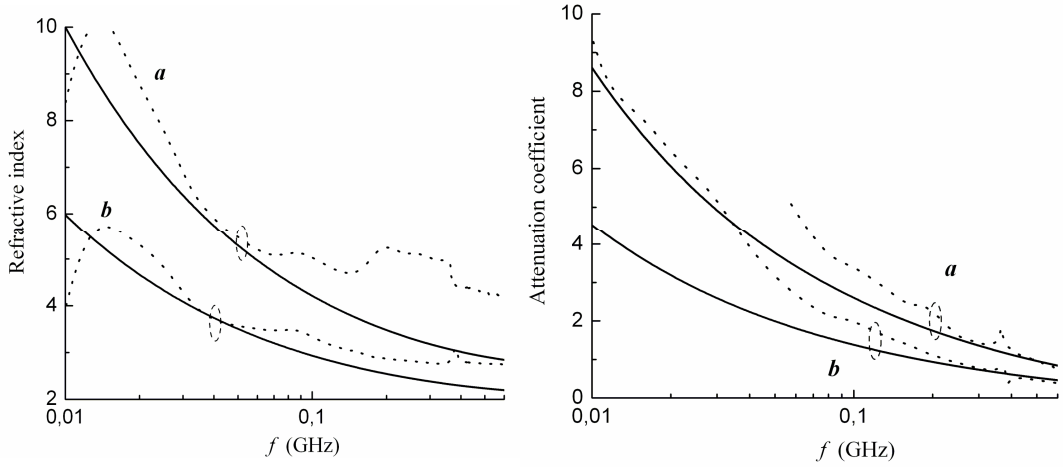

Figure 4: Retrieval spectra of enclosing rock. (a) Flushed zone, (b) native rock. Solid and dot line are a true and retrieved values, respectively.

3. TWO-LAYER MEDIUM. BOREHOLE-OIL-SATURETED ROCK

Two-layer model describes the situation when the layer of flashed zone is not taken into account ($r_1 = r_2$). In the numerical analysis conducted, we considered two type of enclosing rock, permittivities of which corresponded either to the flushed zone or the native oil bearing rock. In this case, the amplitude ratio $U_{12}(\omega)$ and the phase difference $\Delta\varphi(\omega)$ are shown in Fig. 3.

Using the formulas (1), (2) and the results of simulation shown in Fig. 3 we calculated the spectra of the refractive index and attenuation coefficient. These are shown in Fig. 4. As follows from Fig. 4, in the frequency ranges 0.02–0.2 GHz and 0.2–0.6 GHz, the relative errors for refractive index and attenuation coefficient do not exceed 15.6% and 20.5%, respectively.

4. THREE-LAYER MEDIUM FORMED WITH BOREHOLE, FLUSHED ZONE, AND OIL-BEARING ROCK

Some numerical simulation results are given here for a formation containing a flushed zone and native rock. Like in the previous case (see Fig. 3), there were simulated the spectra of amplitude ratio and phase difference as a function of the position of the interface between the flushed zone and native rock, r_2. For a number of frequencies, the results of this simulation are given in Fig. 5.

As seen from Fig. 5, the sensitivity of the amplitude ratio and phase difference to the position of the flushed zone interface decreases when the radius of the flushed zone becomes larger than 0.7 m.

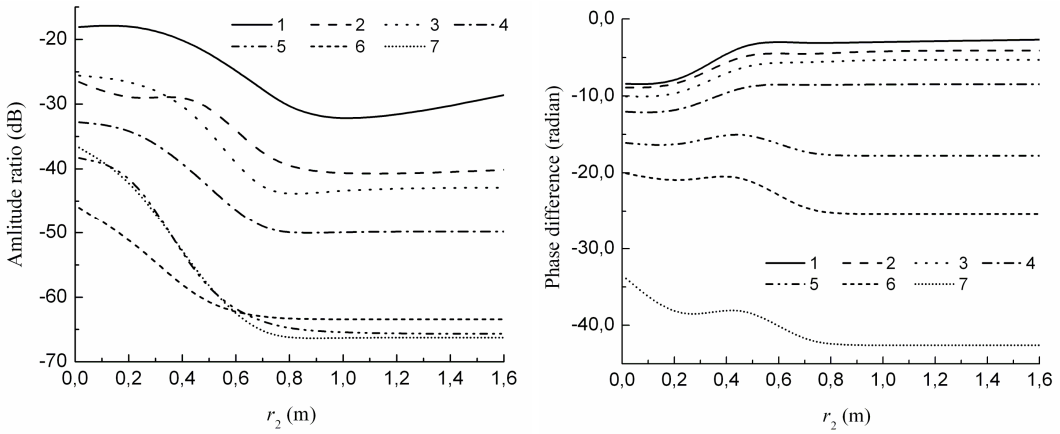

Figure 5: Spectra of amplitude ratio and phase difference at varying thickness of the flushed zone. Frequencies in GHz 1) 0.6, 2) 0.3, 3) 0.2, 4) 0.1, 5) 0.06, 6) 0.04, 7) 0.02.

5. CONCLUSIONS

A broadband borehole electromagnetic logging tool was proved to be feasible for measuring the dielectric properties of the enclosing rock. In the frequency ranges 0.02–0.2 GHz and 0.2–0.6 GHz, the relative errors for refractive index and attenuation coefficient retrieved with the algorithm proposed did not exceed 15.6% and 20.5%, respectively. In addition, the numerical simulations conducted showed that the sensitivity of the amplitude ratio and phase difference, as measured with the borehole tool, to the thickness of the flushed zone is missing if its radius is larger than 0.7 m.

ACKNOWLEDGMENT

This research was supported by the Siberian Branch of the Russian Academy of Sciences under Project No. 10.4.6, under interdisciplinary Project No. 6, and partly by Project No. 6650-8766 (FASIE foundation).

REFERENCES

1. Epov, M. I., V. L. Mironov, K. V. Muzalevskiy, and I. N. Yeltsov, "UWB electromagnetic borehole logging tool," *Proceedings of IGARSS*, 3565–3567, Honolulu, USA, July 2010.
2. Epov, M. I., V. L. Mironov, S. A. Komarov, and K. V. Muzalevsky, "Nanosecond electromagnetic sounding of a fluid-saturated layered formation," *Russian Geology and Geophysics*, Vol. 48, No. 12, 1054–1060, 2007.
3. http://www.slb.com/ds.aspx.
4. Antonov, Yu. N., M. I. Epov, and K. N. Kayurov, "Electromagnetic isoparametric soundings — innovation technique for vertical and horizontal boreholes in West Siberia," *Proceedings of V International Petroleum Conference and Exhibition*, 1, New Delhi, India, January 2003.
5. Daev, D. C., *High-Frequency Electromagnetic Logging Method*, Nedra, Moscow, 1974.
6. Liu, S. and M. Sato, "Electromagnetic logging technique based on borehole radar," *IEEE Transactions on Geoscience and Remote Sensing*, Vol. 40, No. 9, 2083–2092, 2002.
7. Liu, S., M. Sato, and K. Takahashi, "Application of borehole radar for subsurface physical measurement," *J. Geophys. Eng.*, Vol. 1, 221–227, 2004.
8. Chevalier, M. W., R. J. Luebbers, and V. P. Cable, "FDTD local grid with material traverse," *IEEE Trans. Antennas Propagat.*, Vol. 45, 411–421, 1997.

Charge Continuity Equation in the Adjoint Fields

Zi-Hua Weng
School of Physics and Mechanical & Electrical Engineering
Xiamen University, Xiamen 361005, China

Abstract— By means of the features of octonions, the gravitational field generates one adjoint field, while the electromagnetic field originates its adjoint field. The paper discusses the impact of adjoint fields on the conservation laws in the gravitational and electromagnetic fields. When the adjoint fields can not be neglected, it will cause the predictions to departure slightly from the known conservation laws, including the mass continuity equation and the charge continuity equation etc. The study claims that the electromagnetic adjoint field has an effect on the mass continuity equation, while the gravitational adjoint field on the charge continuity equation.

1. INTRODUCTION

The algebra of quaternions [1] can be used to describe the scalar invariants and some conservation laws in the gravitational field. Meanwhile the algebra of octonions [2] can be used to describe the scalar invariants of the electromagnetic field in the presence of the gravitational field, including the conservation of mass [3] and the conservation of charge etc. The above results are only dealt with the quaternion operator. However in some cases, the operator should be extended from the quaternion operator to the octonion operator in the octonion space.

Making use of the octonion operator, the gravitational field [4] demonstrated by the octonion operator will generate an adjoint field. The source of adjoint field includes the adjoint mass and the adjoint linear momentum. In general, the adjoint mass and its movement can not be observed by the conventional tests [5]. When the adjoint mass is combined with the ordinary mass to become one sort of particles, their movements will be accompanied by some effects. And this kind of adjoint mass may exert an influence on the distribution of electric charge. With the invariant property of octonions, we find that the adjoint mass and field strength have the influence on the conservation laws in the gravitational field, under the octonion coordinate transformation.

With the octonion operator, the electromagnetic field [6]demonstrated by the octonion operator will also originate an adjoint field. The source of adjoint field includes the adjoint charge and adjoint electric current. The adjoint charge and its movement can not be observed by usual experiments. When the adjoint charge is combined with the ordinary charge to become the charged particles, their movements will be consorted with some effects. And that this kind of adjoint charge may be considered as one kind of candidate for dark matter [7].

2. OCTONION TRANSFORMATION

In the quaternion space for the gravitational field, the basis vector is $\mathbb{E}_g = (1, \mathbf{i}_1, \mathbf{i}_2, \mathbf{i}_3)$, the radius vector is $\mathbb{R}_g = (r_0, r_1, r_2, r_3)$, and the velocity is $\mathbb{V}_g = (v_0, v_1, v_2, v_3)$. For the electromagnetic field, the basis vector is $\mathbb{E}_e = (\mathbf{I}_0, \mathbf{I}_1, \mathbf{I}_2, \mathbf{I}_3)$, the radius vector is $\mathbb{R}_e = (R_0, R_1, R_2, R_3)$, and the velocity is $\mathbb{V}_e = (V_0, V_1, V_2, V_3)$. The $\mathbb{E}_e$ is independent of the $\mathbb{E}_g$, with $\mathbb{E}_e = \mathbb{E}_g \circ \mathbf{I}_0$. The basis vectors $\mathbb{E}_g$ and $\mathbb{E}_e$ can be combined together to become the octonion basis vector $\mathbb{E} = \mathbb{E}_g + \mathbb{E}_e$.

In the octonion space, the octonion radius vector is $\mathbb{R} = \Sigma(r_i\mathbf{i}_i) + k_x\Sigma(R_i\mathbf{I}_i)$, and the octonion velocity is $\mathbb{V} = \Sigma(v_i\mathbf{i}_i) + k_a\Sigma(V_i\mathbf{I}_i)$. Herein $r_0 = v_0 t$; v_0 is the speed of light, t denotes the time; $R_0 = V_0 T$; V_0 is the quantity similar to the speed of light, T denotes a time-like physical quantity; k_x and k_a are the coefficients for the dimension homogeneity; $\circ$ denotes the octonion multiplication. The quaternion space is considered as the two-dimensional complex space, while the octonion space as the four-dimensional complex space. $i = 0, 1, 2, 3$; $j = 1, 2, 3$; with $\mathbf{i}_0 = 1$.

The octonion $\mathbb{D}(d_0, d_1, d_2, d_3, D_0, D_1, D_2, D_3)$ is defined as, $\mathbb{D} = \Sigma(d_i\mathbf{i}_i) + \Sigma(D_i\mathbf{I}_i)$. When the coordinate system is transformed into the other, the physical quantity $\mathbb{D}$ will be transformed into the new octonion $\mathbb{D}'(d'_0, d'_1, d'_2, d'_3, D'_0, D'_1, D'_2, D'_3)$, with $\mathbb{D}' = \mathbb{K}^* \circ \mathbb{D} \circ \mathbb{K}$. And the $\mathbb{D}$ satisfies,

$$d_0 = d'_0, \tag{1}$$

where d_i, D_i, d'_i, and D'_i are all real. $\mathbb{K}$ is the octonion, and $\mathbb{K}^* \circ \mathbb{K} = 1$; $*$ denotes the conjugate of octonion. The scalar part d_0 is preserved during the octonion coordinates are transforming. And some scalar invariants in the paper will be obtained from this features of the octonion.

3. GRAVITATIONAL FIELD

The gravitational field and its adjoint field both can be demonstrated by the quaternions, although they are quite different from each other indeed.

3.1. Potential and Strength

The field potential is $\mathbb{A}_g = \Sigma(a_i \mathbf{i}_i)$. The field strength $\mathbb{B}_g = \Diamond \circ \mathbb{A}_g = \mathbb{B}_{gg} + \mathbb{B}_{ge}$ consists of the gravitational strength $\mathbb{B}_{gg}$ and adjoint field strength $\mathbb{B}_{ge}$. Herein $\mathbb{B}_{gg} = \Sigma(b_{gi}\mathbf{i}_i)$, $\mathbb{B}_{ge} = \Sigma(B_{gi}\mathbf{I}_i)$; $\Diamond = \Sigma \mathbf{i}_i(\partial/\partial r_i) + k'\Sigma \mathbf{I}_i(\partial/\partial R_i)$. The gauge conditions are $b_{g0} = 0$ and $B_{g0} = 0$. The gravitational strength $\mathbb{B}_{gg}$ includes two components, $\mathbf{g}_g/v_0 = \partial_{g0}\mathbf{a} + \nabla_g a_0$, and $\mathbf{b}_g = \nabla_g \times \mathbf{a}$. And the adjoint field strength $\mathbb{B}_{ge}$ involves two parts, $\mathbf{E}_g/v_0 = \mathbf{I}_0\partial_{e0} \circ \mathbf{a} + \nabla_e a_0$, and $\mathbf{B}_g = \nabla_e \times \mathbf{a}$. The operator $\partial_{gi} = \partial/\partial r_i$, $\nabla_g = \Sigma(\mathbf{i}_j\partial_{gj})$, and $\Diamond_g = \Sigma(\mathbf{i}_i\partial_{gi})$. $\partial_{ei} = \partial/\partial R_i$, $\nabla_e = \Sigma(\mathbf{I}_j\partial_{ej})$, and $\Diamond_e = \Sigma(\mathbf{I}_i\partial_{ei})$. The k' is the coefficient.

The linear momentum density $\mathbb{S}_{gg} = m\mathbb{V}_g$ is the source of gravitational field, and its adjoint linear momentum density $\mathbb{S}_{ge} = \bar{m}\mathbb{V}_e$ is that of adjoint field. They combine together to become the field source $\mathbb{S}_g$,

$$\mu\mathbb{S}_g = -(\mathbb{B}_g/v_0 + \Diamond)^* \circ \mathbb{B}_g = \mu_{gg}\mathbb{S}_{gg} + \mu_{ge}\mathbb{S}_{ge} - \mathbb{B}_g^* \circ \mathbb{B}_g/v_0, \tag{2}$$

where $\bar{m}$ is the adjoint mass density; μ_{gg} and μ_{ge} are the coefficients. $\mathbb{B}_g^* \circ \mathbb{B}_g/(2\mu_{gg})$ is the field energy density, and $\mathbb{B}_g^* \circ \mathbb{B}_g/\mu_{gg} = (\mathbb{B}_{gg}^* \circ \mathbb{B}_{gg} + \mathbb{B}_{ge}^* \circ \mathbb{B}_{ge})/\mu_{gg}$. That means the adjoint field energy makes a contribution to the gravitational mass.

3.2. Conservation of Mass

In the gravitational field with its adjoint field, the linear momentum density $\mathbb{P} = \mu\mathbb{S}_g/\mu_{gg}$ is

$$\mathbb{P} = \widehat{m}v_0 + \Sigma(mv_j\mathbf{i}_j) + \Sigma(M_gV_i\mathbf{I}_i), \tag{3}$$

where $\widehat{m} = m - (\mathbb{B}_g^* \circ \mathbb{B}_g/\mu_{gg})/v_0^2$; $M_g = \bar{m}\mu_{ge}/\mu_{gg}$. $p_0 = \widehat{m}v_0$, $p_j = mv_j$; $P_i = M_gV_i$.

The linear momentum density is, $\mathbb{P}'(p_0', p_1', p_2', p_3', P_0', P_1', P_2', P_3')$, when the octonion coordinate system is rotated. From the definitions of the octonion velocity, linear momentum, and Eq. (1), we obtain some invariant equations, such as $\widehat{m}v_0 = \widehat{m}'v_0'$, $\widehat{m} = \widehat{m}'$, and $v_0 = v_0'$.

The above means that the gravitational mass density $\widehat{m}$ is changed with either the gravitational strength or the adjoint field strength. If we choose the definitions of velocity and linear momentum, the inertial mass density and gravitational mass density will keep unchanged respectively, under the coordinate transformation in the gravitational field with its adjoint field.

3.3. Mass Continuity Equation

In the gravitational field with its adjoint field, the part force density $\mathbb{F} = \Sigma(f_i\mathbf{i}_i) + \Sigma(F_i\mathbf{I}_i)$ is defined from the linear momentum density $\mathbb{P}$,

$$\mathbb{F} = v_0(\mathbb{B}_g/v_0 + \Diamond)^* \circ \mathbb{P}, \tag{4}$$

where the scalar $f_0 = v_0\Sigma(\partial p_i/\partial r_i) + v_0k'\Sigma(\partial P_i/\partial R_i) + \Sigma(b_{gj}p_j + B_{gj}P_j)$.

When the coordinate system rotates, we have the force density $\mathbb{F}'(f_0', f_1', f_2', f_3', F_0', F_1', F_2', F_3')$. By Eqs. (1) and (4), we have $f_0 = f_0'$. When $f_0' = 0$ in the above, we have the conservation of mass

Table 1: The octonion multiplication table.

	1	$\mathbf{i}_1$	$\mathbf{i}_2$	$\mathbf{i}_3$	$\mathbf{I}_0$	$\mathbf{I}_1$	$\mathbf{I}_2$	$\mathbf{I}_3$
1	1	$\mathbf{i}_1$	$\mathbf{i}_2$	$\mathbf{i}_3$	$\mathbf{I}_0$	$\mathbf{I}_1$	$\mathbf{I}_2$	$\mathbf{I}_3$
$\mathbf{i}_1$	$\mathbf{i}_1$	-1	$\mathbf{i}_3$	$-\mathbf{i}_2$	$\mathbf{I}_1$	$-\mathbf{I}_0$	$-\mathbf{I}_3$	$\mathbf{I}_2$
$\mathbf{i}_2$	$\mathbf{i}_2$	$-\mathbf{i}_3$	-1	$\mathbf{i}_1$	$\mathbf{I}_2$	$\mathbf{I}_3$	$-\mathbf{I}_0$	$-\mathbf{I}_1$
$\mathbf{i}_3$	$\mathbf{i}_3$	$\mathbf{i}_2$	$-\mathbf{i}_1$	-1	$\mathbf{I}_3$	$-\mathbf{I}_2$	$\mathbf{I}_1$	$-\mathbf{I}_0$
$\mathbf{I}_0$	$\mathbf{I}_0$	$-\mathbf{I}_1$	$-\mathbf{I}_2$	$-\mathbf{I}_3$	-1	$\mathbf{i}_1$	$\mathbf{i}_2$	$\mathbf{i}_3$
$\mathbf{I}_1$	$\mathbf{I}_1$	$\mathbf{I}_0$	$-\mathbf{I}_3$	$\mathbf{I}_2$	$-\mathbf{i}_1$	-1	$-\mathbf{i}_3$	$\mathbf{i}_2$
$\mathbf{I}_2$	$\mathbf{I}_2$	$\mathbf{I}_3$	$\mathbf{I}_0$	$-\mathbf{I}_1$	$-\mathbf{i}_2$	$\mathbf{i}_3$	-1	$-\mathbf{i}_1$
$\mathbf{I}_3$	$\mathbf{I}_3$	$-\mathbf{I}_2$	$\mathbf{I}_1$	$\mathbf{I}_0$	$-\mathbf{i}_3$	$-\mathbf{i}_2$	$\mathbf{i}_1$	-1

in the case for coexistence of the gravitational field and its adjoint field,

$$\Sigma(\partial p_i/\partial r_i) + k'\Sigma(\partial P_i/\partial R_i) + \Sigma(b_{gj}p_j + B_{gj}P_j)/v_0 = 0. \tag{5}$$

The above will be reduced to, $\partial m/\partial t + \partial M_g/\partial T + \Sigma(\partial p_i/\partial r_i) + k'\Sigma(\partial P_i/\partial R_i) = 0$, if the field strength $b_{gi} = B_{gi} = 0$. And if there is not the adjoint field, we have $\partial m/\partial t + \Sigma(\partial p_j/\partial r_j) = 0$.

The above states that the adjoint field strength, adjoint mass, and gravitational strength have an influence on the conservation of mass in Eq. (5), although the helicity $\Sigma(b_{gj}p_j + B_{gj}P_j)/v_0$ and the $\Sigma(\partial P_i/\partial R_i)$ both are usually very tiny for the fields are weak. In case we choose the definitions of the applied force and velocity in the gravitational field and adjoint field, the conservation of mass will be the invariant under the octonion transformation.

3.4. Conservation of Adjoint Mass

In the adjoint field, a new physical quantity $\mathbb{P}_g = \mathbb{P} \circ \mathbf{I}_0^*$ can be defined as

$$\mathbb{P}_g = M_g V_0 + \Sigma(M_g V_j \mathbf{i}_j) - \{\widehat{m} v_0 \mathbf{I}_0 + \Sigma(m v_j \mathbf{I}_j)\}. \tag{6}$$

Transferring the coordinates, we have the linear momentum density, $\mathbb{P}'_g = \Sigma(P'_i\mathbf{i}'_i - p'_i\mathbf{I}'_i)$. Under the coordinate transformation, the scalar part of $\mathbb{P}_g$ remains unchanged, that is, $M_g V_0 = M'_g V'_0$. Similarly the scalar part of velocity will keep the same, $V_0 = V'_0$. While we obtain the conservation of adjoint mass, $M_g = M'_g$. And M_g is the scalar invariant, which is in direct proportion to the adjoint mass density $\bar{m}$ in the gravitational field with its adjoint field.

The above means that if we emphasize the definitions of velocity and linear momentum, the adjoint mass density will remain the same, under the coordinate transformation in the adjoint field and gravitational field.

3.5. Continuity Equation of Adjoint Mass

In the octonion space, a new physical quantity $\mathbb{F}_g = \mathbb{F} \circ \mathbf{I}_0^*$ can be defined as,

$$\mathbb{F}_g = F_0 + \Sigma(F_j \mathbf{i}_j) - \Sigma(f_i \mathbf{I}_i), \tag{7}$$

where the scalar $F_0 = v_0\Sigma(\partial P_i/\partial r_i) - v_0 k'\Sigma(\partial p_i/\partial R_i) + \Sigma(b_{gj}P_j - B_{gj}p_j)$.

When the coordinate system rotates, we have the octonion density $\mathbb{F}'_g = \Sigma(F'_i\mathbf{i}'_i - f'_i\mathbf{I}'_i)$. Under the coordinate transformation, the scalar part of $\mathbb{F}_g$ remains unchanged, that is, $F_0 = F'_0$. When the right side is equal to zero in the above, we have the continuity equation of adjoint mass in the case for coexistence of the gravitational field and its adjoint field,

$$\Sigma(\partial P_i/\partial r_i) - k'\Sigma(\partial p_i/\partial R_i) + \Sigma(b_{gj}P_j - B_{gj}p_j)/v_0 = 0. \tag{8}$$

If the last term is neglected, the above is reduced to, $\Sigma(\partial P_i/\partial r_i) - k'\Sigma(\partial p_i/\partial R_i) = 0$. Further, if the last term is equal to zero, we have $\Sigma(\partial P_i/\partial r_i) = 0$.

The above states that the gravitational strength and its adjoint strength both have an influence on the continuity equation of adjoint mass, although the term $\Sigma(b_{gj}P_j - B_{gj}p_j)/v_0$ is usually very tiny when the fields are weak.

4. ELECTROMAGNETIC FIELD

The electromagnetic field and its adjoint field both can be demonstrated by the quaternions also, although they are quite different from each other indeed. With the invariant property of octonions, we find that the adjoint charge, adjoint mass, velocity curl, and field strength have an influence on the conservation laws in the electromagnetic field under the octonion transformation.

4.1. Potential and Strength

The electromagnetic field potential is $\mathbb{A}_e = \Sigma(A_i\mathbf{I}_i)$. The electromagnetic potential are combined with the gravitational potential to become the field potential $\mathbb{A} = \mathbb{A}_g + k_a\mathbb{A}_e$. The field strength $\mathbb{B} = \Diamond \circ \mathbb{A} = \mathbb{B}_g + k_b\mathbb{B}_e$ consists of gravitational strength $\mathbb{B}_g$ and electromagnetic strength $\mathbb{B}_e$. The strength $\mathbb{B}_e = \Diamond \circ \mathbb{A}_e = \mathbb{B}_{eg} + \mathbb{B}_{ee}$ consists of the electromagnetic strength $\mathbb{B}_{eg}$ and the adjoint strength $\mathbb{B}_{ee}$, with $\mathbb{B}_{ee} = \Sigma(b_{ei}\mathbf{i}_i)$ and $\mathbb{B}_{eg} = \Sigma(B_{ei}\mathbf{I}_i)$. The electromagnetic strength $\mathbb{B}_{eg}$ includes two components, $\mathbf{E}_e/v_0 = \partial_{g0}\mathbf{A} + \nabla_g \circ \mathbf{A}_0$, and $\mathbf{B}_g = \nabla_g \times \mathbf{A}$. While the adjoint field strength $\mathbb{B}_{ee}$ involves two parts, $\mathbf{g}_e/v_0 = \mathbf{I}_0\partial_{e0} \circ \mathbf{A} + \nabla_e \circ \mathbf{A}_0$, and $\mathbf{b}_e = \nabla_e \times \mathbf{A}$. The gauge conditions are $b_{e0} = 0$ and $B_{e0} = 0$. And the k_b is the coefficient.

The electric current density $\mathbb{S}_{eg} = q\mathbb{V}_e$ is the source of electromagnetic field, and its adjoint electric current density $\mathbb{S}_{ee} = \bar{q}\mathbb{V}_g$ is that of adjoint field. And they combine together to become the field source $\mathbb{S}_e$. In the octonion space, the electromagnetic source $\mathbb{S}_e$ can be combined with the gravitational source $\mathbb{S}_g$ to become the source $\mathbb{S}$,

$$\mu\mathbb{S} = -(\mathbb{B}/v_0 + \Diamond)^* \circ \mathbb{B} = \mu_{gg}\mathbb{S}_{gg} + \mu_{ge}\mathbb{S}_{ge} - \mathbb{B}^* \circ \mathbb{B}/v_0 + k_b(\mu_{ee}\mathbb{S}_{ee} + \mu_{eg}\mathbb{S}_{eg}), \tag{9}$$

where $k_b^2 = \mu_{gg}/\mu_{eg}$; μ_{gg}, μ_{ge}, μ_{ee}, and μ_{eg} are the coefficients. The $\mathbb{B}^* \circ \mathbb{B}/(2\mu_{gg})$ is the field energy density, with $\mathbb{B}^* \circ \mathbb{B}/\mu_{gg} = \mathbb{B}_g^* \circ \mathbb{B}_g/\mu_{gg} + \mathbb{B}_e^* \circ \mathbb{B}_e/\mu_{eg}$.

The above means that the electromagnetic field and its adjoint field make a contribution to the gravitational mass in the octonion space also.

4.2. Conservation of Mass

In the electromagnetic field, gravitational field, and related adjoint fields, the linear momentum density $\mathbb{P} = \mu\mathbb{S}/\mu_{gg}$ is written as

$$\mathbb{P} = \widehat{m}v_0 + \Sigma(mv_j\mathbf{i}_j) + \Sigma(M_gV_i\mathbf{I}_i) + \Sigma(M_qV_i\mathbf{I}_i) + \Sigma(M_ev_i\mathbf{i}_i), \tag{10}$$

where $\widehat{m} = m - (\mathbb{B}^* \circ \mathbb{B}/\mu_{gg})/v_0^2$; $M_q = qk_b\mu_{eg}/\mu_{gg}$; $M_e = \bar{q}k_b\mu_{ee}/\mu_{gg}$.

We may have the linear momentum density, $\mathbb{P}'(p_0', p_1', p_2', p_3', P_0', P_1', P_2', P_3')$, when the octonion coordinate system is rotated. And there are some invariant equations from the velocity and Eqs. (1) and (10), including $(\widehat{m} + M_e)v_0 = (\widehat{m}' + M_e')v_0'$, $\widehat{m} + M_e = \widehat{m}' + M_e'$, and $v_0 = v_0'$.

The above means that the gravitational mass density $\widehat{m}$ is changed with all four kinds of field strengthes in the electromagnetic field, gravitational field, and their adjoint fields. Choosing the definitions of velocity and linear momentum, the inertial mass density $(m + M_e)$ and gravitational mass density $(\widehat{m} + M_e)$ will keep unchanged respectively, under the octonion transformation in the electromagnetic field, gravitational field, and their adjoint fields.

4.3. Mass Continuity Equation

In the electromagnetic field, gravitational field, and their adjoint fields, the part force density $\mathbb{F} = \Sigma(f_i\mathbf{i}_i) + \Sigma(F_i\mathbf{I}_i)$ is defined from the linear momentum density $\mathbb{P} = \Sigma(p_i\mathbf{i}_i) + \Sigma(P_i\mathbf{I}_i)$,

$$\mathbb{F} = v_0(\mathbb{B}/v_0 + \Diamond)^* \circ \mathbb{P}, \tag{11}$$

where the scalar $f_0 = v_0\Sigma(\partial p_i/\partial r_i) + v_0k'\Sigma(\partial P_i/\partial R_i) + \Sigma(b_{gj}p_j + B_{gj}P_j + k_bb_{ej}p_j + k_bB_{ej}P_j)$.

When the coordinate system rotates, we have the force density $\mathbb{F}'(f_0', f_1', f_2', f_3', F_0', F_1', F_2', F_3')$. By Eqs. (1) and (11), we have, $f_0 = f_0'$. When $f_0' = 0$, we have the conservation of mass in the case for coexistence of the electromagnetic field, gravitational field, and their adjoint fields,

$$\Sigma(\partial p_i/\partial r_i) + k'\Sigma(\partial P_i/\partial R_i) + \Sigma(b_{gj}p_j + B_{gj}P_j)/v_0 + \Sigma k_b(b_{ej}p_j + B_{ej}P_j)/v_0 = 0. \tag{12}$$

In case of $b_{gi} = B_{gi} = b_{ei} = B_{ei} = 0$, the above will be reduced to, $\Sigma(\partial p_j/\partial r_j) + \Sigma(\partial P_j/\partial R_j) = 0$. Further, if the last term can be neglected, we have, $\Sigma(\partial p_i/\partial r_i) = 0$.

By the definitions of applied force and velocity in the electromagnetic field, gravitational field, and their adjoint fields, the conservation of mass will be the invariant. The above states also that four kinds of field strengthes, adjoint mass, and adjoint charge have an influence on the conservation of mass, although the impact is usually very small for the fields are weak.

4.4. Conservation of Charge

In the adjoint field, a new physical quantity $\mathbb{P}_q = \mathbb{P} \circ \mathbf{I}_0^*$ can be defined as,

$$\mathbb{P}_q = P_0 + \Sigma(P_j\mathbf{i}_j) - \{p_0\mathbf{I}_0 + \Sigma(p_j\mathbf{I}_j)\}, \tag{13}$$

where $P_0 = (M_g + M_q)V_0$.

We have the linear momentum density, $\mathbb{P}_q' = \Sigma(P_i'\mathbf{i}_i' - p_i'\mathbf{I}_i')$, when the octonion coordinate system is rotated. Under the octonion coordinate transformation, the scalar part of $\mathbb{P}_q$ remains unchanged, that is, $(M_g + M_q)V_0 = (M_g' + M_q')V_0'$, and $V_0 = V_0'$. As a result we obtain the conservation of charge, $M_g + M_q = M_g' + M_q'$. Consequently the $(M_g + M_q)$ is a scalar invariant, which is one function of the adjoint mass density $\bar{m}$ and the ordinary charge q.

The above means if we emphasize definitions of velocity and linear momentum, the charge density $(M_g + M_q)$ will remain the same, under the coordinate transformation in the electromagnetic field, gravitational field, and their adjoint fields.

4.5. Charge Continuity Equation

In the octonion space, a new physical quantity $\mathbb{F}_q = \mathbb{F} \circ \mathbf{I}_0^*$ can be defined as,

$$\mathbb{F}_q = F_0 + \Sigma(F_j \mathbf{i}_j) - \Sigma(f_i \mathbf{I}_i), \tag{14}$$

where the scalar $F_0 = v_0 \Sigma(\partial P_i/\partial r_i) - v_0 k' \Sigma(\partial p_i/\partial R_i) + \Sigma(b_{gj} P_j - B_{gj} p_j + k_b b_{ej} P_j - k_b B_{ej} p_j)$.

When the octonion coordinate system rotates, we have the force density $\mathbb{F}'_q = \Sigma(F'_i \mathbf{i}'_i - f'_i \mathbf{I}'_i)$ under the coordinate transformation. From Eq. (1), the scalar part of $\mathbb{F}_q$ remains unchanged, that is, $F_0 = F'_0$. When the right side is equal to zero, we have the charge continuity equation in the case for coexistence of the gravitational field, electromagnetic field, and adjoint fields,

$$\Sigma(\partial P_i/\partial r_i) - k' \Sigma(\partial p_i/\partial R_i) + \Sigma(b_{gj} P_j - B_{gj} p_j)/v_0 + k_b \Sigma(b_{ej} P_j - B_{ej} p_j) = 0.$$

If last two terms are zeros, the above is reduced to, $\Sigma(\partial P_i/\partial r_i) - k' \Sigma(\partial p_i/\partial R_i) = 0$. Further, if the last term is equal to zero, we have, $\Sigma(\partial P_i/\partial r_i) = 0$.

The above states that the electromagnetic strength, gravitational strength, and adjoint field strengthes have an effect on the charge continuity equation, although the impact is usually very tiny for the fields are weak. And the charge continuity equation is an invariant under the octonion coordinate transformation.

5. CONCLUSIONS

In the octonion space, the gravitational field described by the octonion operator generates its own adjoint field. Meanwhile the electromagnetic field is accompanied by its adjoint field. These two sorts of adjoint fields will exert an influence on the scalar invariants and the conservation laws in the electromagnetic field and gravitational field.

In the case for coexistence of gravitational and electromagnetic fields with their adjoint fields, the electric charge density is influenced by the adjoint mass density $\bar{m}$, ordinary charge density q, and coefficient μ_{ge} etc. And the charge continuity equation will be changed with the electromagnetic strength, gravitational strength, adjoint fields strength, and velocity etc.

It should be noted that the study for some scalar invariants examined only one simple case with the weak field strength in the gravitational field, electromagnetic field, and their adjoint fields. Despite its preliminary character, this study can clearly indicate the field strength and the adjoint fields of the gravitational field and electromagnetic field have the influence on the scalar invariants. For the future studies, the related investigation will concentrate on only the predictions of scalar invariants in the strong strength of adjoint fields in the gravitational and electromagnetic fields.

ACKNOWLEDGMENT

This project was supported partially by the National Natural Science Foundation of China under grant number 60677039.

REFERENCES

1. Hamilton, W. R., *Elements of Quaternions*, Longmans, Green & Co., London, 1866.
2. Cayley, A., *The Collected Mathematical Papers of Arthur Cayley*, The Cambridge University Press, Cambridge, 1889.
3. Lavoisier, A., *Elements of Chemistry*, trans. R. Kerr, Dover Publications Inc., New York, 1965.
4. Newton, I., *The Mathematical Principles of Natural Philosophy*, trans. A. Motte, Dawsons of Pall Mall, London, 1968.
5. Weng, Z.-H., "Adjoint charge in electromagnetic field," *PIERS Proceedings*, 904–907, Moscow, Russia, August 18–21, 2009.
6. Maxwell, J. C., *A Treatise on Electricity and Magnetism*, Dover Publications Inc., New York, 1954.
7. Zwicky, F., "On the masses of nebulae and of clusters of nebulae," *Astrophysical Journal*, Vol. 86, No. 3, 217–246, 1937.

A Generalized Variational Principle of Linear Elastic Materials with Voids

Ji-Huan He
National Engineering Laboratory for Modern Silk, College of Textile and Engineering
Soochow University, 199 Ren-ai Road, Suzhou 215123, China

Abstract— Governing equations for linear elastodynamics analysis of material with voids are reviewed and then cast in the framework of variational statement. Starting from a trial-functional with unknown functions, a family of variational principles are derived through a systematic procedure.

1. INTRODUCTION

The theory of elastic materials with voids or vacuous pores was first established by Nunziato and Cowin [1, 2]. This theory enables us to analyze the behavior of elastic porous solids, which can be widely found in engineering, such as rock and soil, bone, manufactured porous materials.

Ciarletta and Scalia [3] studied a linear thermoelastic theory of material with voids, and established uniqueness and reciprocal theorems. Dhaliwal and Wang [4] proposed a domain of influence theorem for the linear theory of elastic materials with voids. Iesan [5] established a variational theory for thermoelastic materials with voids, and Pi and Jin [6] obtained a generalized variational principle for static linear elastic materials with voids. In this paper we will apply the semi-inverse method [7–9] to establish a variational model for the entitled problem.

2. MATHEMATICAL RELATIONS

Let $x_i\,(i = 1, 2, 3)$ be rectangular Cartesian coordinates and Ω be a regular region of three dimensional space occupied by an elastic material with voids, let $\partial\Omega$ be a piecewise smooth boundary of Ω. According to Cowin and Nunziato's linear elastic theory of elastic materials with voids, we have the following equations [2].

1) Equations of motion

$$\sigma_{ij,j} + \rho\bar{f}_i = \rho u_i'', \tag{1a}$$

$$h_{i,i} + g + \rho l = \rho k\varphi'', \tag{1b}$$

where prime denotes the derivative with respect to time.

2) Constitutive Equations

$$\sigma_{ij} = C_{ijkl}\varepsilon_{kl} + \beta_{ij}\varphi, \tag{2a}$$

$$h_i = \alpha\varphi_{,i}, \tag{2b}$$

$$g = \xi\varphi + \beta_{ij}\varepsilon_{ij}. \tag{2c}$$

3) Geometrical Equations

$$\varepsilon_{ij} = \frac{1}{2}(u_{i,j} + u_{j,i}), \tag{3}$$

in which σ_{ij} is the symmetric stress tensor, u_i is the elastic displacement vector, ε_{ij} is the strain vector, ρ is the mass density, $\bar{f}_i$ is the body force, h_i is the equilibrated stress vector, k is the equilibrated inertia, l and g represent the extrinsic equilibrated body force and the intrinsic equilibrated body force respectively, β_{ij}, α, ω, ξ, C_{ijkl} are characteristic coefficients of material, and the prime denotes the material time derivative while a comma followed by a subscript stands for partial derivatives with respect to the coordinates.

4) Boundary and Initial Conditions

The boundary conditions are

$$u_i = \bar{u}_i \ \text{ on } \ \partial\Omega_1 \times [0, t], \tag{4a}$$

$$\sigma_{ij}n_j = \bar{t}_i \ \text{ on } \ \partial\Omega_1^c \times [0, t], \tag{4b}$$

$$\varphi = \bar{\varphi} \ \text{ on } \ \partial\Omega_2 \times [0, t], \tag{4c}$$

$$h_i n_i = \bar{h} \ \text{ on } \ \partial\Omega_2^c \times [0, t], \tag{4d}$$

with $\partial\Omega_1 \cup \partial\Omega_1^c = \partial\Omega$, $\partial\Omega_2 \cup \partial\Omega_2^c = \partial\Omega$.

The initial conditions are

$$\left.\begin{array}{r} \rho u_i'(\mathbf{x},0) = q_i(\mathbf{x}) \\ \rho k\varphi'(\mathbf{x},0) = \bar{\Phi}(\mathbf{x}) \end{array}\right\} \quad \varphi \in \bar{\Omega}. \tag{4e}$$

3. TRIAL-FUNCTIONAL AND GENERALIZED VARIATIONAL PRINCIPLE

Variational theory is a powerful tool for finite element methods. Recently Romano and Suhubi [10, 11] and Iannece, Romano and Suhubi [12] apply the variational theory to deal with the structure of Weiss domains in ferroelectric crystals.

In this paper, we will use the semi-inverse method to establish a family of variational principles for the above discussed problem. An advantage of the semi-inverse method is that it can provide a powerful tool for the inverse problem of variational calculus.

Supposing a trial-functional with 6 kinds of independent variables (u_i, σ_{ij}, ε_{ij}, φ, h_i, g) can be expressed in the form

$$\begin{aligned} J(u_i,\sigma_{ij},\varepsilon_{ij},\varphi,h_i,g) \;=\; & \int_0^t \iiint_{\Omega} L d\Omega dt + \iiint_{\bar{\Omega}} G_1 d\Omega + \int_0^t \iint_{\partial\Omega_1} G_2 dA dt \\ & + \int_0^t \iint_{\partial\Omega_1^c} G_3 dA dt + \int_0^t \iint_{\partial\Omega_2} G_4 dA dt + \int_0^t \iint_{\partial\Omega_2^c} G_5 dA dt, \end{aligned} \tag{5a}$$

where L is a trial-Lagrangian, one of which can be written in the form

$$L = \frac{1}{2}\rho u_i'^2 + u_i\left(\sigma_{ij,j} + \rho\bar{f}_i\right) + \frac{1}{2}\rho k\varphi'^2 + \varphi(h_{i,i} + g + \rho l) + F, \tag{5b}$$

where F and G_i ($i = 1 \sim 5$) are unknown functions to be further determined.

The above trial-Lagrangian has an advantage that the stationary conditions with respect to u_i and φ are the field Equations (1a) and (1b) respectively if the unknown F is free from the variables u_i and φ and their derivatives.

Now the stationary condition with respect to σ_{ij} reads

$$\delta\sigma_{ij}: \quad -\frac{1}{2}(u_{i,j} + u_{j,i}) + \frac{\delta F}{\delta\sigma_{ij}} = 0, \tag{6}$$

where $\delta F/\delta\sigma_{ij}$ is called variational derivative defined as

$$\frac{\delta F}{\delta\sigma_{ij}} = \frac{\partial F}{\partial\sigma_{ij}} - \left(\frac{\partial F}{\partial\sigma_{ij},j}\right)_{,j}.$$

We search for such an F, so that the trial-Euler Equation (6) satisfies one of the field equations, say Equation (3). Accordingly we have

$$\frac{\delta F}{\delta\sigma_{ij}} = \varepsilon_{ij}, \tag{7}$$

From the above relation, we can readily identify the unknown F, which reads

$$F = \varepsilon_{ij}\sigma_{ij} + F_1, \tag{8}$$

where F_1 is a newly introduced unknown function, which should be free from the variable σ_{ij}.

The trial-Lagrangian, Equation (5b), therefore, can be renewed as

$$L = \frac{1}{2}\rho u_i'^2 + u_i(\sigma_{ij,j} + \rho\bar{f}_i) + \frac{1}{2}\rho k\varphi'^2 + \varphi(h_{i,i} + g + \rho l) + \varepsilon_{ij}\sigma_{ij} + F_1. \tag{5c}$$

The trial-Euler equation for $\delta\varepsilon_{ij}$ reads

$$\delta\varepsilon_{ij}: \quad \sigma_{ij} + \frac{\delta F_1}{\delta\varepsilon_{ij}} = 0, \tag{9}$$

If we set

$$\frac{\delta F_1}{\delta \varepsilon_{ij}} = -(C_{ijkl}\varepsilon_{kl} + \beta_{ij}\varphi), \tag{10}$$

in Equation (9), then Equation (9) becomes Equation (2a). In order to be absent of φ in F_1, we replace φ by using of Equation (2c). We, therefore, can re-write Equation (10) in the form

$$\frac{\delta F_1}{\delta \varepsilon_{ij}} = -\left(C_{ijkl}\varepsilon_{kl} + \frac{1}{\xi}\beta_{ij}g - \frac{1}{\xi}\beta_{ij}\beta_{mn}\varepsilon_{mn}\right), \tag{11}$$

We can identify the unknown function F_1:

$$F_1 = -\left(\frac{1}{2}\varepsilon_{ij}C_{ijkl}\varepsilon_{kl} + \frac{1}{\xi}\varepsilon_{ij}\beta_{ij}g - \frac{1}{2\xi}\varepsilon_{ij}\beta_{ij}\beta_{mn}\varepsilon_{mn}\right) + F_2, \tag{12}$$

where F_2 is a new unknown function free from the variable ε_{ij}. The trial-Lagrangian can be further updated as

$$\begin{aligned} L \;=\; & \frac{1}{2}\rho u_i'^2 + u_i\left(\sigma_{ij,j} + \rho\bar{f}_i\right) + \frac{1}{2}\rho k\varphi'^2 + \varphi(h_{i,i} + g + \rho l) + \varepsilon_{ij}\sigma_{ij} \\ & - \left(\frac{1}{2}\varepsilon_{ij}C_{ijkl}\varepsilon_{kl} + \frac{1}{\xi}\varepsilon_{ij}\beta_{ij}g - \frac{1}{2\xi}\varepsilon_{ij}\beta_{ij}\beta_{mn}\varepsilon_{mn}\right) + F_2 \end{aligned} \tag{5d}$$

Now calculating variation with respect to h_i and g, we have

$$\delta h_i : \quad -\varphi_{,i} + \frac{\delta F_2}{\delta h_i} = 0, \tag{13}$$

$$\delta g : \quad \varphi + \frac{1}{\xi}\varepsilon_{ij}\beta_{ij} + \frac{\delta F_2}{\delta g} = 0. \tag{14}$$

The above two trial-Euler equations should satisfy the left field equations, i.e., Equations (2b) and (2c) respectively. So the unknown F_2 can be determined as

$$F_2 = \frac{1}{2\alpha}h_i h_i - \frac{1}{2\xi}g^2. \tag{15}$$

We finally obtain the necessary Lagrangian, which reads

$$\begin{aligned} L \;=\; & \frac{1}{2}\rho u_i'^2 + u_i\left(\sigma_{ij,j} + \rho\bar{f}_i\right) + \frac{1}{2}\rho k\varphi'^2 + \varphi(h_{i,i} + g + \rho l) + \varepsilon_{ij}\sigma_{ij} \\ & - \left(\frac{1}{2}\varepsilon_{ij}C_{ijkl}\varepsilon_{kl} + \frac{1}{\xi}\varepsilon_{ij}\beta_{ij}g - \frac{1}{2\xi}\varepsilon_{ij}\beta_{ij}\beta_{mn}\varepsilon_{mn}\right) + \frac{1}{2\alpha}h_i h_i - \frac{1}{2\xi}g^2 \end{aligned} \tag{5e}$$

The method of incorporating the boundary/initial conditions into the functional is very similar to the above main method. For example making the functional (5a) with identified Lagrangian (5e) stationary, and applying Green's theory, we obtain the following trial-Euler equations on the boundary $\bar{\Omega}$:

$$\rho u_i' + \frac{\partial G_1}{\partial u_i} \;=\; 0, \tag{16}$$

$$\rho k\varphi' + \frac{\partial G_1}{\partial \varphi} \;=\; 0. \tag{17}$$

The above two equations should satisfy the initial conditions, Equation (4e). Therefore, G_1 can be determined as

$$G_1 = -u_i\bar{q}_i - \varphi\bar{\Phi}. \tag{18a}$$

By simple parallel operation, we can identify the other unknowns as follows

$$G_2 \;=\; -\sigma_{ij}n_j\bar{u}_i, \tag{18b}$$

$$G_3 \;=\; -u_i\left(\sigma_{ij}n_j - \bar{t}_i\right), \tag{18c}$$

$$G_4 \;=\; -h_i n_i\bar{\varphi}, \tag{18d}$$

$$G_5 \;=\; -\varphi\left(h_i n_i - \bar{h}\right). \tag{18e}$$

Constraining the obtained Lagrangian (5e) by selected field equations, or boundary/initial conditions, we can obtain various variational principles under constraints.

4. CONCLUSION

In the paper, we obtain a generalized variational principle, from which the well-known Hellinger-Reissner principle and Hu-Washizu principle of elasticity can be obtained if the void effect is not taken into consideration.

ACKNOWLEDGMENT

The work is supported by National Natural Science Foundation of China.

REFERENCES

1. Nunziato, J. W. and S. C. Cowin, "A nonlinear theory of elastic materials with voids," *Arch. Rational Mech. Anal.*, Vol. 72, 175–201, 1979.
2. Cowin, S. C. and J. W. Nunziato, "Linear elastic materials with voids," *J. Elasticity*, Vol. 13, 125–147, 1983.
3. Clarletta, M. and A. Scalia, "On uniqueness and reciprocity in linear theroelasticity of materials with voids, *J. Elasticity*, Vol. 32, 1–17, 1993.
4. Dhaliwal, R. S. and J. Wang, "Domain of influence theorem in the theory of elastic materials with voids," *Int. J. Engineering Science*, Vol. 32, No. 11, 1823–1828, 1994.
5. Iesan, D., "A theory of Thermoelastic materials with voids," *Acta Mech.*, Vol. 60, 67–89, 1986.
6. Pi, D.-H. and L.-H. Jin, "Structural function theory of generalized variational principles for linear elastic materials with voids," *Applied Math. Mech.*, Vol. 12, No. 6, 565–575, 1991.
7. He, J. H., "Generalized Hellinger-Reissner principle," *ASME Journal of Applied Mechanics*, Vol. 67, No. 2, 326–331, 2000.
8. He, J. H., "Coupled variational principles of piezoelectricity," *Int. J. Engineering Sciences*, Vol. 39, No. 3, 323–341, 2000.
9. He, J. H., "Variational theory for linear magneto-electro-elasticity," *International Journal of Non-Linear Science and Numerical Simulationm*, Vol. 2, No. 4, 309–316, 2001.
10. Romano, A. and E. S. Suhubi, "Structure of Weiss domains in Ferroelectric crystals," *Int. J. Engng. Sci.*, Vol. 30, No. 2, 1715–1729, 1992.
11. Romano, A. and E. S. Suhubi, "Structure of Weiss domains in elastic Ferroelectric crystals," *Int. J. Engng. Sci.*, Vol. 32, No. 12, 1925–1939, 1994.
12. Iannece, D., A. Romano, and E. S. Suhubi, "A thermodynamical approach to the structure of Weiss domains in deformable Ferroelectric crystals," *Int. J. Engng. Sci.*, Vol. 32, No. 12, 1941–1950, 1994.

Using Numerical Analysis for NMR Coils Optimalization

D. Nespor, **K. Bartusek**, **and P. Fiala**
Department of Theoretical and Experimental Electrical Engineering
Brno University of Technology, Kolejni 2906/4, Brno 612 00, Czech Republic

Abstract— Paper contains computing of the B_1 field homogeneity. Basic model is simply planar one-turn coil. This model is solved analytically and numerically [3, 4]. There was made measuring in NMR system too. All results was compared. This the correctness were verified. The next step was computing and size optimalization for maximum B_1 field homogeneity of the saddle coils. The final step was special shaped coils computing.

1. INTRODUCTION

Radio frequency coils create the B_1 field which rotates the magnetization in a pulse sequence. They also detect the transverse magnetization as it precesses in the XY plane. Most RF coils on NMR systems are of the saddle coil design and act as the transmitter of the B_1 field and receiver of RF energy from the sample. You may find one or more RF coils in a probe.

Each of these RF coils must resonate, they must efficiently store energy, at the Larmor frequency of the nucleus being examined with the NMR system. All NMR coils are composed of an inductor, or inductive elements, and a set of capacitive elements. The resonant frequency f_r of an RF coil is determined by the inductance and capacitance of the inductor capacitor circuit.

RF coils used in NMR systems need to be tuned for the specific sample being studied. An RF coil has a bandwidth or specific range of frequencies at which it resonates. When sample was placed a in an RF coil, the conductivity and dielectric constant of the sample affect the resonance frequency. If this frequency is different from the resonance frequency of the studied nucleus, the coil will not efficiently set up the B_1 field and not efficiently detect the signal from the sample.

The B_1 field of an RF coil must be perpendicular to the B_o magnetic field. Another requirement of an RF coil in an NMR system is that the B_1 field needs to be homogeneous over the volume of the sample. If it is not, spins will be rotating by a distribution of rotation angles and spectra will be obtain strange [1, 2].

2. MODEL CREATION

Solved equation:
Magnetostatic:

$$\begin{aligned} \nabla \times \left(\mu_0^{-1}\mu_r^{-1}\nabla \times A\right) &= J \\ B &= \mu_0\mu_r H \\ n \cdot J &= 0 \end{aligned} \tag{1}$$

Boundary conditions:

$$\begin{aligned} n \times A &= 0 \\ n \cdot J &= 0 \end{aligned} \tag{2}$$

Continuity conditions:

$$\begin{aligned} n \cdot (J_1 - J_2) &= 0 \\ n \times (H_1 - H_2) &= 0 \end{aligned} \tag{3}$$

Coil feeding:

$$n \cdot J = 0 \tag{4}$$

For seeking magnetic field homogeneity magneto-static equations were used. Numerical model with basic-shaped coil shows Figure 1. In the middle of the figure is one-turned coil. Feeding of this coil is marked as "terminal" and opposite polarity is marked as "ground". Around of the coil is "computation medium". The computation medium defines whole solution space. The interface of the coil and computation medium define "continuity conditions". The border of the model defines

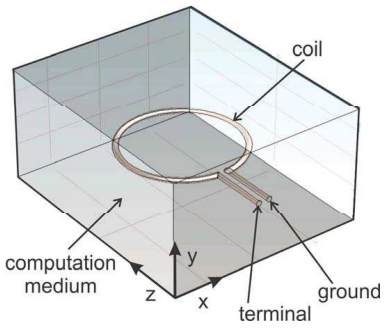

Figure 1: Basic model.

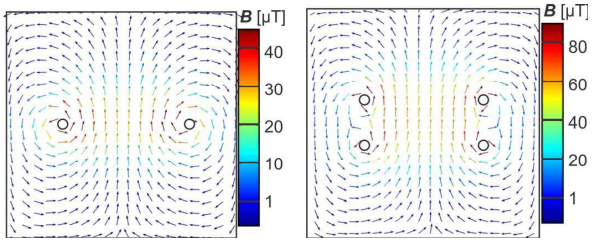

Figure 2: B_1 field of the one and two-turned coil.

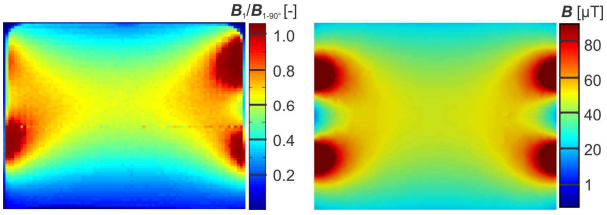

Figure 3: Measured B_1 field and computed B_1 field.

boundary conditions. Boundary conditions working as end of the electromagnetic field. Size of the computation medium area defines as much is electromagnetic field influenced of size of the boundaries conditions. But in this case is important close coil area, so big computation medium is not need. The equations for all cases are listed above. For all cases was used feeding current $I = 1\,\mathrm{A}$.

To confirm the model accuracy was used analytic computation of magnetic vector potential A of the one-turned coil [4]. Computational domain was circle, with radius $r = 10\,\mathrm{mm}$, in the middle of the coil. Analytical result was 175 nWb/m, numerical result was 171 nWb/m. It proves correctness of the model.

3. ONE AND TWO-TURNED COILS

On beginning models of the one and two turned coils were solved. This model was solved rather to illustrated and additional model verification. Both coils are from cylindrical Cu wire. The wire diameter is $d = 2\,\mathrm{mm}$. Radius of the both cols is $r = 20\,\mathrm{mm}$. Distance between turns of the two-turned coils is $l = 14.5\,\mathrm{mm}$. Results are in the Figure 2. In the figure are coils' cross sections. The cross sections are perpendicular to plain coils and are through the centre. Directions of the arrows are consistent with B_1 field. The colour range shows B_1 field value. Left part of the figure shows one-turned coil and right part two-turned coil. For absolutely homogeneous field is necessary to have all arrows in one direction and constant B_1 field value. As is evident from the figure, B_1 field of the one-turned coil is homogeneous only at close quarters coil. The B_1 field of the two-turned coil is much better, but only in the middle of the turns. It could be a problem for measuring of the bigger objects.

In the Figure 3, is B_1 field colour map of the cross section of the two-turned coil. Left part of the figure shows B_1 field which was measured in NMR system. Right part of the figure shows B_1 field which was computed. Both results are very similar. This proves model accuracy again.

4. SADDLE AND WIRE-RECTANGLE COILS

Next solved coils are saddle and wire-rectangle coil. Both coils are from cylindrical Cu wire again. Wire-rectangle coil is like two-turned coil however, turns have not circular shape but they have rectangular shape. Length of the turn is $l = 40\,\mathrm{mm}$, width is $w = 30\,\mathrm{mm}$. Saddle coil has the same construction and sizes as the wire-rectangle coil but in addition is flex as cylinder. Cylinder has radius $r = 15\,\mathrm{mm}$. Results are in the Figure 4. Cross sections are made as in the before case. Left part of the figure shows wire-rectangle coil and right part saddle coil.

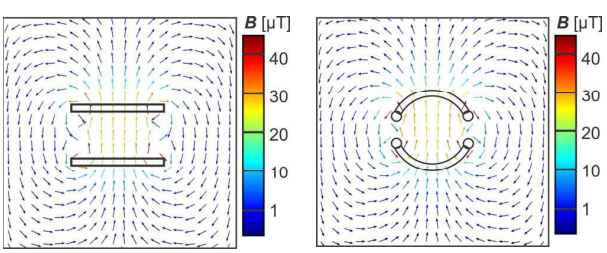

Figure 4: B_1 field of the wire-rectangle coil and saddle coil.

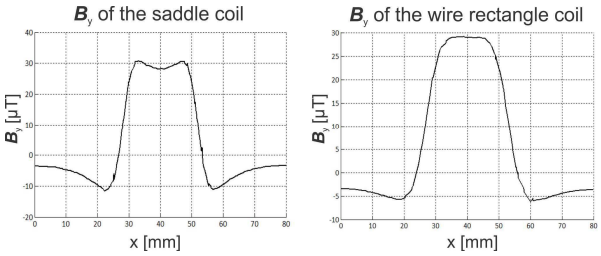

Figure 5: B_y field of the saddle coil and wire-square coil.

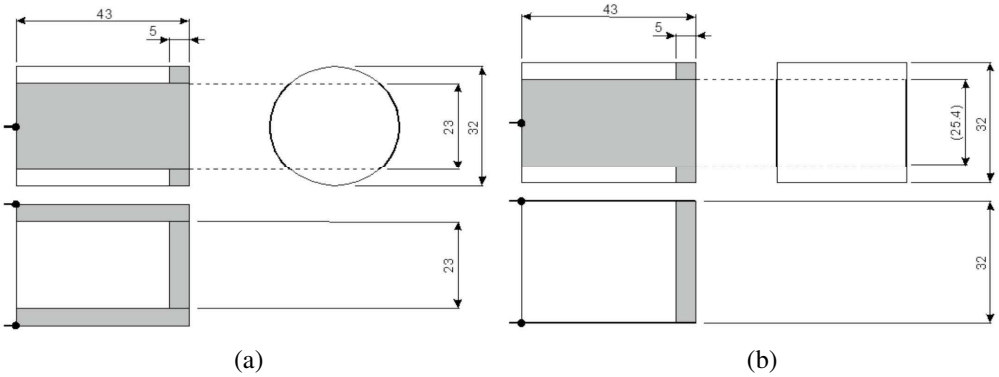

Figure 6: (a) Cylinder strip coil lay-out. (b) Square strip coil lay-out.

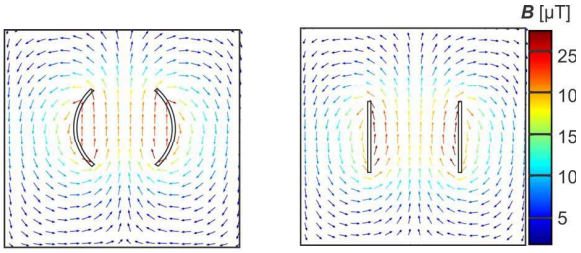

Figure 7: B_1 field of the cylinder strip coil and the square strip coil.

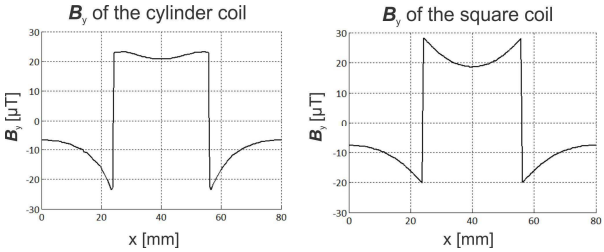

Figure 8: B_y field of the cylinder strip coil and the square strip coil.

In the Figure 5, are behaviours of the B_y field of the both coils. The B_y is domination component of the B_1 field so B_y the best speak about the B_1 field shape. Cross line for the behaviours leads the centre of the coils. Coils' directions corresponded with directions in the Figure 1.

5. CYLINDER AND SQUARE STRIP COILS

The last types are cylinder strip coil [5] and square strip coil. These coils are made from Cu plated. The plate thickness is $t = 0.05\,\text{mm}$. In the Figure 6(a), is lay-out of the cylinder strip coil and in the Figure 6(b) is lay-out of the square strip coil. In the Figure 7, are results. In the Figure 8, are behaviours of the B_y field. All cross sections were made like in the previous cases.

6. SUMMARY OF THE RESULTS

As is evident from previous results one-turned coil is good only for measuring layer at close quarters coil. Two-turned coil has B_1 field homogeneity enough, but another objects shape may not fit. For this cases are useful saddle coils and rectangle-wire coils. These coils have very good B_1 field homogeneity too, plus have better shape for various different object shapes. As is evident from Figure 5, B_y fields of the saddle and rectangle-wire coil are almost identical.

The cylinder strip coil has very good B_1 field homogeneity in the whole volume, plus has good shape for many different objects. The square strip coil has worst B_1 field homogeneity the previous coil, but the shape of this coil could be useful for some object.

This work will be continued to make sizes changing and make different shape coils for special using.

ACKNOWLEDGMENT

The work described in the paper was financially supported by the research project GA102/09/0314, research plan MSM 0021630513 and project of the BUT Grant Agency FEKT-S-10-13.

REFERENCES

1. Mispelter, J., M. Lupu, and A. Briguet, *NMR Probeheads for Biophysical and Biomedical Experiments*, Imperial College Press, 57 Shelton Street, Convent Garden London WC2H 9HE, 2006.
2. Brown, M. A. and R. C. Semelka, *MRI Basic Principles and Applications*, The United States of America, 2010.
3. Stratton, J. A., *Teorie Elektromagnetického Pole*, Státní Nakladatelství Technické Literatury v Praze, 1961.
4. Dědek, L. and J. Dědková, *Elektromagnetismus*, Vysoké Učení Technické v Brně, Vutium, Kounicova 67a, 1996.
5. Benadballah, N., N. Benahmed, B. Benyoucef, R. Bouhmidi, and M. Khelif, *Electromagnetic Analysis of the Slotted-tube Resonator with a Circular Cross Section for MRI Applications*, University of Tlemcen, P. O. Box 119, 13000 Tlemcen, Algeria, 2007.

Limits to the Measurement of the Magnetic Susceptibility Using NMR Method

P. Marcon[1], **K. Bartusek**[2], **and M. Cap**[1]

[1]Department of Theoretical and Experimental Electrical Engineering
Brno University of Technology, Kolejni 2906/4, Brno 612 00, Czech Republic
[2]Institute of Scientific Instruments, Academy of Sciences of the Czech Republic
Kralovopolska 147, Brno 612 64, Czech Republic

Abstract— The paper deals with modeling of the distribution of the magnetic field close to the non-ferromagnetic substances. Non-ferromagnetic cylinders were placed in the center of the cube shaped static magnetic field $B_0 = 4.7\,\mathrm{T}$. Material of the specimen reacts with the static magnetic field and creates a local changes of this field close to the specimen surface. Changes of the static magnetic field hold the possibilities to calculate the magnetic susceptibility of used material. In this article, will be discuss what under conditions is possible to use 1D and 2D method. Model results enable to set up the limits of used method. Consequently, the influence of the relation between length and diameter of the specimen on the accuracy of the magnetic susceptibility calculation is examined. As a specimen materials were used the varied size aluminum, platinum, bismuth and copper cylinders.

1. INTRODUCTION

The magnetic susceptibility is the physical quantity describing material properties in the external magnetic field [1]. Magnetic susceptibility is defined as the ratio between magnetization $\mathbf{M}$ of the material in the magnetic field and the field intensity $\mathbf{H}$:

$$\mathbf{M} = \chi_m \mathbf{H}. \tag{1}$$

Magnetic susceptibility measuring is possible by a several methods. Namely, Inductive method, SQUID, Guoyos balance or MR method is used. In this article, we are focused right on the MR method of magnetic susceptibility measurement. Especially, what under condition is possible to use this method for non-ferromagnetic materials.

One of the MR measurement methods — the Gradient echo (GE) method, is very sensitive to inhomogeneities of the static magnetic field and this can be useful for susceptibility measurement [2, 3]. Because the reaction field is generated proportionally to material susceptibility, it is possible to use the GE method for its measurement.

2. MR METHOD OF MAGNETIC SUSCEPTIBILITY MEASUREMENT

The MR image obtained using the GE technique is phase-modulated. Transversal magnetization $M_\perp$ is for the GE method described by the equation:

$$M_\perp(T_E) = M_0(T_E)\mathrm{e}^{-\frac{T_E}{T_2^*}}\mathrm{e}^{-\mathrm{j}\gamma\Delta B T_E}, \tag{2}$$

where M_0 is the transversal magnetization obtained immediately after excitation, which has been exponentially decreased in time by e^{-T_E/T_2^*}. Here T_2^* is effective relaxation time. The term $\mathrm{e}^{-\mathrm{j}\gamma\Delta B T_E}$ describes the phase modulation of magnetization, induced by reaction field ΔB. It is evident that the phase part of complex image can be used to obtain the spatial distribution of reaction magnetic field ΔB:

$$\Delta B = \frac{\Delta\varphi}{\gamma \cdot T_E}, \tag{3}$$

where γ is the gyromagnetic ratio of reference substance, $\Delta\varphi$ is the phase image, and T_E is the echo time of the GE measuring sequence. From (2), we can see two opposite requirements for the echo time: with longer time T_E we have magnetization which is more sensitive to the reaction field, but due to relaxation time T_2^* we also have a lower signal-to-noise ratio.

Let there be a static magnetic field described by H_0 and B_0, both in the z direction. Assume that a cylindrical specimen of diameter d and length l_s ($l_s \gg d$) is inserted into the magnetic field,

parallel to the direction of B_0. The behaviour of intensity of magnetic field $H_z(x)$ and magnetic induction $B_z(x)$ in the position $y = 0$ and $z = 0$ on a straight line is shown in Fig. 1. The differences between the change of the magnetic field in the specimen vicinity and the value of static magnetic field B_0 is called the reaction field ΔB. For the 1D configuration of the measurement the shape of the reaction field is 1-dimensional and depends on the shape of the specimen being measured.

Equation for magnetic susceptibility calculation of the modeled and measured specimen is derivated from Equations (1) and (3):

$$\chi_m = \frac{\Delta B_{\max} - \Delta B_{\min}}{B_0}. \tag{4}$$

Value $\Delta B_{\max}$ and $\Delta B_{\min}$ represent the maximum value of ΔB in space of the sample and the minimal ΔB value just next to the material sample.

3. EXPERIMENT

Space configuration of the sample is shown in the Fig. 2. Block space ($50 \times 50 \times 80$ mm) filled by air has magnetic susceptibility $\chi_{m1} = 0$, labeled by the number 1 in the Fig. 2. In the center of this space is placed the sample of mentioned materials with different magnetic susceptibility χ_m. The samples are in the shape of a cylinder with a length of 40 mm, labeled by the number 2 in the Fig. 2. The cylinder has a diameter of 5 mm. There were used the paramagnetic samples: aluminum ($\chi_{\mathrm{mAl}} = 2.2 \cdot 10^{-5}$), platinum ($\chi_{\mathrm{mPt}} = 2.65 \cdot 10^{-4}$) and the diamagnetic samples: copper ($\chi_{\mathrm{mCu}} = -9.2 \cdot 10^{-6}$) and bismuth ($\chi_{\mathrm{mBi}} = -1.66 \cdot 10^{-4}$). Section plane is placed to the center of the block space, labeled by the number 3 in the Fig. 2.

The model according to the arrangement shown in the Fig. 2 was designed in the COMSOL environment. The model was calculated with the use of the finite element method (FEM). After the calculation of the magnetic field distribution in x plane ($y = 0$, $z = 0$) the reaction field ΔB was determined by Equation (3). Course of the reaction field is concurrent to the course in Fig. 1. Value of the magnetic susceptibility of the modeled material was calculated from (4). Measurements were provided for cylinder shaped specimens with different size for determination of the method limits.

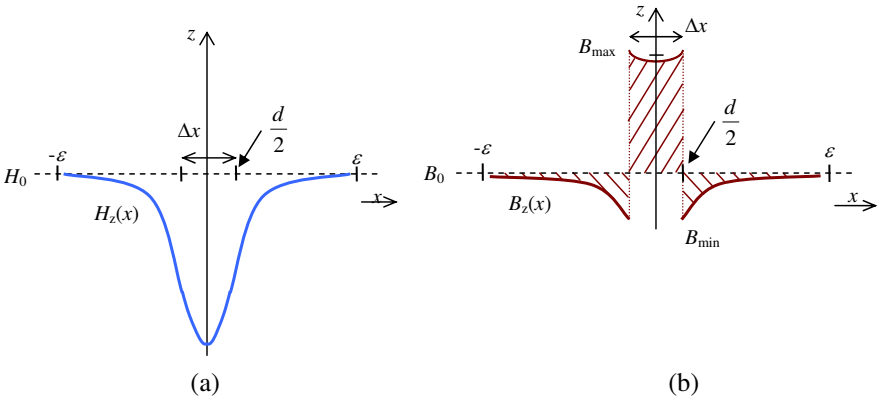

Figure 1: Idealized shape of (a) magnetic intensity $H_z(x)$ and (b) magnetic flux density $B_z(x)$ in paramagnetic specimen and its vicinity. H_0 is the field intensity and B_0 the magnetic flux density of the static field.

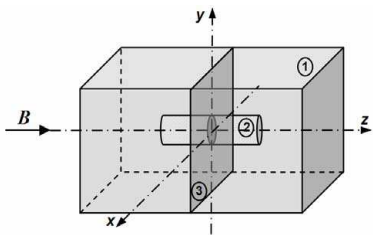

Figure 2: The configuration of the modeled system, cube filled by air with sample.

Table 1: Systematic errors between the value of the magnetic susceptibility χ_m and the calculated value $\delta\chi$.

Samples	χ_t [ppm]	χ_m [ppm]	$\delta\chi_m$ [%]
Cylinder-platinum	265.0	269.0	1.32
Cylinder-aluminum	22.0	22.3	1.26
Cylinder-copper	−9.2	−9.3	1.30
Cylinder-bismuth	−166.0	−168.0	1.29

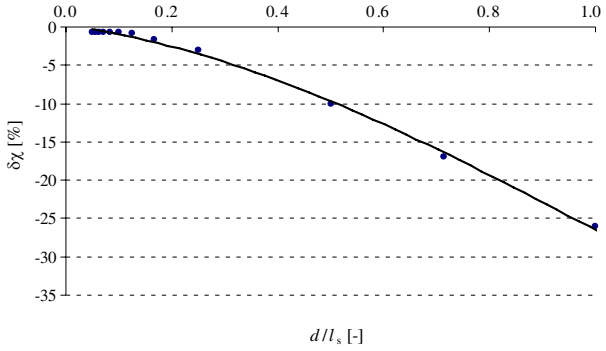

Figure 3: Dependence of the relative susceptibility error $\delta\chi$ on the ratio of diameter d to length l_s of specimen under measurement.

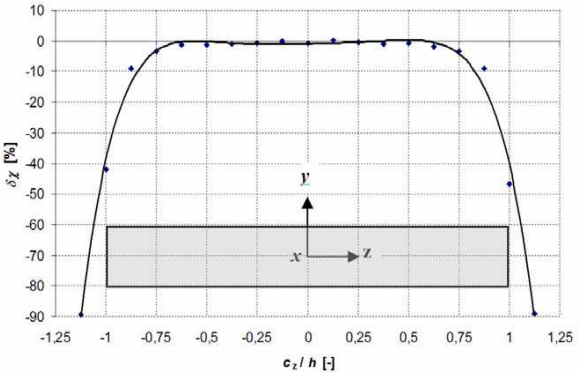

Figure 4: Dependence of relative susceptibility error $\delta\chi$ on the ratio of distance c_z between the plane measured and the specimen centre to specimen half length h.

4. RESULTS

Proposed Equation (4) gives values of the magnetic susceptibility with sufficient accuracy. Higher level of the accuracy is possible with increasing of the element size. In the Table 1 is shown an overview of the actual values of magnetic susceptibility χ_m of measured materials and systematic error $\delta\chi_m$ calculated from the model of individual samples.

5. LIMITS OF THE MAGNETIC SUSCEPTIBILITY CALCULATION

The accuracy of magnetic susceptibility calculation depends on the ratio of cylinder diameter to cylinder length, and on the place of the section from which the susceptibility is calculated. Denoting the specimen length l_s and its diameter d (Fig. 3), the magnitude of magnetic field induction $B_{\max}$ will depend on the d/l_s ratio; in the case of an inappropriate ratio the susceptibility measurement will carry an error. The relative error $\delta\chi$ established via simulation calculation is given in Fig. 3.

A map scanned outside the centre of the specimen being measured may be affected by deformations at the boundaries. The relative susceptibility error due to the finite length of specimen is illustrated in Fig. 4.

The specimen in Fig. 4 is placed in the centre of the coordinate system. Magnetic susceptibility was calculated from sections led through the x, y axis at the distance c_z from the origin of the coordinate system in axis z. For a relative measurement error of less than 5% the specimen diameter/specimen length ratio must be less than 0.3, and the ratio of the position outside the specimen c_z centre to its half length h less than 0.75. The length of specimens of arbitrary shape in section must be greater than the diameter of the circle described on the specimen section and the above conditions are the same.

6. CONCLUSION

In this work, we discuss MR method for magnetic susceptibility measurement. For verifying of the Equation (4) we firstly set up a model in COMSOL. As a modeled samples were chosen 4 non-ferromagnetic cylinders. This material affects the static magnetic field. Changes of the static magnetic field, the reaction field, are corresponding to the magnetic susceptibility of used material. Substitution of the reaction field values in en Equation (4) gives as sufficient accuracy value of the magnetic susceptibility of used material (as we can see in Table 1).

However, it this method has some limitations. For 5% accuracy of the magnetic susceptibility measurement is necessary to use cylindrical specimen. In additional, diameter of the specimen has to be 2.5 times smaller than its length. Value of the magnetic susceptibility is calculated from the 1D cut of the reaction field in the x plane ($y = 0$), see Fig. 2. As is shown in Fig. 4 the reaction field could be measured up to 3/4 of the specimen length from the center of the specimen.

ACKNOWLEDGMENT

The research described in the paper was financially supported by research plan No. MSM 0021630513 ELCOM, and research plan No. MSM 0021630516.

REFERENCES

1. Bartusek, K., M. Cap, P. Marcon, and J. Mikulka, "Magnetic susceptibility modelling using ANSYS," *PIERS Proceedings*, 190–193, Marrakesh, Mar. 20–23, 2011.
2. Steibauer, M. and K. Bartusek, "Magnetic susceptibility measurement using magnetic resonance tomograph," *Acta Technica CSAV*, Vol. 53, 2008.
3. Vladingerbroek, M. T. and J. A. Den Boer, *Magnetic Resonance Imaging*, Springer-Verlag, Heidelberg, Germany, 1999.
4. Bartusek, K., Z. Dokoupil, and E. Gescheidtova, "Mapping of magnetic field around small coils using the magnetic resonance method," *Measurement Science and Technology*, Vol. 18, 2223–2230, 2007.
5. Bartusek, K., Z. Dokoupil, and E. Gescheidtova, "Magnetic field mapping around metal implants using an asymmetric spin-echo MRI sequence," *Measurement Science and Technology*, Vol. 17, No. 12, 3293–3300, 2006.

Sensitivity of the Diffusion Coefficients Measurement to Gradient Field Changes

P. Marcon[1], **K. Bartusek**[2], **and M. Cap**[1]

[1]Department of Theoretical and Experimental Electrical Engineering
Brno University of Technology, Kolejni 2906/4, Brn 612 00o, Czech Republic
[2]Institute of Scientific Instruments, Academy of Sciences of the Czech Republic
Kralovopolska 147, Brno 612 64, Czech Republic

Abstract— The paper deals with accuracy of the diffusion coefficient measurement. Diffusion coefficients were measured by the pulse filed gradient spin echo (PFGSE) method. b-factor value as well as the diffusion coefficients of the measured sample is dependent on the gradient field. As a result is presented relationship between diffusion measurement accuracy and changes of the magnetic field. Consequently, diffusion gradients were modified for the highest accuracy of the measurement. As a specimen by the nickel sulfate water solution filled syringe is used.

1. INTRODUCTION

MRI method is suitable method of research of particles transport in various substances. This motion is according to Stokes-Einstein's equation depended on temperature and on diffusion coefficient of measured substance [1]. This coefficient is in literature named as ADC (Appearent Diffusion Coefficient) D. Diffusion coefficient represents the particles mobility. Method of diffusion coefficient measurement was published in 1965 by O. Stejskal and I. E. Tanner [2]. They describe spectroscopic measurement of diffusion coefficient by the PFGSE (Pulse Field Gradient Spin Echo) method. This method was improved and consequently used for diffusion weighted imaging DWI.

ADC value is calculated from by PGFSE method measured data. One ADC value represents one pixel of DWI image. ADC (usually D) is calculated as:

$$\frac{S}{S_0} = \mathrm{e}^{-bD}, \tag{1}$$

where S is the image measured with gradient or combination of gradients and S_0 is image measured without any gradient. D is depended on the temperature, magnetic field homogeneity and on the parameters of the gradient pulse. For the time intervals and gradient pulse description the value of b-factor is used. The most used PFGSE method with six intervals and sensitivity of the diffusion coefficient on b-factor change are discussed in this article [3].

2. DIFFUSION MEASUREMENT METHOD

The six-interval PFGSE pulse sequence is shown in Fig. 1. During the spin-echo sequence are applied two identical gradient pulses of length δ called the diffusion gradients G. The time interval between gradient pulses is Δ. Optimal parameters of the pulse sequence are selected according to the estimated diffusion. Slower diffusion is suitable to chose the high gradient value G and gradient length δ and increase the time interval between the gradient pulses. Calculation is provided from the ratio of the spin echo size and after the 90° pulse measured FID.

Diffusion gradients G are not necessarily rectangular. In some cases in possible to use trapezoidal or half-sinusoidal gradient pulses. Reasons for use of this pulses is considerable deceleration of the entering and trailing edges, small eddy currents creation close to the conductive materials and considerable decreasing of deformations of the magnetic field gradients. Pulse sequences for three different shapes of diffusion gradient and equations for b-factor calculation are shown in Fig. 1.

Equations for b-factor calculation:

Rectangular diffusion gradient:

$$b = \gamma^2 G^2 \delta^2 \left(\Delta - \frac{\delta}{3}\right), \tag{2}$$

trapezoidal diffusion gradient:

$$b = \gamma^2 G^2 \left(\delta^2 \left(\Delta - \frac{\delta}{3}\right) + \frac{\varepsilon^3}{30} - \frac{\delta\varepsilon^3}{6}\right), \tag{3}$$

half-sinusoidal diffusion gradient:

$$b = 4\pi^{-2}\gamma^2 G^2 \delta^2 \left(\Delta - \frac{\delta}{3}\right), \tag{4}$$

where γ gyromagnetic constant. Constant γ is for hydrogen atom equal to $\gamma_H = 2,67 \cdot 10^8$. G is amplitude of the gradient pulse. Other quantities are time intervals in PFGSE sequence as can be seen in Fig. 1. Quantity δ is the length of the gradient pulse and Δ is the distance of two gradient pulses. Detailed information about PFGSE method is in [4, 5].

3. CHARACTERISTIC SENSITIVITY OF THE DIFFUSION COEFFICIENT

Sensitivity of the diffusion coefficient D on gradient pulse amplitude, length of the gradient pulse and on the distance between the gradients pulses Δ [6] according to mentioned Equations (2), (3) and (4) is investigated. Simulations results proofed the identical sensitivity of the diffusion coefficient change on changes of the diffusion gradient for all gradient pulses shapes.

Figure 2 shows the analysis of the influence of the relative change of the diffusion coefficient (δD) on the relative change of the diffusion gradient. Resulted curves are same for rectangular, trapezoidal and half-sinusoidal gradient.

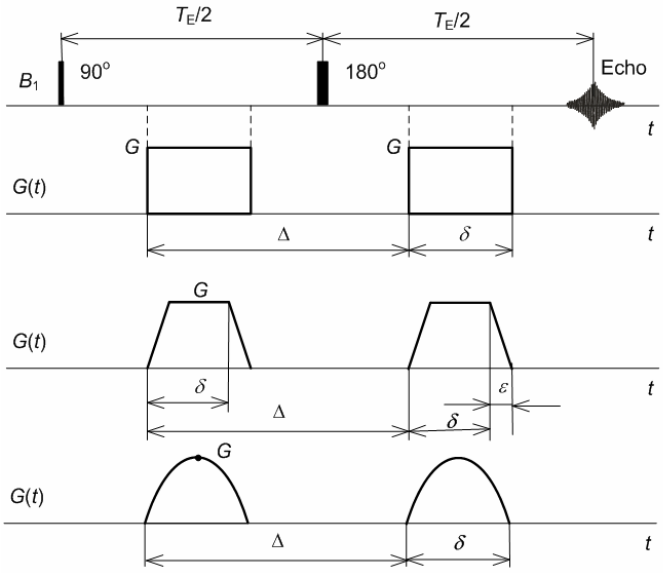

Figure 1: Six-interval pulse sequence for diffusion measurement by use different gradient pulses: rectangular, trapezoidal and half-sinusoidal shapes and corresponding b-factor equations.

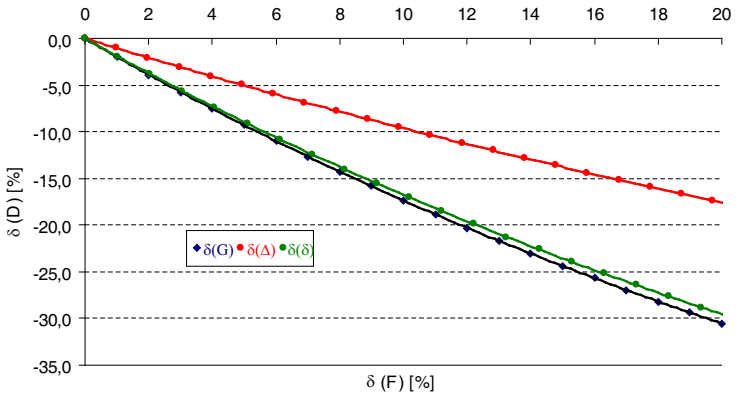

Figure 2: Dependence of relative diffusion error $\delta(D)$ on the activity level $\delta(F)$ of the diffusion gradient.

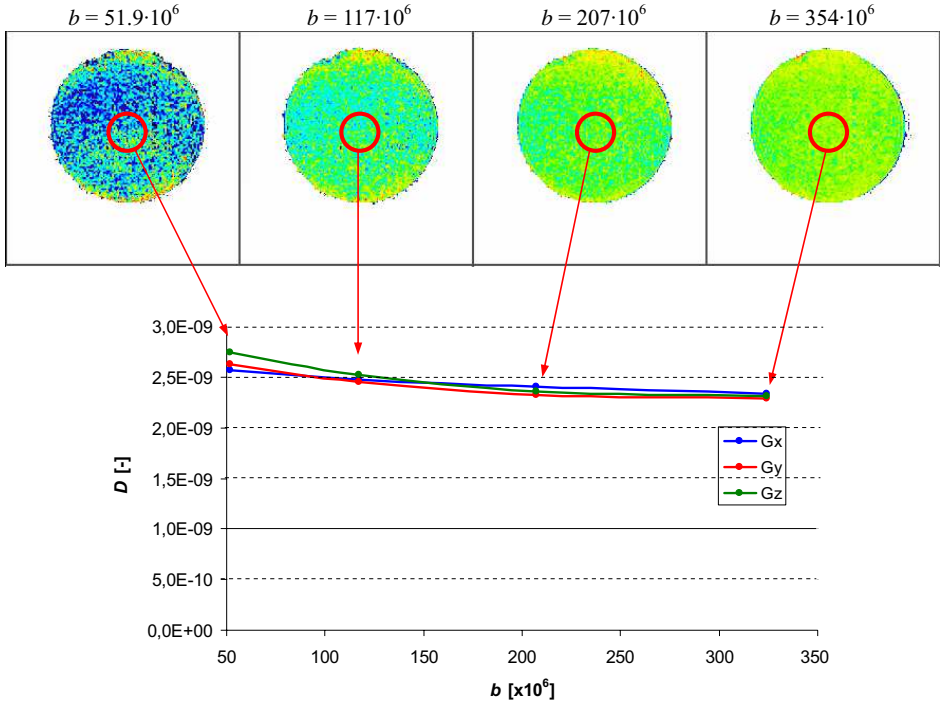

Figure 3: Measured diffusion images for varied b-factor value. Dependencies of the diffusion coefficient on the b-factor value for all x, y and z axis.

Figure 2 shows the highest sensitivity of the diffusion coefficient on the change of the gradient pulse G amplitude and on the gradient pulse length. Lower sensitivity was discovered for distance between two diffusion gradients. Diffusion coefficient measurement with relative error lower than 5% require the following settings: gradient field pulse setting accuracy lower than 3%, length of pulse δ setting accuracy lower than 3% and distance between gradient pulses setting accuracy lower than 5%.

4. EXPERIMENTAL MEASUREMENT OF THE DIFFUSION COEFFICIENT

Experimental measurement of the diffusion coefficient was provided in MR tomograph with static magnetic field $B_0 = 4.7\,\mathrm{T}/120\,\mathrm{mm}$ (i.e., 200 MHz for 1H nuclei). Actively shielded gradient coils yield a maximum gradient field magnitude of 180 mT/m. The diffusion coefficient was measured 3 times for magnetic field inhomogeneity suppression. Measurement was provided without gradient (image S_0), with positive gradient (image S_+) and with negative gradient (image S_-).

Diffusion coefficient was consequently calculate from following equation as:

$$\frac{S_+ + S_-}{2 \cdot S_0} = \mathrm{e}^{-bD}. \tag{5}$$

Detailed description of measurement method is in literature [7] and [8]. NMR method for diffusion measurement require to measure at least in 6 directions of applied diffusion gradient. Result of this process is the anisotropic environment describing diffusion tensor $\mathbf{D}$ [1].

$$\mathbf{D} = \begin{bmatrix} D_{xx} & D_{xy} & D_{xz} \\ D_{yz} & D_{yy} & D_{yz} \\ D_{zx} & D_{zy} & D_{zz} \end{bmatrix}. \tag{6}$$

One of the possible ways of the diffusion tensor measurement is the setting of the gradient pulses G_x, G_y and G_z in accordance with following condition $b = b_{xx} = b_{yy} = b_{zz} = \sqrt{b_x}, \sqrt{b_y} = \sqrt{b_y}, \sqrt{b_z} = \sqrt{b_x}, \sqrt{b_z}$. The time settings need to be provided with highest accuracy. MR tomograph was calibrated for the constant b-factor value in x, y and z axis direction. Consequently, by the nickel sulfate water solution filled syringe (20 mm in diameter) was measured.

Parameters of diffusion gradients were: $\delta = 3.72$ ms, $\Delta = 15.8$ ms and gradient G size was varied. Measurement was provided at temperature 26.3°C.

DWI images with applied diffusion gradient in y axis can be seen in Fig. 3. Measurement was provided with varied diffusion gradient G_y. Diffusion coefficient dependency on the b-factor value was calculated from selected area. Resulted dependencies can be seen in Fig. 3. Graph shows that the diffusion coefficient dependencies are almost constant for b-factor value higher then $b = 117 \cdot 10^6$.

5. CONCLUSION

The paper deals with accuracy of the diffusion coefficient measurement. Diffusion coefficients were measured by the pulse filed gradient spin echo (PFGSE) method. By the change of the gradient field the b-factor value is changing as well as value of the diffusion coefficient of the measured specimen. As a result is presented graphic relationship between diffusion measurement accuracy and changes of the gradient field. According to the obtained dependence the MR tomograph was configured for the highest measurement accuracy. As a specimen by the nickel sulfate water solution filled syringe was used.

In this article is closely discussed the PFGSE method of diffusion coefficients measurement. Dependencies of the relative error of the diffusion coefficient on the relative change of the diffusion gradient parameters are shown in Fig. 1. Fig. 2 shows the highest sensitivity of the diffusion coefficient on the change of the gradient pulse G amplitude and on the gradient pulse length.

In the next part of article was discussed the MR measurement. The diffusion coefficient was measured 3 times for magnetic field inhomogeneity suppression [8]. The setting of the gradient pulses G_x, G_y and G_z in accordance with following condition $b = b_{xx} = b_{yy} = b_{zz}$ was provided. This condition is important for measurement in anisotropic environment and for description of this environment by the diffusion tensor. Setting of the gradient pulses was done for nickel sulfate water solution with high accuracy. Hence, the diffusion coefficients are in all axes almost constant.

ACKNOWLEDGMENT

The research described in the paper was financially supported by research plan No. MSM 0021630513 ELCOM, and research plan No. MSM 0021630516.

REFERENCES

1. Johansen-Berg, H. and T. E. J. Behrens, *Diffusion MRI: From Quantitative Measurement to in vivo Neuroanatomy*, Elsevier, China, 2009.
2. Stejskal, E. O. and J. E. Tanner, "Spin diffusion measurements: Spin echoes in the presence of a time-dependent field gradient," *The Journal of Chemical Physics*, Vol. 42, No. 1, 10–28, 1965.
3. Bartusek, K. and E. Gescheidtova, "MR Measurement technique of rapidly switched gradient magnetic fields in MR tomography," *Applied Magnetic Resonance*, Vol. 29, No. 12, 675–686, 2006.
4. Mansfield, P. and B. Chapman, "Active magnetic screening of gradient coils in NMR imaging," *Journal of Magnetic Resonance*, Vol. 66, 1986.
5. Bartusek, K., *Special Methods of Diffusion Coefficients Measurement by Use of Nuclear Magnetic Resonance*, Inaugural thesis, Brno Univeristy of Technology, Brno, 2007.
6. Bartusek, K. and E. Gescheidtova, "Testing the quality of magnetic gradient fields for studying self-diffusion processes in biological specimens by magnetic resonance methods," *Measurement Science and Technology*, Vol. 17, 2256–2262, 2006.
7. Bartusek, K. and E. Gescheidtova, "MRI method of diffusion measurement in heterogeneous materials," *Measurement Science and Technology*, Vol. 19, 2008.
8. Marcon, P. and K. Bartusek, "Errors in diffusion coefficients measurement," *PIERS Proceedings*, 1035–1039, Cambridge, USA, July 5–8, 2010.

Evaluation of Errors in Manual Image Processing

J. Mikulka, **E. Gescheidtová**, **and K. Bartušek**
Department of Theoretical and Experimental Electrical Engineering
Brno University of Technology, Kolejni 4, Brno 612 00, Czech Republic

Abstract— The article describes kinds of errors which appears in biomedical image processing and possibilities of their evaluation. The research is focused mainly on evaluation of number of objects in image (cells, neurons, tissues). The issue of manual segmentation is also described within the meaning of bounding interesting areas for further processing (area evaluation, visualization). The methodology of manual and automatic processing is proposed and the experimental results are shown.

1. INTRODUCTION

Manual image processing is still the most used approach for evaluating of various parameters and properties of observed objects. This approach has advantages and disadvantages. The main advantage is direct use of processing person knowledge. The main disadvantage is time demand and in case of use of improper approach is high error rate. The article describes kinds of errors which appears in biomedical image processing and possibilities of their evaluation. The research is focused mainly on evaluation of number of objects in image (cells, neurons, tissues). In Figure 1 is shown a case with recognizing the problematic area with several cell nuclei, on the right is shown the result of automatic image processing.

The issue of manual segmentation is also described within the meaning of bounding interesting areas for further processing (area evaluation, visualization) [1, 2]. In Figure 2 is shown example of liver tumor and results of two kinds of segmentation.

In the first case (counting the objects) a tiredness and decreased concentration is expected in long-term manual image processing and thus increasing of error rate. In case of manual segmentation and bounding searched area adds to tiredness effect the error of inaccurate boundary determination. There are described traditional methods of image processing in medical practice. Furthermore, the methodology of automatic and semiautomatic image processing is proposed. Impacts to speed, accuracy and entire efficiency are discussed.

2. CURRENT STATE

Currently the manual evaluation is the most frequently used approach in medical practice. The main problem in manual processing is that this approach is very time-consuming. The error of processing increases in the time of manual processing because of tiredness of people. Also a human factor causes an error in manual processing such as inaccurate boundaries determination. In Figure 3 is example of supposed course of error function in manual counting of object in a set of images and supposed course of error function in automatic counting of objects by a tool.

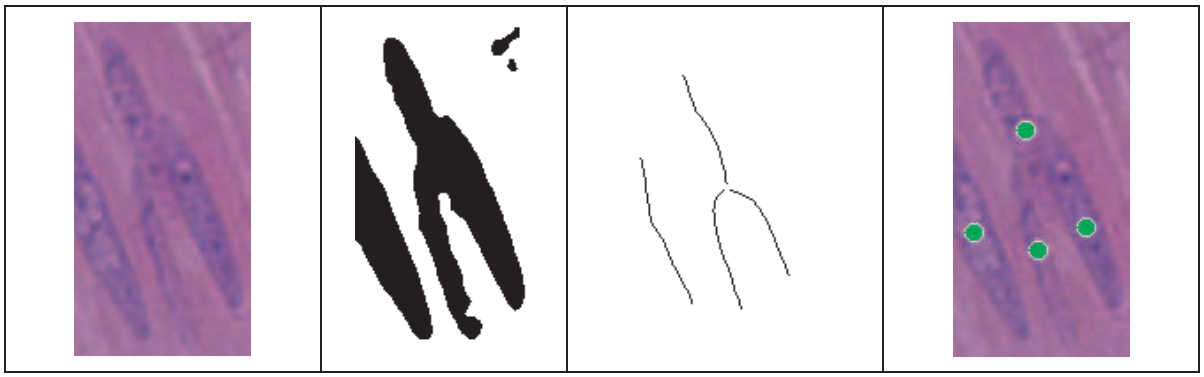

Figure 1: The example of problematic area with several cell nuclei in tissue, (a) original image, (b) thresholding, (c) skeleton, (d) result of automatic cell nuclei counting.

3. PROPOSED APPROACH

We proposed approaches to evaluate two types of errors. The first type of error of manual image processing is evaluation of inaccurate boundaries determination in manual segmentation of images. The aim of this type of error evaluation is to establish the difference between the manual determined boundary and real boundary. This difference corresponds to area given by sum of pixels:

$$E = \sum_{\Omega} \left(I_{\mathrm{A}} - I_{\mathrm{B}}\right) \cup \left(I_{\mathrm{B}} - I_{\mathrm{A}}\right). \tag{1}$$

where E is the error (difference) between area determined manually and segmented by automated tool on image area Ω, I_{A} and I_{B} are sets of pixels on image area Ω, which belong to segmented area of interest by manual approach or reference automated approach. Described operation is shown in Figure 4. The area filled by blue color represents the difference between results of two segmentation methods A and B.

The second type of error arises in counting of objects in image. The error increases in time of processing because of tiredness. The proposed approach is to process set of images manually, write time of processing, duration and number of objects. In counting of objects there are to kinds of error: miss detected object (object in the image which is not marked manually), false detected object (mark in the image which does not correspond with counted objects).

It can be assumed that number of miss detected and false detected objects will increase in the time of processing. The results of automatic processing will be taken as reference real values. For this purpose will be created Java application in ImageJ open-source software. All the mentioned variables will be registered automatically.

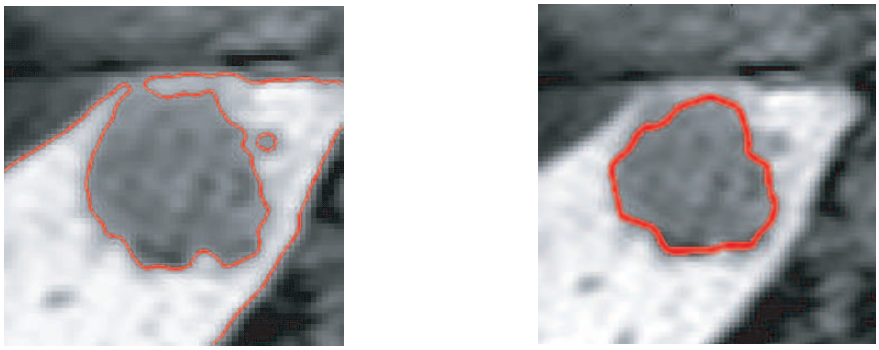

(a) (b)

Figure 2: The example of problematic area with smooth edges of region of interest, (a) segmentation by region-based snakes, (b) segmentation by edge-based snakes.

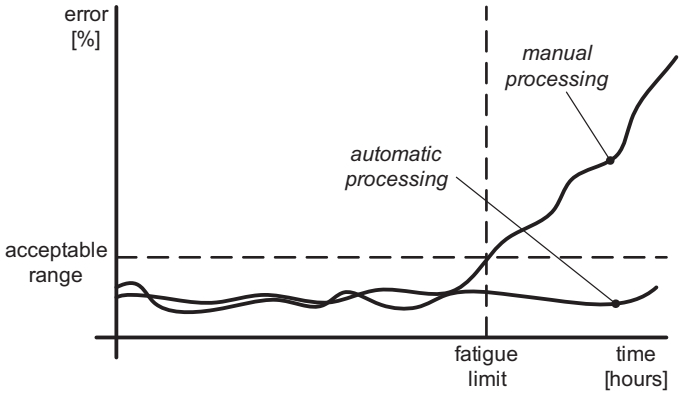

Figure 3: Supposed course of error function in manual counting of object in a set of images and supposed course of error function in automatic counting of objects by a tool.

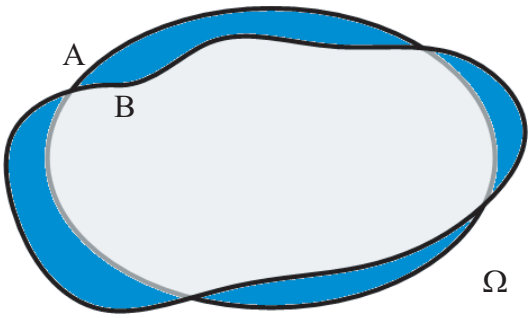

Figure 4: Graphical representation of proposed approach for evaluation of quality of segmentation.

Table 1: Table for evaluation of tiredness error in manual image processing (counting of objects).

Image	**Time of processing [hh:mm]**	**Duration [minutes]**	**Number of objects by manual processing**	**Number of objects by automatic processing**	**Miss detection**	**False detection**
1	08:30	13	35	38	2	4
2	08:45	15	45	48	3	5
n	18:30	25	40	39	10	8

4. CONCLUSIONS

In this article was shown basic ideas of evaluation of quality of manual image processing within the meaning of manual segmentation of image (determining of objects boundary) and manual counting of objects (determining of density). Two kinds of error were described: difference between area determined by manual and automatic segmentation and difference between manual and automatic object counting in the time. In this case has to be established two errors: miss detection and false detection of objects. The first one means number of objects which is not correctly marked, the second one means the number of objects which are marked incorrectly.

ACKNOWLEDGMENT

This work was supported within the framework of the research plan MSM 0021630513 and projects ME10123 and GACR 102/11/0318.

REFERENCES

1. Mikulka, J., E. Gescheidtová, K. Bartušek, and Z. Smékal, "Processing of MR slices of temporomandibular disc for 3D visualization," *PIERS Online*, Vol. 6, No. 3, 204–206, 2010.
2. Mikulka, J., E. Gescheidtová, and K. Bartušek, "Processing of MR slices of human liver for volumetry," *PIERS Proceedings*, 202–204, Xian, China, March 22–26, 2010.
3. "Image Processing and Analysis in Java (ImageJ) software documentation," on the website: http://rsbweb.nih.gov/ij/.

Multiple Reflection from Layered Heterogeneous Medium

R. Kadlec, E. Kroutilová, and P. Fiala
Department of Theoretical and Experimental Electrical Engineering
Brno University of Technology, Kolejní 2906/4, Brno 612 00, Czech Republic

Abstract— The paper presents the problem of algorithm design of propagation, reflection and refraction of the electromagnetic waves on a layered medium. The analytic solution of this issue is very intricate and time demanding. This method is suitable for specific purposes of the detailed analysis of the general issue. Numerical methods are more suitable for analysis of the reflection and refraction of electromagnetic waves on layered heterogeneous medium. Fundamental law for analysis of the reflection and the refraction of electromagnetic waves on the boundary line between two materials are Snell's law for electromagnetic waves. The paper deals with the problem of complex angle of refraction in the losing medium. In non-lossy environment, interpretation of Fresnel relations and Snell's law is simple. For a layered heterogeneous medium, an algorithm was prepared for the reflection on several layers in MatLab program environment. Methods described in this paper are suitable for analysis of beam refraction to the other side from the perpendicular line during the passage through the interface. This phenomenon is occur in metamaterial. These materials with negative parameters constitute a group of media that possesses a negative value, relative permittivity or relative permeability or both.

1. INTRODUCTION

Generally, inhomogeneities and regions with different parameters appear even in the cleanest materials. During the electromagnetic wave passage through a material there occur an amplitude decrease and a wave phase shift, owing to the material characteristics such as conductivity, permittivity, or permeability. If a wave impinges on an inhomogeneity, a change of its propagation there occurs. This change materializes in two forms, namely in reflection and refraction. In addition to this process, polarization and interference may appear in the waves.

2. ELECTROMAGNETIC WAVES IN ISOTROPIC DIELECTRICS MATERIALS

Algorithms were generated in the Matlab program environment that simulates reflection and refraction in a lossy environment on the interface between two dielectrics. This section of the paper is linked to the previous modelling of light applying the related geometrical laws. The reflection and refraction is in accordance with Snell's law for electromagnetic waves as shown in Fig. 1. The form of Snell's law is

$$\frac{\sin\theta_0}{\sin\theta_2} = \frac{k_2}{k_1} = \frac{\sqrt{j\omega\mu_2 \cdot (\gamma_2 + j\omega\varepsilon_2)}}{\sqrt{j\omega\mu_1 \cdot (\gamma_1 + j\omega\varepsilon_1)}}, \tag{1}$$

where k is the wave number, γ is the conductivity, ε the permittivity and μ the permeability. Relation (1) is defining for the boundary line between the dielectrics medium. Generally, k_1 and k_2 are complex; then angle θ_2 is also complex. An electromagnetic wave is understood as the electric field strength and the magnetic field strength. The electric component and magnetic component incident wave according to Fig. 1 follows the formula

$$\mathbf{E}_i = \mathbf{E}_0 e^{-j\mathbf{k}_1\mathbf{u}_{n0}\cdot\mathbf{r}}, \quad \mathbf{H}_i = \frac{\mathbf{u}_{n0} \times \mathbf{E}_i}{\mathbf{Z}_{v1}} \tag{2}$$

where $\mathbf{E}_0$ is the amplitude electric field strength on the boundary line, $\mathbf{r}$ is the positional vector, and $\mathbf{u}_{n0}$ is the unit vector of propagation direction.

The intensity of reflection beams and the intensity of refraction beams are expressed according to the formula

$$\mathbf{E_r} = \mathbf{E}_1 e^{-jk_1\mathbf{u_{n1}}\times\mathbf{r}}, \quad \mathbf{E_t} = \mathbf{E}_2 e^{-jk_2\mathbf{u_{n2}}\times\mathbf{r}}, \tag{3}$$

where $\mathbf{E}_1$ is calculated from the intensity on boundary line $\mathbf{E}_0$ and reflection coefficient ρ_E, and $\mathbf{E}_2$ is calculated from the intensity on boundary line $\boldsymbol{E}_0$ and transmission factor τ_E:

$$\mathbf{E}_1 = \rho_E \cdot \mathbf{E}_0, \quad \mathbf{E_2} = \tau_E \cdot \mathbf{E}_0, \tag{4}$$

magnetic component is calculated from electric component and wave impedance:

$$\mathbf{H}_0 = \frac{\mathbf{E}_0}{\mathbf{Z}_{v1}}, \quad \mathbf{H}_1 = \frac{\mathbf{E}_1}{\mathbf{Z}_{v1}}, \quad \mathbf{H}_2 = \frac{\mathbf{E}_2}{\mathbf{Z}_{v2}}. \tag{5}$$

The calculation of reflection coefficient ρ_E and transmission factor τ_E with utilization of wave impedance Z_v is according to these relations:

$$\rho_E = \frac{\mathbf{E}_1}{\mathbf{E}_0} = \frac{Z_{v2}\cos\theta_1 - Z_{v1}\cos\theta_2}{Z_{v2}\cos\theta_1 + Z_{v1}\cos\theta_2}, \quad \tau_E = \frac{\mathbf{E}_2}{\mathbf{E}_0} = \frac{2Z_{v2}\cos\theta_1}{Z_{v2}\cos\theta_1 + Z_{v1}\cos\theta_2}. \tag{6}$$

For numerical modelling, there is a suitable relation in the form of

$$\begin{aligned} \mathbf{E_r} &= \frac{\mu_2 k_1 \cos\theta_0 - \mu_1\sqrt{k_2^2 - k_1^2\sin^2\theta_0}}{\mu_2 k_1 \cos\theta_0 + \mu_1\sqrt{k_2^2 - k_1^2\sin^2\theta_0}}\mathbf{E}_0 \cdot e^{-jk_1\,\mathbf{u_{n1}}\times\mathbf{r}}, \\ \mathbf{E_t} &= \frac{2\mu_2 k_1 \cos\theta_0}{\mu_2 k_1 \cos\theta_0 + \mu_1\sqrt{k_2^2 - k_1^2\sin^2\theta_0}}\mathbf{E}_0 \cdot e^{-jk_2\,\mathbf{u_{n2}}\times\mathbf{r}}. \end{aligned} \tag{7}$$

These relations are calculated from the basic variable and they facilitate an acceleration of the calculation process.

Interpretation of the Fresnel equations and Snell's laws is simple in the case of the refraction on boundary line between the dielectrics medium. In case of refraction in a lossy medium, angle θ_2 is complex. According to relation (1), angle θ_2 depends on wave numbers k_1 and k_2, which are generally complex; then, in medium 2 an inhomogeneous wave is propagated.

Example of reflection and refraction on a planar boundary line in COMSOL program is shown in Fig. 2 (at the incidence of the wave on the interface at an angle of 45°).

For a layered heterogeneous medium, an algorithm is deduced for the reflection on several layers. The reflection and refraction on a heterogonous material is solved by the help of the numerical method. The reflection on a layered material on n layers generates n primary electromagnetic waves, according to Fig. 4. The interpretation of propagation of electromagnetic waves on a layered heterogeneous medium is according to relation

$$\mathbf{E_{rl}} = \mathbf{E_{il}}\rho_{E\lambda} \cdot e^{-jk_l\,\mathbf{u_{nrl}}\times\mathbf{r_l}}, \quad \mathbf{E_{tl}} = \mathbf{E_{il}}\tau_{E\lambda} \cdot e^{-jk_l\,\mathbf{u_{ntl}}\times\mathbf{r_l}}, \tag{8}$$

where $\mathbf{E}_{rl}$ and $\mathbf{E}_{tl}$ are the reflection and refraction electromagnetic waves on the boundary line ($l = 1, \ldots, \max$) according to Fig. 4, $\mathbf{E}_{il}$ is the amplitude electric field strength on boundary line l,

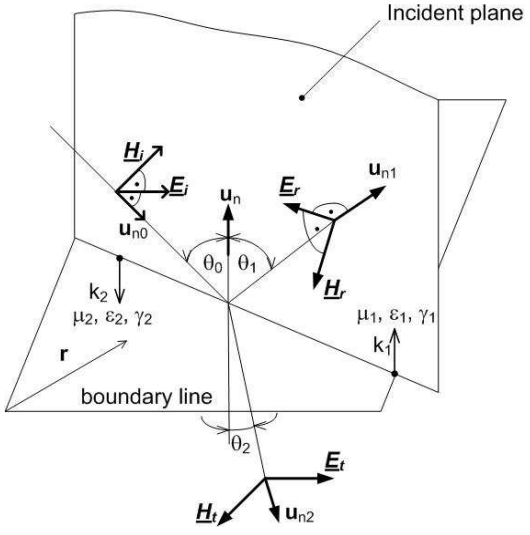

Figure 1: Reflection and refraction of light [1].

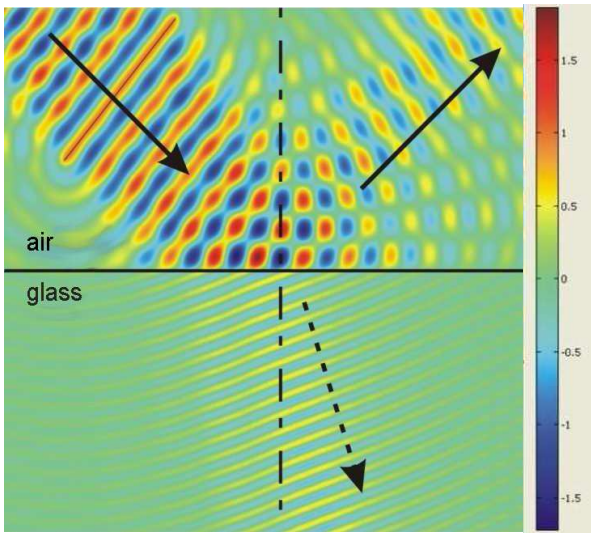

Figure 2: Reflection and refraction on a planar boundary line [2].

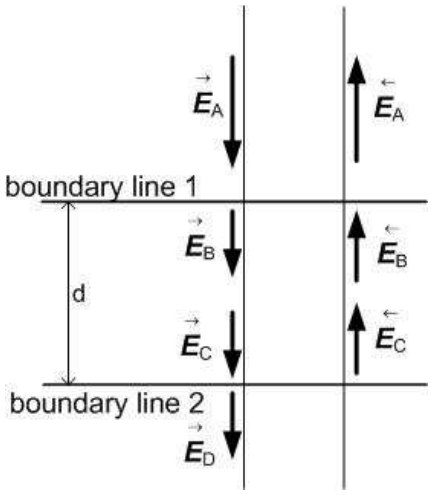

Figure 3: Perpendicular incidence of the wave on layered material.

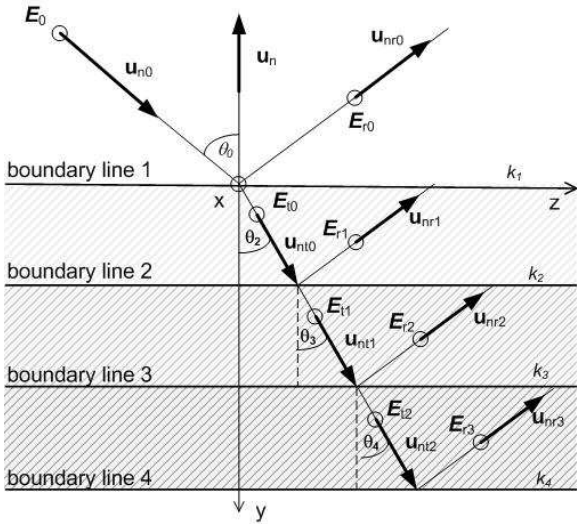

Figure 4: Reflection and refraction on a layered heterogenous material.

ρ_{El} and τ_{El} are the reflection coefficient and transmission factor on boundary line l, k_l is the wave number of layer, $\mathbf{r}_l$ is the electromagnetic wave positional vector on boundary line l, $\boldsymbol{u}_{\mathbf{nt}l}$ and $\boldsymbol{u}_{\mathbf{nr}l}$ are the unit vectors of propagation direction.

Special case is perpendicular incidence of the electromagnetic wave on the interface according to Fig. 3. The interpretation of perpendicular incidence for incident wave $\tilde{\mathbf{E}}_{\mathbf{A}}$ and reflection wave $\overleftarrow{\mathbf{E}}_{\mathbf{A}}$ is according to relation

$$\tilde{\mathbf{E}}_{\mathbf{A}} = \frac{e^{jk_2\cdot\mathbf{u_{nA}}\times\mathbf{r}} + \rho_{12}\rho_{23}\cdot e^{-jk_2\cdot\mathbf{u_{nA}}\times\mathbf{r}}}{\tau_{12}\tau_{23}}\tilde{\mathbf{E}}_{\mathbf{D}}, \quad \overleftarrow{\mathbf{E}}_{\mathbf{A}} = \frac{\rho_{12}e^{jk_2\cdot\mathbf{u_{nA}}\times\mathbf{r}} + \rho_{23}e^{-jk_2\cdot\mathbf{u_{nA}}\times\mathbf{r}}}{\tau_{12}\tau_{23}}\tilde{\mathbf{E}}_{\mathbf{D}}, \tag{9}$$

where ρ_{12} is reflection coefficient of wave in external medium which is reflective on boundary line 1, ρ_{21} is reflection coefficient of wave in internal medium which is reflective on boundary line 1. Transmission factors τ are indexed analogically. k_2 is the wave number internal medium and $\mathbf{u_{nA}}\times\mathbf{r}$ is distance between boundary lines.

With some redefinitions, the formalism of transfer matrices and wave impedances for perpendicular incidence translates almost like to the case of oblique incidence. By separating the fields into transverse and longitudinal components with respect to the direction the dielectrics are stacked (the z-direction), we show that the transverse components satisfy the identical transfer matrix relationships as in the case of perpendicular incidence. The transverse components of the electric fields are defined differently in the two polarization cases. We recall from that an obliquely-moving wave will have, in general, both TM and TE components, then we use generally electric component $\mathbf{E}_T$ with both polarizations, in this paper [5].

Using the matching and propagation matrices for transverse fields we derive here the layer recursions for multiple dielectric slabs at oblique incidence [5]. Fig. 4 shows such a multilayer structure. The layer recursions relate the various field quantities, such as the electric fields and the reflection waves, on the top of each interface.

We assume that there are no incident fields from the down side of the structure. The reflection/refraction angles in each medium are related to each other by Snel's law applied to each of the $M+1$ interfaces:

$$k_1\cdot\sin\theta_0 = k_2\cdot\sin\theta_2 = k_l\cdot\sin\theta_l, \quad l = 1, 2, \ldots, M \tag{10}$$

To obtain the layer recursions for the electric fields, we apply the propagation matrix [5] to the fields on the top of interface $l+1$ and propagate them to the down of the interface l, and then, apply a matching matrix [5] to pass to the left of that interface:

$$\begin{bmatrix} \tilde{\mathbf{E}}_{\mathbf{T}}l \\ \overleftarrow{\mathbf{E}}_{\mathbf{T}}l \end{bmatrix} = \frac{1}{\tau_{Tl}}\begin{bmatrix} 1 & \rho_{Tl} \\ \rho_{Tl} & 1 \end{bmatrix}\begin{bmatrix} e^{jk_l\cdot\mathbf{u}_{\mathbf{n}l}\times\mathbf{r}} & \\ & e^{-jk_l\cdot\mathbf{u}_{\mathbf{n}l}\times\mathbf{r}} \end{bmatrix}\begin{bmatrix} \tilde{\mathbf{E}}_{\mathbf{T},l+1} \\ \overleftarrow{\mathbf{E}}_{\mathbf{T},l+1} \end{bmatrix}. \tag{11}$$

Multiplying the matrix factors, we obtain:

$$\begin{bmatrix} \tilde{\mathbf{E}}_{\mathbf{T}l} \\ \overleftarrow{\mathbf{E}}_{\mathbf{T}l} \end{bmatrix} = \frac{1}{\tau_{Tl}} \begin{bmatrix} e^{jk_l \cdot \mathbf{u}_{\mathbf{n}l} \times \mathbf{r}} & \rho_{Tl} e^{-jk_l \cdot \mathbf{u}_{\mathbf{n}l} \times \mathbf{r}} \\ \rho_{Tl} e^{jk_l \cdot \mathbf{u}_{\mathbf{n}l} \times \mathbf{r}} & e^{-jk_l \cdot \mathbf{u}_{\mathbf{n}l} \times \mathbf{r}} \end{bmatrix} \begin{bmatrix} \tilde{\mathbf{E}}_{\mathbf{T},l+1} \\ \overleftarrow{\mathbf{E}}_{\mathbf{T},l+1} \end{bmatrix}. \tag{12}$$

The recursion is initialized on the to of the $(M+1)$st interface by performing an additional matching to pass to the down of that interface:

$$\begin{bmatrix} \tilde{\mathbf{E}}_{\mathbf{T},M+1} \\ \overleftarrow{\mathbf{E}}_{\mathbf{T},M+1} \end{bmatrix} = \frac{1}{\tau_{Tl,M+1}} \begin{bmatrix} 1 & \rho_{T,M+1} \\ \rho_{T,M+1} & 1 \end{bmatrix} \begin{bmatrix} \tilde{\mathbf{E}}'_{\mathbf{T},M+1} \\ 0 \end{bmatrix}. \tag{13}$$

Similarly, we obtain the following recursions for the total transverse electric and magnetic fields at each interface (they are continuous across each interface):

$$\begin{bmatrix} \mathbf{E}_{\mathbf{T}l} \\ \mathbf{H}_{\mathbf{T}l} \end{bmatrix} = \begin{bmatrix} \cos(k_l \cdot \mathbf{u}_{\mathbf{n}l} \times \mathbf{r}) & j \cdot Z_{vl} \sin(k_l \cdot \mathbf{u}_{\mathbf{n}l} \times \mathbf{r}) \\ j \cdot Z_{vl}^{-1} \sin(k_l \cdot \mathbf{u}_{\mathbf{n}l} \times \mathbf{r}) & \cos(k_l \cdot \mathbf{u}_{\mathbf{n}l} \times \mathbf{r}) \end{bmatrix} \begin{bmatrix} \mathbf{E}_{\mathbf{T},_{l+1}} \\ \mathbf{H}_{\mathbf{T},_{l+1}} \end{bmatrix}. \tag{14}$$

3. CONCLUSIONS

For simple cases (such as a planar interface), the behaviour of an impinging wave can be calculated analytically by the help of Snell's refraction/reflection law and the Fresnel equations, which are fundamental law for analysis of the reflection and the refraction of electromagnetic waves on boundary line between two materials. Problem of algorithm design of propagation, reflection and refraction of the electromagnetic waves on a layered medium is very intricate and time demanding. This method is suitable for specific purposes of detail analysis of general issue. Therefore, numerical methods are applied to facilitate the calculation process, and a wide range of programs like ANSYS, Comsol, or Matlab can be utilized in the realization of numerical modelling.

Methods describe in this paper are suitable for analysis of beam refraction to the other side from the perpendicular line during the passage through the interface. This phenomenon is occur in metamaterials.

Algorithms created in the Matlab environment are verified by the help of programs based on the finite element method, namely programs such as Comsol and ANSYS.

ACKNOWLEDGMENT

The research described in the paper was financially supported by the research program MSM 0021630516 and research plan MSM 0021630513, Ministry of Defence of the CR, Ministry of Industry and Trade of the CR (Diagnostics of Superfast Objects for Safety Testing, FR-TI1/368), Czech Science Foundation (102/09/0314) and project of the BUT Grant Agency FEKT-S-11-5.

REFERENCES

1. Dedek, L. and J. Dedková, *Elektromagnetismus. 2*, 232, VITIUM, Brno, 2000, ISBN 80-214-1548-7.
2. Nešpor, D., "Electromagnetic wave propagation study in heterogeneous structures," 20 s, Supervisor Doc. Ing. Pavel Fiala, Ph.D., 2009.
3. Fiala, P., "Finite element method analysis of a magnetic field inside a microwave pulsed generator," *2nd European Symposium on Non-Lethal Weapons*, SRN, Ettlingen, May 13–15, 2003.
4. Fiala, P., R. Kadlec, P. Drexler, and P. Dohnal, "Tuned periodical structures — Model, experiments in THz band applied in safety application," *PIERS Proceedings*, 1022–1026, Cambridge, USA, July 5–8, 2010.
5. Orfanidis, S., *Electromagnetic Waves and Antennas*, 1031, 2008, Available from WWW: <www.ece.rutgers.edu/ orfanidi/ewa>.

Stochastic Models of Electrodynamics

Pavel Fiala and Martin Friedl
Faculty of Electrical Engineering and Communication
Department of Theoretical and Experimental Electrical Engineering
Brno University of Technology, Kolejní 2906/4, Brno 612 00, Czech Republic

Abstract— The article presents the transient task numerical modelling of the electrodynamic process in gas with a pulsed electric field. Within the numerical model, non-linear electric properties of gas are respected and, by the help of a non-deterministic stochastic model, the possibility of an electric charge generation is analyzed. The authors examine the problem of electric charge probability evaluation; on the basis of testing the tip-tip disposition, a comparison of individual instances of the probability function evaluation is provided.

1. INTRODUCTION

The origins of research in the field of single-shot processes modelling date back deep into the past century. Then, the related problems were solved through the use of experimental methods as applied by Nikola Tesla, the Nestor of electrical engineering [1, 2]. For the solution of the pulse process in an electromagnetic field, models based on the conversion of a physical model into a mathematical one can be classified as stochastic. From the perspective of a macroscopic physical model, the concerned tasks mostly involve a high number of relations of the system elements, with the possibility of description comprising only several external parameters and functions of the system. The models can be further solved as stochastic or deterministic. For numerical models based on finitary methods, it is easier to utilize the stochastic approach [3] in the first approximation This article uses the example of a 2-D model to present the algorithm and parameters of a stochastic model of a discharge generation in an air spark gap, Fig. 1.

2. THE NUMERICAL MODEL

As it was already discussed in study [3], the model is formulated for a quasi-stationary electric field from reduced Maxwell's equations

$$\mathrm{div}\varepsilon\mathbf{E} = q, \quad \mathrm{div}\mathbf{J} = -\frac{\partial q}{\partial t}, \tag{1}$$

$$\mathrm{div}\left(\gamma\mathbf{E}\right) = -\frac{\partial q}{\partial t}, \tag{2}$$

where $\mathbf{E}$ is the electric field intensity, $\mathbf{J}$ is the current density vector, ε is the permittivity, γ the conductivity, and q the electric charge. After modification, the equations from (1) become

$$\mathrm{div}\left(\gamma\mathbf{E} + \frac{\partial\left(\varepsilon\mathbf{E}\right)}{\partial t}\right) = 0, \tag{3}$$

If the formulation of electric intensity vector by the help of potential φ is respected,

$$\mathbf{E} = -\mathrm{grad}\varphi, \tag{4}$$

Figure 1: A simple electrical spark gap, 3D.

then the model according to expression (3) can be written as

$$\mathrm{div}\left(\gamma \mathrm{grad}\varphi + \frac{\partial\left(\varepsilon \mathrm{grad}\varphi\right)}{\partial t}\right) = 0, \tag{5}$$

In expression (5), the partial derivative includes the formulation ε grad φ. If we assume time independence of the environment macroscopic characteristic — permittivity ε, the form can be written in a manner consistent with paper [3]

$$\mathrm{div}\left(\gamma \mathrm{grad}\varphi + \varepsilon \mathrm{grad}\frac{\partial \varphi}{\partial t}\right) = 0, \tag{6}$$

This form, in the dynamical modelling of an electric field shock wave, does not include the effect of permittivity variation. Conversely, conductivity γ, or electrical resistivity ρ as its reversed value, is shown in Fig. 2.

If we assumed the dependence of electrical permittivity ε on time variation and the module of electric intensity **E**, model (5) could be employed to describe more exactly the processes related to an electric discharge. The time behaviour of electric potential variation was preset with parameters of 0.1/50 µs, Fig. 3.

3. A COMPARISON OF THE 2D AND 3D MODELS

If we apply the probabilistic function according to article [3] for the 2D stochastic model based on relation (6)

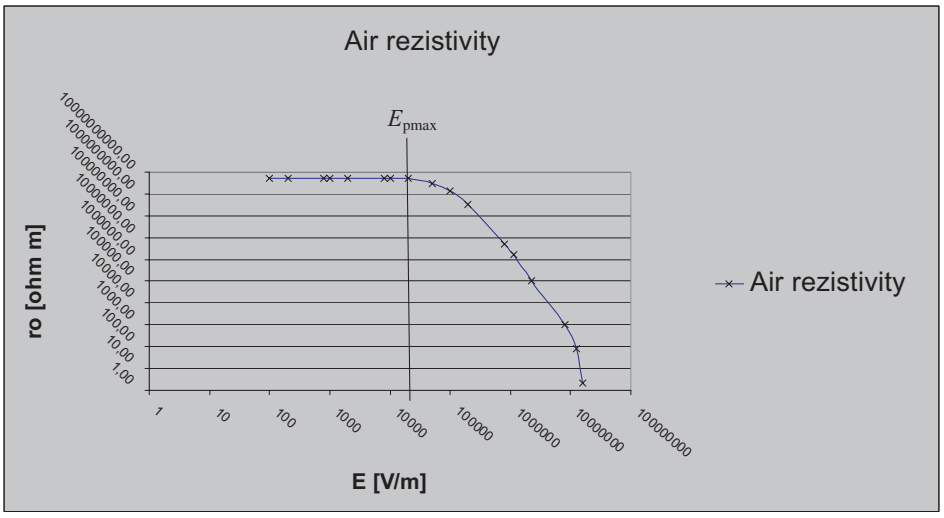

Figure 2: Characteristics of the electrical resistivity dependence on electric field intensity.

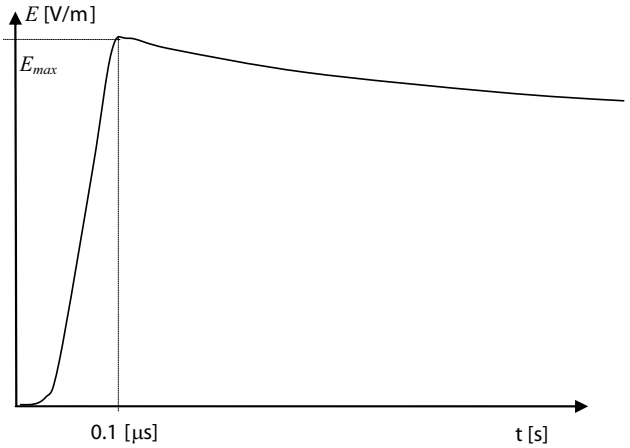

Figure 3: The electric potential time behaviour in model (5).

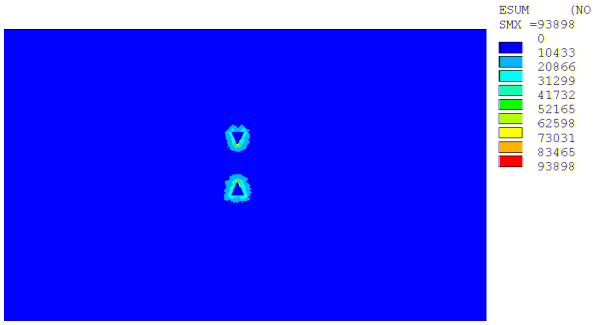

Figure 4: The module distribution of electric intensity $E, t = 0.4\,\mu s$.

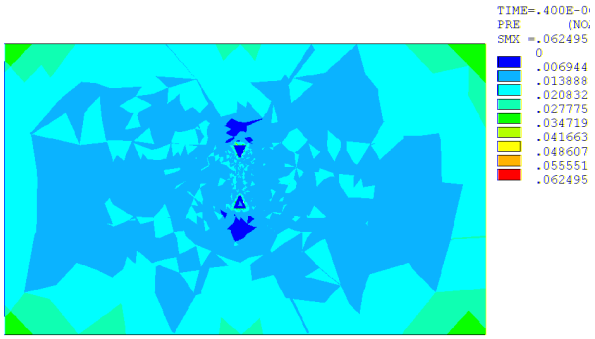

Figure 5: The distribution of probability P, $t = 0.4\,\mu s$.

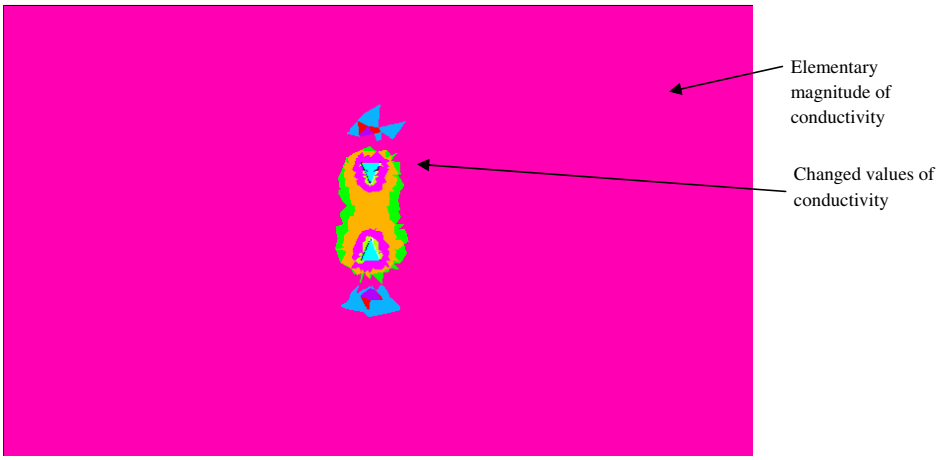

Figure 6: The distribution of the conductivity changed characteristics $\gamma, t = 0.4\,\mu s$.

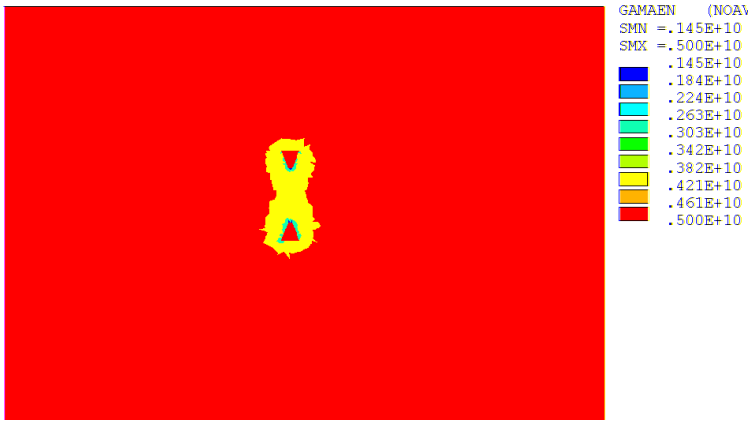

Figure 7: The distribution of conductivity $\gamma, t = 0.4\,\mu s$.

$$P_{i,j} = \frac{(E_{i,j})^{\eta}}{\sum (E_{i,j})^{\eta}}, \tag{7}$$

where E_{ij} is the electric intensity module of the numerical model element solved by means of the finite element method (FEM), η relates the growth probability with the local electric field. The time behaviour of electric potential φ according to Fig. 2, in which we tested the model behaviour for $E_{\max} = 3\,\mathrm{kV/cm}$, 100 kV/cm, is shown in Fig. 3.

For example, for entering the waveform of intensity of electric field E (electric potential φ) from the behaviour described in Fig. 3. $E_{\max} = 3\,\mathrm{kV/cm}$, the distribution of electric field E for the non-uniform mesh of the 3D model elements is shown in Fig. 4. However, for the process described

in paper [3] and the evaluation of probabilistic function (7), probability distribution P in the quasi-stationary 3D model (6) is shown in Fig. 5. Fig. 6 describes, based on the transient process modelling, the distribution of changed characteristics of conductivity γ in the 3D stochastic model. Fig. 7 shows conductivity γ distribution in the model as a function of electric field E intensity according to the characteristics from Fig. 5. Thus, the entire transient process was modelled according to the time behaviour of the exciting quantity from Fig. 3. Also, it was determined that the described probabilistic function from [3] has certain drawbacks for the 3D numerical model; therefore, we used (for example) the Laplace probabilistic function and brought it under testing.

$$L_{i,j} = \frac{p}{2B} e^{\left(\frac{-|E_{i,j}-E_{med}|}{B}\right)} + \frac{1-p}{2C} e^{\left(\frac{-|E_{i,j}-E_{med}|}{B}\right)}, \tag{8}$$

where $p \in \langle 0, 1\rangle$, B, $C > 0$.

4. CONCLUSION

The tests conducted by the help of a 3D numerical model designed for the modelling of the electric discharge stochastic process proved that the quality of the assembled numerical model, uniform distribution, and boundary conditons setting are aspects of fundamental importance to the modelling procedure. As several probabilistic functions were tested, it is possible to conduct a discussion related to forms that are more suitable for faster convergence of the stochastic model.

ACKNOWLEDGMENT

The funding of the project was supported by the Ministry of Industry and Trade of the CR (Diagnostics of superfast objects for safety testing, FR-TI1/368), Ministry of Education, Youth and Sports of the CR, and by institutional resources from the related Research Design — Electronic Communication Systems and New Generation Technologies (ELKOM) MSM0021630513, GAČR 102/09/0314.

REFERENCES

1. http://www.rastko.rs/projekti/tesla/delo/10761
2. http://books.google.cz/books?id=QclcZw7I4yMC&pg=PA112&lpg=PA112&dq=Nikola+Tesla+discharge&source=bl&ots=s1VLwDeNNX&sig=bqNGiCHEwHagK4PnlOSgWgqnbYg&hl=cs&ei=SEGoTd6TCoebOpW0scwJ&sa=X&oi=book_result&ct=result&resnum=2&ved=0C CIQ6AEwAQ#v=onepage&q=Nikola%20Tesla%20discharge&f=false.
3. Enokizono, M. and H. Tsutsumi, "Finite element analysis for discharge phenomenon," *IEEE Transactions on Magnetics*, Vol. 30, No. 5, 2936–2939, Sep. 1994.
4. Fiala, P., "Finite element method analysis of a magnetic field inside a microwave pulsed generator," *2nd European Symposium on Non-Lethal Weapons*, Ettlingen, SRN, May 13–15, 2003.
5. Fiala, P. and P. Drexler, "Measurement methods of pulsed power generators," *4nd European Symposium on Non-Lethal Weapons*, Ettlingen, SRN, May 21–23, 2007.
6. Kikuchi, H., *Electrohydrodynamics in Dusty and Dirty Plasmas, Gravito-electrodynamics and EHD*, Kluwer academic publishers, Dordrecht/Boston/London, 2001.
7. Stratton, J. A., *Theory of Electromagnetic Field*, SNTL Praha, 1961 (in Czech).

EMHD Models Respecting Relativistic Processes of Trivial Geometries

Pavel Fiala, **Zoltán Szabó**, **and Martin Friedl**
Faculty of Electrical Engineering and Communication
Department of Theoretical and Experimental Electrical Engineering
Brno University of Technology, Kolejní 2906/4, Brno 612 00, Czech Republic

Abstract— This paper examines the problem of utilisation of the coupled hybrid magnetic field model and the subject of the conductive area motion in a magnetic field. For exact evaluation of all effects influence one can't neglect the phenomena related to the movement of one system relatively to the other. There is shown that related distinctive effects affects the resultant electromagnetic field distribution from the relative speed $v_0 = 1\,\mathrm{m}\cdot\mathrm{s}^{-1}$ yet.

1. INTRODUCTION

At the present time, the modelling and simulation of technical systems constitute a substantial part of the entire network of modelled problems. Among the modelled tasks there are various problems related to fields with the fastest pace of both the development and the application of modelling, namely to energetic, mechanical engineering, metallurgy, electrical engineering, space and nuclear technologies [1, 2]. This paper examines the problem of utilisation of the coupled hybrid magnetic field model and the subject of the conductive area motion in a magnetic field. The model is dealt with *per partes*: the first aspect solved is a stationary model of a magnetic field, the following aspect consists in a quasi-stationary model for the assumed motion of elements of the task, and the last part constitutes a model respecting the relativistic principle in electromagnetic field modelling [4]. Let us consider an example of conductor movement in stationary or non-stationary magnetic field. It seems to be a trivial problem with straightforward solution. Though, for exact evaluation of all effects influence one can't neglect the phenomena related to the movement of one system relatively to the other. As it was shown in [7] this distinctive effect affects the resultant electromagnetic field distribution from the relative speed $\mathbf{v}_0 = 1\,\mathrm{m}\cdot\mathrm{s}^{-1}$ yet.

2. MODEL DESCRIPTION

In this work the simple model is used for the demonstration of influence of the relativistic approach to the model creation on the analysis results. The physical model is based on the solution of the reduced Maxwell equations [4, 8]. The resulting current density $\mathbf{J}$ is formed by the exciting current density $\mathbf{J}_\mathrm{s} = \rho\mathbf{v}$ with the specific density of electric charge ρ and the current density caused by eddy currents $\mathbf{J}_\mathrm{v}$. Motion effect for the instantaneous velocity vector $\mathbf{v}$ is respected in the model by current density $\mathbf{J}_\mathrm{m}$. The ANSYS program was modified using suitably selected boundary conditions in order to respect the model characteristics described in [6, 8]. The entire problem begins at the moment when the vector of intensities of both the electric and the magnetic fields of the moving system is **relative**. The complete Maxwell equations are covariant in all the systems; therefore, it is not important to specify the system within which the observer moves as the described relations always hold true. After the derivation of the four-vector and respecting the Lorentz transformation, the current density is written in the form

$$\mathbf{J}_\square = \rho\frac{\partial\mathbf{s}}{\partial t} + \mathrm{j}c\rho\mathbf{u}_t, \tag{1}$$

where j is the symbol of the imaginary component of the quantity complex shape, c is the velocity of light module in the vacuum. For the continuity equation there holds

$$\mathrm{div}\,(J_\square) = 0, \tag{2}$$

In order to facilitate simplification, if we assume the motion of one reference system as () (for example, in the x axis of the Cartesian coordinate system), the four-vector of current density can be written, after application of the Lorentz transformation, in the (invariant) form of

$$\mathbf{J}'_\square = \frac{J_x + \mathrm{j}\frac{v_x}{c}J_t}{\sqrt{1-\left(\frac{\|\mathbf{v}\|}{c}\right)^2}}\mathbf{u}_x + J_y\mathbf{u}_y + J_z\mathbf{u}_z + \mathrm{j}\frac{c\rho - \frac{v_x}{c}J_x}{\sqrt{1-\left(\frac{\|\mathbf{v}\|}{c}\right)^2}}\mathbf{u}_t, \tag{3}$$

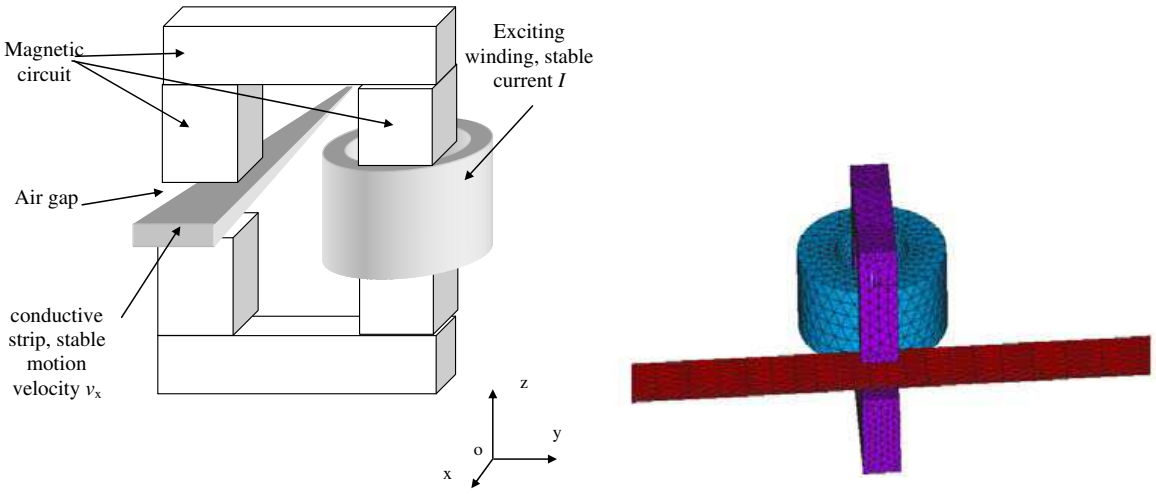

Figure 1: A simple geometry for the verification of the relativistic approach of electrodynamics, numerical model.

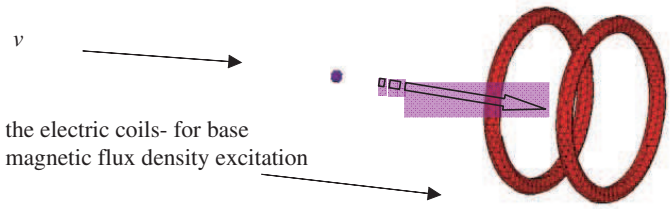

Figure 2: The electrodynamic magnetic field analysis: model of simple ballistic projectile velocity measurement.

$$\rho' = \frac{\rho - \frac{v_x}{c^2} J_x}{\sqrt{1 - \left(\frac{\|\mathbf{v}\|}{c}\right)^2}}, \tag{4}$$

and the electric charge volume density in the reference. There is no problem obtaining, by means of reversal in the sign of velocity, transformed quantities of the opposite system (which is moving) for the above-expressed transformed quantities. Let us have a simple geometric task, Fig. 1. The model example composes of the conductive strip in the air gap which is a part of magnetic circuit. The distribution of magnetic field in the system is evaluated for different case of strip movement and for non-relativistic and relativistic approach.

3. THE MODEL SOLUTION

The conductor was moving in the longitudinal direction at the speed of $v = 1\,\mathrm{m/s}$. The numerical model of ballistic projectile velocity measurement is shown in Fig. 2. There are electric coils for excitation of basic magnetic flux density $\mathbf{B}$, Fig. 3. The secondary magnetic flux density are dependent on the effects on move projectile on the its surface. The effects depend on eddy currents and relativistic theory. The final vector magnetic flux density is measured with classical sensors, Fig. 4(a). It can be shown real and imaginary components of current density module, Fig. 4(b), and results of relativistic contribution of magnetic flux density, $\mathbf{B}_{\mathrm{re}}$, $\mathbf{B}_{\mathrm{im}}$, Fig. 5.

1. Consider a model with stationary excitation by basic magnetic field. The projectile crossing (no matter of the type — conductive/non-conductive) induces similar effects as in model in Fig. 1– Fig. 2. A transient electromagnetic phenomenon occurs, which is possible to sense by means of standard methods. It is possible to show the influence of projectile shape and projectile velocity on the magnetic field gradient shift.

2. We may use a more complicated model (Fig. 2), which is based on basic magnetic field excitation by harmonic signal with frequency, e.g., $f = 15\,\mathrm{MHz}$. Relativistic effects occur in the object,

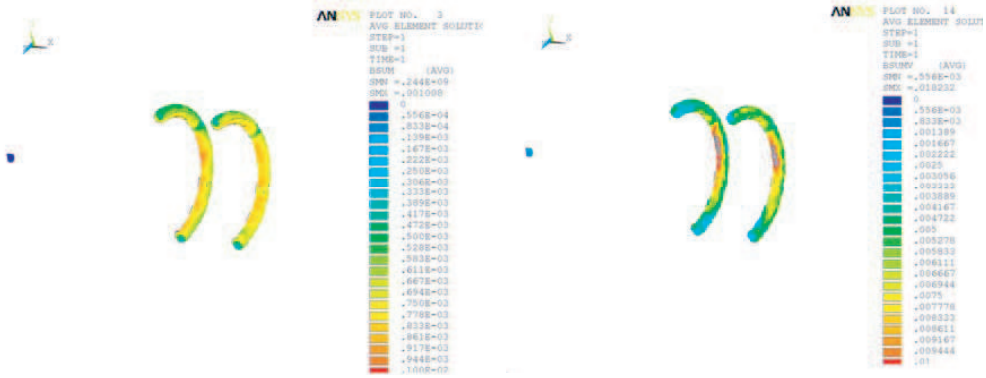

(a) (b)

Figure 3: The electrodynamic magnetic field analysis: (a) the basic magnetic flux density vector module **B** distribution, (b) the final magnetic flux density vector module **B** distribution.

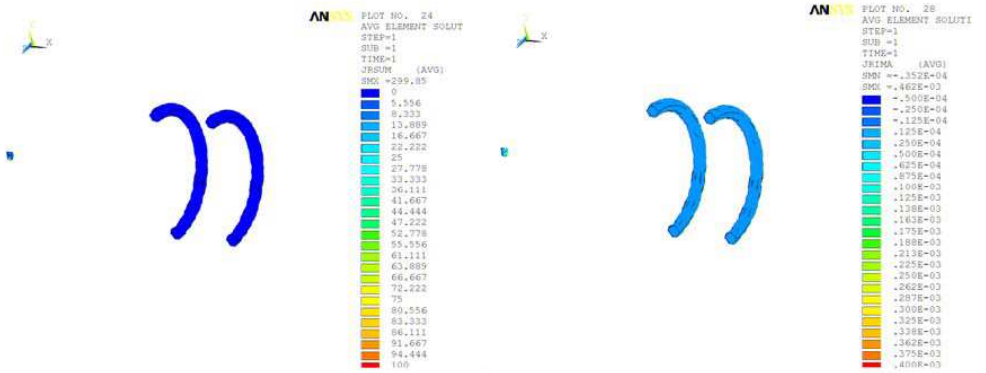

the real component the imaginary component

Figure 4: The electrodynamic magnetic field analysis: the real component current density $\mathbf{J}_{\mathrm{re}}$ vector module distribution, the imaginary component current density $\mathbf{J}_{\mathrm{im}}$ vector module distribution.

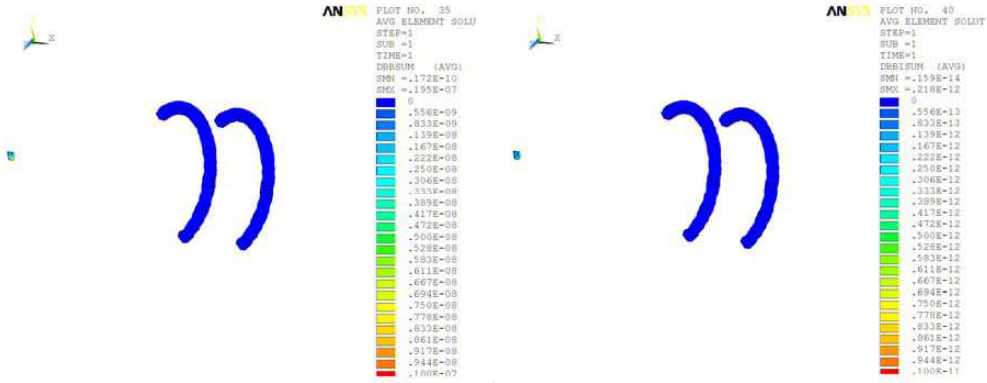

the real component the imaginary component

Figure 5: The electrodynamic magnetic field analysis: the real component of magnetic flux density $\mathbf{B}_{\mathrm{re}}$, the imaginary component of magnetic flux density $\mathbf{B}_{\mathrm{im}}$.

which moves with respect to system of coordinates. Relativistic effect occur in excitation system also. If we carefully analyze the model analysis results, we may evaluate resulting effects for two different excitation coil configurations with respect to projectile trajectory. The coil configuration is determined by excitation magnetic field vector **B**. The influence of excitation on resulting effect

may be described by relation

$$\mathbf{J}'_{\square} = \frac{J_x - v_x \mathrm{div}\left(\frac{\varepsilon}{\gamma}\left(J_x\mathbf{u}_x + J_y\mathbf{u}_y + J_z\mathbf{u}_z\right)\right)}{\sqrt{1-\left(\frac{\|\mathbf{v}\|}{c}\right)^2}}\mathbf{u}_x + J_y\mathbf{u}_y + J_z\mathbf{u}_z + j\frac{c\,\mathrm{div}\left(\frac{\varepsilon}{\gamma}\left(J_x\mathbf{u}_x + J_y\mathbf{u}_y + J_z\mathbf{u}_z\right)\right) - \frac{v_x}{c}J_x}{\sqrt{1-\left(\frac{\|\mathbf{v}\|}{c}\right)^2}}\mathbf{u}_t. \quad (5)$$

4. CONCLUSION

The model makes apparent the distinction by order of the individual phenomena. It is evident that the relativistic electro-magneto-dynamic principle is indispensable and introduces substantial changes into the original non-dynamic conception of this type of simple task analysis.

The effect is apparent of motion on the magnetic field imbalance. A higher value of an elementary magnetic field combines with a decrease in relative magnitude of the electro-magneto-dynamic field influence.

Between the numerical values we may point to $B_{\max} = 0.277{\cdot}10^{-3}$ T for quasi-stationary task and $B_{\max re} = 0.427 \cdot 10^{-1}$ T for electrodynamic model. A distinctive influence of projectile movement on magnetic field symmetry is noticeable.

ACKNOWLEDGMENT

The research described in the paper was financially supported from research plans No. MSM 0021630513 ELCOM, No. MSM 0021630516 and by a grant from the Ministry of Industry and Trade of the Czech Republic (MPO No. FR-TI1/368), GAČR 102/09/0314, BUT Grant Agency FEKT-S-10-13.

REFERENCES

1. Kuneš, J., O. Vavroch, and V. Franta, "Základy modelování," SNTL, Praha, 1989, ISBN 80-03-00147-1.
2. ANSYS, *Theory Reference Manual*, Příloha Programu ANSYS.
3. Dědek, L. and J. Dědková, *Elektromagnetismus*, VUTIUM, Brno, 2000.
4. Stratton, J., *Teorie Elektromagnetického Pole*, Vyd, SNTL, Praha, Str. 51–60 (In Czech).
5. Fiala, P., "Secondary winding model of current transformer-switchable variant," Research Report, Laboratory of Modeling and Optimization Field in Electromagnetic Systems, Brno, Czech Republic, 1999.
6. Fiala, P., "Transformer partial discharge modeling, minimal breakdown value set in critical parts of transformer design," Research Report, Laboratory of Modeling and Optimization Field in Electromagnetic Systems, Brno, Czech Republic, 1999.
7. Haňka, L., *Teorie Elektromagnetického Pole,* Skripta, SNTL, Praha, 1971 (In Czech).
8. Fiala, P., Z. Szabó, T. Bachorec, and P. Dohnal, "EMHD model used for linear moving objects analysis," *PIERS Proceedings*, 1017–1021, Cambridge, USA, Jul. 5–8, 2010.

A Solar Element with Controlled Efficiency

P. Fiala and D. Nešpor
Faculty of Electrical Engineering and Communication
Department of Theoretical and Experimental Electrical Engineering
Brno University of Technology, Kolejní 2906/4, Brno 612 00, Czech Republic

Abstract— The authors propose an analysis of a model solar element based on the principle of a resonance system facilitating the transformation of the external form of impinging energy into electric energy. A similar principle provides the basis for harvesters designed to operate at lower frequencies [1]; in these harvesters, the efficiency of the energy form transformation can be controlled from the frequency spectrum of an external source

1. INTRODUCTION

Initial research studies in the field of mini- and microgenerators conceived as harvesters [8] mainly examined the problem of exploiting a form of energy from the mechanical motion of a system, with special regard paid to possible utilization of the energy for feeding the electronic components of the moving system.

The central issue in the part of the research related to this paper and chiefly solved in the WISE project (6-FP EU) was to develop an independent energy source for a temperature sensor (or other sensor types). The sensor has been applied in an NH-90 helicopter EUROCOPTER. From all the investigated solutions, the Vibration Micro-Generator (MG) was chosen as the independent energy source for the sensor. The MG can provide energy proportionally to the helicopter vibration on a specific resonant frequency [1].

2. TUNED STRUCTURES: THE ACTIVE PART OF A GENERATOR

Tuned structures were partially analyzed and developed in research study [1]. Utilizing the semiconductor technology, the authors designed a resonant element (Fig. 1) [2] which satisfied the basic requirements for resonance (Fig. 2) on the wavelength of the impinging electromagnetic wave. Further conditions for function [1, 4–6] can be formulated as follows: In the course of impingement of an externally generated electromagnetic wave there must not emerge a stationary electromagnetic wave. The elementary resonator (Fig. 3) must pass into a resonant state and reach a multiple amplitude in desired parts of the resonant circuit: the transforming element, Fig. 3. The criterion must be met of the spectrum bandwidth of the impinging electromagnetic wave in order for the structure to be kept in the resonant state under the desired multiple of the impinging amplitude The principle of the resonant circuit (Fig. 4) as a method of converting electromagnetic field components to a processible level was already tested [2].

The principle of a resonance generator (RG) operation is based on the utilization of external vibrations. The basic conception of energy transformation can be described by means of Faraday's

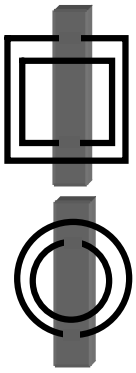

Figure 1: Instances of the basic elements of metamaterials.

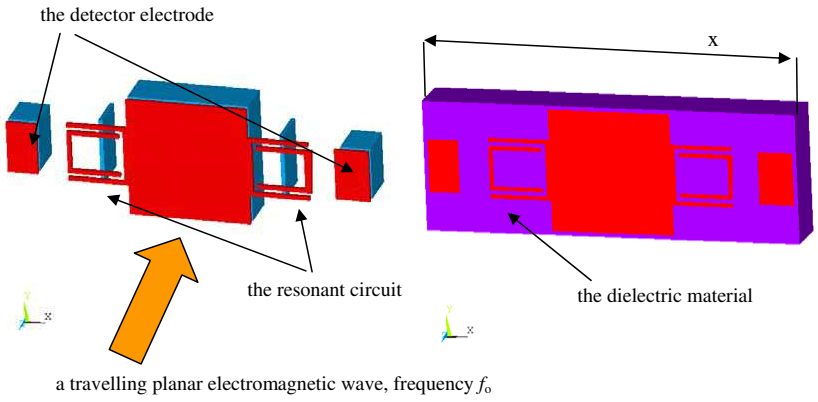

Figure 2: A geometrical model of the resonant circuit basic element.

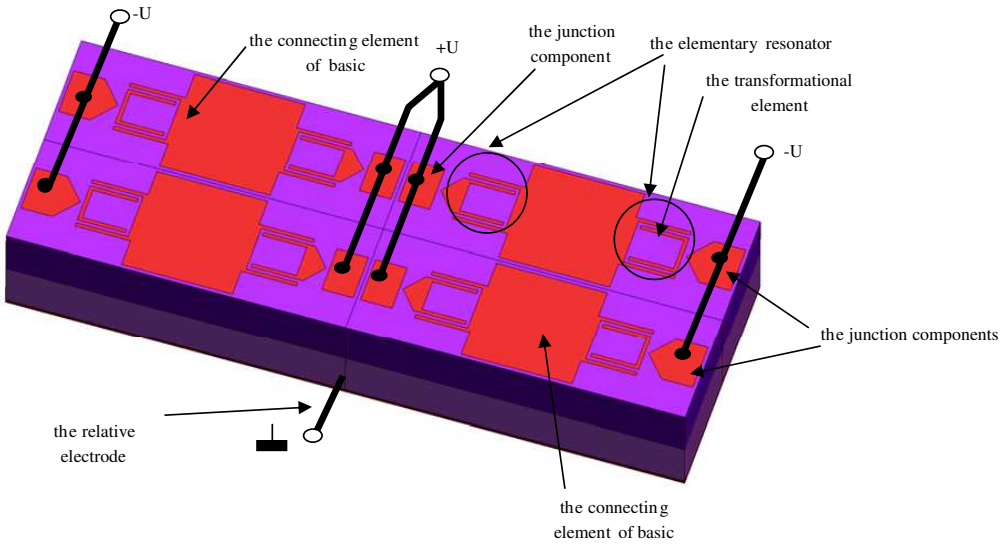

Figure 3: A geometrical model of the resonant circuit structure.

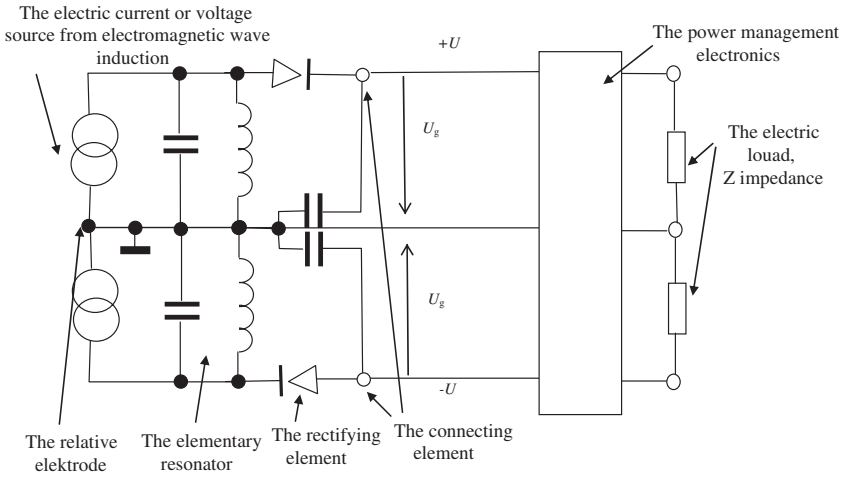

Figure 4: The resonance circuit structure of the generator.

law [3, 7]. The required output power depends on the type of output load, namely on the used impedance. The basic arrangement of the RG is provided in Fig. 4. The generator was conceived on the basis of magnetic field variations owing to mechanical vibrations, and the non-stationary electromagnetic field was excited through the variation of magnetic field in the preset magnetic circuit. The vibrational generator (VG) body is tightly connected with the vibration source; for us, for example in an airplane fuselage and in association with the oscillation of the whole system, the VG core starts moving with respect to the fuselage activity. The mechanical part of the VG is designed in such a manner that the VG core driven by external vibrations performs nondamped oscillations. The design of the VG enables the oscillations of the VG core to fit within a comparatively wide spectrum of external oscillation frequencies. The operation of the VG is based on Faraday's law. The core, which contains ferromagnetic parts and permanent magnets (with a high density of the stored energy, e.g., FeNdB, SmCo) moves with respect to the winding connected to the shell and induces a voltage in it. In relation to this, the connected external current starts carrying a core-braking current. Both the induced voltage and the current in the external circuit are generally complex functions of time.

3. THE STRUCTURE MODEL

The basic model was built in a system based on the finite element method, namely in the ANSYS system, in order to facilitate the retrieval of the basic resonant circuit with maximum efficiency. As the elementary structure basis, the type according to Fig. 1, Fig. 2 was chosen and solved as the model [2]. There occur several points in the design and solution of the model. The first of

these points consists in the solution of impedance matching of the structure and in the possibility of emergence of reflected electromagnetic waves, another one lies in the state of propagation and damping of electromagnetic waves in the space behind the mask and still another one is the designing of the basic geometry with respect to the required utilization of both the electric and the magnetic components of the electromagnetic wave. In Fig. 2, the design is presented of the basic elementary structure as a resonant circuit with the aim to obtain the maximum component of electric field on the detector electrodes.

Figure 3 presents schematically the arrangement of the periodic structure of resonators with their connectivity. The numerical model was analyzed in such a manner that we reached the above-described input conditions of the RG function. Fig. 5 shows the distribution of the module of the electric intensity E component. The model in Figs. 2, 3 were designed for the frequency of 100 THz. The dimension is $x = 9\,\mu\text{m}$. The intensity module of an electromagnetic wave impinging on the structure is $E_{in} = 0.1\,\text{V/m}$, the wave orientation is in the direction of the y axis, and the wave was modeled as linearly polarized. It follows from the analysis that, within the range of excited frequencies, there may occur even a 21-fold amplification of the signal. However, this signal is already processible by means of currently available technologies.

In Fig. 4, a basic schematic expression is provided of a modelled RG including components for shaping the ulilizable form of energy. In order to enable correct functioning of the generator, we

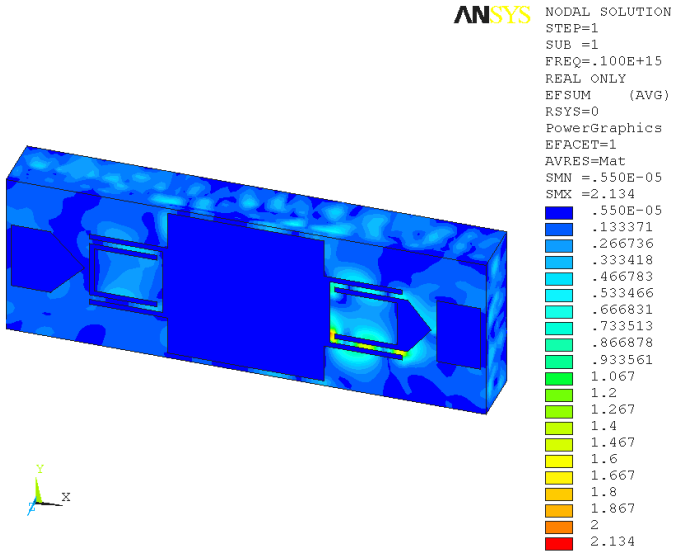

Figure 5: The interpretation of solution of the resonant circuit basic element model, the electric field components.

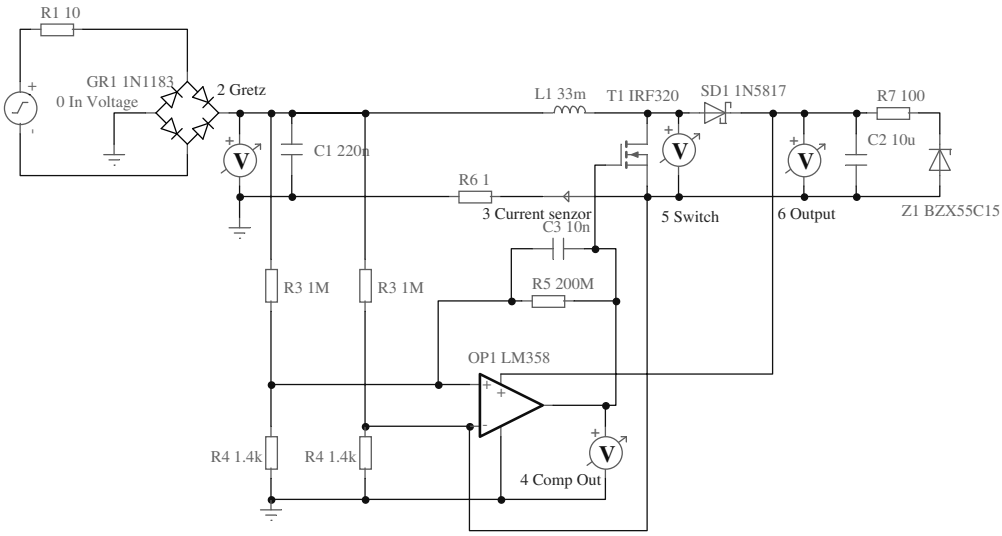

Figure 6: The simulation diagram for power management circuit — PFC.

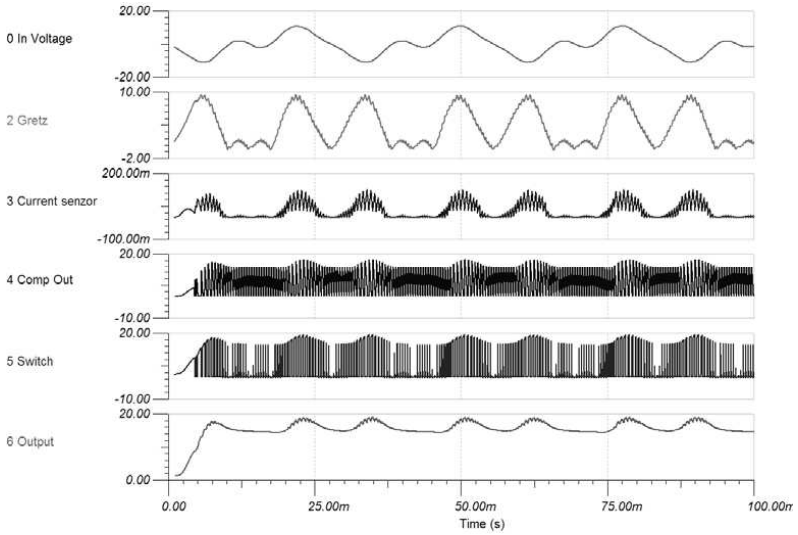

Figure 7: Simulated waveforms for the PFC power management circuit.

have to embed controlling electronics between the electrical load and the junction components of the RG. The electronics will ensure that at any condition on the output of the device, the VG generator is loaded with constant impedance Z in the junction points. This type of connection can be realized, for example, according to the diagram in Fig. 6 (power management circuit); in practice, it was already tested on the mini- and microharvesters, and the simulated behaviour from Fig. 7 corresponds to the measured values. These tests, which were easily measurable and realizable using the generators, enabled us to produce the basic power management circuit design for the RG.

4. CONCLUSION

The experimental VG on a solar element is currently in the process of testing. The applied research of the numerical model periodical structures has brought a considerable sum of experience in the resonant mode modeling; the results of the related analysis are utilized for the manufacturing technology proposals concerning the RGs and their experimental operation.

ACKNOWLEDGMENT

The research described in the paper was financially supported by FRVŠ (a fund of university development), research plan No. MSM 0021630513 ELCOM, No. MSM 0021630516, and a grant provided by the BUT Grant Agency FEKT-S-10-13.

REFERENCES

1. Jirků, T., P. Fiala, and K. Martin, "Magnetic resonant harvesters and power management circuit for magnetic resonant harvesters," *Microsystem Technologies*, Vol. 16, No. 5, 677–690, 2010.
2. Fiala, P. and T. Jirku, "Analysis and design of minigenerator," *PIERS Online*, Vol. 4, No. 7, 706–710, 2008.
3. Kikuchir, H., *Electrohydrodynamics in Dusty and Dirty Plasmas, Gravito-electrodynamics and EHD*, Kluwer Academic Publishers, Dordrecht, Boston, London, 2001.
4. Patent No. PV-2006-571, Czech Republic.
5. Patent No. PUV-2006-18391, Czech Republic.
6. Patent No. PV 2007-331, Czech Republic.
7. Stratton, J. A., *Theory of Electromagnetic Field*, Praha, 1961 (In Czech).
8. Wen, J. L., Z. Wen, and P. K. Wong, *A Micromachined Vibration Induced Power Generator for Low Power Sensors of Robotic Systems*, World Automation Congress, Maui, Hawaii, Jul. 11–16, 2000.

Fusion of the T1, T2 Weighted and Perfusion Weighted Images for Peritumoral Region Evaluation

M. Cap[1], **E. Gescheidtova**[1], **P. Marcon**[1], **K. Bartusek**[1,2], **and A. Sprlakova**[3]

[1]Department of Theoretical and Experimental Electrical Engineering
Brno University of Technology, Kolejni 2906/4, 612 00 Brno, Czech Republic
[2]Institute of Scientific Instruments, Academy of Sciences of the Czech Republic
Kralovopolska 147, 612 64 Brno, Czech Republic
[3]Faculty Hospital Brno, Department of Radiology, Jihlavska 20, 625 00 Brno, Czech Republic

Abstract— MRI is a constantly developing region of medicine, which is suitable for the study of soft tissues. The current methodologies for obtaining images weighted by relaxation times give only an idea of the distribution of soft tissues. Differential diagnosis of a high-grade glioms and solitary metastases is in some cases inconclusive. Investigators in several studies have demonstrated that in perfusion MRI (magnetic resonance imaging) of high-grade glioms and solitary metastases are differences. Analysis of the peritumoral region could be more useful than the analysis of the tumor itself. Precise evaluation of mentioned differences in peritumoral region gives a hopeful chance for tumor diagnosis.

This article describes image processing and fusion of the MR images. T_1 weighted (T1W) and T_2 weighted (T2W) images are processed for tumor and peritumoral region detection. By the fusion of the T1W and T2W images with perfusion weighted images (PWI) is possible to image perfusion in the peritumoral region in the T1W or T2W image.

1. INTRODUCTION

This article deals with fusion of the perfusion weighted images with T_1, T_2 weighted image. The aim of this work is to create system for tumor and peritumoral region detection, image registration and fusion of the T_2 and perfusion weighted images. The importance of the perfusion imaging method lies in its ability to describe anatomy and physiology of the tumor and peritumoral region microvasculature [1]. Several studies have demonstrated that in perfusion MRI of high-grade glioms and solitary metastases are differences [2–4]. In this article, we are focused on the differences in perfusion weighted images in the peritumoral region.

Three sets of images were processed. T_1 and T_2 weighted images are used for detection of the tumor and peritumoral region size and position. These two image sets contain 22 images. Resolution of the T_1 weighted images is 256×256 px ($0.9\,\text{mm} \times 0.9\,\text{mm}$ pixel size), resolution of the T_2 weighted images is 512×512 px ($0.45\,\text{mm} \times 0.45$ mm pixel size). Fig. 1 gives as examples of the processed images. Perfusion images are acquired each 1.22 s with space resolution 64×64 px (pixel size $3.4\,\text{mm} \times 3.4\,\text{mm}$).

Image fusion requires precise image registration. In an effort to obtain the most accurate diagnosis is the image registration the key part of the image fusion algorithm. Hence, the PWI images are processed wit accuracy of ± 1 pixel. With the aim of image fusion the structural image is processed for tumor and peritumoral region detection. Selection of the peritumoral region area in PWI image and its imaging in structural image will be the aim of this work.

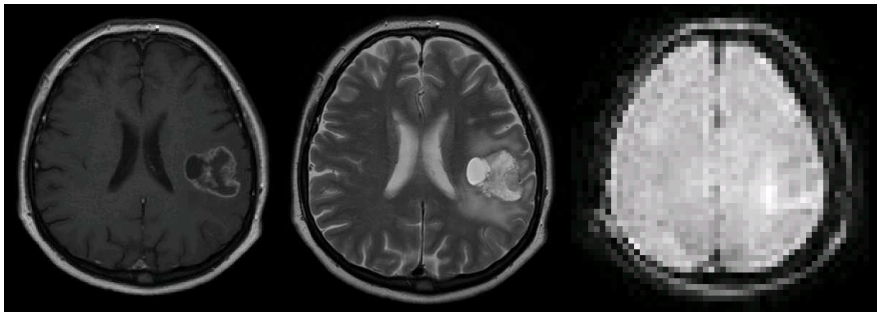

Figure 1: T_1 weighted image, T_2 weighted image and perfusion weighted image of the same slice.

2. METHODS

2.1. Image Registration

The first step for image fusion is the image registration. Precise position detection in both images is necessary for right perfusion evaluation in peritumoral region. Detection of the size and position of the patient's brain is based on the interhemispheric fissure position as can be seen in Fig. 2. Position of the interhemispheric fissure is detected from the local minimum in the frontal and occipital lobe. Each value is calculated as an average of 10 positions of the local minimum in surrounded rows. PW images are acquired with low resolution, only 64×64 px. For size adjustment the bilinear method is used. Pixel is calculated as a weighted average of pixels in the nearest 2-by-2 neighborhood.

2.2. Segmentation

Most important part of the work is the segmentation of the regions of interest. Both structural images are suitable for tumor detection. T2W image was chosen for higher contrast in peritumoral region as you can see in Fig. 1. The goal of segmentation is to find position of the tumor and peritumoral region. As an input for image fusion are used. Segmentation method is based on the detection of the high intensity of the tumor region [6].

Used method has two steps. At first, the high contrast area of the tumor is detected. Tumor area intensity exceeds a threshold which is adjusted according to whole image intensity. Rest of the tumor is detected by the fine detection on the boundaries of previously detected area. The threshold is now lower then before for detection of the parts of the tumor area with smaller image intensity. In the second step the incorrectly detected areas are removed or added. Results of the tumor and peritumoral region detection are in Fig. 3.

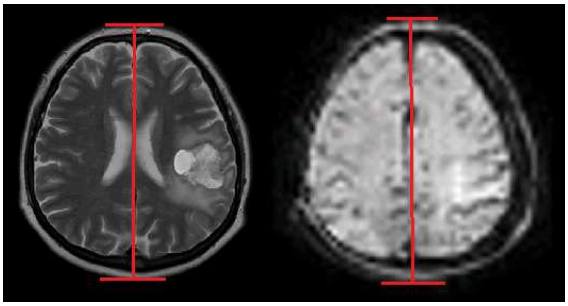

Figure 2: Results of the interhemispheric fissure detection. T2W image left, PWI image right.

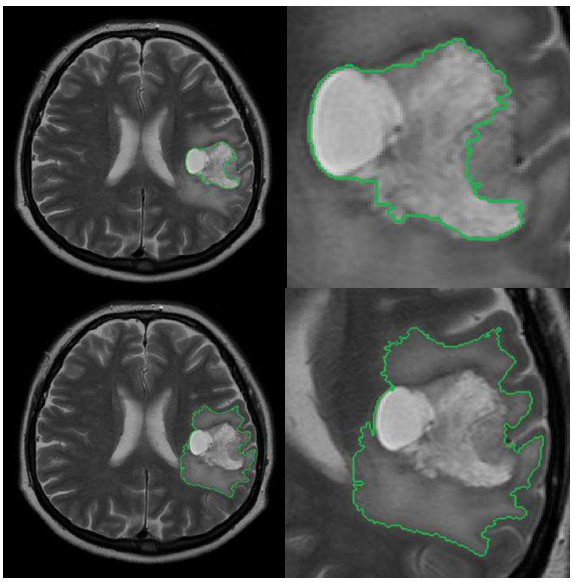

Figure 3: On the top the detected tumor, on bottom the detected peritumoral region in T2W image.

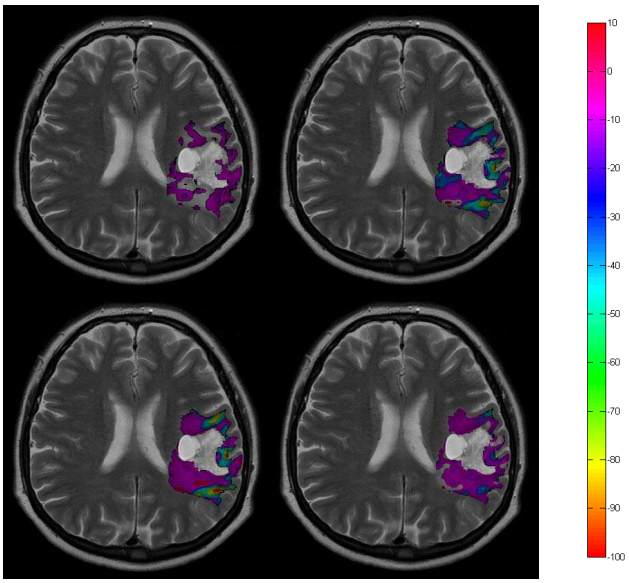

Figure 4: Results of T2W and PWI images fusion.

Signal intensity in peritumoral region is not as significantly higher as is in tumor area. Algorithm for peritumoral region detection uses a similar method to method used for tumor detection. Algorithm detects higher signal intensity close to the tumor and signal loss on the peritumoral region boundaries. By use of a threshold dependent on the signal intensity it was possible to detect the peritumoral region with sufficient accuracy.

2.3. Image Fusion

Detection of the tumor and peritumoral region gave us knowledge about the position of these objects. These positions are used for a mask creating. By multiplying the mask with PWI image the perfusion in peritumoral region is obtained. Results of the image fusion can be seen in Fig. 4.

3. RESULTS

Results of the tumor and peritumoral region detection algorithms are presented in Fig. 4. Result of both algorithms is the mask with the same size as the T2W image. Resulting mask is obtained as the peritumoral region mask reduced about the tumor mask.

Fusion is provided for all 60 PWI images. Four images in Fig. 4 were scanned in time: top left image 3.66 s, top right image 21.96 s, bottom left image 34.16 s and bottom right image 48.80 s. PWI images were processed for size and position correction and fit to T2W image.

4. CONCLUSION

The paper presents registration, segmentation and fusion of the T2W and PWI images. Interhemispheric fissure were localized and used for image registration. Detection of the tumor and peritumoral region was the key part of this work. Precise evaluation of the peritumoral region requires providing all of these detections with high accuracy. Aim of the presented work was the research into methods, which will enable distinguishing between individual types of tumor. Presented result holds possibility to be useful for more precise tumor diagnosis. In the further work the considerable attention will be devoted to the peritumoral region evaluation in all slices as well as a calculation of perfusion time characteristics in selected regions.

ACKNOWLEDGMENT

This work was supported within the framework of projects No. 102/11/0318 of the Grant Agency of the Czech Republic and the research plan MSM 0021630513.

REFERENCES

1. Jackson, A., D. L. Buckley, and G. J. M. Parker, *Dynamic Contrast-enhanced Magnetic Resonance Imaging in Oncology*, 311, Elsevier, 2005.
2. Law, M., S. Cha, E. A. Knopp, G. Johnson, J. Arnett, and A. W. Litt, "High-grade gliomas and solitary metastases: Differentiation by using perfusion and proton spectroscopic MR imaging," *Radiology*, 715–721, 2002.
3. Hakyemez, B., C. Erdogan, N. Bolca, N. Yildirim, G. Gokalp, and M. Parlak, "Evaluation of different cerebral mass lesions by perfusion-weighted MR imaging," *J. Magn. Reson. Imaging*, Vol. 24, 817, 2006.
4. Rollin, N., J. Guyotat, N. Streichenberger, J. Honnorat, V. A. Tran Minh, and F. Cotton, "Clinical relevance of diffusion and perfusion magnetic resonance imaging in assessing intraaxial brain tumors," *Neuroradiology*, Vol. 9, 150, 2006.
5. Cianfoni, A., R. Calandrelli, P. de Bonis, A. Pompucci, L. Lauriola, and C. Colosimo, "Nocardia brain abscess mimicking high-grade necrotic tumor on perfusion MRI," *Journal of Clinical Neuroscience*, Vol. 17, No. 8, 1080–1082, 2010.
6. Mikulka, J., E. Gescheidtova, and K. Bartusek, "Modem edge-based and region-based segmentation methods," *32nd International Conference on Telecommunications and Signal Processing*, 89–91, Dunakiliti, Hungary, 2009.

Thermal Properties of Light-controllable Photonic Liquid Crystal Fibers

Jia-Hong Liou, Ta Lin, and Chin-Ping Yu
Department of Photonics, National Sun Yat-Sen University, Kaohsiung 80424, Taiwan, R.O.C.

Abstract— We have investigated the thermal characteristics of light-controllable photonic liquid crystal fibers (PLCFs) by varying the ambient temperature. The measured results show that as the PLCF is irradiated by a blue laser, the transmission spectrum has a red shift. In addition, the response time of the fabricated PLCF can be reduced by raising the ambient temperature and by increasing the concentration of the photoresponsive LC mixture.

1. INTRODUCTION

Photonic crystal fibers (PCFs) can confine light by the periodic triangular air-hole array in the fiber cladding [1, 2] PCFs possess many attractive optical properties which depend on the air-hole size and air-hole distribution in the cladding region [2, 3]. Owing to the fix geometry after the fabrication, the optical properties of the PCFs are hard to be changed. By infiltrating liquid crystals (LCs) into the air holes of PCFs, one can form tunable photonic liquid crystal fibers (PLCFs). The refractive index of the LC can be modulated by the thermal or electrical effect making the PLCFs useful in many optical applications, such as long period fiber gratings (LPFGs) [4], switches [5], and notch filters [6].

Recently, light-controllable PLCFs have been proposed by using a photoresponsive LC mixture [7, 8]. Under external light illumination, the phase structure of the photoresponsive LC can be switched from anisotropic to isotropic [7–9] and the effective index can then be modulated. Based on this property, Liou et al. have proposed reversible photo-induced LPFGs in PLCFs infiltrated with the photoresponsive LC mixture [8]. However, the temperature effects on the phtoresponsive PLCFs have not been studied yet. In this paper, we investigate the light-controllable PLCF filled with the photoresponsive LC mixture which consists of nematic E7 LC and photochromatic 4-methoxyazobenzene (4MAB) [8, 9]. By irradiating the PLCF with a blue laser, the transmission spectra and the response time of the fabricated PLCF will be measured at variant ambient temperature. In addition, the effect of the concentration of 4MAB on the response time of the photoresponsive LC mixture in the PLCF will also be discussed.

2. FABRICATION AND EXPERIMENT SETUP

The photoresponsive LC mixture prepared in this experiment consists of 75 wt% nematic E7 LC (ECHO Chemical Co.) and 25 wt% 4MAB (TKK Co.). The ordinary (n_o) and extraordinary (n_e) refractive indices of E7 are 1.5024 and 1.697, respectively. Fig. 1 illustrates the photo-induced phase transformation for the photoresponsive LC mixture. The photochromatic 4MAB contains two kinds of isomers, the rod-like *trans*4MAB and bent *cis*4MAB Under suitable external light stimulus, the isomerzation can be induced and is reversible [7–9]. First, the rod-like *trans*-4MAB is parallel to the nematic LC molecules to form an anisotropic LC mixture via the guest-host effect as shown in Fig. 1. As the anisotropic LC mixture is irradiated with a blue laser ($\lambda = 473\,\text{nm}$), the rod-like *trans*4MAB molecules are switched to bent *cis*4MAB and then the phase structure of the LC mixture is destabilized and changed to isotropic. On the contrary, if the isotropic LC mixture is exposed to a green laser ($\lambda = 532\,\text{nm}$), the isomer is transferred from bent *cis*-4MAB to rod-like *trans*-4MAB because of the backward isomerization. The phase structure of the LC mixture returns to anisotropic again.

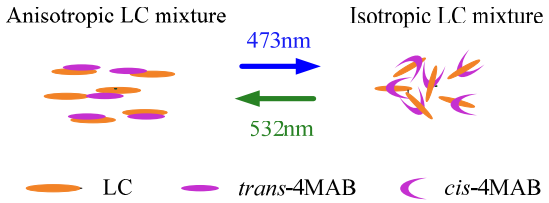

Figure 1: Reversible photo-induced phase transformation of the photoresponsive LC mixture.

Figure 2 shows the experiment setup for finding out the thermal properties of the light-controllable PLCF. The solid-core PCF we used is the LMA10 PCF from NKT Photonics A/S. The fiber has four rings of air holes surrounding the center solid core. The diameter and the lattice constant of the air holes of the LMA10 PCF are $d = 3.1\,\mu m$ and $\Lambda = 7.1\,\mu m$, respectively. By using the vacuum pumping method, we filled the photoresponsive LC mixture into the PCF to form a photoresponsive PLCF which was then spliced to two single-mode fibers (SMFs) at both ends. To investigate the thermal characteristics of the PLCF, the PLCF was placed onto a temperature controller and exposed to a diode-pumped-solid-sate (DPSS) laser as shown in Fig. 2. The wavelength of DPSS lasers we used were 473 nm with a intensity of $5\,mW{\cdot}cm^{-2}$ and 532 nm with a intensity of $100\,mW{\cdot}cm^{-2}$, respectively. To measure the transmission spectra of the photoresponsive PLCF, light from a broadband source (BBS) was launched into the PLCF through a SMF. The output spectra were collected by an optical spectrum analyzer (OSA) through another SMF as shown in Fig. 2.

3. RESULTS AND DISCUSSIONS

First, the PLCF was measured at 27°C and Fig 3(a) displays the transmission spectra for variant blue-laser illumination time. The black solid line represents the initial transmission spectrum without irradiation of the blue laser. One can see that the PLCF is a photonic bandgap (PBG) guiding structure due to the refractive index of the LC mixture is larger than that of silica. As the PLCF was irradiated by a blue laser, the transmission spectrum had a red shift. If we further increased the irradiation time, the effective index of the LC mixture was raised and the transmission losses was increased. As the irradiation time was 15 seconds, the transmission spectrum was almost unchanged as shown in Fig. 3(a) due to the phase structure of the LC mixture was completely switched from anisotropic to isotropic. Then, we can obtain the response time of the photoresponsive LC mixture in the PLCF is 15 seconds at 27°C.

Subsequently, we raised the ambient temperature from 27°C to 29.4°C and the corresponding transmission spectra are shown in Fig. 3(b). Similarly, as we increased the blue-laser irradiation time, the spectrum moved toward longer wavelengths and the phase transformation of the LC mixture can be rapidly changed by blue-laser irradiation. From Fig. 3(b), we can see that the

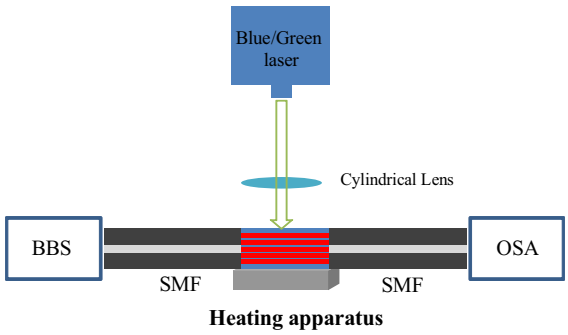

Figure 2: The schematic of experiment setup.

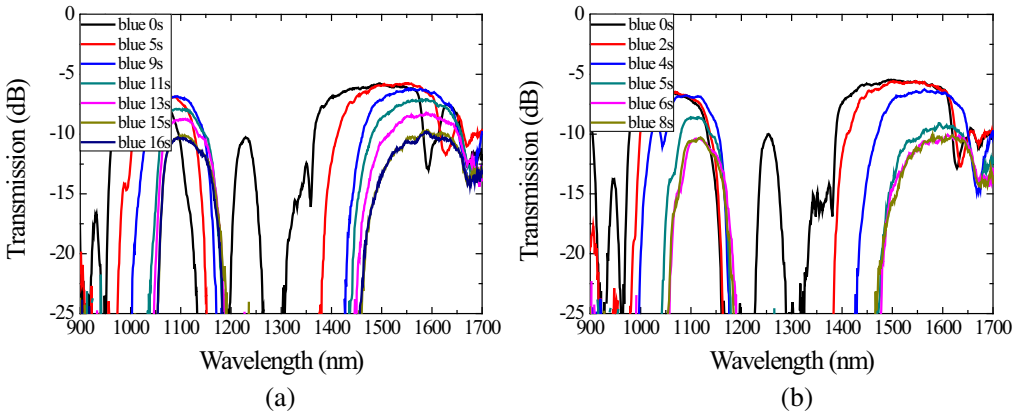

Figure 3: The transmission spectra of the light-controllable PLCF at (a) 27°C and (b) 29.4°C.

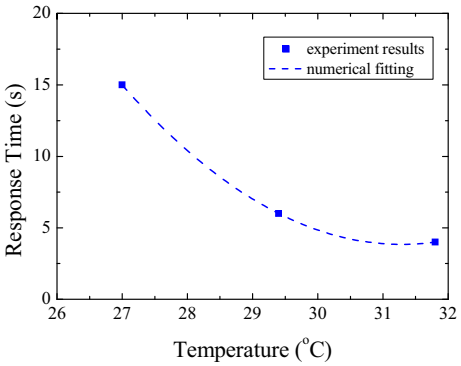

Figure 4: The response time of the PLCF versus the ambient temperatures.

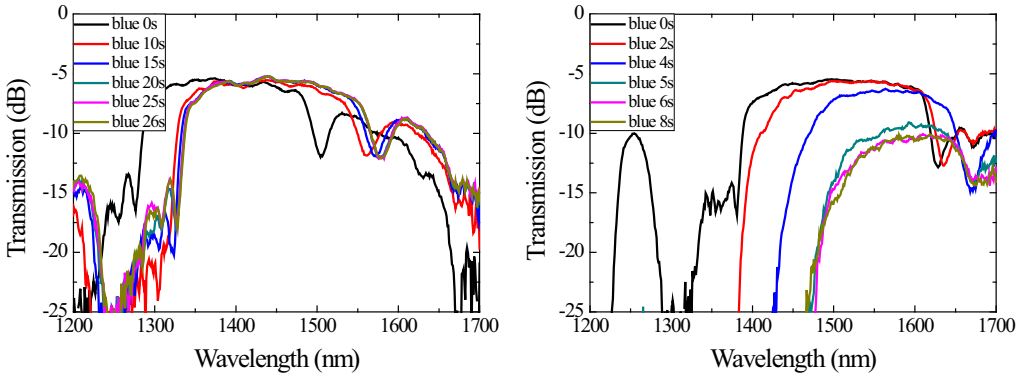

Figure 5: The transmission spectra of the light-controllable PLCF as the 4MAB concentrations is (a) 15 wt% and (b) 25 wt%.

response time was reduced from 15 seconds to 6 seconds owing to the viscosity of the LCs was reduced by the thermal effect. We also measured the response time of phase transformation for variant ambient temperatures as shown in Fig. 4 and a second-order relationship can be observed. However, when the operation temperature reached 34°C, which is the phase transition point of the photoresponsive LC mixture, the phase structure of the LC mixture became isotropic before irradiation and the transmission spectrum cannot be changed by blue-laser illumination.

We also measured the PLCF with variant 4MAB concentrations as the ambient temperature was 29.4°C. The transmission spectra are shown in Figs. 5(a) and 5(b). The transmission band was observed to move toward shorter wavelengths as we decreased the concentration of 4MAB. After the blue-laser exposure, the transmission spectra moved toward longer wavelengths as shown in Fig. 5(a). Compared with Fig. 5(b), one can observe that the response time of the phase transformation was increased with the decreased 4MAB concentrations. From these measured results, it can be seen that the response time of our fabricated light-controllable PLCF can be reduced by raising the ambient temperature near the phase transition point of the photoresponsive LC mixture and by increasing the 4MAB concentration.

4. CONCLUSIONS

In this paper, a light-controllable PLCF is fabricated by filling the PCF with the photoresponsive LC mixture consisting of nematic E7 LC and photochromatic 4MAB. Under blue-laser irradiation, the phase transition of the photoresponsive LC mixture can be switched from anisotropic to isotropic and the refractive index of the LC mixture can be varied. By raising the ambient temperature and the concentrations of 4MAB, the response time of the LC mixture can be reduced. These measured results are useful for applying the photoresponsive PLCFs in further applications of optical devices.

REFERENCES

1. Knight, J. C., T. A. Birks, P. S. J. Rusesel, and D. M. Atkin, "All-silica single-mode optical fiber with photonic crystal cladding," *Opt. Lett.*, Vol. 21, No. 19, 1547–1549, 1996.

2. Knight, J. C., "Photonic crystal fibers," *Nature*, Vol. 424, No. 14, 847–851, 2003.
3. Ferrando, A., E. Silvestre, P. Andrés, J. J. Miret, and M. V. Andrés, "Designing the properties of dispersion flattened photonic crystal fibers," *Opt. Express*, Vol. 9, No. 13, 687–697, 2001.
4. Noordegraaf, D., L. Scolari, J. Lægsgaard, L. Rindorf, and T. T. Alkeskjold, "Electrically and mechanically induced long period gratings in liquid crystal photonic bandgap fibers," *Opt. Express*, Vol. 15, No. 13, 7901–7912, 2007.
5. Du, F., Y. Q. Lu, and S. T. Wu, "Electrically tunable liquid-crystal photonic crystal fiber," *App. Phys. Lett.*, Vol. 85, No. 12, 2181–2183, 2004.
6. Noordegraaf, D., L. Scolari, J. Lægsgaard, T. T. Alkeskjold, G. Tartarini, E. Borelli, P. Bassi, J. Li, and S. T. Wu, "Avoided-crossing-based liquid-crystal photonic-bandgap notch filter," *Opt. Lett.*, Vol. 33, No. 9, 986–988, 2008.
7. Hsiao, V. K. and C. Y. Ko, "Light-controllable photoresponsive liquid-crystal photonic crystal fiber," *Opt. Express*, Vol. 16, No. 17, 12670–12676, 2008.
8. Liou, J. H. T. H. Chang, T. Lin, and C. P. Yu, "Reversible photo-induced long-period fiber gratings in photonic liquid crystal fibers," *Opt. Express*, Vol. 19, No. 7, 6756–6761, 2011.
9. Lee, C. R., J. D. Lin, B. Y. Huang, T. S. Mo, and S. Y. Huang, "All-optically controllable random laser based on a dye-doped liquid crystal added with a photoisomerizable dye," *Opt. Express*, Vol. 18, No. 25, 25896–25905, 2010.

Design Approach of Liquid-filled Dispersion-flattened Photonic Crystal Fibers

Jui-Ming Hsu[1, 2] **and Der-Li Ye**[1]

[1]Department of Electro-Optical Engineering, National United University, Miaoli 360, Taiwan, R.O.C.
[2]Optoelectronics Research Center, National United University, Miaoli 360, Taiwan, R.O.C.

Abstract— A design approach of liquid-filled dispersion-flattened photonic crystal fibers (LF-DFPCF) is proposed. Instead of changing the geometric structure, we fill specific liquid with different index into some cladding-holes of a photonic crystal fiber to design a broadband zero-dispersion PCF. The numeric results indicate that the bandwidth of ultra-flat dispersion values between 0 ± 1.0 ps/nm-km is about 460 nm.

1. INTRODUCTION

Dispersion-flattened fibers (DFF) have potential applications to broadband WDM (wavelength division multiplexing) systems. For a traditional DFF, the chromatic dispersion D is relatively small over a wide wavelength range extending from 1.3 to 1.6 μm [1]. Photonic crystal fibers (PCF) have attracted substantial attention recently because of their outstanding properties and great versatility. Several designs for the dispersion-flattened photonic crystal fiber (DFPCF) have been proposed to achieve the nearly zero ultraflattened chromatic dispersion properties [2–7]. The previous studies involved altering the air hole size of specific layers of PCF to design a DFPCF [2–6]. K. M. Gundu et al. filled same liquid in the holes of two inner layers to achieve small dispersion values between 0 ± 1 ps/nm-km over a bandwidth of about 400 nm [7].

In this study, a design approach of a liquid-filled dispersion-flattened photonic crystal fiber (LF-DFPCF) is proposed. Instead of changing the geometric structure, we fill specific liquid with different index into some cladding-holes of a PCF to achieve the broadband nearly zero dispersion properties. Different from Gundu's work [7], we fill different liquid in the holes located at different layers to design a LF-DFPCF.

2. SIMULATION MODELS

Figure 1 indicates the simulation model of the proposed structure, the cladding is consisted of a triangular lattice of air-holes with a diameter of $d = 1.925$ μm and a pitch (center-to-center distance between the holes) Λ of 3.500 μm in a background of undoped silica. The solid core with a diameter of about 5 μm is formed by removing the central air-hole. Some liquid with different index, which will be designed in this study, are filled in the cladding-holes located at three layers nearest the solid core.

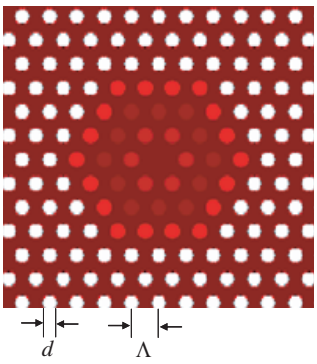

Figure 1: Simulation model of the proposed LF-DFPCF. $\Lambda = 3.500$ μm, $d = 1.925$ μm. Some liquid with different index are filled in the cladding-holes located at three layers nearest the solid core.

3. DESIGNING PROCEDURES

The chromatic dispersion D is a sum of the material dispersion D_M and the waveguide dispersion D_W, $D = D_M + D_W$. For a zero chromatic dispersion at a wavelength of λ, the relation $D(\lambda) = D_M(\lambda) + D_W(\lambda) = 0$ must be satisfied. Therefore, to achieve a nearly zero ultraflattened chromatic dispersion, we can tailor the waveguide dispersion to fit in with

$$D_W(\lambda) \approx -D_M(\lambda) \tag{1}$$

over a bandwidth of as large as possible.

The chromatic dispersion coefficient D, material dispersion coefficient D_M and waveguide dispersion coefficient D_W are defined as

$$D(\lambda) = D_M(\lambda) + D_W(\lambda) = -\frac{\lambda}{c}\frac{d^2 n_{eff}}{d\lambda^2}, \tag{2}$$

$$D_M(\lambda) = \frac{-\lambda}{c}\frac{d^2 n_m}{d\lambda^2}, \tag{3}$$

$$D_W(\lambda) = \frac{-\lambda}{c}\frac{d^2 n_w}{d\lambda^2}, \tag{4}$$

where λ represents the operating wavelength, c is the speed of light in a vacuum, and n_{eff} is the effective index of the fundamental guided mode in a fiber, n_m is the material refractive index (silica in this case), and n_w is the modal refractive index evaluated by consideration of the fact that the material refractive index is wavelength independent.

In this work, the material refractive index (n_m) is computed by using the Sellmeier equation [8]

$$n_m(\lambda) = \left[1 + \frac{0.6961663\lambda^2}{\lambda^2 - (0.0684043)^2} + \frac{0.4079426\lambda^2}{\lambda^2 - (0.1162414)^2} + \frac{0.8974794\lambda^2}{\lambda^2 - (9.896161)^2}\right]^{1/2}, \tag{5}$$

the effective waveguide index (n_w) of the liquid-filled PCF is estimated by using the plane-wave expansion (PWE) method. The material dispersion D_M and waveguide dispersion D_W are then evaluated by substituting n_m and n_w into Equations (3) and (4), respectively.

After several simulation procedures, the tailor-tendency of waveguide dispersion curves, referred to as D_W curves, for the index-altering of each layer holes can be found out. Table 1 indicates the tailor-tendencies generalized from collections of some simulation instances, e.g., Figure 2. Figures 2(a), (b) and (c) indicate the waveguide dispersion distribution for filling different liquid (with indices of n_{L1}, n_{L2} and n_{L3}) in the holes of layers 1, 2 and 3, respectively. The D_W curves in each figure oscillate by wavelength cyclically. As shown in Figure 2(a), the period of D_W curves is almost changeless for altering the n_{L1}. However, for a larger n_{L1}, the amplitude of the curve is smaller, thus the D_W value is smaller at a short wavelength. Therefore, the tailor-tendency of D_W curve for the first layer is the starting point decision at short wavelength. In Figure 2(b), the period and amplitude of D_W curve are all smaller while n_{L2} is enlarged. However, the slopes of the D_W curves are approximately equal in our operating range to cannel out the material dispersion curve (for the curve of $n_{L2} = 1.41$, the range is about 1.2 µm–1.7 µm in the figure). Therefore, one

Table 1: Tailor-tendency of waveguide dispersion curves with the index-altering for each layer holes.

Layer (referred figures)	mainly affected behaviors	Descriptions
Layer1 (Figure 2(a))	Starting point decision at short wavelength.	The smaller the n_{L1}, the larger the starting point of the D_W value.
Layer2 (Figure 2(b))	Wavelength-shift for the D_W curve.	The D_W curve shifts toward a shorter wavelength for a larger n_{L2}.
Layer3 (Figure 2(c))	Slope-variation for the D_W curve.	The larger the n_{L3}, the steeper the D_W curve.

can shift a D_W curve and nearly hold on an invariable slope by exchanging liquid of second layer. As shown in Figure 2(c), the period of D_W curve shrinks obviously for a larger n_{L3}. Therefore, the tailor-tendency of D_W curve for the third layer is slope-variation.

The curve of $-D_M$ can be plotted as a criterion of D_W-tailoring. According to Equation (1), to achieve a nearly zero chromatic dispersion, tailoring the D_W curve to overlap the $-D_M$ curve over a bandwidth of as large as possible is the designing policy. According to the tailor-tendency in Table 1, refractive indices of liquid filled in the holes at each layer are modified to tailor the D_W value to overlap its curve with the $-D_M$ curve over a bandwidth of as large as possible.

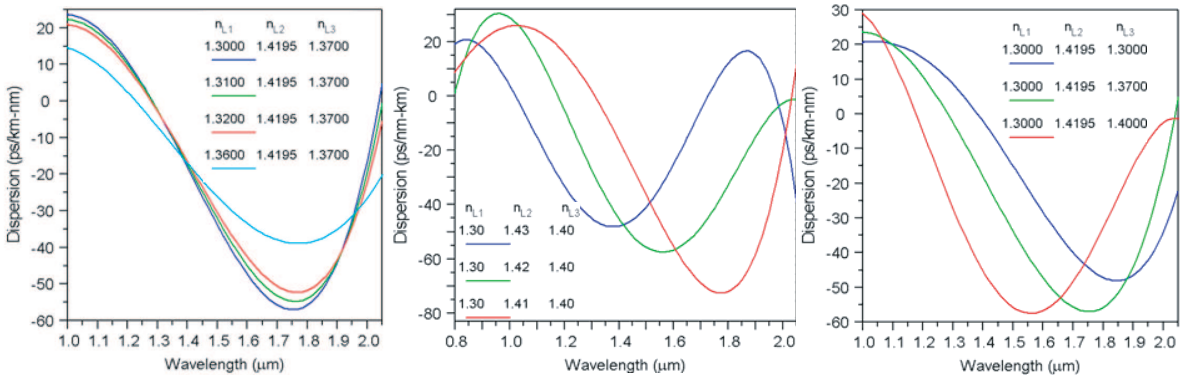

(a) (b) (c)

Figure 2: Some simulation examples for the tailor-tendency inference of waveguide dispersion for a liquid-filled PCF.

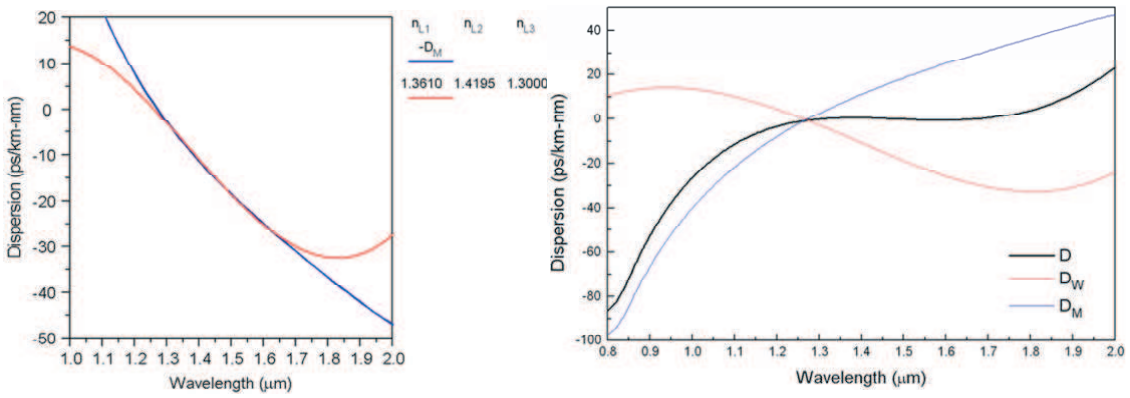

(a) (b)

Figure 3: Dependence of dispersions on wavelength for the proposed LF-DFPCF. (a) Negative material dispersion ($-D_M$, blue line) and waveguide dispersion (D_W, red line), (b) material dispersion (D_M), waveguide dispersion (D_W) and chromatic dispersion ($D = D_M + D_W$). $\Lambda = 3.500\,\mu$m, $d = 1.925\,\mu$m, $n_{L1} = 1.3610$, $n_{L2} = 1.4195$, and $n_{L3} = 1.3000$.

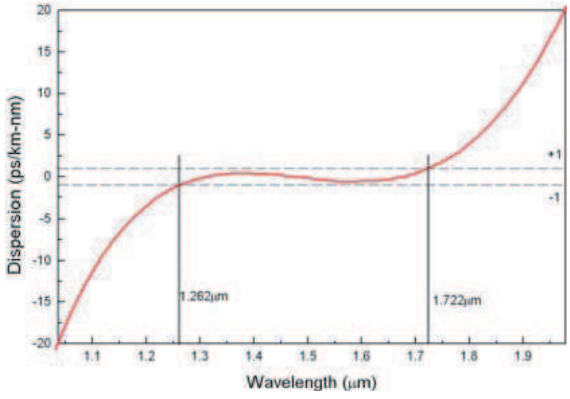

Figure 4: Dependence of chromatic dispersion on wavelength for the proposed LF-DFPCF.

Figure 3(a) indicates the dependence of D_W and $-D_M$ on wavelength for the tailored result of $n_{L1} = 1.3610$, $n_{L2} = 1.4195$, and $n_{L3} = 1.3000$. Figure 3(b) depicts the relation of D_W, D_M and D $(= D_W + D_M)$ versus wavelength. As shown in Figures 3(a) and (b), the material dispersion is nullified by the tailored waveguide dispersion, this results in a zero chromatic dispersion, in a very wide wavelength window. To clearly exhibit the chromatic dispersion behavior, the dependence of chromatic dispersion on wavelength with a tolerant range of 0 ± 1 ps/nm-km is shown in Figure 4. The wavelength window for which the fiber dispersion remains between the tolerant ranges of 0 ± 1 ps/nm-km is from 1262 to 1722 nm. The flattened zero-dispersion bandwidth is approximately 460 nm.

4. CONCLUSIONS

This article proposes an approach to design a liquid-filled dispersion-flattened photonic crystal fiber (LF-DFPCF). Instead of changing the geometric size of cladding holes, we fill specific liquid with different index into some cladding-holes of the PCF to design a broadband zero-dispersion PCF. After several simulation procedures, we found out the tailor-tendencies of waveguide dispersion distribution for changing liquid filled in the holes of each layer. According to these tailor-tendencies, the waveguide dispersion is tailored to nullify the material dispersion within a wide range of wavelength. The wavelength window for which the fiber dispersion remains between 0 ± 1 ps/nm-km is from 1262 to 1722 nm. The flattened zero-dispersion bandwidth is approximately 460 nm.

REFERENCES

1. Agrawal, G. P., *Fiber-optic Communication Systems*, John Wiley & Sons, 3rd Edition, New York, 2002.
2. Ferrando, A., E. Silvestre, J. J. Miret, and P. Andres, "Nearly zero ultraflattened dispersion in photonic crystal fibers," *Opt. Lett.*, Vol. 25, No. 11, 790–792, 2000.
3. Ferrando, A., E. Silvestre, and P. Andres, "Designing the properties of dispersion-flattened photonic crystal fiber," *Opt. Express*, Vol. 9, No. 13, 687–697, 2001.
4. Reeves, W. H., J. C. Knight, and P. St. J. Russell, "Demonstration of ultra-flattened dispersion in photonic crystal fibers," *Opt. Express*, Vol. 10, No. 14, 609–613, 2002.
5. Saitoh, K., M. Koshiba, T. Hasegawa, and E. Sasaoka, "Chromatic dispersion control in photonic crystal fibers: Application to ultra-flattened dispersion," *Opt. Express*, Vol. 11, No. 8, 843–852, 2003.
6. Wu, T. L. and C. H. Chao, "A novel ultraflattened dispersion photonic crystal fiber," *IEEE Photon. Technol. Lett.*, Vol. 17, No. 1, 67–69, 2005.
7. Gundu, K. M., M. Kolesik, and J. V. Moloney, "Ultra-flattened-dispersion selectively liquid-filled photonic crystal fibers," *Opt. Express*, Vol. 14, No. 15, 6870–6878, 2006.
8. Malitson, I. H., "Interspecimen comparison of the refractive index of fused silica," *J. Opt. Soc. Am.*, Vol. 55, No. 10, 1205–1209, 1965.

The Use of Magnetic Spectroscopy in the Investigation of the Magnetic Viscosity of Nanoparticles at Microwave Frequencies

P. C. Fannin[1] **and C. N. Marin**[2]

[1]Department of Electronic and Electrical Engineering, Trinity College, Dublin 2, Ireland
[2]Faculty of Physics, West University of Timisoara, Bd. V. Parvan no. 2, Timisoara, Romania

Abstract— In the case of uniaxial single domain superparamagnetic particles, the magnetic moment, m, may switch between two anti-parallel equilibrium positions, however, the switching does not happen instantaneously and parameters which influence this action in the particles are the magnetic viscosity, η_m, the interwell and intrawell relaxation times, τ_N and τ_0. Here, by measurement of the field and frequency dependence of the complex magnetic susceptibility, $\chi(\omega) = \chi'(\omega) - i\chi''(\omega)$, these values are determined for two colloidal suspensions of manganese ferrite in isopar-m of approximately the same particle size and magnetisation but differing stoichiometry, x, with a view to determining, what effect, if any, the value of x has on η_m and hence the switching time of the magnetic moment.

1. INTRODUCTION

The magnetic viscosity, η_m, of the magnetic moment, m, of nano-particles is of particular interest in investigating the performance quality of a single-domain nanoparticle used as a signal processing device, such as a binary switch. Such devices are governed by the signal-to-noise ratio (SNR) characteristic of the particle which is found to be inversely proportional to the magnetic viscosity, η_m [1]; hence the need to investigate this parameter together with the actual switching time, τ_N and its prefactor τ_0. Here these parameters are investigated through the medium of magnetic fluids which comprise of a distribution of particles having radii ranging from approximately 2 to 10 nm. These particles are in the single domain region, with, m, given by $m = M_s v$, where $M_s(T)$ denotes the saturation magnetisation and v is the magnetic volume of the particle.

The direction of m fluctuates in a random manner for two reasons. Firstly, within the particle, m can change from one easy direction of magnetisation to another by surmounting an energy barrier which for uniaxial anisotropy is given by Kv. K is the anisotropy constant of the particle. This process is characterised by the Néel switching time τ_N. Secondly as the particle is surrounded by a viscous fluid it can perform Brownian rotation diffusion [2] with a a relaxation time, τ_B.

For anisotropic particles the probability of the magnetic moments surmounting the anisotropy energy barrier is approximately equal to $\exp(\sigma)$, where σ is the ratio of anisotropy energy to thermal energy, (Kv/kT). This reversal or switching time, τ_N, was estimated by Néel to be $\tau_N = \tau_o \exp(\sigma)$.

$\tau_o = Ms/2\alpha\gamma K$, where α is the Landau and Liftshitz damping parameter [3], whilst γ is the magneto-mechanical ratio; both parameters are evaluated here for the two samples. Brown [4] proposed expressions for τ_N for low and high anisotropy barriers, with;

$$\tau_N = \tau_o \sigma \qquad \sigma < 1 \tag{1}$$

$$\tau_N = \tau_o \sigma^{-1/2} \exp(\sigma) \quad \sigma \geq 2 \tag{2}$$

2. MAGNETIC VISCOSITY

The magnetic moment does not switch instantaneously within a particle and this arises because of the particles 'magnetic viscosity', η_m. By means of the Landau and Lifshitz [3] equation, $\dot{M}_s = \gamma(M_s \times H) + \frac{\alpha\gamma}{M_s}(M_s \times H) \times M_s$, one can determine an equation for η_m in terms of the two parameters, α and γ, where the coefficient $\alpha\gamma/\mathrm{M}_S$, preceeding the relaxational or dissipative term signifies rotary mobility which has the inverse units of viscosity. The Einstein formula gives the coefficient of the internal rotational diffusion of the magnetic moment, m, as $D = \alpha\gamma kT/m$ [2]. Thus the characteristic time of the orientational diffusion of the magnetic moment, m, is, $\tau_D = \frac{1}{2D} = \frac{M_s v}{2\alpha\gamma kT}$.

Analogous to the Brownian relaxation case, this is generally written in the more convenient form, $\tau_D = 3\, v\eta_m/kT$ where the parameter,

$$\eta_m = M_s/6\alpha\gamma \tag{3}$$

is the internal 'magnetic viscosity' which inhibits the movement of the magnetic vector and has the same units (Nsm^{-2}) as viscosity.

3. COMPLEX SUSCEPTIBILITY

$\chi(\omega)$ of an assembly of single domain particles can be described in terms of its parallel, $\chi_{||}(\omega)$, and perpendicular, $\chi_{\perp}(\omega)$, components, with $\chi(\omega) = \frac{1}{3}\left(\chi_{||}(\omega) + 2\chi_{\perp}(\omega)\right)$ [5]. $\chi_{||}(\omega)$, can be described by the Debye equation [2, 6], with $\chi_{||}(\omega) = \frac{\chi_{||}(0)}{1+i\omega\tau_{||}}$, where $\chi_{||}(0)$ is the static parallel susceptibility and $\tau_{||}$ is the parallel relaxation time which is related to the frequency, $f_{\max}$, at which the imaginary component of $\chi''(\omega)$ is a maximum, by the expression $f_{\max} = 1/(2\pi\tau_{||})$.

Over the high frequency range considered here $\tau_{||}$ will be considered to be dominated by the Néel relaxation mechanism τ_N. In equilibrium, m would be directed along this easy axis if it were not for thermal fluctuations. The angular resonant frequency ω_{res}, is given by, $\omega_{res} = \gamma H_A$. H_A is the internal field for a particle with uniaxial anisotropy and where the polar angle between the easy axis and the magnetic moment is small, has magnitude, $H_A = 2K/M_s$. Applying an external H, results in an increase in ω_{res} given by

$$\omega_{res} = 2\pi f_{res} = \gamma(H + H_A) \tag{4}$$

3.1. Experimental and Results

Measurements of the complex magnetic susceptibility $\chi(\omega) = \chi'(\omega) - i\chi''(\omega)$ over the frequency range 100 MHz to 6 GHz, and for 12 values of polarizing field over the range of 0–104 $\mathrm{kAm^{-1}}$, were made by means of the coaxial transmission line technique [7, 8]. For the measurements a Hewlett-Packard(HP) 50 Ω coaxial line incorporating a coaxial cell was used in conjunction with a HP 8753C network analyzer. The samples were placed in the coaxial cell and standard HP open-circuit and short-circuittest devices used as terminations and then the input impedance of the line containing the sample was measured and from these measurements the complex components, were determined.

The two magnetic fluids, namely Sample 1, and Sample 2, used in this study consisted of colloidal suspensions of manganese ferrite particles, $Mn_xFe_{1-x}Fe_20_4$, colloidally dispersed in isopar M and stabilised with oleic acid. x had values of 0.3 and 0.5, and the samples had saturation magnetisations of 360 G and 330 G, and corresponding particle median diameters of 10.5 nm and 9.9 nm, respectively.

Figure 1 shows the polarised results obtained in the case of Sample 1 and these results are typical of those obtained for both samples. From Fig. 1, it is seen that resonance, occurs at a frequency $f_{res} = 1.6$ GHz whilst the maximum of the $\chi''(\omega)$ loss-peak is also shown to occur at a frequency of $f_{\max} = 1.0$ GHz. Variation H over the stated range results in f_{res} and $f_{\max}$ increasing up to frequencies of 6.0 GHz and 5.9 GHz, respectively. A plot of f_{res} against H for the sample is shown in Fig. 2. and as $\omega_{res} = 2\pi f_{res} = \gamma(H + H_A)$, a value of $H_A = 43.8\,\mathrm{kAm^{-1}}$, corresponding to a, K value of 5.9 10^3 $\mathrm{J/m^3}$, was determined. From the slope of Fig. 2 the magneto-mechanical ratio, γ, is found to be 2.48 10^5 $\mathrm{S^{-1}A^{-1}m}$.

A value of α is obtained by a method reported in Ref. [9] where it is shown that in the region

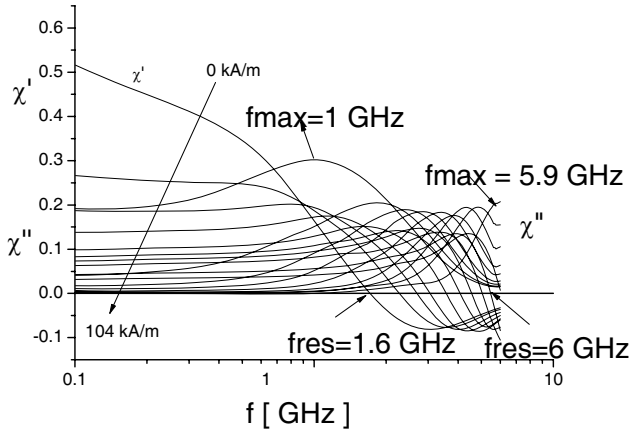

Figure 1: Plot of χ' (ω, H) and χ'' (ω, H) against f (Hz), for Sample 1.

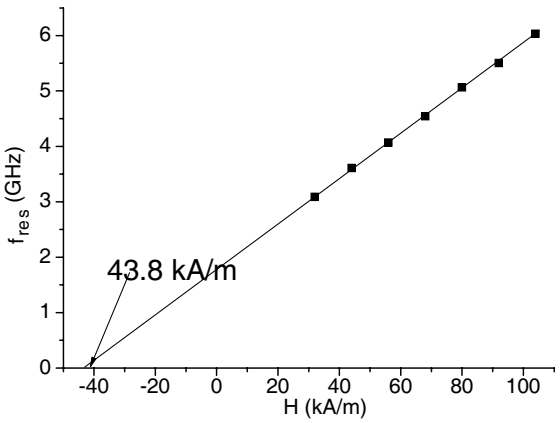

Figure 2: Plot of f_{res} against polarising field, H, for Sample 1.

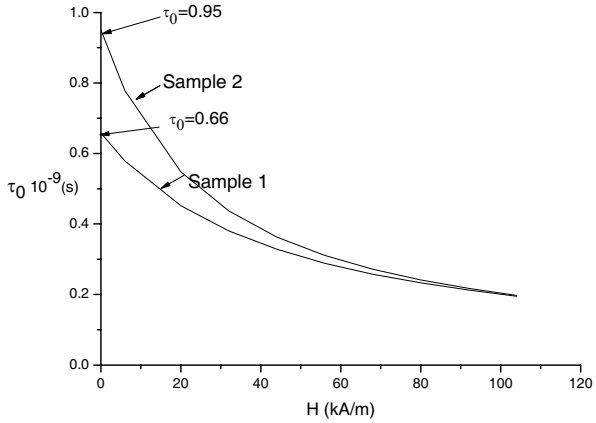

Figure 3: Plot of $t(s)$ against H for Samples 1 and 2.

Table 1.

sample	$\bar{H}_A$ kAm^{-1}	γ s^{-1}A^{-1}m	α	$\eta_m 10^{-6}$Nsm^{-2}	τ_o 10^{-9}s	$\tau_N 10^{-9}$s
1	43.8	2.48 10^5	0.21	0.864	0.66	0.56
2	35	2.42 10^5	0.135	1.377	0.95	0.55

of strong polarizing fields, ($H > H_A$),

$$\alpha = \sqrt{\frac{1-(f_{\max}/f_{res})^2}{1+(f_{\max}/f_{res})^2}} \tag{5}$$

In this case it was found that for $H > 80\,\mathrm{kA/m}$, the ratio $f_{\max}/f_{res}$ tends to have a constant value of 0.953 and using this value in Eq. (5) results in $\alpha = 0.21$. This method of determining α is a more accurate method than that previously used [10] since the effect of the large polarising field is to reduce to a minimum the influence of any Brownian relaxation which may be present.

Having determined values of α and γ for the sample, the value of η_m was found from Eq. (3). Thus, for $\alpha = 0.21, \gamma = 2.4810^5\,\mathrm{S^{-1}A^{-1}\,m}$ and $M_S = 0.27\,\mathrm{T}$, η_m is found to have a value of 0.864 $10^{-6}\mathrm{Nsm^{-2}}$.

$$\frac{B}{b(0)} = \frac{\left(1/\tau_o\right)}{\left(1/\tau_o\right)^2 + \omega_{res}^2} = \frac{\tau_o}{1+\omega_{res}^2\tau_o^2} \tag{6}$$

τ_o was determined by means of the after-effect technique reported in [11], through Equation (6), where B is the area under the after-effect function $b(t)$, of the susceptibility and $b(o)$ is the value of $b(t)$ at time $t = 0$. From the plot of Fig. 3, ($t(s)$ against H), τ_o is determined as 0.66 10^{-9} s for Sample 1. τ_N is found to have a value of 0.56 10^{-9} s. The above procedure was performed for both samples and the results obtained are shown in Table 1 below.

4. CONCLUSIONS

The switching action of a nano-particles magnetic moment, m, is influenced by the interwell and intrawell relaxation times, τ_N, and τ_0, and the magnetic viscosity coefficient, η_m. In order to evaluate these parameters it is necessary to determine values for the damping parameter, α, the gyromagnetic constant, γ, and the anisotropy constant K of the nanoparticles. Here these values are determined for two colloidal suspensions of manganese ferrite in isopar m by measurement of the complex magnetic susceptibility as a function of frequency and H.

From plots of f_{res} against H, values of γ were determined. The damping parameters were found by means of the method reported in Ref. [9] and the values of 0.21 and 0.135, respectively, were obtained.

The parameters, τ_N, τ_0, and η_m, were then evaluated. As can be seen from Table 1, η_m was found to have values of $0.86410^{-6}\,\mathrm{N{\cdot}s{\cdot}m^{-2}}$and $1.377\ 10^{-6}\,\mathrm{N{\cdot}s{\cdot}m^{-2}}$. The values of τ_N for

those samples were estimated as 0.56×10^{-9} s and 0.55×10^{-9} s, both latter values being within the normally accepted range for this parameter. If it is assumed that the time, τ_N, is short compared with the time the magnetic moment spends in a particular direction, relative to the particle, then the changes in sign of the magnetisation may be treated as a Poisson process which is a stochastic function that changes between levels of $+1$ and -1, i.e., a binary switching action, an electronic switch. Therefore, as τ_N is approximately the same in each case, one can conclude that in the case of samples with the same approximate particle size and magnetisation, the difference in stoichiometry has no apparent detrimental effect on the switching performance of the particles.

ACKNOWLEDGMENT

P. C. Fannin acknowledges ESA for part funding of this work whilst C. N. Marin acknowledges support of CNMP grant no. 1-32155/2008. Thanks are also due to Dr. C. Cooper.

REFERENCES

1. Fannin, P. C., Y. L. Raikher, A. T. Giannitsis, and S. W. Charles, "Investigation of the influence which material parameters have on the signal-to-noise ratio of nanoparticles," *J. Magn. Magn. Mater.*, Vol. 252, 114, 2002.
2. Raikher, Y. L. and M. I. Shliomis, "Relaxation phenomena in condensed matter," *Adv. Chem. Phys.*, Vol. 87, 595, 1994.
3. Landau, L. D. and E. M. Lifhitz, *Phys. Z. Sowjetunion*, 8, 153, 1935; reprinted in *Collected Works of L. Landau*, No. 18, Pergamon Press, London, 1965.
4. Brown, Jr, W. F., "Thermal fluctuations of a single-domain particle," *Phys. Rev.*, Vol. 130, 1677, 1963.
5. Raikher, Y. L. and M. I. Shliomis, "Theory of dispersion of the magnetic susceptibility of fine ferromagnetic particles," *Sov. Phys. JETP*, Vol. 40, 526, 1975.
6. Debye, P. and P. Molecules, *The Chemical Catalog Company*, New York, 1929.
7. Roberts, S. and A. R. von Hippel, "A new method for measuring dielectric constant and loss in the range of centimeter waves," *J. Appl. Phys.*, Vol. 17, 610, 1946.
8. Fannin, P. C., C. MacOireachtaigh, and C. Couper, "An improved technique for the measurement of the complex susceptibility of magnetic colloids in the microwave region," *J. Magn. Magn. Mater.*, Vol. 322, 2428, 2010.
9. Fannin, P. C. and C. N. Marin, "Determination of the Landau-Lifshitz damping parameter by means of complex susceptibility measurements," *J. Magn. Magn. Mater.*, Vol. 299, 425, 2006.
10. Fannin, P. C., T. Relihan, and S. W. Charles, "Experimental and theoretical profiles of the frequency-dependent complex susceptibility of systems containing nanometer-sized magnetic particles," *Phys. Rev. B*, Vol. 55, 14423, 1997.
11. Fannin, P. C., C. Couper, and C. N. Marin, "Precessional decay time of nanoparticles in magnetic fluids," *J. Magn. Magn. Mater.*, Vol. 323, 1242, 2010.

Concealing an Electromagnetic Sensing System Using Three Kinds of Isotropic Homogeneous Single-negative Materials

Xuefeng Zhu, **Xinye Zou**, **Qian Chen**, **Bin Liang**, **and Jian-Chun Cheng**
Key Laboratory of Modern Acoustics, MOE, Department of Physics, Institute of Acoustics
Nanjing University, Nanjing 210093, China

Abstract— We have proposed a multi-layer structure for concealing an electromagnetic sensing system (a sensor is inserted into a scatterer), using isotropic single-negative materials whose material parameters are completely independent of those of the host matrix and the concealed system. The numerical results show that only three kinds of different isotropic homogeneous materials are sufficient to yield the cloaking effect even in the presence of weak loss. This may significantly facilitate the experimental realization of a well-performed sensor-cloaking device.

1. INTRODUCTION

The past decade has witnessed substantial efforts dedicated to the investigation on various cloaking devices [1–9]. One approach to achieving an invisibility cloak is to exclude electromagnetic (EM) waves from the inner domain without perturbing the exterior fields [1–7]. But this approach cannot be used to cloak a sensor [8], which dramatically limits its potential applications. To solve such a difficulty, another approach was then presented to realize the so-called "external cloaking" [9], in which the cloaked object can share information with the surroundings. Henceforth, Zhu et al. [10] have proposed a different cloaking approach called "superlens cloaking" to cloak an acoustic sensor by employing SNG materials in a double-shell structure, which remarkably simplifies the experimental realization and improves the operating bandwidth for an acoustic cloak.

In this paper, we present a multi-layer cloaking scheme to cloak an electromagnetic sensing system (an EM sensor is inserted into a scatterer) using three kinds of isotropic homogeneous SNG materials only. It is shown that the external field is almost undisturbed when an EM sensor is inserted into a bare scatterer to form a sensing system, with the employment of the three different kinds of isotropic materials whose material parameters are homogeneous and completely independent of those of the host matrix and the concealed system.

2. THEORY

For simplicity, we focus our attention within two-dimensional cases. During coordinate transformation, i.e., transforming a piece of space $(A+B)$ into another $(A'+B)$, a hole C may form, which is inaccessible to the EM field. Since the transformed space $(A'+B)$ is an unconnected domain as seen in Fig. 1(a), the hole C can be filled with complementary media to keep the continuity of EM field. As a result, the object A' $(0 < r' < a)$ can be regarded as being cloaked by the cloak in C $(a < r' < c)$.

According to the transformation optics, the permittivity ε' and permeability μ' in the transformed space $\mathbf{x}'$ are given by $\varepsilon' = \mathbf{H}\varepsilon\mathbf{H}^{\mathbf{T}}/\det\mathbf{H}$ and $\mu' = \mathbf{H}\mu\mathbf{H}^{\mathbf{T}}/\det\mathbf{H}$, where ε and μ are the permittivity and permeability in the original space $\mathbf{x}$. $\mathbf{H}$ is the Jacobian transformation tensor with components $H_{ij} = (h_{x_i'}/h_{x_j})(\partial x_i'/\partial x_j)$, in which h_{x_i} and $h_{x_i'}$ are the scale factors in spaces $\mathbf{x}$ and $\mathbf{x}'$ respectively. For the mapping $A \leftrightarrow A'$ and $B \leftrightarrow B$, the transforming equations can be written as $r = f(r')$, $\vartheta = \vartheta'$ with $f(r') = r'c/a$ $(0 < r' < a)$ and $f(r') = r'$ $(r' > c)$, respectively. In the mapping $A \leftrightarrow A'$, the scale factors are $h_r = 1$, $h_\vartheta = r = f(r') = r'c/a$ and $h_{r'} = 1$, $h_{\vartheta'} = r'$. For the TE waves (E along the z direction), the parameters ε and μ of A are assumed to be $\varepsilon_z = 1$ and $\mu_r = \mu_\vartheta = 1$, respectively. Then the parameters ε' and μ' of A' are $\varepsilon_z' = (c/a)^2 > 1$ and $\mu_r' = \mu_\vartheta' = 1$, respectively. In the mapping $B \leftrightarrow B$, the medium is unchanged apparently. For the hole region C, we first consider the case of the mapping between C_1 $(a < r' < b)$ and C_2 $(b < r'' < c)$, which is given by $r' = f(r'')$, $\vartheta' = \vartheta''$ with:

$$f\left(r''\right) = ca/r'' \qquad b < r'' < c \tag{1}$$

where $b = \sqrt{ac}$ as shown in Fig. 1(b). For the mapping $C_1 \leftrightarrow C_2$, the scale factors are $h_r' = 1$, $h_{\vartheta'} = r' = f(r'') = ca/r''$ and $h_{r''} = h_{z''} = 1$, $h_{\vartheta''} = r''$. Then, we divide C_1 equally into N smaller sections D_n $(n = 1, \ldots, N)$, in which $a + [(b-a)/N](n-1) < r_n' < a + [(b-a)/N]n$. Accordingly,

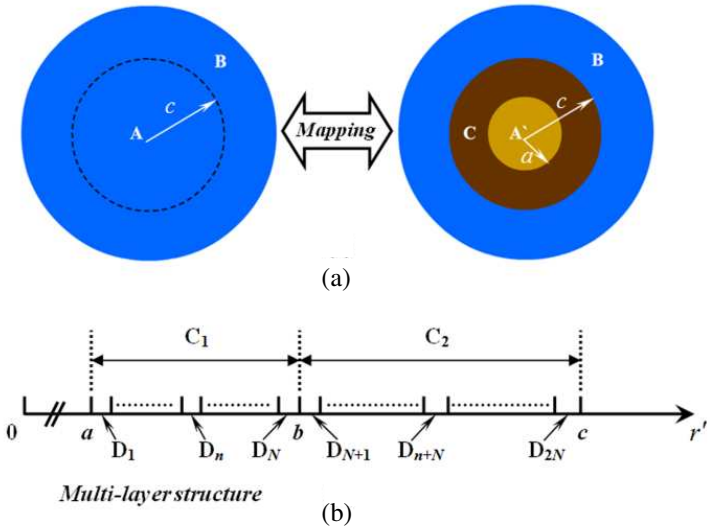

Figure 1: (a) the scheme of our mapping approach where $A \leftrightarrow A'$, $B \leftrightarrow B$. A' is the cloaked object $(0 < r' < a)$, while C is the hole filled with the cloaking shell made of single-negative parameters. (b) The scheme of multi-layer structure where $C_1 \leftrightarrow C_2$, $D_n \leftrightarrow D_{n+N}$ $(n = 1, \ldots, N)$ in the folding transformation.

D_{n+N} $(n = 1, \ldots, N)$ in C_2 can be obtained through the folding transformation which is similar in the form to the Eq. (1), in which $\{a + [(b-a)/N](n-1)\}(b/a) < r'_n < \{a + [(b-a)/N]n\}(b/a)$. Since the total phase shift when the EM wave passes across D_n and D_{n+N} $(n = 1, \ldots, N)$ must be exactly zero, the permittivity ε_n and ε_{n+N} in D_n and D_{n+N}, which are opposite in sign due to the folding transformation, must satisfy the following equation:

$$\phi_n = \sqrt{|\varepsilon_n|}(b-a)/N - \sqrt{|\varepsilon_{n+N}|}[(b-a)/N](b/a) = 0 \tag{2}$$

which finally gives $\varepsilon_n = -\varepsilon_{n+N}(b/a)^2$. Here the permeability in D_n and D_{n+N} has the relationship $\mu_n = -\mu_{n+N}$ from the folding transformation. It needs to mention that the ENG and MNG layers are preferred to stack alternatively to make the surface-plasmon-polaritons strongly coupled between the front and rear surfaces of the multi-layer cloak. With all the recipes mentioned above, the material parameters of the cloak can be derived in the following two steps. In the first step, we set N to be an odd number to ensure the alternatively stacking of ENG and MNG layers. The material parameters of D_{2n-1} $[n = 1, \ldots, (N+1)/2]$ are set to be $\varepsilon_{2n-1} = -\varepsilon_0$ and $\mu_{2n-1} = \mu_0$, in which ε_0 and μ_0 are arbitrary numbers, respectively. Based on Eq. (2), the material parameters of D_{2n-1+N} $[n = 1, \ldots, (N+1)/2]$ are calculated to be $\varepsilon_{2n-1+N} = \varepsilon_0(a/b)^2$ and $\mu_{2n-1+N} = -\mu_0$, respectively. In the second step, the material parameters of D_{2n} $[n = 1, \ldots, (N-1)/2]$ are set to be $\varepsilon_{2n} = \varepsilon_0(a/b)^2$, $\mu_{2n} = -\mu_0$ in order to reduce the number of required materials in the cloak. Then, the material parameters of D_{2n+N} $[n = 1, \ldots, (N-1)/2]$ are calculated to be $\varepsilon_{2n+N} = -\varepsilon_0(a/b)^4$ and $\mu_{2n+N} = \mu_0$, respectively. As a result, the number of material parameters in the cloak is reduced into three, and the parameters can be chosen flexibly as required in the fabrication process.

3. NUMERICAL RESULTS AND DISCUSSION

In the simulations, the wavelength of the TE wave is chosen to be $\lambda = 0.7$ unit. The electric fields are normalized throughout the section. For the host matrix $(r' > c)$, the permittivity and permeability are chosen to be $\varepsilon_M = 1$ and $\mu_M = 1$, respectively. The cloaked region $(0 < r' < a)$ is filled with a bare scatterer with the permittivity, the permeability and the radius chosen to be $\varepsilon_O = 2.7778$, $\mu_O = 1$ and $a = 0.6$, respectively. Then, the outer radii of C_1 and C_2 can be readily determined as $b = 0.775$ and $c = 1$, respectively. It is worth pointing out that the cloaked region can also be treated as filling with a homogeneous "effective" medium whose permittivity and permeability in fact refer to the effective ones. To give an example, we choose $N = 7$ and assume the material parameters of D_{2n-1} $[n = 1, \ldots, (N+1)/2]$ to be $\varepsilon_{2n-1} = -2.5$ and $\mu_{2n-1} = 1$, respectively, then the material parameters of D_{2n-1+N} $[n = 1, \ldots, (N+1)/2]$ are $\varepsilon_{2n-1+N} = 1.4984$ and $\mu_{2n-1+N} = -1$, respectively. If the material parameters of D_{2n} $[n = 1, \ldots, (N-1)/2]$ are also set to be $\varepsilon_{2n} = 1.4984$ and $\mu_{2n} = -1$, the material parameters of D_{2n+N} $[n = 1, \ldots, (N-1)/2]$ are $\varepsilon_{2n+N} = -0.8981$ and $\mu_{2n+N} = 1$, respectively.

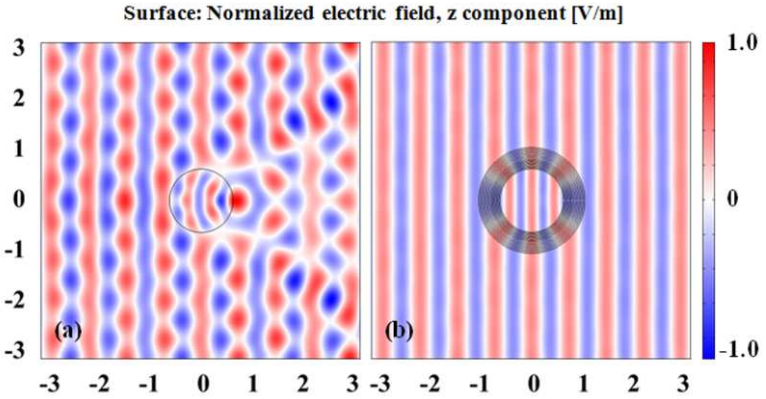

Figure 2: Normalized electric field distribution for plane EM wave incident from the left. A bare scatterer is shielded by (a) nothing, (b) lossless multi-layer cloak.

We first investigate the case of a bare scatterer illuminated by a plane wave, which is launched by a sheet of uniform current density on the left edge of the domain. The top and bottom boundaries are perfect magnetic conductors so that the plane wave with its electric field pointed in z direction can terminate without reflection on these edges. The right edge of the domain is set to be non-scattering, which simulates the infinite domain. The electric field around the bare scatterer is shown in Fig. 2(a). It is seen that the plane wave is strongly disturbed by the scatterer, which results in much backward reflection and heavily-perturbed shadow. Fig. 2(b) shows the cloaking effect, where the bare scatterer is perfectly concealed by the designed multi-layer cloak. It is noteworthy that the plane wave can penetrate into the cloaked region without changing the shape of wavefront. In addition, the wave field in the cloaked scatterer is of no phase distortion, due to the fact that the total phase shift is exactly zero when the EM wave passes across the cloak.

ACKNOWLEDGMENT

The work is supported by National Basic Research Program 973 from Ministry of Science and Technology of China (Grant No. 2011CB707900), the National Science Foundation of China under Grant Nos. 10804050, 10874086, 10834009 and 10904068.

REFERENCES

1. Pendry, J. B., D. Schurig, and D. R. Smith, *Science*, Vol. 312, 1780, 2006.
2. Schurig, D., J. J. Mock, B. J. Justice, S. A. Cummer, J. B. Pendry, A. F. Starr, and D. R. Smith, *Science*, Vol. 314, 977, 2006.
3. Popa, B. I. and S. A. Cummer, *Phys. Rev. A*, Vol. 79, 023806, 2009.
4. Cai, W., U. K. Chettiar, A. V. Kildishev, and V. M. Shalaev, *Nat. Photonic*, Vol. 1, 224, 2007.
5. Yu, G. X., W. X. Jiang, and T. J. Cui, *Appl. Phys. Lett.*, Vol. 94, 041904, 2009.
6. Zhang, J. J., Y. Luo, and N. A. Mortensen, *Appl. Phys. Lett.*, Vol. 96, 113511, 2010.
7. Andkjær, J. and O. Sigmund, *Appl. Phys. Lett.*, Vol. 98, 021112, 2011.
8. Alù, A. and N. Engheta, *Phys. Rev. Lett.*, Vol. 102, 233901, 2009.
9. Lai, Y., H. Y. Chen, Z. Q. Zhang, and C. T. Chan, *Phys. Rev. Lett.*, Vol. 102, 093901, 2009.
10. Zhu, X. F., B. Liang, W. W. Kan, X. Y. Zou, and J. C. Cheng, *Phys. Rev. Lett.*, Vol. 106, 014301, 2011.

Results of the SMOS Data Validation over a Steppe and Forest Area in Siberia

P. P. Bobrov[1], **O. V. Kondratieva**[1], **V. L. Mironov**[2,4], **E. Shvetsov**[3], **A. I. Sukhinin**[3,4], **and A. S. Yashchenko**[1]

[1]Omsk State Pedagogical University, Omsk, Russia
[2]Kirensky Institute of Physics, SB RAS, Krasnoyarsk, Russia
[3]Sukachev Institute of Forest, SB RAS, Krasnoyarsk, Russia
[4]Reshetnev Aerospace State University, Krasnoyarsk, Russia

Abstract— The results of in situ measurements of radiobrightness temperature at the frequency 1.4 GHz and soil moisture in the surface layer of the test area located in Western Siberia near Omsk are given. It is shown that at low soil moisture these data are in satisfactory agreement with the SMOS data of the levels 1c and 2. In addition, correlation analysis between the topsoil moisture provided with the SMOS, on the one hand, and the forest fire danger index derived on the basis of rainfalls and temperatures recorded by the net of weather stations located in the area of the city of Krasnoyarsk Eastern Siberia was carried out. This effort was made to investigate if the SMOS data can be used to estimate forest fire danger over the areas where no weather stations are availabe. The correlation analysis showed good relationships between SMOS soil moisture data and fire danger indices.

1. INTRODUCTION

Analysis of incoming SMOS data shows that in some cases, the brightness value exceeds the possible value for the dry soil, sometimes there is a mismatch of the brightness temperature and retrieval soil moisture values. This causes the necessary of the SMOS data validation on levels 1c and 2 by comparison with in situ measurements. Such field measurements we have performed in 2010. The test site was located in the southern part of the Omsk Region West Siberia at the interface of the steppe and forest landscape zones. In addition, we studied the possibility of using the SMOS data of soil moisture for fire danger index estimation.

We carried out validation for the Levels 1c and 2 SMOS data over two areas in Western and Eastern Siberia through the Summer and Autumn 2010 periods. The first test sites was located in the southern part of the Omsk Region West Siberia at the interface of the steppe and forest landscape zones. While the second one was situated 50 km far from the city of Krasnoyarsk in the area of boreal forests. There were conducted in field radiobrightness measurement for the first test site, and analysis of forest fire index along with the moisture data provided by the SMOS was developed.

2. VALIDATION OF THE RADIOBRIGHTNESS AND SOIL MOISTURE SMOS DATA OVER THE FIRST SITE

Figure 1 shows a general view of the experimental installation. The radiobrightness was measured at the look angle of 30° relative to nadir. The bandwidth of the 1.4 GHz radiometer was equal to 60 MHz, with its fluctuation sensitivity being of 0.3 K. The width of antenna pattern at the 3 dB level was about 22°. The metal sheet reflecting the sky radiation and the smooth water surface were used as standards to calibrate the radiometer. The radiobrightness of metal sheets were assigned to be of 3 K. The radiobrightness of the smooth water surface was estimated according to the Fresnel reflection coefficient and Debye model for the water permittivity. An absolute error of calibration was estimated to be of 3–5 K. The measurements of radiobrightness, T_b, were carried out with 60 to 120 minutes intervals. There were measured both bare and grass covered plots.

Analysis of the SMOS data relating to the footprint, with the ground based radiometer being included, and the on the ground attained radiobrightnesses measured in the Summer 2010 showed for these data sets to be in good agreement, with deviation from each other not exceeding 6 to 8 K (See Fig. 2). This suggests the SMOS footprint observed to consist of either bare or low and dry vegetation areas. Some difference between the SMOS and field measurements could be caused by either the heterogeneity of soil moisture over the SMOS footprint or the the footprint size variations. During the ground-based measurement in the case of grass covered plot, we registered

Figure 1: Radiometric installation and test sites view. 1 — 1.4 GHz radiometer; 2 — 6.9 GHz radiometer; 3 — bare soil, 4 — soil covered with grass; 5 — water basin.

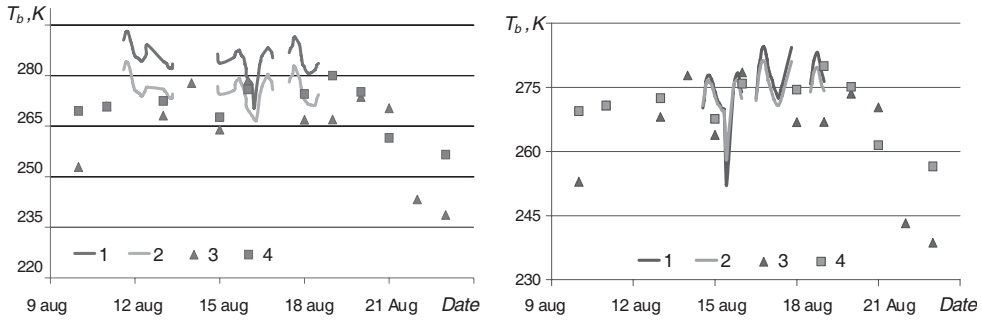

Figure 2: The time series of radiobrightness for the (a) plot covered with grass (b) and bare soil plot, 1 — ground-based measurements, horizontal polarization; 2 — ground-base measurements, vertical polarization; 3 — SMOS data, horizontal polarization; 4 — SMOS data, vertical polarization.

a noticeable excess of the H-polarization radiobrightness over that related to the V-polarization radiobrightness, which may be attributed to the anisotropic permittivity of the grass layer. Such a phenomenon was sometimes registered regarding the SMOS radiobrightnesses observed. Using the radiobrighnesses measured in the field, we retrieved the time series of topsoil moisture in the course of 2010 summer/autumn period. The moistures measured with the thermostatic-weighted method for the field plot and those retrieved from the SMOS radiobrightnesses were found to be of 3–8% and 2–4%, respectively.

In autumn 2010, we carried out field measurements of the radiobrightness in the case of frozen topsoil. Once the soil moisture was too low during this measurement, in contrast to the results disscussed in [1, 2], the daily fluctuations of the radiobrightness, was seen to be only in the limits of 9 K, We entirely attributed these variations to the respective fluctuations of the thermodynamic temperature, being observed in the limits of 18 K.

3. CORRELATIONS BETWEEN THE FIRE DANGER INDICES AND THE SMOS LEVEL 2 SOIL MOISTURE

Soil moisture measurements made by SMOS satellite were compared with weather forest fire danger indices, calculated on the basis of meteorological parameters measured by the ground weather station. Such indices characterize the moisture of forest litter. Russian PV-1 fire danger index, reflecting the balance of the factors of forest fuels moistening and drying and Canadian Fire Weather Index (FWI) [3] were used for comparison. Additionally, correlations were estimated not only for FWI index itself, but also for its components, such as Duff Moisture Code (DMC), which characterizes the moisture of medium litter layers and Drought Code (DC) describing the moisture of lower humus layers (Forestry Canada, 1992). Such fire danger indices are widely used in forecasting wildfire occurrence probability and possible fire danger.

The comparison was made using time series of measurements made during summer fire season

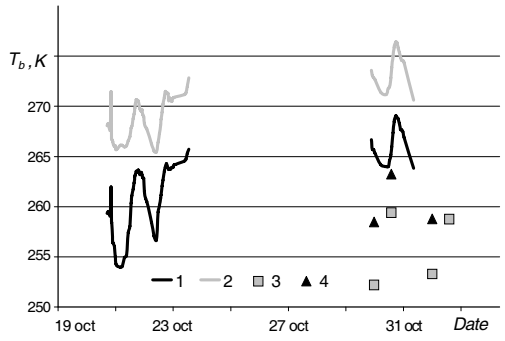

Figure 3: The time series of radiobrightness related to the bare soil plot at the lower temperatures. 1 — ground-based measurement, horizontal polarization; 2 — ground-based measurement, vertical polarization; 3 — SMOS data, horizontal polarization; 4 — SMOS data, vertical polarization.

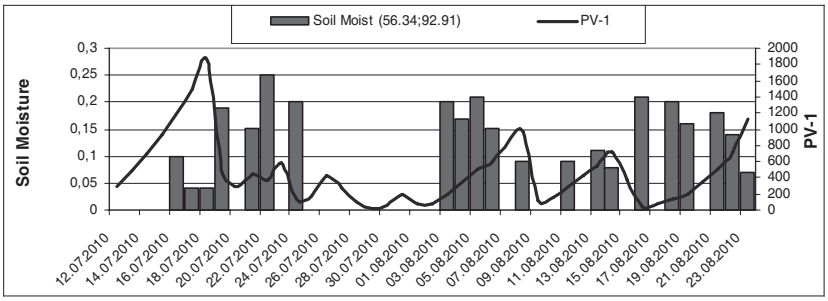

(a)

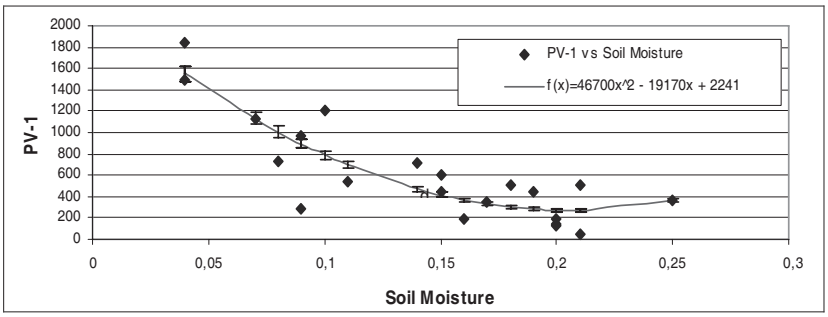

(b)

Figure 4: (a) Dynamics of PV-1 fire danger index change during fire season from 12 July 2010 to 23 August 2010. Corresponding soil moisture measurements are also shown. (b) Dependencies between PV-1 and FWI indices and soil moisture measurements. Plots are made for the SMOS pixel located at 56.34°N, 92.91°E.

from 12 July 2010 to 23 August 2010. The study area was located near Pogorelka village, approximately 30 km to the north from Krasnoyarsk city. SMOS measurements were retrieved for three pixels nearest to the test plot. The coordinates of the center points of these pixels were: 56.34°N, 92.91°E; 56.37°N, 93.16°E; 56.24°N, 93.06°E.

Correlation analysis performed showed the existence of relationship between SMOS measurements and fire danger indices, calculated based on ground measurements of meteorological parameters. It should be noted that the best relationships existed for PV-1 and FWI indices. For all points considered the correlation coefficients for these parameters and SMOS data were the largest. Generally, correlation coefficients between all fire danger indices considered and SMOS data were in range $-0.5 \sim -0.8$. The negative correlation coefficients indicate inverse dependence between soil moisture and fire danger indices. The only exception was DC (Drought Code) index, for which lower correlation coefficients were registered ($-0.3 \sim -0.55$).

Figure 4(a) shows the dynamics of PV-1 index change for the Krasnoyarsk weather station, the nearest to the test point, and soil moisture measurements made by SMOS satellite from 12 July to 23 August. As it can be seen from plot 5a, high soil moisture values were registered for low

Table 1: Correlation coefficients between soil moisture measurements and fire danger indices.

Point	PV-1	FWI	DC	DMC
(56.24; 93.06)	−0059	−0061	−0031	−0051
(56.34; 92.91)	−0080	−0079	−0040	−0061
(56.37; 93.16)	−0065	−0062	−0056	−0064

values of PV-1 fire danger index. Fig. 4(b) shows the dependency plot between PV-1 index and soil moisture according SMOS data and quadratic fitting curve. Given plots correspond to SMOS pixel nearest to the Pogorelka, i.e., with center located at 56.34°N, 92.91°E.

PV-1 points were approximated by quadratic polynomial equation, with correlation coefficient of 0.87. Relationships between soil moisture measurements and fire danger indices differ for various regions and can be determined using weather station data or field studies. Such relationships can have significant practical value in the regions where no weather stations exist.

Table 1 shows the correlation coefficients between soil moisture measurements and fire danger indices calculated by Krasnoyarsk ground weather station. All indices except DC show rather good relationship with soil moisture measurements.

At the moment the comparison results are available only for three SMOS pixels near Pogorelka village. However, if good correlation values will be found for the other areas in different regions, SMOS soil moisture values can provide valuable information on weather fire danger in the areas where no weather stations information available.

4. CONCLUSION

Comparison of the measured radiobrightness temperature and soil moisture from SMOS data showed that the results of summer measurements at low soil moisture to be in good agreement with the SMOS data. Significantly large differences in brightness temperatures (above 10 K) were observed at air temperatures below zero.

Correlation analysis showed the existence of relationship between SMOS measurements and fire danger indices. It should be noted that the best relationships existed for PV-1 and FWI indices.

REFERENCES

1. Bobrov, P. P., V. L. Mironov, and A. S. Yashchenko, "Diurnal dynamics of soil brightness temperatures observed at frequencies of 1.4 and 6.9 GHz in the processes of freezing and thawing," *Journal of Communications Technology and Electronics*, Vol. 55, No. 4, 395–403, 2010.
2. Mironov, V. L., P. P. Bobrov, P. V. Zhirov, S. V. Krivaltsevitsh, A. S. Jaschenko, and R. D. De Roo, "Radiobrightness dynamics of freezing/thawing processes for different soils," *IEEE Geoscience and Remote Sensing Symposium and the 28th Canadian Symposium on Remote Sensing*, Vol. 6, 3015–3018, Denver, Colorado, USA, 2006.
3. Forestry Canada Fire Danger Group, "Development and structure of the canadian forest fire behavior prediction system," *Science and Sustainable Development Directorate*, Inf. Rep. ST-X-3, Ottawa, 1992.

Infrared Imaging Detection of Hidden Danger in Mine Engineering

Shanjun Liu[1], **Zhongyin Xu**[1], **Lixin Wu**[1, 2], **Baodong Ma**[1], **and Xin Liu**[1]

[1]Institute for Geo-informatics & Digital Mine Research
Northeastern University, Shenyang 110819, China
[2]Academe of Disaster Reduction and Emergency Management
Beijing Normal University, Beijing 100875, China

Abstract— Thermal infrared (TIR) imaging has been successfully applied in the indoor and outdoor thermographic inspection of the defects of solid materials and building structures in the engineering scale. In this paper, TIR imaging detection experiments were conducted in some mines of China to detect the mine hidden danger, including self ignition of coal gangue, high-stress area of underground mine, water-seeping in underground mine, landslide of opencast mine. The experimental result indicates TIR imaging technology can detect the mine safe problems, which is very helpful for preventing the happening of mine disasters.

1. INTRODUCTION

A thermal imager can generate radiometric images, also called thermography in the infrared (IR) band, that can be transformed — under specific conditions — into thermal maps. It provides data for the comparative analysis of thermal differences between detected objects and their environment. Thermal infrared (TIR) imaging is an all-weather, full-area, noncontact, and nondestructive technology. Hence, it has been successfully applied in the indoor and outdoor thermographic inspection of the defects of solid materials and building structures in the engineering scale [1–4]. The mine disasters caused by rock stress and catastrophe, such as rock burst, roof caving, water inrush and slope landslide etc., are the main disasters in mine. The effective detection and identifying of precursor of these disasters are an important basis to predict and prevent the disasters happening.

The past experimental research [5–9] showed that the infrared radiation of loaded rock appeared staged variation in the process of loading and fracturing. There were abnormal precursors appearing before rock fracture. When the rock was close the failure thermal images appeared radiation anomaly strip along the position of future fracture. The shear fracture appeared temperature-increase anomaly, and tension fracture appeared temperature-decrease anomaly. The experimental result indicates that it is possible that the stress and the fracturing process of rock can be detected by infrared imaging technology.

In this paper, TIR imaging detection experiments were conducted in some mines of China to detect the mine safety problems, and a infrared imaging system was applied to detect the temperature field of objects.

2. INFRARED IMAGING DETECTION OF HIDDEN DANGERS IN MINE

2.1. Infrared Imaging Detection of Self Ignition of Coal Gangue

Coal gangue is a kind of waste rock in coal mine. There are thousands of coal waste dumps in China, and thirty percent of which is burning. The burning of coal gangue can produce a mass of harmful gas and explosion, and when coal gangue dump slides and collapses will probably cause casualties. Therefore, the detection of burning state of coal gangue is important for preventing the happening of coal gangue disaster.

We carried out the infrared imaging detection in a coal mine of China to find out the temperature field distribution of the coal gangue dump. Fig. 1 is the thermal images of a coal gangue dump. From the figure you can see that the temperature in the top of gangue is higher, and some coal is burning and smoking. The highest temperature of the dump is up to 106°C. The temperature becomes lower gradually with the decrease of height. In the bottom the temperature of the dump is only 36.2°C.

Figure 2 is the detection result of a part in dump. The highest temperature is up to 93°C. The photo shows the color of high-temperature area is black due to the burning of coal gangue.

The result of the detection indicates that infrared imaging technology is effective for detecting the self ignition of coal gangue.

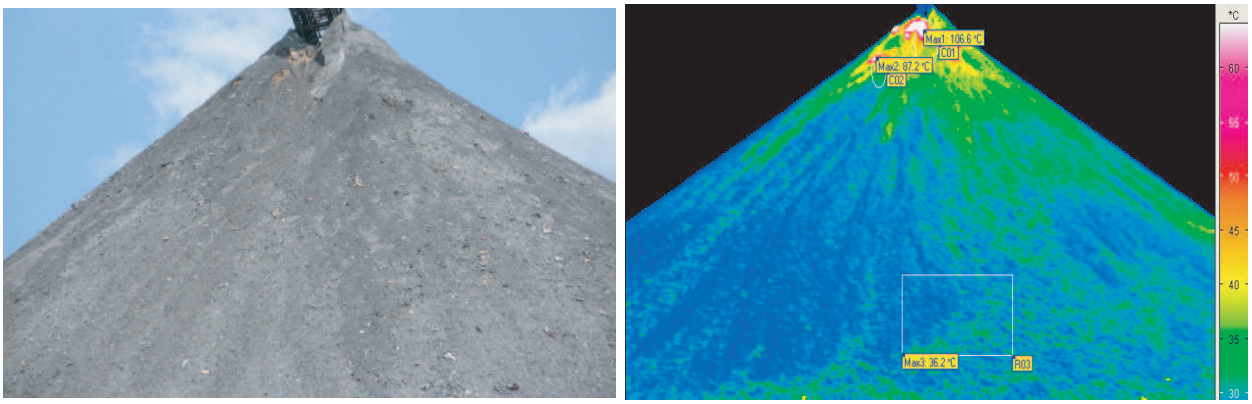

(a) (b)

Figure 1: (b) Thermal image and (a) photo of a coal gangue dump.

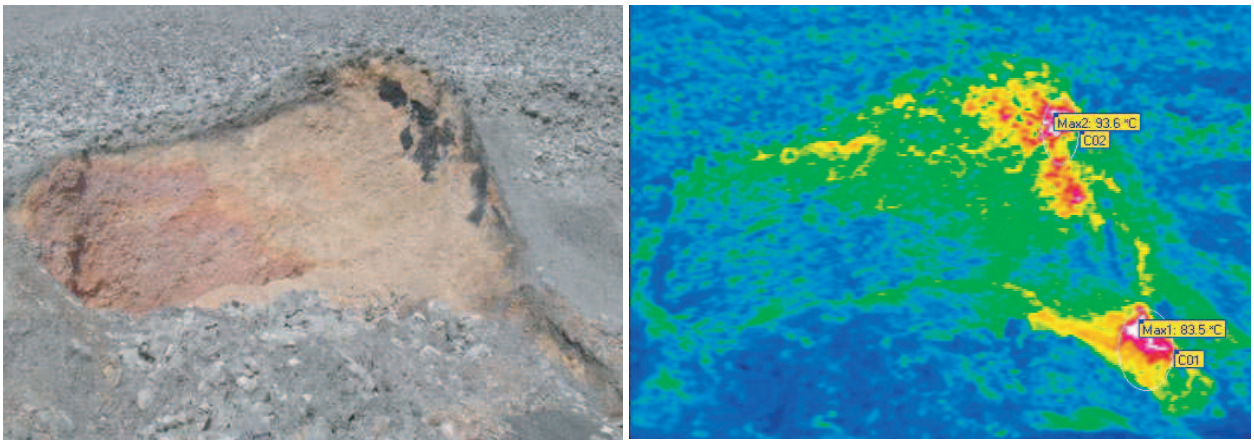

Figure 2: Infrared imaging detection result of a part in coal gangue dump.

2.2. Infrared Imaging Detection of High-stress Area in Underground Mine

The past experiments [7–10] showed that when rock was loaded the infrared radiation temperature of rock surface would vary. In the high-stress area the radiation temperature was higher. When the rock was close the failure the temperature anomaly strip appeared along the future fractures, and the high-temperature anomaly strip was along the shear fracture and the low-temperature anomaly strip was along the tension fracture. Fig. 3 is the infrared imaging detection result of different rock samples in the loading process. It shows that in the high-stress area (see the circle area of Fig. 3). the radiation temperature is higher, and high-temperature anomaly strip (see the ellipse area of Fig. 3) distributes along the shear fracture.

Figure 4 is the infrared imaging detection result of a rock tunnel in an underground mine of China. In can be founded that a rock pillar supports above rock mass, the stress in their connecting area is higher than surrounding area. Meanwhile the thermal image shows the infrared radiation temperature in the connecting area is also higher than surrounding rock (see the circle area of Fig. 4). This indicates that the temperature of high-stress area is higher than that of the low-stress area. It is also inferred the high-temperature area is the dangerous area to happen rock burst disaster.

Besides, the collapse of loose rock block in the mine tunnel often causes worker injured, so we also carried out an infrared detection of loose rock block in an underground mine. Fig. 5 is the thermal image of a mine tunnel wall. The figure shows a loose rock block (see the enclosing area of Fig. 5) in the tunnel wall. The temperature of the loose rock block is lower than the surrounding rock, and the border of loose rock is clearer in the thermal image than in the visible photo. This indicates that thermal imager can detect the loose rock block of mine tunnel, so it is beneficial to prevent the roof collapse.

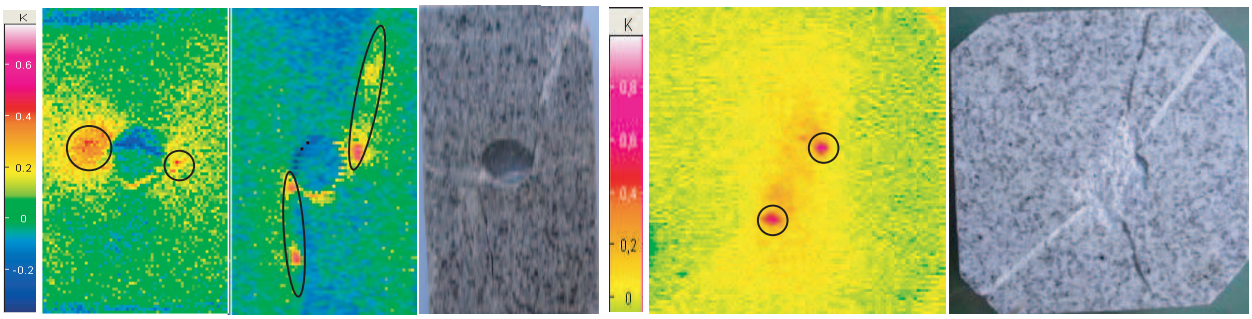

(a) Rock sample with circular hole (b) Rock sample with unconnected faults

Figure 3: Thermal images and photos of different rock samples in the loading process.

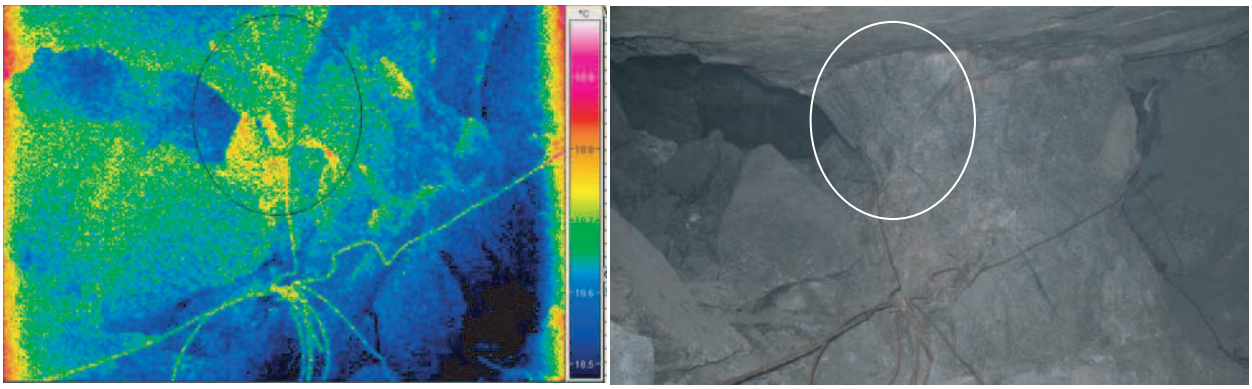

(a) (b)

Figure 4: (a) Thermal image of rock pillar and (b) its photo.

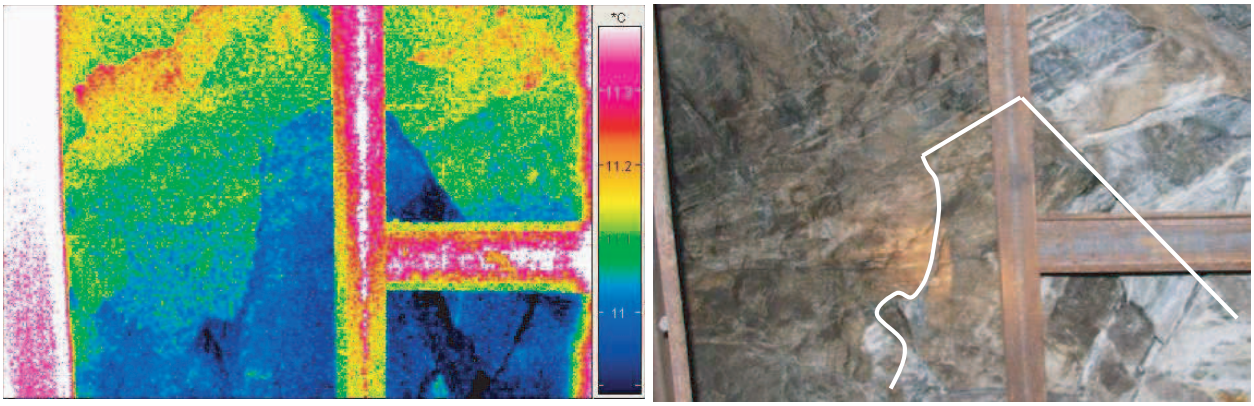

(a) (b)

Figure 5: (a) Thermal image of a rock panel and (b) its photo.

2.3. Infrared Imaging Detection of Water-seeping Area in Underground Mine

Underground water is a kind of dangerous resource to the mine extraction. Many mine disasters are related to underground water, so the detection of underground water is important to the underground mine. Past research [11] showed that the temperature decreased when the water seeped from the inner of concrete (see Fig. 6). Fig. 7 is an infrared imaging detection result of a mine tunnel in China. The figure shows there are two seeping spot in the floor of the tunnel (see the circle area of Fig. 7), and the temperature of the seeping water area is lower than the surrounding rock area. The shorter the distance to the seeping position, the lower the temperature is. Meanwhile, the temperature of water-seeping tunnel is several degrees lower than the normal dry tunnel.

Above result indicates the infrared imaging technology is an effective method to detect the water-seeping area in underground mine. It is beneficial to prevent the happening of water inrush.

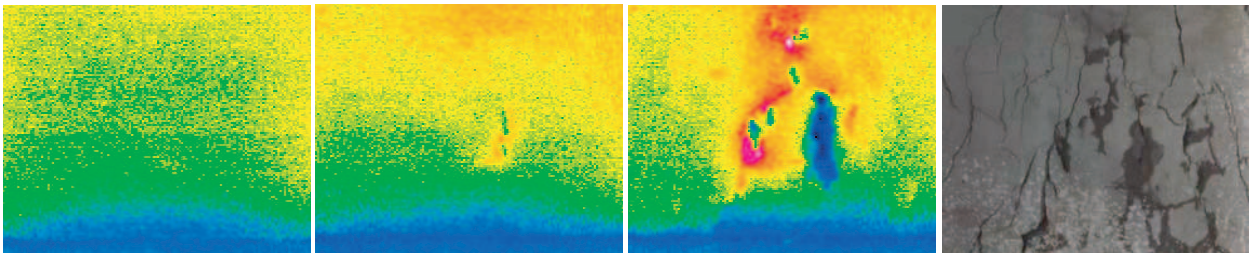

Figure 6: Thermal image variation of concrete in the fracturing and seeping process.

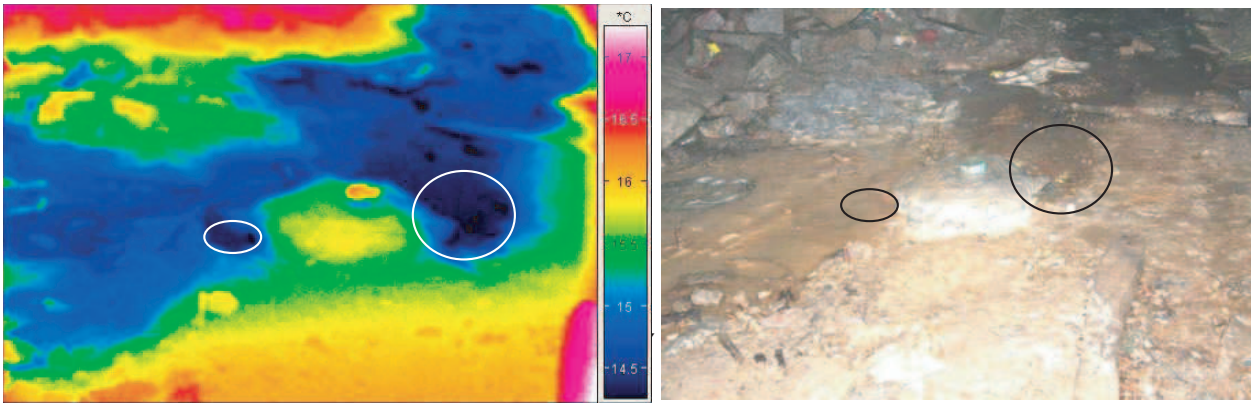

(a) (b)

Figure 7: (a) Thermal image of seeping laneway and (b) its photo (enclosing areas is the seeping spots).

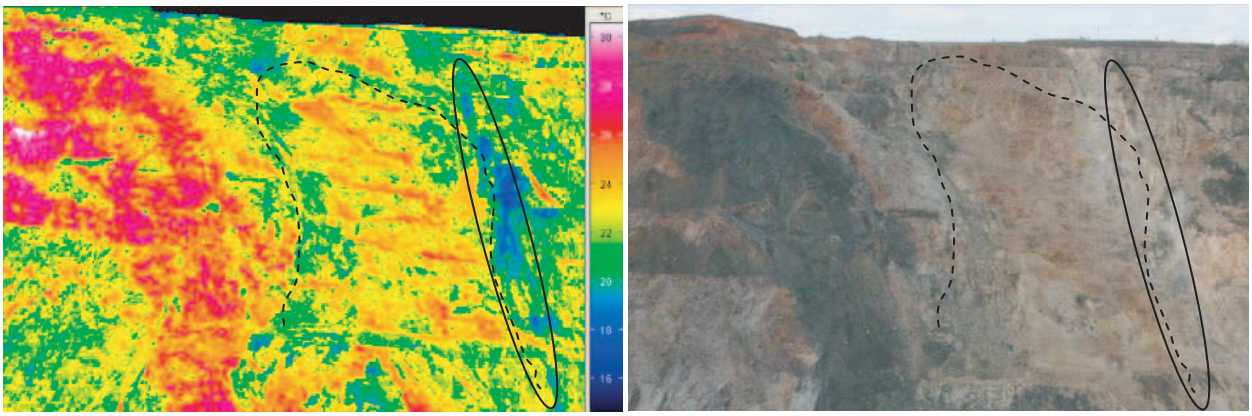

(a) (b)

Figure 8: (a) Thermal image of slope in open-pit mine and (b) its photo.

2.4. Infrared Imaging Detection of Landslide in Opencast Mine

Landslide is a high-danger geological disaster in opencast mine. It often causes casualties and mine equipments destroyed. How to find out the existence of landslide and its distribution is very important for taking precautions against the disaster. Usually the rock or the soil in landslide area is looser and more fractured than the normal rock or soil, especially some faults or fractures often distribute along the edge of the landslide, and some water is contained in the faults. Therefore the temperatures in the landslide and its edge are different from the surrounding rock.

Figure 8 is the result of infrared imaging detection of a slope in an opencast mine. It can be founded the temperature along the broken line is lower than the inner and external area. Especially, the temperature of right edge (see the ellipse area) of the area is much lower. It is known through the scene survey that the area with lower temperature in the left and right edges distributes

respectively a compressive zone and a fault (see the photo in Fig. 7). The temperature in the middle area between the compressive zone and the fault is higher than the two strips. The reason to cause the temperature lower is analyzed. It is thought that loosing and fracturing of rock in the two strips causes more water is contained in the area. So the temperature in the fault and the compressive zone are lower.

The detection result indicates a landslide existing probably in the ellipse area due to the feature that two fractured zone surround a middle area. The guess has confirmed by the worker of the mine, and some rock has been scraped from the landslide area to lower the danger.

3. CONCLUSION

In this paper some TIR imaging detection experiments were conducted in some mines of China to detect the hidden danger. The experimental results showed that:

(1) In the high stress area of rock the infrared radiation temperature is higher. Hence, TIR imaging technology can detect the high-stress area of rock, which is very important for preventing the happening of rock burst.
(2) In the area of loose rock block the infrared radiation temperature is lower. Hence, TIR imaging technology can detect the loose rock block in the roof of laneway, which is very important for preventing the happening of collapse of roof rock occurring at underground mines.
(3) When water seeps from fracturing rock the infrared radiation temperature will became low. The experimental result indicates TIR imaging technology can detect the water-seeping spot, which is very important for preventing the happening of the water inrush.
(4) In the landslide area of opencast mine the pattern of infrared radiation temperature field is different from that of the surrounding rock area. The experimental result indicates TIR imaging technology can detect the landslide of mine, which is very helpful for preventing the happening of landslide disaster.

ACKNOWLEDGMENT

This work is supported by the National Natural Science Foundations of China (No. 50774017; 41074127)

REFERENCES

1. Wong, B. S., C. G. Tui, and W. Bai, "Thermographic evaluation of diseases in composite materials," *Insight*, Vol. 41, No. 8, 504–509, Aug. 1999.
2. McCann, D. M. and M. C. Forde, "Review of NDT methods in the assessment of concrete and masonry structures," *NDT, E Int.*, Vol. 34, No. 2, 71–84, Mar. 2001.
3. Cramer, K. E., W. P. Winfree, and P. A. Howell, "Thermographic imaging of cracks in thin metal sheets," *Proc. SPIE Thermosense XIV*, Vol. 1682, 162–170, 1992.
4. Avdelidis, N. P. and A. Moropoulou, "Applications of infrared thermography for the investigation of historic structures," *J. Cultural Heritage*, Vol. 5, No. 1, 119–127, Jan.–Mar. 2004.
5. Geng, N. G., C. G. Cui, and M. D. Deng, "Remote sensing detection of rock fracturing experiment and the beginning of remote rock mechanics," *Acta Seismologica Sinica*, Vol. 14, 645–652, 1992.
6. Deng, M. D., C. X. Cui, and N. G. Geng, "Application of principle of remote sensing to earthquake prediction and the experimental results," *Earthquake Research in China*, Vol. 9, No. 2, 163–169, 1993.
7. Wu, L., C. Cui, N. Geng, et al., "Remote sensing rock mechanics (RSRM) and associated experimental studies," *Int. J. Rock Mech. & Mining Sci.*, Vol. 37, No. 6, 879–888, 2000.
8. Wu, L., S. Liu, Y. Wu, et al., "Precursors for rock fracturing and failure — Part I: IRR image abnormalities," *Int. J. Rock Mech. & Mining Sci.*, Vol. 43, No. 3, 473–482, 2006.
9. Wu, L., S. Liu, Y. Wu, et al., "Precursors for rock fracturing and failure — Part II: IRR T-Curve abnormalities," *Int. J. Rock Mech. & Mining Sci.*, Vol. 43, No. 3, 483–493, 2006.
10. Wu, L., S. Liu, Y. Zhang, et al., "Evolutive features of thermal radiation of tortuously non-connected fault in the loading and instability process," *Chinese Journal of Rock Mechanics and Engineering*, Vol. 28, No. 2, 3342–3348, 2009.
11. Liu, S., Y. Zhang, L. Wu, et al., "Infrared radiation feature of concrete during fracturing and water seepage process," *Chinese Journal of Rock Mechanics and Engineering*, Vol. 28, No. 1, 53–58, 2009.

Magnetic Anomaly Detection in Ferromagnetic Material

J. Atzlesberger and B. G. Zagar
Institute for Measurement Technology, Johannes Kepler University, Austria

Abstract— This paper discusses a non-destructive testing (NDT) technique based on the magnetic flux leakage (MFL) method, which is able to detect magnetic anomalies in ferromagnetic material. The goal is the detection of very small inhomogeneities not only on the surface but also anywhere in the cross section of magneto-conductive objects by scanning their surfaces using low-cost GMR (giant magneto resistance) sensors at rather high scanning speeds (up to 1 m/s) in order to enable an automatic inspection and to minimize test time. The measured magnetic flux density variations due to the expected inhomogeneities are down to only some nT (depending on the inhomogeneity size and position) on a pedestal of some mT, therefore the system must realize a very high resolution and all parameters affecting the system's sensitivity (geometrical arrangement, sensors and electronics, signal acquisition, signal processing, etc.) have to be optimized in order to get a robust and highly sensitive measuring system. As a pilot survey, some test specimen were prepared (by inserting artificial inhomogeneities into otherwise homogeneous, isotropic magneto conductive objects) and inspected with a prototype measuring system.

1. INTRODUCTION

Since many years non-destructive testing (NDT) methods are of a great concern in measurement and testing technology. The oldest NDT method for inspecting ferromagnetic material was already applied in 1870. For the detection of flaws in railway tracks and in gun barrels a compass needle as indicator was used [1]. Moving the compass across blemished material, a deflection of the compass needle can be seen. In 1922 William E. Hooke discovered, that swarf on a magnetic fixed steel sheet form a pattern that was according to the pattern built by visible surface cracks on the steel sheet [1]. This was the hour of birth of the magnetic particle inspection (MPI) [2]. Since then different magnetic NDT methods were developed for the detection of anomalies in ferromagnetic material. These anomalies can be caused for example by thickness variation of the inspected test specimen [3], corrosion [4], residual stresses [5], cracks [6], flaws, non-metallic inclusions, material blemishes and/or surface-defects [7].

2. MEASURING PRINCIPLE

One possible magnetic anomaly detection principle is the magnetic flux leakage (MFL) method [8] as shown in Fig. 1. An electro magnet magnetizes the ferromagnetic specimen. Any inhomogeneity inside the specimen produces a variation of the magnetic flux density on and near the surface of the specimen and this variation can be detected by scanning the specimen's surface using appropriate magnetic field sensors. In the past flux gate sensors, hall-sensors or AMR sensors (anisotropic magneto resistance) were used. In 1988 the giant magneto resistive effect (GMR) [9] was discovered in Fe/Cr/Fe trilayers [10, 11] and this effect is much more sensitive than the AMR effect. Furthermore GMR sensors can be built much smaller than flux gates and therefore allow a better spatial resolution thus GMR sensors were used for the measurement set-ups described in this paper. The advantages of MFL is that there is no couple medium needed (vs. ultrasonic testing), that there incurs no radiation burden (vs. X-ray inspection) and due to the small sensor sizes array processing is easily possible.

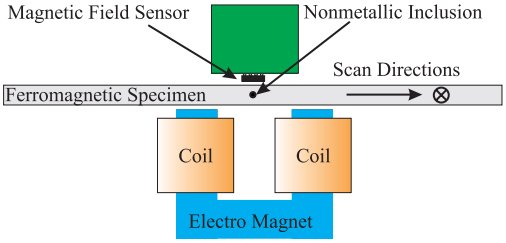

Figure 1: Schematic test set-up of the magnetic flux leakage method using an electro magnet for the magnetic excitation and a GMR sensor which measures the magnetic flux density near the surface of the ferromagnetic specimen.

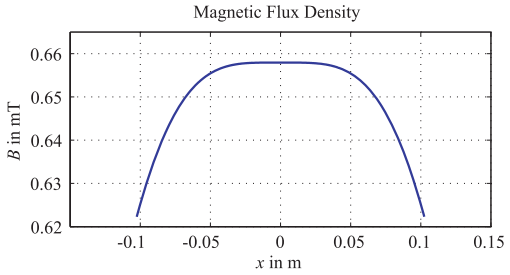

(a) The calculated magnetic flux density of a Helmholtz coil pair (Eq. (1)) at an excitation current of $I = 3$ A, $N = 50$ turns and $R = a = 205$ mm.

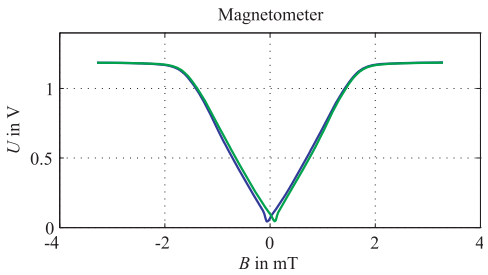

(b) Measured magnetometer characteristic at a supply voltage of $U = \pm 10$ V.

Figure 2: Distribution of the magnetic flux density between two coaxial air coils of a Helmholtz arrangement and the characteristic of the used magnetometer.

3. SENSOR TYPES

Different types of GMRs (magnetometer, gradiometer, spin valve sensors, etc.) were considered whereat this paper deals with a magnetometer and a gradiometer.

3.1. Magnetometer

The used GMR magnetometer is a magnetic field sensor which measures the absolute value of the magnetic field strength and accordingly the magnetic flux density[1]. In order to obtain the magnetometer's characteristic (see Fig. 2(b)) the sensor was positioned in the center of a Helmholtz coil arrangement (which consists of two coaxial air coils on the x-axis with equal magnetic flux orientation through the two coils) and the excitation current through the two coils was varied. If the origin of the coordinate system is placed symmetrically between the two air coils, the magnetic flux density on the x-axis can be calculated using Biot-Savart's law [12] and superpositioning the magnetic flux densities produced by the two air coils

$$\vec{B}(x) = \frac{\mu_0 INR^2}{2\left(R^2 + \left(\frac{a}{2} + x\right)^2\right)^{\frac{3}{2}}} \cdot \vec{e_x} + \frac{\mu_0 INR^2}{2\left(R^2 + \left(\frac{a}{2} - x\right)^2\right)^{\frac{3}{2}}} \cdot \vec{e_x}. \tag{1}$$

With I, excitation current through the two coils, N number of turns per coil, R the radius of and a the distance between the two coils. For $a = R$, the first and the second derivative of the magnetic flux density (on the x-axis) with respect to location are equal to zero in the origin therefore positioning the sensor (actually in the center of the Helmholtz coil pair) doesn't need to be very precise as it can be seen from the horizontal magnetic flux density distribution in the range close to the central point ($x = 0$) (see Fig. 2(a)).

Equation (1) evaluated in the center of the Helmholtz coil arrangement ($x = 0$) results in

$$\vec{B}_{tot} = \frac{\mu_0 \cdot 8 \cdot NI}{\sqrt{125}R} \cdot \vec{e_x}. \tag{2}$$

So the magnetic flux densities $\vec{B}(x)$ and $\vec{B}_{tot}$ only depend on the geometric parameter R (radius and the distance between the two coils), the number of windings N of the coils and are linearly related to the excitation current I.

3.2. Gradiometer

The gradiometer measures the gradient of the magnetic flux density, so the characteristic in Fig. 3(b) was obtained by positioning the sensor in the center of a Maxwell coil arrangement[2] and varying the excitation current through the two coils. Superpositioning the magnetic flux densities of both coils and calculating the magnetic flux density's first spatial derivative (gradient) with respect to location results in

$$\operatorname{grad}\left(\vec{B}\right) = \frac{3}{4} \cdot \frac{\mu_0 INR^2(2x - a)}{\left(R^2 + \left(\frac{a}{2} - x\right)^2\right)^{\frac{5}{2}}} \cdot \vec{e_x} - \frac{3}{4} \cdot \frac{\mu_0 INR^2(2x + a)}{\left(R^2 + \left(\frac{a}{2} + x\right)^2\right)^{\frac{5}{2}}} \cdot \vec{e_x}. \tag{3}$$

[1] In air the magnetic flux density $\vec{B}$ is linear to the magnetic field strength $\vec{H}$ and can be calculated as $\vec{B} = \mu \cdot \vec{H}$ with the magnetic permeability $\mu = \mu_0 = 4\pi \cdot 10^{-7} \frac{Vs}{Am}$, but in general μ is a tensor.

[2] A Maxwell coil arrangement consists of two coaxial coils with different magnetic flux orientations through the two coils.

The gradient of the magnetic field is linearly related to the excitation current I and depends on the coil radius R, the coil separation a and the number of windings N. For $a = \sqrt{3}R$, the first and the second derivative of the magnetic flux density gradient on the x-axis with respect to location are equal to zero in the center between the two coils as shown in Fig. 3(a).

4. LOCK-IN-AMPLIFIER

For measuring very small flux density variations and increasing the SNR (signal-to-noise ratio) a lock-in-amplifier was used. The schematic diagram of an analog lock-in-amplifier is shown in Fig. 4. For a sinusoidal reference signal with frequency f_{ref} and a sensor signal $U_{in}(t)$ the output signal $U_{out}(t)$ for an analog lock-in-amplifier can be calculated as

$$U_{out}(t) = \frac{1}{T}\int_{t-T}^{t} \sin\left(2\pi f_{ref} s + \Delta\phi\right) U_{in}(s) ds. \tag{4}$$

The maximum of the output voltage is obtained, if the reference and the input signal are in-phase ($\Delta\phi = 0$) and can be adjusted by using the phase shift block in Fig. 4. A lock-in-amplifier can be considered as a band-pass filter with it's center frequency equal to the reference frequency and it's bandwidth inversely proportional to the integration time T. For a digital lock-in-amplifier Eq. (4) can be rewritten to

$$U_{out}(n) = \frac{1}{N}\sum_{n-N}^{n} \sin\left(2\pi \frac{f_{ref}}{f_s} n + n_\phi\right) U_{in}(n), \tag{5}$$

with sample frequency f_s. For finding out the smallest detectable flux density variation of the magnetometer, the excitation current I through the two coils of the Helmholtz arrangement was varied sinusoidal with a frequency of $f = 75\,\text{Hz}$ and the magnetic flux density was measured. The digitalized unbiased magnetometer signal (sample frequency = 10 kHz) was subsequently filtered using a software implemented lock-in-amplifier (Eq. (5) with $N = 10000$). A flux density variation of 1.25 nT could be measured even under the influence of interference as large as 100 nT.

5. PRELIMINARY MEASUREMENT RESULTS

5.1. Static Detection of Surface Parallel Blind Holes

A hot rolled steel sheet with a thickness of 3.3 mm containing drilled blind holes and a broken magnetizable spiral drill with a diameter of 500 µm was scanned using a GMR gradiometer type system (pointwise measurement). In Fig. 5 a one- and a two-dimensional gradiometer scan are

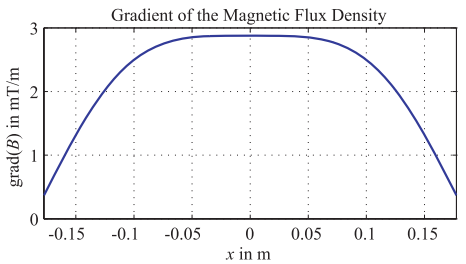

(a) The calculated magnetic flux density of a Maxwell coil pair (Eq. (3)) at an excitation current of $I = 3$ A, $N = 50$ turns and $R = a = 205$ mm.

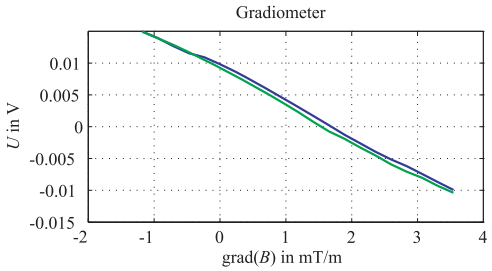

(b) Measured gradiometer characteristic at a supply voltage of $U = \pm 10$ V.

Figure 3: Distribution of the magnetic flux density between two coaxial air coils of a Maxwell arrangement and the characteristic of the used gradiometer.

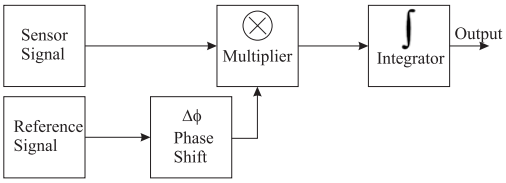

Figure 4: Schematic diagram of a lock-in-amplifier.

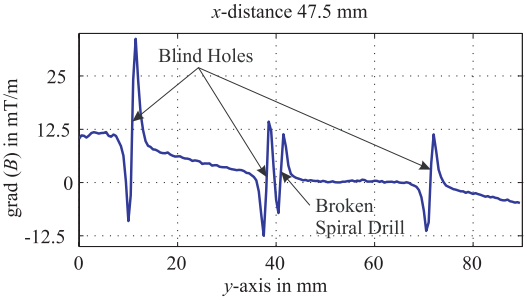

(a) Gradiometer signal of a line scan at an x-distance of 47.5 mm.

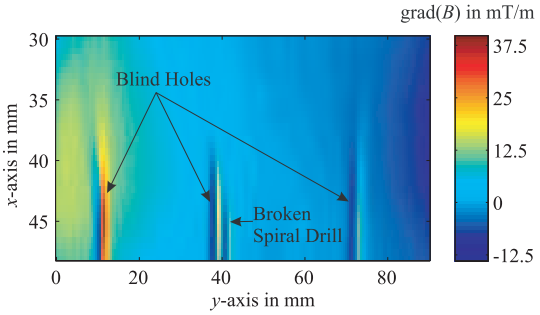

(b) Two-dimensional gradiometer scan of the hot rolled steel sheet containing artificial inclusions.

Figure 5: One- and two-dimensional gradiometer scan of a hot rolled steel sheet. The steep flanks in the gradiometer signal in (a) indicate the hole's and the spiral drill's positions.

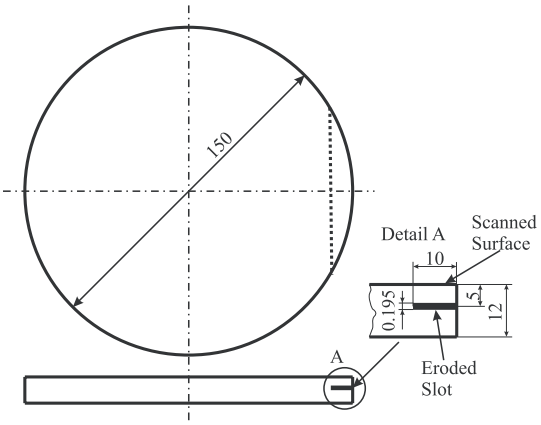

(a) Horizontal and sheer plan of the specimen.

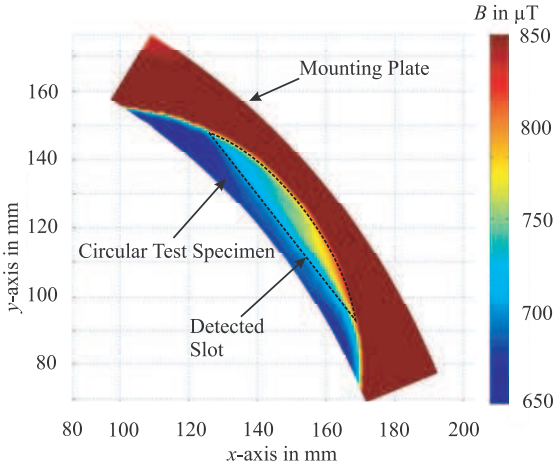

(b) Measurement result of the circular test specimen.

Figure 6: The horizontal and sheer plan of a specimen containing a surface parallel eroded slot and the measurement result obtained by scanning the specimen's surface with a GMR magnetometer.

shown. The holes and the air gap between the specimen and the spiral drill (which is partly filled with magnetizable swarf and therefore the effective air gap is even smaller) simulate elongated, nonmagnetic, subsurface inclusions.

5.2. Dynamic Detection of a Surface Parallel Slot

A circular steel sheet with a thickness of 12 mm containing a central eroded slot (width = 195 µm) was prepared. The horizontal, the sheer plan and the measurement result are shown in Fig. 6. The circular specimen was fixed in a mounting plate which was rotated by a variable speed motor and during the rotation an electro magnet magnetized the specimen and the magnetic flux density near the specimen's surface was measured with a magnetometer. The average circumferential speed was 1 m/s. The dashed line in Fig. 6(b) indicates the detected slot which simulates an elongated, nonmagnetic, subsurface defect.

6. CONCLUSION

An effective measurement system using GMR sensors for detecting magnetic anomalies was introduced. Magnetizable objects inside of ferromagnetic material and even inclusions with a very small cross section (as compared to the specimen's total cross section) oriented parallel to the magnetic flux lines could be detected. For increasing the signal-to-noise ratio and to investigate the magnetometer's sensitivity limit a software implemented lock-in-amplifier was used and a magnetic flux density variation of only 1.25 nT could be verified.

ACKNOWLEDGMENT

The authors gratefully acknowledge the partial financial support for the work presented in this paper by the Austrian Center of Competence in Mechatronics (ACCM).

REFERENCES

1. Gauss, G., et al., "Oberflächenrissprüfung nach dem Magnetpulver-Verfahren," *Zerstörungsgreie Werkstück- und Werkstoffprüfung*, 133–177, 2nd Edition, 1993.
2. Lovejoy, D., *Magnetic Particle Inspection — A Practical Guide*, Kluwer Academic Publisher, 1993.
3. Niese, F., "Wall thickness measurement sensor for pipeline inspection using EMAT technology in combination with pulsed eddy current and MFL," *ECNDT*, 2006.
4. Coughlin, C. R., et al., "Effects of stress on MFL responses from elongated corrosion pits in pipeline steel," *NDT & E International*, Vol. 33, 118–188, 2000.
5. Ricken, W., "GMR and eddy current sensor in use of stress measurement," *Sensors and Actuators*, 42–45, 2001.
6. Göktepe, M., "Non-destructive crack detection by capturing local flux leakage field," *Sensors and Actuators*, 70–72, 2001.
7. Atzlesberger, J. and B. G. Zagar, "Detection of inhomogeneities in magneto-conductive objects," *Proc. of the SSD'11*, Sousse, Tunisia, Mar. 2011.
8. Blitz, J., *Electrical and Magnetic Methods of Non-destructive Testing*, 2nd Edition, Chapman & Hall, London, 1997.
9. Hauser, H., et al., "Magnetoresistors," *Magnetic Sensors and Magnetometers*, 129–171, 2001.
10. Binasch, G., et al., "Enhanced magnetoresistance in layered magnetic structures with antiferromagnetic interlayer exchange," *Physical Review*, Vol. 39, 4828–4830, 1989.
11. Grünberg, P., et al., "Layered magnetic structures: Evidence for antiferromagnetic coupling of Fe layers across Cr interlayers," *Physical Review Letters*, Vol. 57, 2442–2445, 1986.
12. Strassacker, G. and P. Strassacker, *Analytische und Numerische Methoden der Feldberechnung*, Teubner, Germany, 1993.

A New Analytical Method for Calculation of Eddy Current Distribution and Its Application to a System of Conductor-slab and Rectangular Coil

T. Itaya[1], **K. Ishida**[2], **A. Tanaka**[3], **N. Takehira**[2], **and T. Miki**[4]

[1]Suzuka National College of Technology, Japan
[2]Tokuyama College of Technology, Japan
[3]Ube National College of Technology, Japan
[4]Yamaguchi University, Japan

Abstract— This study proposes an analytical method for the eddy current distribution analyses, and provides the eddy current distribution in conductor slab with rectangular coils arranged perpendicular to the slab. Our analytical method utilizes double Fourier transform to derive a set of equations for determining the eddy current distribution. The eddy current density is derived from the analytical solution called stream function. The spatial distribution of eddy current, which is dependent upon the frequency of coil current, the thickness and velocity of a conductor slab, is successfully obtained. Our analytical method is usable for calculations of varieties of eddy current problems, and we demonstrate the eddy current distributions in a conductor slab facing to a rectangular coil.

1. INTRODUCTION

The eddy current analysis is widely used in solving the problems on magnetic interaction between an electrically conductive material and an excitation coil that carries an AC current, e.g., the eddy current problems of magnetic resonance diagnosis in medical field, nondestructive testing (NDT) and magnetic sensing in industrial measurement field, induction heating in industrial power application field, etc. Numerical methods such as the finite element method (FEM) and/or boundary element method (BEM) are often employed, and recent increase of computer power have enabled three-dimensional eddy current analysis [1–3], Recently, eddy current distribution (ECD) imaging has also been developed by several research groups [4–6]. ECD imaging of a moving conductor facing to an excitation coil is useful for developing more precise and sophisticated magnetic sensing as well as other varieties of applications. Although the FEM is a potential tool for solving eddy current problems, it is hardly applied to the eddy current problems with moving conductors because of long computational time. Instead, the authors have proposed a new analytical method that enables to obtain the exact solution of magnetic field in a moving conductor facing to a rectangular excitation coil [7, 8]. Using this analytical method, we have developed optional NDT and magnetic sensing techniques, for instance, the thickness and velocity measurements of moving conductors. This article presents an analytical method of ECD in a moving conductor slab facing to a rectangular coil. The ECDs have been obtained using a set of analytical formulae derived by double Fourier transform of Maxwells equations. A shape function is introduced for analyzing ECD excited by an arbitrarily-shaped coil [9, 10], and numerical ECD calculations were carried out with a conventional personal computer. In this article, we demonstrate the ECDs dependent upon the excitation frequency of the coil as well as the thickness and velocity of the moving conductor slab.

2. THEORETICAL ANALYSIS

Figure 1 shows a schematic drawing of the coil-conductor arrangement studied in this work. The plane of a rectangular coil is perpendicularly arranged to the conductor slab. In our ECD analyses, we have simply assumed:

(1) The moving conductor is isotropic and infinitely wide.

(2) The coil is one-turn, and it carries an AC current with a given effective RMS value and angular frequency ω. The coil wire is assumed to be infinitely thin.

(3) Conductivity σ, permeability μ and conductor velocity v are all constant.

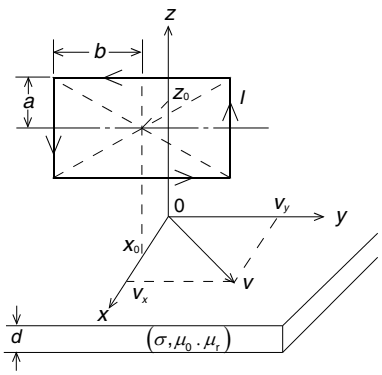

Figure 1: Arrangement of analytical model.

2.1. Magnetic Flux Density

In our previous papers [9], we have introduced shape function to analyze the magnetic field produced by an arbitrarily-shaped coil. However, because of high symmetry of rectangular coil, one can simply express the magnetic flux density for this coil-conductor system in Fig. 1. According to Refs. [7, 8], the x-, y- and z-components of the magnetic flux density $\overline{B}_1$ in the conductor slab are given by the following equations:

$$\begin{aligned} B_{1x} &= -\frac{\mu_0\mu_r I}{4\pi^2}\int_{-\infty}^{\infty}\int_{-\infty}^{\infty}\frac{\xi^2 e^{jx_0\xi}}{\eta\left(\xi^2+\eta^2\right)}\ \frac{\sin(b\eta)}{1-e^{2\gamma d}}\left[\left\{-\left(1+\lambda_0\right)e^{2\gamma d}+\nu_0 e^{-\left(\sqrt{\xi^2+\eta^2}-\gamma\right)d}\right\}e^{rz}\right. \\ &\quad \left.+\left\{1+\lambda_0-\nu_0 e^{-\left(\sqrt{\xi^2+\eta^2}-\gamma\right)d}\right\}e^{-rz}\right]e^{-z_0\sqrt{\xi^2+\eta^2}}\left(e^{a\sqrt{\xi^2+\eta^2}}-e^{-a\sqrt{\xi^2+\eta^2}}\right)e^{-j(x\xi+y\eta)}d\xi d\eta, \quad (1) \\ B_{1y} &= -\frac{\mu_0\mu_r I}{4\pi^2}\int_{-\infty}^{\infty}\int_{-\infty}^{\infty}\frac{\xi e^{jx_0\xi}}{\xi^2+\eta^2}\ \frac{\sin(b\eta)}{1-e^{2\gamma d}}\left[\left\{-\left(1+\lambda_0\right)e^{2\gamma d}+\nu_0 e^{-\left(\sqrt{\xi^2+\eta^2}-\gamma\right)d}\right\}e^{rz}\right. \\ &\quad \left.+\left\{1+\lambda_0-\nu_0 e^{-\left(\sqrt{\xi^2+\eta^2}-\gamma\right)d}\right\}e^{-rz}\right]e^{-z_0\sqrt{\xi^2+\eta^2}}\left(e^{a\sqrt{\xi^2+\eta^2}}-e^{-a\sqrt{\xi^2+\eta^2}}\right)e^{-j(x\xi+y\eta)}d\xi d\eta, \quad (2) \\ B_{1z} &= -j\frac{\mu_0\mu_r I}{4\pi^2}\int_{-\infty}^{\infty}\int_{-\infty}^{\infty}\frac{\xi e^{jx_0\xi}}{\eta\gamma}\ \frac{\sin(b\eta)}{1-e^{2\gamma d}}\left[\left\{-\left(1+\lambda_0\right)e^{2\gamma d}+\nu_0 e^{-\left(\sqrt{\xi^2+\eta^2}-\gamma\right)d}\right\}e^{rz}\right. \\ &\quad \left.-\left\{1+\lambda_0-\nu_0 e^{-\left(\sqrt{\xi^2+\eta^2}-\gamma\right)d}\right\}e^{-rz}\right]e^{-z_0\sqrt{\xi^2+\eta^2}}\left(e^{a\sqrt{\xi^2+\eta^2}}-e^{-a\sqrt{\xi^2+\eta^2}}\right)e^{-j(x\xi+y\eta)}d\xi d\eta. \quad (3) \end{aligned}$$

Here,

$$\gamma = \sqrt{\xi^2+\eta^2-j\sigma\mu_0\mu_r\left(v_x\xi+v_y\eta\right)+j\omega\sigma\mu_0\mu_r}, \quad (4)$$

$$\lambda_0 = \frac{\left\{\gamma^2-\mu_r^2\left(\xi^2+\eta^2\right)\right\}\left(1-e^{-2\gamma d}\right)}{\left(\gamma+\mu_r\sqrt{\xi^2+\eta^2}\right)^2-\left(\gamma-\mu_r\sqrt{\xi^2+\eta^2}\right)^2 e^{-2\gamma d}}, \quad (5)$$

$$v_0 = \frac{4\mu_r\sqrt{\xi^2+\eta^2}\gamma e^{\left(\sqrt{\xi^2+\eta^2}-\gamma\right)d}}{\left(\gamma+\mu_r\sqrt{\xi^2+\eta^2}\right)^2-\left(\gamma-\mu_r\sqrt{\xi^2+\eta^2}\right)^2 e^{-2\gamma d}}. \quad (6)$$

Here, σ is the conductivity of the conductor; d is its thickness; v_x and v_y are the x- and y-components of the conductor velocity, respectively; μ_r is the relative permeability of the conductor; μ_0 is permeability of vacuum. The quantities ξ and η are the integration variables of the Fourier transform. The values and depend on the angular frequency of the excitation current, conductor thickness, velocity, and material properties as well as the coil geometry.

2.2. Eddy Current Density

The x- and y-components of ECD in the conductor slab is expressed by the following equations:

$$J_{1x} = \frac{1}{\mu_0\mu_r}\left(\frac{\partial B_{1z}}{\partial y} - \frac{\partial B_{1y}}{\partial z}\right), \tag{7}$$

$$J_{1y} = \frac{1}{\mu_0\mu_r}\left(\frac{\partial B_{1x}}{\partial z} - \frac{\partial B_{1z}}{\partial x}\right). \tag{8}$$

2.3. Stream function

We introduce stream function to derive ECDs. The following equation expresses streamline of eddy current that satisfies $J_x = J_{1x}(x, y, z)$ and $J_y = J_{1y}(x, y, z)$ in the x-y plane is

$$\frac{dy}{dx} = \frac{\mathrm{Re}\,(J_y)}{\mathrm{Re}\,(J_x)}. \tag{9}$$

Therefore,

$$\mathrm{Re}\,(J_y)\,dx - \mathrm{Re}\,(J_x)\,dy = 0, \tag{10}$$

where, Re(...) returns the real part of the arguments and gives the instantaneous value of the eddy current density. The stream function $U(x, y)$ in the x-y plane is given by

$$U\,(x, y) = \mathrm{Re}\left(\int J_y dx\right) = k = \text{constant}, \tag{11}$$

or

$$U\,(x, y) = \mathrm{Re}\left(\int -J_x dy\right) = k = \text{constant}. \tag{12}$$

2.4. Stream Function Including Time t

Since the eddy current in conductor slab is a function of time t, the stream function $U(x, y, z, t)$ is given by

$$U\,(x, y, z, t) = \mathrm{Re}\left(\int J_y dx\sqrt{2}e^{j\omega t}\right) = \sqrt{2}\left[\mathrm{Re}\left(\int J_y dx\right)\cos\omega t - \mathrm{Im}\left(\int J_y dx\right)\sin\omega t\right] = k \tag{13}$$

where, Im(...) returns the imaginary part of its arguments and gives the instantaneous value of the eddy current density. The stream function on the z'-plane at time t' is given by

$$U\left(x, y, z', t'\right) = k = \text{constant}. \tag{14}$$

From Eq. (14), the constant k is obtained by changing (x, y) and connecting point (x, y) with the equivalent value k. In this way, ECDs on various z-planes are obtained.

3. RESULTS AND DISCUSSION

From Eq. (13), one obtained ECDs dependent upon the excitation frequency f, conductor velocity v and conductor thickness d. The ECDs were calculated by adjusting the integration range of the integral using the Gauss-Legendre integration method, and the contour plots were obtained by using MATLAB. In this research, we have calculated the ECDs in metallic aluminum slabs. The specifications of the conductor slab are given in Table 1, and the dimensions of rectangular coil are shown in Table 2. The contour plots shown hereafter are the ECDs at $z = 0$ and $t = 0$. For

Table 1: Specifications for conductor slab.

Aluminum
$d = 10\,\mathrm{mm}$
$\sigma = 3 \times 10^7\,\mathrm{S/m}$
$\mu = \mu_0 = 4\pi \times 10^{-7}\,\mathrm{H/m}$

Table 2: Specifications for coils.

Rectangular coil
$a = 25\,\mathrm{mm}$
$b = 25\,\mathrm{mm}$
$z_0 = 55\,\mathrm{mm}$
$x_0 = 0\,\mathrm{mm}$

Table 3: Comparison between our technique and FEM.

	Proposed method	FEM
Computational accuracy	exact solution	dependent on mesh size
Computational time	within two seconds	10 times longer

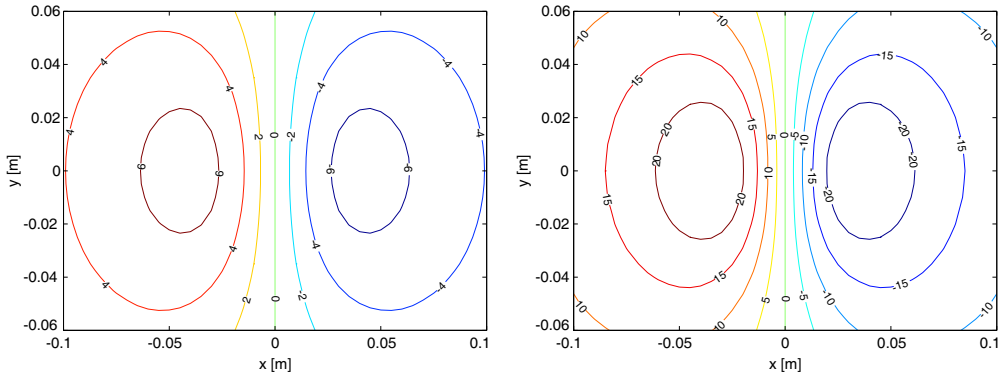

Figure 2: Effect of excitation frequency on ECD of standstill conductor. (a) ECD at $f = 100\,\mathrm{Hz}$ and (b) ECD at $f = 1\,\mathrm{kHz}$.

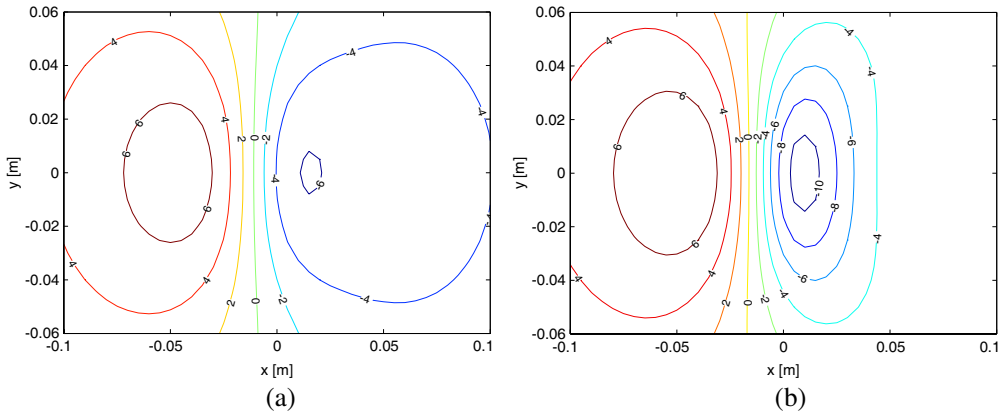

Figure 3: Effect of sliding motion of conductor slab on ECD in the slab with a thickness of 10 mm. The excitation frequency is $f = 100\,\mathrm{Hz}$. (a) ECD for $v_x = 10\,\mathrm{m/s}$ and (b) ECD for $v_x = 20\,\mathrm{m/s}$.

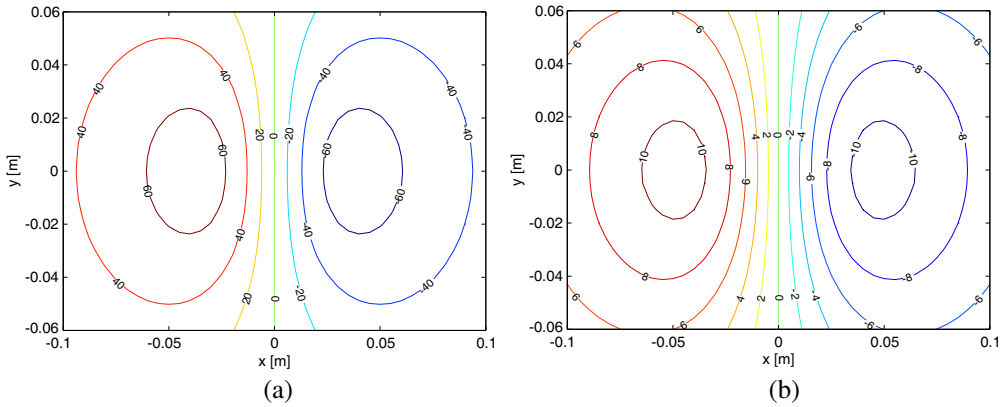

Figure 4: The ECDs of conductor-slab with thicknesses of (a) $d = 1\,\mathrm{mm}$ and (b) $d = 5\,\mathrm{mm}$. The excitation frequency is $f = 1\,\mathrm{kHz}$.

separate computation of the real and imaginary part of the ECDs, in double precision, the CPU time for one ECD calculation on a 3.2 GHz Core i5 PC is about 1.2 s. The comparison between our

technique and the FEM are shown in Table 3. The accurate solution of ECDs can also be obtained using the FEM. However, it requires a long computational time than our technique.

First, the velocity of conductor slab was set to be $v_x = v_y = 0$. Figs. 2(a) and (b) show the ECDs at $f = 1\,\text{kHz}$ and $10\,\text{kHz}$, respectively. The direction of eddy currents on either side of the $x = 0$ line is opposite each other, which is concordant with our common sense. Upon increasing frequency f, the magnitude of eddy current increases, and the ECD becomes more concentrated around the portions where two intense eddy currents arise. Next, we investigated the effect of the sliding motion of conductor slab on ECDs. Figs. 3(a) and (b) show the ECDs at $v_x = 10$ and $20\,\text{m/s}$, respectively, and $v_y = 0$. The excitation frequency was chosen to be $f = 100\,\text{Hz}$. The contour plots of Fig. 3 indicate that the sliding motion causes asymmetric ECDs. Two types of eddy currents, one is shown by counter-clockwise vectors and the other by clockwise vectors in Fig. 3, simultaneously shift towards the $-x$ direction. The ECD shift becomes larger, as the slab velocity increases. The effect of excitation frequency on the ECD shift was also examined. It is found that the sliding motion of conductor slab gives rise to no significant change in ECD at $f = 1\,\text{kHz}$, when v_x is less than $20\,\text{m/s}$. Figs. 4(a) and (b) show the ECDs of conductor slabs with thicknesses of $d = 1\,\text{mm}$ and $d = 5\,\text{mm}$. The ECDs are calculated at $v_x = v_y = 0$ and at $f = 1\,\text{kHz}$. The magnitude of the surface eddy current of thin conductor is larger than that of thicker slab. The eddy current is strongly influenced when the conductor slab thickness is smaller than the flux penetration depth. Since the penetration depth is about $2.68\,\text{mm}$ in aluminum at $f = 1\,\text{kHz}$, high eddy current for the aluminum slab with $d = 1\,\text{mm}$ reflects the penetration effect.

4. CONCLUSION

In this paper, a theoretical solution was derived that exactly displays the eddy current distribution occurring when a rectangular coil is arranged perpendicular to the conductor slab, which was until now unsolved. The flow of the eddy current, which arises in the conductor as a function of excitation frequency, thickness of the conductor slab, and speed of the slab, has been clarified by this theoretical solution. This analysis method enables the immediate determination of the eddy current irrespective of whether the conductor slab is moving. Moreover, it is considered useful not only in sophisticated analyses of eddy currents but also in other types of eddy current analyses.

ACKNOWLEDGMENT

The authors gratefully acknowledge Mr. K. Nawata for his cooperation.

REFERENCES

1. Cacciola, M., S. Calcagno, G. Megali, D. Pellicano, M. Versaci, and F. C. Morabito, "Eddy current modeling in composite materials," *PIERS Online*, Vol. 5, No. 6, 591–595, 2009.
2. Tsuboi, H., N. Seshima, I. Sebestyn, J. Pv, S. Gyimthy, and A. Gasparics, "Transient eddy current analysis of pulsed eddy current testing by finite element method," *IEEE Trans. on Magnetics*, Vol. 40, No. 2, 1330–1333, 2004.
3. Preis, K., O. Biro, and I. Ticar, "FEM analysis of eddy current losses in nonlinear laminated iron cores," *IEEE Trans. on Magnetics*, Vol. 41, No. 5, 1412–1415, 2005.
4. Theodoulidis, T. P. and E. E. Kriezis, "Impedance evaluation of rectangular coils for eddy current testing of planar media," *NDT and E International*, Vol. 35, 407–414, 2002.
5. Yin, W. and A. Peyton, "Sensitivity formulation including velocity effects for electromagnetic induction systems," *IEEE Trans. on Magnetics*, Vol. 46, No. 5, 1172–1176, 2010.
6. He, Y., F. Luo, and M. Pan, "Defect characterisation based on pulsed eddy current imaging technique," *Sensors and Actuators*, Vol. A, No. 164, 1–7, 2010.
7. Tanaka, A., N. Takehira, and K. Toda, "Analysis of a rectangular coil facing moving sheet conductor," *IEEJ. Trans. A*, Vol. 101, No. 8, 405–412, 1981.
8. Itaya, T., K. Ishida, A. Tanaka, and N. Takehira, "Analysis of a fork-shaped rectangular coil facing moving sheet conductors," *IET Science, Measurement and Technology*, Vol. 3, No. 5, 279–285, 2009.
9. Ishida, K., T. Itaya, A. Tanaka, and N. Takehira, "Magnetic field analysis of an arbitrary shaped coil using shape functions," *IEEE Trans. on Magnetics*, Vol. 45, No. 1, 104–112, 2009.
10. Ishida, K., T. Itaya, A. Tanaka, N. Takehira, and T. Miki, "Arbitrary-shaped single-layer coil self-inductance using shape functions," *IET Science, Measurement and Technology*, Vol. 45, No. 1, 21–27, 2010.

High Performance 2D and 3D Approaches for Adjoint Variable Method Suitable for Inverse Problems

Ahmed Gomaa Radwan[1, 2]

[1]Cairo University, Egypt
[2]King Abdullah University of Science and Technology (KAUST), Saudi Arabia

Abstract— The Transmission-Line Modeling (TLM) is used in the analysis of many electromagnetic problems. Recently, inverse biomedical problems can be solved using TLM method and its sensitivities. During the last few decades, it was recommended to use the Adjoint Variable Method(AVM) over the conventional difference techniques to obtain the sensitivity analysis of engineering problems.In this paper a new formulation of the scattering matrix which needs less storage and speeds up the simulation will be presented. In addition, another technique which joins the scattering and connection processes into a single system of equations is also introduced for the first time. The derivative of the scattering matrix with respect to all parameters will be calculated through some scalar values. These derivatives are required in the AVM technique which in turn is used for the solutions of many inverse problems.

1. INTRODUCTION

Sensitivity analysis [1–4] has received unlimited attention due to its relation with the inverse problem techniques which affect many fields such as geophysical, biological and electromagnetic sciences. Transmission Line Modeling (TLM) is considered one of the most famous electromagnetic numerical techniques [5, 6]. Also, the AVM has been used in the analysis of electromagnetic problems [7], and its advantages appear for the sensitivity analysis of problems which have a large number of parameters. An extra single simulation loop is required independent of the number of parameters unlike the forward approach which needs the same or double the parameters to calculate the sensitivity. Recently, several articles have been presented and discuss the use of AVM in the TLM techniques [8–10] using only one extra loop independent of the number of system parameters.

2. CONVENTIONAL TLM METHOD

In this section, we will simplify the computational efforts related to the 2D-TLM shunt-node model and the 3D Symmetrical-Condensed-Node (SCN) in the case of lossless materials [5, 6]. There are many advantages of the TLM technique since, it is the only technique based on equivalent circuit models and physical meaning. The incident and reflected impulses which are calculated at each step have direct relations with the incident and reflected fields.

The major problems of the TLM technique are that it requires huge storage area and large simulation time. As we know the conventional TLM technique needs two steps, the scattering and the connection processes. The number of voltage links of N cells are $5N$ (or $18N$) in 2D (or 3D) structure at a certain time step. The scattering matrix relates the reflected voltage to the incident impulses of the same cell, however the connection matrix interchange the voltages by handshaking as a preparation stage before the next time-step. The basic iteration for a TLM problem with no dispersive boundaries is given by:

$$V_{(k+1)\Delta t} = CSV_{k\Delta t} + V^S_{k\Delta t} \tag{1}$$

$$\begin{bmatrix} V_1^r \\ V_2^r \\ V_3^r \\ V_4^r \\ V_5^r \end{bmatrix} = \frac{1}{y} \begin{bmatrix} 2-y & 2 & 2 & 2 & 2y_0 \\ 2 & 2-y & 2 & 2 & 2y_0 \\ 2 & 2 & 2-y & 2 & 2y_0 \\ 2 & 2 & 2 & 2 & 2y_0-y \end{bmatrix} \begin{bmatrix} cV_1^i \\ V_2^i \\ V_3^i \\ V_4^i \\ V_5^i \end{bmatrix} \tag{2}$$

where $V_{k\Delta t}$ is the vector of incident impulses for all links and all nodes at k time-index. The matrix S is a block diagonal matrix whose jth diagonal block is the scattering matrix of the jth node, and $V^S_{k\Delta t}$ is the vector of the source excitation at the k time-index. The relationship between the reflected and incident impulses is described in (2) for the 2D nondispersive system, where $y_o = 4(\epsilon_r - 1)$, and $y = 4\epsilon_r + \frac{\sigma_e \Delta L}{\sqrt{\mu_o/\epsilon_o}}$.

The scattering matrix in the 3D-case is very large as in (3) and requires large time for scattering and $18N$ storage unit for both the reflected and incident impulses. Also, the connection process is more complex in order to interconnect between the 18th links for each cell with its neighboring cells.

$$\begin{bmatrix} V_1^r \\ V_2^r \\ V_3^r \\ V_4^r \\ V_5^r \\ V_6^r \\ V_7^r \\ V_8^r \\ V_9^r \\ V_{10}^r \\ V_{11}^r \\ V_{12}^r \\ V_{13}^r \\ V_{14}^r \\ V_{15}^r \\ V_{16}^r \\ V_{17}^r \\ V_{18}^r \end{bmatrix} = \begin{bmatrix} a & b & d & 0 & 0 & 0 & 0 & 0 & b & 0 & -d & c & g & 0 & 0 & 0 & 0 & i \\ b & a & 0 & 0 & 0 & d & 0 & 0 & c & -d & 0 & b & g & 0 & 0 & 0 & -i & 0 \\ d & 0 & a & b & 0 & 0 & 0 & b & 0 & 0 & c & -d & 0 & g & 0 & 0 & 0 & i \\ 0 & 0 & b & a & d & 0 & -d & c & 0 & 0 & b & 0 & 0 & g & 0 & i & 0 & 0 \\ 0 & 0 & 0 & d & a & b & c & -d & 0 & b & 0 & 0 & 0 & 0 & g & -i & 0 & 0 \\ 0 & d & 0 & 0 & b & a & b & 0 & -d & c & 0 & 0 & 0 & 0 & g & 0 & i & 0 \\ 0 & 0 & 0 & -d & c & b & a & d & 0 & b & 0 & 0 & 0 & 0 & g & i & 0 & 0 \\ 0 & 0 & b & c & -d & 0 & d & a & 0 & 0 & b & 0 & 0 & g & 0 & -i & 0 & 0 \\ b & c & 0 & 0 & 0 & b & 0 & 0 & a & d & 0 & b & g & 0 & 0 & 0 & i & 0 \\ 0 & -d & 0 & 0 & b & c & b & 0 & d & a & 0 & 0 & 0 & 0 & g & 0 & -i & 0 \\ -d & 0 & c & b & 0 & 0 & 0 & b & 0 & 0 & a & d & 0 & g & 0 & 0 & 0 & i \\ c & b & -d & 0 & 0 & 0 & 0 & 0 & b & 0 & d & a & g & 0 & 0 & 0 & 0 & -i \\ g & g & 0 & 0 & 0 & 0 & 0 & 0 & g & 0 & 0 & g & h & 0 & 0 & 0 & 0 & 0 \\ 0 & 0 & g & g & 0 & 0 & 0 & g & 0 & 0 & g & 0 & 0 & h & 0 & 0 & 0 & 0 \\ 0 & 0 & 0 & 0 & g & g & g & 0 & 0 & g & 0 & 0 & 0 & 0 & h & 0 & 0 & 0 \\ 0 & 0 & 0 & f & -f & 0 & f & -f & 0 & 0 & 0 & 0 & 0 & 0 & 0 & j & 0 & 0 \\ 0 & -f & 0 & 0 & 0 & f & 0 & 0 & f & -f & 0 & 0 & 0 & 0 & 0 & 0 & j & 0 \\ f & 0 & -f & 0 & 0 & 0 & 0 & 0 & 0 & 0 & f & -f & 0 & 0 & 0 & 0 & 0 & j \end{bmatrix} \begin{bmatrix} V_1^i \\ V_2^i \\ V_3^i \\ V_4^i \\ V_5^i \\ V_6^i \\ V_7^i \\ V_8^i \\ V_9^i \\ V_{10}^i \\ V_{11}^i \\ V_{12}^i \\ V_{13}^i \\ V_{14}^i \\ V_{15}^i \\ V_{16}^i \\ V_{17}^i \\ V_{18}^i \end{bmatrix} \tag{3}$$

The conventional SCN scattering matrix in (3) is a function of 10 variables which depend on another four variables $\hat{Z}$, $\hat{Y}$, $\hat{G}$, and $\hat{R}$ as shown in the following relations

$$\begin{aligned} a &= -\frac{\hat{Y}+\hat{G}}{2\left(4+\hat{Y}+\hat{G}\right)} + \frac{\hat{Z}+\hat{R}}{2\left(4+\hat{Z}+\hat{R}\right)}, \quad b = \frac{2}{\left(4+\hat{Y}+\hat{G}\right)}, \\ c &= -\frac{\hat{Y}+\hat{G}}{2\left(4+\hat{Y}+\hat{G}\right)} - \frac{\hat{Z}+\hat{R}}{2\left(4+\hat{Z}+\hat{R}\right)} \end{aligned} \tag{4a}$$

$$\begin{aligned} d &= \frac{2}{\left(4+\hat{Z}+\hat{R}\right)}, \quad e = b, \quad f = \hat{Z}d, \quad g = \hat{Y}b, \quad i = d, \\ h &= \frac{\hat{Y}-\hat{G}-4}{\left(4+\hat{Y}+\hat{G}\right)}, \quad j = \frac{4-\hat{Z}-\hat{R}}{\left(4+\hat{Z}+\hat{R}\right)} \end{aligned} \tag{4b}$$

The relations between these four variables and the electromagnetic parameters are

$$\begin{aligned} u_o &= \frac{1}{\sqrt{\mu_o \epsilon_o}} = 0.5\frac{\Delta L}{\Delta t}, \quad \hat{Y} = 4\left(\epsilon_r - 1\right), \quad \hat{Z} = 4\left(\mu_r - 1\right), \\ \hat{G} &= \sigma_e \frac{\Delta L}{Y_o}, \quad Y_o = \sqrt{\frac{\epsilon_o}{\mu_o}}, \quad \hat{R} = \sigma_m \frac{\Delta L}{Z_o}, \quad Z_o = \frac{1}{Y_o} \end{aligned} \tag{5}$$

One of the major parameters in the AVM when applied to the TLM technique [8–10] is to calculate the parameter η for each link as a function of the time-index k and cell location j as in (6). This parameter depends on the scattering derivatives with respect to all cell properties x_i.

$$\eta_{j,k,i} = C\frac{\Delta S_j}{\Delta x_i} V_{j,k} \tag{6}$$

3. HIGH PERFORMANCE 2D FORMULATIONS

3.1. Scattering Matrix Simplifications

Assuming a structure has N cells, then the scattering phase using these equations faces storage and execution time problems. A temporary matrix size $5N$ is needed to store the reflected pulses of all cells, then this matrix will be copied into the incident matrix at the next time step which consumes an effective time as long as N is large. Therefore, the scattering matrix (2) will affect the storage and speed simultaneously. These problems increase as long as ΔL decreases (fine mesh). Returning to (2), and extracting $V^r_{1,(k+1)\Delta t}$ then, the incident voltage $V^i_{1,k\Delta t}$ can be expressed in terms of the new voltage $V^r_{1,(k+1)\Delta t}$ as follows

$$V^i_{1,k\Delta t} = \frac{V^r_{1,(k+1)\Delta t} - 2\left(V^i_{2,k\Delta t}+V^i_{3,k\Delta t}+V^i_{4,k\Delta t}+y_o V^i_{5,k\Delta t}\right)/y}{2/y-1} \tag{7}$$

Similarly for the other links' voltage and then substituting in (2) we got the following equation

$$V^r_{m,(k+1)\Delta t} = \frac{2}{2(m-1)-y}\left(\sum_{j=1}^{m-1} V^r_{j,(k+1)\Delta t} - \sum_{j=m}^{4} V^i_{j,k\Delta t} - y_o V^i_{5,k\Delta t}\right) - V^i_{m,k\Delta t} \tag{8}$$

$$\frac{\partial S_j}{\partial x_i}V_{j,k} = \frac{-2}{y^2}\left(\sum_{j=1}^{4} V^i_{j,k\Delta t} + y_o V^i_{5,k\Delta t}\right)\frac{\partial y}{\partial x_i} + \frac{2}{y}\sum_{j=1}^{5} V^i_{j,k\Delta t}\frac{\partial y_o}{\partial x_i} \tag{9}$$

Thus, $V^r_{m,(k+1)\Delta t}$ is a function of the reflected voltages of the previous links at the $(k+1)$ time-index and the incident voltages of the next links at the previous k time-index as in (8).Therefore,there is no need to store the incident voltages at the previous links in a temporary place which will solve both problems. Fig. 1(a) shows the percentage time saving using (8) instead of (2) in a square 2D structure with variable length L using $\Delta L = 0.5\,\text{mm}$ and $k_{\max}$= 5000. The derivatives of the scattering matrix with respect to all possible parameters, which are required in the AVM for the inverse problem [8–10], can be obtained by (9).

4. SINGLE STEP 2D-TLM TECHNIQUE

For the first time, a new formulation of the conventional TLM method by combining both the scattering and connection into a single step is introduced. Equation (2) can be simply rewritten as in (10) which relates each reflected link directly with its opposite link in the same cell and at the same time-index k. By applying the connection process a system of equations which relate the incident pulses of each link at $(k+1)$ time-index to the previous incident of the same link at the neighboring cell as shown in (11) is obtained. Fig. 1(b) shows the percentage time saving by using this method as compared with the previous two methods.

$$\begin{bmatrix} V^{r,(x,z)}_{1,(k+1)\Delta t} \\ V^{r,(x,z)}_{2,(k+1)\Delta t} \\ V^{r,(x,z)}_{3,(k+1)\Delta t} \\ V^{r,(x,z)}_{4,(k+1)\Delta t} \\ V^{r,(x,z)}_{5,(k+1)\Delta t} \end{bmatrix} = \frac{1}{y}\begin{bmatrix} 2-y & 2 & 2+y & 2 & 2y_0 \\ 2 & 2-y & 2 & 2+y & 2y_0 \\ 2+y & 2 & 2-y & 2 & 2y_0 \\ 2 & 2+y & 2 & 2-y & 2y_0 \\ 2 & 2 & 2 & 2 & 2y_0 \end{bmatrix}\begin{bmatrix} V^{i,(x,z)}_{1,k\Delta t} \\ V^{i,(x,z)}_{2,k\Delta t} \\ V^{i,(x,z)}_{3,k\Delta t} \\ V^{i,(x,z)}_{4,k\Delta t} \\ V^{i,(x,z)}_{5,k\Delta t} \end{bmatrix} - \begin{bmatrix} V^{i,(x,z)}_{3,k\Delta t} \\ V^{i,(x,z)}_{4,k\Delta t} \\ V^{i,(x,z)}_{1,k\Delta t} \\ V^{i,(x,z)}_{2,k\Delta t} \\ V^{i,(x,z)}_{5,k\Delta t} \end{bmatrix} \tag{10}$$

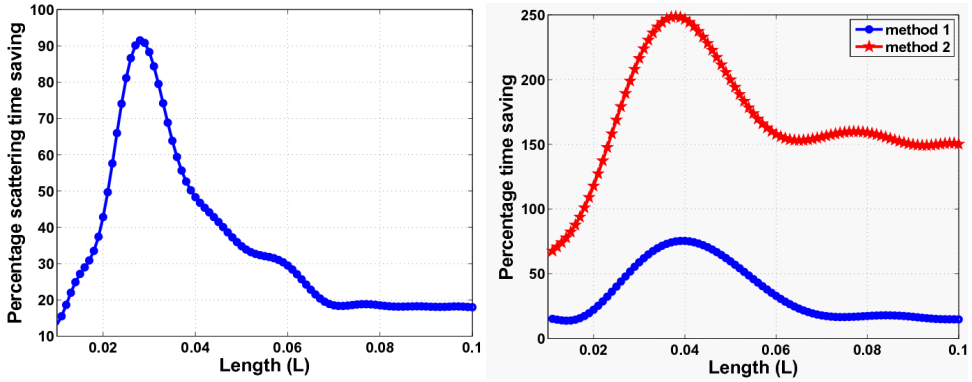

(a) (b)

Figure 1: (a) Percentage scattering time saving using (8) instead of (2), and (b) is the percentage total time (plus connection) saving of the problem using (10) as compared with method 1 and method 2 using Equations (1) and (8).

$$\begin{bmatrix} V^{r,(x,z)}_{1,(k+1)\Delta t} \\ V^{r,(x,z)}_{2,(k+1)\Delta t} \\ V^{r,(x,z)}_{3,(k+1)\Delta t} \\ V^{r,(x,z)}_{4,(k+1)\Delta t} \\ V^{r,(x,z)}_{5,(k+1)\Delta t} \end{bmatrix} = \begin{bmatrix} w_1+w_2 \\ w_1+w_3 \\ w_1-w_2 \\ w_1-w_3 \\ w_1 \end{bmatrix} - \begin{bmatrix} V^{i,(x,z)}_{3,k\Delta t} \\ V^{i,(x,z)}_{4,k\Delta t} \\ V^{i,(x,z)}_{1,k\Delta t} \\ V^{i,(x,z)}_{2,k\Delta t} \\ V^{i,(x,z)}_{5,k\Delta t} \end{bmatrix} = \begin{bmatrix} V^{i,(x,z-1)}_{3,(k+1)\Delta t} \\ V^{i,(x-1,z)}_{4,(k+1)\Delta t} \\ V^{i,(x,z+1)}_{1,(k+1)\Delta t} \\ V^{i,(x+1,z)}_{2,(k+1)\Delta t} \\ V^{i,(x,z)}_{5,(k+1)\Delta t} \end{bmatrix} \tag{11a}$$

$$w_1 = \frac{2}{y}\left(V^{i,(x,z)}_{1,k\Delta t} + V^{i,(x,z)}_{2,k\Delta t} + V^{i,(x,z)}_{3,k\Delta t} + V^{i,(x,z)}_{4,k\Delta t} + y_o V^{i,(x,z)}_{5,k\Delta t}\right) \tag{11b}$$

$$w_2 = -V^{i,(x,z)}_{1,k\Delta t} + V^{i,(x,z)}_{3,k\Delta t},\ w_3 = -V^{i,(x,z)}_{2,k\Delta t} + V^{i,(x,z)}_{4,k\Delta t} \tag{11c}$$

5. SCATTERING SIMPLIFICATION IN 3D STRUCTURES

Similarly with the 3D Symmetrical-Condensed-Node (SCN) we can modify the system described in (3) as follows. First, let us define γ and δ as in (12) which simplify the ten variables in (3) and (4) into (13) as follows

$$\gamma = \frac{2}{4+\hat{Y}+\hat{G}}, \quad \delta = \frac{2}{4+\hat{Z}+\hat{R}} \tag{12}$$

$$a=\gamma-\delta, \quad e=b=\gamma, \quad c=\gamma+\delta-1, \quad i=d=\delta, \quad f=\hat{Z}\delta, \quad g=\gamma\hat{Y}, \quad h=\gamma\hat{Y}-1, \quad j=4\delta-1 \tag{13}$$

The scattering matrix can be factorized into small matrices which are a function of the scalar values γ, δ, $\hat{Z}$, and $\hat{Y}$ as (14a) where these matrices are calculated from six equations as shown in (14b) and (14c). The matrix $BV_{k\Delta t}$ is similar to the connection process such that $V_1 \leftrightarrow V_{12}$, $V_2 \leftrightarrow V_9$, $V_3 \leftrightarrow V_{11}$, $V_4 \leftrightarrow V_8 V_5 \leftrightarrow V_7$, $V_6 \leftrightarrow V_{10}$, $V_{[13-18]} \leftrightarrow V_{[13-18]}$.

$$SV_{(k+1)\Delta t} = \left(\gamma\left(A_1 + A_2\hat{Y}\right) + \delta\left(A_3 + A_4\hat{Z}\right) - B\right)V_{k\Delta t} = (S_{a12} + S_{a34} - B)V_{k\Delta t} \tag{14a}$$

$$S_{a12}V_{k\Delta t} = \begin{cases} k_1 = \sum\limits_{j=1,2,9,12} V^i_{j,k\Delta t} + V^i_{13,k\Delta t}\hat{Y} & \text{for links } 1,2,9,12, \text{ and } 13 \\ k_2 = \sum\limits_{j=3,4,8,11} V^i_{j,k\Delta t} + V^i_{14,k\Delta t}\hat{Y} & \text{for links } 3,4,8,11, \text{ and } 14 \\ k_3 = \sum\limits_{j=5,6,7,10} V^i_{j,k\Delta t} + V^i_{15k\Delta t}\hat{Y} & \text{for links } 5,6,7,10, \text{ and } 15 \end{cases} \tag{14b}$$

$$S_{a34}V_{k\Delta t} = \begin{cases} -V^i_{1,k\Delta t} + V^i_{3,k\Delta t} - V^i_{11,k\Delta t} + V^i_{12,k\Delta t} + V^i_{18,k\Delta t} & \text{for links } 1,3,11,12, \text{ and } 18 \\ V^i_{2,k\Delta t} - V^i_{6,k\Delta t} - V^i_{9,k\Delta t} + V^i_{10,k\Delta t} + V^i_{17,k\Delta t} & \text{for links } 2,6,9,10, \text{ and } 17 \\ -V^i_{4,k\Delta t} + V^i_{5,k\Delta t} - V^i_{7,k\Delta t} + V^i_{8,k\Delta t} + V^i_{16,k\Delta t} & \text{for links for links } 4,5,7,8, \text{ and } 16 \end{cases} \tag{14c}$$

Therefore, by calculating six values we can get the reflected voltages which speed up the system and decreases the required storage needed for scattering. For most conventional cases, $\sigma_m = 0$, $\mu_r = 0$ which will simplify (14a) into (15) as follows

$$SV_{(k+1)\Delta t} = \left(\gamma\left(A_1 + A_2\hat{Y}\right) + 0.5A_3 - B\right)V_{k\Delta t} \tag{15}$$

The sensitivity analysis of the scattering matrix with respect to ϵ_r and σ_e can be calculated for the whole links by three scalar values as shown in (16).Therefore, some scalar values can be enough to get the reflected voltages and also the scattering derivatives which are a key factor in the AVM technique. These simplifications will speed up the calculation of sensitivity analysis which is required for gradient based optimization to detect and investigate many inverse problem applications [8–10].

$$\frac{\partial S}{\partial \epsilon_r}V_{k\Delta t} = \begin{cases} \frac{-8Y_o^2}{\gamma^2}k_1 + 8\frac{Y_o}{\gamma}V_{13,k\Delta t} & \text{for links } 1, 2, 9, 12, \text{ and } 13 \\ \frac{-8Y_o^2}{\gamma^2}k_2 + 8\frac{Y_o}{\gamma}V_{14,k\Delta t} & \text{for links } 3, 4, 8, 11, \text{ and } 14 \\ \frac{-8Y_o^2}{\gamma^2}k_3 + 8\frac{Y_o}{\gamma}V_{15,k\Delta t} & \text{for links } 5, 6, 7, 10 \text{ and } 15 \end{cases} \tag{16a}$$

$$\frac{\partial S}{\partial \sigma_e}V_{k\Delta t} = \begin{cases} \frac{-2Y_o\Delta L}{\gamma^2}k_1 & \text{for links } 1, 2, 9, 12, \text{ and } 13 \\ \frac{-2Y_o^2\Delta L}{\gamma^2}k_2 & \text{for links } 3, 4, 8, 11, \text{ and } 14 \\ \frac{-2Y_o^2\Delta L}{\gamma^2}k_3 & \text{for links} 5, 6, 7, 10 \text{ and } 15 \end{cases} \tag{16b}$$

6. CONCLUSION

We present a novel efficient 2D and 3D computational approach for sensitivity analysis using the Adjoint Variable Method (AVM) combined with Time Domain Transmission-Line-Modeling (TD-TLM) using only one extra TD-TLM simulation. This approach is based on computing the necessary variables. The total variables needed are decreased by a rate of 80% in the 2D case and 83% in the 3D cases as compared with the conventional technique. This improvement will certainly reduce the necessary physical memory needed and will speed up the solution process by a considerable factor. By using these techniques, we can study the sensitivity analysis of larger discontinuous bodies inside the partially computational or completely computational domain. A Comparison table and examples are introduced to emphasis the importance of these techniques.

REFERENCES

1. Chung, Y.-S., J. Ryu, C. Cheon, I. H. Park, and S.-Y. Hahn, "Optimal design method for microwave device using time domain method and design sensitivity analysis — Part I: FETD case," *IEEE Trans. on Magnetics*, Vol. 37, No. 5, 3289–3293, Sep. 2001.
2. Nikolova, N. K., R. Safian, E. A. Soliman, and M. H. Bakr, "Accelerated gradient based optimization using adjoint sensitivities," *IEEE Trans. Antennas and Propagation*, Vol. 52, 2147–2157, Aug. 2004.
3. Nikolova, N. K., H. W. Tam, and M. H. Bakr, "Sensitivity analysis with the FDTD method on structured grids," *IEEE Trans. Microwave Theory Tech.*, Vol. 52, No. 4, 1207–1216, Apr. 2004.
4. Nikolova, N. K., Y. Li, and M. H. Bakr, "Sensitivity analysis of scattering parameters with electromagnetic time-domain simulators," *IEEE Trans. Microwave Theory Tech.*, Vol. 54, No. 4, 1598–1610, Apr. 2006.
5. Christopoulos, C., *The Transmission-Line-Method TLM*, IEEE Press, 1995.
6. Johns, P. B. and R. L. Beurle, "Numerical modeling of 2-dimensional scattering problems using a transmission line matrix," *Proceedings of IEE*, Vol. 118, No. 9, 1203–1208, Sep. 1971.
7. Basl, P. A. W., M. H. Bakr, and N. K. Nikolova, "The theory of self-adjoint S-parameter sensitivities for lossless nonhomogeneous TLM problems," *IET Microw. Antennas Propagation*, Vol. 2, No. 3, 211–220, 2008.
8. Bakr, M. H., P. Zhao, and N. K. Nikolova, "Adjoint first order sensitivities of time domain responses and their applications in solution of inverse problems," *IEEE Trans. Antennas and Propagation*, Vol. 57, No. 7, 2137–2146, 2009.
9. Radwan, A. G., M. H. Bakr, and N. K. Nikolova, "Transient adjoint sensitivities for discontinuities with Gaussian material distributions," *Progress In Electromagnetics Research B*, Vol. 27, 1–19, 2011.

10. Radwan, A. G., M. H. Bakr, and N. K. Nikolova, "Transient adjoint sensitivities for problems with multiple discontinuities exhibiting space dependent properties," *The 26th Annual Review of Progress in Applied Computational Electromagnetics*, 108–113, Finland, Apr. 2010.

Reconstruction of Target Properties for Different Distributions Using Transient Adjoint Technique

Ahmed G. Radwan[1, 2]

[1]Faculty of Engineering, Applied Engineering Mathematics Department, Cairo University, Egypt
[2]King Abdullah University of Science and Technology (KAUST), Thuwal, Saudi Arabia

Abstract— This paper discusses the sensitivity analysis and the inverse problem solution using the Adjoint Variable Method (AVM) integrated with Transmission Line Modeling (TLM) for many examples having different distributions. The sensitivity analyses of the Gaussian function relative to its parameters is introduced where, great discrimination is observed of the sensitivity magnitude which reflects on the electromagnetic sensitivity and the solution of the inverse problem. Different obstacles with properties (ϵ_r, σ) having Gaussian, Poisson and exponential distributions are investigated.

1. INTRODUCTION

Computational electromagnetic techniques play a vital role in the analysis, design and fabrication of many applications. Moreover, they affect many bioengineering applications through the inverse problem electromagnetic approaches. These approaches have the ability to detect and recognize the shape and properties of obstacles through electromagnetic scattering phenomena [1]. One of the most important techniques is the known Transmission Line Modeling (TLM) technique which models the computational domain into voxels with electrical properties [2]. Many applications have been studied using this technique as in [3–7]. For better detection in the inverse problem, gradient based optimization techniques are recommended which need the calculation of the sensitivity analysis with respect to all (N) parameters. Although the forward, backward, and central difference schemes are usually used to get the sensitivity, they need N, N, and $2N$ extra simulation loops for calculations. Another technique which has been recently used is the AVM which enables us to obtain the sensitivities using one extra simulation loop.

Many recent researches are merging both the TLM with AVM for studying the sensitivities and the inverse problem. Many inverse problems for single obstacle with constant properties [4], single obstacle with Gaussian properties [5] and for multiple obstacles [6] are studied. The conventional TLM technique consists of two steps which are the scattering and the connection processes with big matrices. However, these calculations can be simplified which in turn will speed up the computational time and decrease the required memory as in [7]. In this paper we will discuss mathematically the sensitivities of the Gaussian function with respect to each parameter. In addition, the sensitivity of multiple obstacles with different distributions such as polar, Gaussian, Poisson, and exponential will be discussed with some inverse problem.

2. SENSITIVITY OF THE GAUSSIAN DISTRIBUTION FUNCTION

The Gaussian function in 2D can be written as (1), where ϵ_m is the background relative dielectric and (x_c, z_c) is the center point of the Gaussian distribution. The parameters a, b, and c are given by (2) as a function of the angle θ and the standard deviations σ_x and σ_z.

$$\epsilon_r = \epsilon_m + f(x,z) = \epsilon_m + \epsilon_{\max} e^{-\left(a(x-x_c)^2 + 2b(x-x_c)(z-z_c) + c(z-z_c)^2\right)} \tag{1}$$

$$a = \frac{\cos^2(\theta)}{2\sigma_x^2} + \frac{\sin^2(\theta)}{2\sigma_z^2}, \quad b = -\frac{\sin(2\theta)}{4\sigma_x^2} + \frac{\sin(2\theta)}{4\sigma_z^2}, \quad c = \frac{\sin^2(\theta)}{2\sigma_x^2} + \frac{\cos^2(\theta)}{2\sigma_z^2} \tag{2}$$

The sensitivity magnitude of the function $f(x,z)$ has a big range with respect to each parameter. Generally, The Gaussian function confined in the region bounded by $|x-x_c| \leq \frac{3}{\sqrt{2a}}$ and $|z-z_c| \leq \frac{3}{\sqrt{2c}}$ shows more than 98% of the changes. In the following subsections, we will make a small change in each parameter Δp_i and obtain Δf due to this small change. Let us assume that the initial situation at $\theta_i = 0$. Two factors of interest will be studied as follows

- The peaks and their locations.

Table 1: Comparison between the effective area, critical points, maximum and average parameters of Gaussian function.

P_i	Effective area (R)	Critical points at	$\max\lvert\Delta f/\Delta P_i\rvert$	Average
A	$\lvert x-x_c\rvert \le 3\sigma_x$, and $\lvert z-z_c\rvert \le 3\sigma_z$	(x_c, z_c)	1	$\pi/18$
z_c	$\lvert x-x_c\rvert \le 3\sigma_x$, and $\lvert z-z_c-\Delta z\rvert \le 3\sigma_z$	$(x_c, z_c \pm \sigma_z)$	$A/(\sigma_z\sqrt{e})$	$0.2089A\Delta z_c/\sigma_z^2$
σ_z	$\lvert x-x_c\rvert \le 3\sigma_x$, and $\lvert z-z_c\rvert \le 3(\sigma_z+\Delta\sigma_z)$	$(x_c, z_c \pm \sqrt{2}\sigma_z)$	$2A/(\sigma_z e)$	$0.17A/\sigma_z$
σ_r	$\lVert(x,z)-(x_c,z_c)\rVert \le 3(\sigma_z+\Delta\sigma_r)$	$\lVert(x,z)-(x_c,z_c)\rVert = \sqrt{2}\sigma_r$	$2A/(\sigma_r e)$	$0.3365A/\sigma_r$
θ	$\lvert x-x_c\rvert$ and $\lvert z-z_c\rvert \le 3\max(\sigma_z, \sigma_x)$	$(x_c \pm \sigma_x, z_c \pm \sigma_z)$, $(x_c \mp \sigma_x, z_c \pm \sigma_z)$	$A(\sigma_z^2-\sigma_x^2)/(\sigma_x\sigma_z e)$	very small

- The effective average value of each parameter; which can be defined as

$$\bar{p_i} = \frac{\left|\iint_R \frac{\Delta f}{\Delta p_i} dR\right|}{R} \tag{3}$$

where R is the region affected by the change of the parameter p_i given in Table 1.

2.1. Sensitivity with Respect to z_c

Assume that z_c changes to $z_c - \Delta L$, then Δf_{z_c} has two extremes z^*, which satisfy the following equation

$$e^{\frac{\Delta L}{2\sigma_z^2}(2(z^*-z_c)+\Delta L)} = 1 + \frac{\Delta L}{z^*-z_c} \tag{4}$$

When $\Delta L \to 0$, then the critical values are $(x_c, z_c \pm \sigma_z)$, one gives maximum and the other gives minimum. The absolute peak of the sensitivity of $f(x,z)$ with respect to z_c is given by $\frac{\Delta f_{z_c}}{\Delta L}_{(x_c,z^*)} = \frac{A}{\sigma_z\sqrt{e}}$. Since z_c is shifted left by ΔL the function has been studied in the interval $|x-x_c| \le 3\sigma_x$ and $|z-z_c| \in [-3\sigma_z - \Delta L, 3\sigma_z]$ which is the affected region R_{z_c}. Therefore, if ΔL is small, the locations and the magnitude of the critical points is independent on ΔL. By applying (3), the average value will be $\bar{z_c} \approx \frac{\sqrt{\pi}A\Delta L}{6\sqrt{2}\sigma_z^2}$. Although, the peak is independent of ΔL, the average value is proportional to it.

2.2. Sensitivity with Respect to σ_z, where $\sigma_x \neq \sigma_z$

Repeating the same procedure for σ_z, assuming that σ_z changes to $\sigma_z + \Delta\sigma_z$. Then, Δf_{σ_z} has two maximum and one minimum points. The minimum exists at $z^*_{\min} = 0$ where $\Delta f_{\sigma_z}(x_c, z^*_{\min}) = 0$, While the maximum value is given by

$$z^*_{\max} = z_c \pm 2\sigma_z(1+\delta)\sqrt{\frac{\ln(1+\delta)}{\delta(2+\delta)}}, \qquad \frac{\Delta f_{\sigma_z}}{\Delta\sigma_z}_{z=z^*_{\max}} = \frac{A}{\sigma_z}(2+\delta)\left(\frac{1}{1+\delta}\right)^{\frac{2(1+\delta)^2}{\delta(2+\delta)}} \tag{5}$$

where $\delta = \Delta\sigma_z/\sigma_z$. Table 1 summarizes the effective area, the critical points, maximum sensitivity magnitude and the average of the sensitivity analysis for Gaussian function with respect to each parameter.

3. SENSITIVITY ANALYSIS EXAMPLES

Two different examples, one with multiple obstacles and the other with Gaussian distributions are discussed. In these two structures, we used the TLM method with the AVM technique as described in [5] to discuss the sensitivity analysis. The excitation's parameters are $(f_c, BW, \bar{t}) = (3\,\text{GHz}, 1\,\text{GHz}, 2.9463\,\text{nSec})$ and is done at the first column of z, while the observation point is in the midpoint of the last column of z. The discretization cell is $\Delta L = 0.5\,\text{mm}$.

3.1. Example 1: — Many Obstacles with Different Properties

Assume a square shape of size 20 mm bounded from two sides by magnetic walls ($x = 0$, and $x = 20$ mm) and the other two sides by ABC boundary. we have two constant obstacles with square shape whose corner is (9 mm, 6 mm) and size of 3 mm with properties $(\epsilon_{\rm r}, \sigma) = (7, 0.8)$, and rectangular shape whose corner is (13 mm, 16 mm) and dimensions 2 mm × 3 mm with properties $(\epsilon_r, \sigma) = (5, 0.6)$. The third obstacle is space dependent where its properties are $\epsilon_r = \epsilon_{\max} -$

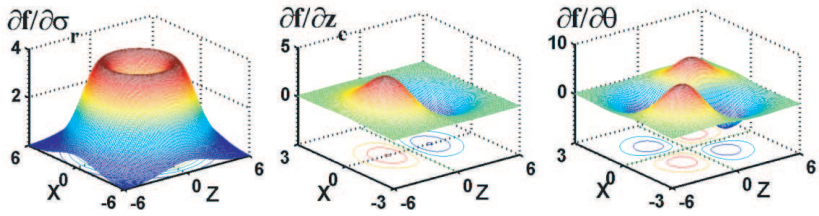

Figure 1: The sensitivity of the Gaussian function with respect to σ_r for polar Gaussian, z_c and θ showing the critical points and magnitude response.

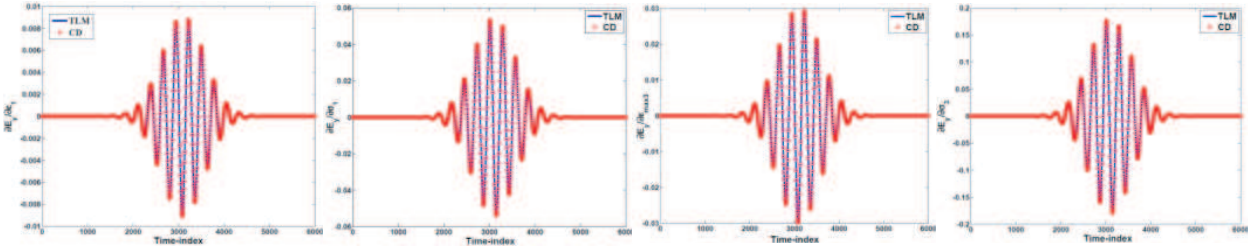

Figure 2: The sensitivity analysis of E_y w.r.t. ϵ_1, σ_1, $\sigma_{\max 3}$, and σ_3 of example 1.

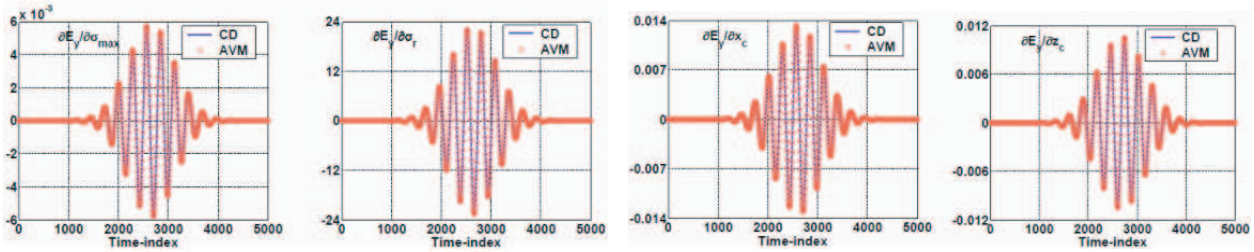

Figure 3: The sensitivity analysis of E_y w.r.t $\sigma_{\max}$, σ_r, x_c, and z_c of example 2.

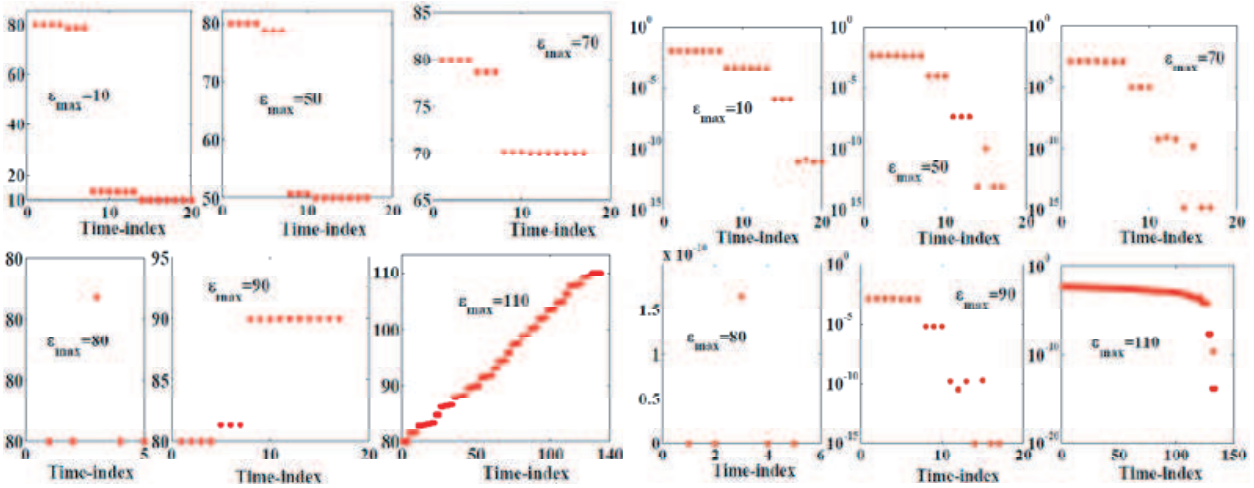

(a) (b)

Figure 4: The inverse problem results of six different cases of the Poisson distribution function (a) $\epsilon_{\max}$ output of the optimization, and (b) the error function for each case.

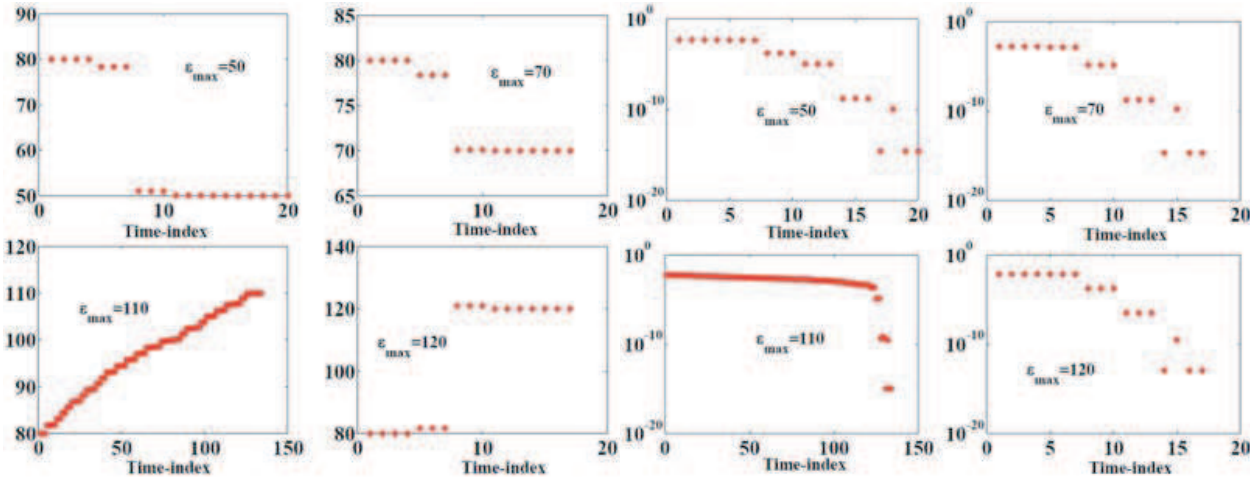

Figure 5: The inverse problem results of six different cases of the Exponential distribution function (a) $\epsilon_{\max}$ output of the optimization, and (b) the maximum error function for each case.

$(r\backslash a)^2$, $\forall r < a$ with values $\sigma = 0.5$, $\epsilon_{\max} = 6$, and $a = 3\,\text{mm}$. Its shape is a circle with center (6 mm, 12 mm) and radius 3 mm. The sensitivity analyses of the electric fields are shown in Fig. 2.

3.2. Example 2: ϵ_t and σ_t Same Polar Gaussian Function ($\sigma_x = \sigma_z = \sigma_r$)

For a rectangular computational domain of similar conditions with size 14 mm and 30 mm in x and z respectively. If the obstacle has a circle shape (the effective area of the tumour is a circle), so the distribution of its parameters is a polar Gaussian function. Then assume that ϵ_t and σ_t have the same following properties $(x_c, z_c, \sigma_r, \epsilon_{\max}, \sigma_{\max}) = (7\,\text{mm}, 15\,\text{mm}, 0.5\,\text{mm}, 5, 0.5)$. Fig. 3 shows the sensitivity analysis using the AVM and CD techniques for some parameters showing different magnitudes.

4. INVERSE PROBLEM EXAMPLES

In this section we will apply the inverse problem technique discussed in [5, 6] for Gaussian distribution function into the known Poisson and exponential distribution functions.

4.1. Poisson Distribution Function

The 2D Poisson function can be written as (6). For simplicity, we will run the inverse problem for single parameter $\epsilon_{\max}$ for different values as shown in Fig. 4, where the TLM technique with the sensitivity analysis using AVM [5] is able to detect the exact value; the initial value for all cases is $\epsilon_{\max i} = 80$.

$$f_\epsilon = \epsilon_m + \frac{\epsilon_{\max}}{\Gamma(x - x_c + 1)\,\Gamma(z - z_c + 1)} \lambda_1^{(x-x_c)}\, \lambda_2^{(z-z_c)} e^{-\lambda_1 - \lambda_2} \tag{6}$$

4.2. Exponential Distribution Function

Similarly, the 2D of the Exponential function can be written as (7). Fig. 5 shows the optimization output for six different cases with their maximum error versus the number of iterations.

$$f_\epsilon = \epsilon_m + \epsilon_{\max} e^{-\lambda_1 |x - x_c| - \lambda_2 |z - zc|} \tag{7}$$

5. CONCLUSION

In this paper, we discussed the use of the TLM with the sensitivity analysis through the AVM technique for different obstacles with constant properties, showing polar, Gaussian, Poisson, and exponential distributions. Also, the sensitivity analyses of the Gaussian function with respect to its parameters which reflects on the sensitivity magnitude of the output electric field for these parameters.

REFERENCES

1. Nikolova, N. K., Y. Li, and M. H. Bakr, "Sensitivity analysis of scattering parameters with electromagnetic time-domain simulators," *IEEE Trans. Microwave Theory Tech.*, Vol. 54, No. 4, 1598–1610, April 2006.
2. Christopoulos, C., *The Transmission-Line-Method TLM*, IEEE Press, 1995.
3. Basl, P. A. W., M. H. Bakr, and N. K. Nikolova, "The theory of self-adjoint S-parameter sensitivities for lossless nonhomogeneous TLM problems," *IET Microw. Antennas Propagation*, Vol. 2, No. 3, 211–220, 2008.
4. Bakr, M. H., P. Zhao, and N. K. Nikolova, "Adjoint first order sensitivities of time domain responses and their applications in solution of inverse problems," *IEEE Trans. on Antennas and Propagation*, Vol. 57, No. 7, 2137–2146, 2009.
5. Radwan, A. G., M. H. Bakr, and N. K. Nikolova, "Transient adjoint sensitivities for discontinuities with gaussian material distributions," *Progress In Electromagnetics Research B*, Vol. 27, 1–19, 2011.
6. Radwan, A. G., M. H. Bakr, and N. K. Nikolova, "Transient adjoint sensitivities for problems with multiple discontinuities exhibiting space dependent properties," *The 26th Annual Review of Progress in Applied Computational Electromagnetics*, 108–113, Finland, April 2010.
7. Radwan, A. G., "High performance 2D and 3D approaches for adjoint variable method suitable for inverse problems," *PIERS Proceedings*, Suzhou, China, September 12–16, 2011.

A Novel Imaging Method for Inverse Scattering Problem Using Stepped-frequency Waveforms

Wei Yan, Nai-Zhi Wang, Amna Ajaz, and Jia-Dong Xu
School of Electronic and Information, Northwestern Ploytechnical University, Xi'an, Shaanxi, China

Abstract— Previously, many algorithms have been used to reconstruct an unknown object from backward scattering data. For the object on a turntable in microwave chamber, inverse synthetic aperture radar (ISAR) method is often used to acquire the image of the object. In this paper, circular synthetic aperture radar (CSAR) algorithm is applied to inverse scattering problem of the object. It can utilize the scattering sampled data of a 360 degree rotation of the objects on the turntable system. Compared to traditional ISAR method, CSAR algorithm can provide the reflective image of the target with high resolution. First, it transforms the scattering field to spatial frequency domain, and compensates the difference in height between the plane of antenna and the turntable. Then, circular spectrum theory is used to obtain the spatial frequency domain of the objects. After FFT transformation, the reflective image of the objects, which is also the spatial domain of the objects, is reconstructed. The point spread function (PSF) is given for the objects in the middle of turntable system. Finally, the simulations for the model of a plane are done both by CSAR algorithm and ISAR method. The results show that the method in this paper has high resolution. Then, an experiment with a metal plate on the turntable is done in microwave chamber at X band. The result shows the algorithm in this paper has high accuracy using stepped-frequency waveforms.

1. INTRODUCTION

Conventional ISAR imaging techniques are based on coherent radars, which process received signals to obtain an image of the illuminated target. The resolution of the obtained image depends on bandwidth of the transmitted signal in range domain and extent of the rotated angle in cross-range domain. The individual target scattering points must be smaller than the Doppler resolution to prevent distortion in cross-range [1–3]. For the large angle rotation problem, the image of the targets will be unfocused taking into account arbitrary range migration and cross-range phase errors.

CSAR system can acquire high resolution image through full-rotation of targets. It is based on the Fourier analysis of Green's function to reconstruct the target function. However, it was proposed for the case of slant mode which leads to Doppler spread on the ground plane [4–7].

In this paper, CSAR imaging system is introduced for inverse scattering problem with full rotation on the ground plane. The advantage of this method is that it can avoid the Doppler spread which makes the imaging process accurate. The proposed method can compensate the range migration and cross-range phase errors in spatial frequency domain. The two dimension FFT can be used to transform the spatial frequency domain to the spatial domain of the targets. The results form experiment is compared with the simulation of the same model, which shows the algorithm in this paper has high accuracy using stepped-frequency waveforms.

2. FORMULATION OF THE MODEL

The geometry of a turntable system is illustrated in Fig. 1 in cylindrical coordinates, in which the position of the scattering targets with reflection coefficient $\psi(x, y)$ is placed at (x, y) on the turntable. R is the distance between the antenna and the centre of turntable and d stands for the distance from antenna to the targets. θ is the angle through which the turntable rotates.

The scattering electric field of targets can be expressed as [8]

$$E_s(f,\theta) = \int_0^{\infty}\int_0^{\infty} \psi(x,y)\, G(x,y;f,\theta)\, dxdy \tag{1}$$

where, $G(x, y; f, \theta) = \frac{e^{-jk\times 2d}}{d^2}$, $d = \sqrt{R^2 + \rho^2 + 2R\rho\cos(\phi - \theta)}$.

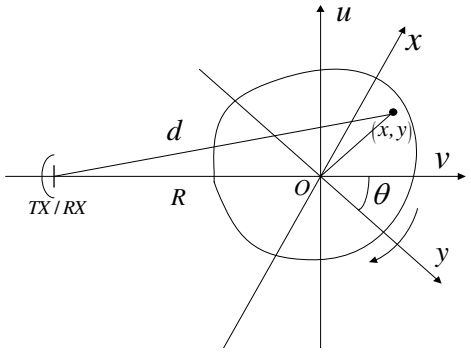

Figure 1: Illustration of the model.

To make a computational inversion for imaging, we first transform the spatial domain of targets to the spatial frequency domain. The relationship between them can be expressed as

$$\psi\left(f_x, f_y\right) = \int_{-\infty}^{\infty}\int_{-\infty}^{\infty} \psi\left(x, y\right) \cdot e^{-2\pi(x \cdot f_x + y \cdot f_y)} dxdy \tag{2}$$

Here, $f_x = \frac{2f}{c}\cos\theta$ and $f_y = \frac{2f}{c}\sin\theta$ are the spatial frequency domain of x and y.

Note that if $R \gg \rho$, the distance d and green function G can be expressed as

$$d \approx R + \rho\cos\left(\phi - \theta\right) \qquad d^2 = R^2 \qquad G\left(x, y; f, \theta\right) = \frac{e^{-j2k[R+\rho\cos(\phi-\theta)]}}{R^2} \tag{3}$$

According to Parseval's theory, the scattering electric field can be expressed as

$$E_s\left(f, \theta\right) = \int_0^{\infty}\int_0^{\infty} \psi\left(-f_x, -f_y\right) G\left(f_x, f_y; f, \theta\right) df_x df_y = \int_0^{\infty}\int_0^{\infty} \sigma\left(f_x, f_y\right) G\left(f_x, f_y; f, \theta\right) df_x df_y \tag{4}$$

where, $\psi(f_x, f_y)$ is the special frequency domain of reflective distribution $\psi(x, y)$. $\sigma(f_x, f_y)$ is the scattering pattern of the targets which can be express as $\sigma(f_x, f_y) = \psi(-f_x, -f_y)$. Special frequency domain can also be expressed in polar format as (f', ϕ). As the scattering field can only be sampled within an extent of frequency band, the special frequency domain f' can be given as $f' = 2f/c$.

For a single frequency, it can be expressed as

$$E_s\left(f, \theta\right) = f' \int_0^{2\pi} \sigma\left(f', \phi\right) G\left(f'; \theta - \phi\right) d\theta = f'\sigma\left(f', \theta\right) * G\left(f', \theta\right) \tag{5}$$

According to Fourier spectrum theory,

$$\sigma\left(f', \theta\right) = Ifft_\theta\left\{FFt_\theta\left[E_s\left(f', \theta\right)/f'\right]/FFt_\theta\left[G\left(f', \theta\right)\right]\right\} \tag{6}$$

For each frequency, the reflectivity spatial distribution of the targets can be acquired by the same way. To acquire the reflectivity distribution of the targets, scattering pattern of the targets $\sigma(f', \theta)$ should be transformed to $\sigma(f_x, f_y)$ by the bilinear interpolation method. The reflectivity distribution of the targets can easily obtained by the 2-D inverse Fourier transformation.

The resolution of this method can be shown by the point spreading function (PSF) of the targets at the origin position. In this case, the point spread function of this target in the spatial domain can be expressed as

$$\psi_n\left(x, y\right) = 2k_{\max}\frac{J_1\left(rk_{\max}\right)}{r} - 2k_{\min}\frac{J_1\left(rk_{\min}\right)}{r} \tag{7}$$

3. SIMULATION RESULTS

The validity of the presented approach is demonstrated by simulation example. In this paper, several point targets with the reflectivity 1 are simulated. The position of the targets is shown in Fig. 2. It is both simulated by the CSAR imaging and ISAR imaging. Table 1 is the simulation parameters of CSAR.

The results from CSAR imaging is compared with the ISAR imaging. It shows that CSAR imaging can have high resolution which can distinguish the image blurs cause by small angle rotation. Although the confocal focus method can solve the range migration caused by the large angle rotation of targets, it always needs several hours to acquire the image. The processing time using CSAR imaging only need 1minutes. Although the resolution in Fig. 2(a) is higher than Fig. 2(b), the points are not focused very well. The reason may be caused by the bilinear interpolation in spatial frequency domain of targets.

Table 1: Simulation parameters of CSAR.

Simulation Parameters	
frequency	8–12 GHz
Total angle	360 degree
R_0	3 m
h	0 m
Sampling numbers in frequency	401
Sampling numbers in angle	361

Table 2: Simulation parameter of ISAR.

Simulation Parameters	
frequency	8–12 GHz
Total angle	30 degree
R_0	3 m
h	0 m
Sampling numbers in frequency	401
Sampling numbers in angle	301

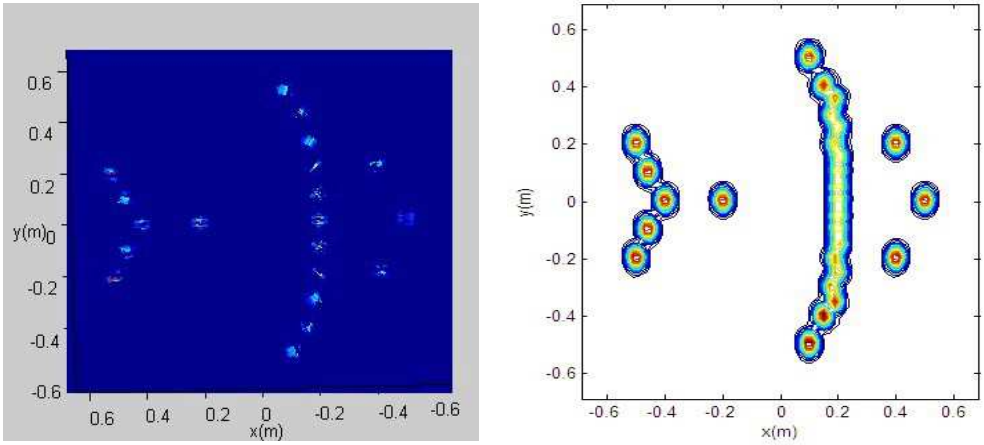

Figure 2: Results of imaging. (a) CSAR imaging. (b) ISAR imaging.

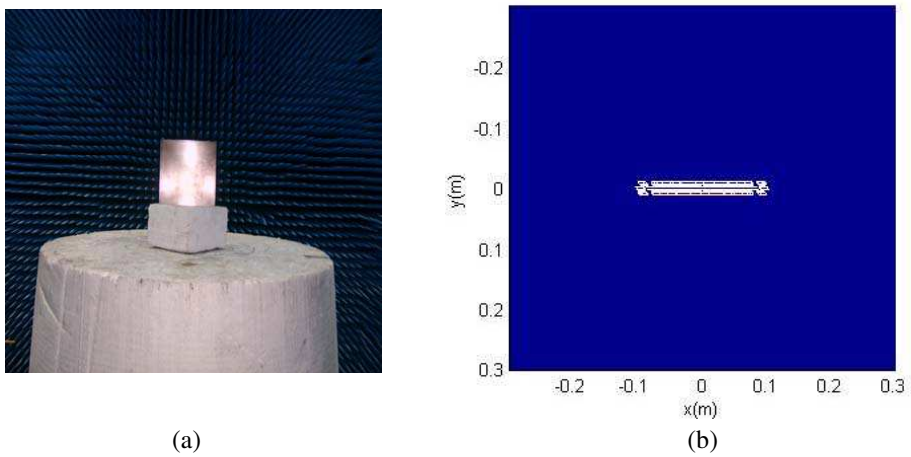

Figure 3: The metal plate with the imaging result. (a) The actual plate. (b) The imaging result.

Experiment is also done in microwave chamber. The target is a metal plate with size of 0.2 m by 0.2 m on the turntable, as shown in Fig. 3(a). The working frequency is 10 GHz and horn antennas are used for transmitting and receiving electromagnetic wave. Agilent network analyzer 8363A is used for measuring scattering field. The result is shown in Fig. 3(b), which validates the method in this letter has high accuracy. The error may caused by the turntable supporter and environment.

4. CONCLUSION

CSAR imaging using stepped-frequency waveforms has been introduced to the turntable system. The difference between the algorithm in this paper and conventional full rotation algorithm is that this algorithm transform the spatial domain of targets to spatial frequency domain, can do motion compensation in spatial frequency domain. This algorithm can be efficiently used in the case of radar cross-section (RCS) reduction in stealth design.

REFERENCES

1. Ausherman, D. A., A. Kozma, J. L. Walker, H. M. Jones, and E. C. Poggio, "Developments in radar imaging," *IEEE Transactions on Aerospace and Electronic Systems*, Vol. 20, No. 4, 363–400, 1984.
2. Thayaparan, T., G. Lampropoulos, and L. Stankovic, "Motion compensation in ISAR imaging using the registration-restoration-fusion approach," *IET Signal Processing*, Vol. 2, No. 3, 223-236, 2008.
3. Ishimaru, A., T.-K. Chan, and Y. Kuga, "An imaging technique using confocal circular synthetic aperture radar," *IEEE Transactions on Geoscience and Remote Sensing*, Vol. 36, No. 5, 1524–1530, Sep. 1998.
4. Soumekh, M., "Reconnaissance with slant plane circular SAR imaging," *IEEE Transactions on Image Processing*, Vol. 5, No. 8, 1252–1265, 1996.
5. Bryant, M. L., L. L. Gostin, and M. Soumekh, "3-D E-CSAR imaging of a T-72 tank and synthesis of its SAR reconstructions," *IEEE Transactions on Aerospace and Electronic Systems*, Vol. 39, No. 1, 211–227, 2003.
6. Burki, J. and C. F. Barnes, "Slant plane CSAR processing using householder transform," *IEEE Transactions on Image Processing*, Vol. 17, No. 10, 1900-1907, 2008.
7. Wu, X.-F., Y.-P. Wang, W.-X. Tan, W. Hong, and Y.-R. Wu, "Multi reference plane projected confocal 3-D imaging algorithm for CSAR," *1st Asian and Pacific Conference on Synthetic Aperture Radar*, 37–40, 2007.
8. Broquetas, A., J. Palau, L. Jofre, and A. Cardama, "Spherical wave near-field imaging and radar cross-section measurement," *IEEE Transactions on Antennas and Propagation*, Vol. 46, No. 5, 730–735, 1998.

Mathematics behind the Fractional-order Smith Chart

A. G. Radwan[1, 2], **A. Shamim**[2], **and K. N. Salama**[2]

[1]Engineering Mathematics Department, Cairo University, Egypt
[2]Physical Sciences and Engineering
King Abdullah University of Science and Technology, Saudi Arabia

Abstract— This paper derives the theory for a fractional order Smith chart and provides a comparison between the impedance and admittance fractional order Smith charts. Basic chart features such as boundaries, critical points, peak values, matching (unity) circle, and the central angle are investigated and compared. Mathematical analysis for these basic features and standard Smith chart functions is also described. This Smith chart can be used to study the scattering parameters in fractional-order RF designs. In addition, it may be used for inverse problems whose models depend on fractional-order electrical elements.

1. INTRODUCTION

Although, the known integer order elements inductors, capacitors, and resistors have been extensively studied and have been the foundation of the electronic revolution, the search for a new generic element that demonstrates innovative characteristics has always been a core objective of the researchers [1, 2]. One such promising element is a fractional element, which has found its roots from fractional calculus. Fractional calculus is as old as integer order calculus. However, it did not become popular until the scientists found that the modeling of dynamical systems is much better and more accurate using the fractional or non-integer derivatives in 1960 [2]. Recently, several good realizations of fractional-elements were introduced and are based on different principles such as mathematical approximation, chemical-probe, fractal design and RC branches [3–6]. These elements can now verify experimentally the generalized fractional order theorems utilized in circuit designs [7, 8], electromagnetics [9], and in bioengineering fields [10]. A fractional element is one whose impedance is proportional to s^{α} where $\alpha \in [-2, 2)$, where the phase difference between the voltage across its two terminals and the current entering these terminals is $\alpha\pi/2$. This means that the integer based resistor (R), inductor (L), capacitor (C), and frequency dependent negative resistor (FDNR) used at present are only special cases of fractional based elements and correspond to $\alpha = 0, 1, -1, -2$ respectively. In addition, the magnitude of the fractional element impedance is $|z_f| = \omega^{\alpha}L$, and $\frac{1}{\omega^{\alpha}C}$ for fractional order inductor and capacitor respectively. Therefore, the effect of frequency can be controlled by the proper choice of the fractional-order parameter. The impedance of the fractional-order element is given by:

$$Z_f = |Z_f| \left(\cos(0.5|\alpha|\pi) \pm j \sin(0.5|\alpha|\pi)\right) \tag{1}$$

2. CONVENTIONAL SMITH CHART

Although the Smith chart is known since 1939, it is still considered as one of the most used charts till now [reference to smith chart). It is critical for high frequency (RF, microwave frequency range) impedance matching problems. Basically, it is a polar plot of the voltage reflection coefficient $\Gamma = \Gamma_r + j\Gamma_i$, where the magnitude $|\Gamma|$ is plotted as a radius ($|\Gamma| < 1$) from the center, and the angle $\theta(-180^{\circ} < \theta \leq 180^{\circ})$ is measured from the right hand side of the horizontal diameter [11]. The real advantage of smith chart lies in its ability to transform from reflection coefficients to normalized impedances and vice versa. By conventional matching techniques, any load can be matched with two elements [11].

The standard smith chart can be used for normalized admittance in the same way as it is used for normalized impedances, and it can be used to convert between impedance and admittance. Since a complete revolution around the Smith chart corresponds to a length of $\lambda/2$, a $\lambda/4$ transformation is equivalent to rotating the chart by 180°; this is also equivalent to imaging a given impedance (or admittance) point across the center of the chart to obtain the corresponding admittance (or impedance) point. Thus, the same Smith chart can be used for both impedance and admittance calculations during the solution of a given problem. Recently, the spherical Smith chart was also studied in [12, 13].

Our previous work presented a novel generalized Smith chart suitable for fractional order circuits and the technique for plotting and impedance matching [14, 15]. This paper furthers our work by providing detailed mathematical analysis of the fractional-order Smith-chart and a comparison between impedance and admittance fractional order Smith charts. The effect of the fractional-order parameter on the critical points of the Smith chart is introduced.

3. THE FAMILY OF THE FRACTIONAL-ORDER SMITH CHARTS

The existence of the fractional order parameter (α) increases the system's degree of freedom. Then instead of the conventional Smith chart being based on (Γ_r, Γ_i), it is now based on $(\Gamma_r, \Gamma_i, \alpha)$. Therefore the fractional Smith chart is no longer a 2D polar plot as known, but it is now a 3D plot as shown in Fig. 1(b) for the matching surfaces of both the Z and Y Smith charts. The reflection coefficient Γ can be calculated from $\Gamma = (z-1)/(z+1)$ where z is the normalized load impedance. Table 1 shows the basic equations of the fractional-order impedance and admittance Smith charts. These equations are developed based on the definition of the fractional-order impedance (1), and using some algebraic simplifications. In addition, the generic equations of circles for each constant element with their special case in the conventional Smith chart are introduced. It is clear, that symmetry still holds between both Z and Y charts even in the fractional-order domain. Fig. 1(a) shows four different cases of the fractional order Smith charts when $\alpha = 0.5$ and 1.2 for the impedance (left) and admittance (right) charts.

From the table below, any equation represents a family of circles that has a common radical axis which is defined as the locus of points at which tangents drawn to all these circles have the same length. For example, the radical axis of the constant $|Z_f|$ circles is $\Gamma_r = 0$ for both α and $|Z_f|$ parameters. However, the radical axis of the constant r circles depends on two parameters (r and α) as follows

$$\Gamma_r + \frac{(r_2+1)\csc(0.5|\alpha_1|\pi) - (r_1+1)\csc(0.5|\alpha_2|\pi)}{(r_2-r_1)}\Gamma_i - 1 = 0 \tag{2}$$

For constant r and variable α the radical axis becomes $\Gamma_i = 0$, while for constant α and variable r the radical axis tends to $\Gamma_r + \csc(0.5|\alpha|\pi)\Gamma_i - 1 = 0$.

4. QUALITATIVE STUDY OF THE FRACTIONAL-ORDER Y-SMITH CHART

The reflection coefficients of the Y Smith chart generally as a function of $(\alpha, g, |y_f|)$ are given by

$$\begin{aligned}\Gamma_r &= \frac{(1-g^2) - y_f(|y_f| + 2g\cos(0.5|\alpha|\pi))}{(1+g)((1+g) + 2|y_f|\cos(0.5|\alpha|\pi)) + |y_f|^2} \\ \Gamma_i &= \frac{2|y_f|\sin(0.5|\alpha|\pi)}{(1+g)((1+g) + 2|y_f|\cos(0.5|\alpha|\pi)) + |y_f|^2}\end{aligned} \tag{3}$$

Let us consider a normalized load impedance of $z_L = 1.35 + 0.35j$ plotted in the half-order impedance ($|\alpha| = 0.5$) Smith chart, shown in Fig. 2(a). This impedance has a complex reflection coefficient of $\Gamma + A = 0.167 + 0.124j$, which is plotted as point A. In order to convert this impedance into the corresponding admittance, a circle is drawn with a radius equal to $OA = 0.21$. Drawing a straight line through the center which meets the circle at the other end (point B in Fig. 2(a)),

Table 1: Comparison of fractional-order Z and Y Smith charts.

	Fractional-order Y-Smith chart	Fractional order Z-Smith chart
Load impedance	$z = \frac{1}{y}$, $y = \lvert y_f\rvert(\cos(\frac{\lvert\alpha\rvert\pi}{2}) - j\sin(\frac{\lvert\alpha\rvert\pi}{2})) + g$	$z = z_{fe} + r$ $= \lvert z_f\rvert(\cos(\frac{\lvert\alpha\rvert\pi}{2}) + j\sin(\frac{\lvert\alpha\rvert\pi}{2})) + r$
Constant $\lvert y_f\rvert$ or $\lvert z_f\rvert$ circles	$(\Gamma_r+1)^2 + (\Gamma_i \mp \frac{\csc(0.5\lvert\alpha\rvert\pi)}{\lvert y_f\rvert})^2$ $= (\frac{\csc(0.5\lvert\alpha\rvert\pi)}{\lvert y_f\rvert})^2$	$(\Gamma_r-1)^2 + (\Gamma_i \pm \frac{\csc(0.5\lvert\alpha\rvert\pi)}{\lvert z_f\rvert})^2$ $= (\frac{\csc(0.5\lvert\alpha\rvert\pi)}{\lvert z_f\rvert})^2$
Constant g or r circles	$(\Gamma_r + \frac{g}{(g+1)})^2 + (\Gamma_i \pm \frac{\cot(0.5\lvert\alpha\rvert\pi)}{(g+1)})^2$ $= (\frac{\csc(0.5\lvert\alpha\rvert\pi)}{(g+1)})^2$	$(\Gamma_r - \frac{r}{r+1})^2 + (\Gamma_i \pm \frac{\cot(0.5\lvert\alpha\rvert\pi)}{r+1})^2$ $= (\frac{\csc(0.5\lvert\alpha\rvert\pi)}{r+1})^2$
Conventional equations ($\alpha = 1$)	$(\Gamma_r+1)^2 + (\Gamma_i \mp \frac{1}{y_1})^2 = (\frac{1}{y_1})^2$	$(\Gamma_r-1)^2 + (\Gamma_i \pm \frac{1}{z_1})^2 = (\frac{1}{z_1})^2$
	$(\Gamma_r + \frac{g}{g+1})^2 + \Gamma_i^2 = (\frac{1}{g+1})^2$	$(\Gamma_r - \frac{r}{r+1})^2 + \Gamma_i^2 = (\frac{1}{r+1})^2$

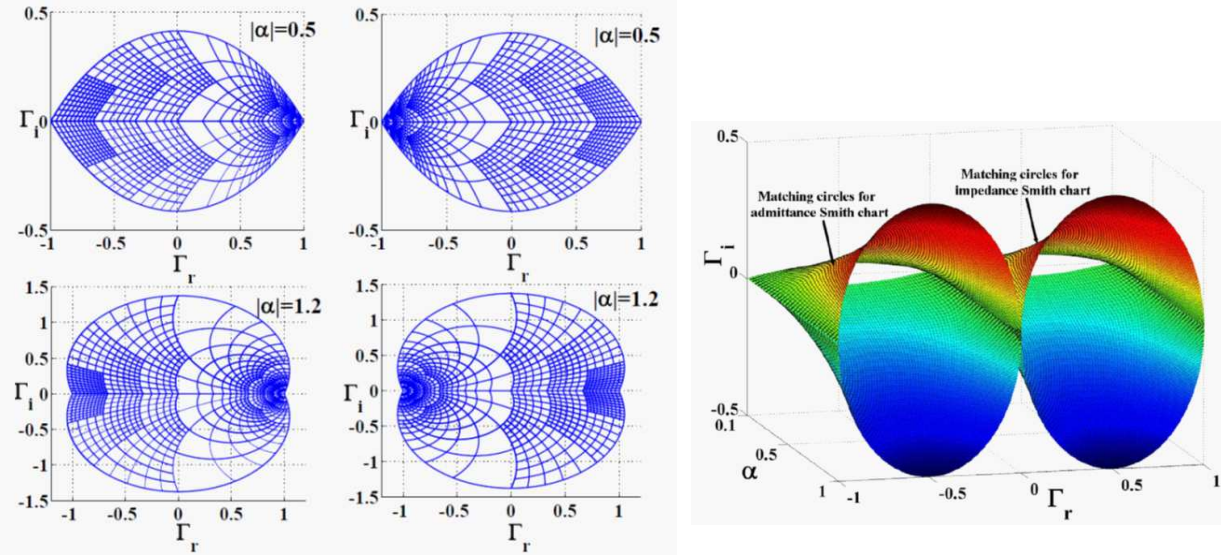

(a) (b)

Figure 1: (a) The impedance and admittance fractional-order Smith chart for two different values of the fractional-order $\alpha = \{0.5, 1.2\}$, and (b) the matching circles for both the impedance and admittance Smith-chart when the fractional-order parameter $\alpha \in [0.1, 1]$.

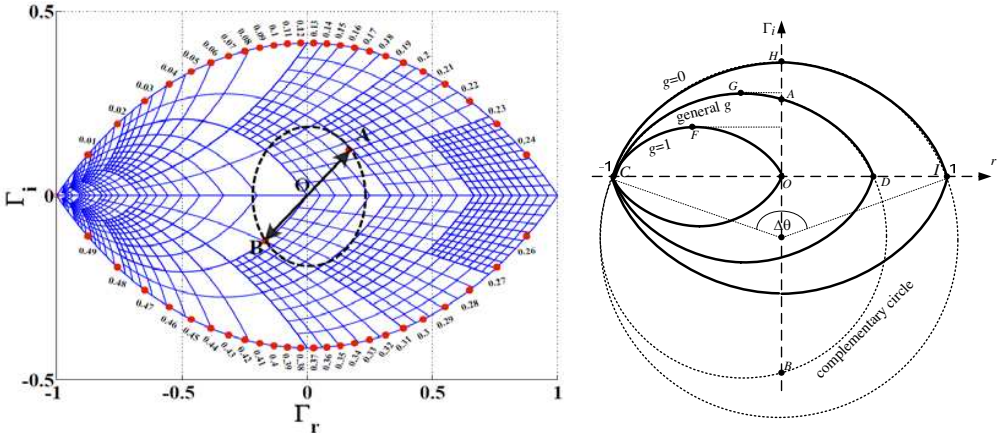

(a) (b)

Figure 2: (a) The half-order Y Smith chart with frequency response, and (b) the general schematic for the most important points in the fractional-order Y Smith chart.

gives the corresponding admittance, $Y = G + B = 0.6941 - 0.18j$. This procedure is consistent with the standard Smith chart operation to convert impedances into admittances.

The following points will discuss some interesting features of the fractional-order Y Smith chart with the help of Fig. 2(b).

i. $\mathbf{\Gamma_r = 0}$: (reflection coefficient is totally imaginary such as A, B, O, and H points) at $|y_f|_{1,2} = \frac{g^2}{g\cos(0.5|\alpha|\pi) \pm \sqrt{1-g^2\sin^2(0.5|\alpha|\pi)}}$ according to whether we are working with fractional inductor of order $|\alpha|$ (point A) or its complementary circle (fractional capacitor) of order $(2 - |\alpha|)$ such as point B. For $g = 1$ (matching circles), the values of $|y_f|_{1,2}$ are ∞ or $0.5|\alpha|\pi$ (point O and its complementary point (not shown)). Generally, these values are different due to the nonsymmetrical circles, however in the conventional case ($|\alpha| = 1$), $|y_f|_{1,2} = \frac{\pm g^2}{\sqrt{1-g^2}}$ due to the half-circle symmetry of the Smith-chart. Point H is the maximum imaginary reflection coefficient of this chart.

ii. $\mathbf{\Gamma_i = 0}$: (Reflection coefficient is totally real such as C, D, O, and I) when $\{g = 0 \,\text{or}\, |y_f| = 0\}$, which are the same conditions in the conventional case. When $|y_f| = 0$, the real-component

of the reflection coefficient is $\Gamma_r = \frac{1-g^2}{(1+g)^2}$ as C, D, O, and I which are independent of the fractional-order α which means that these points are fixed for all fractional-orders.

iii. **Peak value $\frac{\partial \mathbf{\Gamma_i}}{\partial |\mathbf{y_f}|} = \mathbf{0}$:** (critical values of the Γ_i such as F, G, and H points) at $|y_f|_{3,4} = 1+g$, which means that the location of maximum for the inductive part (point G, same as minimum for capacitive part) imaginary reflection coefficient is independent of the fractional order α. Then for a given r and α, the magnitude of this maximum is $\Gamma_{i_{\max}} = \frac{\tan(0.25|\alpha|\pi)}{1+g}$ (at point G) which is partially dependent on α. For constant $|\alpha|$ Smith chart, this value can be obtained when $g = 0$ (boundary circle) and its value is $(\Gamma_{i_{\max}})$ such as point H. As a special case, when $|\alpha| = 1$ the conventional Smith chart, $(\Gamma_{i_{\max}})_{\alpha=1} = 1$ as known. For half-order Smith chart ($|\alpha| = 0.5$) the maximum value is $(\Gamma_{i_{\max}})_{\alpha=0.5} = \tan(\frac{\pi}{8}) = \sqrt{2}-1$ as in the Z Smith-chart [14]. Note that: the maximum magnitude at the matching circles is half $(\Gamma_{i_{\max}})_{fixed\alpha}$ of the same $|\alpha|$ chart as in point F.

iv. **Area inside the fractional-order Smith chart:** Since the equations of the Y-Smith chart are circles. The boundary curve ($g = 0$) which begins at point C and ends at point I is an arc from a big circle whose center is $0, \cot(0.5|\alpha|\pi)$ and whose radius is $\csc(0.5|\alpha|\pi)$. Then by using some algebraic calculations, the central angle of this arc can be easily given as $\Delta\theta = |\alpha|\pi$. Moreover, all the arcs have the same central angle $\Delta\theta$. Therefore, the area inside the upper half of the Smith-chart can be calculated as $A_{\alpha-upper} = \frac{|\alpha|\pi - \sin|\alpha|\pi}{2\sin^2(0.5|\alpha|\pi)}$. For conventional case, this value will be equal to $(\pi/2)$ as known. Similarly, the area inside the matching circle ($g = 1$) is given by $A_{matching} = 0.25A_{\alpha-upper}$.

v. **Matching:** If the load point lies on the matching circle (Z or Y) Smith chart of a certain α, then this load needs a (series or parallel) element of order $(2-|\alpha|)$; its complement circle; and an opposite to the load's property, inductive if the load is capacitive and vice versa. Therefore, the conventional Smith chart is two identical circles overlapped together.

vi. **Mapping:** The necessary and sufficient condition for any load Z_L such that its representation to be inside the Smith-chart is $|\angle Z_f < 0.5|\alpha|\pi|$. Then, as α increases, the Smith chart includes more and more load impedances which can't be represented in lower fractional-orders.

5. CONCLUSION

This paper presents a comparison between the fundamental equations of the impedance/admittance fractional-order Smith chart, intersection points with both the real and imaginary reflection coefficients, the peak value associated with each fractional-order chart, area inside, central angle, and the necessary condition of the plotting for any load impedance.

REFERENCES

1. Strukov, D. B., G. S. Snider, D. R. Stuwart, and R. S. Williams, "The missing memristor found," *Nature*, Vol. 453, 80–83, 2008.
2. Sabatier, J., O. P. Agrawal, and J. A. Tenreiro Machado, *Advances in Fractional Calculus; Theoretical Developments and Applications in Physics and Engineering*, Springer, 2007.
3. Carlson, G. and C. Halijak, "Approximation of fractional capacitors $(1/s)^{1/n}$ by a regular Newton process," *IEEE Transactions on Circuits and Systems I*, Vol. 11, 210–213, 1964.
4. Biswas, K., S. Sen, and P. Dutta, "Realization of a constant phase element and its performance study in a differentiator circuits," *IEEE Transactions on Circuits and Systems III*, Vol. 53, 802–806, 2006.
5. Haba, T. C., G. Ablart, T. Camps, and F. Olivie, "Influence of the electrical parameters on the input impedance of a fractal structure realised on silicon," *Chaos, Solitons and Fractals*, Vol. 24, 479–490. 2005.
6. Nakagawa, M. and K. Sorimachi, "Basic characteristics of a fractance device," *IEICE Transactions on Fundamentals of Electronics Communications and Computer Sciences*, Vol. E75, No. 12, 1814–1819, 1992.
7. Radwan, A. G., A. S. Elwakil, and A. M. Soliman, "Fractional-order sinusoidal oscillators: Design procedure and practical examples," *IEEE Transactions on Circuits and Systems I*, Vol. 55, No. 7, 2051–2063, 2008.

8. Radwan, A. G., A. S. Elwakil, and A. M. Soliman, "On the generalization of second-order filters to fractional-order domain," *Journal of Circuits Systems & Computers*, Vol. 18, No. 2, 361–386, 2009.
9. Machado, J., I. S. Jesus, A. Galhano, and J. B. Cunha, "Fractional order electromagnetics," *Signal Processing*, Vol. 86, 2637–2644, 2006.
10. Magin, R. L., *Fractional Calculus in Bioengineering*, Begell House, Connecticut, 2006.
11. Pozar, D. M., *Microwave Engineering*, 3rd Edition, 64–66, 223–227, John Wiley & Sons, 2005.
12. Zelley, C., "A spherical representation of the Smith chart," *IEEE Microwave Magazine*, Vol. 8, No. 3, 60–66, Jun. 2007.
13. Wu, Y., Y. Zhang, Y. Liu, and H. Huang, "Theory of the spherical generalized smith chart," *Microwave and Optical Technology Letters*, Vol. 51, No. 1, 95–97, Jan. 2009.
14. Shamim, A., A. G. Radwan, and K. N. Salama, "Fractional smith chart theory and application," *IEEE Microwave and Wireless Components Letters*, Vol. 21, No. 3, 117–119, 2011.
15. Radwan, A. G., A. Shamim, and K. N. Salama, "Theory of fractional order elements based impedance matching networks," *IEEE Microwave and Wireless Components Letters*, Vol. 21, No. 3, 120–122, 2011.

Algorithm Improvement for Real Time ILIDS Analysis in Airborne Research

Huanhuan Shen[1], **Marc Brunel**[1], **Gérard Grehan**[1], **Arnaud Querel**[2], **Pascal Lemaitre**[2], **and Emmanuel Porcheron**[2]

[1]UMR 6614 CORIA CNRS, Université de Rouen, France
[2]IRSN/DSU/SERAC/LECEV, Saclay, France

Abstract— We present a real-time algorithm to analyse ILIDS interferograms in airborne research, and propose a numerical implementation of image stretching to replace Scheimpflug systems, and simplify the design of the airborne instrument.

1. INTRODUCTION

Our objective is to develop an airborne optical spectrometer for atmospheric water droplets measurements (droplets diameters in the range 20–200 micrometers). The technique used is Interferometric Laser Imaging Droplet Sizing (ILIDS) which provides the instantaneous size and spatial distribution of transparent and spherical particles in a section of a flow [1, 2]. In ILIDS, the images of the droplets are captured with a CCD camera positioned in a non-focal plane (out-of-focus imaging). The camera records the interferometric pattern of the laser light scattered by the particles. In our airborne system, the analysis must be fast enough to perform real-time processing during a flight through clouds. In order to realize a high-speed analysis of ILIDS interferograms, a Fourier analysis based on fast-Fourier transforms has been developed. Experimentally, a frequency-doubled pulsed Nd: YAG laser is extended using a cylindrical lens in order to create a laser sheet. The ILIDS scattered field is recorded at a scattering angle of 66° (which allows to obtain the best fringe contrast). As the camera is not perpendicular to the laser sheet, the images suffer some aberrations: focusing properties are indeed not identical on both right hand-side and left hand-side of the images. A Scheimpflug apparatus has thus to be added to correct this property [3]. In the present paper we show that our high speed analysis can be improved to avoid the use of a Scheimpflug apparatus. The Scheimpflug is indeed an obstacle to the compact integration of the whole system in an airborne device. We present in this communication a numerical alternative. The communication will be organized as follows: we will first recall the principle of our airborne ILIDS system, and the principle of the algorithm that has been developed for real time analysis. In a second time, we will present the principle of an image distortion that can be done numerically to avoid the introduction of a Scheimpflug system in the set-up.

2. REAL-TIME ALGORITHM FOR ILIDS ANALYSIS

The principle of ILIDS is detailed in Figure 1. A pulsed laser sheet is sent toward a group of droplets. The scattering light is collected by a receiving optics. The images are captured with a CCD camera positioned in a non-focal plane (out-of-focus imaging). The camera records the interferometric pattern of the laser light scattered by the particles. This pattern results from the interference between the light reflected at the droplet surface and the light refracted within the droplet (i.e., the glare points). Each droplet is thus associated to a circular fringe pattern. For each droplet, the number of fringes (or the fringe frequency) is linked to the droplet diameter, by a factor which depends on the receiving optics parameters (numerical aperture, focal length, out-of-focus distance ...). To illustrate the method, Figure 2 shows an experimental ILIDS interferogram, and a synthesized interferogram.

Using a geometrical optic approach it can be shown that the droplet diameter d is linked to the number of fringes, and thus to the fringe frequency of an out-of-focus particle image. With this approach, the particle diameter d can be indeed related to the number of fringes N appearing in the interferometric image through the relation:

$$d = \frac{2\lambda N}{\alpha}\left(\cos(\theta/2) - \frac{m\sin(\theta/2)}{\sqrt{m^2 - 2m\cos(\theta/2)+1}}\right)^{-1} \quad (1)$$

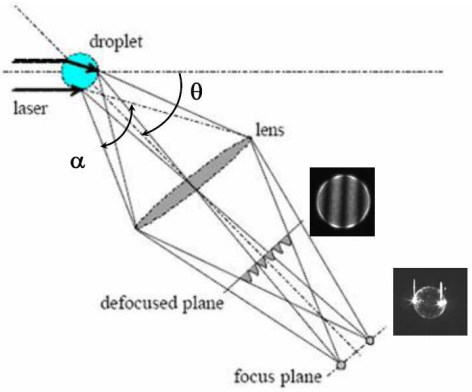

Figure 1: ILIDS set-up.

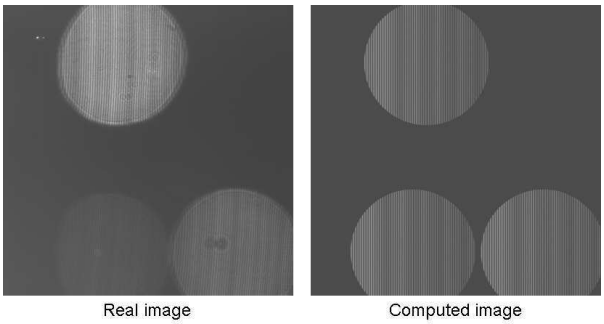

Figure 2: Experimental and simulated ILIDS interferograms.

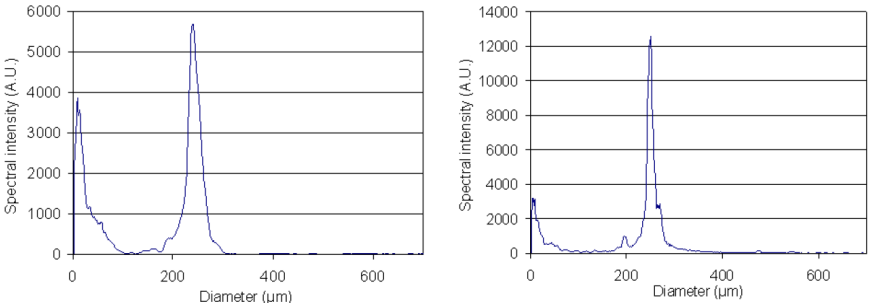

Figure 3: Dropplet's histogram obtained from real and simulated ILIDS interferograms.

where θ is the scattering angle, α is the aperture angle of the collecting imaging system, d and m are the diameter and the refractive index of the droplet respectively, and λ the wavelength of the laser sheet. In this case, the surrounding medium is air. The common approach for ILIDS interferogram analysis is to detect each fringe pattern present in the image and then determine the droplet size distribution using Equation (1). The drawback of this method for our application is the computation time due to the detection of each fringe pattern. In our case, the analysis must be fast enough to perform real-time processing during a flight through clouds. We do not look for any local analysis per droplet but we need a global image analysis. In order to realize a high-speed analysis of ILIDS interferogram, a Fourier analysis has thus been developed. Let us consider an ILIDS interferogram with vertical fringes (as in Figure 2). Our analysis require 2 major steps:

- First a Fourier transform along the x-axis of this image,
- Then a Radon transform of angle 0° (i.e., for each abscissa, summation of the intensity of all pixels present in the corresponding column) with an x-axis calibration to visualize directly the droplet size scale instead of the fringe frequency. This step will require the relation (1).

Based solely on one fast Fourier transform, this algorithm allows high speed numerical analysis. For example, Figure 3 shows the histograms obtained applying our algorithm to the images of Figure 2. More details can be found in reference [3].

3. NUMERICAL CORRECTION OF FRINGE'S CHIRP IN PLACE OF SCHEIMPFLUG SYSTEM

Our scattering angle is around $\theta = 66°$ (this angle allows to obtain the best fringe contrast). As the camera is not perpendicular to the laser sheet, the images suffer some aberrations: we should indeed observe a progressive chirp of the fringe frequency along the x-axis of the images in Figure 2, which is actually corrected experimentally by a Scheimpflug apparatus. We show now how ILIDS images can be numerically stretched to correct this fringe frequency distortion, in place of an experimental Scheimpflug system.

Figure 4 details the problem. Using a scattering angle $\theta = 90°$, we would observe the out-of-focus image of droplet A (symbolized by its two glare points). As the scattering angle is $\theta = 66°$, we observe actually the out-of-focus image of droplet B (symbolized by its two glare points). For a

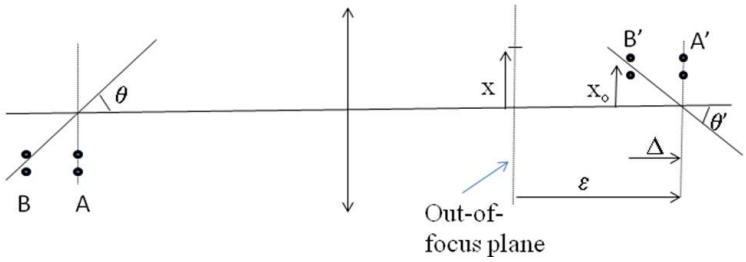

Figure 4: Calibration curve giving inter-glare points distance versus droplets diameter.

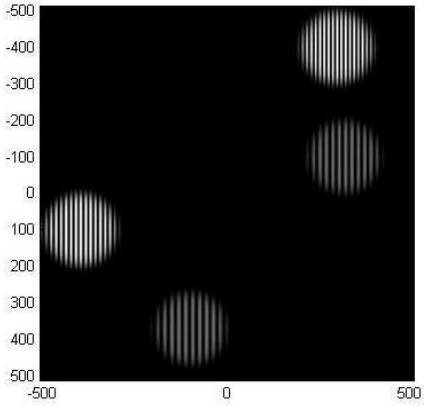

Figure 5: ILIDS image with fringe's chirp due to the 66° scattering angle.

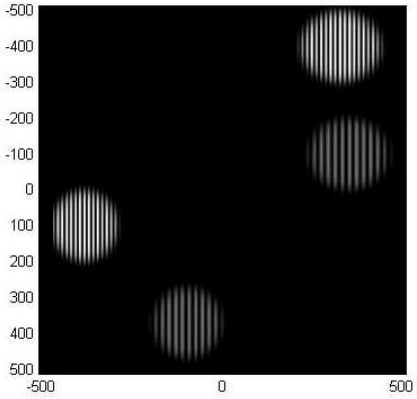

Figure 6: Stretched ILIDS image where the fringe's chirp is numerically corrected.

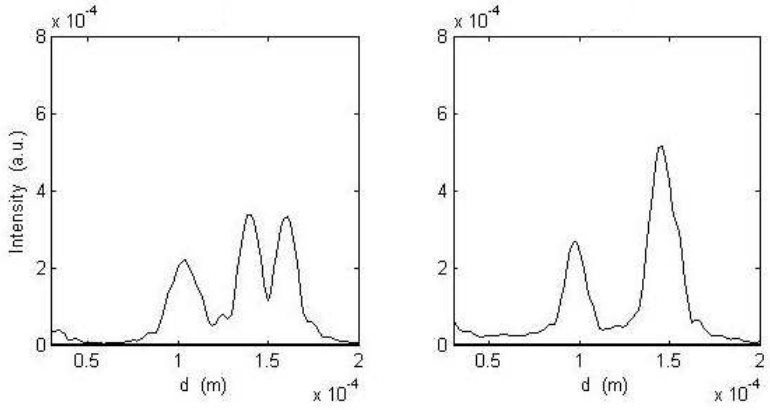

Figure 7: (a) Histograms obtained from ILIDS image affected by a frequency's chirp, and (b) the corrected stretched image.

droplet of diameter d, the distance between the two glare points can be noted βd (with $\beta < 1$). In the out-of-focus plane of the CCD, at abscissa x, the path way difference δ for the droplet whose focus image B' is located at x_o can be expressed by relation:

$$\frac{x - x_o}{\varepsilon - \Delta} \approx \frac{\delta}{\beta\, d} \quad \text{where} \quad \Delta = x_o / \tan(\theta').$$

In ILIDS images, the fringe frequency is proportional to δ. In first approximation, the fringe frequency can thus be related to the droplet's image position x_o through relation:

$$\text{fringe frequeny} \quad \propto \quad \frac{x - x_o}{\varepsilon - x_o / \tan(\theta')} \tag{2}$$

Figure 5 shows an example of distorted image. We have developed an algorithm to stretch numerically this image, inversely to relation (2). The stretched image is presented in Figure 6.

Figure 7 shows finally the histograms obtained applying our real-time ILIDS analysis to the original image of Figure 5 and to the numerically stretched image of Figure 6. The images were obtained considering droplets whose diameters are 100 or 150 µm. The real-time ILIDS analysis delivers an erronate histogram using the ILIDS image of Figure 5 affected by fringe's chirp Figure 7(a). The image stretching allows to correct this error Figure 7(b).

4. CONCLUSION

In conclusion, we have presented a real-time algorithm to analyse ILIDS interferograms, and proposed a numerical implementation of image stretching to replace Scheimpflug systems. Next developments will concern the experimental validation of image stretching implementation, and the development of an airborne system combining ILIDS images and digital holography techniques [4] to improve the range of droplet's diameters to be analysed.

ACKNOWLEDGMENT

This work is supported by the European EUFAR project.

REFERENCES

1. König, G., K. Anders, and A. Frohn, "A new light-scattering technique to measure the diameter of periodically generated moving droplets," *J. Aerosol Sci.*, Vol. 17, 157, 1986.
2. Glover, A. R., S. M. Skippon, and R. D. Boyle, "Interferometric laser imaging for droplet sizing: A method for droplet-size measurement in sparse spray systems," *Appl. Opt.*, Vol. 34, 8409, 1995.
3. Quérel, A., P. Lemaitre, M. Brunel, E. Porcheron, and G. Gréhan, "Real time global interferometric laser imaging for droplet sizing (ILIDS) analysis for airbone research," *Measurement Science and Technology*, Vol. 21, 015306, 2010.
4. Brunel, M., S. Coëtmellec, D. Lebrun, and K. Aït Ameur, "Digital phase contrast with the fractional Fourier transform," *Appl. Opt.*, Vol. 48, 579–583, 2009.

An Improved Inverse Scattering Transform for DNLS$^+$ Equation under Nonvanishing Boundary Condition

Guo-Quan Zhou[1, 2]

[1]Department of Physics, Wuhan University, Wuhan 430072, China
[2]Department of Mathematics, The University of Vermont, Burlington, VT 05401, USA

Abstract— A revised inverse scattering transform (IST for brevity) for the derivative nonlinear Schrödinger (DNLS$^+$) equation with nonvanishing boundary condition (NVBC) and normal group velocity dispersion is proposed by introducing an affine parameter in Zakharov-Shabat integral; the explicit breather-type one soliton solution has been derived, which can reproduce the one pure soliton at the degenerate case and the the one bright soliton solution at the limit of vanishing boundary, verifying the validity of the improved IST.

1. INTRODUCTION

One of the several typical and rarely intelgrable nonlinear models, the derivative nonlinear Schrödinger (DNLS for brevity) equation,

$$iu_t - u_{xx} + i\left(|u|^2 u\right)_x = 0, \tag{1}$$

can be used to describe nonlinear waves with normal group velocity dispersion in many fields, especially the Alften wave in plasma, the pulse in optical fibers, the weak nonlinear electromagnetic waves in (anti-) ferromagnetic or dielectric systems under external magnetic field [1–6].

Kaup and Newell proposed a modified IST in Reference [2] to make a convergent integral of the Cauchy contour. The soliton solution gotten from their IST for the VBC case had a self-dependent and complicated phase factor. For the DNLS equation with NVBC, many heuristic and interesting results had been attained [3, 4]. Reference [1] had attained a pure single dark/bright soliton solution to the DNLS equation with NVBC. By introducing an affine parameter in the Zakharov-Shabat integral kern, Reference [3] had found their pure N-soliton solution for a special case that all the simple poles (zeros of $a(\lambda)$) were located on a circle of radius ρ centered at the origin. Reference [4] had found its multi-soliton solution for some extended case with N poles on a circle and M poles out of the circle, and further developed its perturbation theory based on IST. References [3, 4] constructed their theory based on modified IST which is similar to that was used by Kaup and Newell to deal with the VBC case for DNLS equation and further adopted a good idea of introducing an affine parameter to avoid the trouble caused by multi-value problem in Riemann sheets, but their results are assumed N-soliton solutions because Reference [3] should verify an identity demanded by the standard form of a soliton solution. (see expression (51) in Reference [3]). Such an identity is rather difficult to prove for $N \geq 2$ case even by use of computer techniques and Mathematica. And author of Reference [4] also admits that his soliton solution is short of a rigorous verification. A newly revised IST is thus proposed to avoid the dual difficulty and the excessive complexity. The resulted one soliton solution can naturally tend to the well-established conclusions and appears to be strict and reliable.

2. THE FUNDAMENTAL CONCEPTS FOR THE IST THEORY OF DNLS EQUATION

Under a Galileo transformation $(x, t) \to (x + \rho^2 t, t)$, the DNLS$^+$ Equation (1) can be changed into

$$iu_t - u_{xx} + i\left[\left(|u|^2 - \rho^2\right)u\right]_x = 0 \tag{2}$$

with nonvanishing boundary condition $|u| \to \rho$, as $|x| \to \infty$. According to References [2, 3], the phase difference between the two infinite ends should be zero. The Lax pair of DNLS$^+$ Equation (2) is

$$\mathbf{L} = -i\lambda^2\sigma_3 + \lambda\mathbf{U}, \quad \mathbf{U} = \begin{pmatrix} 0 & u \\ \bar{u} & 0 \end{pmatrix} = u\sigma_+ + \bar{u}\sigma_- \tag{3}$$

$$\mathbf{M} = i2\lambda^4\sigma_3 - 2\lambda^3\mathbf{U} + i\lambda^2\left(U^2 - \rho^2\right)\sigma_3 - \lambda\left(U^2 - \rho^2\right)\mathbf{U} + i\lambda U_x\sigma_3 \tag{4}$$

where σ_3 and σ_+, σ_- involve standard Pauli's matrices and their linear combination. Here and hereafter a bar over a variable represents complex conjugate. An affine parameter ζ and two aided

parameters $\kappa \equiv (\zeta - \rho^2\zeta^{-1})/2$, and $\lambda \equiv (\zeta + \rho^2\zeta^{-1})/2$, are introduced to avoid the trouble caused by treatment of double-valued function on Riemann sheets.

The Jost functions satisfy equation $\partial_x \mathbf{F}(x,\zeta) = \mathbf{L}(x,\zeta)\mathbf{F}(x,\zeta)$; $\mathbf{F}(x,\zeta) \in \{\Psi(x,\zeta), \Phi(x,\zeta)\}$,

$$\Psi(x,\zeta) = (\tilde{\psi}(x,\zeta), \psi(x,\zeta)) \to \mathbf{E}(x,\zeta), \quad \text{as} \quad x \to \infty \tag{5}$$

$$\Phi(x,\zeta) = (\phi(x,\zeta), \tilde{\phi}(x,\zeta)) \to \mathbf{E}(x,\zeta), \quad \text{as} \quad x \to -\infty \tag{6}$$

The free Jost functions $\mathbf{E}(x,\zeta)$, an 2×2 matrix function, can be easily attained and expressed as

$$\mathbf{E}(x,\zeta) = (\mathbf{I} + \rho\zeta^{-1}\sigma_2)\exp(-i\lambda\kappa x\sigma_3). \tag{7}$$

The monodramy or transition matrix is

$$\mathbf{T}(\zeta) = \begin{pmatrix} a(\zeta) & \tilde{b}(\zeta) \\ b(\zeta) & \tilde{a}(\zeta) \end{pmatrix}, \tag{8}$$

which satisfies $\Phi(x,\zeta) = \Psi(x,\zeta)\mathbf{T}(\zeta)$. Some useful and important symmetry properties can be found

$$\sigma_1\bar{\mathbf{L}}(\zeta)\sigma_1 = \mathbf{L}(\bar{\zeta}), \quad \sigma_3\mathbf{L}(-\zeta)\sigma_3 = \mathbf{L}(\zeta) \tag{9}$$

$$\tilde{\psi}(x,\zeta) = \sigma_1\overline{\psi(x,\bar{\zeta})} \quad , \tilde{\phi}(x,\zeta) = \sigma_1\overline{\phi(x,\bar{\zeta})} \tag{10}$$

$$\tilde{\psi}(x,-\zeta) = \sigma_3\tilde{\psi}(x,\zeta), \quad \psi(x,-\zeta) = -\sigma_3\psi(x,\zeta) \tag{11}$$

$$\tilde{a}(\bar{\zeta}) = \overline{a(\zeta)}, \quad \tilde{b}(\zeta) = \overline{b(\zeta)}, \quad a(-\zeta) = a(\zeta), \quad b(-\zeta) = -b(\zeta). \tag{12}$$

Other important symmetry properties called reduction relation can also be easily found

$$\lambda\left(\rho^2\zeta^{-1}\right) = \lambda(\zeta), \quad \kappa\left(\rho^2\zeta^{-1}\right) = -\kappa(\zeta) \tag{13}$$

$$\mathbf{E}\left(x,\rho^2\zeta^{-1}\right) = \rho^{-1}\zeta\left(\mathbf{I} + \rho\zeta^{-1}\sigma_2\right)e^{-i\kappa\lambda x\sigma_3}\sigma_2 \tag{14}$$

$$\tilde{\psi}\left(x,\rho^2\zeta^{-1}\right) = i\rho^{-1}\zeta\psi(x,\zeta), \quad \psi\left(x,\rho^2\zeta^{-1}\right) = -i\rho^{-1}\zeta\tilde{\psi}(x,\zeta) \tag{15}$$

$$\phi\left(x,\rho^2\zeta^{-1}\right) = i\rho^{-1}\zeta\tilde{\phi}(x,\zeta), \quad \tilde{\phi}\left(x,\rho^2\zeta^{-1}\right) = -i\rho^{-1}\zeta\phi(x,\zeta) \tag{16}$$

$$\tilde{a}\left(\rho^2\zeta^{-1}\right) = a(\zeta), \quad \tilde{b}\left(\rho^2\zeta^{-1}\right) = -b(\zeta). \tag{17}$$

On the other hand, the single simple poles, or zeros of $a(\zeta)$, appear in pairs, and can be designed by ζ_n, $(n = 1, 2, \ldots, 2N)$, in the I quadrant, and $\zeta_{n+2N} = -\zeta_n$ in the III quadrant. Considering (12) and (17), the subset of zero points is $\{\zeta_1, \zeta_2 = \rho^2\bar{\zeta}_1^{-1}, \zeta_3 = -\zeta_1, \zeta_4 = -\zeta_2 = -\rho^2\bar{\zeta}_1^{-1}\}$.

According to the standard procedure, the discrete part of $a(\zeta)$ can be deduced to be

$$a(\zeta) = \prod_{n=1}^{2N} \frac{\zeta^2 - \zeta_n^2}{\zeta^2 - \overline{\zeta_n^2}} \frac{\overline{\zeta_n}}{\zeta_n} \tag{18}$$

At ζ_n, the zeros of $a(\zeta)$, we have

$$\phi(x,\zeta_n) = b_n\psi(x,\zeta_n), \quad \dot{a}(-\zeta_n) = -\dot{a}(\zeta_n) \tag{19}$$

By the asymptotic behaviors of the Jost solutions in the limit of $|\zeta| \to \infty$, we find a useful formula for relation between the solution and Jost functions of DNLS$^+$ equation

$$\bar{u} = -i \lim_{|\zeta|\to\infty} \frac{\zeta\tilde{\psi}_2(x,\zeta)}{\tilde{\psi}_1(x,\zeta)} \tag{20}$$

3. ZAKHAROV-SHABAT EQUATIONS AND THE BREATHER-TYPE N-SOLITON SOLUTION

A 2×1 column Function $\Pi(x,\lambda)$ is introduced as usual

$$\Pi(x,\zeta) \equiv \begin{cases} \frac{1}{a(\zeta)}\phi(x,\zeta), & \text{as } \zeta \text{ in I, III quadrants.} \\ \tilde{\psi}(x,\zeta), & \text{as } \zeta \text{ in II, IV quadrants.} \end{cases} \tag{21}$$

There is an abrupt jump for $\Pi(x,\zeta)$ across both real and imaginary axes

$$a(\zeta)^{-1}\phi(x,\zeta)-\tilde{\psi}(x,\zeta)=r(\zeta)\psi(x,\zeta) \tag{22}$$

where $r(\zeta)=b(\zeta)/a(\zeta)$, is called the reflection coefficient. The usual procedure of constructing the IST equation by a Cauchy contour integral was proved difficult. In view of the abortive experience, we proposed a revised method to derive a suitable IST and the corresponding Z-S equation by multiplying an inverse spectral parameter $1/\lambda$, $\lambda=(\zeta+\rho^2\zeta^{-1})/2$ before the Z-S integral kern. Meanwhile, our modification produces no new poles since the Lax operator $\mathbf{L}\to 0$, as $\lambda\to 0$. Under reflectionless case, i.e., $r(\zeta)=0$, the Cauchy integral along with contour Γ shown as Figure 1 gives

$$\frac{1}{\lambda}\left\{\Pi(x,\zeta)-\mathbf{E}_{\cdot 1}(x,\zeta)\right\}e^{i\lambda\kappa x}=\frac{1}{2\pi i}\oint_{\Gamma}d\zeta'\frac{1}{\zeta'-\zeta}\frac{1}{\lambda'}\left\{\Pi(x,\zeta')-\mathbf{E}_{\cdot 1}(x,\zeta')\right\}e^{i\lambda'\kappa' x} \tag{23}$$

$$\text{Or}\qquad \psi(x,\zeta)=e^{-i\lambda\kappa x}+\lambda\left\{-\sum_{n=1}^{4}\frac{1}{\lambda_n}\frac{1}{\zeta_n-\zeta}c_n\psi(x,\zeta_n)e^{i\lambda_n\kappa_n x}\right\}e^{-i\lambda\kappa x} \tag{24}$$

where $c_n\equiv b_n/\dot{a}(\zeta_n)$. Note (7) and (21) has been used in (23)–(24). The minus sign before the sum of residue number in (24) comes from the clock-wise contour integrals around every single simple pole.

By a standard procedure, the time dependences of b_n and c_n can be derived as follows

$$b_n(t)=b_{n0}e^{-i4\lambda_n^3\kappa_n t},\quad c_n=c_n(0)e^{-i4\lambda_n^3\kappa t},\quad c_n(0)=b_{n0}/dota_n \tag{25}$$

In the reflectionless case, the Zakharov-Shabat equations for DNLS$^+$ equation can be derived from (24)

$$\tilde{\psi}_1(x,\zeta)\;=\;e^{-i\Lambda x}+\lambda\left[\sum_{n=1}^{2}\frac{2\zeta}{\lambda_n}\frac{1}{\zeta^2-\zeta_n^2}c_n\psi_1(x,\zeta_n)e^{i\Lambda_n x}\right]e^{-i\Lambda x} \tag{26}$$

$$\tilde{\psi}_2(x,\zeta)\;=\;i\rho\zeta^{-1}e^{-i\Lambda x}+\lambda\left[\sum_{n=1}^{2}\frac{2\zeta_n}{\lambda_n}\frac{1}{\zeta^2-\zeta_n^2}c_n\psi_2(x,\zeta_n)e^{i\Lambda_n x}\right]e^{-i\Lambda x} \tag{27}$$

here $\Lambda\equiv\lambda\kappa$, $\Lambda_n\equiv\lambda(\zeta_n)\kappa(\zeta_n)=\lambda_n\kappa_n$. Note that in Equations (26) and (27), the terms corresponding to poles ζ_n, $(n=1,2,\ldots,2N)$, have been combined with the terms related to poles $\zeta_{n+2N}=-\zeta_n$. Substituting Equations (26) and (27) into formula (20) and letting $\zeta\to\infty$, we thus attain the conjugate of the raw N-soliton solution (time dependence is suppressed)

$$\bar{u}_N\;=U_N/V_N \tag{28}$$

$$U_N\;\equiv\rho\left[1-\sum_{n=1}^{2N}i\frac{\zeta_n}{\rho\lambda_n}c_n\psi_2(x,\zeta_n)e^{i\Lambda_n x}\right];\quad V_N\equiv 1+\sum_{n=1}^{2N}\frac{c_n}{\lambda_n}\psi_1(x,\zeta_n)e^{i\Lambda_n x} \tag{29}$$

Letting $\zeta=\rho^2\zeta_m^{-1}$, $(m=1,2,\ldots,2N)$ respectively in Equations (26) and (27), by use of reduction symmetry relations (15)–(17), we can further change Equations (26)–(27) into following form

$$\psi_1(x,\zeta_m)\;=\;-i\rho\zeta_m^{-1}e^{i\Lambda_m x}+\sum_{n=1}^{2N}\frac{\lambda_m c_n}{\lambda_n\zeta_m^2}\frac{2\rho^3}{i\left(\rho^4\zeta_m^{-2}-\zeta_n^{-2}\right)}\psi_1(x,\zeta_n)e^{i(\Lambda_n+\Lambda_m)x} \tag{30}$$

$$\psi_2(x,\zeta_m)\;=\;e^{i\Lambda_m x}+\sum_{n=1}^{2N}\frac{\lambda_m\zeta_n c_n}{\lambda_n\zeta_m}\cdot\frac{2\rho}{i\left(\rho^4\zeta_m^{-2}-\zeta_n^{-2}\right)}\psi_2(x,\zeta_n)e^{i(\Lambda_n+\Lambda_m)x} \tag{31}$$

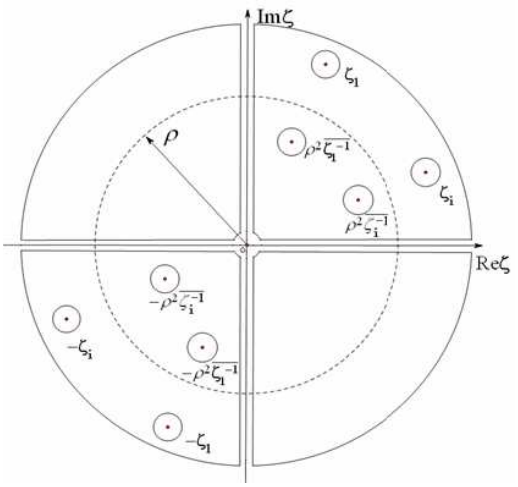

Figure 1: The integral path for IST of the DNLS$^+$.

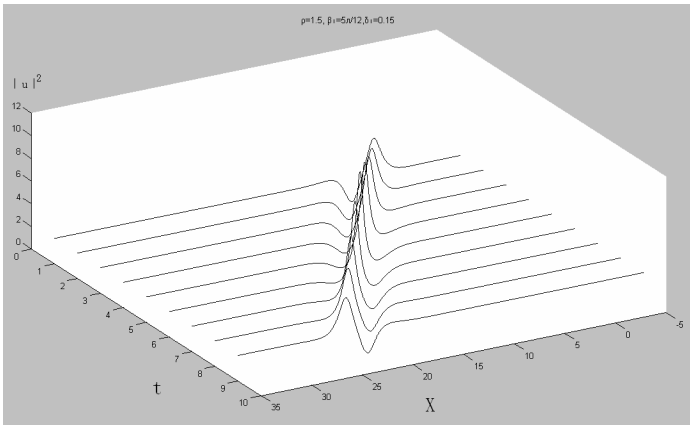

Figure 2: Evolution of one breather solution.

$m = 1, 2, \ldots, 2N$. To solve Equation (31), we define that

$$(\varphi_2)_n \equiv i\frac{\zeta_n}{\rho\lambda_n}\sqrt{\frac{c_n}{2}}\psi_2(x,\zeta_n), \quad \varphi_2 \equiv ((\varphi_2)_1, (\varphi_2)_2, \ldots (\varphi_2)_{2N}) \tag{32}$$

$$f_n \equiv \sqrt{2c_n}e^{i\Lambda_n x}, \quad g_n \equiv i\sqrt{\frac{c_n}{2}}\frac{\zeta_n}{\rho\lambda_n}e^{i\Lambda_n x} = \frac{i\zeta_n}{2\rho\lambda_n}f_n, \quad n = 1, 2, \ldots, 2N \tag{33}$$

$$\mathbf{f} \equiv (f_1, f_2, \ldots, f_{2N}), \quad \mathbf{g} \equiv (g_1, g_2, \ldots, g_{2N}) \tag{34}$$

$$\mathbf{B} \equiv Matrix(B_{nm})_{2N\times 2N} \text{ with } B_{nm} \equiv f_n\frac{\rho}{i\left(\zeta_n^2 - \rho^4\zeta_m^{-2}\right)}f_m, \quad m, n = 1, 2, \ldots, 2N.$$

Then Equation (31) can be rewritten in compact form

$$\varphi_2 = \mathbf{g} - \varphi_2\mathbf{B}; \quad \text{or} \quad \varphi_2 = \mathbf{g}(\mathbf{I}+\mathbf{B})^{-1} \tag{35}$$

On the other hand, according to (29) and (35), U_N can be rewritten as

$$U_N = \rho\left[1 - \varphi_2\mathbf{f}^T\right] = \rho\left[1 - \mathbf{g}(\mathbf{I}+\mathbf{B})^{-1}\mathbf{f}^T\right] = \rho\frac{\det(\mathbf{I}+\mathbf{B}-\mathbf{f}^T\mathbf{g})}{\det(\mathbf{I}+\mathbf{B})} = \rho\frac{\det(\mathbf{I}+\mathbf{A})}{\det(\mathbf{I}+\mathbf{B})} \tag{36}$$

where $\mathbf{A} \equiv \mathbf{B} - \mathbf{f}^T\mathbf{g}$, with $A_{nm} \equiv B_{nm} - f_n g_m = \frac{\zeta_m\zeta_n\lambda_n}{\rho^2\lambda_m}B_{nm}$. Superscript "$T$" represents transposing of a matrix. To solve Equation (30), we define that

$$(\varphi_\mathbf{1})_m \equiv i\sqrt{\frac{c_m}{2}}\frac{\zeta_m}{\rho\lambda_m}\psi_1(x,\zeta_m), \quad \varphi_1 \equiv ((\varphi_1)_1, (\varphi_1)_2, \ldots, (\varphi_1)_{2N}) \tag{37}$$

$$f_m^{'} \equiv i\sqrt{2c_m}\cdot\frac{\rho}{\zeta_m}e^{i\Lambda_m x} = i\frac{\rho}{\zeta_m}f_m, \quad g_m^{'} = \sqrt{\frac{c_m}{2}}\cdot\frac{1}{\lambda_m}e^{i\Lambda_m x} = \frac{-i\zeta_m}{2\rho\lambda_m}f_m^{'} \tag{38}$$

$$\mathbf{f}^{'} = \left(f_1^{'}, f_2^{'}, \ldots, f_{2N}^{'}\right); \quad \mathbf{g}^{'} = (g_1^{'}, g_2^{'}, \ldots, g_{2N}^{'}); \tag{39}$$

$$D_{nm}^{'} \equiv f_n^{'}\left[\frac{-\rho}{i(\zeta_n^2 - \rho^4\zeta_m^{-2})}\right]f_m^{'} = \frac{\rho^2}{\zeta_n\zeta_m}B_{nm} \tag{40}$$

with $n, m = 1, 2, \ldots, 2N$. Then Equation (30) can be rewritten in a compact form

$$\varphi_1 = \mathbf{g}^{'} - \varphi_1\mathbf{D}^{'}, \quad \text{or} \quad \varphi_1 = \mathbf{g}^{'}(\mathbf{I}+\mathbf{D}^{'})^{-1} \tag{41}$$

On the other hand, according to (29) and (41), V_N can be rewritten as

$$\begin{aligned} V_N &= 1-\sum_{n=1}^{2N}(\varphi_1)_n f_n^{'} = 1-\varphi_1 \mathbf{f}^{'T} = 1-\mathbf{g}^{'}(\mathbf{I}+\mathbf{D})^{-1}\mathbf{f}^{'T} \\ &= \frac{\det(\mathbf{I}+\mathbf{D}^{'}-\mathbf{f}^{'T}\mathbf{g}^{'})}{\det(\mathbf{I}+\mathbf{D}^{'})} \equiv \frac{\det(\mathbf{I}+\mathbf{B}^{'})}{\det(\mathbf{I}+\mathbf{D}^{'})} \end{aligned} \tag{42}$$

where use is made of formula $B'_{nm} \equiv (D' - f'^T g')_{nm} = \frac{\zeta_m \zeta_n \lambda_n}{\rho^2 \lambda_m} D'_{nm} = \frac{\lambda_n}{\lambda_m} B_{nm}$.

In the end, by substituting (36) and (42) into (28), we attain the N-soliton solution to the DNLS$^+$ Equation (2) under NVBC in the reflectionless case (Note that the time dependence of the soliton solution naturally emerged in $c_n(t)$),

$$\bar{u}(x,t) = \frac{U_N}{V_N} = \rho \frac{\det(\mathbf{I}+\mathbf{A})\det(\mathbf{I}+\mathbf{D}')}{\det(\mathbf{I}+\mathbf{B})\det(\mathbf{I}+\mathbf{B}')} \equiv \rho \frac{C_N D_N}{\overline{D_N}^2}, \tag{43}$$

here $C_N \equiv \det(\mathbf{I}+\mathbf{A})$, $\overline{D}_N \equiv \det(\mathbf{I}+\mathbf{B})$. The solution has a standard form due to

$$\det(\mathbf{I}+\mathbf{B}') = \det(\mathbf{I}+\mathbf{B}), \quad \overline{\det(\mathbf{I}+\mathbf{D}')} = \det(\mathbf{I}+\mathbf{B}), \tag{44}$$

which can be proved by direct calculation for the $N=1$ case and by some special algebra techniques for the $N>1$ case. In order to get an explicit N-soliton solution to the DNLS$^+$ Equation (1) with NVBC, firstly we need to make an inverse Galileo transformation of (2) by $(x,t) \to (x-\rho^2 t, t)$. If we define $\zeta_n \equiv \rho e^{\delta_n + i\beta_n}$, with $\delta_n > 0$, $\beta_n \in (0, \pi/2)$, then some typical expressions for soliton solution are as follows

$$B_{nn} = f_n^2 \frac{\rho}{i(\zeta_n^2 - \rho^4 \zeta_n^{-2})} = \frac{2\rho}{i(\zeta_n^2 - \rho^4 \zeta_n^{-2})} \frac{b_n(0)}{\dot{a}(\zeta_n)} \exp i2\Lambda_n \left[(x - (2\lambda_n^2 + \rho^2)t\right] \tag{45}$$

$$b_n(0) \exp i2\Lambda_n \left[(x - (2\lambda_n^2 + \rho^2)t\right] \equiv \exp(-\theta_n + i\phi_n) \tag{46}$$

$$\theta_n(x,t) \equiv \nu_n(x - \upsilon_n t - x_{n0}); \quad \varphi_n(x,t) \equiv \mu_n(x - \eta_n t) + \varphi_{n0} \tag{47}$$

$$\mu_n = \rho^2 \cos 2\beta_n sh2\delta_n; \quad \nu_n = \rho^2 \sin 2\beta_n ch2\delta_n \tag{48}$$

$$\upsilon_n = \rho^2 \left(2 + ch4\delta_n \cos 2\beta_n / ch2\delta_n\right), \quad \eta_n = \rho^2 \left(2 + ch2\delta_n \cos 4\beta_n / \cos 2\beta_n\right) \tag{49}$$

$$b_n(0) \equiv \exp(\nu_n x_{n0}) \exp(i\varphi_{n0}) \tag{50}$$

where $n = 1, 2, \ldots, 2N$; and the n'th constant factor $b_n(0)$ has been absorbed by redefinition of the n'th soliton center and initial phase in (47) by (50).

4. THE BREATHER-TYPE AND PURE ONE-SOLITON SOLUTIONS

We give two concrete examples — the one breather-type soliton solution and one pure soliton solution in illustration of the improved IST and the general explicit N-soliton formula.

In the case of one-soliton solution, $N=1$, $\zeta_1 \equiv \rho e^{\delta_1} e^{i\beta_1}$, $\zeta_2 \equiv \rho^2 \bar{\zeta}_1^{-1} = \rho e^{-\delta_1} e^{i\beta_1}$, and $\delta_1 > 0$, $\beta_1 \in (0, \pi/2)$, then direct calculation can verify (44). We finally attain

$$\bar{D}_1 = 1 + \frac{\sin 2\beta_1}{\sinh 2\delta_1} e^{i\beta_1} e^{-\theta_1} (e^{\delta_1} e^{i\varphi_1} + e^{-\delta_1} e^{-i\varphi_1}) - e^{i2\beta_1} e^{-2\theta_1} \tag{51}$$

$$C_1 = 1 + \frac{\sin 2\beta_1}{\sinh 2\delta_1} e^{i3\beta_1} e^{-\theta_1} (e^{3\delta_1} e^{i\varphi_1} + e^{-3\delta_1} e^{-i\varphi_1}) - e^{i6\beta_1} e^{-2\theta_1} \tag{52}$$

here we define $b_{10} e^{i2\lambda_1\kappa_1(x-2\lambda_1^2 t)} \equiv e^{-\theta_1} e^{i\varphi_1}$; $b_{10} = e^{\nu_1 x_{10}} e^{i\varphi_{10}}$; $-b_{20} e^{i2\lambda_2\kappa_2(x-2\lambda_2^2 t)} \equiv e^{-\theta_2} e^{i\varphi_2}$, and

$$\theta_1(x,t) \equiv \nu_1(x - \upsilon_1 t - x_{10}), \quad \varphi_1(x,t) \equiv \mu_1(x - \eta_1 t) + \varphi_{10} \tag{53}$$

with $\mu_1 = \rho^2 \cos 2\beta_1 sh2\delta_1$, $\nu_1 = \rho^2 \sin 2\beta_1 ch2\delta_1$

$$\upsilon_1 = \rho^2 \left(2 + ch4\delta_1 \cos 2\beta_1 / ch2\delta_1\right), \quad \eta_1 = \rho^2 \left(2 + ch2\delta_1 \cos 4\beta_1 / \cos 2\beta_1\right) \tag{54}$$

Due to $\theta_2 = \theta_1$, $\varphi_2 = -\varphi_1$; $-b_{20} = \bar{b}_{10}$, substituting (51)–(52) into following formula gives the one-soliton solution of DNLS$^+$ Equation (1)

$$\bar{u}_1(x,t) = \rho C_1 D_1/\bar{D}_1^2 = q_1(x,t), \quad \text{or} \quad u_1(x,t) = \rho \bar{C}_1 \bar{D}_1/D_1^2 \tag{55}$$

which is generally called one breather solution and shown in Figure 2.

Formula (55) contains the bright one-soliton solution of the DNLS equation with VBC as its special case. In the limit of $\rho \to 0$, $\delta_1 \to \infty$ but ρe^{δ_1} invariant, we have

$$\rho C_1 \to 4|\lambda_1| \sin 2\beta_1 e^{i3\beta_1} e^{-\theta_1} e^{i\varphi_1}; \quad \bar{D}_1 \to 1 - e^{i2\beta_1} e^{-2\theta_1}; \quad D_1 \to 1 - e^{-i2\beta_1} e^{-2\theta_1} \tag{56}$$

Substituting (56) into (55), we can attain

$$u_1(x,t) = 4|\lambda_1| \sin 2\beta_1 e^{-i3\beta_1} e^{-\theta_1} e^{-i\varphi_1} \left(1 - e^{i2\beta_1} e^{-2\theta_1}\right) / \left(1 - e^{-i2\beta_1} e^{-2\theta_1}\right)^2 \tag{57}$$

If we redefine $\zeta_1 = \rho e^{\delta_1} e^{i(\pi/2-\beta_1')}$, $\zeta_2 = \rho e^{-\delta_1} e^{i(\pi/2-\beta_1')}$, then $\bar{u}_1(x,t) = q(x,t)$, the complex conjugate of one-soliton solution in (57), perfectly reproduce the one-soliton solution that gotten in [2, 5, 6] for DNLS equation with VBC case, up to a permitted global constant phase factor. This verifies the validity of our formula of soliton solution and the reliability of the improved IST for the DNLS$^+$ with NVBC.

The degenerate case for $N = 1$, or the so-called pure one soliton, is also a typical illustration of the present improved IST. It can be dealt with by letting $\delta_1 \to 0$. The simple poles $\zeta_1 (= \rho e^{i\beta_1})$ and $\zeta_2 (= \rho^2 \bar{\zeta}_1^{-1} = \rho e^{i\beta_1})$ are coincident, so do $\zeta_3 (= -\zeta_1)$ and $\zeta_4 (= -\rho e^{i\beta_1})$. Meanwhile, from (45)–(50), $\mu_1 \to 0$, $\varphi_1 \to 0$, $\nu_1 = \rho^2 \sin 2\beta_1$, $-ib_{10} \in \Re$. Especially for the degenerate case, we have

$$a(\zeta) = \frac{\zeta^2 - \zeta_1^2}{\zeta^2 - \overline{\zeta_1^2}} \frac{\overline{\zeta_1}}{\zeta_1}, \quad c_1(0) = \frac{b_{10}}{\dot{a}(\zeta_1)} = b_{10} \frac{\zeta_1^2 - \bar{\zeta}_1^2}{2\zeta_1} \frac{\zeta_1}{\bar{\zeta}_1} \tag{58}$$

$$-ib_{10} e^{i2\lambda_1\kappa_1(x-2\lambda_1^2 t)} \equiv \varepsilon e^{-\theta_1}, \quad \theta_1(x,t) \equiv \nu_1(x - \upsilon_1 t - x_{10}) \tag{59}$$

with $\nu_1 = \rho^2 \sin 2\beta_1$, $\upsilon_1 = \rho^2(1 + 2\cos^2\beta_1)$, $\varepsilon = sgn(-ib_{10})$. Then from (45)–(50) we have

$$\bar{D} = 1 + \varepsilon e^{i\beta_1} e^{-\theta_1}, \quad \text{or} \quad D = 1 + \varepsilon e^{-i\beta_1} e^{-\theta_1}; \quad C = 1 + \frac{\zeta_1^2}{\rho^2} F_1 = 1 + \varepsilon e^{i3\beta_1} e^{-\theta_1} \tag{60}$$

$$\begin{aligned} \bar{u}_1(x,t) &= \rho \frac{C_1 D_1}{\bar{D}_1^2} = \rho \frac{(1 + \varepsilon e^{i3\beta_1} e^{-\theta_1})(1 + \varepsilon e^{-i\beta_1} e^{-\theta_1})}{(1 + \varepsilon e^{i\beta_1} e^{-\theta_1})^2} \\ &= \rho \left[1 - \frac{4\varepsilon \sin^2\beta_1}{e^{\theta_1} e^{-i\beta_1} + e^{-\theta_1} e^{i\beta_1} + 2\varepsilon}\right] \end{aligned} \tag{61}$$

where $\varepsilon = 1(-1)$ corresponds to dark (bright) soliton, Similarly if we redefine that $\beta_1 \equiv \pi/2 - \beta_1'$, then solution (61) is just the same as that gotten in [1] and [3, 4], and called one-parameter pure soliton. This further convinces us of the validity of our soliton solution and the reliability of the revised IST for NVBC.

5. CONCLUDING REMARKS

By introducing a suitable affine parameter in the IST, a revised inverse scattering transform for the DNLS$^+$ equation with NVBC and normal dispersion is proposed, the corresponding Z-S equations have been solved in a matrix form. The breather-type one-soliton solution has been given as a typical example of the unified formula of the N-soliton. It can perfectly reproduce the established conclusions, especially for the VBC case and the pure degenerate case, verifying the validity of the improved IST for DNLS equation with NVBC.

REFERENCES

1. Mjϕlhus, E., "Nonlinear Alfven waves and the DNLS equation: Oblique aspects," *Phys. Scr.*, Vol. 40, 227, 1989.
2. Kaup, D. J. and A. C. Newell, "An exact solution for a derivative nonlinear Schrödinger equation," *Journal of Mathematical Physics*, Vol. 19, 798, 1978.

3. Chen, X.-J., et al., "N-soliton solution for the derivative nonlinear Schrödinger equation with nonvanishing boundary condition," *Journal of Physics A. Gen.*, Vol. 39, 3263–3274, IOP Publishing, 2006.
4. Lashkin, V. M., "N-soliton solutions and perturbation theory for DNLS with nonvanishing condition," *J. Phys. A*, Vol. 40, 6119–6132, 2007.
5. Zhou, G.-Q., et al., "An N-soliton solution to the DNLS equation based on revised inverse scattering transform," *Journal of Physics A: Mathematical and Theoretical*, Vol. 40, 13607–13623, 2007.
6. Zhou, G.-Q., "Soliton solution of the DNLS equation based on Hirota's bilinear derivative transform," *Wuhan Univ. J. Nat. Sci.*, Vol. 14, No. 6, 505–510, 2009.

Glare Point Reconstruction in Digital Holographic Microscopy for Droplet Characterization

Huanhuan Shen[1], **Marc Brunel**[1], **Sébastien Coetmellec**[1], **Gérard Grehan**[1], **Denis Lebrun**[1], **Xuecheng Wu**[2], **and Kefa Cen**[2]

[1]UMR 6614 CORIA CNRS, Université de Rouen, France
[2]State Key Laboratory, Zhejiang University, China

Abstract— We present in this communication our studies carried out in the domain of off-axis numerical holographic microscopy. Combining Generalized Lorenz-Mie Theory (GLMT) to compute the field scattered by transparent droplets and digital holography, we show that a numerical reconstruction based on the fractional Fourier transform allows to characterize the particles in terms of diameter of the droplet, and position.

1. INTRODUCTION

Digital in-line holography can bring many informations in particle analysis. In the last decade, many configurations have been tested. In particular, the development of numerical anamorphous reconstruction has brought much progress to in situ characterizations of flows in pipes and micropipes [1]. Of main importance is now the possibility to distinguish clearly opaque, semi-transparent or transparent particles in a flow. Some first works have been done through digital in-line phase contrast experiments [2], but much has still to be done. For the characterization of transparent or semi-transparent objects, the digital off-axis holography has important potentialities. It should indeed allow to determine simultaneously the position, the diameter, the real and imaginary parts of the refractive index of particles present in a flow.

We present in this communication our studies carried out in the domain of off-axis numerical holographic microscopy. Combining Generalized Lorenz-Mie Theory (GLMT) to compute the field scattered by transparent droplets and digital holography [3], we show that a numerical reconstruction based on the fractional Fourier transform allows to characterize particles in terms of diameter of the droplet, and position.

The configuration under study is as follows: a laser illuminates some droplet. A camera records the hologram made by interference of a reference wave and of the laser light scattered by the particle. This pattern results essentially from the interference between the reference wave and both the light reflected at the droplet surface and the light refracted within the droplet. These two ways act as if two laser sources were issued from the droplet (i.e., the glare points). Using GLMT, we compute theoretical off-axis numerical holograms. In a second step, a fractional-order Fourier reconstruction is done and we show that the two glare points can be reconstructed. This reconstruction process allows then to determine characteristics of the droplets as position, diameter and refractive index.

In this communication, we will first present the principle of our GLMT calculations to predict numerical holograms, and our technique of numerical reconstruction using the fractional-order Fourier transformation. The results concerning the reconstruction of the glare points and the droplet characterization will then be detailed.

2. DESCRIPTION OF THE NUMERICAL TOOLS

2.1. Lorenz-Mie Theory for Predicting the Field Scattered by the Particle and Numerical Prediction of the Hologram

The configuration under study is schematized in Figure 1. A plane wave, called incident wave, impinges a spherical particle. The particle is characterized by its coordinates x_i, y_i and z_i relatively to a Cartesian coordinate system (OXYZ). A detector, assumed to be represented by a section of a plane, is located in the angular direction at a distance R ($R = OO'$) of the center of the Cartesian coordinate system. On this detector the interference between the light scattered by the particles and a reference beam (assumed to be a plane wave and impinging perpendicularly on the detector) are recorded. Note that in the particular case of inline Gabor holography the reference wave is the incident wave; for other configurations the reference beam can be arbitrarily defined. The particle is assumed to be a Mie scatter center (a perfectly spherical, isotropic and homogeneous particle with a diameter d and a complex refractive index m).

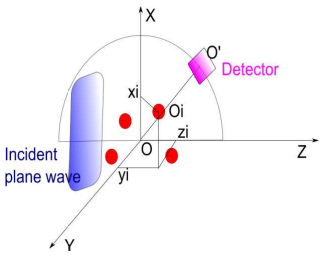

Figure 1: Off-axis set-up under consideration for digital holography.

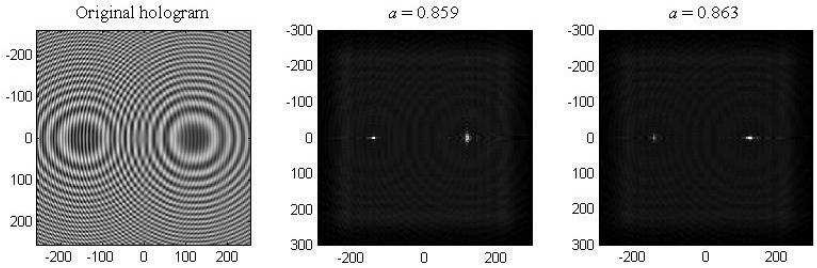

(a) (b) (c)

Figure 2: Original off-axis hologram for 1 droplet (a), and optimal reconstructions of both glare points ((b) and (c)).

2.2. Two-dimensional Fractional Order Fourier Transform for Numerical Reconstruction of the Holograms

The Fractional order Fourier transform (FRFT) has many applications in image processing. Its mathematical definition is given in Refs. [4–6]. The two-dimensional fractional Fourier transformation of order α_x along the x-axis and α_y along the y-axis of a 2D-function $I(x, y)$ is defined by

$$\Im_{\alpha_x,\alpha_y}[I(x,y)](x_a,y_a) = \iint_{\Re^2} N_{\alpha_x}(x,x_a)\, N_{\alpha_y}(y,y_a)\, I(x,y)\, dx\, dy$$

with $\alpha_p = a_p\pi/2$ ($p = x$ or y) and $0 \leq |\alpha_p| \leq \pi/2$, and where the kernel of the fractional operator is defined by

$$N_{\alpha_p}(x,x_a) = \frac{\exp\left(-i\left(\frac{\pi}{4}\mathrm{sign}(\sin(\alpha_p)) - \frac{\alpha_p}{2}\right)\right)}{\left|s_p^2 \sin\alpha_p\right|^{1/2}} \exp\left(i\,\pi\frac{x^2+x_a^2}{s_p^2\tan\alpha_p}\right) \exp\left(-\frac{i\;2\pi x x_a}{s_p^2\sin\alpha_p}\right)$$

The parameter s_p is defined from the experimental conditions according to $s_p^2 = N_p \cdot \delta_p^2$. N_p is the number of samples of the image along the x or y axes. The constant δ_p is the sampling period along the two previous axes of the image. One of the most important FRFT features is its ability to transform a linear chirp into a Dirac impulse when the right orders α_p are selected.

3. DROPPLET'S ANALYSIS THROUGH NUMERICAL RECONSTRUCTION OF GLARE POINTS FROM OFF-AXIS HOLOGRAMS

Figure 2(a) shows a digital hologram predicted using the Lorenz-Mie theory. The characteristics of the droplet are a refractive index of 1.33, a diameter of 140 µm. The droplet is transparent. The scattering angle is in the interval: [62°, 76°]. The angle is converted automatically by our simulator into transverse coordinates in the plane of a CCD sensor. The pattern is composed of two systems of concentric rings. It results essentially from the interference between the reference wave, and both the light reflected at the droplet surface and the light refracted within the droplet (without any internal reflection). Figure 2(b) shows now the pattern obtained when applying a fractional order Fourier transformation of order 0.859 to the hologram, while Figure 2(c) shows the pattern obtained when applying a transformation of order 0.863. For both reconstructions, the left-hand side point is due to refraction within the droplet while the right-hand side point is due to reflection on the droplet. Each of these two FRFT acts as a refocusing on one glare point: Figure 2(b) on

the glare point due to the refraction within the droplet, and Figure 2(c) on glare point due to the reflection on the droplet. Both orders are different as the two path ways (reflection and refraction within the droplet) are different.

Figure 3 shows the geometric schematic representation of the two glare points. In traditional in-line holography using an incident plane wave, the optimal order of reconstruction can be linked to the distance z_c between the object and the CCD camera through the following relation:

$$\tan(\alpha_{opt}) = \frac{\lambda z_c}{s_P^2}$$

Using this relation, we can evaluate the distances between both glare points and the plane of the CCD sensor: 0.985 mm for the reflected point A and 1.014 mm for the refracted point B ($\lambda = 532\,\text{nm}$, $N_p = 512$ and $s_p = 0.48\,\mu\text{m}$ in the calculus). We can then evaluate the transverse distance between both glare points. It gives in this case: 120 µm. Such reconstructions can be done for different values of the droplet's diameter. It is then possible to obtain a calibration curve giving the inter-distance between reconstructed glare points versus the droplet's diameter. Figure 4 shows this curve. This curve can now act as a calibration curve for droplet diameter characterization.

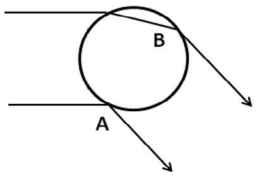

Figure 3: geometric schematic representation of the two glare points.

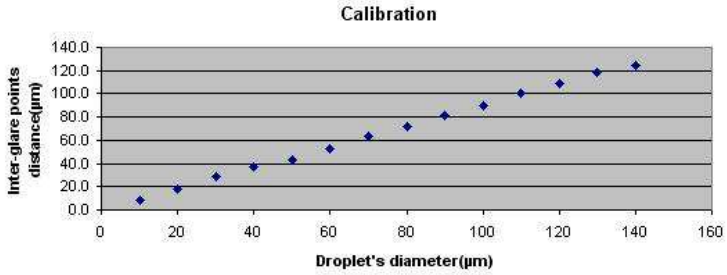

Figure 4: Calibration curve giving inter-glare points distance versus droplets diameter.

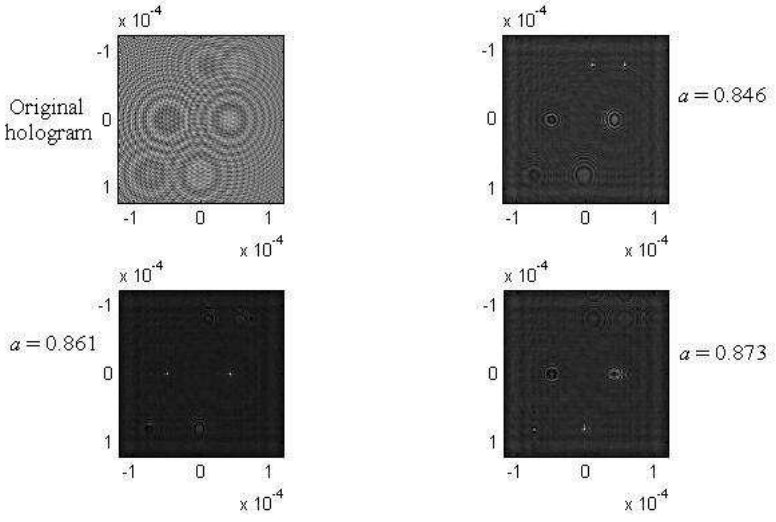

Figure 5: Original hologram and optimal glare point reconstructions of the 3 dropplets.

4. MULTI-DROPPLET RECONSTRUCTION

Figure 5 shows now the hologram simulated assuming the presence of 3 particles at different positions. The three optimal orders of reconstruction for the three particles are: 0.846, 0.861, 0.873. These three fractional orders allow to evaluate the position in depth of the three particles. The distance between each droplet and the CCD sensor plane is 0.99 mm, 0.89 mm and 1.1 mm respectively. For comparison, the theoretical values are: 1 mm, 0.90 mm and 1.1 mm. Reconstruction allows a relatively good localization of the particles.

The second step is to determine the droplets diameters. For each droplet, the inter-distance between the two reconstructed glare points is 46 µm, 90 µm, and 74 µm respectively. These values allow to evaluate the droplet's diameters according to the calibration curve of Figure 4. We obtain: 50 µm, 100 µm, and 80 µm respectively. Those are indeed the theoretical values used to compute the original hologram.

5. CONCLUSION

Combining Generalized Lorenz-Mie Theory (GLMT) to compute the field scattered by transparent droplets and digital holography, we show that a numerical reconstruction based on the fractional Fourier transform allows to characterize the particles in terms of diameter of the droplet, and position.

REFERENCES

1. Verrier, N., C. Rémacha, M. Brunel, D. Lebrun, and S. Coëtmellec, "Micropipe flow visualization using digital in-line holographic microscopy," *Opt. Express*, Vol. 18, 7807–7819, 2010.
2. Brunel, M., S. Coëtmellec, D. Lebrun, and K. Aït Ameur, "Digital phase contrast with the fractional Fourier transform," *Appl. Opt.*, Vol. 48, 579–583, 2009.
3. Wu, X., G. Gréhan, S. Meunier-Guttin-Cluzel, L. Chen, and K. Cen, "Sizing of particles smaller than 5 µm in digital holographic microscopy," *Opt. Lett.*, Vol. 34, 857–859, 2009.
4. McBride, A. C. and F. H. Kerr, "On Namias's fractional Fourier transforms," *IMA J. Appl. Math.*, Vol. 39, 159–175, 1987.
5. Namias, V., "The fractional order Fourier transform and its application to quantum mechanics," *J. Inst. Maths. Its Applics*, Vol. 25, 241–265, 1980.
6. Lohmann, A. W., "Image rotation, Wigner rotation, and the fractional Fourier transform," *J. Opt. Soc. Am. A*, Vol. 10, 2181–2186, 1993.

Efficient Partial Concealment of Convex Conductive Body

A. M. Lebedev and A. I. Fedorenko
Institute for Theoretical and Applied Electromagnetics, Russian Academy of Sciences, Russia

Abstract— The principal solution to the problem of partial concealment (PC) of big convex conductive body through the application of radar absorbing material (RAM) is discussed. Efficient PC means the reduction of backscatter radar cross section (RCS) of conductive body to the levels as for the body, fully coated with RAM, in relatively small angular interval of concealment, while applying RAM only in comparable angular interval. The classical apparatus of Fresnel zones (FZs) is used. Coating with RAM of apparently mostly scattering part of surface is shown not enough for controllable RCS reduction. However, coating with lengthy enough gradual transition (GT) RAM-conductor is proven to provide PC.

1. INTRODUCTION

Let the scatterer be a convex conductive body with characteristic dimensions and minimum radius of curvature much greater than the radar wavelength λ. Further only backscattering, characterized by (backscatter) RCS, will be considered. The backscattering is calculated here in physical optics approximation.

PC means RCS reduction to the levels as for the body, fully coated with RAM (reduction in about R_P times, where R_P is a coefficient of power reflection from RAM on the metal surface), and in relatively small angular interval of concealment $\Delta\varphi_{PC}$, which is much smaller than the interval of normal to the surface direction variation $\Delta\varphi_N$. RAM application onto the whole surface of the body solves the task of PC; however this solution is not efficient. Efficient PC means that angular interval of coating with RAM $\Delta\varphi_{RAM}$ only slightly exceeds $\Delta\varphi_{PC}$ and, correspondingly, is only a small part of $\Delta\varphi_N$.

The suggestions about RCS reduction of sizeable conductive bodies in certain directions through RAM application onto the first FZ (as a variant — onto a definite number of first FZs), determined in respect to these directions, can occasionally be met in literature. As applied to backscatter RCS calculation, the scatterer is divided into FZs by planes, perpendicular to direction of irradiation-observation, with distance $\lambda/4$ between planes (as in Fig. 1(a)). The phase of contributions from FZ parts into backscattering differs within π.

Calculations with the stationary phase method can lead to conclusion on existence of effectively scattering part of surface. The existence of effectively scattering fragment of surface around the point of backward reflection of ray is reported in [1]; the phase of contributions from elements of this fragment differs not more than $\pi/4$. RCS of this fragment is really equal to RCS of singly and doubly curved conductive surfaces. Hence in order to obtain efficient PC, it may seem to be necessary just to coat all effectively scattering parts of surface for all directions in $\Delta\varphi_{PC}$.

2. IMPOSSIBILITY OF EFFICIENT PARTIAL CONSEALMENT THROUGH APPLICATION OF RAM WITH ABRUPT TERMINATION

Without loss of generality, PC of circular conductive cylinder will be considered. Fig. 2 shows the situations of interest: (a) uncoated cylinder, (b) coating with abrupt termination is applied, (c), (d) coating with GT RAM-conductor is applied.

Spiral in Fig. 2(a) demonstrates how the backscattering from the cylinder is formed by contributions of sequent elements of surface. The spiral has a leg and a relatively slowly converging "almost round" part. Vector 1, connecting the beginning of spiral and point of its convergence, characterizes the scattered field. Vector 2 corresponds to the field of effectively scattering fragment [1]. Its length is really equal to the length of vector 1. The end of vector 2 can tentatively be considered as the spiral leg's end. The phase of the field, presented by vector 2, differs noticeably from the phase of really scattered field. As a result, vector 2A represents the substantial field — the backscattered field after coating of the effectively scattering fragment [1] with ideal RAM.

Vectors 3 and 4 depict backscattering from the first FZ and the first four FZs, and vectors 3A and 4A correspond to backscattering after coating of these regions with ideal RAM.

The presence of big residual scattered fields indicates difficulty in PC by coating some portion of surface, unless it corresponds to coating of the whole lit part of surface. There exists some level

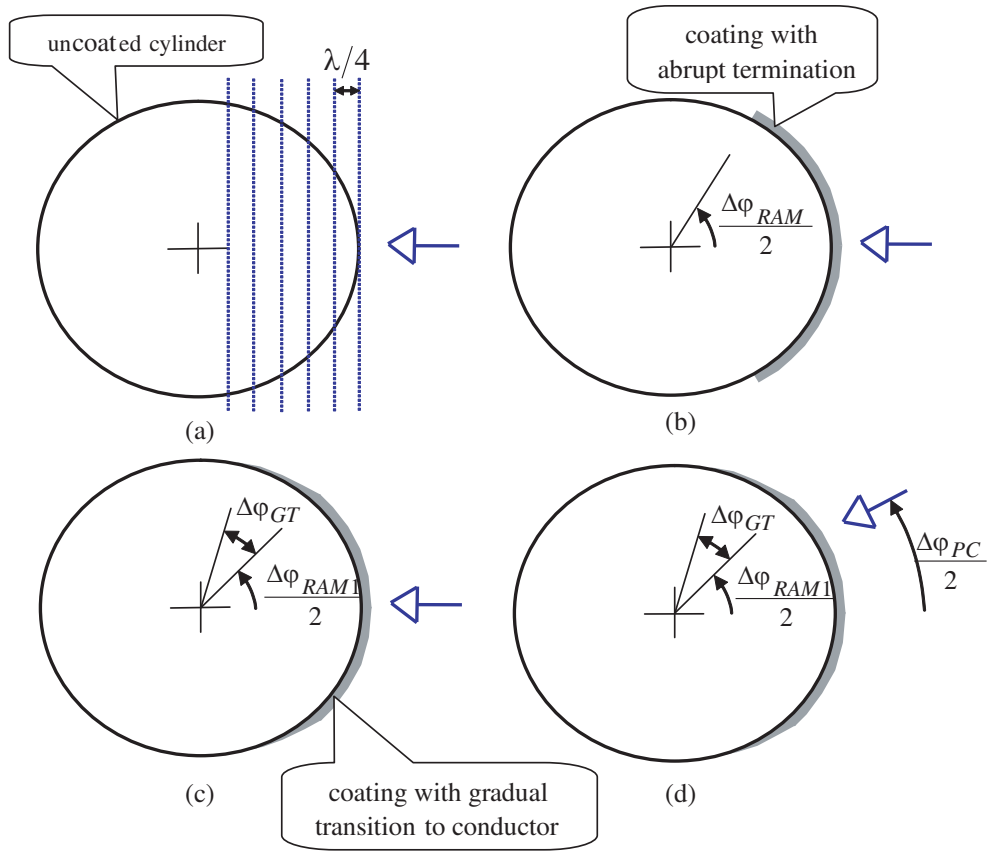

Figure 1: Schemes of circular conductive cylinder coating with RAM. The direction of irradiation is (a)–(c) central $\varphi = 0$, or (d) along the boundary of PC interval $\varphi = \Delta\varphi_{PC}/2$.

of RCS diagram saturation, corresponding to coating of the portion with ideal RAM — RCS can not obviously be reduced below this level by improving quality of RAM.

Figure 2(b) convincingly shows impossibility of PC of the scatterer by applying coating with abrupt termination onto the part of its lit surface as in Fig. 1(b). Piece of spiral for fully coated body (thin grey curve) is followed by piece of spiral for uncoated body (blue curve of medium thickness). Due to great difference in coefficients of reflection, the end of the resulting spiral is carried out far from the convergence point of the spiral for fully coated body.

3. PRINCIPAL POSSIBILITY OF EFFICIENT PARTIAL CONCEALMENT THROUGH COATING WITH GRADUAL TRANSITION RAM-CONDUCTOR

For situation as in Fig. 1(c), when coating has gradual transition RAM-conductor, part of spiral for fully coated body is followed by a piece of slowly widening spiral, corresponding to GT RAM-conductor (grey curve of big thickness) and then a part of spiral for uncoated conductor (see Fig. 2(c)). Importantly, point of convergence of the spiral is kept in small neighborhood of point of convergence of the spiral for fully coated body.

Now let the irradiation direction be on the boundary of PC angular interval $\varphi = \Delta\varphi_{PC}/2$ (Fig. 1(d)). Then spiral is conveniently divided into upper and lower branches, presenting the contributions from, correspondingly, upper and lower body parts in respect to the irradiation direction. GT RAM-conductor slowly increases radius of the spiral on transition from lower to upper branches, keeping the convergence point of the upper branch close to convergence point of spiral for fully coated conductor.

Maintenance of convergence point of spiral in small neighborhood of the corresponding point for fully coated body in angular interval $\Delta\varphi_{PC}$ just exactly means realization of PC.

4. THE EXAMPLES OF EFFICIENT PARTIAL CONCEALMENT OF CIRCULAR CYLINDERS

Two-dimensional RCS diagrams of circular conductive cylinders of radii $R = 4\lambda$ and $R = 30\lambda$ were calculated for application of RAMs with $R_P = 0.12^2$ and $R_P = 0.04^2$ according to two coating schemes in Fig. 1. The results are presented in Fig. 3, where the values of characteristic angles

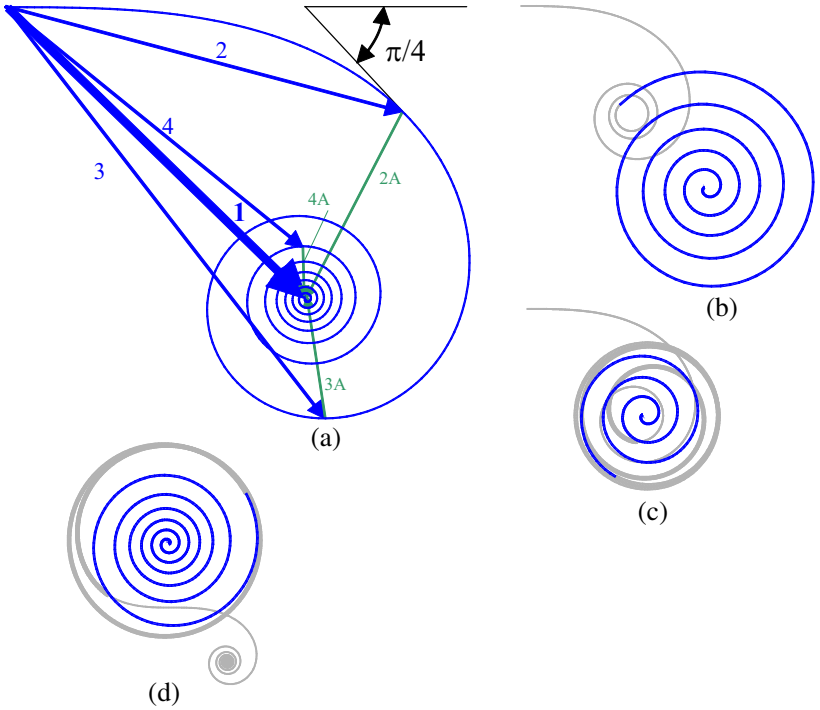

Figure 2: The spiral of backscattered field formation for (a) uncoated conducting cylinder, (b) same cylinder with abruptly terminated coating, (c) (d) cylinder with coating, having gradual transition RAM-conductor. Irradiation is central $\varphi = 0$ (a)–(c), of along the boundary of PC interval $\varphi = \Delta\varphi_{PC}/2$ (d).

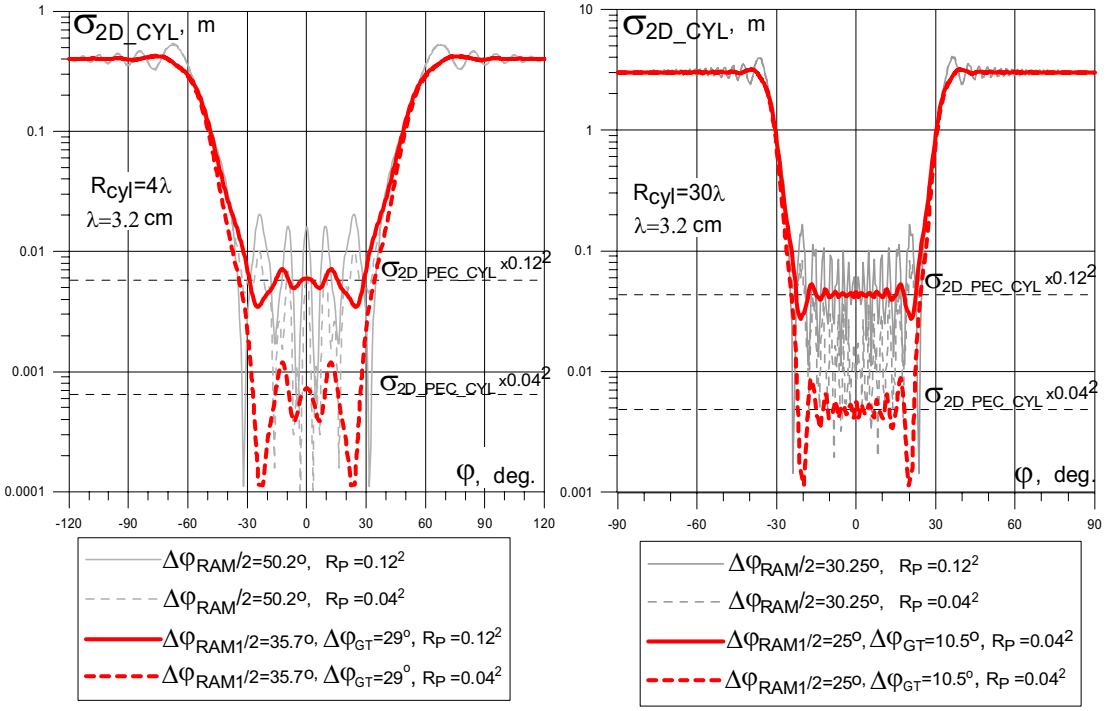

Figure 3: 2D RCS diagrams of conductive cylinders, coated with RAM according to schemes in Fig. 1.

$\Delta\varphi_{RAM}$, $\Delta\varphi_{RAM1}$ and $\Delta\varphi_{GT}$ are pointed out in legends to graphs. Note, that interval $\Delta\varphi_{GT}$ corresponds to two first FZs from the direction $\varphi = \Delta\varphi_{RAM1}$, and $\Delta\varphi_{RAM} = \Delta\varphi_{RAM1} + \Delta\varphi_{GT}$ was taken.

For both coating schemes, reduction of RCS is seen in the same angular intervals. However, for the abruptly terminated coating (diagrams are shown in grey) strong RCS oscillations around the levels generally higher, than $R_P \cdot \sigma_C$, are observed, where σ_C is the RCS of conductive cylinder, whereas for coating with gradual transition RAM-conductor (diagrams are shown in red) RCS diagrams definitely reduce to levels $R_P \cdot \sigma_C$ in the angular intervals of PC.

Interval $\Delta\varphi_{PC}$ is less than the interval $\Delta\varphi_{RAM1}$ of regular RAM coating. For irradiation from direction $\varphi = \Delta\varphi_{PC}/2$ contribution from the interval $\Delta\varphi_{RAM1}/2 - \Delta\varphi_{PC}/2$ approximately corresponds to the leg of the upper branch of spiral.

5. RAM-CONDUCTOR GRADUAL TRANSITION SPECIFICATIONS

The condition on minimum length of gradual transition RAM-conductor follows from the requirement of approximate maintenance of convergence point of spiral. At least two FZs, related to the irradiation in the direction on the boundary of PC angular interval, must be located along the gradual transition. Really, transition at two FZs corresponds to going 360° around the tentative convergence point along the trajectory with monotone increasing of curvature radius. For comparison, the rotation center can not be kept in case of gradual transition at one FZ — the center of the following oscillations is inevitably shifted during transition.

Besides the proper length of GT, obtaining PC in interval $\Delta\varphi_{PC}$ requires application of RAM in interval $\Delta\varphi_{RAM1}$ slightly wider than $\Delta\varphi_{PC}$. While irradiating from the boundary direction $\varphi = \Delta\varphi_{PC}/2$, contribution into backscattering from the part of surface in the interval $\frac{\Delta\varphi_{RAM1}-\Delta\varphi_{PC}}{2}$ must approximately correspond to the leg of the spiral branch. Then GT will occur at "almost round" part of spiral.

6. CONCLUSIONS

Principal possibility of concealment of big convex conductive body in relatively small angular interval by applying a spot of RAM with gradual transition RAM-conductor is shown.

REFERENCES

1. Knott, E. F., J. F. Shaeffer, and M. T. Tuley, *Radar Cross Section*, 548–550, Artech House, Boston, London, 1993.

Some Helicities in Electromagnetic Fields

Zi-Hua Weng
School of Physics and Mechanical & Electrical Engineering
Xiamen University, Xiamen 361005, China

Abstract— The paper discusses the influences of the helicity on the gravitational mass density, the field source, and the mass continuity equation etc. in the electromagnetic and gravitational fields. With the algebra of octonions, the magnetic helicity, the current helicity, the cross helicity, the kinetic helicity, the field energy, the enstrophy, and some new helicity terms can be derived from the octonion definitions of the linear momentum and the force in some fields with different operators. The study claims that the gravitational mass density and the mass continuity equation are impacted by the helicity, the field strength, and the vorticity of the rotational objects and the spinning charged objects in the gravitational and electromagnetic fields.

1. INTRODUCTION

The concept of the helicity [1] was originated by C. F. Gauss's studying of the orbits of the comet and the asteroid in the astronomy. Recently it is extended to the researches regarding the double helix structure of DNA molecular chain [2], the solar electromagnetic field, the fluid dynamics, the meteorology, and the topology etc. In the astronomy the helicity can be used to investigate the helical structure of the solar magnetic field, including the magnetic helicity, the current helicity, the cross helicity [3], and the kinetic helicity. In the fluid dynamics [4] the helicity can be used to illustrate the vorticity fields, the kinetic helicity, and the enstrophy. It is found that the helicity will impact the gravitational mass density and the mass continuity equation.

The quaternion was invented by W. R. Hamilton, and was first used by J. C. Maxwell [5] to depict the electromagnetic theory. Later the algebra of quaternions is used to represent the physical properties of the gravitational field. The quaternion space for the gravitational field is independent to that for the electromagnetic field. Two quaternion spaces are perpendicular to each other [6], and are combined together to become one octonion space, which is related to the algebra of octonions. The latter was invented by A. Cayley etc. Consequently the algebra of octonions can be used to describe the physical features of the gravitational field and the electromagnetic field simultaneously, including the mass continuity equation, the gravitational mass, and the helicity etc.

In terms of the octonions, the helicity of the rotational objects and the spinning charged objects in the electromagnetic field and the gravitational field can be found in the definition of the field source and the force-power in the octonion space. The helicities cover all known helicity terms in the classical theories, including the magnetic helicity, the current helicity [7], the cross helicity, the kinetic helicity, the field energy, the enstrophy, and some new helicity terms.

2. OCTONION SPACES

In the electromagnetic field and gravitational field, the operator $\Diamond$ with the field potential and the field strength can draw out directly the physical properties of these two fields, including the field potential, the field strength, the field source, the linear momentum, the angular momentum, the energy, the torque, the power, the force, and some helicities of the rotational objects and the spinning charged objects etc. It is found that the helicity, the field strength, and the field source will impact the gravitational mass and the mass continuity equation.

2.1. Octonion Space with the Operator $(\Diamond, \mathbb{B})$

The octonion space with the operator $(\Diamond, \mathbb{B})$ can derive the current helicity etc., and impact the mass continuity equation. In the quaternion space for the gravitational field, the basis vector is $\mathbb{E}_g = (\mathbf{i}_0, \mathbf{i}_1, \mathbf{i}_2, \mathbf{i}_3)$, the radius vector is $\mathbb{R}_g = (r_0, r_1, r_2, r_3)$, and the velocity is $\mathbb{V}_g = (v_0, v_1, v_2, v_3)$. In the quaternion space for the electromagnetic field, the basis vector is $\mathbb{E}_e = (\mathbf{I}_0, \mathbf{I}_1, \mathbf{I}_2, \mathbf{I}_3)$, the radius vector is $\mathbb{R}_e = (R_0, R_1, R_2, R_3)$, and the velocity is $\mathbb{V}_e = (V_0, V_1, V_2, V_3)$. The $\mathbb{E}_e$ is independent of the $\mathbb{E}_g$, with $\mathbb{E}_e = \mathbb{E}_g \circ \mathbf{I}_0$, and that they can combine together to become the basis vector of octonion space, $\mathbb{E} = (\mathbf{i}_0, \mathbf{i}_1, \mathbf{i}_2, \mathbf{i}_3, \mathbf{I}_0, \mathbf{I}_1, \mathbf{I}_2, \mathbf{I}_3)$.

The octonion radius vector is $\mathbb{R} = \Sigma(\mathbf{i}_i r_i + k_{eg}\mathbf{I}_i R_i)$, and the octonion velocity is $\mathbb{V} = \Sigma(\mathbf{i}_i v_i + k_{eg}\mathbf{I}_i V_i)$ in the octonion space. Herein $\mathbf{i}_0 = 1$; $r_0 = v_0 t$, t is the time. The symbol $\circ$ denotes the

octonion multiplication. v_0 and k_{eg} are the coefficients for the dimensional homogeneity, while the v_0 is the speed of light by comparison with the classical theory.

The gravitational potential, $\mathbb{A}_g = (a_0, a_1, a_2, a_3)$, combines with the electromagnetic potential, $\mathbb{A}_e = (A_0, A_1, A_2, A_3)$, to become the octonion field potential, $\mathbb{A} = \mathbb{A}_g + k_{eg}\mathbb{A}_e$. The field strength $\mathbb{B} = \Diamond \circ \mathbb{A} = \mathbb{B}_g + k_{eg}\mathbb{B}_e$ consists of the gravitational strength, $\mathbb{B}_g = \Sigma(h_i \mathbf{i}_i)$, and the electromagnetic strength, $\mathbb{B}_e = \Sigma(H_i \mathbf{I}_i)$. The gauge equations are $h_0 = 0$ and $H_0 = 0$. The gravitational strength $\mathbb{B}_g$ includes two parts, $\mathbf{g}/v_0 = \partial_0 \mathbf{a} + \nabla a_0$ and $\mathbf{b} = \nabla \times \mathbf{a}$, and the electromagnetic strength $\mathbb{B}_e$ involves two components, $\mathbf{E}/v_0 = \partial_0 \mathbf{A} + \nabla \circ \mathbf{A}_0$ and $\mathbf{B} = \nabla \times \mathbf{A}$. The linear momentum density $\mathbb{S}_g = m\mathbb{V}_g$ is the source for the gravitational field, while the electric current density $\mathbb{S}_e = q\mathbb{V}_e$ is that for the electromagnetic field. Herein q is the electric charge density; m is the inertial mass density; $\mathbf{a} = \Sigma(a_j \mathbf{i}_j)$, $\mathbf{A} = \Sigma(A_j \mathbf{I}_j)$, $\mathbf{A}_0 = A_0 \mathbf{I}_0$; $\Diamond = \Sigma(\mathbf{i}_i \partial_i)$, with $\partial_i = \partial/\partial r_i$. $i = 0, 1, 2, 3$. $j = 1, 2, 3$.

2.2. Octonion Space with the Operator $(\Diamond, \bar{\mathbb{A}}, \bar{\mathbb{B}})$

The octonion space with the operator $(\Diamond, \bar{\mathbb{A}}, \bar{\mathbb{B}})$ can deduce the magnetic helicity, the current helicity, the cross helicity, the kinetic helicity, the field energy, the enstrophy, and some new helicity terms etc. In the octonion space with the basis vector $\mathbb{E} = (1, \mathbf{i}_1, \mathbf{i}_2, \mathbf{i}_3, \mathbf{I}_0, \mathbf{I}_1, \mathbf{I}_2, \mathbf{I}_3)$, the octonion radius vector is $\mathbb{R} = \Sigma(\mathbf{i}_i r_i + k_{eg} \mathbf{I}_i R_i)$, and the octonion velocity is $\mathbb{V} = \Sigma(\mathbf{i}_i v_i + k_{eg} \mathbf{I}_i V_i)$. The octonion field potential is $\mathbb{A} = \mathbb{A}_g + k_{eg}\mathbb{A}_e$, while the octonion field strength is $\mathbb{B} = (\Diamond + k_a \mathbb{A}) \circ \mathbb{A} = \mathbb{B}_g + k_{eg}\mathbb{B}_e$. In this space the gravitational strength is $\mathbb{B}_g = \Sigma(h_i \mathbf{i}_i) = \Diamond \circ \mathbb{A}_g + k_a(\mathbb{A}_g \circ \mathbb{A}_g + k_{eg}^2 \mathbb{A}_e \circ \mathbb{A}_e)$, and the electromagnetic strength is $\mathbb{B}_e = \Sigma(H_i \mathbf{I}_i) = \Diamond \circ \mathbb{A}_e + k_a k_{eg}(\mathbb{A}_e \circ \mathbb{A}_g + \mathbb{A}_g \circ \mathbb{A}_e)$. Herein k_a and $k_b = 1/v_0$ are the coefficients.

The radius vector $\mathbb{R}$ and octonion $\mathbb{X}$ in the octonion space can be combined together to become the compounding radius vector $\bar{\mathbb{R}} = \mathbb{R} + k_{rx}\mathbb{X}$, and the compounding quantity $\bar{\mathbb{X}} = \mathbb{X} + K_{rx}\mathbb{R} = \Sigma(\bar{x}_i \mathbf{i}_i + k_{eg} \bar{X}_i \mathbf{I}_i)$. The derivation of the octonion quantity $\mathbb{X}$ will yield the gravitational potential and the electromagnetic potential. The related space is called as the octonion compounding space, which is one kind of function space. In this octonion compounding space, the coordinates are the $\bar{r}_i = r_i + k_{rx} x_i$ for the basis vector $\mathbf{i}_i$, while the $\bar{R}_i = R_i + k_{rx} X_i$ for the basis vector $\mathbf{I}_i$, and the radius vector is $\bar{\mathbb{R}} = \Sigma(\mathbf{i}_i \bar{r}_i + k_{eg} \mathbf{I}_i \bar{R}_i)$. The compounding field potential is $\bar{\mathbb{A}} = \Diamond \circ \bar{\mathbb{X}} = \mathbb{A} + K_{rx}\mathbb{V}/v_0 = \Sigma(\bar{a}_i \mathbf{i}_i + k_{eg} \bar{A}_i \mathbf{I}_i)$, and the compounding velocity is $\bar{\mathbb{V}} = \mathbb{V} + v_0 k_{rx} \mathbb{A} = \Sigma(\bar{v}_i \mathbf{i}_i + k_{eg} \bar{V}_i \mathbf{I}_i)$. The octonion field strength is $\bar{\mathbb{B}} = (\Diamond + k_a \bar{\mathbb{A}}) \circ \bar{\mathbb{A}} = \bar{\mathbb{B}}_g + k_{eg}\bar{\mathbb{B}}_e$, and is defined from the octonion field potential $\bar{\mathbb{A}} = \bar{\mathbb{A}}_g + k_{eg}\bar{\mathbb{A}}_e$. And the gravitational strength is $\bar{\mathbb{B}}_g = \Sigma(\bar{h}_i \mathbf{i}_i) = \Diamond \circ \bar{\mathbb{A}}_g + k_a(\bar{\mathbb{A}}_g \circ \bar{\mathbb{A}}_g + k_{eg}^2 \bar{\mathbb{A}}_e \circ \bar{\mathbb{A}}_e)$, while the electromagnetic strength is $\bar{\mathbb{B}}_e = \Sigma(\bar{H}_i \mathbf{I}_i) = \Diamond \circ \bar{\mathbb{A}}_e + k_a(\bar{\mathbb{A}}_e \circ \bar{\mathbb{A}}_g + \bar{\mathbb{A}}_g \circ \bar{\mathbb{A}}_e)$. The gauge equations are $\bar{h}_0 = 0$ and $\bar{H}_0 = 0$. Herein $k_{rx} = 1/v_0$ and $K_{rx} = 1/k_{rx}$ are the coefficients.

3. FIELD SOURCE AND TORQUE

In the electromagnetic field and gravitational field, the operator $(\Diamond + k_a \bar{\mathbb{A}} + k_b \bar{\mathbb{B}})$ can deduce some physical properties of two fields, including the octonion field potential, the octonion field strength, the octonion field source, the octonion linear momentum, the octonion angular momentum, the energy, the torque, the power, the force, and some helicities of the rotational objects and the spinning charged objects. The helicity terms cover the current helicity, magnetic helicity, cross helicity, and kinetic helicity etc. It is found that the helicity, the field strength, and the field source will impact the gravitational mass and the mass continuity equation etc.

In the electromagnetic and gravitational fields with the operator $(\Diamond + k_a \bar{\mathbb{A}} + k_b \bar{\mathbb{B}})$, the linear momentum density $\bar{\mathbb{S}}_g$ is the source for the gravitational field, and the electric current density $\bar{\mathbb{S}}_e$

Table 1: The octonion multiplication table.

	1	$\mathbf{i}_1$	$\mathbf{i}_2$	$\mathbf{i}_3$	$\mathbf{I}_0$	$\mathbf{I}_1$	$\mathbf{I}_2$	$\mathbf{I}_3$
1	1	$\mathbf{i}_1$	$\mathbf{i}_2$	$\mathbf{i}_3$	$\mathbf{I}_0$	$\mathbf{I}_1$	$\mathbf{I}_2$	$\mathbf{I}_3$
$\mathbf{i}_1$	$\mathbf{i}_1$	-1	$\mathbf{i}_3$	$-\mathbf{i}_2$	$\mathbf{I}_1$	$-\mathbf{I}_0$	$-\mathbf{I}_3$	$\mathbf{I}_2$
$\mathbf{i}_2$	$\mathbf{i}_2$	$-\mathbf{i}_3$	-1	$\mathbf{i}_1$	$\mathbf{I}_2$	$\mathbf{I}_3$	$-\mathbf{I}_0$	$-\mathbf{I}_1$
$\mathbf{i}_3$	$\mathbf{i}_3$	$\mathbf{i}_2$	$-\mathbf{i}_1$	-1	$\mathbf{I}_3$	$-\mathbf{I}_2$	$\mathbf{I}_1$	$-\mathbf{I}_0$
$\mathbf{I}_0$	$\mathbf{I}_0$	$-\mathbf{I}_1$	$-\mathbf{I}_2$	$-\mathbf{I}_3$	-1	$\mathbf{i}_1$	$\mathbf{i}_2$	$\mathbf{i}_3$
$\mathbf{I}_1$	$\mathbf{I}_1$	$\mathbf{I}_0$	$-\mathbf{I}_3$	$\mathbf{I}_2$	$-\mathbf{i}_1$	-1	$-\mathbf{i}_3$	$\mathbf{i}_2$
$\mathbf{I}_2$	$\mathbf{I}_2$	$\mathbf{I}_3$	$\mathbf{I}_0$	$-\mathbf{I}_1$	$-\mathbf{i}_2$	$\mathbf{i}_3$	-1	$-\mathbf{i}_1$
$\mathbf{I}_3$	$\mathbf{I}_3$	$-\mathbf{I}_2$	$\mathbf{I}_1$	$\mathbf{I}_0$	$-\mathbf{i}_3$	$-\mathbf{i}_2$	$\mathbf{i}_1$	-1

Table 2: The operator and multiplication of the physical quantity in the octonion space.

definitions	meanings
$\nabla \cdot \mathbf{a}$	$-(\partial_1 a_1 + \partial_2 a_2 + \partial_3 a_3)$
$\nabla \times \mathbf{a}$	$\mathbf{i}_1(\partial_2 a_3 - \partial_3 a_2) + \mathbf{i}_2(\partial_3 a_1 - \partial_1 a_3) + \mathbf{i}_3(\partial_1 a_2 - \partial_2 a_1)$
∇a_0	$\mathbf{i}_1\partial_1 a_0 + \mathbf{i}_2\partial_2 a_0 + \mathbf{i}_3\partial_3 a_0$
$\partial_0 \mathbf{a}$	$\mathbf{i}_1\partial_0 a_1 + \mathbf{i}_2\partial_0 a_2 + \mathbf{i}_3\partial_0 a_3$
$\nabla \cdot \mathbf{P}$	$-(\partial_1 P_1 + \partial_2 P_2 + \partial_3 P_3)\mathbf{I}_0$
$\nabla \times \mathbf{P}$	$-\mathbf{I}_1(\partial_2 P_3 - \partial_3 P_2) - \mathbf{I}_2(\partial_3 P_1 - \partial_1 P_3) - \mathbf{I}_3(\partial_1 P_2 - \partial_2 P_1)$
$\nabla \circ \mathbf{P}_0$	$\mathbf{I}_1\partial_1 P_0 + \mathbf{I}_2\partial_2 P_0 + \mathbf{I}_3\partial_3 P_0$
$\partial_0 \mathbf{P}$	$\mathbf{I}_1\partial_0 P_1 + \mathbf{I}_2\partial_0 P_2 + \mathbf{I}_3\partial_0 P_3$

is that for the electromagnetic field. The octonion field source $\bar{\mathbb{S}}$ satisfies

$$\mu\bar{\mathbb{S}} = -(\lozenge + k_a\bar{\mathbb{A}} + k_b\bar{\mathbb{B}})^* \circ \bar{\mathbb{B}} = \mu_g\bar{\mathbb{S}}_g + k_{eg}\mu_e\bar{\mathbb{S}}_e - k_a\bar{\mathbb{A}}^* \circ \bar{\mathbb{B}} - k_b\bar{\mathbb{B}}^* \circ \bar{\mathbb{B}}, \tag{1}$$

where $(k_a\bar{\mathbb{A}}^* \cdot \bar{\mathbb{B}} + k_b\bar{\mathbb{B}}^* \cdot \bar{\mathbb{B}})$ is the field strength helicity, and $(k_a\bar{\mathbb{A}}^* \cdot \bar{\mathbb{B}} + k_b\bar{\mathbb{B}}^* \cdot \bar{\mathbb{B}})/(2\mu_g)$ is the field energy density. $\bar{\mathbb{A}}^* \cdot \bar{\mathbb{B}}$ denotes the scalar of the octonion $\bar{\mathbb{A}}^* \circ \bar{\mathbb{B}}$. And $\mathbb{B}^* \circ \mathbb{B}/\mu_g = \mathbb{B}_g^* \circ \mathbb{B}_g/\mu_g + \mathbb{B}_e^* \circ \mathbb{B}_e/\mu_e$; $k_{eg}^2 = \mu_g/\mu_e$; μ_g and μ_e are the gravitational and electromagnetic constants respectively.

The octonion linear momentum density is $\bar{\mathbb{P}} = \mu\bar{\mathbb{S}}/\mu_g = \Sigma(\bar{p}_i\mathbf{i}_i + \bar{P}_i\mathbf{I}_i)$, and the octonion angular momentum density is $\bar{\mathbb{L}} = \bar{\mathbb{R}} \circ \bar{\mathbb{P}} = \Sigma(\bar{l}_i\mathbf{i}_i + \bar{L}_i\mathbf{I}_i)$. The octonion torque-energy density $\bar{\mathbb{W}}$ is defined from the angular momentum density $\bar{\mathbb{L}}$, the field potential $\bar{\mathbb{A}}$, and the field strength $\bar{\mathbb{B}}$,

$$\bar{\mathbb{W}} = v_0(\lozenge + k_a\bar{\mathbb{A}} + k_b\bar{\mathbb{B}}) \circ \bar{\mathbb{L}}, \tag{2}$$

where $\bar{\mathbb{W}} = \Sigma(\bar{w}_i\mathbf{i}_i) + \Sigma(\bar{W}_i\mathbf{I}_i)$; the $-\bar{w}_0/2$ is the energy density, the $\bar{\mathbf{w}}/2 = \Sigma(\bar{w}_j\mathbf{i}_j)/2$ is the torque density. $\bar{\mathbf{p}} = \Sigma(\bar{p}_j\mathbf{i}_j)$; $\bar{\mathbf{P}}_0 = \bar{P}_0\mathbf{I}_0$; $\bar{\mathbf{P}} = \Sigma(\bar{P}_j\mathbf{I}_j)$.

The scalar $\bar{w}_0$ of $\bar{\mathbb{W}}$ is written as,

$$\bar{w}_0/v_0 = \partial_0\bar{l}_0 + \nabla \cdot \bar{\mathbf{l}} + k_a\bar{\mathbf{a}} \cdot \bar{\mathbf{l}} + k_a\bar{a}_0\bar{l}_0 + k_{eg}k_a(\bar{\mathbf{A}} \cdot \bar{\mathbf{L}} + \bar{\mathbf{A}}_0 \circ \bar{\mathbf{L}}_0) + k_b(\bar{\mathbf{h}} \cdot \bar{\mathbf{l}} + k_{eg}\bar{\mathbf{H}} \cdot \bar{\mathbf{L}}),$$

where $-\bar{w}_0/2$ includes the kinetic energy, gravitational potential energy, electric potential energy, magnetic potential energy, field energy, work, the interacting energy between the dipole moment with the fields, and some new energy terms. $\bar{\mathbf{a}} = \Sigma(\bar{a}_j\mathbf{i}_j)$, $\bar{\mathbf{A}}_0 = \bar{A}_0\mathbf{I}_0$, $\bar{\mathbf{A}} = \Sigma(\bar{A}_j\mathbf{I}_j)$. $\bar{\mathbf{l}} = \Sigma(\bar{l}_j\mathbf{i}_j)$, $\bar{\mathbf{L}}_0 = \bar{L}_0\mathbf{I}_0$, $\bar{\mathbf{L}} = \Sigma(\bar{L}_j\mathbf{I}_j)$.

In a similar way, expressing the torque density $\bar{\mathbf{w}}$ of $\bar{\mathbb{W}}$ as

$$\begin{aligned}\bar{\mathbf{w}}/v_0 \;=\; & \partial_0\bar{\mathbf{l}} + \nabla\bar{l}_0 + \nabla \times \bar{\mathbf{l}} + k_b\bar{l}_0\bar{\mathbf{h}} + k_b\bar{\mathbf{h}} \times \bar{\mathbf{l}} + k_{eg}k_b(\bar{\mathbf{H}} \times \bar{\mathbf{L}} + \bar{\mathbf{H}} \circ \bar{\mathbf{L}}_0) \\ & + k_a\bar{\mathbf{a}}\bar{l}_0 + k_a\bar{\mathbf{a}} \times \bar{\mathbf{l}} + k_a\bar{a}_0\bar{\mathbf{l}} + k_{eg}k_a(\bar{\mathbf{A}} \times \bar{\mathbf{L}} + \bar{\mathbf{A}}_0 \circ \bar{\mathbf{L}} + \bar{\mathbf{A}} \circ \bar{\mathbf{L}}_0),\end{aligned} \tag{3}$$

where the above encompasses some new terms of the torque density.

4. FORCE

In the octonion compounding space with the operator $(\lozenge + k_a\bar{\mathbb{A}} + k_b\bar{\mathbb{B}})$, the octonion force-power density, $\bar{\mathbb{N}} = \Sigma(\bar{n}_i\mathbf{i}_i) + \Sigma(\bar{N}_i\mathbf{I}_i)$, is defined from the torque-energy density $\bar{\mathbb{W}}$,

$$\bar{\mathbb{N}} = v_0(\lozenge + k_a\bar{\mathbb{A}} + k_b\bar{\mathbb{B}})^* \circ \bar{\mathbb{W}}, \tag{4}$$

where the power density is $\bar{f}_0 = -\bar{n}_0/(2v_0)$, and the force density is $\bar{\mathbf{f}} = -\bar{\mathbf{n}}/(2v_0)$. The vectorial parts are $\bar{\mathbf{n}} = \Sigma(\bar{n}_j\mathbf{i}_j)$, $\bar{\mathbf{N}}_0 = \bar{N}_0\mathbf{I}_0$, and $\bar{\mathbf{N}} = \Sigma(\bar{N}_j\mathbf{I}_j)$.

Further expressing the scalar $\bar{n}_0$ of $\bar{\mathbb{N}}$ as

$$\begin{aligned}\bar{n}_0/v_0 \;=\; & \partial_0\bar{w}_0 + \nabla^* \cdot \bar{\mathbf{w}} + k_a(\bar{\mathbf{a}}^* \cdot \bar{\mathbf{w}} + \bar{a}_0\bar{w}_0) \\ & + k_{eg}k_a(\bar{\mathbf{A}}^* \cdot \bar{\mathbf{W}} + \bar{\mathbf{A}}_0^* \circ \bar{\mathbf{W}}_0) + k_b(\bar{\mathbf{h}}^* \cdot \bar{\mathbf{w}} + k_{eg}\bar{\mathbf{H}}^* \cdot \bar{\mathbf{W}}).\end{aligned}$$

In the gravitational field and electromagnetic field with the operator $(\lozenge + k_a\bar{\mathbb{A}} + k_b\bar{\mathbb{B}})$, the force density $\bar{\mathbf{f}}$ can be defined from the vectorial part $\bar{\mathbf{n}}$ of $\bar{\mathbb{N}}$,

$$\begin{aligned}-2\bar{\mathbf{f}} \;=\; & \partial_0\bar{\mathbf{w}} + \nabla^*\bar{w}_0 + \nabla^* \times \bar{\mathbf{w}} + k_b\bar{w}_0\bar{\mathbf{h}}^* + k_b\bar{\mathbf{h}}^* \times \bar{\mathbf{w}} + k_{eg}k_b(\bar{\mathbf{H}}^* \times \bar{\mathbf{W}} + \bar{\mathbf{H}}^* \circ \bar{\mathbf{W}}_0) \\ & + k_a(\bar{\mathbf{a}}^*\bar{w}_0 + \bar{\mathbf{a}}^* \times \bar{\mathbf{w}} + \bar{a}_0\bar{\mathbf{w}}) + k_{eg}k_a(\bar{\mathbf{A}}^* \times \bar{\mathbf{W}} + \bar{\mathbf{A}}_0^* \circ \bar{\mathbf{W}} + \bar{\mathbf{A}}^* \circ \bar{\mathbf{W}}_0),\end{aligned} \tag{5}$$

where the force density $\bar{\mathbf{f}}$ includes that of the inertial force, gravitational force, gradient of energy, Lorentz force, and the interacting force between the dipole moment with the fields etc. This force definition is much more complicated than that in the classical field theory, and includes more new force terms regarding the gradient of energy, the field potential, and the angular velocity etc. In case the vorticity $\mathbb{U} = \Diamond \circ \mathbb{V}$ is quick enough, the force terms about the vorticity will be detected.

5. FIELD STRENGTH HELICITY

In the electromagnetic and gravitational fields, as one necessary part of the octonion compounding space with the operator $(\Diamond + k_a\bar{\mathbb{A}} + k_b\bar{\mathbb{B}})$, the helicity will impact the gravitational mass density and the mass continuity equation etc.

The octonion linear momentum density $\bar{\mathbb{P}} = \mu\bar{\mathbb{S}}/\mu_g$ can be defined from the octonion field source $\bar{\mathbb{S}}$ in the octonion compounding space with the operator $(\Diamond + k_a\bar{\mathbb{A}} + k_b\bar{\mathbb{B}})$,

$$\bar{\mathbb{P}} = \widehat{m}\bar{v}_0 + \Sigma(m\bar{v}_j\mathbf{i}_j) + \Sigma(M\bar{V}_i\mathbf{I}_i), \tag{6}$$

where $\widehat{m} = m(\bar{v}_0^{\delta}/\bar{v}_0) + \triangle m$, $\triangle m = -(k_a\bar{\mathbb{A}}^* \cdot \bar{\mathbb{B}} + k_b\bar{\mathbb{B}}^* \cdot \bar{\mathbb{B}})/(\bar{v}_0\mu_g)$. $M = k_{eg}q\mu_e/\mu_g$. $\bar{v}_0^{\delta} = v_0\Diamond \cdot \bar{\mathbb{R}}$, and the $\Diamond \cdot \bar{\mathbb{R}}$ is the scalar part of the $\Diamond \circ \bar{\mathbb{R}}$. The $\bar{r}_0$ is rewritten as the $\bar{r}_0 = \bar{v}_0 t$, with the $\bar{v}_0$ being the coefficient for the dimensional homogeneity.

According to the octonion features, the gravitational mass $\widehat{m}$ is one reserved scalar in the above, and is changed with the field strength $\bar{\mathbb{B}}_g$ and $\bar{\mathbb{B}}_e$, the field potential $\bar{\mathbb{A}}_g$ and $\bar{\mathbb{A}}_e$, the enstrophy $\mathbf{u}^* \cdot \mathbf{u}/8$, and the helicity $(k_a\bar{\mathbb{A}}^* \cdot \bar{\mathbb{B}} + k_b\bar{\mathbb{B}}^* \cdot \bar{\mathbb{B}})$ etc. The helicity covers the magnetic helicity $\bar{\mathbf{A}} \cdot \bar{\mathbf{B}}$, the kinetic helicity $\bar{\mathbf{V}} \cdot \bar{\mathbf{U}}$, the cross helicity $\bar{\mathbf{V}} \cdot \bar{\mathbf{B}}$, and one new helicity term $\bar{\mathbf{A}} \cdot \bar{\mathbf{U}}$ etc. Herein $\bar{\mathbb{U}} = \Diamond \circ \bar{\mathbb{V}} = \Sigma(\mathbf{i}_i\bar{u}_i + k_{eg}\mathbf{I}_i\bar{U}_i)$; $\bar{\mathbf{A}} = \Sigma(\bar{A}_j\mathbf{I}_j)$, $\bar{\mathbf{B}} = \Sigma(\bar{B}_j\mathbf{I}_j)$, $\bar{\mathbf{V}} = \Sigma(\bar{V}_j\mathbf{I}_j)$, $\bar{\mathbf{U}} = \Sigma(\bar{U}_j\mathbf{I}_j)$.

6. FIELD SOURCE HELICITY

The part force density $\bar{\mathbb{F}}$ of the octonion force-power density $\bar{\mathbb{N}}$ is defined from the octonion linear momentum density $\bar{\mathbb{P}}$,

$$\bar{\mathbb{F}} = v_0(\Diamond + k_a\bar{\mathbb{A}} + k_b\bar{\mathbb{B}})^* \circ \bar{\mathbb{P}}, \tag{7}$$

where the part force density includes that of the inertial force, gravitational force, Lorentz force, and the interacting force between the fields with the dipoles etc.

The scalar $\bar{f}_0$ of $\bar{\mathbb{F}}$ is written as,

$$\begin{aligned} \bar{f}_0/v_0 \;=\; & \partial_0\bar{p}_0 + \nabla^* \cdot \bar{\mathbf{p}} + k_a(\bar{\mathbf{a}}^* \cdot \bar{\mathbf{p}} + \bar{a}_0\bar{p}_0) + k_{eg}k_a(\bar{\mathbf{A}}^* \cdot \bar{\mathbf{P}} + \bar{\mathbf{A}}_0^* \circ \bar{\mathbf{P}}_0) \\ & + k_b(\bar{\mathbf{h}}^* \cdot \bar{\mathbf{p}} + k_{eg}\bar{\mathbf{H}}^* \cdot \bar{\mathbf{P}}), \end{aligned}$$

Table 3: Some physical quantities in the octonion compounding spaces with the operator $(\Diamond + k_a\bar{\mathbb{A}} + k_b\bar{\mathbb{B}})$.

definitions	meanings
$\bar{\mathbb{X}}$	field quantity
$\bar{\mathbb{A}} = \Diamond \circ \bar{\mathbb{X}}$	field potential
$\bar{\mathbb{B}} = (\Diamond + k_a\bar{\mathbb{A}}) \circ \bar{\mathbb{A}}$	field strength
$\bar{\mathbb{R}}$	radius vector
$\bar{\mathbb{V}} = v_0\Diamond \circ \bar{\mathbb{R}}$	velocity
$\bar{\mathbb{U}} = \Diamond \circ \bar{\mathbb{V}}$	velocity curl
$\mu\bar{\mathbb{S}} = -(\Diamond + k_a\bar{\mathbb{A}} + k_b\bar{\mathbb{B}})^* \circ \bar{\mathbb{B}}$	field source
$\bar{\mathbb{H}}_b = (k_a\bar{\mathbb{A}} + k_b\bar{\mathbb{B}})^* \cdot \bar{\mathbb{B}}$	field strength helicity
$\bar{\mathbb{P}} = \mu\bar{\mathbb{S}}/\mu_g$	linear momentum density
$\bar{\mathbb{R}} = \mathbb{R} + k_{rx}\mathbb{X}$	compounding radius vector
$\bar{\mathbb{L}} = \bar{\mathbb{R}} \circ \bar{\mathbb{P}}$	angular momentum density
$\bar{\mathbb{W}} = v_0(\Diamond + k_a\bar{\mathbb{A}} + k_b\bar{\mathbb{B}}) \circ \bar{\mathbb{L}}$	torque-energy densities
$\bar{\mathbb{N}} = v_0(\Diamond + k_a\bar{\mathbb{A}} + k_b\bar{\mathbb{B}})^* \circ \bar{\mathbb{W}}$	force-power density
$\bar{\mathbb{F}} = -\bar{\mathbb{N}}/(2v_0)$	force density
$\bar{\mathbb{H}}_s = (k_a\bar{\mathbb{A}} + k_b\bar{\mathbb{B}})^* \cdot \bar{\mathbb{P}}$	field source helicity

where the terms $(\bar{\mathbf{a}}^* \cdot \bar{\mathbf{p}} + \bar{a}_0 \bar{p}_0)$, $(\bar{\mathbf{A}}^* \cdot \bar{\mathbf{P}} + \bar{\mathbf{A}}_0^* \circ \bar{\mathbf{P}}_0)$, and $(\bar{\mathbf{h}}^* \cdot \bar{\mathbf{p}} + k_{eg} \bar{\mathbf{H}}^* \cdot \bar{\mathbf{P}})$ are the helicity in the fields with the operator $(\lozenge + k_a \bar{\mathbb{A}} + k_b \bar{\mathbb{B}})$. The helicity covers the magnetic helicity $\mathbf{A} \cdot \mathbf{B}$, the kinetic helicity $\mathbf{V} \cdot \mathbf{U}$, the cross helicity $\mathbf{V} \cdot \mathbf{B}$, and the current helicity $\mathbf{B}^* \cdot \mathbf{P}$ etc.

The above is the mass continuity equation in the electromagnetic and gravitational fields with the operator $(\lozenge + k_a \bar{\mathbb{A}} + k_b \bar{\mathbb{B}})$, and it is influenced by the helicity of electromagnetic field and of gravitational field. The impact of the helicity may be significant especially in the strong fields.

7. CONCLUSIONS

In the octonion compounding space with the operator $\lozenge$ and the compounding field strength, the features of the electromagnetic field and the gravitational field can be depicted by the algebra of octonions, including the field source, the gravitational mass density, and the mass continuity equation etc. And the physical quantities are influenced by the current helicity, the field energy, and the enstrophy in the electromagnetic field and the gravitational field.

Similarly to the above compounding fields, there may exist other kinds of fields with different operators. The magnetic helicity, the cross helicity, and the kinetic helicity cause these fields with different kinds of operators combine together to become one compounding field. In the octonion compounding space with the operator $\lozenge$ and the octonion quantity $\bar{\mathbb{X}}$, the field potential $\bar{\mathbb{A}}$, the field strength $\bar{\mathbb{B}}$, and the field source $\bar{\mathbb{S}}$ etc., much more helicity terms can be concluded in the electromagnetic field and the gravitational field, including the magnetic helicity, the current helicity, the cross helicity, the kinetic helicity, the enstrophy, the field energy, and some other helicity terms. It is found that those helicity terms will effect the gravitational mass density and the mass continuity equation etc. directly. The impact of these helicity terms may be significant in the strong fields of the electromagnetic field and the gravitational field.

It should be noted that the study for the helicity terms with different kinds of operators examined only some simple cases in the electromagnetic field and gravitational field. Despite its preliminary features, this study can clearly indicate the above helicity terms and the enstrophy are only some simple inferences of the field strength helicity and the field source helicity. They will impact the gravitational mass density and the mass continuity equation in the electromagnetic and gravitational fields. For the future studies, the research will concentrate on only the predictions about some new cross helicity terms related to different physical quantities in the case of the high velocity curl and the strong strength in the electromagnetic field and gravitational field.

ACKNOWLEDGMENT

This project was supported partially by the National Natural Science Foundation of China under grant number 60677039.

REFERENCES

1. Seehafer, N., M. Gellert, K. M. Kuzanyan, and V. V. Pipin, "Helicity and the solar dynano," *Advances in Space Research*, Vol. 32, No. 10, 1819–1833, 2003.
2. Malyshev, A. V., "DNA double helices for single molecule electronics," *Physical Review Letters*, Vol. 98, No. 9, 096801, 4 pages, 2007.
3. Podesta, J. J. and A. Bhattacharjee, "Theory of incompressible magnetohydrodynamic turbulence with scale-dependent alignment and cross-helicity," *The Astrophysical Journal*, Vol. 718, No. 2, 1151–1157, 2010.
4. Trueba, J. L. and M. Arrayas, "Vorticity field, helicity integral and persistence of entanglement in reaction-diffusion systems," *Journal of Physics A: Mathematical and Theoretical*, Vol. 42, No. 28, 282001, 6 pages, 2009.
5. Maxwell, J. C., *A Treatise on Electricity and Magnetism*, Dover Publications Inc., New York, 1954.
6. Weng, Z.-H., "Electromagnetic forces on charged particles," *PIERS Proceedings*, 361–363, Moscow, Russia, August 18–21, 2009.
7. Yeates, A. R., D. H. Mackay, and A. A. van Ballegooijen, "Evolution and distribution of current helicity in full-sun simulations," *The Astrophysical Journal*, Vol. 680, No. 2, L165–L168, 2008.

Comparative Analysis of the Dynamic Stark Effect in Spectra of Rare Gas Atoms and Ions

E. V. Koryukina[1] and V. I. Koryukin[2]

[1]Tomsk State University, Lenin Avenue 36, Tomsk 634050, Russia
[2]Siberian State Medical University, Moscow Road 2, Tomsk 634050, Russia

Abstract— In this work, theoretical *ab initio* calculations and comparative analysis of splitting and shifts of energy levels of rare gas atoms and ions in an alternating circularly polarized electric field are performed. The behavior of the spectra of rare gas atoms and ions was investigated as function of the electric field frequency and strength as well as the atomic/ionic nucleus charge.

1. INTRODUCTION

In the study of plasma by spectroscopic methods, both atomic and ionic emission spectra of an active medium are recorded in experiments. The behavior of the spectra induced by an alternating electric field is characterized by shifts and splitting of spectral lines and strongly depends on the frequency and strength of this field. In order to interpret the experimental data accurately, one needs a correct choice of theoretical calculation method, computer simulation of the considered spectra on the basis of this method, and comparison of the simulation data with experiment.

Some attempts were made to derive formulas allowing calculation of shifts and splitting of energy levels in the electric field of any strength and frequency. However, these attempts were successful only in some particular cases. A number of formulas were obtained for calculating energy level shifts for the systems in the one- and two-level approximations [1]. Further, in the framework of non-stationary perturbation theory, formulas for calculating the energy shifts in the electric field of any polarization were obtained for the case of isolated atomic level in the absence of resonances with the electric field (see [2] and the references therein). All formulas obtained in [2] are applicable only to calculations of Rydberg states of atoms. Furthermore, the application of perturbation theory is limited by the requirements of a low electric field strength, the smallness of splitting of energy levels and the necessity of calculating resonance and non-resonance perturbation by different methods. This status quo lends impetus to a search for a new theoretical approach for solving the foregoing problem.

For the case of a circularly polarized field (the electric field of such polarization can be observed in a high-frequency inductive discharge, under laser excitation, and at collisions with charged particles at ultra-low energies), the non-stationary Schrödinger equation can be reduced to the stationary one due to separation of spatial and time variables in the framework of the rotating-wave approximation [3]. It is obvious, a solution to the stationary Schrödinger equation is much simpler than that to the non-stationary one; however, even in this case, no general method for calculating shifts and splitting of spectral lines in the electric field of any strength and frequency has been developed so far, because the limitations inherent in stationary perturbation theory remain valid.

A theoretical approach suitable for calculating atomic and ionic spectra in an alternating circularly polarized electric field of an arbitrary strength and frequency was developed in [4]. This method, free from limitations inherent in perturbation theory and allowing calculations in the many-level approximation, was applied to calculating emission spectra of rare gas atoms He, Ne, Ar and Kr [4–7]. The method gave good results in simulation of the spectra of neutral atoms in the electric field. In this work, the theoretical approach under consideration is applied to calculating the dynamic Stark effect for rare gas ions.

2. THEORETICAL METHOD

In a circularly polarized electric field, the non-stationary Schrödinger equation is written as

$$i\frac{\partial\psi_n(\vec{r},t)}{\partial t} = \left(\widehat{H}_0\left(\vec{r}\right) - eF\left(x\cos\omega t \pm y\sin\omega t\right)\right)\psi_n(\vec{r},t), \tag{1}$$

where ψ_n is the wave function of the n-th state of the system, $\widehat{H}_0(\vec{r})$ is the unperturbed Hamiltonian, and the operator $-eF(x\cos\omega t \pm y\sin\omega t)$ describes perturbation induced by the interaction of an

atom or ion with a circularly polarized field of frequency ω and strength F. The "+" and "−" signs correspond to the right and left polarization of the field, respectively. To go to the stationary Schrödinger equation, it is necessary to use the rotating-wave approximation [3].

In the framework of this approximation, the wave function in the coordinate system rotating around the Z-axis with the frequency ω, has the form

$$\varphi\left(\vec{r},t\right)=\exp\left(i\omega t\widehat{J}_z\right)\psi(\vec{r},t), \tag{2}$$

where $\widehat{J}_z$ is the z-component of the total angular momentum operator. On substituting Eq. (2) in Eq. (1), we get

$$i\frac{\partial\varphi(\vec{r},t)}{\partial t}=\widehat{Q}\varphi(\vec{r},t),\quad \widehat{Q}=\left(\widehat{H}_0-\omega\widehat{J}_z\pm F\widehat{D}_x\right). \tag{3}$$

As seen from Eq. (3), the operator $\widehat{Q}$ is time-independent. Hence, in the rotating-wave approximation, it is possible to go from the non-stationary Schrödinger Eq. (1) to the stationary one, and we have

$$\widehat{Q}\varphi(\vec{r})=\varepsilon\varphi(\vec{r}),\quad \varphi(\vec{r},t)=\exp(-i\varepsilon t)\varphi(\vec{r}) \tag{4}$$

where $\widehat{Q}$ is the operator of energy of an atom/ion in the electric field, and ε and $\varphi(\vec{r},t)$ are the energy and wave function of an atom/ion in the electric field in the rotating coordinate system. Instead of solving the Schrödinger equation within perturbation theory, it is much more convenient to solve this equation by the method of the energy matrix diagonalization [4]. It was shown in [4] that the wave functions and energies of the atom and ion, being solutions to the Schrödinger Eq. (4), are determined from diagonalization of the energy matrix with elements

$$Q_{mn}=E_n^{(0)}\delta_{mn}-\omega\left\langle\varphi_m^{(0)}(\vec{r})\left|\widehat{J}_z\right|\varphi_n^{(0)}(\vec{r})\right\rangle\pm F\left\langle\varphi_m^{(0)}\left|D_x\right|\varphi_n^{(0)}\right\rangle, \tag{5}$$

where $\varphi_n^{(0)}$ and $E_n^{(0)}$ are the wave function and energy of the n-th state of an atom/ion in the absence of external electric field, and D_x is the x-component of the dipole transition operator. Diagonalization of the energy matrix with elements (5) gives a set of wave functions and an energy spectrum for the n-states of the atom/ion in the electric field. Upon diagonalization of the $\widehat{Q}$ matrix, we get the energies ε_n and wave functions as

$$\varphi_n(\vec{r},t)=e^{-i\varepsilon_n t}\sum_k C_{nk}\varphi_k^{(0)}(r) \tag{6}$$

for the n states of the atom/ion in the electric field in the rotating coordinate system. The coefficients C_{nk} in the wave functions (6) depend on the electric field frequency and strength. To find the average energies of the atom/ion in the initial coordinate system, it is necessary to perform averaging over the oscillation period. Upon averaging, the average energy of the system in the electric field in the initial coordinate system is written in the following form

$$\bar{E}_n=\left\langle\psi_n(\vec{r},t)\left|H(\vec{r},t)\right|\psi_n(\vec{r},t)\right\rangle=\varepsilon_n+\omega\left\langle\varphi_n(\vec{r})\left|\widehat{J}_z\right|\varphi_n(\vec{r})\right\rangle. \tag{7}$$

It follows from Eq. (7) that $\bar{E}_n$ is time-independent. The matrix elements of the D_x operator in Eq. (5) are calculated as follows

$$\begin{aligned}\left\langle\varphi_m^{(0)}\left|D_x\right|\varphi_n^{(0)}\right\rangle &= \left\langle\gamma JM\left|D_x\right|\gamma' J'M'\right\rangle\\ &= \frac{(-1)^{J-M}}{\sqrt{2}}\left[\begin{pmatrix} J & 1 & J'\\ -M & -1 & M'\end{pmatrix}-\begin{pmatrix} J & 1 & J'\\ -M & 1 & M'\end{pmatrix}\right]\left\langle\gamma J\left\|D\right\|\gamma' J'\right\rangle\end{aligned} \tag{8}$$

where the reduced matrix elements $\langle\gamma J\|D\|\gamma' J'\rangle$ are calculated depending on a coupling scheme and transition type. There are three transition types for atoms and ions in calculations of the matrix elements of the operator D_x in Eq. (8), a namely: the $(\gamma S_1L_1)l_1T_1T_2J-(\gamma' S_1'L_1')l_2U_1'U_2'J'$ transitions of I type, the $(\gamma S_1L_1)l_1^{N_1}T_1T_2J-(\gamma' S_1'L_1')l_1^{N_1-1}$, $l_2U_1'U_2'J'$ transitions of II type, and the

$(\gamma_1 S_1 L_1) l_1^{N_1} (\gamma_2 S_2 L_2) l_2^{N_2} T_1 T_2 J - (\gamma_1' S_1' L_1') l_1^{N_1 - 1} (\gamma_2' S_2' L_2') l_2^{N_2+1} U_1' U_2' J'$ transitions of III type, where $T_1 T_2 J$ and $U_1' U_2' J'$ are the quantum numbers of the term in a coupling scheme. The states of rare gas atoms and ions are calculated within the *LS*-coupling scheme and *Jl*-coupling scheme.

As seen from the above reasoning, the proposed approach is free from limitations inherent in perturbation theory, and it may be applied to calculations of the dynamic Stark effect for any atom or ion in a circularly polarized electric field of an arbitrary strength and frequency. Additionally, we can take into account the interaction of the energy levels induced by the electric field. Finally, this method allows us to calculate both resonance and non-resonance excitations using a unique approach, rather than two different techniques, as in perturbation theory.

3. RESULTS AND DISCUSSION

The developed theoretical approach was implemented in a special software package written in FORTRAN. This software was used to investigate the energy level shifts and splitting for rare gas atoms and ions in the electric field of strength up to 10 kV/cm. The calculations were carried out for different frequencies of the electric fields generated by real excitation sources, namely, $\omega = 100$ MHz (a high-frequency discharge HFD), $\omega = 151.91 \cdot 10^3$ MHz (an NH_3 laser), and $\omega = 243.52 \cdot 10^4$ MHz (an HCN laser). The calculations were performed within the *LS*-coupling scheme for the He atom, and the *Jl*-coupling scheme for the rest rare gas atoms (the ground states of the Ne, Ar, and Kr atoms were calculated within the *LS*-coupling scheme). In calculations of the energy matrix of the Ne^+ and Ar^+ ions, the *ns*-, *np*-, and *nd*-states were computed using the *LS*-coupling scheme, while the *nf*-states were calculated using the *Jl*-coupling scheme. The behavior of all examined *ns*-, *np*-, *nd*-, and *nf*-states was investigated as a function of the changes in the electric field frequency ω and strength F as well as the changes in the nucleus charge Z.

In computations of atomic and ionic spectra, it is necessary to take into account the difference the energy matrix structures for rare gas atoms and ions. This difference results from a distinction in the electronic structure of rare gas atoms and ions. The spectra of the Ne, Ar, and Kr atoms are formed by the $n_1 s^2 n_2 p^6$ and $n_1 s^2 n_2 p^5 [^2P] n_3 l$ configurations, whereas those of the Ne, Ar, and Kr ions are formed by the $n_1 s^2 n_2 p^5$, $n_1 s n_2 p^6$, and $n_1 s^2 n_2 p^4 [^{2S+1}L] n_3 l$ configurations. Whence it follows that the dimension of the energy matrix for an ion is much bigger than that of the corresponding atom. Moreover, in contrast to atomic spectra, where only the type I and type II transitions are taken into account in calculation of the matrix elements $\langle \varphi_m^{(0)} | D_x | \varphi_n^{(0)} \rangle$, ionic spectra must be calculated with allowance for all three transition types. In addition, in calculations of the atomic energy matrix, we have to deal with the *LS*-*Jl* transitions only from the ground $n_1 s^2 n_2 p^5 {}^2P$ state to excited states, whereas in calculations of the ionic energy matrix we must consider a bundle of the *LS*-*Jl* transitions between $n_2 p^4 [^{2S+1}L] n_3 l - n_2 p^4 [^{2S+1}L] n_3' f$ configurations. Lastly, unlike the atomic spectra, where the type I transitions constitute the major portion of all transitions, in the ionic spectra, the presence of configurations with a different core leads to an additional sparseness of the energy matrix due to the selection rules. This sparseness leads to a decrease in the ionic energy level interactions as compared with the atomic ones.

Modeling the emission spectra of rare gas atoms and ions in the electric field allowed us to reveal some regularities in the behavior of the Stark effect depending on the electric field parameters and the nucleus charge.

The F-dependence. The dependence of the energy level shifts on the electric field strength is quadratic. The sequence of levels in the electric field depends monotonically on the principal quantum number of an electron of an outer shell (see Fig. 1). For rare gas atoms, there are levels with the quantum number $J = 0$ which undergo shift alone without splitting under the influence of the electric field. As for ions, all energy levels have half-integer values of J, therefore, all these levels must split in the electric field. However, calculations show that all energy levels with the minimal value $J = 1/2$ do not split in the electric field due to weak energy level interactions.

The ω-dependence. A decrease in the splitting of energy levels is observed with an increase in the electric field frequency (see Fig. 2). This regularity is explained by the fact that an increase in the electric field frequency leads to an isolation of the energy level, and this isolation is achieved faster for ions than for atoms. The dependence on the electric field frequency is not monotonic owing to the presence of the resonances with the electric field.

The Z-dependence. For rare gas atoms and ions, the same energy levels are shifted in opposite directions with an increase in the electric field strength (see Fig. 1). The shift direction also depends on the energy level parity. In particular, at $\omega = 100$ MHz, even and odd energy levels of the He

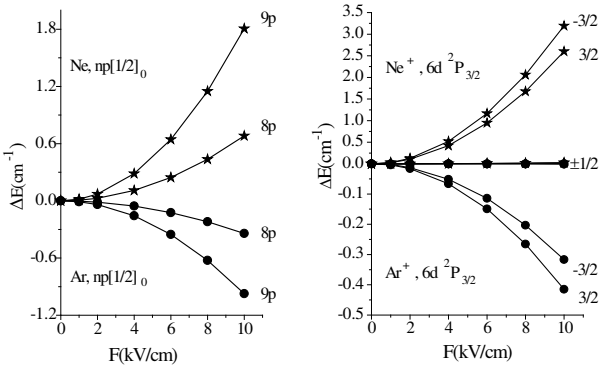

Figure 1: The behavior of atomic and ionic energy levels in the electric field ($\omega = 100\,\mathrm{MHz}$).

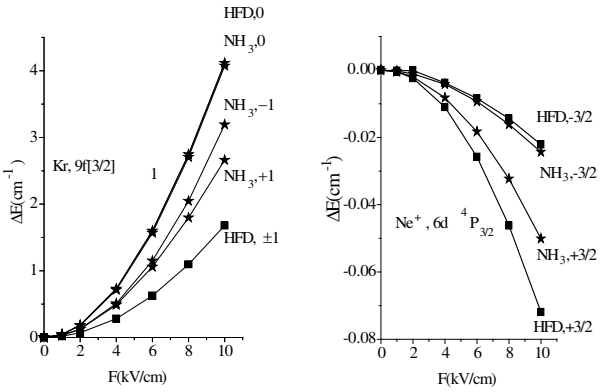

Figure 2: The ω-dependence of the energy levels for rare gas atoms and ions.

and Ne atoms are shifted in opposite directions with an increase in the electric field strength. For all considered Z, the ns-levels are shifted toward the IR region whereas the nf-levels are shifted toward the UV region.

All the foregoing regularities are valid at weak energy level interactions. If this interaction is strong, at least one of these regularities is broken.

4. CONCLUSION

The results obtained are of interest both from a theoretical point of view and for practical applications of the developed theoretical approach. The simulation data allow us to reveal regularities inherent in the behavior of shifts and splitting of atomic and ionic spectral lines in the electric fields of arbitrary frequency and strength. The results of modeling the emission spectra can also be used for plasma diagnostics and for solution of problems in plasma spectroscopy.

It should be noted that the quadratic dependence of the energy level shifts on the electric field strength is well known from perturbation theory. The rest regularities in the behavior of energy levels of atoms and ions depending on the changes in the electric field strength, frequency, and nucleus charge Z have been derived for the first time.

ACKNOWLEDGMENT

This work is continuation of the investigations initiated by grant INTAS No. 01-0200.

REFERENCES

1. Kochanov, V. P., "Dynamic Stark effect in the two- and one-level quantum schemes under a field of intensive radiation of an arbitrary frequency," *Opt. and Spectrosc.*, Vol. 84, No. 1, 4–11, 1998.
2. Delone, N. B. and V. P. Krainov, *Atoms in Strong Light Fields*, Atompress, Moscow, 1984.
3. Bunkin, F. V. and A. M. Prohorov, "Excitation and ionization of atoms in a strong radiation field," *Zh. Eksp Teor. Fiz.*, Vol. 46, No. 3, 1090–1097, 1964 (in Russian).
4. Koryukina, E. V., "Modelling of the dynamic stark effect and calculation of the transition probabilities for an Ar atom," *J. Phys. D: Appl. Phys.*, Vol. 38, No. 17, 326–3303, 2005.
5. Koryukina, E. V., "Investigation of the regularities of the transition probabilities for a Kr atom in an alternating electric field," *Proc. SPIE*, Vol. 6263, 62630O-1–62630O-11, 2006.
6. Koryukina, E. V., "Calculation of transition probabilities and lifetimes for He atom stark states in an alternating electric field," *Atm. and Oceanic Optics*, Vol. 19, No. 7, 519–525, 2006.
7. Koryukina, E. V., "Special features of the neon emission spectrum in a high-frequency discharge and laser fields for the transitions with J, $J \leq 2$," *Atm. and Oceanic Optics*, Vol. 22, No. 11, 1070–1076, 2009.

Spectral Theory of Beam Scattering by Random Curved Surfaces for Imaging Laser Radar

Yasumitsu Miyazaki
Department of Media Informatics, Aichi University of Technology
50-2 Manori, Nishihasama-cho, Gamagori 443-0047, Japan

Abstract— In Information Transport Systems, technical and social subjects of automatic driving system and safety transport and traffic system are very important problems. Automatic driving and cruising systems using optical and millimeter radars in the cars are sensor systems for measurements of distances among driving car detection of obstacles, and intelligent recognition of road environments. Optical and millimeter wave radars of short wavelengths and high frequency using short pulses of optical and millimeter wave carriers yield precise distance measurement and shape image recognition. Distance measurement using short pulse optical carriers is derived by time differences between transmitted pulse and received pulse, and image information are given by reflected waves by scanning optical beam waves of laser, as optical vision information. Comparing with millimeter waves optical waves have comparative attenuation characteristics due to rains, mist, fog, and snows, and can give high size resolution. Shape image recognition systems of car bodies complex objects using scattered and reflected waves in scanning laser radars, are very useful for ITS and object recognition. Temporal and spatial characteristics of electromagnetic scattering and reflection by driving car bodies and complex objects are studied Fundamental characteristics and application of scanning laser radars and image recognition of car body and objects are shown.

1. INTRODUCTION

Fundamental theory of scattering characteristics of laser beam wave has been studied for optical beam waveguides, optical resonators and optical beam circuit elements. Particularly, reflection and scattering characteristics by curved surfaces of lens waveguide are typical examples. The author showed analytical theory of boundary value problem for beam wave scattering by general curved surfaces [1–3]. Recently, we studied beam wave scattering theory concerning distance control system between driving automobiles and shape image recognition system using millimeter wave sensors [4–6]. With the shape image recognition system of objects using millimeter electromagnetic waves, the system using laser radar is considered as effective autocruising system. In this paper, statistical scattering theory by random curved surface using spectral function is discussed. This theory is fundamental for laser radar sensors and applicable to optical ray tracing and CG [7–9].

Optical wave radar, and laser radar of short wavelengths using short pulses of optical wave carriers yield precise distance measurement and image processing. ITS applications of laser radar are distance control system between driving automobiles, and auto-breaking system. Shape image recognition systems of car bodies receiving scattered and reflected waves in scanning laser radars, are very useful for ITS. Temporal and spatial characteristics of electromagnetic scattering and reflection by driving car bodies are studied.

Gaussian laser beam waves with temporal Gaussian impulse radiated from laser radar incident to complicated targets are considered. Spatial and temporal spectral functions are introduced using transverse wave number spectrum for the spatial space and angular frequencies for time domain. Spatial spectral functions concerned with Hermite-Gaussian eigenfunctions are expressed for incident and scattering electromagnetic fields. Asymptotic expressions are derived for the incident Gaussian beam, and reflected and scattered waves, using parameters of beam waist and beam spot size. Radiating optical beam packets from laser radars and reflected beam packets of temporal Gaussian pulse form and spatial Gaussian beam form are expressed as Fourier components for time coordinates and as spectral functions expanded by Hermite-Gaussian functions for space coordinates. Incident, reflected and scattered fields are studied using beam mode expansions derived by Hermite-Gaussian spectral functions.

Scattered and transmitted waves are discussed using eigenfunction orthogonalities, satisfying boundary conditions on complicated target shape for spectral functions of incident, reflected and transmitted waves. Boundary conditions of objects are applied to derive reflected and scattered fields for spectral components. Based on temporal and spatial characteristics of laser beam wave scattering, image recognitions of object targets are shown with computer image processing.

2. OBJECT SHAPE RECOGNITION BY LASER RADAR

Fundamental architectures of scanning laser radars for object image processing are shown in Figs. 1(a) and (b). Distances between the laser and object are given by pulse time difference measurement of transmitting optical pulse and receiving pulse. Measurement situation of laser and object, and laser radar system for image processing are shown in Fig. 2.

Figure 1(b) shows object shape recognition systems using scanning millimeter wave radar. S_{ij} are radiation apertures of scanning laser pulse radar and f_{ij} are multiple laser wave frequencies.

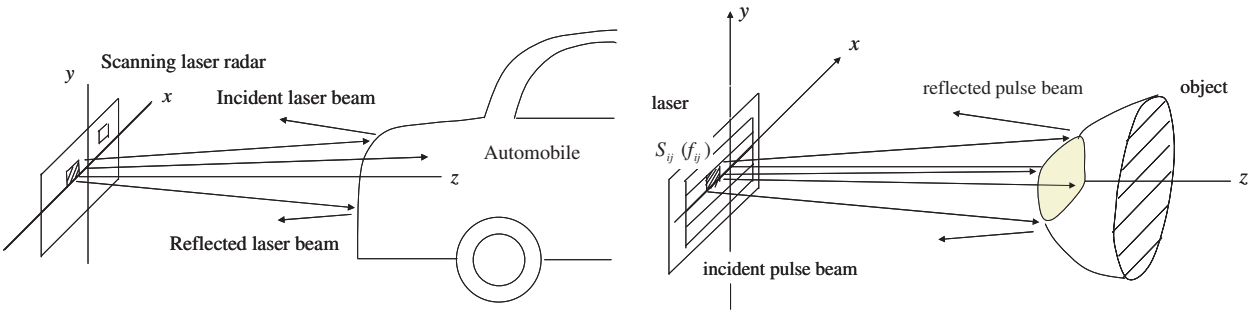

(a) Automobile laser radar

(b) Laser beam and object

Figure 1: Laser radar system.

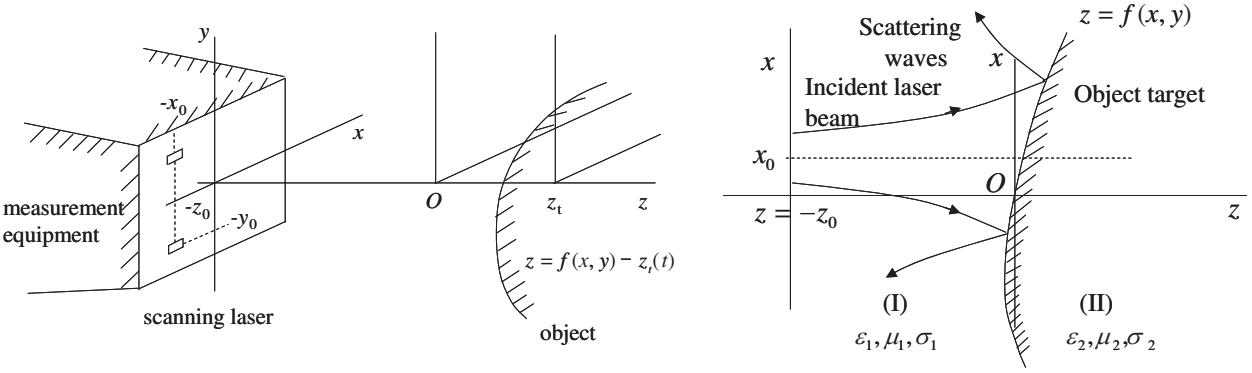

(a) Reflection and scattering of laser pulse beam

(b) Object imaging and beam scattering

Figure 2: Image processing laser and measured object.

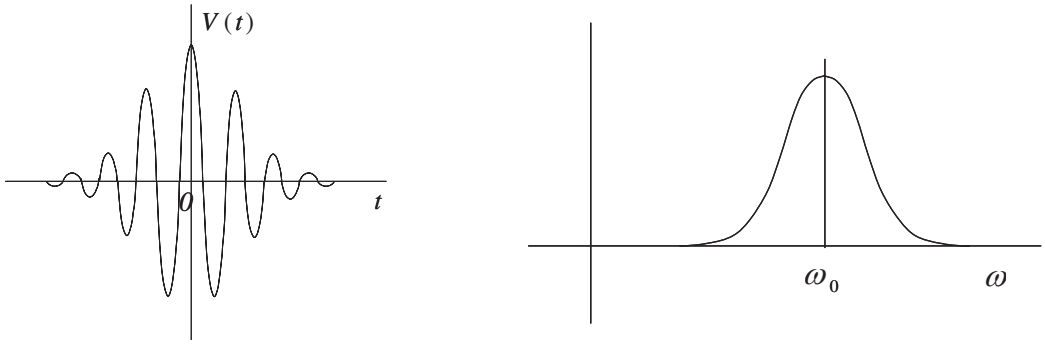

(a) Temporal characteristics of laser radar

(b) Frequency characteristics of laser pulse

Figure 3: Pulse characteristics of incident beam.

3. REFLECTION AND SCATTERING OF OPTICAL WAVE PULSES

Beam waves with beam spot size $1/a$ and beam center $(x_0,\ y_0)$ of optical pulses are radiated from laser at position $z=-z_0$ as shown in Fig. 2. Object surfaces at time t are given by random curved surfaces $z=f(x,y)+z_t(t)$ of position center z_t. Beam wave in the region I of material constants $(\varepsilon_1,\mu_{1,}\sigma_1)$ is incident to object of material constants $(\varepsilon_2,\mu_{2,}\sigma_2)$ in the region II with boundary S, $z=f(x,y)+z_t$.

Incident pulses as shown in Fig. 3 are

$$\mathbf{E}^{(i)}(\mathbf{r},t)=\frac{1}{2\pi}\int_{-\infty}^{\infty}\tilde{V}(\omega)\,\tilde{\mathbf{E}}^{(i)}(\mathbf{r},\omega)\,e^{j\omega t}d\omega \tag{1}$$

where temporal function $V(t)$ and spectral function $\tilde{V}(\omega)$ are

$$\begin{aligned} V(t)&=e^{-\left(\frac{2t}{T}\right)^2}e^{j\omega_0 t}=\frac{1}{2\pi}\int\tilde{V}(\omega)\,e^{j\omega t}d\omega \\ \tilde{V}(\omega)&=\frac{\sqrt{\pi}T}{2}e^{-\left(\frac{(\omega-\omega_0)T}{4}\right)^2} \end{aligned} \tag{2}$$

and when the fundamental beam mode with y polarization is incident, in case of two dimensional space,

$$\tilde{\mathbf{E}}^{(i)}=E_0\mathbf{i}_y e^{-j\beta(z+z_0)}\frac{1}{\sqrt{1-j\zeta}}e^{-\frac{a^2(x-x_0)^2}{2(1-j\zeta)}} \tag{3}$$

where $\zeta=\frac{(z+z_0)}{\beta}a^2$.

Object surface $z=f(x)$ separates the region of free space I and region of object II as shown in Fig. 2. Incident wave, reflected wave and transmitted wave are $\tilde{\mathbf{E}}_i$, $\tilde{\mathbf{E}}_r$ and $\tilde{\mathbf{E}}_t$. In the region I, $\tilde{\mathbf{E}}^{(I)}=\tilde{\mathbf{E}}_i+\tilde{\mathbf{E}}_r$, and in the region II, $\tilde{\mathbf{E}}^{(II)}=\tilde{\mathbf{E}}_t$.

$$\begin{aligned} \mathbf{E}_n(\mathbf{r}_j,t)&=\frac{1}{2\pi}\int_{-\infty}^{\infty}\tilde{\mathbf{E}}_n(\mathbf{r}_j,\omega)\,e^{j\omega t}d\omega \\ \tilde{\mathbf{E}}_n(\mathbf{r}_n,\omega)&=F^{-1}\hat{\mathbf{E}}_n(\beta_{tn})=\int_{-\infty}^{\infty}\hat{\mathbf{E}}_n(\beta_{tn})\,e^{-j\beta_{tn}x_n-j\sqrt{\beta_n^2-\beta_{tn}^2}z}d\beta_{tn} \end{aligned} \tag{4}$$

Wave numbers β_n are $\beta_i=\beta_r=\beta_1=\omega\sqrt{\varepsilon_1^*\mu_1}$, $\beta_t=\beta_2=\omega\sqrt{\varepsilon_2^*\mu_2}$, $\varepsilon_i^*=\varepsilon_i-j\sigma_i/\omega$. β_{tn} are β_{ti}, β_{tr} and β_{tt}.

If β_{tn} are small, we can use asymptotic approximation of $\sqrt{\beta_n^2-\beta_{tn}^2}\cong\beta_{tn}-\frac{1}{2}\frac{\beta_{tn}^2}{\beta_n}-\frac{1}{8}\frac{\beta_{tn}^4}{\beta_n^3}$, and $\hat{\mathbf{E}}_n(\beta_{tn})$ can be expanded as series of Hermite-Gaussian functions, using spectral parameter α_n,

$$\hat{\mathbf{E}}_n(\beta_{tn})=\sum_{m=0}^{\infty}a_{mn}\phi_m(\beta_{tn})\tau_n \tag{5}$$

where

$$\phi_m(\beta_{tn})=\frac{1}{\sqrt{\alpha_n\left(2^m m!\sqrt{\pi}\right)^{\frac{1}{2}}}}e^{-\frac{1}{2}\beta_n'^2}H_m\left(\beta_n'\right)\qquad\beta_n'=\beta_{tn}/\alpha_n \tag{6}$$

and coefficients a_{nm} are

$$a_{nm}\cong\int_{-\infty}^{\infty}\hat{\mathbf{E}}_n(\beta_{tn})\,\phi_m(\beta_{tn})\,\tau_n d\beta_{tn} \tag{7}$$

When incident beam wave is beam wave with the polarization of y-direction, using incident coordinates (x_i,z_i), incident beam waves are

$$\begin{aligned} \tilde{E}_{iy}&=\int_{-\infty}^{\infty}\hat{E}_i(\beta_{ti})\,e^{-j\beta_{ti}x_i-j\sqrt{\beta_1^2-\beta_{ti}^2}(z_i+z_{oi})}d\beta_{ti}, \\ \tilde{H}_{ix}&=\int_{-\infty}^{\infty}\hat{E}_i(\beta_{ti})\,\frac{(j\omega\varepsilon_1+\sigma_1)\left(-j\sqrt{\beta_1^2-\beta_{ti}^2}\right)}{-\beta_1^2}e^{-j\beta_{ti}x_i-j\sqrt{\beta_1^2-\beta_{ti}^2}(z_i+z_{oi})}d\beta_{ti} \\ \tilde{H}_{iz}&=\int_{-\infty}^{\infty}\hat{E}_i(\beta_{ti})\,\frac{(j\omega\varepsilon_1+\sigma_1)(-j\beta_{ti})}{-\beta_1^2}e^{-j\beta_{ti}x_i-j\sqrt{\beta_1^2-\beta_{ti}^2}(z_i+z_{oi})}d\beta_{ti} \end{aligned} \tag{8}$$

Transmitted waves are obtained as like Eq. (8), using transmission coordinates (x_t, z_t). Reflected waves are using

$$\tilde{E}_{ry} = \int_{-\infty}^{\infty} \hat{E}_r(\beta_{tr})\, e^{-j\beta_{tr}x_r + j\sqrt{\beta_1^2-\beta_{tr}^2}(z-z_{or})} d\beta_{tr}, \quad \tilde{E}_{ty} = \int_{-\infty}^{\infty} \hat{E}_t(\beta_{tt})\, e^{-j\beta_{tt}x_t + j\sqrt{\beta_2^2-\beta_{tt}^2}(z-z_{ot})} d\beta_{tt} \quad (9)$$

On the boundary, normal unit vector $\mathbf{n}$ and line element are

$$\mathbf{n} = \left(\gamma \frac{\partial f}{\partial x}, -\gamma\right), \quad ds = \gamma^{-1} dx \quad (10)$$

where $\gamma = \left[1 + \left(\frac{\partial f}{\partial x}\right)^2\right]^{-1/2}$.

Boundary conditions on object surface $z = f(x)$ are when the electromagnetic fields in regions I and II are $\mathbf{E}^{(1)}$, $\mathbf{H}^{(1)}$ and $\mathbf{E}^{(2)}$, $\mathbf{H}^{(2)}$

$$\mathbf{n} \times \left(\mathbf{E}^{(1)} - \mathbf{E}^{(2)}\right) = \mathbf{0}, \quad \mathbf{n} \times \left(\mathbf{H}^{(1)} - \mathbf{H}^{(2)}\right) = \mathbf{0} \quad (11)$$

Here, $\mathbf{E}^{(1)} = \mathbf{E}_i + \mathbf{E}_r$ and $\mathbf{E}^{(2)} = \mathbf{E}_t$, $\eta_i = \frac{\omega\varepsilon_i + \sigma/j}{\beta_i^2}$, the following reflected and transmitted waves are obtained

$$\begin{aligned} \hat{E}_r(\beta_t) &= \frac{\eta_1\sqrt{\beta_1^2-\beta_t^2} - \eta_2\sqrt{\beta_2^2-\beta_t^2}}{\eta_1\sqrt{\beta_1^2-\beta_t^2} + \eta_2\sqrt{\beta_2^2-\beta_t^2}} \frac{B_i(\beta_t)}{B_t(\beta_t)} e^{-j\sqrt{\beta_1^2-\beta_t^2}z_o} \hat{E}_i(\beta_t), \\ \hat{E}_t(\beta_t) &= \frac{2\eta_1\sqrt{\beta_1^2-\beta_t^2}}{\eta_1\sqrt{\beta_1^2-\beta_t^2} + \eta_2\sqrt{\beta_2^2-\beta_t^2}} \frac{B_i(\beta_t)}{B_t(\beta_t)} e^{-j\sqrt{\beta_1^2-\beta_t^2}z_o} \hat{E}_z(\beta_t) \end{aligned} \quad (12)$$

and defining $\varphi^{(0)} = |\tilde{E}_i(x,0)|$, we obtained asymptotically

$$B_r(\beta_t) = \int_{-\infty}^{\infty} e^{\mp j\sqrt{\beta_1^2-\beta_t^2}f(x)} e^{-j\beta_t x} \varphi^{(0)}(x)\, dx, \quad B_t(\beta_t) = \int_{-\infty}^{\infty} e^{-j\sqrt{\beta_2^2-\beta_t^2}f(x)} e^{-j\beta_t x} \varphi^{(0)}(x)\, dx \quad (13)$$

From Eq. (13), back scattered and reflected waves are obtained. Pulse responses due to back scattering by objects are derived by Eq. (13).

When incident fundamental beam expressed in Eq. (3) is reflected by object surface of convex curvature with the radius R at $z = 0$, reflected beam is as in Fig. 4

$$\tilde{\mathbf{E}}^{(r)} = E_0 \mathbf{i}_y e^{+j\beta(z+z_0-z_r)} \frac{1}{\sqrt{1-j\zeta_r}} e^{-\frac{a_r^2 x^2}{2(1-j\zeta_r)}} \quad (14)$$

where $\zeta_r = \frac{2(z-z_r)}{\beta} a_r^2$, $z_r = \frac{R}{2+R/z_0}$ and $a_r = \frac{R}{2z_0+R} a$.

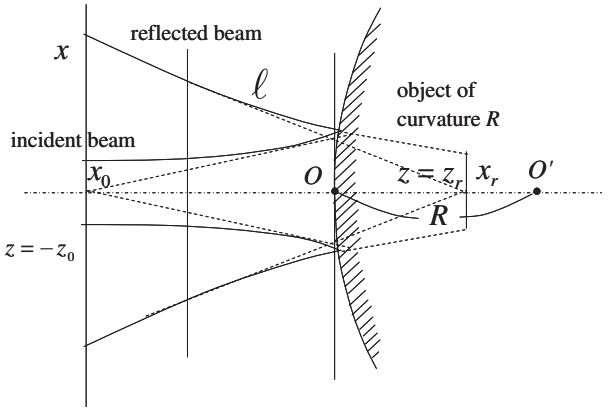

Figure 4: Scanning laser radar and reflected beam.

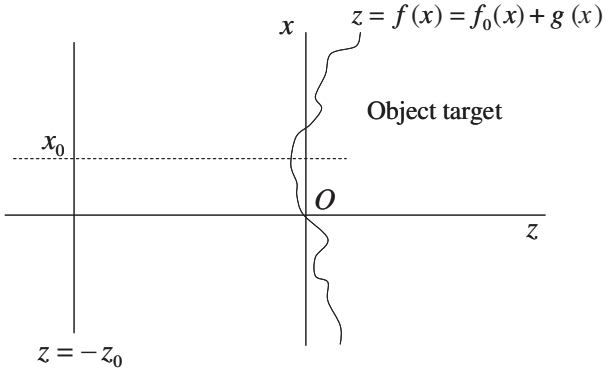

Figure 5: Scattering of laser beam by random curved surface.

Received pulse responses are, when reflection coefficient of object is R_s

$$\mathbf{E}^{(r)}(\mathbf{r},t) = E_0 R_s e^{j\omega_0 t - j\beta_0(z+z_0-z_r)} e^{-\frac{a_T^2}{2}x^2} e^{-\left(\frac{2}{T}\right)^2\left(t-\frac{\ell}{c}\right)^2}\mathbf{i}_\tau \tag{15}$$

where $\ell(x, z_0, z_r, R)$ is ray path of incident beam and reflected beam.

Scattering characteristics of beam wave by wedge and complex object surfaces are also shown using Eq. (13).

4. STATISTICAL CHARACTERISTICS OF REFLECTED AND SCATTERED WAVES

On the random curved surface of car bodies and objects, we define $z = f(x) = f_0(x) + g(x)$ with random function $g(x)$, under the condition of $g(x) \ll f_0(x)$ and correlation function of $g(x)$ with correlation length ℓ_g as

$$\langle g(x_1)\, g(x_2)\rangle = (\Delta g)^2 e^{-\frac{(x_1-x_2)^2}{\ell_g}} \tag{16}$$

Covariance and coherent functions of reflected and scattered fields are, derived by spectral Eqs. (12), (13) and statistical boundary Eq. (16), as

$$\begin{aligned}\operatorname{cov}\left[\tilde{E}_r(\mathbf{r}_1,\omega)\,\tilde{E}_r^*(\mathbf{r}_2,\omega)\right] &= \int_{-\infty}^{\infty} d\beta_{x1}\int_{-\infty}^{\infty} d\beta_{x2} e^{-j\beta_{x1}x_1 + j\sqrt{\beta_1^2-\beta_{x1}^2}(z_1-z_{0r})} \\ &\quad \cdot e^{j\beta_{x2}x_2 - j\sqrt{\beta_1^2-\beta_{x2}^2}(z_2-z_{0r})}\left\langle \hat{E}_r(\beta_{x1})\,\hat{E}_r^*(\beta_{x2})\right\rangle\end{aligned} \tag{17}$$

Here,

$$\begin{aligned}\left\langle \hat{E}_r(\beta_{x1})\,\hat{E}_r^*(\beta_{x2})\right\rangle &= \left|\frac{\eta_1\sqrt{\beta_1^2-\beta_x^2}-\eta_2\sqrt{\beta_2^2-\beta_x^2}}{\eta_1\sqrt{\beta_1^2-\beta_x^2}+\eta_2\sqrt{\beta_2^2-\beta_x^2}}\right|^2 \left\langle \frac{B_i(\beta_{x1})\,B_i^*(\beta_{x2})}{B_r(\beta_{x1})\,B_r^*(\beta_{x2})}\right\rangle \\ &\quad \cdot e^{-j\sqrt{\beta_1^2-\beta_{x1}^2}z_0 + j\sqrt{\beta_1^2-\beta_{x2}^2}z_0}\,\hat{E}_i(\beta_{x1})\,\hat{E}_i^*(\beta_{x2})\end{aligned} \tag{18}$$

5. CONCLUSION

Image processing using optical and millimeter wave pulses is very useful technique for ITS. Object shape detection and recognition system are based on electromagnetic reflection and scattering. Object shape detection by using scanning laser radar is discussed by electromagnetic field theory with spectral functions of Gaussian beams for random curved surfaces of car bodies and objects. Laser radar system for ITS may be accomplished, based on this fundamental theory for object image recognition.

REFERENCES

1. Miyazaki, Y. and Y. Akao, "Reflection and mode conversion of beam wave through a curved interface between dielectrics and thick dielectric lens," *Trans. of IECE, Japan*, Vol. 51-B, No. 1, 25–31, 1968.
2. Miyazaki, Y., "Asymptotic beam mode characteristics of nanometer electromagnetic waves in gradient X-ray waveguides," *Proc. 2001 URSI International Symp. on EM Theory*, 431–433, Victoria, 2001.
3. Miyazaki, Y., "Space-time impulse responses of electromagnetic backscatterings of beam waves for sensing," *Proc. of OFSET 2000*, 361–364, 2000.
4. Takahashi, K. and Y. Miyazaki, "Scattering analysis of millimeter wave radar for collision avoidance using FDTD method," *Trans. IEE, Japan*, Vol. 120C-1, No. 1, 111–116, 2000.
5. Tanaka, M. and Y. Miyazaki, "Microwave simulation characteristics of electromagnetic wave scattering by automobile," *Trans. of IECE, Japan*, Vol. J66-B, No. 8, 1005–1012 1983.
6. Takahashi, K. and Y. Miyazaki, "FDTD computer simulation of millimeter wave driving radar for ITS," *11th World Congress on ITS Nagoya*, Vol. 4088, 6, 2004.
7. Miyazaki, Y., "Electromagnetic scattering and filtering in random media for image sensing," *PIERS Proceedings*, 689–697, Cambridge, USA, July 2–6, 2008.
8. Miyazaki, Y., "Electromagnetic scattering theory of car body imaging using scanning millimeter wave radar," *PIERS Proceedings*, 1423–1428, Beijing, China, March 23–27, 2009.
9. Mizuno, K., "Imaging arrays in the millimeter wave region: Millimeter wave camera," *J. of IEICE, Japan*, Vol. 9, No. 2, 177–181, 1996.

Propagation of TE-waves through a Nonlinear Metamaterial Layer with Arbitrary Nonlinearity

D. V. Valovik
Penza State University, 40 Krasnay Street, Penza 440026, Russia

Abstract— Propagation of TE-waves through a nonlinear layer is considered. The problem for Maxwell equations is reduced to the nonlinear boundary eigenvalue problem. Dispersion equation (DE) for propagation constants is derived. The DE can be used for analytical and numerical study of the problem. Some numerical results are also presented.

1. INTRODUCTION

Problems of electromagnetic waves propagation in nonlinear waveguide structures are intensively investigated during last decades. The article [1] is the first one, where the problems of electromagnetic waves propagation in a layer and a circular cylindrical waveguide with Kerr nonlinearities are considered in strict electromagnetic statement. At least from 1970-th till now these problems attract attention (for bibliography see [2–5]). The problems of propagation TE- and TM-waves in layers with Kerr nonlinearity have been solved in [2, 3], respectively. Then, in [6] the problem of TE-waves propagation in a metamaterial layer with Kerr nonlinearity is considered and many numerical results are also presented. The articles [3–8] are devoted to the studies of TM-waves in nonlinear layers also for nonlinear metamaterials.

2. MAXWELL EQUATIONS AND STATEMENT OF THE PROBLEM

Let us consider electromagnetic waves propagating through a homogeneous isotropic nonmagnetic dielectric layer. The layer is located between two half-spaces: $x < 0$ and $x > h$ in Cartesian coordinate system $Oxyz$. The half-spaces are filled with isotropic nonmagnetic media without any sources and characterized by permittivities $\varepsilon_1 \geq \varepsilon_0$ and $\varepsilon_3 \geq \varepsilon_0$, respectively, where ε_0 is the permittivity of free space. Assume that everywhere $\mu = \mu_0$ is the permeability of free space.

Electromagnetic field harmonically depends on time [1]: $\tilde{\mathbf{E}}(x,y,z,t) = \mathbf{E}_+ \cos\omega t + \mathbf{E}_- \sin\omega t$, $\tilde{\mathbf{H}}(x,y,z,t) = \mathbf{H}_+ \cos\omega t + \mathbf{H}_- \sin\omega t$, where ω is the circular frequency; $\mathbf{E}_+$, $\mathbf{E}_-$, $\mathbf{H}_+$, $\mathbf{H}_-$ are real functions of three spatial variables. Below the time multipliers are omitted. Expressions $\mathbf{E} = \mathbf{E}_+ + i\mathbf{E}_-$, $\mathbf{H} = \mathbf{H}_+ + i\mathbf{H}_-$ are complex amplitudes and $\mathbf{E} = (E_x, E_y, E_z)^T$, $\mathbf{H} = (H_x, H_y, H_z)^T$.

Electromagnetic field $(\mathbf{E}, \mathbf{H})$ satisfies Maxwell equations

$$\operatorname{rot}\mathbf{H} = -i\omega\varepsilon\mathbf{E}, \quad \operatorname{rot}\mathbf{E} = i\omega\mu\mathbf{H}, \tag{1}$$

the continuity condition for the tangential field components on the media interfaces $x = 0$, $x = h$ and the radiation condition at infinity: the electromagnetic field exponentially decays as $|x| \to \infty$ in the domains $x < 0$ and $x > h$.

Let f be an analytical function[1]. The permittivity inside the layer is $\varepsilon = \varepsilon_2 + \varepsilon_0 f\left(|\mathbf{E}|^2\right)$. We seek γ under condition $\max(\varepsilon_1, \varepsilon_3) < \gamma^2 < \varepsilon_2$. This condition corresponds to classical problem of TE-waves propagating in a linear layer (where $f \equiv 0$), when $\varepsilon_1 \geq \varepsilon_0$, $\varepsilon_3 \geq \varepsilon_0$ and $\varepsilon_2 > \max(\varepsilon_1, \varepsilon_3)$. Therefore we use it to derive the DEs for a nonlinear layer. The solution to the Maxwell equations are sought in the entire space.

3. TE-WAVES

Let us consider TE-waves: $\mathbf{E} = (0, E_y, 0)^T$, $\mathbf{H} = (H_x, 0, H_z)^T$. It is easy to prove that the components do not depend on y. Waves propagating along medium interface z harmonically depend on z. It means that the components have the form $E_y = E_y(x)e^{i\gamma z}$, $H_x = H_x(x)e^{i\gamma z}$, $H_z = H_z(x)e^{i\gamma z}$. So we obtain from system (1) the equation $\gamma^2 E_y(x) - E_y''(x) = \omega^2\mu\varepsilon E_y(x)$, where $(\cdot)' \equiv \frac{d}{dx}$ and γ is an unknown spectral parameter (propagation constant).

Let us denote $k_0^2 = \omega^2\mu_0\varepsilon_0$, and perform the normalization according to the formulas $\tilde{x} = k_0 x$, $\frac{d}{dx} = k_0\frac{d}{d\tilde{x}}$, $\tilde{\gamma} = \frac{\gamma}{k_0}$, $\tilde{\varepsilon}_j = \frac{\varepsilon_j}{\varepsilon_0}$ $(j = 1, 2, 3)$. Denoting $E_y(\tilde{x}) \equiv Y(\tilde{x})$ and omitting the tilde symbol,

[1]Everywhere below when we consider an analytical function we mean that it is the analytical function of real variable.

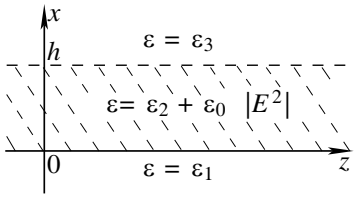

Figure 1: The geometry of the problem.

from the latter equation we have $Y''(x) = \gamma^2 Y(x) - \varepsilon Y(x)$. Introducing new function $Z(x) = Y'(x)$ we can consider this equation as the system of equations:

$$Y'(x) = Z(x), \quad Z'(x) = \left(\gamma^2 - \varepsilon\right) Y(x). \tag{2}$$

It is necessary to find eigenvalues γ of the problem that correspond to surface waves propagating along boundaries of the layer $0 < x < h$, i.e., the eigenvalues corresponding to the eigenmodes of the structure. We seek the real values of spectral parameter γ, such that real solutions $Y(x)$ and $Z(x)$ to system (2) exist[2].

Also we assume that functions Y and Z are differentiable: $Y(x) \in C(-\infty, +\infty) \cap C^1(-\infty, +\infty) \cap \cap C^2(-\infty, 0) \cap C^2(0, h) \cap C^2(h, +\infty)$, $Z(x) \in C(-\infty, +\infty) \cap C^1(-\infty, 0) \cap C^1(0, h) \cap C^1(h, +\infty)$. These conditions follow from physical nature of the problem.

4. SOLVING THE SYSTEM OF DIFFERENTIAL EQUATIONS

In the domain $x < 0$ we have $\varepsilon = \varepsilon_1$. In accordance with the radiation condition we obtain the solution of system (2)

$$Y(x) = Ae^{x\sqrt{\gamma^2 - \varepsilon_1}}, \quad Z(x) = A\sqrt{\gamma^2 - \varepsilon_1} e^{x\sqrt{\gamma^2 - \varepsilon_1}}. \tag{3}$$

We assume that $\gamma^2 - \varepsilon_1 > 0$ otherwise it will be impossible to satisfy the radiation condition.

In the domain $x > h$ we have $\varepsilon = \varepsilon_3$. In accordance with the radiation condition we obtain the solution of system (2)

$$Y(x) = Be^{-(x-h)\sqrt{\gamma^2 - \varepsilon_3}}, \quad Z(x) = -\sqrt{\gamma^2 - \varepsilon_3} Be^{-(x-h)\sqrt{\gamma^2 - \varepsilon_3}}. \tag{4}$$

Here for the same reason as above we consider that $\gamma^2 - \varepsilon_3 > 0$.

Constants A and B in (3) and (4) are defined by transmission conditions and initial conditions.

Inside the layer $0 < x < h$ system (2) has the form

$$Y'(x) = Z(x), \quad Z'(x) = \left(\gamma^2 - \varepsilon_2 - f\left(Y^2\right)\right) Y(x). \tag{5}$$

System (5) has the first integral. So, we can study the first-order equation (either first or second in (5)) with the first integral instead of the second-order equation. Divide the second equation in (5) by the other one we obtain $ZdZ + \left(\varepsilon_2 - \gamma^2 + f\left(Y^2\right)\right) YdY = 0$. This equation is the total differential equation. Its general solution has the form

$$Z^2 + (\varepsilon_2 - \gamma^2)Y^2 + \varphi(Y^2) = C, \tag{6}$$

where $\varphi(Y^2) = \int f(u)du\big|_{u=Y^2}$, and C is the constant of integration.

5. TRANSMISSION CONDITIONS AND TRANSMISSION PROBLEM

Tangential components of electromagnetic field are known to be continuous at media interfaces. In this case tangential components are E_y and H_z. Hence we obtain $E_y(h+0) = E_y(h-0)$, $E_y(0-0) = E_y(0+0)$, $H_z(h+0) = H_z(h-0)$, $H_z(0-0) = H_z(0+0)$. Taking it into account we have $Y'(h) = Z(h)$, $Y'(0) = Z(0)$. It means that $B = Y_h$, $A = Y_0$; we denote $Y_0 = Y(0) = E_y(0-0)$ and $Y_h = Y(h) = E_y(h+0)$. Constant Y_h is supposed to be known (initial condition). Let $Z_0 = Z(0) = H_z(0-0)$, $Z_h = Z(h) = H_z(h+0)$. Then $Z_h = -\sqrt{\gamma^2 - \varepsilon_3} Y_h$ and $Z_0 = \sqrt{\gamma^2 - \varepsilon_1} Y_0$.

[2]In this case, $|\mathbf{E}|^2$ does not depend on z. Since $\mathbf{E} = \left(0, E_y(x)e^{i\gamma z}, 0\right) = e^{i\gamma z}(0, E_y, 0)$ then $|\mathbf{E}| = |e^{i\gamma z}| \cdot |E_y|$. It is known that $|e^{i\gamma z}| = 1$ as $\mathrm{Im}\gamma = 0$. Let $\gamma = \gamma' + i\gamma''$. Then, we obtain $|e^{i\gamma z}| = |e^{i\gamma' z}| \cdot |e^{-\gamma'' z}| = e^{-\gamma'' z}$. If $\gamma'' \neq 0$ then $e^{-\gamma'' z}$ is a function on z. In this case the component E_y depends on z, but it contradicts to the choice of $E_y(x)$.

All above implies the transmission conditions for functions Y, Z

$$[Y]_{x=0} = 0, \quad [Y]_{x=h} = 0, \quad [Z]_{x=0} = 0, \quad [Z]_{x=h} = 0, \tag{7}$$

where $[f]_{x=x_0} = \lim_{x\to x_0-0} f(x) - \lim_{x\to x_0+0} f(x)$.

We also suppose that functions $Y(x)$, $Z(x)$ satisfy the condition

$$Y(x) = O\left(|x|^{-1}\right), \quad Z(x) = O\left(|x|^{-1}\right) \text{ as } |x| \to \infty. \tag{8}$$

Let $\mathrm{D} = \begin{pmatrix} d/dx & 0 \\ 0 & d/dx \end{pmatrix}$, $\mathbf{F}(X,Z) = (X,Z)^T$, $\mathbf{G}(\mathbf{F},\gamma) = (G_1,G_2)^T$, where $Y \equiv Y(x)$, $Z \equiv Z(x)$ are unknown functions, $G_1 \equiv G_1(\mathbf{F},\gamma)$, $G_2 \equiv G_2(\mathbf{F},\gamma)$ are right-hand sides of system (5). The value γ is a spectral parameter. Rewrite the problem using new notations.

For the half-space $x < 0$ and $\varepsilon = \varepsilon_1$, we obtain

$$\mathrm{D}\mathbf{F} - \begin{pmatrix} 0 & 1 \\ \gamma^2 - \varepsilon_1 & 0 \end{pmatrix} \mathbf{F} = 0. \tag{9}$$

Inside the layer $0 < x < h$ and $\varepsilon = \varepsilon_2 + f\left(Y^2\right)$, we have

$$\mathrm{L}(\mathbf{F},\gamma) \equiv \mathrm{D}\mathbf{F} - \mathbf{G}(\mathbf{F},\gamma) = 0. \tag{10}$$

For the half-space $x > h$ and $\varepsilon = \varepsilon_3$, we obtain

$$\mathrm{D}\mathbf{F} - \begin{pmatrix} 0 & 1 \\ \gamma^2 - \varepsilon_3 & 0 \end{pmatrix} \mathbf{F} = 0. \tag{11}$$

Using $Z_h = -\sqrt{\gamma^2 - \varepsilon_3} Y_h$ and (6) we find the value $C_h^Y := C|_{x=h} = (\varepsilon_2 - \varepsilon_3)Y_h^2 + \varphi(Y_h^2)$. Transmission conditions (7) and first integral (6) imply the equation with respect to Y_0:

$$(\varepsilon_2 - \varepsilon_3)Y_h^2 + \varphi\left(Y_h^2\right) = (\varepsilon_2 - \varepsilon_1)Y_0^2 + \varphi\left(Y_0^2\right). \tag{12}$$

Let us formulate the transmission problem. *It is necessary to find eigenvalues γ and corresponding to them nonzero vectors* $\mathbf{F}$ *such that* $\mathbf{F}$ *satisfies to Equations* (9)–(11). *Components of the vector* $\mathbf{F}$ *satisfy transmission conditions* (7), *condition* (8), *and* $Y(0) \equiv Y_0$ *is defined from Equation* (12).

Definition 1. The value $\gamma = \gamma_0$ such that nonzero solution $\mathbf{F}$ to problem (9)–(11) exists under conditions (7), (8), and (12) is called an eigenvalue of the problem. Solution $\mathbf{F}$, corresponding to the eigenvalue is called an eigenvector of the problem, and components $Y(x)$ and $Z(x)$ of vector $\mathbf{F}$ are called eigenfunctions.

6. THE DISPERSION EQUATION AND THE THEOREM OF EQUIVALENCE

Introduce the new variables $\tau(x) = \varepsilon_2 + Y^2(x)$, $\eta(x) = \frac{Z(x)}{Y(x)}$.

System (5) takes the form

$$\tau' = 2(\tau - \varepsilon_2)\eta, \quad \eta' = \left(\gamma^2 - \varepsilon_2 - f(\tau - \varepsilon_2) - \eta^2\right). \tag{13}$$

First integral (6) has the form

$$(\tau - \varepsilon_2)\eta^2 + (\varepsilon_2 - \gamma^2)(\tau - \varepsilon_2) + \varphi(\tau - \varepsilon_2) = C. \tag{14}$$

If nonlinearity function f is a polynomial one then Equation (14) is an algebraic equation with respect to τ. Polarization vector in constitutive relations in Maxwell equations can be expanded into a series in $|\mathbf{E}|$. Cutting off the series we obtain a polynomial function.

Further, we have $\tau(0) = \varepsilon_2 + Y_0^2$, $\tau(h) = \varepsilon_2 + Y_h^2$; since Y_h is known, so is $\tau(h)$. In accordance with the transmission conditions for $\eta(0)$ and $\eta(h)$ we have

$$\eta(0) = \sqrt{\gamma^2 - \varepsilon_1} > 0, \quad \eta(h) = -\sqrt{\gamma^2 - \varepsilon_3} < 0. \tag{15}$$

Substituting $x = h$ into (14) we find $C_h^\tau := C|_{x=h} = (\varepsilon_2 - \varepsilon_3)(\tau(h) - \varepsilon_2) + \varphi(\tau(h) - \varepsilon_2)$.

From (14), using (15) and C_h^τ, we find equation with respect to $\tau(0)$:

$$(\tau(0)-\varepsilon_2)(\varepsilon_2-\varepsilon_1)+\varphi(\tau(0)-\varepsilon_2)=(\varepsilon_2-\varepsilon_3)(\tau(h)-\varepsilon_2)+\varphi(\tau(h)-\varepsilon_2). \tag{16}$$

It is obvious that $\tau(0)\geq\varepsilon_2$ since $\tau(0)=\varepsilon_2+Y_0^2$ and $\varepsilon_2>0$. For existing the root $\tau(0)\geq\varepsilon_2$ of Equation (16) it is necessary to impose some conditions on function f. For example, if f is polynomial function with nonnegative coefficients then the suitable root exists.

It should be noticed that from Equation (16), we can see that if $\varepsilon_1=\varepsilon_3$ then one of the roots of this equation will be $\tau(h)$, that is $\tau(0)=\tau(h)$. In original variables we obtain $Y_0^2=Y_h^2$. The situation is almost the same for the case of a linear layer. There is a slight difference here between the case of a nonlinear layer and the case of a linear layer. In the linear case it is always $Y_0^2=Y_h^2$ when $\varepsilon_1=\varepsilon_3$. In the nonlinear case this is only one root of Equation (16).

We suppose that function f satisfies the condition $\left(\gamma^2-\varepsilon_2-f(\tau-\varepsilon_2)-\eta^2\right)<0$. It is surely true if f is a polynomial function with nonnegative coefficients.

In this case right-hand side of the second equation of system (13) is negative. It means that function η decreases when $x\in(0,h)$. From formulas (15), we can see that $\eta(0)>0$ and $\eta(h)<0$. However, it is possible that there are zeros of the function Y. Since Y and Z are analytical functions, so is η. It means that η has discontinuities of the second kind at the points with $Y=0$. These points are poles of function η.

From first integral (14), we have $\eta^2=\frac{C_h^\tau-\varphi(\tau-\varepsilon_2)-(\varepsilon_2-\gamma^2)(\tau-\varepsilon_2)}{\tau-\varepsilon_2}$. The poles are zeros of the denominator of this expression. Then, in these points $\tau^*=\tau(x^*)$ is such that $\eta^*=\pm\infty$.

Let us suppose that there are $(N+1)$ points of discontinuities: $x_0,\ldots,x_N$ on interval $x\in(0,h)$.

The properties of function $\eta=\eta(x)$ imply $\eta(x_i-0)=-\infty$, $\eta(x_i+0)=+\infty$, where $i=\overline{0,N}$.

Denote $w=-\left[\gamma^2-\varepsilon_2-f(\tau-\varepsilon_2)-\eta^2\right]^{-1}$, where $w\equiv w(\eta)$; and $\tau=\tau(\eta)$ is expressed from first integral (14). It is necessary to seek to the solutions on each interval $[0\,,x_0)$, (x_0,x_1), …, $(x_N\,,h]$. Introduce the notation $T\equiv\int_{-\infty}^{+\infty}\omega d\eta$. It can be shown that $0<x_{i+1}-x_i=T<h$, where $i=\overline{0,N-1}$. This implies the convergence of the improper integral.

It can be proved that the DE has the form

$$J(\gamma,N):=\int_{-\sqrt{\gamma^2-\varepsilon_3}}^{\sqrt{\gamma^2-\varepsilon_1}}w d\eta+(N+1)\,T=h, \tag{17}$$

where $N\geq0$ is an integer. Expression (17) is the DE which holds for any finite h. There are several DEs for different N when $N\neq0$. It is necessary to solve with respect to γ each equation.

Theorem 1. *The set of solutions of DE* (17) *contains the set of solutions* (*eigenvalues*) *of the boundary eigenvalue problem* (9)–(11) *with conditions* (7), (8), (12).

Theorem 2 (*of equivalence*). *If equation* (16) *has the unique solution* $\tau(0)\geq\varepsilon_2$ *then boundary eigenvalue problem* (9)–(11) *with conditions* (7), (8), (12) *has a solution* (*an eigenvalue*) *if and only if this eigenvalue is a solution of DE* (17).

Let $h_{\inf}^k=\inf\limits_{\gamma^2\in(\max(\varepsilon_1,\varepsilon_3),\varepsilon_2)}J(\gamma,k)$, $h_{\sup}^k=\sup\limits_{\gamma^2\in(\max(\varepsilon_1,\varepsilon_3),\varepsilon_2)}J(\gamma,k)$ and $k=\overline{0,N}$.

Theorem 3. *Let* h *satisfies the following two-sided inequality* $h_{\inf}^k<h<h_{\sup}^k$ *for certain* $k=\overline{0,N}$. Then the boundary eigenvalue problem (9)–(11) *with conditions* (7), (8), (12) *has at least one solution* (*an eigenvalue*).

Quantities $h_{\inf}^k$ and $h_{\sup}^k$ can be numerically calculated.

It can be also proved that the DE for arbitrary real value ε_2 and $\max(\varepsilon_1,\varepsilon_3)<\gamma^2<+\infty$ has the form (17), where $N=0,\pm1,\pm2,\ldots$

Note 1. If there is a certain value γ_*^2 such that some of the integrals in DEs (17) diverge in certain inner points it simply means that the value γ_*^2 is not a solution of chosen DE and the value γ_*^2 is not an eigenvalue of the problem.

Note 2. It is necessary to emphasize that this nonlinear problem essentially depends on initial condition Y_h. The transmission problem for a linear layer does not depend on initial condition.

7. NUMERICAL RESULTS

In the Fig. 2, the behavior of dispersion curves (DC) is shown. For both cases the nonlinearity function $f=aY^2+bY^4+cY^6+dY^8$ and others parameters $\varepsilon_1=\varepsilon_3=1$, $\varepsilon_2=3$, $Y_h=1$ are used.

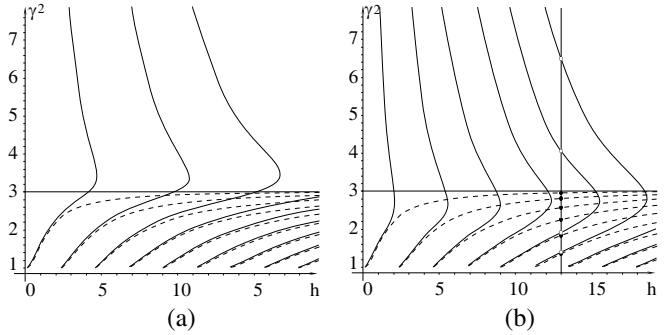

Figure 2: (a) $a = b = c = d = 0.05$; (b) $a = 0.05$, $b = c = d = 0.005$.

The dashed curves are DCs for the linear layer (when $f \equiv 0$), the lines $\gamma^2 = 3$ are asymptotes for DCs in the linear case, solid curves are DCs for the nonlinear case (solutions of DE (17)).

It follows from numerical calculations (for the case of Kerr nonlinearity it can be proved strictly) that the function $h \equiv h(\gamma)$ defined from Equation (17) when $f > 0$ has the following property: $\lim_{\gamma^2 \to +\infty} h(\gamma) = 0$. This means that in the nonlinear case every DC has an asymptote, and the asymptote is $h = 0$. How are the value of the propagation constant and its number defined? For example, see Fig. 2(b). The line $h = 13$ corresponds to the layer's thickness. For the linear layer in this case there are 6 propagation constants (black dots where the line $h = 13$ intersects the dashed DCs). These propagation constants are eigenvalues of the problem correspond to the eigenmodes. In the case of the nonlinear layer in Fig. 2(b) are shown 4 eigenvalues (uncolored dots). These eigenvalues corresponds to 4 eigenmodes. Taking the above into account it is easy to understand that in the nonlinear case there are infinite number of eigenvalues.

8. CONCLUSION

In conclusion, I would like to stress some important distinctions between linear and nonlinear cases. As the reader can see from the previous in the nonlinear case there are infinite number of eigenmodes. At the same time, in the linear case there are always finite number of eigenmodes. And also in the linear case there are no eigenvalues in the region $\varepsilon_2 < \gamma^2 < +\infty$.

ACKNOWLEDGMENT

This study was supported by the Russian Federation President Grant, project No. MK-2074.2011.1 and the Russian Foundation for Basic Research, project No. 11-07-00330-A. I also should like to thank Yu. G. Smirnov for valuable advice.

REFERENCES

1. Eleonskii, P. N., L. G. Oganes'ants, and V. P. Silin, "Cylindrical nonlinear waveguides," *Sov. Phys. JETP*, Vol. 35, No. 1, 44–47, 1972.
2. Shürmann, H. W., V. S. Serov, and Y. V. Shestopalov, "TE-polarized waves guided by a lossless nonlinear three-layer structure," *Physical Review E*, Vol. 58, No. 1, 1040–1050, 1998.
3. Valovik, D. V. and Y. G. Smirnov, "Calculation of the propagation constants of TM electromagnetic waves in a nonlinear layer," *Journal of Communications Technology and Electronics*, Vol. 53, No. 8, 883–889, 2008.
4. Joseph, R. I. and D. N. Christodoulides, "Exact field decomposition for TM waves in nonlinear media," *Optics Letters*, Vol. 12, No. 10, 826–828, 1987.
5. Leung, K. M., "Scattering of transverse-magnetic waves with a nonlinear film: Formal field solutions solutions in quadratures," *Physical Review B*, Vol. 44, No. 10, 5007–5012, 1991.
6. Valovik, D. V., "Propagation of electromagnetic waves in a nonlinear metamaterial layer," *Journal of Communications Technology and Electronics*, Vol. 56, No. 5, 544–556, 2011.
7. Valovik, D. V. and Y. G. Smirnov, "Calculation of the propagation constants and fields of polarized electromagnetic TM waves in a nonlinear anysotropic layer," *Journal of Communications Technology and Electronics*, Vol. 54, No. 4, 391–398, 2009.
8. Valovik, D. V. and Y. G. Smirnov, "Nonlinear effects in the problem of propagation of TM electromagnetic waves in a Kerr nonlinear layer," *Journal of Communications Technology and Electronics*, Vol. 56, No. 3, 283–288, 2011.

Stopband and Resonance Characteristics of Cylindrical Electromagnetic Bandgap Structures

Vakhtang Jandieri[1] and Kiyotoshi Yasumoto[2]

[1]School of Electrical Engineering and Computer Science, Kyungpook National University
Daegu 702-701, Republic of Korea
[2]Kyushu University, 2-13-11 Mainosato, Koga, Fukuoka 811-3114, Japan

Abstract— The radiation from an infinite line current source located in a cylindrical electromagnetic bandgap (EBG) structure is analyzed using a semi-analytical method based on the cylindrical Floquet mode expansion. The cylindrical EBG structure consists of parallel metallic rods periodically distributed in the concentrically or eccentrically layered cylindrical geometry. The transmission spectra of the cylindrical structure and the radiation patterns of the line source are numerically investigated.

1. INTRODUCTION

Recently the cylindrical EBG structures, which consist of parallel circular rods periodically distributed in the layered cylindrical geometry, have received a growing attention because of their potential applications to the designs of beam forming antennas. The radiation characteristics of an infinite or finite line current source coupled to the cylindrical EBG structures have been analyzed [1, 2] using the finite different time domain method and an approximate analytical method based on the fundamental cylindrical Floquet mode.

In this paper, we shall present a semi-analytical, rigorous method to analyze the radiation characteristics of an infinite line current source located in a cylindrical EBG structure formed by parallel metallic rods distributed in the concentrically or eccentrically layered cylindrical geometry. The method takes into account all of the cylindrical Floquet modes and their interactions between the cylindrical layers. The proposed method is used to numerically investigate the transmission spectra of the cylindrical EBG structure and the radiation patterns of the line source. It is demonstrated that the directivity of radiation of the line source is closely related to the resonance characteristics in the transmission spectra of the cylindrical EBG structure.

2. FORMULATION OF THE PROBLEM

The cylindrical EBG structures are formed by N-layered cylindrical arrays of circular rods located in a homogeneous background medium with material constants ε_0 and μ_0 as shown in Fig. 1. The M_ν circular rods with radius r_ν are periodically distributed on each of N circular rings with radii R_ν ($\nu = 1, 2, \ldots, N$). The rods are infinitely long in the z direction and parallel to each other. The rods in different layers of the arrays need not be identical in material properties and dimensions. The $\#\nu$ circular ring with radius R_ν separates two cylindrical regions $(\nu - 1)$ and (ν). Figs. 1(a) and (b) show the *concentric* and *eccentric* configurations of cylindrical EBG structures, respectively. The center O_1 of the innermost #1 ring in the *eccentric* configuration is chosen as the global origin O.

We assume the excitation by a line source which is uniform in the z direction and located at the global origin O of the (a) *concentric* and (b) *eccentric* configurations in Fig. 1. The two-dimensional radiation problem is formulated in terms of E_z field. We consider first the *concentric* configuration. The total field in regions (ν) and $(\nu + 1)$ separated by the ν-th layer of the array is expressed in matrix form as follows:

$$E_z^{(\nu)}(\rho, \varphi) = \mathbf{\Phi}^T \cdot \mathbf{b}^{(\nu)} + \mathbf{\Psi}^T \cdot \mathbf{c}^{(\nu)}, \quad E_z^{(\nu+1)}(\rho, \varphi) = \mathbf{\Phi}^T \cdot \mathbf{b}^{(\nu+1)} + \mathbf{\Psi}^T \cdot \mathbf{c}^{(\nu+1)} \tag{1}$$

with

$$\mathbf{\Phi} = [J_m(k_0\rho)e^{im\varphi}], \quad \mathbf{\Psi} = [H_m^{(1)}(k_0\rho)e^{im\varphi}], \quad \mathbf{b}^{(\nu)} = [b_m^{(\nu)}], \quad \mathbf{c}^{(\nu)} = [c_m^{(\nu)}] \tag{2}$$

where $\{b_m^{(\nu)}\}$ represent the unknown amplitudes of the *incoming* cylindrical waves, $\{c_m^{(\nu)}\}$ are those of the *outgoing* cylindrical waves, and J_m and $H_m^{(1)}$ are the Bessel and Hankel functions of the m-th order. The superscript T denotes the transpose of the indicated vectors. Using the semi-analytical approach reported in [3, 4], we can obtain the following relations between four unknown amplitude vectors:

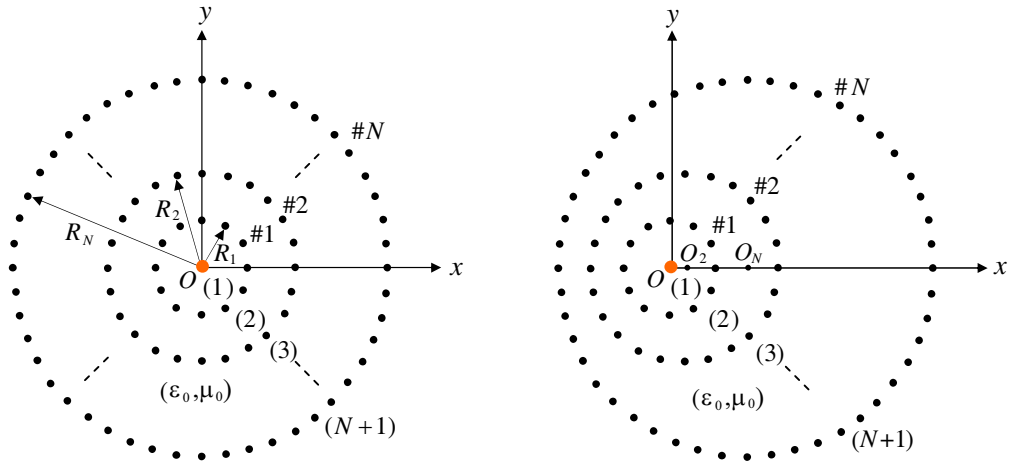

(a) Concentric configuration (b) Eccentric configuration

Figure 1: Cylindrical EBG structures formed by M_ν circular rods with radius r_ν periodically distributed on each of N circular rings with radii R_ν ($\nu = 1, 2, \ldots, N$).

$$\mathbf{c}^{(\nu+1)} = \mathbf{R}_{\nu+1,\nu} \cdot \mathbf{b}^{(\nu+1)} + \mathbf{F}_{\nu+1,\nu} \cdot \mathbf{c}^{(\nu)}, \quad \mathbf{b}^{(\nu)} = \mathbf{F}_{\nu,\nu+1} \cdot \mathbf{b}^{(\nu+1)} + \mathbf{R}_{\nu,\nu+1} \cdot \mathbf{c}^{(\nu)} \quad (\nu \geq 1) \tag{3}$$

where $\mathbf{R}_{\nu+1,\nu}$ and $\mathbf{F}_{\nu,\nu+1}$ represents the reflection and transmission matrices of the ν-th layer of the array for the *incoming* cylindrical waves with $\{b_m^{(\nu+1)}\}$, whereas $\mathbf{R}_{\nu,\nu+1}$ and $\mathbf{F}_{\nu+1,\nu}$ are the corresponding matrices for the *outgoing* cylindrical waves with $\{c_m^{(\nu)}\}$. The closed form expressions for $\mathbf{R}_{\nu+1,\nu}$, $\mathbf{F}_{\nu,\nu+1}$, $\mathbf{R}_{\nu,\nu+1}$, and $\mathbf{F}_{\nu+1,\nu}$, which are related to the T-matrix of a circular rod in isolation and the geometrical parameters characterizing the periodic distribution of the circular rod, are given in [3]. The initial field in region (1) excited by the line source located at the origin O is expressed as follows:

$$E_z^i = \frac{i}{4}\mathbf{\Psi}^T \cdot \mathbf{c}^{(1)}, \quad \mathbf{c}^{(1)} = [\delta_{m0}]. \tag{4}$$

Equation (3) are concatenated from region (1) to region $(N+1)$. Following the same procedure as reported in [3], the radiated field into the outermost region $(N+1)$ shown in Fig. 1(a) is obtained as

$$E_z^{(N+1)} = \frac{i}{4}\mathbf{\Psi}^T \cdot \mathbf{F}^{(N+1)} \cdot \mathbf{c}^{(1)} \tag{5}$$

with

$$\mathbf{F}^{(N+1)} = \mathbf{\Lambda}_{N+1,N}\mathbf{\Lambda}_{N,N-1}, \ldots, \mathbf{\Lambda}_{3,2}\mathbf{\Lambda}_{2,1}, \quad \mathbf{\Lambda}_{\nu+1,\nu} = (\mathbf{I} - \mathbf{R}_{\nu+1,\nu}\bar{\bar{\mathbf{R}}}_{\nu+1,\nu+2})^{-1}\mathbf{F}_{\nu+1,\nu} \tag{6}$$

$$\bar{\bar{\mathbf{R}}}_{\nu,\nu+1} = \mathbf{R}_{\nu,\nu+1} + \mathbf{F}_{\nu,\nu+1}\bar{\bar{\mathbf{R}}}_{\nu+1,\nu+2}\mathbf{\Lambda}_{\nu+1}, \quad \bar{\bar{\mathbf{R}}}_{N+1,N+2} = \mathbf{0} \tag{7}$$

where $\mathbf{F}^{(N+1)}$ represents the generalized transmission matrix of the N-layered *concentric* cylindrical arrays. The matrices $\mathbf{\Lambda}_{\nu+1,\nu}$ and $\bar{\bar{\mathbf{R}}}_{\nu,\nu+1}$ are calculated from Equations (6) and (7) through the N times recursion process starting with $\bar{\bar{\mathbf{R}}}_{N+1,N+2} = \mathbf{0}$.

Next, we consider the case of the *eccentric* configuration shown in Fig. 1(b). In this case, the total field in regions (ν)- and $(\nu+1)$ are expressed in the following form:

$$E_z^{(\nu)}(\rho,\varphi) = \mathbf{\Phi}_\nu^T \cdot \mathbf{b}^{(\nu)} + \mathbf{\Psi}_\nu^T \cdot \mathbf{c}^{(\nu)}, \quad E_z^{(\nu+1)}(\rho,\varphi) = \mathbf{\Phi}_{\nu+1}^T \cdot \mathbf{b}^{(\nu+1)} + \mathbf{\Psi}_{\nu+1}^T \cdot \mathbf{c}^{(\nu+1)} \tag{8}$$

with

$$\mathbf{\Phi}_\nu = [J_m(k_0\rho_\nu)e^{im\varphi_\nu}], \quad \mathbf{\Psi}_\nu = [H_m^{(1)}(k_0\rho_\nu)e^{im\varphi_\nu}] \tag{9}$$

$$\mathbf{\Phi}_{\nu+1} = [J_m(k_0\rho_{\nu+1})e^{im\varphi_{\nu+1}}], \quad \mathbf{\Psi}_{\nu+1} = [H_m^{(1)}(k_0\rho_{\nu+1})e^{im\varphi_{\nu+1}}] \tag{10}$$

where $(\rho_\nu,\ \varphi_\nu)$ and $(\rho_{\nu+1},\ \varphi_{\nu+1})$ denote the local polar coordinates systems with their origins at the centers of the $\#\nu$ and $\#(\nu+1)$ rings. Since the basis functions in the cylindrical harmonic expansion are different in two regions, the scattering amplitude vectors $(\mathbf{b}^{(\nu)},\ \mathbf{c}^{(\nu)})$ and $(\mathbf{b}^{(\nu+1)},\ \mathbf{c}^{(\nu+1)})$ are connected after transforming the basis functions in region $(\nu+1)$ to those in region (ν). From straightforward manipulations, we have the following relations:

$$\mathbf{U}_{\nu,\nu+1}\cdot\mathbf{c}^{(\nu+1)} = \mathbf{R}_{\nu+1,\nu}\mathbf{U}_{\nu,\nu+1}\cdot\mathbf{b}^{(\nu+1)} + \mathbf{F}_{\nu+1,\nu}\cdot\mathbf{c}^{(\nu)} \tag{11}$$

$$\mathbf{b}^{(\nu)} = \mathbf{F}_{\nu,\nu+1}\mathbf{U}_{\nu,\nu+1}\cdot\mathbf{b}^{(\nu+1)} + \mathbf{R}_{\nu,\nu+1}\cdot\mathbf{c}^{(\nu)}, \quad \mathbf{U}_{\nu,\nu+1} = [J_{m-n}(k_0 d_{\nu,\nu+1})] \tag{12}$$

where $\mathbf{U}_{\nu,\nu+1}$ is the translation matrix which transforms $\mathbf{\Phi}_{\nu+1}$ and $\mathbf{\Psi}_{\nu+1}$ to $\mathbf{\Phi}_{\nu}$ and $\mathbf{\Psi}_{\nu}$, respectively and $d_{\nu,\nu+1}$ denotes the distance between two origins O_ν and $O_{\nu+1}$. Equations (11) and (12) are concatenated from region (1) to region $(N+1)$. Finally, the radiated field $E_z^{(N+1)}$ is expressed in terms of the global coordinate and the generalized transmission matrix $\mathbf{F}^{(N+1)}$ to be used in Equation (5) is obtained as

$$\mathbf{F}^{(N+1)} = \mathbf{U}_{1,N}\mathbf{\Gamma}_{N+1,N}\mathbf{\Gamma}_{N,N-1},\ldots,\mathbf{\Gamma}_{3,2}\mathbf{\Gamma}_{2,1}, \quad \mathbf{U}_{1,N} = [J_{m-n}(k_0 d_{1,N})] \tag{13}$$

with

$$\mathbf{\Gamma}_{\nu+1,\nu} = (\mathbf{I} - \mathbf{U}_{\nu,\nu+1}^{-1}\mathbf{R}_{\nu+1,\nu}\mathbf{U}_{\nu,\nu+1}\bar{\bar{\mathbf{R}}}_{\nu+1,\nu+2})^{-1}\mathbf{U}_{\nu,\nu+1}^{-1}\mathbf{F}_{\nu+1,\nu} \tag{14}$$

$$\bar{\bar{\mathbf{R}}}_{\nu,\nu+1} = \mathbf{R}_{\nu,\nu+1} + \mathbf{F}_{\nu,\nu+1}\mathbf{U}_{\nu,\nu+1}\bar{\bar{\mathbf{R}}}_{\nu+1,\nu+2}\mathbf{\Gamma}_{\nu+1,\nu}, \quad \bar{\bar{\mathbf{R}}}_{N+1,N+2} = \mathbf{0}. \tag{15}$$

where $d_{1,N}$ denotes the distance between two origins O and O_N. If $d_{\nu,\nu+1} = 0$ $(\nu = 1,2,\ldots,N)$, we have $\mathbf{U}_{\nu,\nu+1} = \mathbf{U}_{1,N} = \mathbf{I}$, and Equations (13)–(15) are reduced to Equations (6) and (7) for the *concentric* configuration.

Using the asymptotic behavior of $H_m^{(1)}(k_0\rho)$ for$k_0\rho \gg 1$, from Equation (5) the radiated field in the far zone in the outermost region $(N+1)$ and the directivity of radiation $D(\varphi)$ are given as follows:

$$E_z^{(N+1)}(\rho,\varphi) = \frac{(1-i)}{\sqrt{\pi k_0}}\frac{e^{ik_0\rho}}{\sqrt{\rho}}\sum_{m=-\infty}^{\infty}(-i)^m F_{m,0}^{(N+1)} e^{im\varphi} \tag{16}$$

$$D(\varphi) = 10\log_{10}\left(\left|\sum_{m=-\infty}^{\infty}(-i)^m F_{m,0}^{(N+1)} e^{im\varphi}\right|^2 \Big/ \sum_{m=-\infty}^{\infty}\left|F_{m,0}^{(N+1)}\right|^2\right) \tag{17}$$

where $F_{m,0}^{(N+1)}$ is the $(m,0)$ element of the generalized transmission matrix $\mathbf{F}^{(N+1)}$ and represents the spectral amplitudes of the m-th order cylindrical Floquet mode in the radiated field.

3. NUMERICAL EXAMPLES AND DISCUSSIONS

From Equations (16) and (17) it follows that the directivity of radiation are closely related to the spectral response of the transmission coefficient $F_{m,0}^{(N+1)}$. Although a substantial number of numerical examples could be generated, we discuss here a three-layered structure consisting of the identical circular rods of perfect conductor where $r_1 = r_2 = r_3 = 2\,\text{mm}$, $R_1 = 40\,\text{mm}$, $R_2 = 2R_1$, $R_3 = 3R_1$, $M_1 = 12$, $M_2 = 24$, and $M_3 = 36$. For the numerical calculation, the reflection and transmission matrices were truncated by $m = n = \pm 36$ after confirming the convergence of solutions.

Figure 2 shows the transmission spectra calculated for the *concentric* configuration illustrated in Fig. 1(a) as functions of frequency over $0.4\,\text{GHz} \sim 12\,\text{GHz}$. Because of the symmetry of the

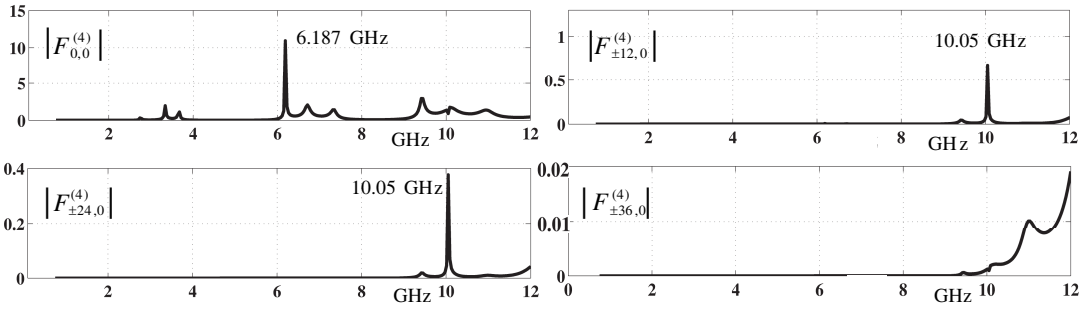

Figure 2: Transmission coefficients $|F_{m,0}^{(4)}|$ as functions of the frequency for the *concentric* three-layered structure shown in Fig. 1(a), where $M_1 = 12$, $M_2 = 24$, $M_3 = 36$, $r_1 = r_2 = r_3 = 2\,\text{mm}$, $R_1 = 40\,\text{mm}$, $R_2 = 2R_1$, and $R_3 = 3R_1$.

cylindrical structure, only the cylindrical Floquet modes $F_{m,0}^{(N+1)}$ with $m = 0$, $m = \pm 12$, $m = \pm 24$, and $m = \pm 36$ are excited under the assumed truncation order. From Fig. 2 we can see that there exist a series of stopbands and passbands for each of the excited Floquet modes. The transmission is very small in the stopbands, whereas a sharp resonant peak appears in the passbands. The major resonance occurs at 6.187 GHz for $|F_{0,0}^{(4)}|$ and at 10.05 GHz for $|F_{\pm 12,0}^{(4)}|$ and $|F_{\pm 24,0}^{(4)}|$.The radiation patterns for these two resonance frequencies are plotted in Fig. 3. The radiation pattern for 6.187 GHz is omnidirectional as shown in Fig. 3(a) because only the fundamental mode with $F_{0,0}^{(4)}$ is propagating at this frequency. For 10.05 GHz, the higher-order modes with $F_{\pm 12,0}^{(4)}$ and $F_{\pm 24,0}^{(4)}$ resonate to the cylindrical structure and the directive pattern with 12 beams is formed as shown in Fig. 3(b).

Figure 4 shows the transmission spectra for the *eccentric* configuration shown in Fig. 1(b), where $d_{12} = \overline{OO}_2 = 0.1R_1$, $d_{13} = \overline{OO}_3 = 0.2R_1$ and other parameters are the same as those given in Fig. 2. Since the symmetry of the structure breaks, all of the cylindrical Floquet modes up to $m = \pm 36$ are excited. In Fig. 4, the results only for the lowest five modes, which have significant values of the transmission coefficient, are shown. In the passbands, there exist special resonance frequencies: 6.1125 GHz and 6.3 GHz, at which all of the Floquet modes simultaneously resonate. The radiation patterns for these two resonance frequencies and for 10.05 GHz are plotted in Fig. 5. The radiation pattern at the multiple-resonance frequency produces generally a single beam as shown in Fig. 5(a) but the beam width is rather moderate. The spectral amplitudes of the resonated five Floquet modes are properly balanced at 6.3 GHz as shown in Fig. 4, and a narrow single beam is obtained for this frequency as shown in Fig. 5(b). The radiation pattern for 10.05 GHz shown in Fig. 5(c) is quite different from that of Fig. 3(b) for the *concentric* configuration. The interference between all of the excited Floquet modes significantly modifies the pattern.

From Figs. 2 and 4 it is noted that several peak values of $|F_{m,0}^{(4)}|$ at resonance exceed unity.

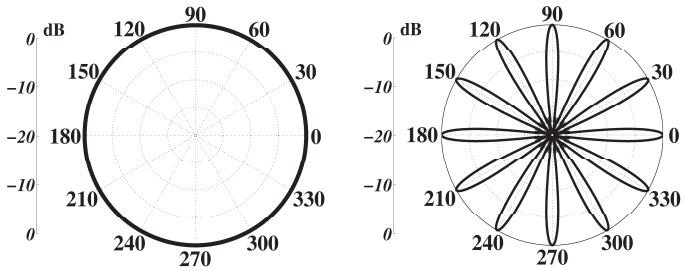

Figure 3: Radiation patterns of the line source for two different resonance frequencies of the *concentric* three-layered structure as shown in Fig. 2; (a) 6.187 GHz and (b)10.05 GHz.

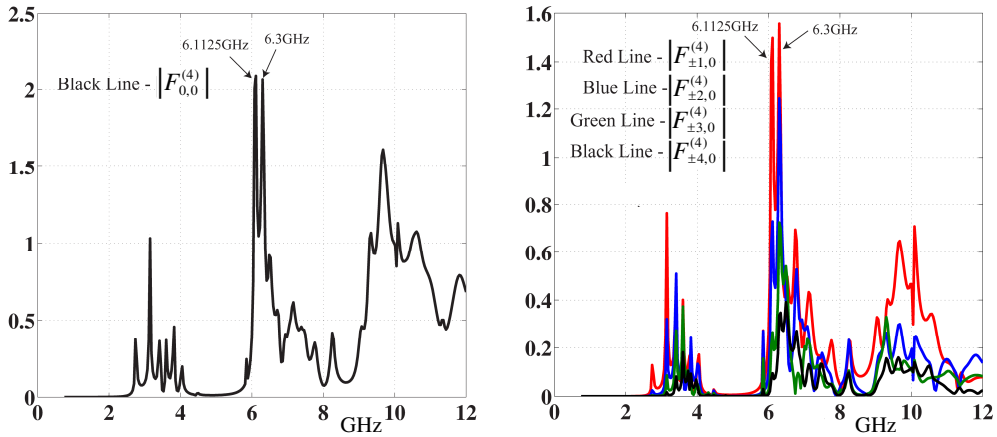

Figure 4: Transmission coefficients $|F_{m,0}^{(4)}|$ as functions of the frequency for the *eccentric* three-layered structure shown in Fig. 1(b), where $d_{12} = \overline{OO}_2 = 0.1R_1$, $d_{13} = \overline{OO}_3 = 0.2R_1$, and other parameters are the same as those given in Fig. 2.

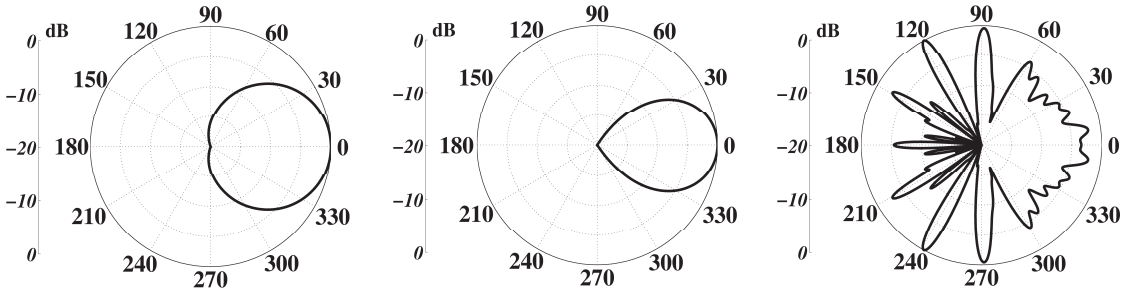

(a) 6.1125 GHz (b) 6.3 GHz (c) 10.05 GHz

Figure 5: Radiation patterns of the line source for three different resonance frequencies of the *eccentric* three-layered structure as shown in Fig. 4; (a) 6.1125 GHz , (b) 6.3, GHz , and (c)10.05 GHz .

This is due to the interaction of the initial source field with the surrounding cylindrical structure and does not violate the energy conservation principle. We briefly explain the energy conservation relation for this excitation problem. Calculating the net power flow across two cylindrical surfaces with $\rho = \rho_1 = R_1 - r_1$ and $\rho = \rho_N = R_N + r_N$ per unit length in the z direction, the incident power $P^{inc}(\rho_1)$ and the reflected power $P^{ref}(\rho_1)$ in region (1) and the transmitted power $P^{tra}(\rho_N)$ in region $(N+1)$ are obtained as follows:

$$\begin{aligned} P^{inc}(\rho_1) &= \sqrt{\frac{\varepsilon_0}{\mu_0}}\frac{2}{k_0}\left|1+\frac{1}{2}\bar{\bar{R}}_{1,2;0,0}\right|^2, \quad P^{ref}(\rho_1) = \sqrt{\frac{\varepsilon_0}{\mu_0}}\frac{2}{k_0}\left|\frac{1}{2}\bar{\bar{R}}_{1,2;0,0}\right|^2, \\ P^{tra}(\rho_N) &= \sqrt{\frac{\varepsilon_0}{\mu_0}}\frac{2}{k_0}\sum_{m=-\infty}^{\infty}\left|\bar{\bar{F}}_{m,0}^{(N+1)}\right|^2 \end{aligned} \tag{18}$$

where $\bar{\bar{R}}_{1,2;0,0}$ denotes the $(0,0)$ element of the matrix $\bar{\bar{\mathbf{R}}}_{1,2}$ defined by Equations (7) and (15). The energy conservation principle requires that $P^{inc}(\rho_1) = P^{ref}(\rho_1) + P^{tra}(\rho_N)$. This leads to the following relation:

$$1 = \eta_1 + \sum_{m=-\infty}^{\infty}\tau_m^{(N+1)}, \quad \eta_1 = \left|\bar{\bar{R}}_{1,2;0,0}\right|^2 \Big/ \left|2+\bar{\bar{R}}_{1,2;0,0}\right|^2, \quad \tau_m^{(N+1)} = 4\left|\bar{\bar{F}}_{m,0}^{(N+1)}\right|^2 \Big/ \left|2+\bar{\bar{R}}_{1,2;0,0}\right|^2 \tag{19}$$

where η_1 represents the power reflection coefficient in the innermost region (1) and $\tau_m^{(N+1)}$ is the power transmission coefficient for the m-th Floquet mode in the outermost region $(N+1)$. The transmission coefficient $|F_{m,0}^{(4)}|$ presented in Figs. 2 and 4 always satisfy the energy conservation relation (19).

4. CONCLUSIONS

We have analyzed the radiation characteristics of an infinite line current source located in a cylindrical EBG structure using a semi-analytical methods based on the cylindrical Floquet mode expansion. It is shown that the radiation patterns are closely correlated with the transmission spectra of the cylindrical structure which are controllable by the structural parameters.

REFERENCES

1. Boutayeb, H., T. A. Denidni, K. Mahdjoubi, A.-C. Tarot, A.-R. Sebak, and L. Talbi, "Analysis and design of a cylindrical EBG-based directive antenna," *IEEE Trans. Antennas Propag.*, Vol. 54, No. 1, 211–219, Jan. 2006.
2. Biancotto, C. and P. Record, "Design of a beam forming dielectric cylindrical EBG antenna," *Progress In Electromagnetics Research B*, Vol. 18, 327–346, 2009.
3. Yasumoto, K., V. Jandieri, and B. Gupta, "Guidance and scattering of electromagnetic waves by layered cylindrical arrays of circular rods," *Proc. of 2009 IEEE Applied Electromagnetics Conference*, No. CEM-6-4418, Kolkata, Dec. 2009.
4. Jandieri, V. and K. Yasumoto, "Electromagnetic scattering by layered cylindrical arrays of circular rods," *IEEE Trans. Antennas Propag.*, Vol. 59, No. 6, 2011, accepted for publication.

Parallelized FDTD-TDPO Algorithm Based on MPI Platform

Xiangqin Zhu[1], **Jianguo Wang**[1, 2], **and Libing Cai**[1]

[1]Northwest Institute of Nuclear Technology, Xi'an 710024, China
[2]School of Electronic and Information Engineering, Xi'an Jiaotong University
Xi'an 710049, China

Abstract— A parallelized FDTD-TDPO algorithm based on MPI (Message Passing Interface) platform is presented in this paper for simulation of reflector antennas, which can not be done on a personal computer due to over long time and prohibitive computation resources. The speedup factor and efficiency for parallel FDTD-TDPO code are measured on high performance computers. The computational results are in good agreement with those obtained by FDTD-TDPO method using single process. In addition, numerical results show that the speed up ratio is approximately equal to N, where N is the number of processes.

1. INTRODUCTION

Reflector antennas are intensively applied in the radars, communication, and guidance, etc. Considering that reflector antennas are electrically large but the dimensions of the antenna feeds are on the order of the wavelength, a hybrid method combining finite-difference time-domain (FDTD) method [1] and time-domain physical optics (TDPO) method [2] by means of Kirchhoff's surface integral representation (KSIR) [3] is presented to compute the radiation fields of reflector antennas. The near-fields of antenna feeds are analyzed by FDTD method. The surface of reflectors is discretized with triangular meshes and the radiation fields of reflectors are computed by TDPO method. While the reflector is very large and the number of triangular meshes on its surface is quite huge, long time is needed and computation resources are lacking as radiation fields of the reflector antenna are computed by FDTD-TDPO method on a personal computer.

In other hand, MPI (Message Passing Interface) [4, 5] is applied in IBM PC/Windows, Linux work stations, and parallel computers. Parallel FDTD Method [6, 7], parallel moment method (MoM) [8, 9], and parallel UTD Method [10, 11] based on MPI platform are recently used to analyze large-scale computational electromagnetic problems.

A parallel FDTD-TDPO method based on MPI platform is developed in this paper. By using this method, the computing time is saved by dividing the computing task into many sub-tasks and performing them on the supercomputer.

2. APPLICATION OF PARALLELIZED FDTD-TDPO ALGORITHM

The induced current on each surface mesh of reflectors is independent of other surface meshes. So the computing tasks are decomposed according to the spatial place of each surface mesh. The parallel design pattern is shown in Fig. 1.

As shown in Fig. 1, Firstly, simulation parameters including geometry parameters of reflector antennas are input to root process. And the computing tasks are divided by root process based on load balancing. The triangular meshes on the reflector's surface are distributed into given process

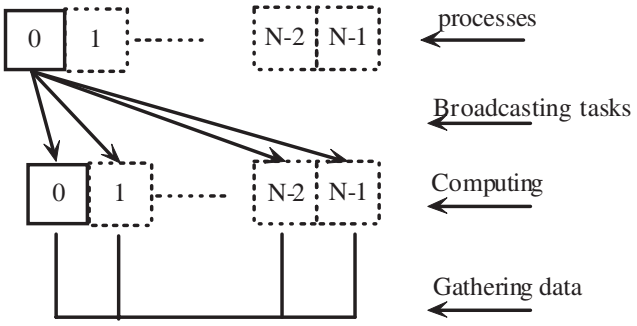

Figure 1: Design of the parallel program (N processes used).

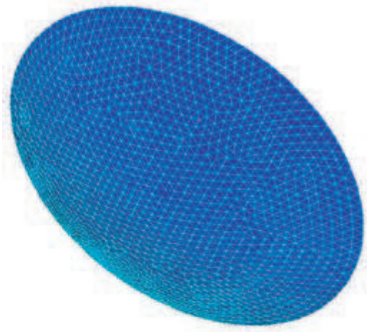

Figure 2: Meshes on the illuminated zone of reflector.

according to the ID numbers of triangles in turn. Secondly, the corresponding parameters are broadcasted into corresponding sub-domains (that is corresponding process, root process included) by root process. Thirdly, TDPO method is used in given computational domain by corresponding process. Lastly, radiation fields of reflectors are gathered into root process and saved in a file after all sub-tasks are completed. The main steps of parallel FDTD-TDPO method used on a reflector antenna are shown as follows:

(1) MPI initialization (MPI_Init());
(2) The computing task is divided by root process.
(3) Radiation fields of the reflector are computed by each process.
(4) Computing results of each process are gathered into root process with the procedure "MPI_Gatherv".

    Each process keeps synchronous to avoid communication conflict when root process gathers data from all processes after the computation is finished using parallel TDPO method.
(5) End (MPI_Finalize()).

3. NUMERICAL EXAMPLES

3.1. Validated Examples

The related frequency is 4.0 GHz and the corresponding wavelength is $\lambda = 0.075$ m. The aperture size of a paraboloid reflector is $D = 10\lambda$ and the proportion of the focal length to the aperture size is 0.4. A dipole is placed on the focus of the reflector. The sizes of FDTD cell in three dimensions are $\delta_x = \delta_y = \delta_z = 2.5$ mm and the time alternation for FDTD method is $\Delta t_1 = 4.166667 \times 10^{-12}$ s. The point source is located at the origin. The source is expressed as

$$E_z^n = p^n \tag{1}$$

where

$$p(t) = \exp\left[-(t - t_0)^2 \Big/ T_w^2\right] \tag{2}$$

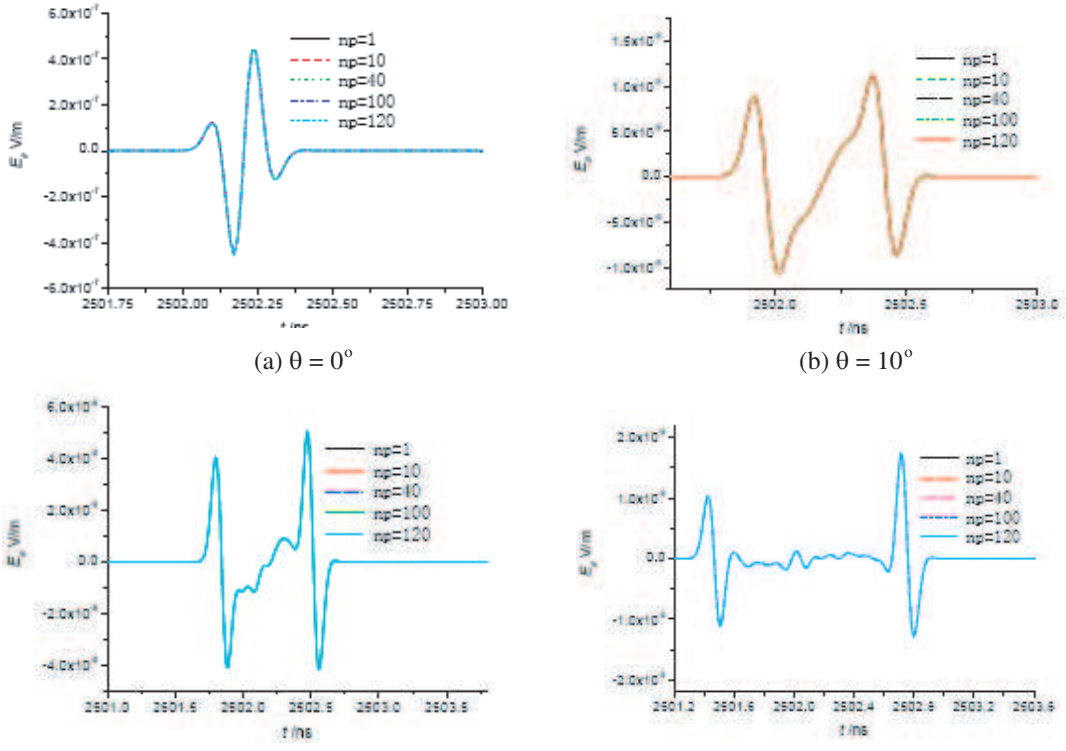

(a) θ = 0° (b) θ = 10°

(c) θ = 15° (d) θ = 30°

Figure 3: Radiation field E_θ at $r = 750$ m for $\phi = 90°$ and different θ.

$T_w = 6.25 \times 10^{-11}$ s, $t_0 = 1.875 \times 10^{-10}$ s. The near-fields of antenna feed are computed by FDTD method. The illuminated surface of the reflector is divided into 5376 triangular meshes, as shown in Fig. 2.

By using parallel FDTD-TDPO method on high performance computers, the variation of radiated electric fields E_θ with time is shown in Fig. 3 when the received angle is $\phi = 90°$, $\theta = 0°$, $\theta = 10°$, $\theta = 15°$ and $\theta = 30°$. Note that the results don't include the far-fields of the feed. The variation of radiated electric fields E_φ with time is shown in Fig. 4. The results of parallel FDTD-TDPO method using many processes should agree with those of parallel FDTD-TDPO method using single process. In fact, the two kinds of results agree absolutely as shown in Fig. 3 and Fig. 4.

3.2. Parallel Speedup Factors

All geometry and computation parameters of the reflector and its feed are same with the last example. Speedup efficiency is measured on a high performance computer with some processors. The speedup factor and efficiency, when the total number of processes is changed, are shown in Table 1. It can be seen from this table that the saved time increases linearly as the process's number increases. That is because the fields computing in each sub-domain (corresponding to each sub-task

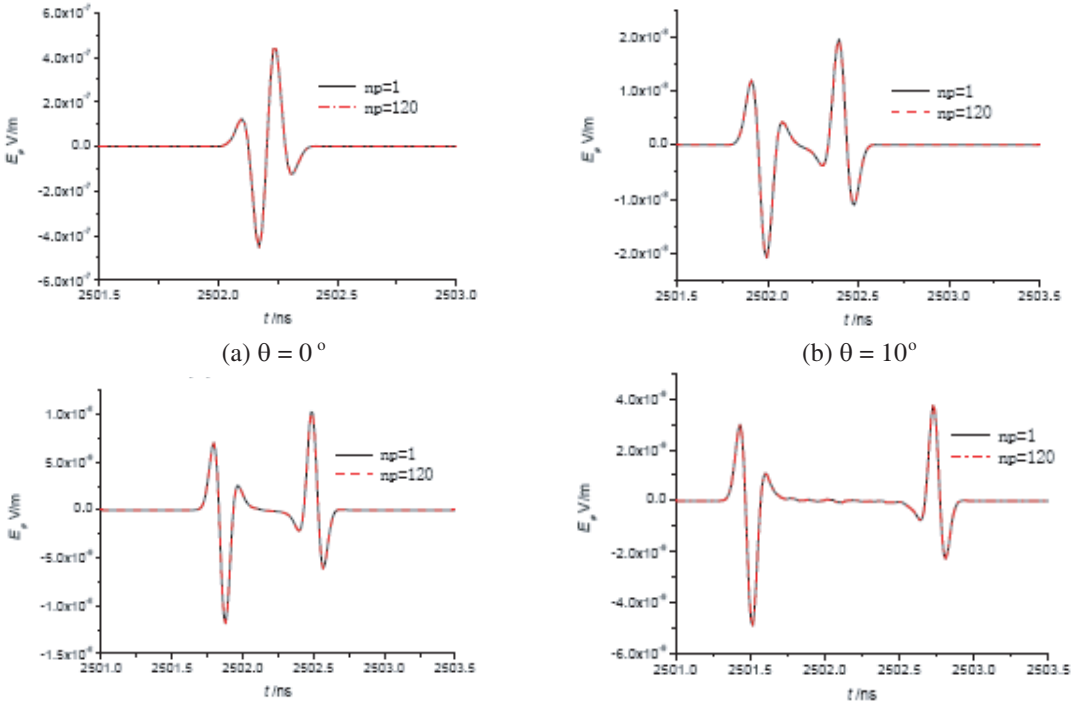

Figure 4: Radiation field E_φ at $r = 750$ m for $\phi = 0°$ and different θ.

Table 1: Parallel performance of parallel FDTD-TDPO program for computing radiation fields of a paraboloid reflector (Total number of time step is 1100).

No. of processes	Computing time	Saved time	Speedup factor S'_p	Parallel efficiency
1	52769.9810 s	—	1	100%
2	26389.2802 s	49.992%	1.9997	99.985%
8	6627.3696 s	87.441%	7.9624	99.530%
20	2672.1489 s	94.936%	19.7481	98.740%
80	698.8808 s	98.676%	75.5064	94.383%
120	472.8578 s	99.104%	111.5980	92.998%

or each process) is independent, and there is no data exchange between every two sub-domains as the parallel program is run except at the beginning of broadcasting tasks and end of the computing in each sub-domain. That is, the ratio of communication time to the total computing time is very little as parallel TDPO method is used. Based on that, it's concluded that more computing time is saved as more CPUs are used. Speedup factor approaches N If N processes are used.

4. CONCLUSIONS

In this paper, a parallel FDTD-TDPO method with MPI functions is developed to analyze the radiation fields of large-scale reflector antennas as the problem couldn't be done on a personal computer due to over long time and prohibitive computation resources. The computational results obtained by parallel FDTD-TDPO method using some processes are in good agreement with those obtained by the method using single process. The parallel performance of the parallel TDPO program is measured. And the results show that the speed up ratio is approximately equal to the number of processes.

REFERENCES

1. Ge, D. and Y.-B. Yan, *Inite-Difference Time-Domain Method for Electromagnetic Waves*, Xidian Press, April 2002, in Chinese.
2. Sun, E.-Y. and W. V. T. Rusch, "Time-domain physical-optics," *IEEE Trans. Antenna Propagat.*, Vol. 42, No. 1, 9–15, 1994.
3. Ramahi, O. M., "Near- and far-field calculations in FDTD simulations using Kirchhoff surface integral representation," *IEEE Trans. Antenna Propagat.*, Vol. 45, No. 5, 753–759, 1997.
4. Pacheco, P., *Parallel Programming with MPI*, Morgan Kaufman, San Francisco, CA, 1997.
5. Du, Z.-H., *Parallel Programming for High Performance Computing-parallel Programming with MPI*, Tsinghua University Press, 2001, in Chinese.
6. Guiffaut, C. and K. Mahdjoubi, "A parallel FDTD algorithm using the MPI Library," *IEEE Ant. Prop. Mag.*, Vol. 43, No. 2, 94–103, 2001.
7. Raouf, A. E. and E. Hany, "A class of finite difference time domain (FDTD) technique for solving large electromagnetic structures," *International Conference on RF and Microwave*, 301–305, 2006.
8. Zhang, Y., T. Su, H.-Q. Zhai, et al., "Study on applications of parallel MoM on PC clusters," *Acta Electronica Sinica*, Vol. 31, No. 9, 1368–1371, 2003 (in Chinese).
9. Zhang, Y, M. Wang, C.-H. Liang, et al., "Study of parallel MoM on PC clusters," *Journal of Electronics & Information Technology*, Vol. 27, No. 4, 647–650, 2005.
10. Zhang, Y. and C.-H. Liang, "Parallel UTD algorithm and its application to the analysis of airborne antennas," *Acta Electronica Sinica*, Vol. 31, No. 3, 332–334, 2003 (in Chinese).

A Fan-beam Millimeter-wave Antenna Based on Modified Luneberg Cylindrical Lens

Changzhou Hua[1,2], **Xidong Wu**[1], **Nan Yang**[1], **Huixian Wu**[1], **Bo Li**[1,2], **and Wen Wu**[2]

[1]Department of Information Science and Electronic Engineering, Zhejiang University
Hangzhou 310027, China
[2]Ministerial Key Laboratory of JGMT, Nanjing University of Science and Technology
Nanjing 210094, China

Abstract— A new design of lens antenna at millimeter-wave frequencies is introduced with special focus on ease of manufacturing and reliability. The system is composed of a modified Luneberg cylindrical lens and a feed antenna. The modified Luneberg cylindrical lens consists of two parallel plates with the space between plates only filled with air, thus free of dielectric loss. A planar linear tapered slot antenna (LTSA) is inserted into the air region between the parallel plates at the edge of the lens as a feed antenna. A combined ray-optics method and CST-MWS are used to analyze and design this cylindrical lens antenna at 30 GHz. Due to its spherical symmetry, the proposed lens can be used to launch multiple beams by implementing an arc array of planar LTSA elements at the periphery of the lens. The proposed antenna can be easily extended for higher mm-wave frequencies, and is well suitable for scanning fan-beam applications, such as aircraft landing systems.

1. INTRODUCTION

In recent years, wide-angle scanning antennas are required in many mm-wave applications such as modern wireless communications, automotive radars, and imaging systems. And there has been an increased research interest in spherical lens antennas to launch pencil beams [1–3]. For some applications, such as aircraft landing system [4], it is more desirable to launch fan-beam scanning in one plane. In [5], a two-dimensional Luneberg lens based on partially-filled parallel plate technique was designed to launch scanning fan beams. In this paper, an air-filled modified Luneberg cylindrical lens is proposed for mm-wave multiple fan beam applications.

2. STRUCTURE OF THE MODIFIED LUNEBERG CYLINDRICAL LENS ANTENNA

The proposed modified Luneberg cylindrical lens is designed by using the technique of parallel plates propagating the TE_{10} mode. It is well-known that the TE_{10} mode's wave number k for a parallel-plate waveguide can be written as,

$$k = k_0\sqrt{1-\left(\frac{\lambda_0}{2h}\right)^2}, \tag{1}$$

and the effective index of refraction is given by,

$$n = k/k_0, \tag{2}$$

where λ_0 is wavelength in free space, k_0 is the free space wave number and h is the plate spacing.

Figure 1 shows the structure of the proposed lens antenna. As shown, it consists of two parallel plates filled with air. The plate spacing $h(r)$ is varied with the normalized radius r in order to achieve the general Luneberg's variation of the effective index of refraction,

$$n = N_0\sqrt{2-\delta r^2}, \tag{3}$$

where N_0 and δ are two adjustable parameters. When N_0 and δ are chosen to be equal to 1, it will reduce to the Luneberg's Law. Then, we can determine the $h(r)$ by using (1)–(3). The modified Luneberg lens antenna is fed with a LTSA, which excites TE_{10} mode (horizontal polarization) between the two parallel plates when the height h is chosen to be $\lambda_0/2 < h < \lambda_0$. In order to achieve the best illumination, the phase-center of the LTSA should coincide with the focal position of the lens.

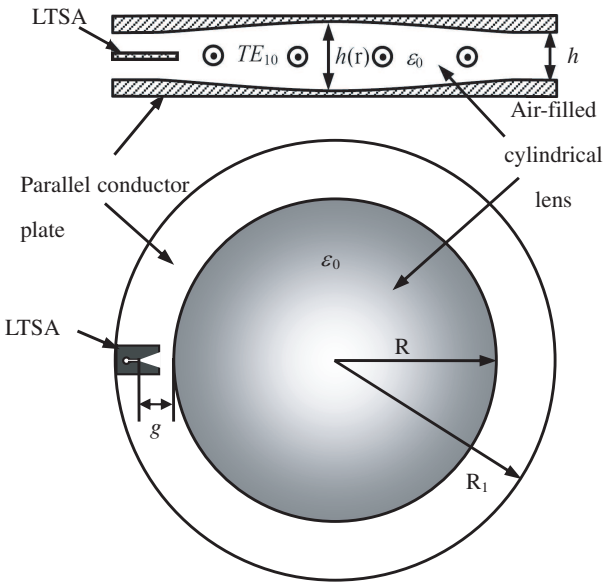

Figure 1: Structure of the proposed lens antenna.

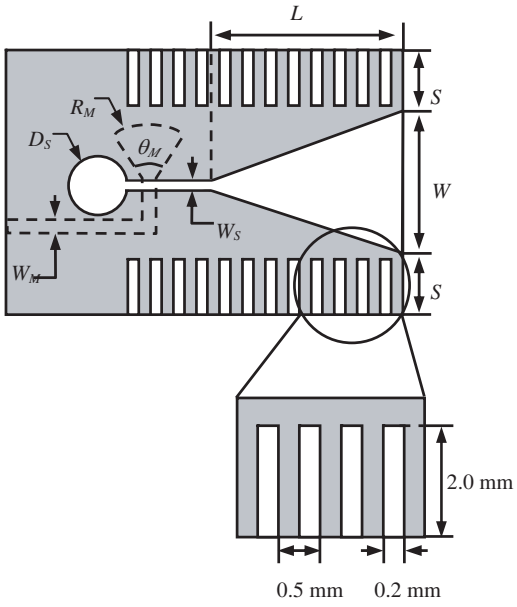

Figure 2: Structure of the feed LTSA.

In Fig. 2, the feed LTSA with a microstrip/slotline transition is integrated on a dielectric substrate Duroid 5870 with a thickness of 0.254 mm and a relative permittivity of 2.33. The main structural parameters as defined in Fig. 1 and Fig. 2 are given as follow: $R = 50$ mm, $R_1 = 62$ mm, $h = 6.6$ mm, $L = 6.1$ mm, $W = 3.5$ mm, $S = 2.3$ mm, $W_S = 0.25$ mm, $W_M = 0.76$ mm, $D_S = 1.5$ mm, $R_M = 1.4$ mm and $\theta_M = 80°$. Simulations and designs are carried out using the commercial software CST-MWS. The length of the tapered slot line (L) is much shorter than that of conventional LTSA to generate a wide H-plane pattern, ensuring a smooth transition to TE_{10} mode excitation. The opening of the LTSA (W) is adjusted to generate the required illumination beamwidth in E-plane. The periodic arrangement of slits along the LTSA edges is used to minimize the back radiation. The proper selection of the parameters of the microstrip/slotline transition is crucial to the wideband performance of the LTSA. Finally, the simulated LTSA patterns in free space exhibit a 10-dB beamwidth of 98° in the E-plane and 122° in the H-plane at 30 GHz.

3. THEORETICAL ANALYSIS AND DISCUSSION

The ray-tracing technique is used to analyze the focusing property of the modified Luneberg cylindrical lens [3]. In this way, the optimum focal position d/R of the cylindrical lens can be easily determined. Fig. 3 shows the ray tracing from a point source at a distance d from the edge of the proposed cylindrical lens. The main difference here is that the index of refraction n is a function of the distance r from the origin. The angle θ can be obtained from the integral equation [6],

$$\theta = \theta_0 \pm e \int_{r_0}^{r} \frac{dr}{r\sqrt{n^2 r^2 - e^2}}, \tag{4}$$

with

$$e = nr \sin \phi,$$

where φ denotes the angle from the positive direction along the ray to the direction of increasing r, and e is constant for a particular ray. The constant e and the ambiguous sign are determined by the direction of the ray at the initial point (r_0, θ_0). In order to achieve a diffraction-limited pattern, which means a maximum directivity, whose limit is given by the size of the aperture, the exit angle θ_e should be as small as possible for all input angles θ_s. As shown in Fig. 4, the optimum focal position is obtained for $d/R \approx 0.14$ ($N_0 = 0.685$, $\delta = 1.17$). Then, the focusing properties of the designed cylindrical lens and their dependence on the phase-center of the LTSA are studied by adjusting the insertion depth of the feeding LTSA. With the aid of CST-MWS, we find that diffraction-limited patterns occur at the position of $g = 10.5$ mm, indicating that the phase-center of the LTSA is about $6.1 - (10.5 - 0.14 \times 50) = 2.6$ mm away from its opening tip.

To calculate the far-field pattern of the proposed cylindrical lens, a combined ray-tracing/diffraction method is used follows the technique described in [5]. Fig. 5 shows the calculated and simulated

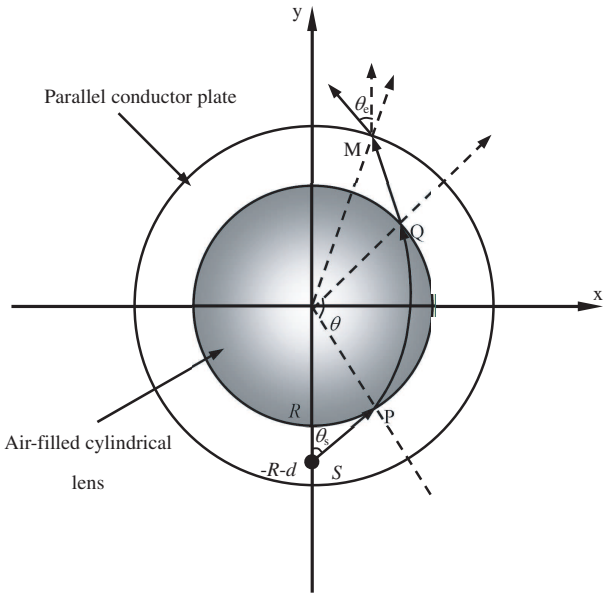

Figure 3: Ray-tracing of the proposed lens antenna.

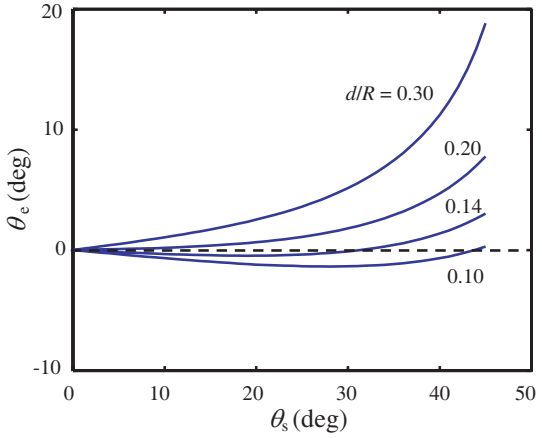

Figure 4: Exit angle θ_e as a function of the input angle θ_s for different d/R.

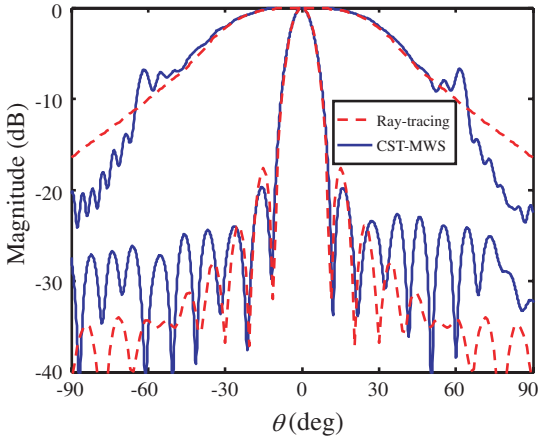

Figure 5: Calculated and simulated radiation patterns of the proposed lens antenna at 30 GHz.

radiation patterns of the proposed lens antenna at the design frequency of 30 GHz. As shown, the theoretical calculations in both E- and H-planes agree well with the CST-MWS simulations. The calculated 3-dB E- and H-plane beamwidths are about 8.9° and 67.8°, respectively, which agrees very well with the beamwidths of 9.0° and 68.0° simulated by CST-MWS. The simulated first sidelobe level in E-plane is −19.8 dB, whereas the theoretical level is −17.6 dB. The disagreement between theoretical calculations and simulations for higher order sidelobes is due to the approximate feed pattern. Meanwhile, no reflections from the lens-air interface have been taken into account in ray-tracing analysis.

The aperture efficiency of the lens antenna is given by,

$$\eta = D_0/D_{\max}, \tag{5}$$

with

$$D_{\max} = \frac{8}{\pi^2}\left[4\pi\left(\frac{2Rh}{\lambda_0^2}\right)\right],$$

where D_0 is the directivity of the designed lens antenna, and $D_{\max}$ is the maximum directivity which the TE_{10} mode distribution aperture can achieve. The simulated directivity is 15.7 dB, and the corresponding aperture efficiency is about 55%.

Due to its spherical symmetry, the proposed modified Luneberg cylindrical lens can be used to launch multiple beams by implementing an arc array of planar LTSA elements at the periphery

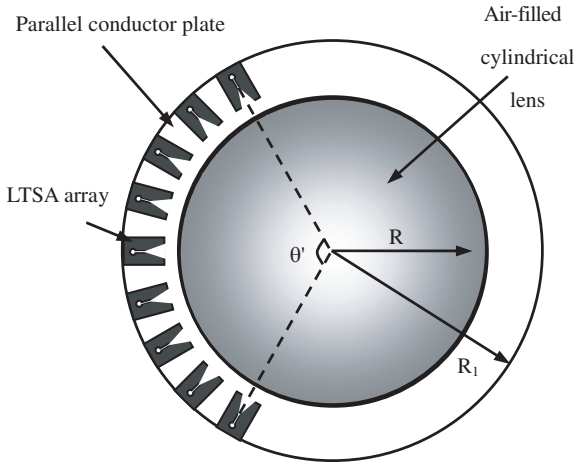

Figure 6: Top view of the proposed multiple-beam lens antenna.

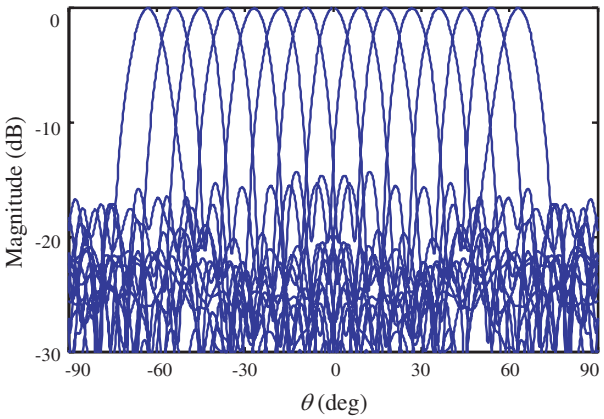

Figure 7: Simulated E-plane patterns at 30 GHz of the 15 beam array with a crossover of -3 dB.

of the lens. Beam scanning can be achieved by switching among the feed antenna elements. A top view of the proposed multiple-beam lens antenna is shown in Fig. 6. In our design, the LTSA elements are placed on the $d = 7.0$ mm arc with a center-to-center spacing of 9.4 mm. This results in a beam scan of 9° between any two adjacent antenna elements, and the pattern crossover occurs at the 3 dB level. A total of 15 LTSA elements are required to cover total 135° scan angle, and the simulated patterns are shown in Fig. 7. As shown, the designed 15-element array results in virtually no directivity loss over the entire 135° scan angle, which proves to be a wide scan-angle antenna at millimeter-wave frequencies.

4. CONCLUSIONS

A modified Luneberg cylindrical lens at mm-wave frequencies which utilizes the technique of parallel plates propagating the TE_{10} mode has been designed. The effective index of refraction of the mode TE_{10} can be easily obtained by controlling the spacing between the parallel plates. A combined ray-tracing/diffraction method is used to analyze the modified Luneberg cylindrical lens antenna system. Then, a modified Luneberg cylindrical lens at 30 GHz was designed. For this prototype, a directivity of 15.7 dB with 3-dB E- and H-plane beamwidths of 9.0° and 68.0° is achieved at the design frequency of 30 GHz, and the sidelobe level in the E-plane is -19.8 dB. Due to its spherical symmetry, the proposed modified Luneberg cylindrical lens can be used to launch multiple beams by implementing an arc array of planar LTSA elements at the periphery of the lens. In conclusion, the proposed lens antenna system is suits for wide-angle scanning fan-beam applications due to its low weight and high performance.

ACKNOWLEDGMENT

This work is supported by Ministry of Science and Technology of China under Project 863 Grant 2009AA01Z226 and by NSFC under grant # 60871010.

REFERENCES

1. Sanford, J. R., "Scattering by spherically stratified microwave lens antennas," *IEEE Trans. Antennas Propag.*, Vol. 42, No. 5, 690–698, 1994.
2. Sanford, J., "A Luneberg lens update," *IEEE Mag. Antennas Propag.*, Vol. 37, No. 1, 76–79, 1995.
3. Schoenlinner, B., et al., "Wide-scan spherical lens antenna for automotive radars," *IEEE Trans. Microw. Theory Tech.*, Vol. 50, No. 9, 2166–2175, 2002.
4. Bui, L. Q., Y. Alon, and T. Morton, "94 GHz FMCW radar for low visibility aircraft landing system," *IEEE MTT-S Microwave Symp. Dig.*, 1147–1150, Boston, MA, July 1991.
5. Wu, X. and J. Laurin, "Fan-beam millimeter-wave antenna design based on the cylindrical luneberg lens," *IEEE Trans. Antennas Propag.*, Vol. 55, No. 8, 2147–2156, 2007.
6. Morgan, S. P., "General solution of the Luneburg lens problem," *J. Appl. Phys.*, Vol. 29, No. 9, 1358–1368, 1958.

A Dual Frequency Rectangular Dielectric Resonator Antenna Fed by a Coaxial Probe

Huixian Wu[1], **Xidong Wu**[1], **Changzhou Hua**[1, 2], **and Nan Yang**[1]

[1]Department of Information Science & Electronic Engineering
Zhejiang University, Hangzhou 310027, China
[2]Ministerial Key Laboratory of JGMT
Nanjing University of Science & Technology, Nanjing 210094, China

Abstract— A dual frequency hybrid dielectric resonator antenna (DRA) is presented for wireless communications. The proposed DRA consists of a rectangular dielectric resonator and a printed rectangular patch on top of it in order to achieve dual-band operation without significant increase in antenna size. The proposed antenna is analyzed and designed using CST-MWS. The simulated results show the -10dB bandwidths are from 19.0 GHz–20.4 GHz (BW_1 = 1.4 GHz) and 29.6 GHz–31.4 GHz (BW_2 = 1.8 GHz), respectively. The frequency ratio of the two resonant frequencies is 1.54, which is relatively larger than that of conventional designs.

1. INTRODUCTION

Dielectric resonator antenna (DRA) has many attractive advantages, such as small volume, high efficiency, wide bandwidth, design flexibility [1, 2]. All these features make DRA widely used in wireless communications, for example, mobile terminals, wireless access points, base stations and other communication systems. In order to achieve dual-band operation without significant increase in antenna size, hybrid DRA structures have been developed recently by combining single DRA with other kinds of planar radiator such as parasitic loop [3], rectangular slot [4].

In this paper, a compact dual frequency hybrid DRA is presented. The DRA consists of a probe-fed rectangular dielectric resonator and a rectangular patch antenna on top of it. The rectangular dielectric resonator provides the first resonance frequency while the patch antenna resonates at the second frequency. Its detailed design consideration is described, and the simulated results are presented and discussed.

2. ANTENNA STRUCTURE

Figure 1 shows the geometry of the proposed rectangular DRA (ε_{r1}) with size of $a \times a \times h$. A printed patch antenna with size of $b \times b$ on a substrate (ε_{r2}) is placed on the top of the dielectric resonator. The DRA is fed using a coaxial probe, with a distance x_0 from the center of the DRA. The height of the feed probe above the ground plane is l. By optimizing the structure parameters, the DRA and the patch antenna can resonate at two different frequencies. The rectangular dielectric resonator provides the first resonance frequency f_1 while the patch antenna resonates at the second frequency f_2.

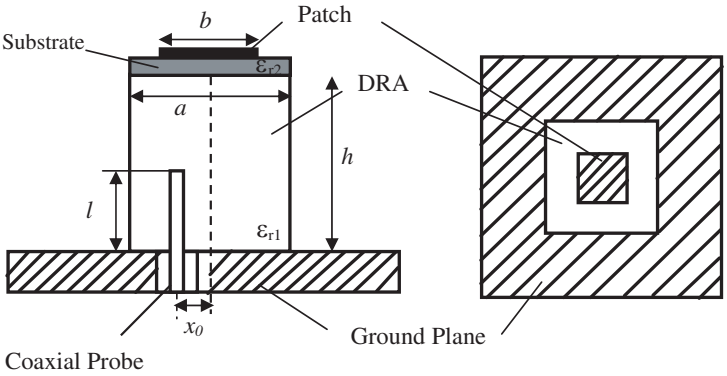

(a) Side view (b) Top view

Figure 1: Configuration of proposed antenna.

3. ANTENNA DESIGN AND RESULTS

The resonant properties of the designed DRA are studied by adjusting the values of different parameters using CST-MWS. For this purpose, the relative permittivity of the rectangular DRA is chosen to be $\varepsilon_{r1} = 12$, and the relative permittivity of the patch substrate is chosen to be $\varepsilon_{r2} = 2.2$. Fig. 2 shows the simulated return loss for different DRA size a. As shown, two resonances are achieved, which are DRA mode and patch mode, respectively. Both the two resonant frequencies decrease with the DRA size a. In the same spirit, Fig. 3 shows the simulated return loss for different patch size b. As expected, both the two resonant frequencies decrease with the patch size b too. It should be noted that the DRA size provides more sensitivity than the patch size. The feed position and the depth of feed probe can be adjusted for matching purpose.

After the above parametric studies, the dimensions of the designed dual frequency DRA are given as follows: $a = 2.5\,\text{mm}$, $b = 2.0\,\text{mm}$, $h = 2.0\,\text{mm}$, $x_0 = 0.8\,\text{mm}$ and $l = 1.2\,\text{mm}$. The simulated return loss is then given in Fig. 4. The two resonant frequencies are realized at 19.5 GHz and 30.0 GHz, respectively. The $-10\,\text{dB}$ bandwidths are from 19.0 GHz–20.4 GHz ($BW_1 = 1.4\,\text{GHz}$) and 29.6 GHz–31.4 GHz ($BW_2 = 1.8\,\text{GHz}$), respectively. The corresponding E- and H-plane patterns at these two frequencies are shown in Fig. 5. The realized gains are all equal to 5.6 dBi at these two resonant frequencies.

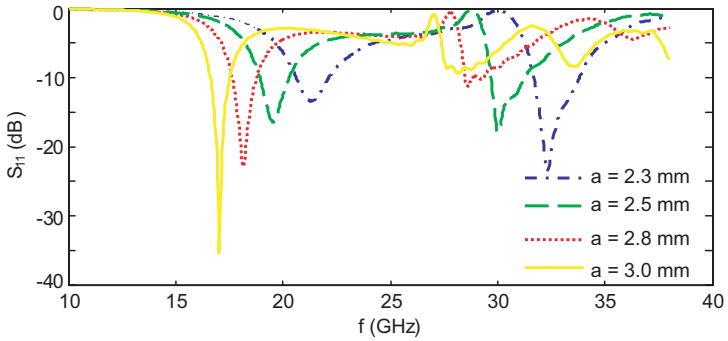

Figure 2: Return loss of different DRA sizes with $h = 2.0\,\text{mm}$, $b = 2.0\,\text{mm}$, $x_0 = 0.8\,\text{mm}$, $l = 1.3\,\text{mm}$.

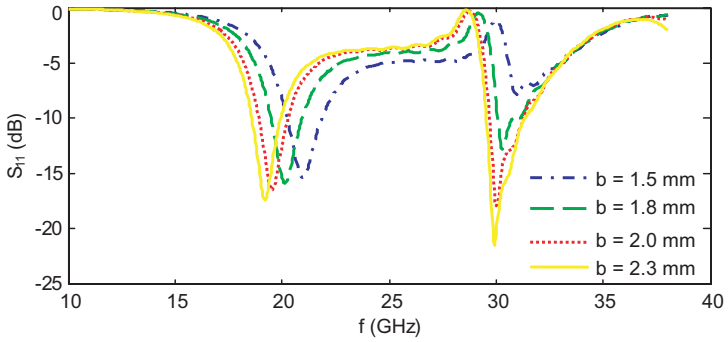

Figure 3: Return loss of different patch sizes with $a = 2.5\,\text{mm}$, $h = 2.0\,\text{mm}$, $x_0 = 0.8\,\text{mm}$, $l = 1.3\,\text{mm}$.

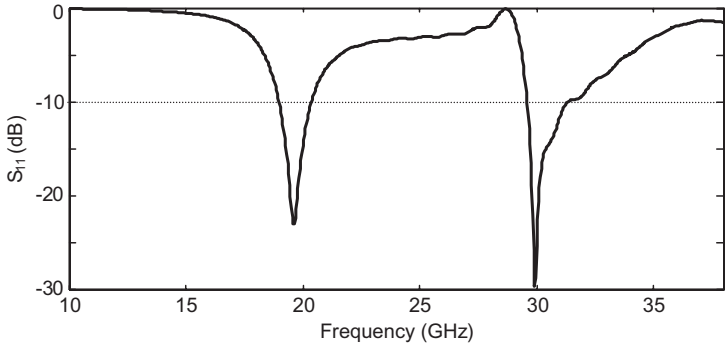

Figure 4: Return loss of the dual frequency DRA with $a = 2.5\,\text{mm}$, $h = 2.0\,\text{mm}$, $b = 2.0\,\text{mm}$, $x_0 = 0.8\,\text{mm}$, and $l = 1.2\,\text{mm}$.

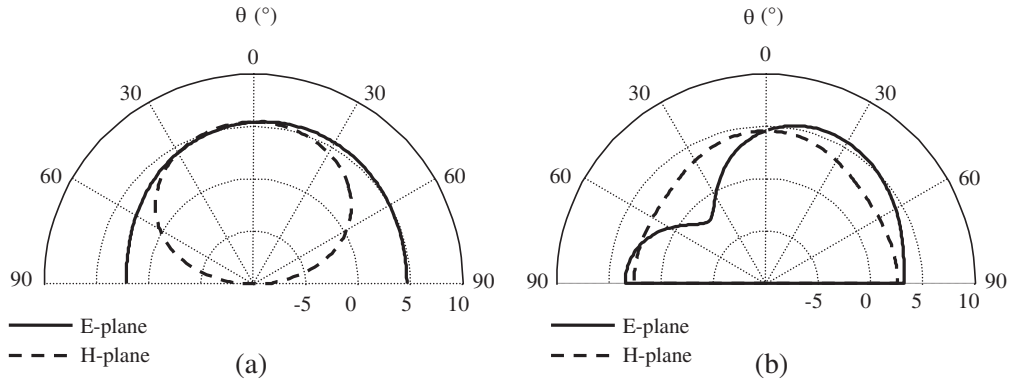

Figure 5: Radiation patterns of the dual frequency DRA with $a = 2.5\,\text{mm}$, $h = 2.0\,\text{mm}$, $b = 2.0\,\text{mm}$, $x_0 = 0.8\,\text{mm}$, and $l = 1.2\,\text{mm}$ at (a) $f_1 = 19.5\,\text{GHz}$ and (b) $f_2 = 30.0\,\text{GHz}$.

4. CONCLUSIONS

This paper presents a dual frequency hybrid DRA which is composed of a probe-fed rectangular dielectric resonator and a rectangular patch antenna on top of it. The radiation characteristics of the proposed antenna have been investigated using CST-MWS. Two resonant frequencies are realized at 19.5 GHz and 30.0 GHz, with bandwidth from 19.0 GHz–20.4 GHz and 29.6 GHz-31.4 GHz respectively. Such a hybrid antenna with compact size can provide sufficient impedance bandwidth and good radiation patterns across the desired frequency bands, which are very attractive for WLAN applications.

ACKNOWLEDGMENT

This work is supported by Ministry of Science and Technology of China under Project 863 Grant 2009AA01Z226 and by NSFC under grant # 60871010.

REFERENCES

1. Kishk, A. A., X. Zhang, A. W. Glisson, and D. Kajfez, "Numerical analysis of stacked dielectric resonator antennas excited by a coaxial probe for wideband applications," *IEEE Trans. Antennas Propag. Lett.*, Vol. 51, No. 8, 1996–2006, 2003.
2. Rao, Q., T. A. Denidni, and A. R. Sebak, "Design, analysis and measurement of a new dual-band compact hybrid resonator antenna," *IEEE-NEWCAS Conference*, 275–278, Québec, Canada, June 2005.
3. Gao, Y., B.-L. Ooi, and M.-S. Leong, "Dual-band hybrid dielectric resonator antenna for WLAN," *IEEE Trans. Antennas Propag. Soc.*, 1–4, San Diego, CA, July 2008.
4. Buerkle, A., K. Sarabandi, and H. Mosallaei, "Compact slot and dielectric resonator antenna with dual-resonance, broadband characteristics," *IEEE Trans. Antennas propag.*, Vol. 53, No. 3, 1020–1027, 2005.

Use of Frequency Selective Surface to Prevent SAR and Improve Antenna Performance of Cellular Phones

Han-Nien Lin[1], **Ke-Wen Lin**[2], **and Sheng-Chun Chen**[1]

[1]Department of Communications Engineering, Feng-Chia University
100 Wen-Hua Rd., Taichung 40724, Taiwan, R.O.C.
[2]Department of Electrical Engineering, National Chiao-Tung University
1001 University Road, Hsinchu 300, Taiwan, R.O.C.

Abstract— The purpose of this study is to design the low-cost planar inverted-F antenna (PIFA) applicably built in cellular phones with finite integration technique (FIT) for simulation of surface current distribution, radiation efficiency, radiation pattern, and gain. The prototype antenna is constructed with aluminum foil and low-cost FR4 PCB substrate. The antenna is designed with quarter wavelength ($\lambda/4$) of resonant frequencies and fed with 50 Ω matching microstrip. It owns the industrial demanding characteristics of light weight, compactness, low profile, and easy fabrication. The target frequency band is designed for the following cellular phone systems: GSM (Global system for mobile communication: 880–960 MHz), DCS (Digital communication system: 1.71–1.88 GHz, PCS (Personal communication system: 1.85–1.99 GHz), and IMT-2000 (3G: (1.92–2.17 GHz). However, since the bio-effect of specific absorption rate (SAR) by cellular phone gains popular concern, we also try to utilize the unique band-stop or band-pass features of frequency selective surface (FSS) to reduce the SAR. Finally, we design the finite size 2-dimensional periodic structure to integrate with antenna for SAR reduction by decreasing backward radiation. The result shows that the integrated PIFA-FSS module not only reduces the SAR but also improve the antenna gain and radiation efficiency of the cellular phone.

1. INTRODUCTION

Due to the ever increasing popularization of all kinds of mobile communication devices in recent years, there is urgent demanding for antennas with characteristics of low-profile, light-weight, compactness, easy-fabrication, low-cost, and easy-integration with PCB. We therefore dedicated to advantageous PIFA (planar inverted-F antenna) with center frequencies around 900 MHz and 1800 MHz in this study for popular communication systems, such as GSM (Global system for mobile communication: 880–960 MHz), DCS (Digital communication system: 1.71–1.88 GHz), PCS (Personal communication system: 1.85–1.99 GHz), and IMT-2000 (3G communications: 1.92–2.17 GHz). Nowadays the electromagnetic band-gap (EBG) structure [1] has gained the most attention in the microwave community and become a major research topic. The most attractive characteristic of EBG material is the band-stop and slow-wave response from the periodic arrangement of structure or component. It thus results in high surface impedance and energy band-gap (stop-band or pass-band) due to impedance discontinuity between air and high-impedance surface, and therefore prevents electromagnetic wave propagating through the periodic structure. However, this kind of special electromagnetic material does not exist itself in nature, it is often categorized as artificial magnetic conductor (AMC), perfect magnetic conductor (PMC), or even meta-material [2] by Yen et al.. The frequency selective surfaces (FSS) [3] frequently found in 2-dimensional applications belongs to this category.

Due to periodic dimension of EBG structure commonly being about half-wavelength of the stop-band, the large size has limited the applications of EBG structure in low frequency range. In this paper we introduce folded bends to lengthen the electric current path and thus increase equivalent inductance. We also utilize the longer edge-coupling effect to lengthen the magnetic current path and thus increase equivalent capacitance. Therefore, we are able to design compact EBG structure for low frequency applications using the above techniques.

Since we try to utilize the unique band-stop or band-pass features of frequency selective surface (FSS) to reduce the SAR, We thus design the finite size 2-dimensional periodic structure to integrate with antenna for SAR reduction by decreasing backward radiation. The result shows that the integrated PIFA-FSS module not only reduces the SAR but also improve the antenna gain and radiation efficiency of the cellular phone.

2. EBG STRUCTURE DESIGN FOR ANTENNA MODULE

The stop-band and center frequency of EBG structure presented in this paper are around 900 MHz and 1800 MHz respectively. When PET (ε_{eff} = 3.3 and thickness 50 μm) used as substrate in this design, the resonant wavelength in dielectric and unit cell dimension λ_{EBG} can be calculated from Equations (1) and (2) respectively. While conventional EBG structure is capacitive itself between periodic metallic components, we introduced folding bend metallic components to reduce dimension of metallic patch L according to Equations (3) and (4) due to effective inductance of metallic component itself. The effect of increased equivalent inductance and capacitance is able to shift stop-band or energy band-gap to lower frequency. The designed dimensions and configuration is shown in Figure 1. The EBG structure investigated in this paper is 3 × 3 Unit cells as shown in Figure 2, where the thickness of the silver powder printing slot nets is 35 μm.

$$fr = \frac{c}{\lambda_0 \sqrt{\frac{\varepsilon_r+1}{2}}} \tag{1}$$

$$\lambda_{EBG} = \frac{\lambda_0}{2} \tag{2}$$

$$fr = \frac{1}{2\pi\sqrt{LC}} \tag{3}$$

$$BW = \sqrt{\frac{L}{C}}\frac{1}{\eta} \tag{4}$$

The design parameters above are the following: c is the speed of light in free space, ε_{eff} the equivalent dielectric constant, λ_{EBG} the wavelength of metallic component periodic dimension, λ_0 the wavelength of light in free space, fr the resonant frequency, and η is the free space wave impedance.

We first calculated the basic design parameters from the above equations, and then utilized the full-wave FDTD (Finite-Difference Time-Domain) electromagnetic simulation software for the optimal geometric structure design of periodic pattern.

3. SIMULATION AND MEASUREMENT COMPARISON OF PIFA ANTENNA

The radiating part of the investigated PIFA is made of aluminum foil with 0.05 mm thickness by fabricating with Laser cutting process. The 0.05 mm thickness ground plane is printed on FR4 substrate. The FR4 substrate has the following characteristics: equivalent dielectric constant ε_{eff} = 4.4 loss tangent 0.0245, and 0.8 mm thickness. The radiator of PIFA is fixed on ABS plastic material as usually found in cellular phone enclosure. The ABS plastic has the following parameters: dielectric constant ε_{eff} = 2.25, loss tangent 0.0004. The dimension of antenna is shown in Figure 3 when PIFA antenna equals quarter-wavelength with center frequency fr = 900 MHz. Two feeding methods are applied for the design: one is to feed antenna with coaxial-like structure, and the other is using stripline or microstrip structure for easy fabrication purpose in laboratory. Figure 4 shows the good characteristic agreement between simulated and measured results. The 2-dimensional radiation pattern of the PIFA antennas for 900 MHz and 1800 MHz are shown in Figures 5 and 6 respectively.

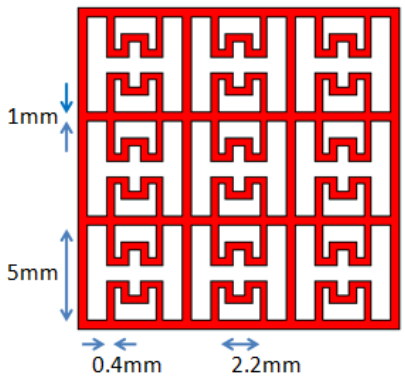

Figure 1: Dimensions of periodic structure.

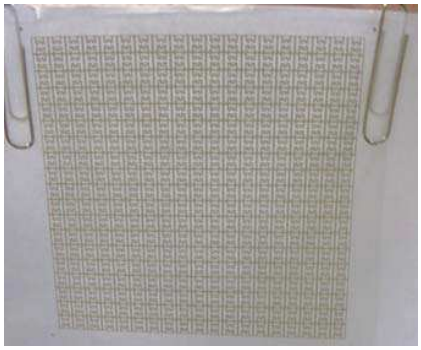

Figure 2: Photograph of periodic structure.

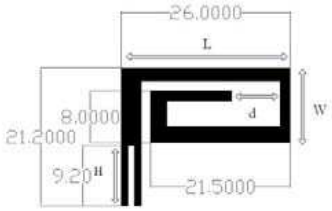

Figure 3: Dimension of PIFA antenna.

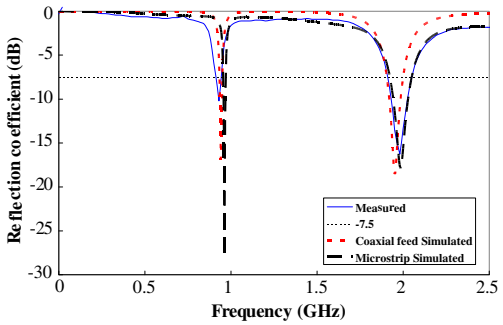

Figure 4: Simulation and measurement comparison of PIFA antenna.

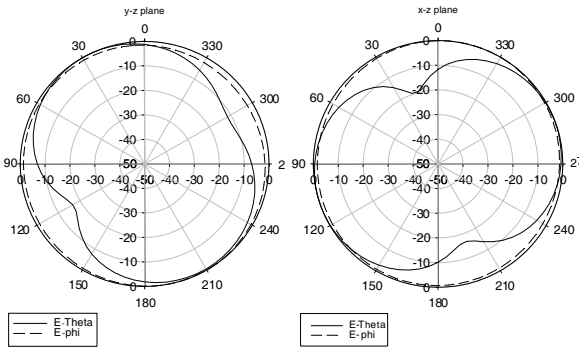

Figure 5: 2D radiation pattern of PIFA (@900 MHz).

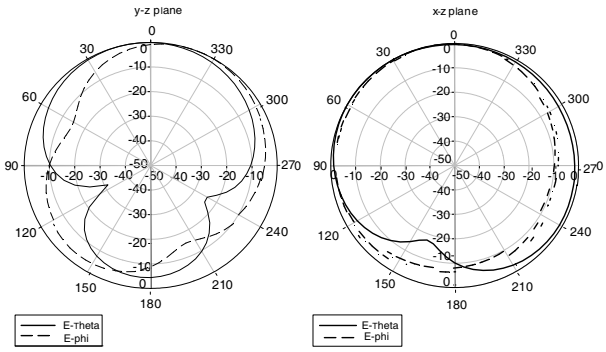

Figure 6: 2D radiation pattern of PIFA (@1900 MHz).

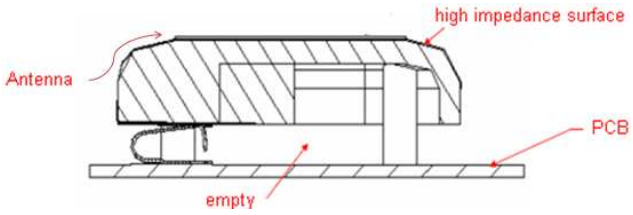

Figure 7: Schematic of PIFA on FSS.

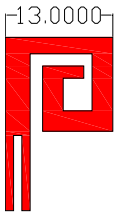

Figure 8: Dimension of Reduced PIFA antenna.

4. ANALYSIS OF PEC AND EBG REFLECTOR STRUCTURE EFFECT ON PIFA ANTENNA PERFORMANCE

We first placed the slotted FSS structure beneath the PIFA antenna to work as reflector as shown in Figure 7. Since the slotted FSS structure also became part of radiator, the periodic slotted array therefore induced magnetic current and further to lower the resonant frequency. To tune back the originally designed frequency, the dimension of PIFA is thus reduced as shown in Figure 8. The physical combination of the PIFA antenna with periodic structure as reflector is shown in Figure 9. The integration of slotted FSS and antenna can effectively reduce the radiator's dimension and be efficiently implemented for compact cellular phone. The comparison of S parameter between original antenna and FSS combined antenna is shown in Figure 10. It could be found that antenna with slotted FSS structure not only reduces total dimension, but also achieves better S parameter. The 2-dimensional radiation pattern of the FSS combined antennas for 900 MHz, 950 MHz, 1800 MHz and 1900 MHz are shown through Figures 11 to 14 respectively. Finally, we show in Table 1 the antenna gain and radiation efficiency comparison for the original antenna and FSS combined antenna. It is obvious that both antenna gain and radiation efficiency improve effectively with FSS implemented. We thus proposed the antenna module with combination of FSS and antenna to meet the cellular phone application with better performance.

5. INFLUENCE OF CELLULAR PHONE WITH FSS ON SAR

We use BENQ S88 cellular phone for SAR test to verify if the slotted FSS film studied in this paper can effectively reduce the SAR. We first measured the SAR for cellular alone, and then put the FSS film on top or bottom side of its antenna for performance comparison. When FSS film is placed in front of LCD (i.e., in the bottom side of antenna) as shown in Figure 13, the configuration is defined as with FSS front side. On the other hand, it is defined as "with FSS back side" when FSS film is placed in the back of cellular phone.

We find from the measured results (Table 2) that SAR could be effectively reduced with slotted FSS film attached in front of LCD panel (with FSS front side). It is explained that the high impedance surface (provided by slotted FSS film) under antenna can effectively reduce the back-

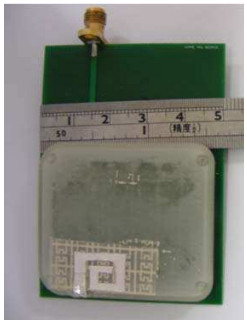

Figure 9: Physical arrangement of PIFA.

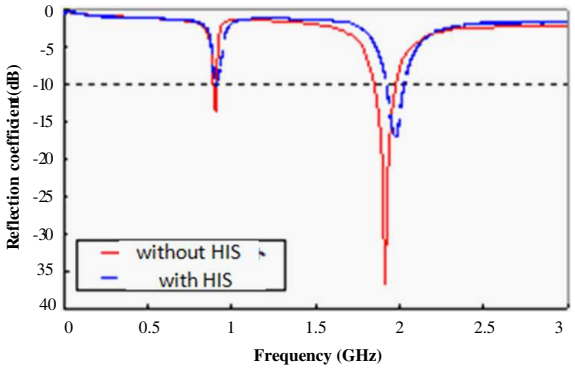

Figure 10: S_{11} comparison between original and FSS.

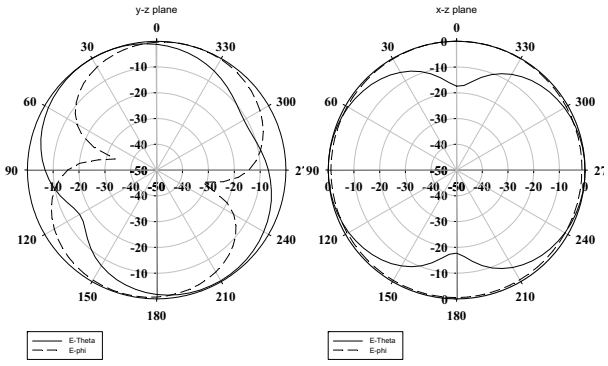

Figure 11: 2D radiation pattern (@900 MHz).

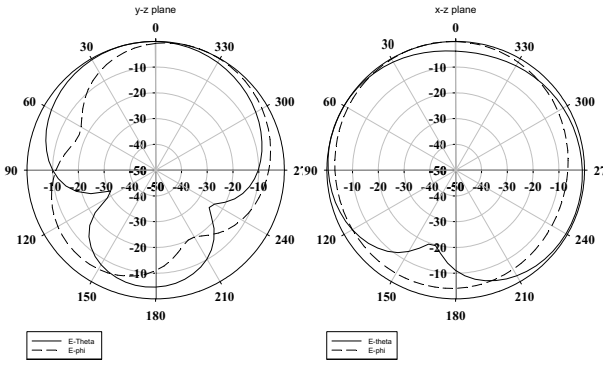

Figure 12: 2D radiation pattern (@1900 MHz).

Figure 13: Photograph of slotted FSS film placed on mobile phone for experiment.

Table 1: Performance comparison.

frequency	Gain (dB)	Radiation Efficiency (%)	frequency	Gain (dB)	Radiation Efficiency (%)
900 MHz	0.7083	79.48	1900 MHz	3.454	91.31
900 MHz with FSS	1.073	92.92	1900 MHz with FSS	3.517	95.93

Table 2: SAR Comparison for cellular phone with/without slotted FSS film.

Frequency (MHz)	with FSS back/front side.	SAR (1 g) = mW/g;	SAR (10 g) = mW/g;	Frequency (MHz)	with FSS back/front side.	SAR (1 g) = mW/g;	SAR (10 g) = mW/g;
1747.4	non	0.501	0.290	1784.8	non	0.598	0.351
1747.4	back	0.717	0.418	1784.8	back	0.695	0.378
1747.4	front	0.140	0.075	1784.8	front	0.22	0.118

lobe radiation and hence improve SAR performance. On the other hand, the SAR will increase when slotted FSS film is place on top of antenna because of backward radiation enhanced.

6. CONCLUSIONS

In this paper we have successful reduced the size of antenna structure by utilizing the frequency selective surface (FSS). The antenna module with combination of FSS and antenna has shown the improvement in antenna gain and radiation efficiency. In the meantime, the SAR performance for cellular phone has improved from the measurement and verifies the reduction of back lobe radiation. Therefore, the antenna module proposed in this paper not only provides better service quality of mobile communications, but also effectively reduces SAR of cellular for user's health.

REFERENCES

1. Yang, F., *Electromagnetic Band Gap Structures in Antenna Engineering*, The Cambridge RF and Microwave Engineering Series, New York, 2009.
2. Caloz, C. and T. Itoh., *Electromagnetic Metamaterials: Theory and Design*, Wiley-Interscience, New Jersey, 2006.
3. Munk, B. A., *Frequency Selective Surfaces: Theory and Design*, Wiley-Interscience, New York, 2000.
4. Jo, Y., et al., *Dual Band Spiral Shaped Antenna*, US Patent Application Publication, Pub. No.: US2003/0117325 A1, Jun. 26, 2003.
5. Jo, Y. and F. Caimi, *Independently Tunable Multi-band Meanderline Loaded Antenna*, US Patent Application Publication, Pub. No.: US2004/0125031 A1, Jul. 1, 2004.

Receiving Performance Enhancement of Active GPS Antenna with Periodic Structure

Han-Nien Lin[1], **Ke-Wen Lin**[1, 2], **Chung-Wei Kuo**[3], **and Yu-Jie Huang**[1]

[1]Department of Communications Engineering, Feng-Chia University
100 Wen-Hua Road, Taichung 40724, Taiwan, R.O.C.
[2]Department of Electrical Engineering, National Chiao-Tung University
1001 University Road, Hsinchu 300, Taiwan, R.O.C.
[3]Ph.D. Program in Electrical and Communications Engineering
Feng-Chia University, 100 Wen-Hua Road, Taichung 40724, Taiwan, R.O.C.

Abstract— The purpose of this study is to design the high gain active GPS antenna module and analyze the performance improvement implemented with periodic structure. Since the utilization of high-impedance surface of periodic structures as reflector not only significantly reduces the antenna profile with phase enhancement, but it will also enhance its gain and directivity performance. We first investigated the electromagnetic radiation suppression characteristic of Electromagnetic Band-Gap (EBG) structure and utilized the microstrip measurement method to verify the simulation result for required stopband and performance. In this study, we design microstrip antenna and periodic structure with center frequency at 1.575 GHz for Global Positioning System (GPS) to investigate the effect with applications of EBG structure on antenna. Microstrip antenna has the industrial demanding characteristics of light weight, low profile, and easy integration with circuits on PCB. We investigated surface wave suppression and axial ratio improvement with the antenna surrounded by matching resonant EBG structure. Finally, we design the front-end low noise amplifier (LNA) with center frequency at 1.575 GHz to integrate with antenna to further improve GPS receiving sensitivity.

1. INTRODUCTION

Due to the ever increasing popularization of navigation devices in recent years, there is urgent demanding for antennas with characteristics of low-profile, light-weight, compactness, easy-fabrication, low-cost, and easy-integration with PCB. We therefore dedicated to advantageous micristrip antenna with center frequencies around 1575 MHz in this study for popular Global Positioning System (GPS) applications. The electromagnetic band-gap (EBG) structure [1] has gained the most attention in the microwave community and becomes a major research topic recently. The most attractive characteristic of EBG material is the band-stop and slow-wave response from the periodic arrangement of structure or component. It thus results in high surface impedance and energy band-gap (stop-band or pass-band) due to impedance discontinuity between air and high-impedance surface, and therefore prevents electromagnetic wave propagating out of the periodic structure. However, this kind of special electromagnetic material does not exist itself in nature, it is often categorized as artificial magnetic conductor (AMC), perfect magnetic conductor (PMC), or even meta-material [2] by Yen et al.. The frequency selective surfaces (FSS) [3] frequently found in 2-dimensional applications also belongs to this category.

Since microstrip antenna is an resonant structure, its radiation loss and Q factor are both inverse proportional to substrate thickness. Therefore the thicker the substrate is, the wider the impedance-matching bandwidth will be. However, the increasing coupling of the energy also results in more surface wave occurring adverse coupling at substrate or edge of antenna. The implementation of periodic structure on microstrip antenna can suppress the surface wave propagation and obtain better axial ratio by reducing interfering scattering from surface wave. In addition to surface wave suppression by periodic structure, the integration of antenna and low-noise amplifier can further improve receiving sensitivity with increasing S/N ratio.

2. ANALYSIS OF EBG STRUCTURE DESIGN

From Bragg condition [2], the completely constructed reflection phenomena from radiation would result from periodic structure with half-wavelength or its integral multiple as period dimension and further result in energy band-gap characteristics. The stop-band is usually determined by periodic separation λ_{EBG} between metallic components. The stop-band and center frequency of EBG structure presented in this paper is around 1.575 GHz for GPS system. When FR4 substrate

($\varepsilon_r = 4.4$ and thickness 1.6 mm) is used in this design, the resonant wavelength in dielectric and unit cell dimension λ_{EBG} can be calculated from Equations (1) and (2) respectively. While conventional EBG structure is capacitive itself between periodic metallic components, we also implement vias to reduce dimension of metallic patch by introducing L according to Equations (3) and (4) due to effective inductance of via loop itself. The effect of increased equivalent inductance and capacitance is able to shift stop-band or energy band-gap to lower frequency. The dimension and EBG structure investigated in this paper are 5×5 Unit cells as shown in Figure 1 and Table 1 respectively. The design parameters can be calculated from the following:

$$L = \mu_0 \times h \tag{1}$$

$$C = \frac{W\varepsilon_0(1+\varepsilon_r)}{\pi} \cosh^{-1}\left(\frac{2W+g}{g}\right) \tag{2}$$

$$\omega = \frac{1}{\sqrt{LC}} \tag{3}$$

$$BW = \frac{\Delta\omega}{\omega} = \frac{1}{\eta}\sqrt{\frac{L}{C}} \tag{4}$$

where L is the equivalent inductance, μ_0 the permeability in free space, h the thickness of substrate, C the equivalent capacitance, W the width of metallic patch, ε_r the equivalent dielectric constant, g the spacing between metallic patches, ω_0 the resonant angular frequency, and η the intrinsic impedance of free space.

We first calculated the basic design parameters from the above equations, and then utilized the full-wave FDTD (Finite-Difference Time-Domain) electromagnetic simulation software to obtain the optimal geometric structure design of periodic pattern. The resulted transmission characteristic is shown in Figure 2, where the bandwidth of stop-band is around 600 MHz (1.4∼2 GHz) to meet −20 dB attenuation specification.

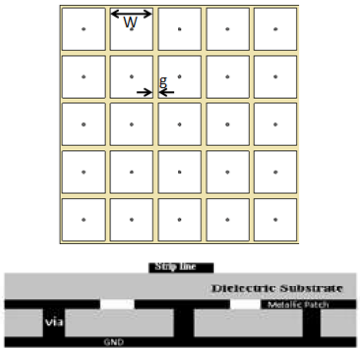

Figure 1: Schematic of periodic structure.

	size
Width of metallic patch (W)	16 mm
Spacing (g)	2 mm
Substrate thickness (h)	1.6 mm
Radius of via	0.5 mm

Table 1: Dimensions of periodic structure.

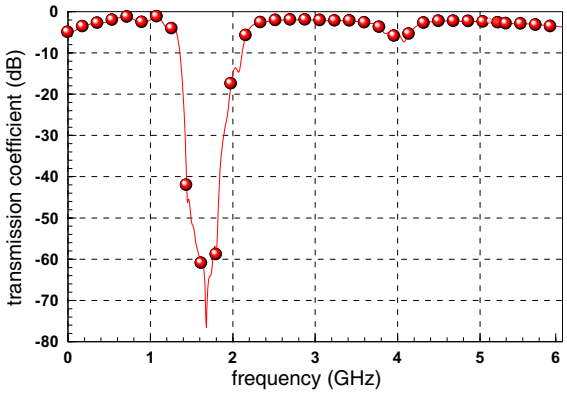

Figure 2: Simulated transmission coefficient of periodic structure.

3. SIMULATION AND MEASUREMENT COMPARISON OF ACTIVE MICROSTRIP ANTENNA

The low noise amplifier with center frequency $fr = 1.575$ GHz is designed on FR4 substrate, where the dielectric constant $\varepsilon_r = 4.4$ and thickness is 1.6 mm. The physical circuit of LNA is shown in Figure 3. The measured characteristic S parameters, noise figure, and simulated stability results of low noise amplifier are shown in Figure 4 to 6 respectively.

When FR4 substrate ($\varepsilon_r = 4.4$ and thickness 1.6 mm) is used for mircostrip antenna design, the dimension is designed as one half of resonant wavelength in dielectric with resonant frequency $fr = 1.575$ GHz as shown in Figure 7. It could be found that the excellent agreement between simulation and measurement results has been achieved in Figure 8, and also the increasing bandwidth after low noise amplifier added to the antenna. Figure 9 shows that the simulated and measured axial-ratio (AR) of antenna both fall between 5 and 6. The measured 3-dimensional radiation pattern of the microstrip antenna is shown in Figure 10.

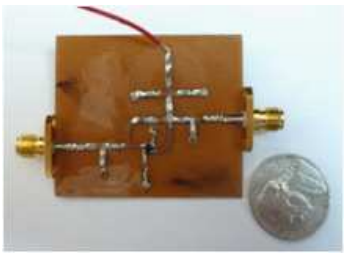

Figure 3: Photograph of low noise amplifier.

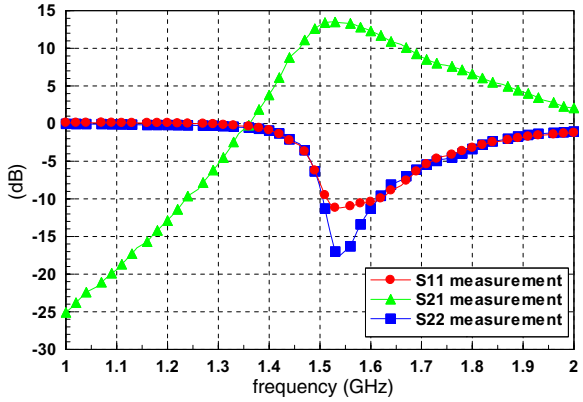

Figure 4: Measured characteristic parameters of LNA.

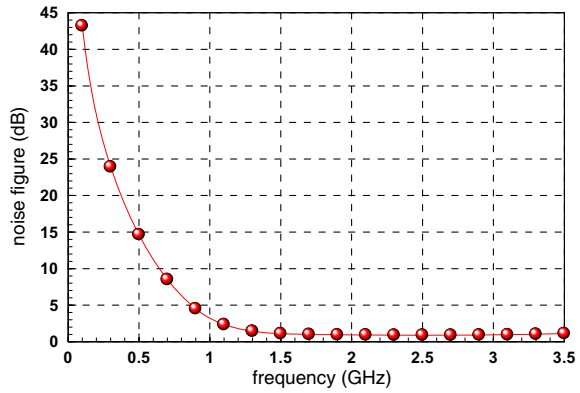

Figure 5: Simulated noise figure of LNA.

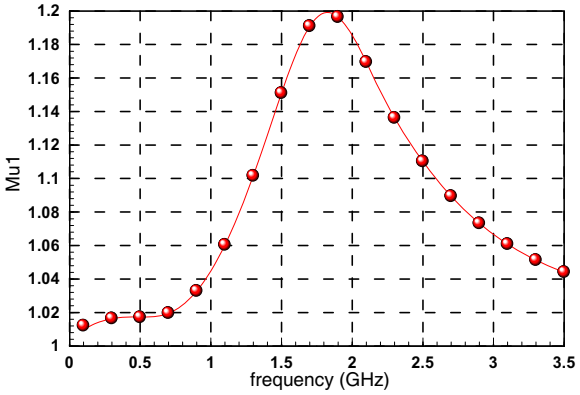

Figure 6: Simulated stability of LNA.

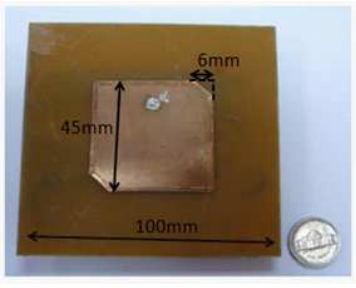

Figure 7: Dimensions of antenna.

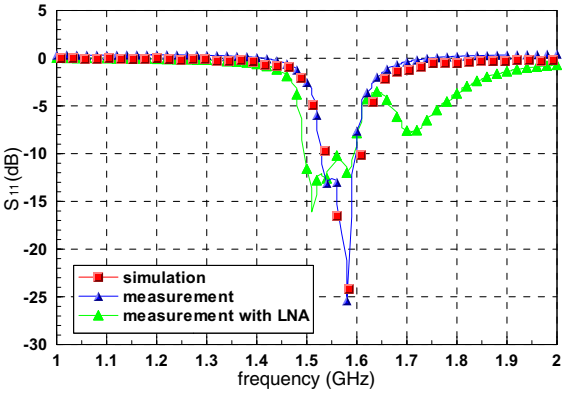

Figure 8: S_{11} comparison between simulation and measurement.

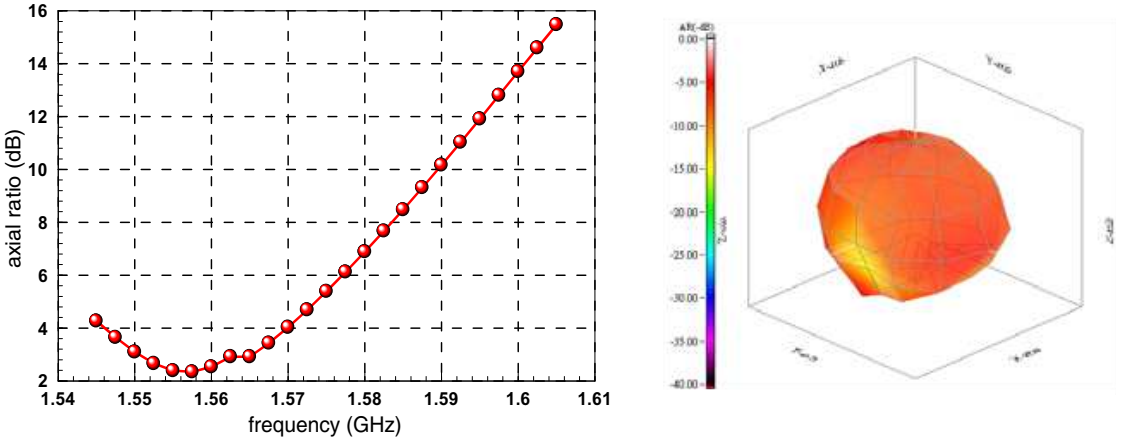

Figure 9: Simulated and measured axial-ratio (AR) of antenna around and @1.575 GHz.

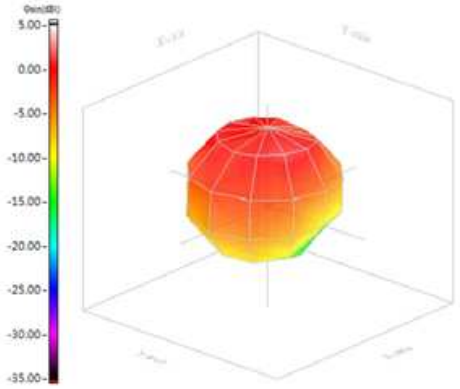

Figure 10: 3-dimensional radiation pattern of the microstrip antenna @1.575 GHz.

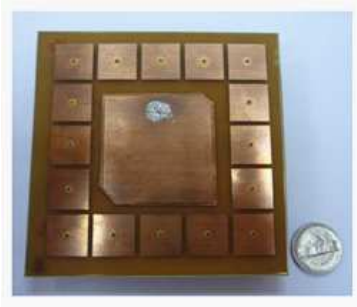

Figure 11: Photograph of antenna and EBG combination.

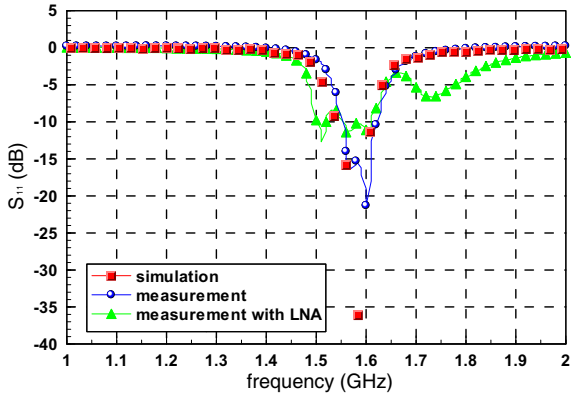

Figure 12: Simulated and measured S_{11} comparison.

4. INTEGRATION MODULE OF ANTENNA AND PERIODIC STRUCTURE

To suppress the surface on PCB substrate, we implement the periodic structure around the microstrip antenna to form the integrated antenna module as shown in Figure 11. The simulated and measured S_{11} parameters are shown in Figure 12. It could be found from the results that the resonant frequency shifts upward due to resonant dimension reduction of antenna. The simulated and measured axial-ratios are shown in Figure 13, and it reveals that the AR gains 1–2 dB improvement after implementing periodic structure. The measured 3-dimensional radiation pattern of the integration of microstrip antenna and EBG structure is shown in Figure 14. In the last, we show in Table 2 the performance comparison before and after periodic structure is added to the microstrip antenna.

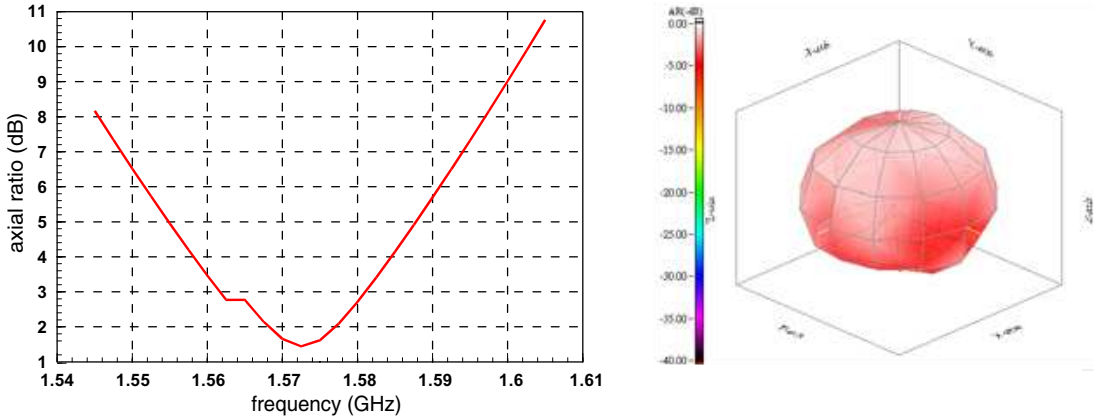

Figure 13: Simulated and measured axial-ratio (AR) of antenna surrounded by periodic structure around and @1.575 GHz.

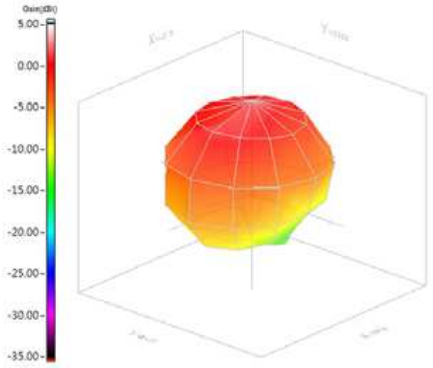

Figure 14: 3-dimensional radiation pattern of the microstrip antenna surrounded by periodic structure @1.575 GHz.

Table 2: Performance comparison for antennas.

Antenna structure	Input return loss (dB)	Measured gain (dBi)	Measured directivity (dB)	Measured efficiency	AR (dB)
Microstrip antenna	−21.20	1.02 dBi	6.46(dB)	28.61%	5.4
Microstrip antenna with periodic structure	−16.59	1.28 dBi	7.15(dB)	25.86%	1.5

5. CONCLUSIONS

In this paper, we have successfully improved axial ratio characteristic for GPS antenna (AR from 5.4 dB to 1.5 dB) by surrounding the periodic structure around microstrip antenna. Not only 3 dB AR requirement for circular polarization is met from this study, but antenna gain is also increased as well. We also integrate the GPS antenna with low noise amplifier to improve SNR and receiving sensitivity as shown in simulated and measured results. The resultant active antenna also shows the increasing bandwidth for the system.

REFERENCES

1. Yang., F., "Electromagnetic band gap structures in antenna engineering," *The Cambridge RF and Microwave Engineering Series*, New York, 2009.
2. Caloz, C. and T. Itoh., *Electromagnetic Metamaterials: Theory and Design*, Wiley-Interscience, New Jersey, 2006.
3. Munk., B. A., *Frequency Selective Surfaces: Theory and Design*, Wiley-Interscience, New York, 2000.
4. Sievenpiper, D. F., "Sievenpiper, high-impedance electromagnetic surfaces," Ph.D. thesis, UCLA, 1999.

Finite Different Ground Shapes Printed Spiral Antennas for Multi Wide Band Applications Using PPPC Feeding Scheme

A. A. Jamali[1], **A. Gaafar**[1], **and A. A. Abd Elaziz**[2]

[1]Department of Electronics and Communications Engineering, AAST, Egypt
[2]Department of Electronics and Communications Engineering, MUST, Egypt

Abstract— In this paper, three printed spiral antennas are proposed taking into account eliminating the presence of ground plane under the radiating element for not to affect on the spiral radiation characteristics. This can be done through choosing L, U and rectangular shape as a finite ground plane. The proposed antennas consists of two FR4 (dielectric constant of 4.65 and thickness of 1.5 mm) layers with foam (dielectric constant of 1.05 and thickness of 1.6 mm) layer inserted between them. Upper layer, two arms spiral antenna placed on its top where the lower layer has microstrip phase shifter etched on the surface and finite ground plane on its bottom. Parallel-plane perpendicular-current (PPPC) feed method will be used through connecting the spiral antenna arms with the microstrip phase shifter using shorted vias. The proposed antennas are fabricated and its reflection coefficients are measured and compared with its computed counterparts. Gain, directivity, axial ratio and other antenna parameters are studied using the IE3D Method of moments based software.

1. INTRODUCTION

In the era of modern wireless communication systems, antennas capable of operating at broad frequency band range are increasingly demanded. Various antenna design which enable antennas with low profile, light weight, enhanced dual or wideband frequency capabilities have been developed. However, such antennas mostly need a large size of ground plane which increases manufacturing cost. Among the proposed antenna designs, a spiral structure appears to be promising for wideband application due to its broadband impedance characteristic and compact size. The spiral antenna is a self-complementary structure [1] that has the input impedance close to theoretical value of 60π however practical realizations [2] usually achieve less values of impedance. Ideally, the electrical size of such antennas would remain constant over the entire electromagnetic spectrum. This ideal state requires that the spiral antenna be infinite to fulfill the self-scaling and self-complementary conditions. For a certain range of parameters, the spiral antenna can be truncated and still retain the properties of the infinite structures over a very wide band. The practical frequency independent structure is truncated, which limits the antenna's upper and lower frequency limits [2, 3]. A broadband antenna could find wide application in many systems such as given by [4] where the design was suitable for the WiMAX band (3.4–3.6 GHz)] . Recent studies are highly focused on antenna design in Ku-Band. Since the Ku-band has enough available bandwidth for satellite links, these systems are widely used in satellite communications, especially in the mobile antenna systems used in vehicles. There are also other application areas of Ku-band systems such as weather radars and redetection radars [7]. The first commercial television network to extensively utilize the Ku Band for most of its affiliate feeds was NBC, back in 1983. The ITU Region 2 segments covering the majority of the Americas are between 11.7 and 12.2 GHz. The 12.2 to 12.7 GHz segment of the Ku Band spectrum is allocated to the broadcasting satellite service (BSS). The ITU Region 1 segments of the Ku spectrum represent Africa and Europe (11.45 to 11.7 GHz band range and 12.5 to 12.75 GHz band range) is reserved for the fixed satellite service (FSS), with the uplink frequency range between 14.0 and 14.5 GHz).

2. ANTENNA GEOMETRY AND PROPERTIES

Printed spiral antenna was fed using different methods of excitation such given by [5] where the spiral consists of three arms, two outer lines and one middle line which form the spiral structure. The middle line connected directly to the inner conductor of the coax, and the outer lines connected to the ground conductor of the coax another one proposed by [6] where a parallel-plane perpendicular-current feed was used. This feed receives its name because its feed lies in a plane parallel to the spiral's surface and the currents traveling down this feed line are approximately perpendicular to the currents on the spiral's arms where the feed line passes underneath. Placing the feed in a plane parallel to the spiral minimizes the overall volume of the structure. Forcing the currents to cross

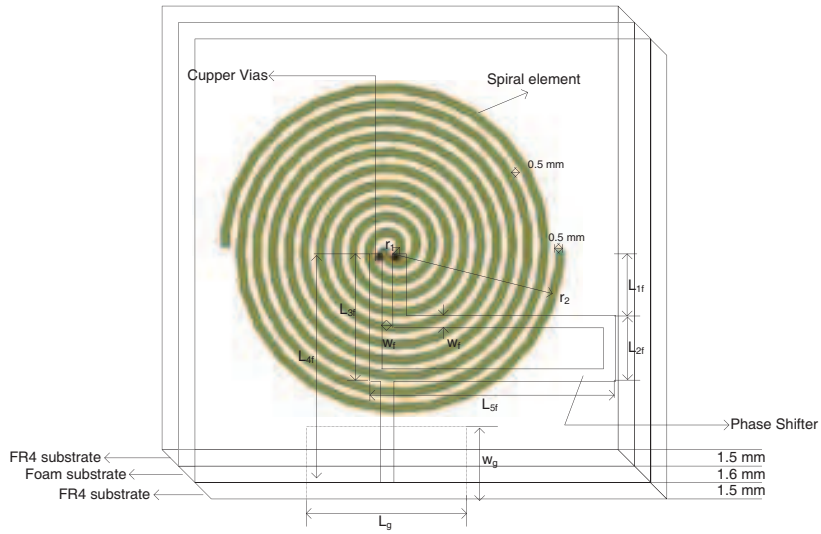

Figure 1: Top view of feeding system.

each other at near perpendicular angles minimizes the interactions of fields from the spiral with fields from the transmission line. With minimized interactions between radiation and transmission line fields, the antenna radiates most efficiently with an optimal return loss. The proposed antennas use the concept of parallel-plane perpendicular-current feed through the two vias connecting the radiating spiral element with the phase shifter as shown in Figure 1. The spiral consists of two identical arms which are shifted by 180° with respect to each other. The spiral curve is described by Equation (1) [3]:

$$r = r_o e^{a(\varphi+\theta)} \tag{1}$$

where r_o is the starting distance at $\varphi = 0°$, a determines the increasing rate of radius r, θ is the variable angle and φ determines rotation of the curve. The impedance transformer is based on a microstrip phase shifter on a finite ground plane with different shapes. The size and the shape of the ground plane are optimized for matching the radiator to the 50 Ω coaxial line. Based on the traditional equations of printed spiral antenna and covering the range from 2–10 GHz, so we can substitute for $f_{low} = 2\,\text{GHz}$ and $f_{high} = 13\,\text{GHz}$ in Equations (2) and (3) where f_{low} and f_{high} are the lower and the higher frequency limits and c is the light velocity.

$$f_{low} = \frac{c}{2\pi r_2} \tag{2}$$

$$f_{high} = \frac{c}{2\pi r_1} \tag{3}$$

Inner spiral radius r_1 and outer spiral radius r_2 found to be 3.672 mm and 23.873 mm respectively. As shown in Figure 1, the radiated element placed on the top of the substrate while the feeding scheme placed on another substrate where a rectangular finite ground plane with length L_g and width W_g lies beneath. Both substrates are integrated together through two vias connecting the feeding scheme with the radiator element passing through the foam layer between them. With these design parameters, the width w of the arms are the same as the spacing s between the arms and the structure is self-complementary, which gives the most frequency independent parameters [2]. After optimization using IE3D, the width of the arms are found to be 0.5 mm. The spiral antenna with rectangular ground plane shape has a radius of 10.5 mm for the spiral element and $4 \times 5\,\text{mm}^2$ for the ground plane shape. Both spiral antenna with U and L ground plane shapes have equal radii of 8.5 mm for spiral elements and $23 \times 35\,\text{mm}^2$ and $20 \times 35\,\text{mm}^2$ for ground plane respectively. The phase shifter dimensions for the three structure are $l_{1f} = 3\,\text{mm}$, $l_{2f} = 3\,\text{mm}$, $l_{3f} = 6\,\text{mm}$, $l_{4f} = 11\,\text{mm}$, and $l_{5f} = 11.5\,\text{mm}$. The proposed spiral antenna is fabricated on two FR-4 substrates with thickness of 1.5 mm and a relative dielectric constant (ε_r) of 4.65 with foam layer with 1.6 mm thickness and ε_r of 1.05 inserted between them.

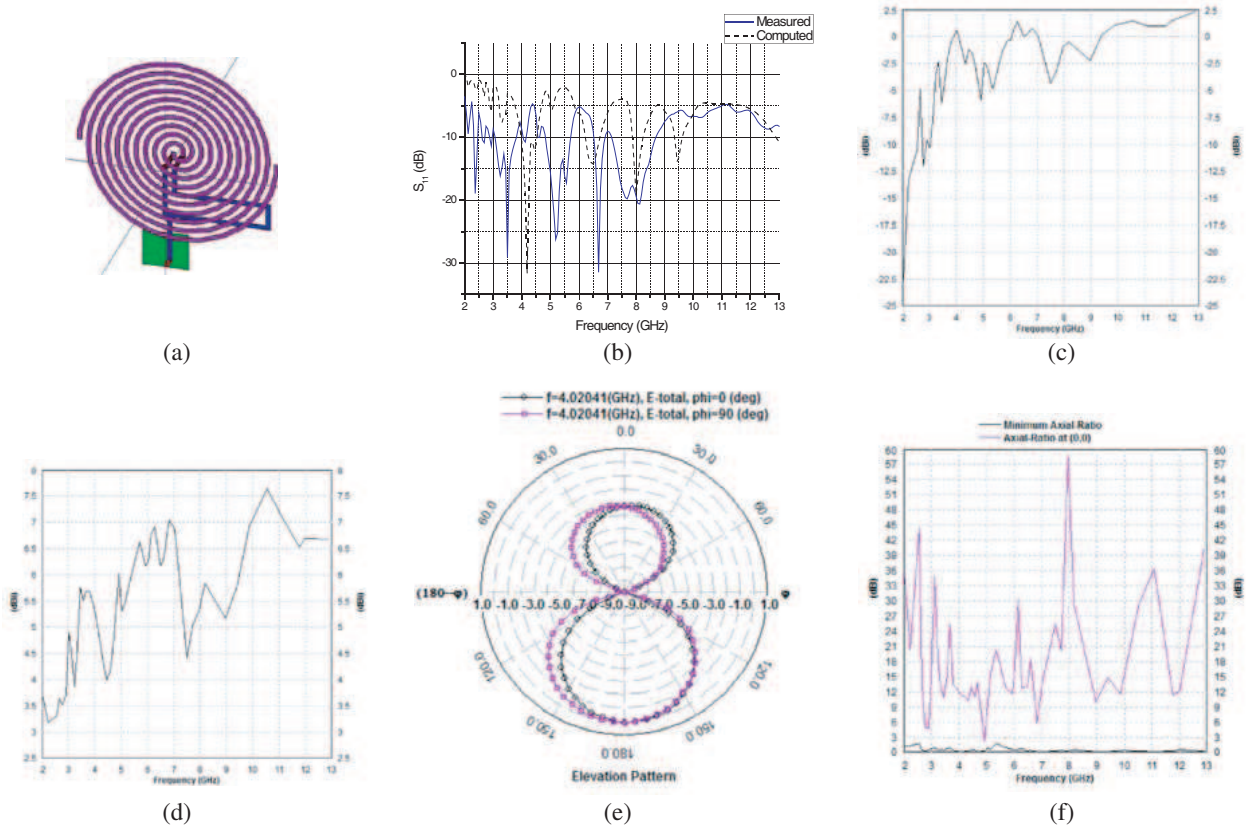

(a) (b) (c) (d) (e) (f)

Figure 2: (a) Proposed rectangular shape ground plane spiral antenna. (b) Reflection coefficient versus frequency of rectangular shape ground plane spiral antenna. (c) Gain versus frequency for rectangular ground plane shape spiral antenna. (d) Directivity versus frequency for rectangular ground plane shape spiral antenna. (e) Radiation pattern for rectangular ground plane shape spiral antenna. (f) Axial and minimum axial ratio versus frequency for rectangular ground plane shape spiral antenna.

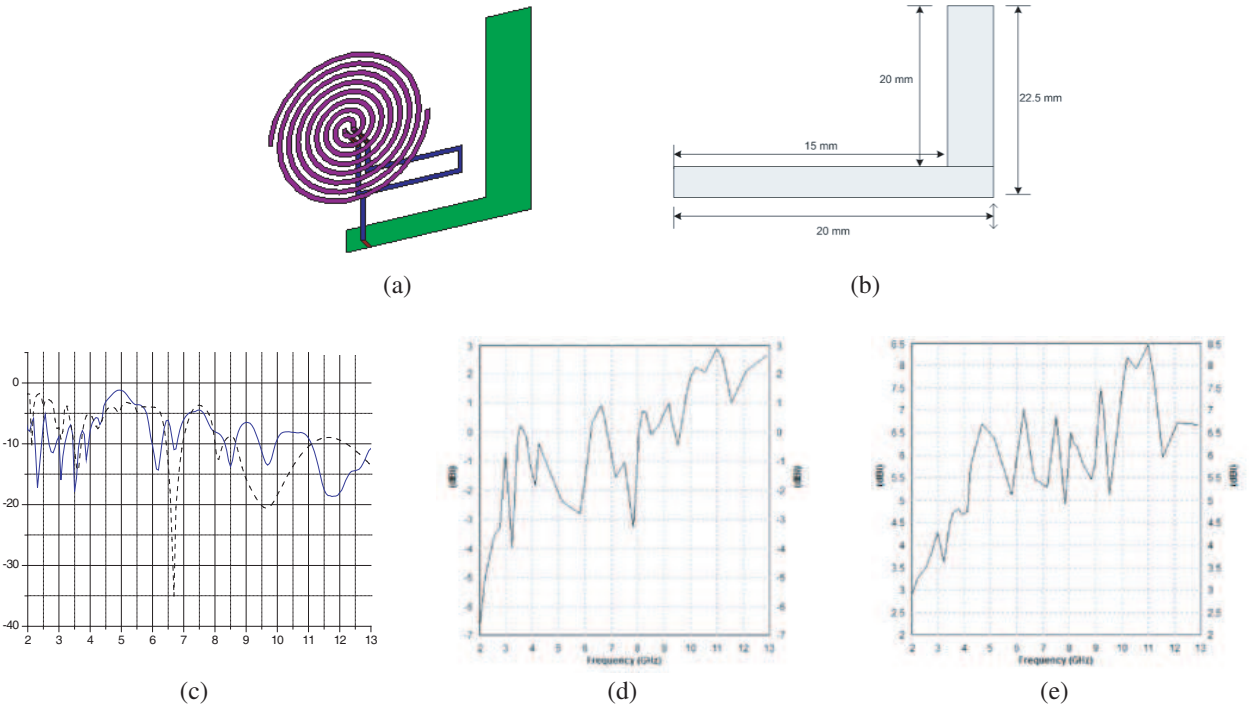

(a) (b) (c) (d) (e)

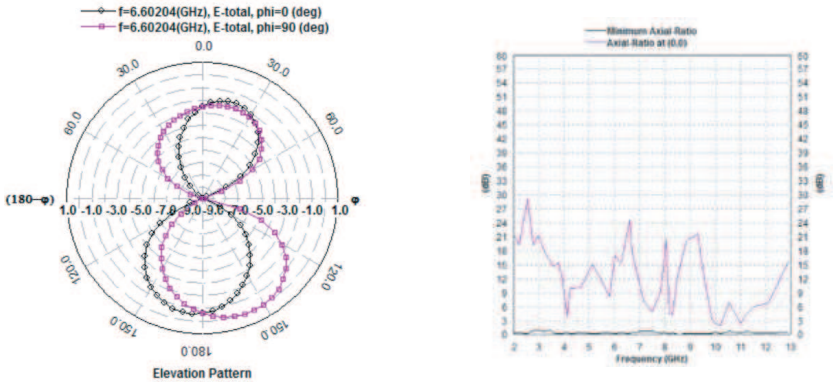

(f) (g)

Figure 3: (a) Proposed L shape ground plane spiral antenna. (b) Ground plane shape for the L shape ground plane spiral antenna. (c) Reflection coefficient versus frequency of L shape ground plane spiral antenna. (d) Gain versus frequency for L ground plane shape spiral antenna. (e) Directivity versus frequency for L ground plane shape spiral antenna. (f) Radiation pattern for L ground plane shape spiral antenna. (g) Axial and minimum axial ratio versus frequency for L ground plane shape spiral antenna.

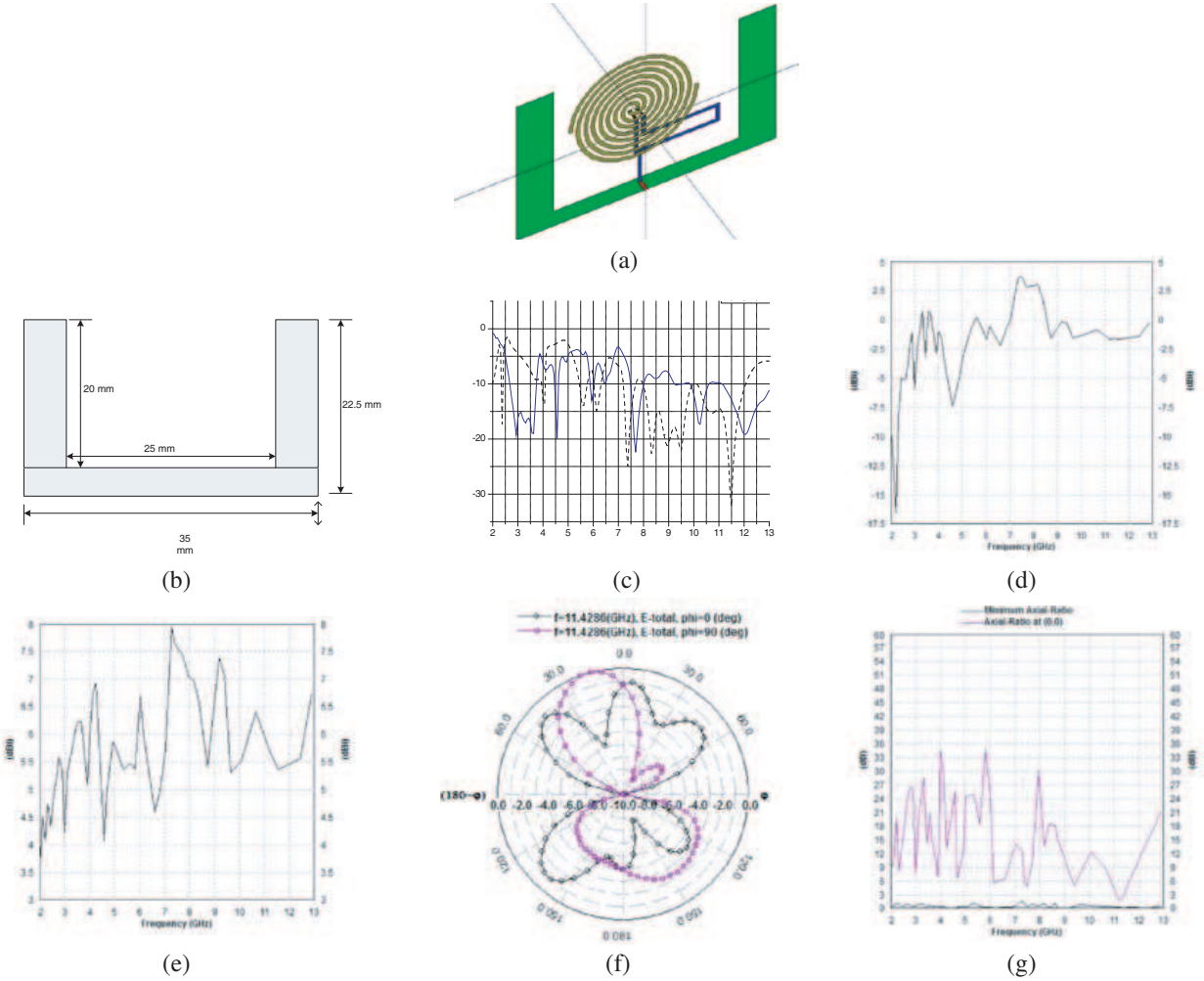

(a) (b) (c) (d) (e) (f) (g)

Figure 4: (a) Proposed antenna with three substrates and U shape ground plane. (b) Ground plane for the U ground plane shape spiral antenna. (c) Reflection coefficient versus frequency of U shape ground plane spiral antenna. (d) Gain versus frequency for U ground plane shape spiral antenna. (e) Directivity versus frequency for U ground plane shape spiral antenna. (f) Radiation pattern for U ground plane shape spiral antenna. (g) Axial and minimum axial ratio versus frequency for U ground plane shape spiral antenna.

3. NUMERICAL AND EXPERIMENTAL RESULTS

The whole design of the spiral antenna and its parallel-plane perpendicular-current feed system impedance transformer with foam layer are simulated for rectangular, L and U shape ground plane. The structure for the rectangular ground plane shape spiral antenna is shown in Figure 2(a) and its reflection coefficient is shown in Figure 2(b) where we can notice that the measured reflection coefficient is better than the computed one such it covers the ranges from 3.0625 GHz to 3.8125 GHz, 4.812 GHz to 5.6875 GHz, 6.5 GHz to 6.937 GHz and 7.125 GHz to 8.6875 GHz. The computed gain, directivity, radiation pattern and axial ratio are shown in Figures 2(c)–2(f) respectively. The L ground plane shape spiral antenna structure, ground plane dimensions and its reflection coefficient are shown in Figures 3(a)–3(c) respectively. The measured bandwidth extends from 9.44 GHz to 10 GHz and 11.0625 GHz to 13 GHz. The computed gain, directivity, radiation pattern and axial ratio are shown in Figures 3(d)–3(g) respectively. The U ground plane shape spiral antenna structure, ground plane dimensions and its reflection coefficient are shown in Figures 4(a)–4(c) respectively. we notice that the measured reflection coefficient extends from 2.6875 GHz to 3.75 GHz, 7.5 GHz to 8.06 GHz and 9.2 GHz to 13 GHz. The computed gain, directivity, radiation pattern and axial ratio are shown in Figures 5(d)–5(g) respectively. The fabricated rectangular, L and U ground shape antennas top and bottom view are shown in Figures 5(a), 5(b), 6(a), 6(b), 7(a) and 7(b) respectively.

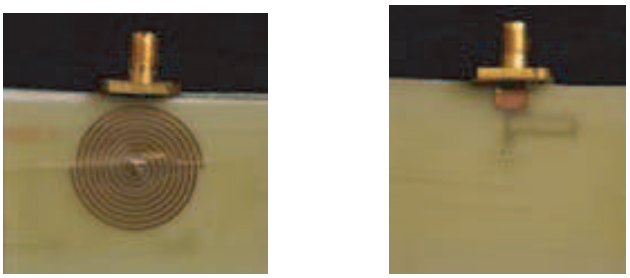

(a) (b)

Figure 5: (a) Rectangular ground plane spiral antenna, top view. (b) Rectangular ground plane spiral antenna, bottom view.

(a) (b)

Figure 6: (a) L ground plane spiral antenna, top view. (b) L ground plane spiral antenna, bottom view.

(a) (b)

Figure 7: (a) U ground plane spiral antenna, top view. (b) U ground plane spiral antenna, bottom view.

4. CONCLUSIONS

This article discussed the design and the fabrication of three antennas suitable for operate for the wide band applications and how the bandwidth affected by the ground plane shape. All the antennas uses parallel-plane perpendicular-current feed through the vias which connect the feeding system with the radiating element. The proposed feeding system consists of a phase shifter over a finite ground plane which take different shapes such as rectangular L and U shapes. In the bandwidth enhancement trend, we find that the U shape is the one which achieve the widest bandwidths among all (almost 4 GHz). The electromagnetic simulation program IE3D has been used to simulate the performance of the spiral antenna. The wide bandwidth are achieved for both simulated and its measured counterpart. Finally, the proposed antennas are cheap, compact and introduce a suitable antenna gain, directivity and bandwidth suitable for WiMAX band and wide band applications especially for the Ku band.

REFERENCES

1. Mushiake, Y., "Self-complementary antennas," *IEEE Trans. Antennas and Propagation*, Vol. 34, 23–29, December 1992.
2. Dyson, J. D., "The equiangular spiral antenna," *IRE Trans. Antennas and Propagation*, Vol. 7, 181–187, April 1959.
3. Thaysen, J., "Numerical and experimental investigation of a coplanar waveguide-fed spiral antenna," *IEEE 24th QMW Antenna Symposium*, 13–16, 2000.
4. Cheng, N. C. and H. C. Wen, "A novel dual-band spiral antenna for a satellite and terrestrial communication system," *IEEE AWPL*, Vol. 8, 624–626, 2009.
5. Kimiagarov, N. and H. Matzner, "A wide band flat spiral antenna with planar unbalanced feed," *IEEE Trans. IC*
6. Eubanks, T. W. and C. Kai, "A compact parallel-plane perpendicular-current feed for a modified equiangular spiral antenna" *IEEE Trans. Antennas and Propagation*, Vol. 58, 2193–2202, 2010.
7. Dogan, M., K. Özsoym, and I. Tekin, "Printed dipole array fed with parallel stripline for ku-band applications," *PIERS Proceedings*, 194–196, Moscow, Russia, August 18–21, 2009.

Dual-band Printed Monopole Antenna with 1-D EBG Ground Plane

S. H. Kim, D. J. Kim, J. Y. Lee, B. H. Shin, and J. H. Jang
School of Information and Communications, WCU Department of Nanobio Materials and Electronics
Gwangju Institute of Science and Technology (GIST)
261 Cheomdan-gwagiro, Buk-gu, Gwangju 500-712, Korea

Abstract— A dual-band printed monopole antenna was designed and realized at the corner of a rectangular one-dimensional electromagnetic bangap (1-D EBG) ground plane. Two monopole antennas with different polarization are placed on two different edges of the ground plane and are fed by a port at the corner of the rectangular ground plane. The lengths of the two monopoles are also different, which leads to different resonant frequencies. When each monopole is positioned horizontally close to an ordinary ground plane, the antenna cannot radiate energy efficiently. In order to make the antenna radiates efficiently, 1-D EBG structures with different energy bandgaps were inserted at different edges of the ground plane. The improved radiation efficiency of the dual-band 1-D EBG backed antenna is due to the in-phase reflection characteristics within a certain frequency band; these characteristics are similar to those of a 2-D mushroomlike EBG structure.

The designed antenna covers DCS 1800 (1.71 GHz $\sim$ 1.88 GHz), PCS (1.85 GHz $\sim$ 1.99 GHz), and WLAN 802.11 b/g (2.4 GHz $\sim$ 2.4835 GHz) frequency bands. Because the frequency bands of the antenna are within the operating bandwidth of each 1-D EBG structure, the degradation of the radiation performance of the antenna is minimized. The radiation efficiency was measured to be higher than 70% within all the operating frequency bands. In addition, the radiation pattern is y-directive in the lower frequency band and the radiation pattern is x-directive in the higher frequency band, because of the effect of the 1-D EBG ground plane. The designed antenna could be applied to rectangular type wireless communication devices supporting 3G and WLAN environments, such as tablet personal computers and laptop computers.

1. INTRODUCTION

Various electromagnetic bandgap (EBG) structures have been widely studied and applied to antennas and microwave components [1–3]. In particular, mushroom-like EBG structures proposed by D. Sievenpiper have been utilized to the ground plane of low-profile antennas [4, 5]. The major property of these structures is that they reflect incident wave in-phase rather than out-of-phase. The structural resonances of the mushroom-like EBG structure result in high surface impedance in a certain frequency band, and thus the EBG ground plane can be regarded as a magnetic conductor. Due to the properties of the EBG structure, a radiating element can be placed very close to the EBG ground plane so that incident and reflected waves interfere constructively. Therefore, an antenna backed with the mushroom-like EBG ground plane has high radiation efficiency even if the distance between the radiator and the ground plane is very close. However, mushroom-like EBG structures having a two-dimensional (2-D) configuration cannot be directly used as a ground plane for a printed antenna on a single printed circuit board (PCB). Recently, a one-dimensional (1-D) EBG structure, which can be directly designed on a single PCB, was proposed [6]. The ground plane with a 1-D EBG structure operates like the 2-D EBG ground plane in that the 1-D EBG ground plane has in-phase reflection characteristics. A printed antenna backed with a 1-D EBG ground plane also has a low-profile and directional radiation characteristics.

In this study, a dual-band printed monopole antenna with a 1-D EBG ground plane was designed and realized. Two monopoles located at one corner of the rectangular ground plane were utilized for dual-band operation of the antenna and the arrayed 1-D EBG cells were integrated to the ground plane for efficient radiation of the monopoles. The frequency response and radiation characteristics of the antenna were evaluated by simulations and experiments.

2. ANTENNA DESIGN

A monopole antenna positioned horizontally close to a normal ground plane has low radiation efficiency. In this case, the radiation performance of the monopole antenna can be improved by utilizing a 1-D EBG ground plane because of the in-phase reflection property of the EBG structures. The designed dual-band monopole antenna backed with the 1-D EBG ground plane is depicted in Figure 1(a). Two monopoles are placed at one corner of the rectangular ground plane. The lengths

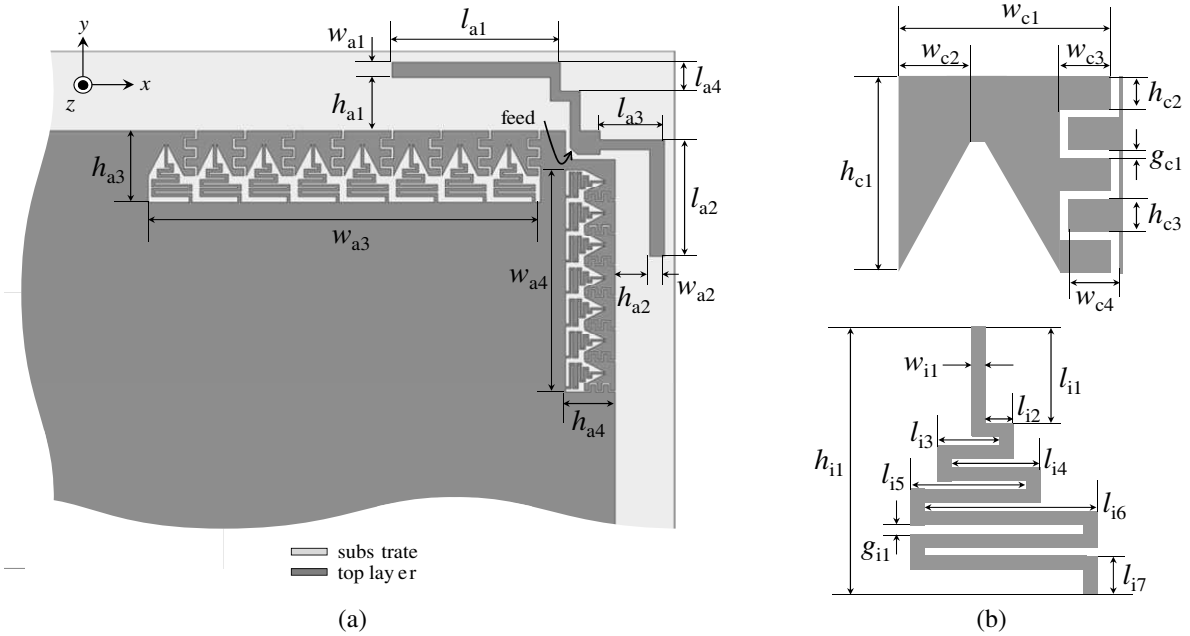

Figure 1: Configuration of (a) the designed dual-band monopole antenna and (b) the metal patch and the meanderline of the 1-D EBG structure.

of the radiator's arms are different, leading to different resonant frequencies. Also, each arm supports different polarization. Therefore, 1-D EBG structures with different resonant frequencies were inserted to different edges of the ground plane to reflect the radiated waves from each monopole in-phase, rather than out-of-phase. The detailed configuration of the 1-D EBG structure is shown in Figure 1(b). The 1-D EBG cell is composed of a metal patch and a meanderline strip line. The electric fields between the adjacent metal patches create capacitance and the current flows through the meanderline and the ground plane result in inductance; the 1-D EBG structure consequently resonates at a certain frequency and has high impedance near the frequency.

The longer and shorter arms were designed to be resonant at the 1.8 GHz and 2.5 GHz bands, respectively. The 1-D EBG structures placed below each radiator were also designed to be resonant near each frequency band. The design parameters of the antenna in Figure 1(a) are as follows: $l_{a1} = 17$ mm, $l_{a2} = 12$ mm, $l_{a3} = 6.5$ mm, $l_{a4} = 3$ mm, $w_{a1} = 1.5$ mm, $w_{a2} = 1.5$ mm, $w_{a3} = 39.6$ mm, $w_{a4} = 23.1$ mm, $h_{a1} = 5.5$ mm, $h_{a2} = 3.5$ mm, $h_{a3} = 7.5$ mm, and $h_{a4} = 5$ mm. The design parameters of the y-arrayed 1-D EBG cells shown in Figure 1(b) are as follows: $w_{c1} = 3.15$ mm, $w_{c2} = 1.1$ mm, $w_{c3} = 0.75$ mm, $w_{c4} = 0.75$ mm, $h_{c1} = 3.1$ mm, $h_{c2} = 0.5$ mm, $h_{c3} = 0.5$ mm, $g_{c1} = 0.15$ mm, $w_{i1} = 0.2$ mm, $l_{i1} = 1.3$ mm, $l_{i2} = 0.4$ mm, $l_{i3} = 0.9$ mm, $l_{i4} = 1.3$ mm, $l_{i5} = 1.7$ mm, $l_{i6} = 2.55$ mm, $l_{i7} = 0.6$ mm, $h_{i1} = 4$ mm, and $g_{i1} = 0.15$ mm. The parameters of the x-arrayed 1-D EBG cells have 1.5 times scaled values along the x- and y-direction as compare to the presented parameters of the y-arrayed 1-D EBG cells in order to realize resonance at lower frequency. A conventional 50 Ω coaxial cable was used for feeding and a FR4 substrate with a height of 1.2 mm and a dielectric constant of 4.4 was applied for the design. The thickness of the metal (copper) is 0.035 mm.

3. ANTENNA PERFORMANCE

The simulated and measured reflection coefficients of the designed antenna are shown in Figure 2. Two different resonances are observed due to the monopoles with different lengths. The lower band was measured from 1.508 GHz to 1.999 GHz and the higher band was measured from 2.36 GHz to 2.57 GHz. They cover DCS 1800 (1.71 GHz ∼ 1.88 GHz), PCS 1900 (1.85 GHz ∼ 1.99 GHz), and WLAN 802.11 b/g (2.4 GHz ∼ 2.4835 GHz) frequency bands. Even though the radiator is placed very close to the ground plane, the antenna shows good impedance matching at each frequency band due to the effect of the 1-D EBG patterns at the edge of the ground plane.

The simulated and measured radiation patterns of the antenna are shown in Figure 3. Because of the effect of the 1-D EBG ground plane, the radiation patterns are y-directive in the lower frequency band and x-directive in the higher frequency band. The measured radiation efficiency

and antenna gain in the operating frequency bands are plotted in Figure 4. The designed antenna has radiation efficiency of more than 70% in the operating frequency bands and stable antenna gains were obtained in all frequency ranges. The antenna could be applied to rectangular type wireless communication devices supporting 3G and WLAN environments such as tablet personal computers and laptop computers.

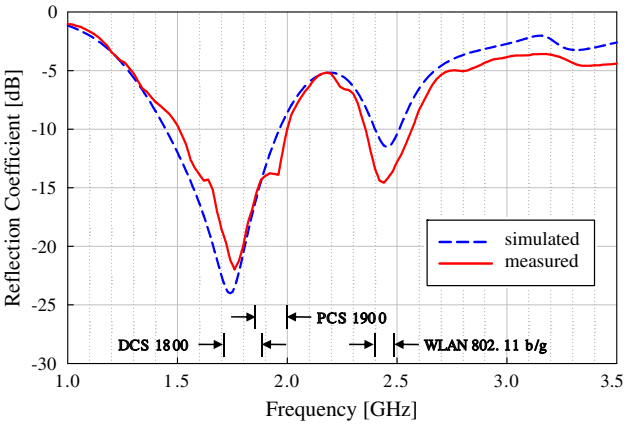

Figure 2: Simulated and measured reflection coefficients of the designed dual-band monopole antenna.

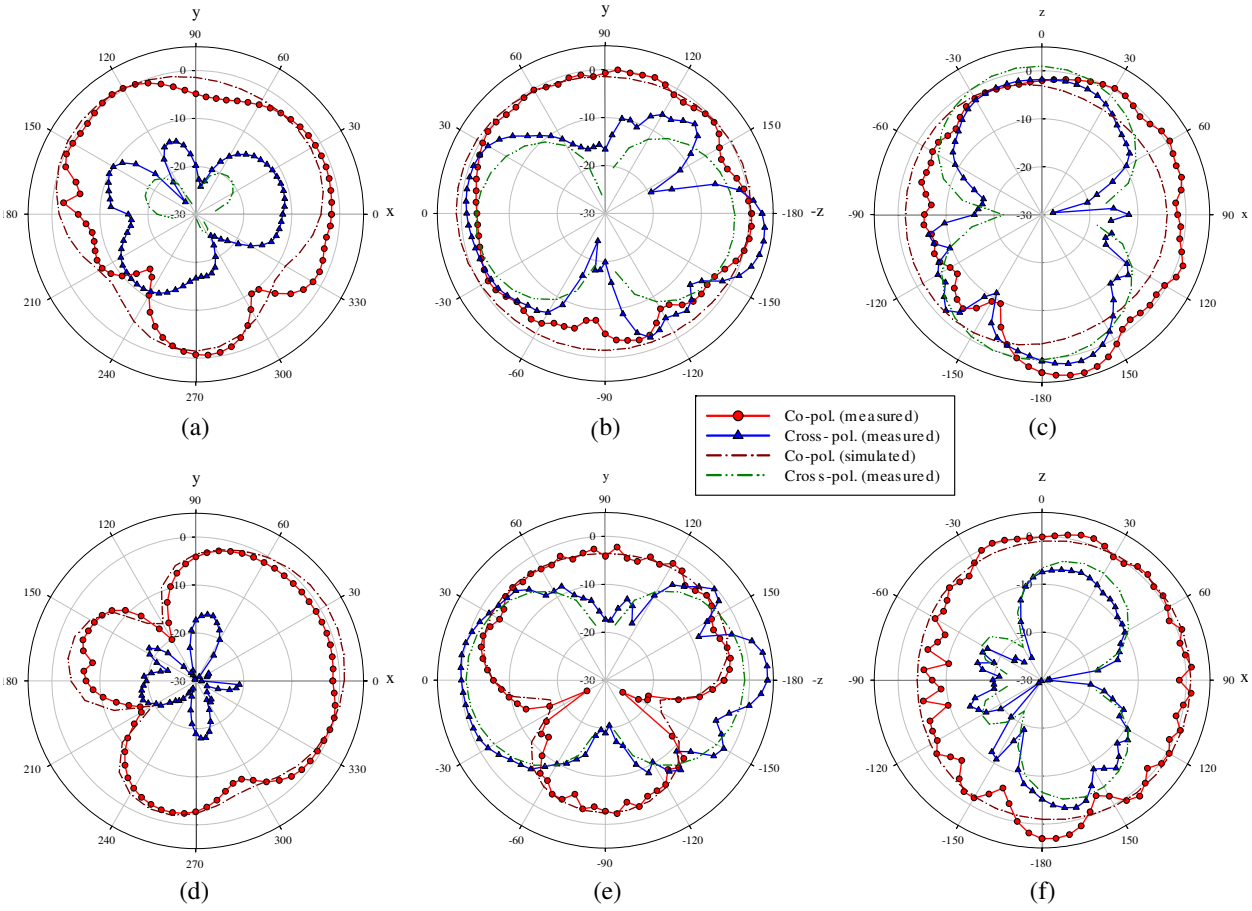

Figure 3: Simulated and measured radiation patterns of the designed dual-band monopole antenna. (a) xy-plane, (b) yz-plane, and (c) zx-plane at the lower resonant frequency, (d) xy-plane, (e) yz-plane, and (f) zx-plane at the higher resonant frequency.

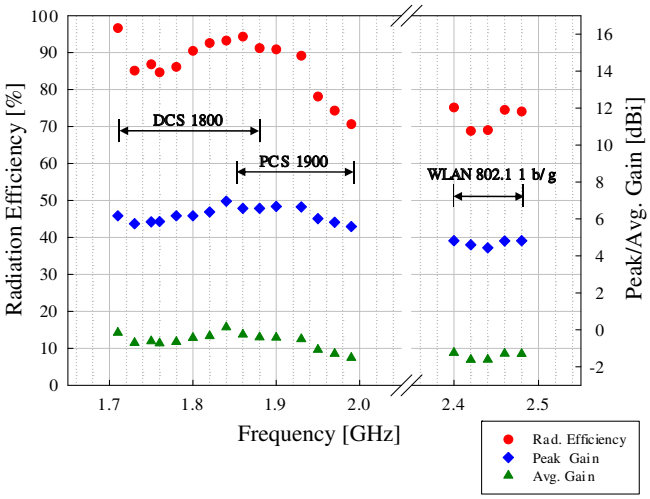

Figure 4: Measured radiation efficiency and antenna gains of the designed dual-band monopole antenna within the frequency range of the DCS 1800, PCS 1900, and WLAN 802.11 b/g bands.

4. CONCLUSIONS

A dual-band printed monopole antenna was designed and realized at the corner of a rectangular 1-D EBG ground plane. Two monopoles with different lengths and polarization were placed horizontally close to the 1-D EBG ground plane. The designed antenna covers the DCS 1800 (1.71 GHz $\sim$ 1.88 GHz), PCS 1900 (1.85 GHz $\sim$ 1.99 GHz), and WLAN 802.11 b/g (2.4 GHz $\sim$ 2.4835 GHz) frequency bands. The antenna has different radiation patterns in the different operating frequency bands and reasonable radiation efficiency throughout the frequency range due to the effects of the 1-D EBG ground plane.

ACKNOWLEDGMENT

This work was partially supported by the World Class University (WCU) program at GIST through a grant provided by the Ministry of Education, Science and Technology (MEST) of Korea (Project No. R31-20008-000-10026-0) and the Center for Distributed Sensor Network at GIST.

REFERENCES

1. Yang, F. and Y. Rahmat-Samii, "Microstrip antennas integrated with electromagnetic band-gap (EBG) structures: A low mutual coupling design for array applications," *IEEE Transactions on Antennas and Propagation*, Vol. 51, No. 10, 2936–2946, 2003.
2. Yang, F.-R., K.-P. Ma, Y. Qian, and T. Itoh, "A uniplanar compact photonic-bandgap (UC-PBG) structure and its applications for microwave circuits," *IEEE Transactions on Microwave Theory and Techniques*, Vol. 47, No. 8, 1509–1514, 1999.
3. Sohn, J. R., K. Y. Kim, H.-S. Tae, and J.-H. Lee, "Comparative study on various artificial magnetic conductors for low-profile antenna," *Progress In Electromagnetic Research*, Vol. 61, 27–37, 2006.
4. Sievenpiper, D., L. Zhang, R. F. J. Broas, N. G. Alexopolus, and E. Yablonovich, "High-impedance electromagnetic surface with a forbidden frequency band," *IEEE Transactions on Microwave Theory and Techniques*, Vol. 47, 2059–2074, 1999.
5. Yang, F. and Y. Rahmat-Samii, "Reflection phase characterizations of the EBG ground plane for low profile wire antenna applications," *IEEE Transactions on Antennas and Propagation*, Vol. 51, 2691–2703, 2003.
6. Kim, S.-H, T. T. Nguyen, D.-J. Kim, and J. H. Jang, "Printed dipole antenna with a 1-D EBG ground plane," *Antennas and Propagation Society International Symposium (APS/USRI)*, Toronto, Canada, July 2010.

Wideband Antenna Design by the Stacked Koch Fractal Structures

Homayoon Oraizi and Shahram Hedayati
Department of Electrical Engineering, Iran University of Science and Technology, Iran

Abstract— In this paper, a novel multiband stacked microstrip antenna is introduced, which is composed of an active patch, under which three parasitic patches are placed. The geometry of each patch is shaped as a Koch fractal of third generation. The antenna feed is made of a coaxial probe, which passes through a cylindrical cavity also shaped into a Koch fractal. In order to obtain wider frequency bandwidths, the active and parasitic patches on different substrates are displaced with respect to each other. Wide and multiband frequency characteristics are achieved for the radiation patterns and impedance matching. Another configuration is proposed for modifying performance of the stacked Koch antenna (SKA), wherein a space-filling slot in the form of Hilbert fractal geometry is cut into the active patch. High-directivity microstrip antennas comprising a driven patch and at least one parasitic element placed on the same plane, operate at a frequency larger than the fundamental mode of the driven patch in order to obtain a resonance frequency with a high-directivity broadside radiation pattern. The gap defined between the driven and parasitic patched is used to control the resonance frequency where the high-directivity behavior is obtained.

1. INTRODUCTION

We observe in nature various self-similar configurations, which are usually referred as fractal geometries. For example, tree branches and cloud shapes may represent fractal geometries. Mandelbrot first introduced the fractal geometry in 1975 [1], in which each sub-section has the characteristics of the whole structure in a smaller scale. This is the basic property of self-similarity. Fractal geometries have been applied in various science and technologies, such as antennas and radiators. The intrinsic properties of fractal geometries may produce appropriate characteristics in antennas, radiators and reflectors, which make them perform effectively in the propagation media. Generally, the utilization of fractal geometries in antennas tends to reduce their physical sizes and produce multiband response in their radiation characteristics. Since fractal structures have a repetitive geometry, they can generate long paths in a limited volume. Accordingly, we may refer to fractal geometries, such as the Koch, Minkowski, Hilbert and tree fractals, which have been used for dipole and ring antennas.

Antennas design methods have been commonly used in a narrow frequency band. Moreover, if the antenna size is less than a quarter wavelength, it does not become an efficient radiator, but fractal geometries can overcome such shortcomings. It has been shown that a limited number of iterations of fractal geometries, can make an antenna multiband. As the number of fractal repetitions increases, the lowest antenna resonant frequency decreases, and additional higher resonant frequencies appear. The fractal geometries were first introduce in 1993 as serious candidates for the design of wide band and multiband antennas [3]. The fractal or fractional dimension (as opposed to the Euclidean dimension) is defined for fractal geometries which may be used for their comparison and space-filling capability. The property of self-similarity of fractal geometries is used to achieve multiband operations from fractal antennas and their space-filling property is used for the antenna miniaturization.

However, in this paper we intend to investigate the characteristics of a novel multiband microstrip antenna composed of stacked a Koch fractal structure. It is composed of an active element under which three parasitic elements are placed. All the elements are formed as Koch fractals of third iteration. The antenna feed is by a coaxial cable through the parasitic elements inside a cylindrical cavity, whose periphery is also cut as a third order Koch geometry. (See Fig. 1.). We thus introduce a new class of microstrip antennas, in which all the elements are formed into Koch fractals and parasitic elements are placed on different substrates under the active one. In order to increase the frequency bandwidth, the microstrip patches on different substrates are displaced with respect to each other.

2. DESCRIPTION OF THE STACKED KOCH ANTENNA

The proposed stacked Koch antenna (SKA) is composed of an active patch over the FR4-epoxy substrate (with dielectric constant $\varepsilon_r = 4.4$ and height $h = 1.6\,\text{mm}$) situated at a distance of

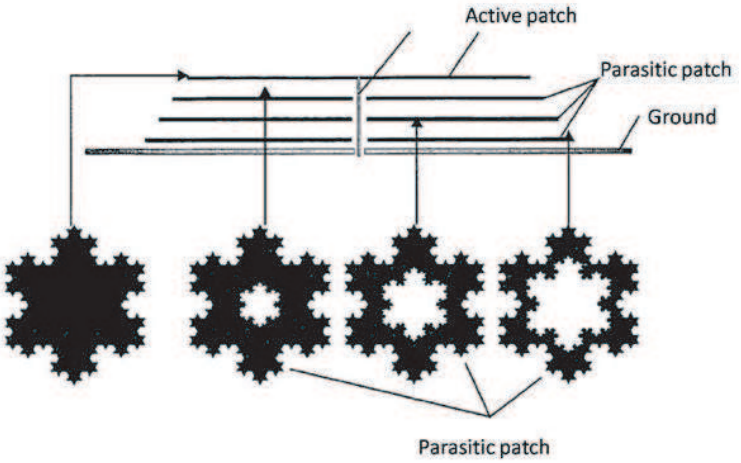

Figure 1: Basic proposed structure.

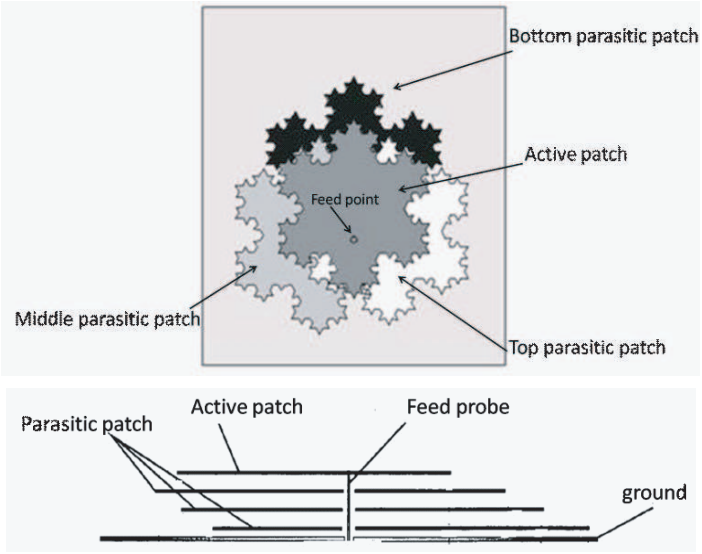

Figure 2: First proposed structure.

Table 1.

	Band I	**Band II**	**Band III**
Center freq (GHz)	1.58	2.12	4.2
Bandwidth (MHz)	60	10	2670
Band limits (GHz)	1.54–1.6	2.05–2.15	2.82–5.49
Percentage BW	4%	0.5%	57%

6.4 mm above the ground plane. The three parasitic patches are placed under the active patch at distances of 4.8, 3.2 and 1.6 mm from the ground plane. The lowest parasitic patch is over the Rogers RT/Duroid 5880 substrate (with dielectric constant $\varepsilon_r = 2.2$ and height $h = 1.6$ mm). The other two parasitic patches are over the same FR4 substrate. However, in order to achieve the highest possible bandwidths, the patch centers are displaced horizontally. (See Fig. 2.) Assuming the center of active patch to be coincident with the origin of coordinate system, then the bottom parasitic patch is displaced by 4 mm along the X-axis. The middle and top parasitic patches are displaced along the Y-axis by 8 mm and along the X-axis by 16 mm. Another configuration is proposed for the stacked Koch antenna (SKA), wherein a space-filling slot in the form of Hilbert fractal geometry is cut into the active patch, as shown in Fig. 3.

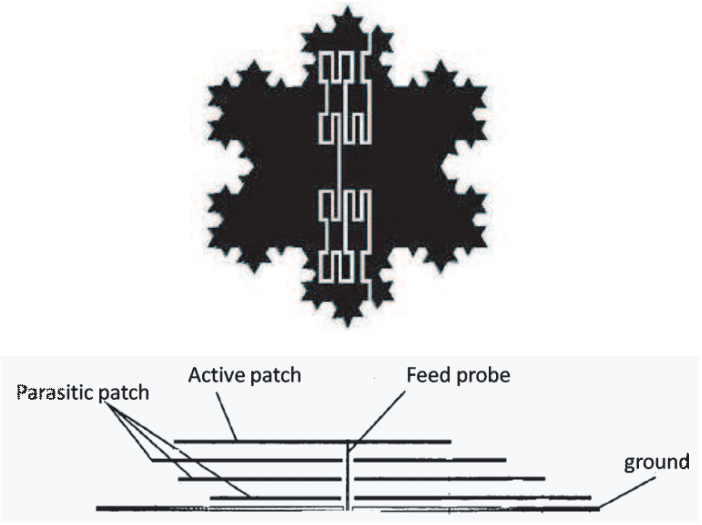

Figure 3: Proposed structure for active patch (Second proposed structure.

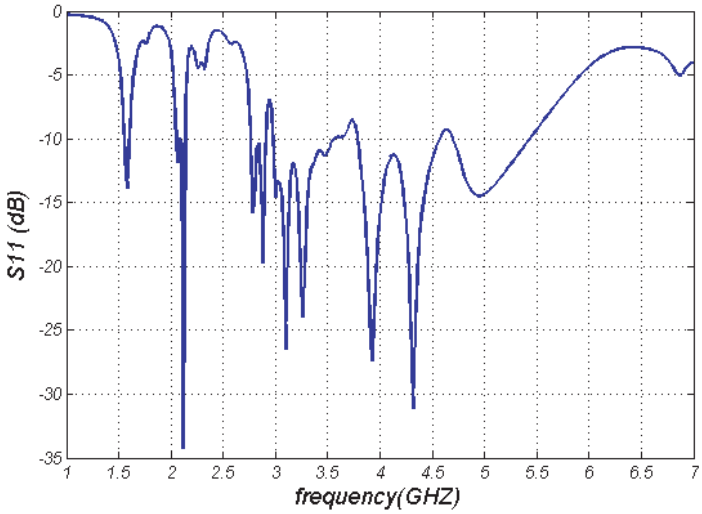

Figure 4: Simulated result of S11 spectrum for first proposed structure.

Table 2.

	Band I	**Band II**	**Band III**
Center freq (GHz)	1.62	2.98	4.4
Bandwidth (MHz)	280	70	1280
Band limits (GHz)	1.54–1.82	2.05–2.75	4.02–5.5
Percentage BW	17%	3%	29%

3. COMPUTER SIMULATIONS

The HFSS software is used for the simulation and design of SKA. The return loss (as S_{11}) of the first SKA is drawn versus frequency in Fig. 4. Observe that the first resonant frequency is located at $f_r = 1.58\,\text{GHz}$ with a bandwidth of $BW = 60\,\text{MHz}$, the second at $f_r = 2.12\,\text{GHz}$ with a bandwidth of $BW = 70\,\text{MHz}$ and the third at $f_r = 4.2\,\text{GHz}$ with a bandwidth of $BW = 2470\,\text{MHz}$. These results are shown in Table 1. The radiation patterns of the first proposed antenna are drawn in the xz-plane (E-plane) and yz-plane (H-plane) and is shown in Fig. 5. The return loss (as S_{11}) of the second SKA is drawn versus frequency in Fig. 7. Observe that the first resonant frequency is located at $f_r = 1.62\,\text{GHz}$ with a bandwidth of $BW = 280\,\text{MHz}$, the second at $f_r = 2.98\,\text{GHz}$ with a bandwidth of $BW = 70\,\text{MHz}$ and the third at $f_r = 4.4\,\text{GHz}$ with a bandwidth of $BW = 1280\,\text{MHz}$. Observe that the bandwidth of the first resonant frequency has increased. These results shown

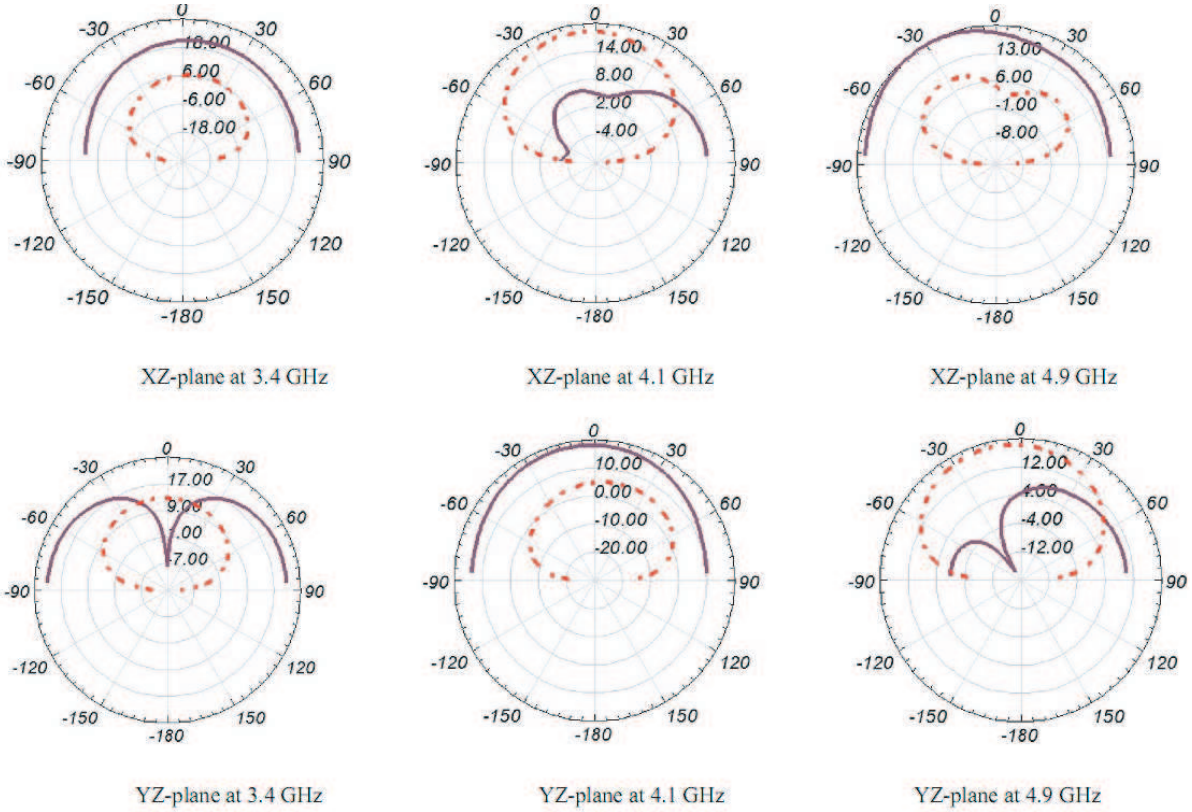

Figure 5. Computer simulated radiation patterns of the first proposed antenna.

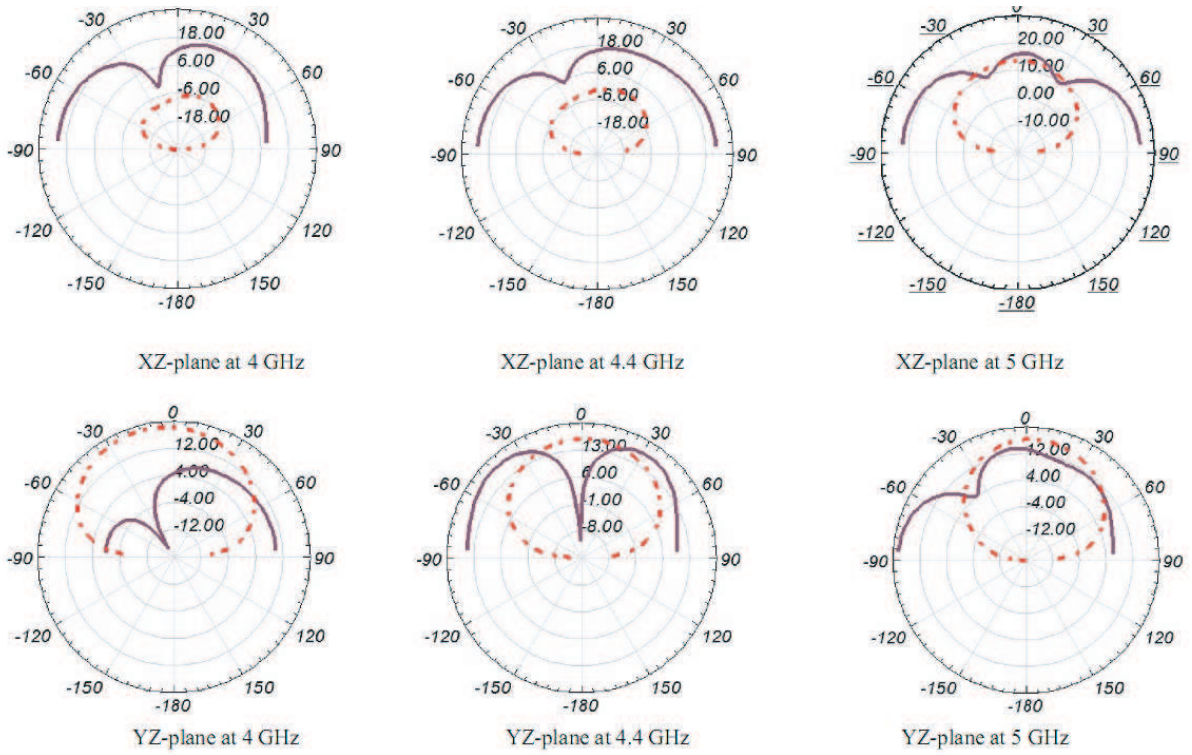

Figure 6. Computer simulated radiation patterns of the second proposed antenna.

in Table 2. The radiation patterns of the second proposed antenna are drawn in the xz-plane (E-plane) and yz-plane (H-plane) and is shown in Fig. 6. The gain of first and second antenna as obtained by the computer simulation is drawn in Fig. 8 and Fig. 9 Observe that the maximum gain for second antenna greater than first one and is about 7 dB.

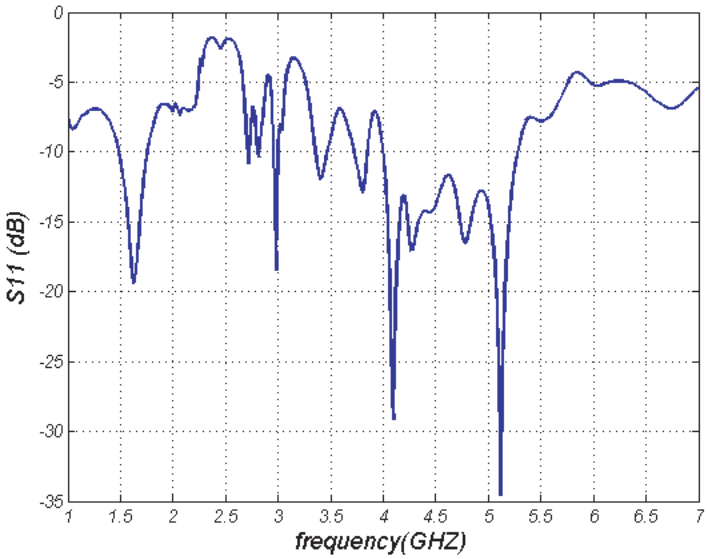

Figure 7. Simulated result of S_{11} spectrum for second proposed structure.

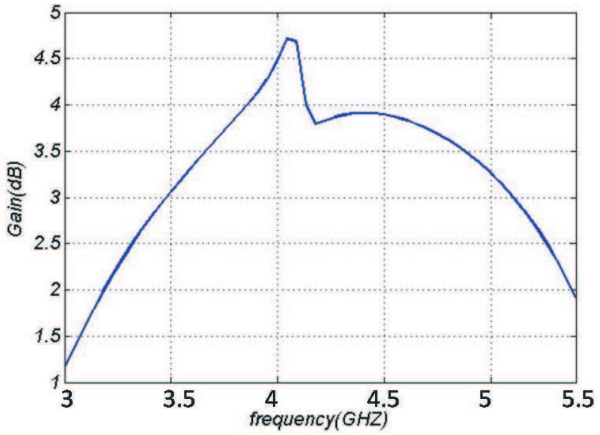

Figure 8. Gain of the first proposed antenna.

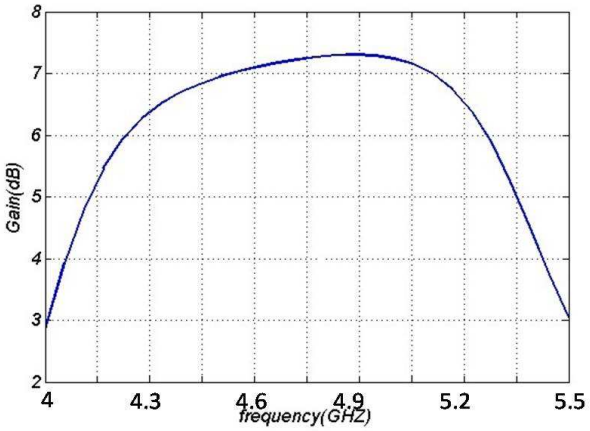

Figure 9. Gain of the second antenna.

4. CONCLUSIONS

In this paper, a novel multiband stacked microstrip antenna is introduced, which uses the Koch fractals for the active and parasitic fractals. By adjusting the dimensions and relative positions of patches, it has become possible to obtain multiband and wideband radiation characteristics specifically 60% in the bands the adjustment of the Koch fractal cylindrical surface around the feed coaxial probe, it has also been possible to obtain good impedance matching. Furthermore, cutting a slot in the form of Hilbert fractal in the center of the active patch, the frequency band width of the first band also increases. It has been shown that the application of fractal geometries have great possibilities to realize various radiation characteristics of antennas.

REFERENCES

1. Werner, D. H. and R. Mittra, *Frontiers in Electromagnetics*, 48–81, IEEE Press, Piscataway, NJ, 2000.
2. Baliarda, C. P., J. Romeu, and A. Cardama, *The Koch Monopole: A Small Fractal Antenna & Propagation*, Vol. 48, No. 11, November 2000.
3. Puente_Baliaada, C., J. Romeu, and R. Cardama, "On the behavior of the Sierpinski multiband fractal antenna," *IEEE Transaction on Antenna and Propagation*, Vol. 46, No. 4, April 1998.
4. Wernerm D. H. and S. Ganguly, "An overview of fractal antenna engineering research," *IEEE Antenna and Propagation Mag.*, Vol. 45, No. 1, February 2003.

A Compact Planar Microstrip-Fed Feed Patch Antenna Using High Permittivity Substrate

C. H. Hsu[1], **C. H. Lai**[2], **and Y. S. Chang**[1]

[1]Department of Electrical Engineering, National United University, Taiwan
[2]Department of Electronic Engineering, National United University, Taiwan

Abstract— A compact-size Microstrip-Fed Feed Patch antenna is investigated by employing high-permittivity and low-loss substrate (i.e., high $Q \times f$ value) for 1.9-GHz application. The antenna was fabricated on ZnO-doped $Nd(Co_{1/2}Ti_{1/2})O_3$ ($\varepsilon_r = 27.4$, $Q \times f$ value of 147,000 GHz) substrate. The high permittivity and low-loss ceramic substrate (ZnO-doped $Nd(Co_{1/2}Ti_{1/2})O_3$) was used to reduce the microstrip antenna dimension on patch size. The proposed antenna occupies a size of 2.25 cm^2 and obtains the operation bandwidth of about 10 MHz. Good antenna gain and CP radiation patterns have also been observed. The measured results of the performance of the antenna are presented.

1. INTRODUCTION

Microwave dielectric ceramics with high permittivity are commonly applied in several microwave communication components. Since high-permittivity dielectrics can be used as substrates for antennas, with advantages of compact size and low-profile, the development of ceramic substrate antennas for mobile communication handsets has been rapidly growing recently. The microstrip antenna, with compact size, has been a very attractive antenna for circularly polarized (CP) operation [1, 2]. Typically, a cornertruncated square microstrip antenna is used on a substrate with high dielectric constant. Such a compact CP antenna has adequate bandwidth and axial ratio, and can greatly reduce the packing cost of the final product. With the development of the efficiency enhancement techniques for the microstrip antenna, a chip resistor [3] and a lossy conducting patch have been used. In this paper, the use of low loss substrates (ZnO-doped $Nd(Co_{1/2}Ti_{1/2})O_3$) is studied to enhance the efficiency of the proposed antenna. The design and fabrication of a right-hand circular polarized microstrip antenna [4] applied to 1.9 GHz is demonstrated. Details of the proposed antenna and the measured results are presented and discussed.

2. ANTENNA DESIGN AND EXPERIMENTAL RESULTS

The geometry of the proposed compact circularly polarized antenna using ZnO-doped $Nd(Co_{1/2}Ti_{1/2})O_3$ material loss substrates for 1.9 GHz application is depicted in Fig. 1. The dielectric materials are ZnO-doped $Nd(Co_{1/2}Ti_{1/2})O_3$ ($\varepsilon_r = 27.4$, $Q \times f$ value of 147,000 GHz, thickness of 0.9 mm) substrate. High dielectric constant can reduce patch size [5]. Parameters of antenna are the size of slot and feed position. The dimension of the proposed antenna with high-permittivity ceramic substrate is provided in Table 1. The measured return loss of the CP antenna using ZnO-doped $Nd(Co_{1/2}Ti_{1/2})O_3$ substrate are demonstrated in Fig. 2. The obtained 10-dB return loss bandwidth is 10 MHz at the frequency of 1.89 GHz.

Figure 3 presented the measured RHCP radiation patterns at 1.89 GHz in two orthogonal x-z and y-z planes of the investigated antenna. It is observed that broadside field patterns are obtained, as expected. A slight asymmetry in radiation patterns is observed, which is probably owing to the introduction asymmetry in the proposed structure. It can also be found from the pattern that the 3 dB beam widths are about 151° (−73°–78°) in the x-z plane and 96° (−34°–62°) in the y-z plane. Measured co- and cross-polarized radiation patterns of the antenna are shown in Fig. 4. The difference between co- and cross-polarized level is higher than 10 dB in the broadside direction (near 0°) for all cases. Fig. 5 presented measured gain and axial ratio for the introduction antenna. This figure demonstrated a very much stable gain variation and a CP bandwidth of 80 MHz (4.23%) centered at 1.89 GHz for the proposed antenna.

Table 1: Dimensions of proposed antenna with ceramic substrate.

Design (mm)	a	b	c	d
ZnO-doped $Nd(Co_{1/2}Ti_{1/2})O_3$ Ceramic Substrate	15	15	0.5	1.75

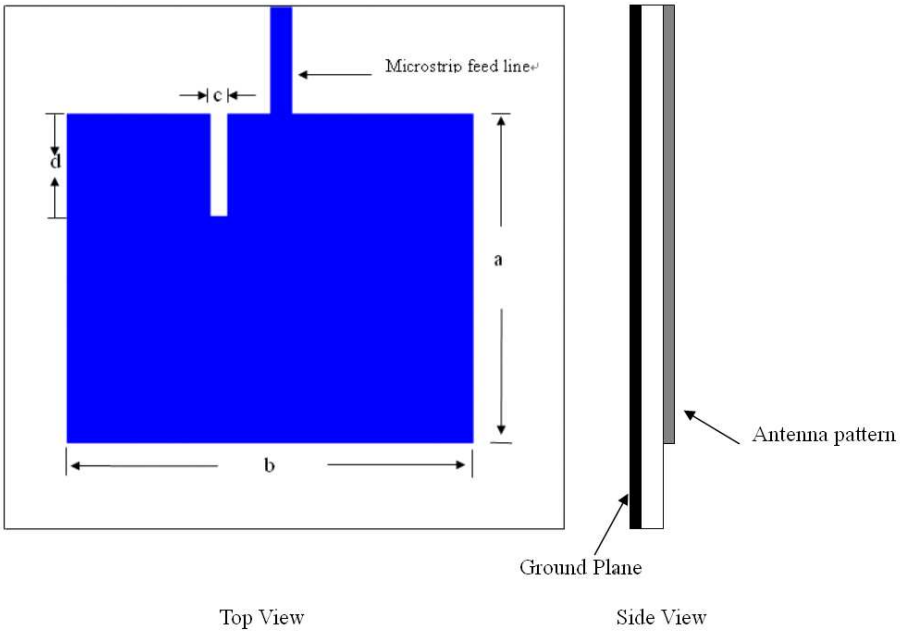

Figure 1: Geometry of the proposed planar monopole antenna, (a) top view, (b) side view.

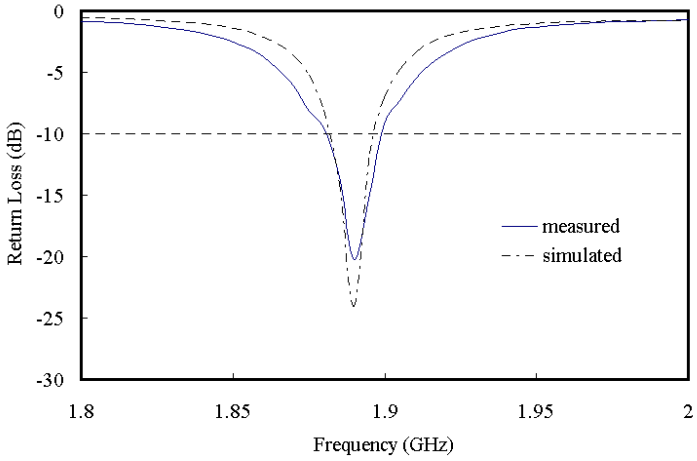

Figure 2: Simulated and measured return loss of the antenna.

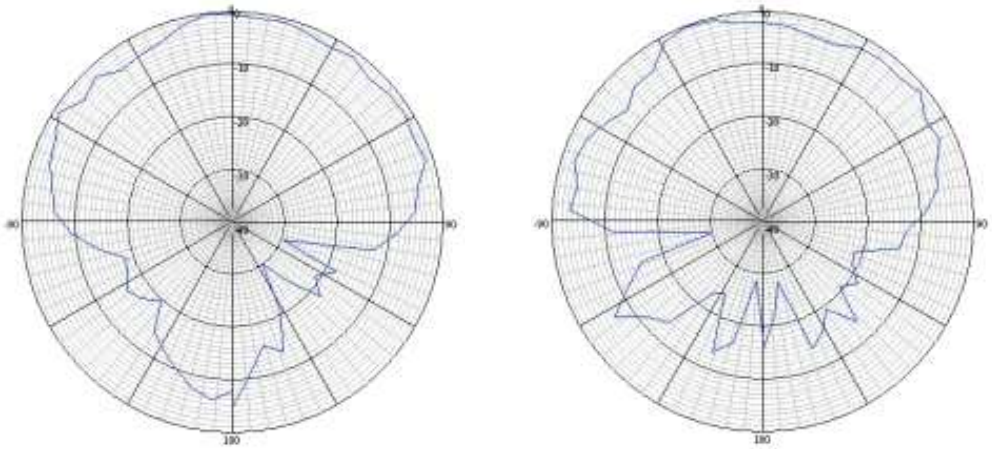

(a) (b)

Figure 3: Measured RHCP radiation patterns at 1.89 GHz for (a) x-z plane (b) y-z plane.

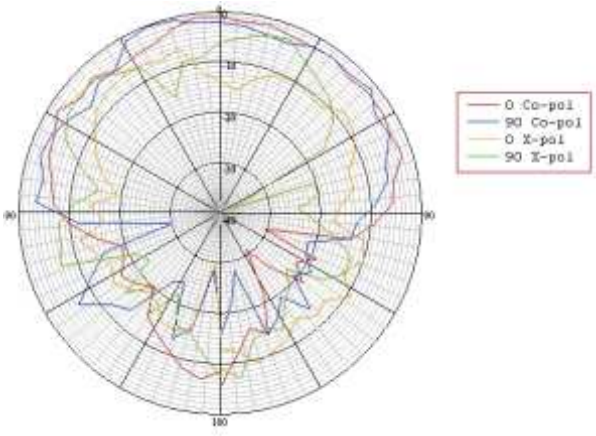

Figure 4: Measured co-polarization and cross-polarization at 1.89 GHz of proposed antenna on phi = 0° and 90°.

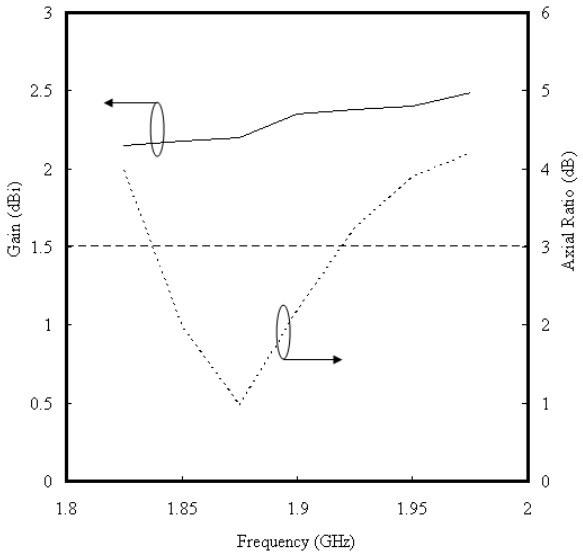

Figure 5: Measured antenna gain and axial ratio versus frequency for the proposed antenna.

3. CONCLUSIONS

A compact circularly polarized antenna using ZnO-doped $Nd(Co_{1/2}Ti_{1/2})O_3$ substrate (high-permittivity and low-loss substrate) operated at 1.9 GHz has been proposed. The proposed antenna occupies a size of 22.5 cm^2. Moreover, the circularly polarized antenna fabricated on ZnO-doped $Nd(Co_{1/2}Ti_{1/2})O_3$ substrate can achieve a 4.32% (80 MHz) 3-dB axial ratio bandwidth. It is not only a low-profile antenna but also exhibits the advantages of smaller size, wider CP bandwidth, better gain, and good RHCP with ZnO-doped $Nd(Co_{1/2}Ti_{1/2})O_3$ substrate.

ACKNOWLEDGMENT

This work was supported by National Science Council of the Republic of China under NSC 99-2628-E-239-002.

REFERENCES

1. Microwave, J., *A Miniature Patch Antenna for GPS Application*, Toko America Inc., Vol. 40, 116–118, 1997.
2. Zhong, S. S., J. H. Cui, R. F. Xue, and J. W. Niu, "Compact circularly polarized microstrip antenna on organic magnetic substrate," *Microwave Opt. Technol. Lett.*, Vol. 46, 497–500, 2004.
3. Wong, K. L. and Y. F. Lin, "Small broadband rectangular microstrip antenna with chip-resistor loading," *Electron. Lett.*, Vol. 33, 1593–1594, 1997.
4. Sharma, P. C. and K. C. Gupta, "Analysis and optimized design of single feed circularly polarized microstrip antennas," *IEEE Trans. Antennas Propagat.*, Vol. 31, 949–955, 1983.
5. Huang, C. L., C. H. Hsu, and C. M. Tsai, "Miniaturization of hairpin bandpass filters using high-permittivity substrate," *Microwave Opt. Technol Lett.*, Vol. 45, 229–232, 2005.

Design of Microstrip Antenna with Modified Annular-ring Slot for GPS Application

C. F. Tseng, S. C. Lu, and Y. C. Hsu
Department of Electronic Engineering, National United University, Taiwan

Abstract— A circularly polarized annular ring slot antenna with broadband impedance and circularly polarized bandwidth characteristics has been presented in this paper. By introducing proper asymmetry in the annular ring slot structure in the form of two pairs of slits, and feeding the ring slot using a 50 Ω microstrip line, the bandwidth is increased, and the circularly polarized antenna is also formed for GPS application. The measured results agree with the simulation, showing that the proposed antenna has a wide return loss and AR bandwidth (AR < 3 dB) of more than 40% referred to the resonant frequency 1.575 GHz. The measured radiation patterns are stable and symmetric with respect to the broadside direction. Moreover, a prototype antenna with an average gain of 3.2 dBi over a CP bandwidth is shown.

1. INTRODUCTION

Circularly polarized (CP) antennas have an advantage in reducing the loss caused due to polarization misalignment between signals and receiving antennas. A well-known method of generating circular polarization is by creating different shapes of radiating elements with a single feed, such as a square patch with truncated corners or a circular patch with notches [1–5]. These antennas have a 10 dB impedance bandwidth of only about 3%, which tends to become less than 1% for 3 dB axial-ratio (AR) bandwidths. In comparison with microstrip antennas, the printed ring slot antennas not only have low profile, light weight and wide impedance bandwidth, but are also easy to manufacture and have wider circular polarization bandwidth. Many ring slot antenna designs producing CP radiation have been proposed. In [6], a square-ring slot antenna with 38.7% impedance bandwidth and 12.9% 3 dB AR bandwidth is presented. In [7], a printed slot antenna is excited by an L-shaped strip and has CP and impedance bandwidths of approximately 44% and 38% respectively, referred to the resonant frequency. This antenna has a simple structure and is easy to implement.

In this paper, the geometry of the antenna was developed from the designs described in [2] and [8]. The ring slot antenna in [8] has an asymmetric ring slot structure, feeding the ring slot using a microstrip line at 45° from the asymmetry. In our design, the annular ring slot design with two pairs of slits is proposed. By adjusting the length of slits, the impedance and CP bandwidths can be improved. The designed antenna is successfully implemented and the experimental results are presented.

2. ANTENNA DESIGN AND EXPERIMENTAL RESULTS

The geometry of the proposed microstrip line fed CP annular-ring slot antenna is shown in Fig. 1. The total area of antenna is $70 \times 50\,\text{mm}^2$ with an FR4 dielectric substrate, which has relative permittivity 4.4, loss tangent 0.02 and thickness 1.6 mm. On the top of the substrate is the ground plane, etched to form an annular ring slot, which has an inner radius $R_1 = 17\,\text{mm}$, outside radius $R_2 = 23.5\,\text{mm}$ and two slots. The fundamental resonant frequency of the annular-ring slot antenna can be calculated according to the following [8]:

$$f_r = \frac{c}{\pi\,(R_1 + R_2)}\sqrt{\frac{1+\varepsilon_r}{2\varepsilon_r}} \tag{1}$$

where c is the speed of light in free space; $\pi(R_1 + R_2)$ is the mean circumference of the annular ring slot around the patch; the second term in (1) is the correction factor considering the presence of different dielectric media on either side of the slot antenna. To excite two orthogonal near-degenerate resonant modes for CP radiation, the annular ring has a pair of truncated slots of dimensions $4.25 \times 6.72\,\text{mm}$. Moreover, the slots are placed along the line that is 45° away from the vertical line, as shown in Fig. 1.

To improve impedance bandwidth and CP bandwidth, two pairs of opposite slits are introduced in the annular ring slot. All the slits are 1.5 mm wide. The lengths of slits 1 and slit 2 are a and b

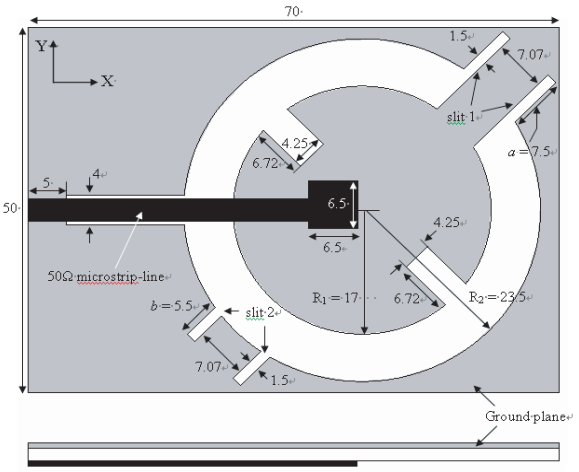

Figure 1: Geometry of the annular ring slot antenna.

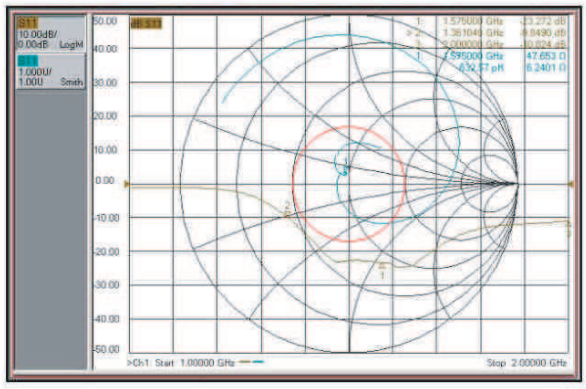

Figure 2: Measured return loss and input impedance on a Smith chart for the proposed antenna.

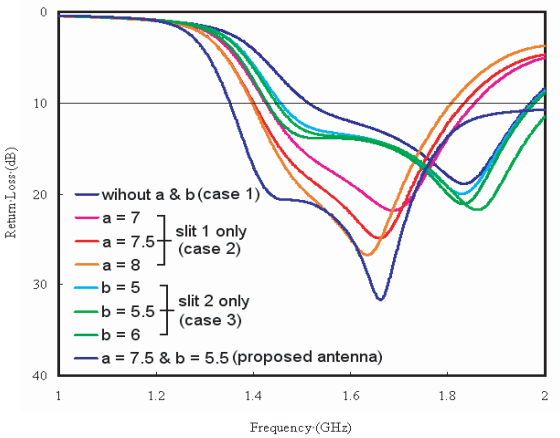

Figure 3: Simulated return loss for different lengths of a and b.

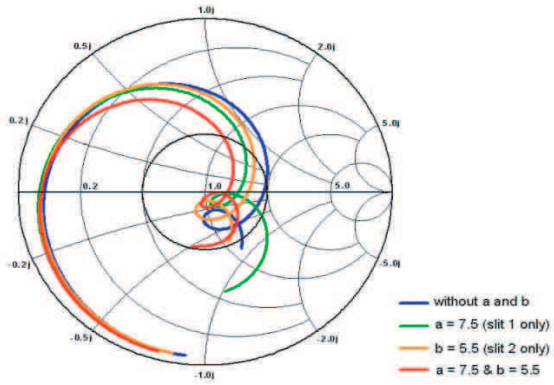

Figure 4: Simulated input impedance on Smith chart for different lengths of a and b.

mm respectively. A 50 Ω microstrip feed line with a widened square stub of length 6.5 mm is placed on the bottom of the substrate. The optimized dimensions for the proposed antenna are as shown in Fig. 1.

The characteristics of the ARSA were calculated by Ansoft High Frequency Structure Simulator (HFSS) software and measured by Agilent N5230A network analyzer. Fig. 2 shows the measured return loss and input impedance on a Smith chart for the proposed antenna. It is clearly observed that a very small loop is formed at approximately 1.575 GHz and occurs close to the center of the Smith chart obtained. This characteristic usually indicates that two resonant modes are excited at close frequencies [9], creating CP radiation. The impedance bandwidth ($S_{11} \leq 10$ dB) is more than 640 MHz (or about $> 40.6\%$), around the center frequency $f = 1.575$ GHz.

To study further the effect of the added slits 1 and 2, the simulated return losses of the proposed antenna are shown in Fig. 3 and Table 1; the table also shows different values of a and b, the lengths of the two pairs of slits. The impedance bandwidth of the proposed antenna without use of the two pairs of slits ($a = 0$, $b = 0$; case 1) is only about 455 MHz. Large variations are observed in the excited resonant mode for case 2, and the resonant modes are shifted to lower frequency by using slit 1 only, as compared with that case 1. On the other hand, the frequency modes of case 3 are only slightly shifted. With the addition of slit 2, the lowest resonant frequency moves toward lower frequency, and the second resonant frequency moves toward higher frequency. The results verify that cutting slit 2 in the radiator can increase impedance bandwidth. From Fig. 3 and Table 1, it appears that the impedance bandwidth is the largest from 1.44 to more than 2 GHz as $b = 5.5$ mm. However, the obtained CP bandwidth cannot cover the GPS band for the antenna. According to

these study results of a and b, the resonant frequency is mainly controlled by a, and the impedance bandwidth is mainly controlled by b. Therefore, the widest bandwidth for GPS application can be obtained by combining slits 1 and 2 and properly tuning a and b.

Figure 4 presents the simulated input impedance for various a and b on the Smith chart. It is noted that the loop of Smith curve is condensed due to introduction of the slits. By cutting slits 1 and 2, the frequency at the loop can be shifted to approach 1.575 GHz and the loop size of impedance loci can be decreased as two degenerate modes get close to each other. The resultant CP axial ratios against frequency are shown in Fig. 5. From the simulated results, it can also be observed that CP bandwidth (defined as 3 dB AR) increases by more than 340 MHz when ARSA cuts the two-pair slits.

The measured and simulated antenna gain over the entire operation region is shown in Fig. 6. The obtained gain in CP bandwidth range varies from 2.8 to 3.5 dBi. It is also observed that, within

Table 1: Performance of the proposed antenna with different values of a and b in Fig. 1.

a (mm)	b (mm)	BW (MHz)	CP BW (MHz)
0	0	455 (1515 ~1970)	313 (1595 ~ 1977)
7	0	430 (1426 ~1856)	-
7.5	0	440 (1394 ~1836)	418 (1378 ~ 1796)
8	0	410 (1398 ~1807)	-
0	5	518 (1456 ~1974)	-
0	5.5	>560 (1440 ~ >2000)	404 (1586 ~ 1990)
0	6	550 (1429 ~1979)	-
7.5	5.5	>648 (1352 ~ >2000)	>660 (1340 ~ >2000)

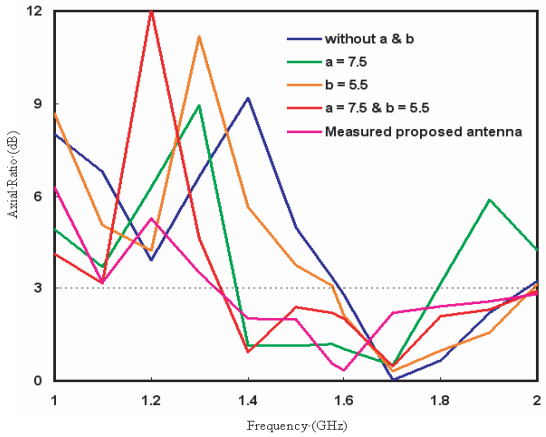

Figure 5: Simulated and measured axial ratio versus frequency for different lengths of a and b.

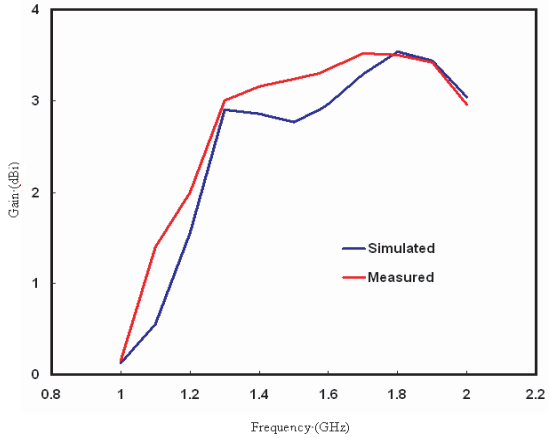

Figure 6: Measured and simulated antenna gain versus frequency for the proposed antenna.

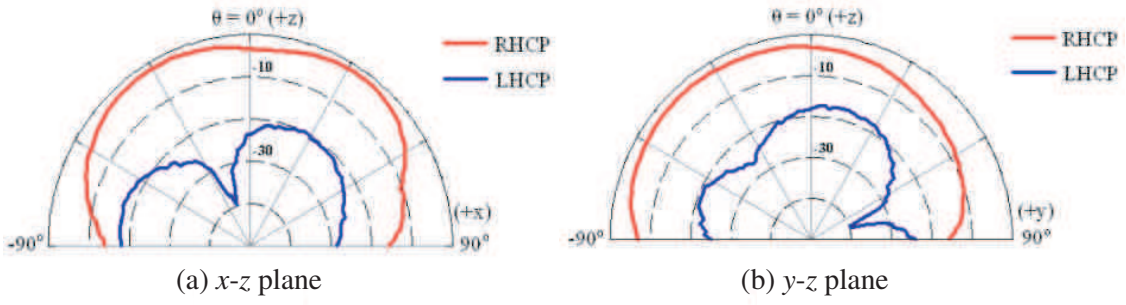

(a) x-z plane (b) y-z plane

Figure 7: Measured radiation patterns of proposed antenna at 1.575 GHz. (a) x-z plane, (b) y-z plane.

the 3 dB AR bandwidth, the antenna gain variations are less than 1.0 dBi, with peak antenna gains of approximately 3.5 (measured) and 3.2 dBi (simulated). The measured radiation patterns of the proposed ARSA at frequency 1.575 GHz in the two principal planes are plotted in Fig. 7, demonstrating that the bi-directional radiation with opposite polarization is achieved. It can be observed that the antenna operates in a right-hand CP mode, with more than 15 dB isolation between the right-hand and left-hand fields in the main beam direction ($\theta = 0°$).

3. CONCLUSIONS

A CP annular ring slot antenna with broadband impedance and CP bandwidth characteristics has been presented in this paper. To improve impedance and CP bandwidths, the annular ring slot with the use of two pairs of slits is investigated. The measured results agree with the simulation, showing that the proposed antenna has a wide return loss and AR bandwidth (AR $<$ 3 dB) of more than 40% referred to the resonant frequency 1.575 GHz. The measured radiation patterns are stable and symmetric with respect to the broadside direction. Moreover, a prototype antenna with an average gain of 3.2 dBi over a CP bandwidth is shown.

ACKNOWLEDGMENT

This work was supported by National Science Council of the Republic of China under NSC 97-2221-E-239-006-MY2.

REFERENCES

1. Kim, S. M., K. S. Yoon, and W. G. Yang, "Dual-band circular polarization square patch antenna for GPS and DMB," *Microwave Opt. Technol. Lett.*, Vol. 49, 2925–2926, 2007.
2. Chen, H. M. and K. L. Wong, "On the circular polarization operation of annular-ring microstrip antennas," *IEEE Trans. Antennas Propag.*, Vol. 47, 1289–1292, 1999.
3. Wong, K. L. and Y. F. Lin, "Circularly polarized microstrip antenna with a tuning stub," *Electron. Lett.*, Vol. 34, 831–832, 1998.
4. Row, J. S., "Dual-frequency circularly polarized annular-ring microstrip antenna," *Electron. Lett.*, Vol. 40, 153–154, 2004.
5. Wong, K. L., W. H. Hsu, and C. K. Wu, "Single-feed circularly polarized microstrip antenna with a slit," *Microwave Opt. Technol. Lett.*, Vol. 18, 306–308, 1998.
6. Chang, K. M., R. J. Lin, C. Deng, and Q. X. Ke, "A novel design of a microstrip-fed shorted square-ring slot antenna for circular polarization," *Microwave Opt. Technol. Lett.*, Vol. 49 1684–1687, 2007.
7. Tseng, L. Y. and T. Y. Han, "Microstrip-fed circular slot antenna for circular polarization," *Microwave Opt. Technol. Lett.,* Vol. 50, 1056–1058, 2008.
8. Wong, K. L., C. C. Huang, and W. S. Chen, "Printed ring slot antenna for circular polarization," *IEEE Trans. Antennas Propag.*, Vol. 50, 75–77, 2002.
9. Wong, K. L. and T. W. Chiou, "Broad-band single-patch circularly polarized microstrip antenna with dual capacitively-coupled feeds," *IEEE Trans. Antennas Propag.*, Vol. 49, 41–44, 2001.

Miniaturized Ultra-wideband Circular Metallic Plate Antenna Suspended by Shorting Pins

Homayoon Oraizi and Mehdi Hamidkhani
Department of Electrical Engineering, Iran University of Science and Technology, Narmak, Iran

Abstract— In this paper, a circular metallic plate antenna suspended by shorting pins over a ground plate with a novel stepped coaxial feed is proposed for miniaturized ultra-wideband applications in the frequency range 2.6–13.2 GHz. This antenna achieves acceptable miniaturization and provides excellent UWB input impedance bandwidths and stable radiation patterns. It achieves about 110 percent bandwidth. The proposed antenna achieves both miniaturization and high bandwidths in UWB wireless applications, which are quite contrary and opposing characteristics. The performance of the proposed antenna is quite good compared to other similar structures.

1. INTRODUCTION

The recent wide spread applications of military and civilian wireless communication systems have increased the need for inexpensive, lightweight and small antennas having the capability of integration with other system components [1]. The ultra-wideband (UWB) frequency is specified in the range 3.1–10.6 GHz. The UWB systems should have the advantage of low power consumption, which also leads to the reduction of adverse radiation effects of communication systems on the human body, high security of military communication systems achieved by low transmission powers, high immunity against the background noise (which is expected to be low in parts of the bandwidth, even though it may be high in other intervals), high performance in multipath channels and high penetration capability [2].

Microstrip patch antennas are appropriate candidates for UWB application. However, they have mostly narrow input impedance bandwidths. The antennas mostly used in UWB systems are monopole, coplanar and slot antennas. However, these radiating structures have lower radiation efficiencies than the microstrip antennas.

For the TM_{mn} modes in circular patch microstrip antenna, the radius of circular patch is $(k_{mn}\lambda)/(2\pi\sqrt{\varepsilon_r})$, where λ is the wavelength in free space, ε_r is the dielectric constant of the substrate and K_{mn} is the n'th zero of the derivative of the Bessel function of order m. For the dominant mode TM_{11}, the constant is $K_{11} = 1.84118$.

Various methods are proposed for the miniaturization of such antennas in the literature [3]. However, different limitations are encountered as a result of antenna miniaturization, such as the reduction of impedance bandwidth. Generally it may be inferred that the reduction of antenna size and increase of its bandwidth are inversely proportional. However, there are several methods for the enhancement of antenna impedance bandwidth, such as thicker substrate heights (h) [4], lower substrate dielectric constants (ε_r) [4], use of various techniques for antenna feeds and impedance matching [4], use of parasitic elements [3] and application of various configurations of slot antennas [2].

In this paper, we propose a technique to increase the antenna impedance bandwidth, which combines a proper antenna feed, impedance matching and higher substrate heights. It also leads to the effective miniaturization of the antenna configuration. Its size is further reduced by placing shorting pins to the ground plane [8, 9]. The antennas are designed for the standard ultra-wideband (UWB) frequency interval namely 2.6 to 13.2 GHz.

2. THE PROPOSED ANTENNA CONFIGURATION

The proposed antenna configuration is shown in Fig. 1. The antenna feed is made by a probe through a coaxial cable, which has several advantages relative to the microstrip line, such as lower losses and less spurious radiation from the feed line and the capability of input impedance adjustment by varying the position of probe. Generally, the microstrip antenna with probe feedings has lower impedance bandwidths due to their high Q factors. On the other hand, higher substrate heights lead to the reduction of Q and increase of the bandwidth. However, longer probes have higher inductance, which imposes a limitation on the enhancement of bandwidth. Several techniques are proposed to counteract this effect in the literature, such as a folded patch feed.

In this paper, we use a two-section cylindrical probe feed with different radii and lengths, which effectively decreases its inductive effects and increases its bandwidth. (Multisection cylindrical probe feed could also be used for better results.) The electrical length of the probe has actually increased, which leads to the reduction of the antenna size. The height of the air substrate is h_2 and the length of the lower section of probe is h_1. Moreover, for the further reduction of antenna size, three shorting pins are also inserted in the antenna structure.

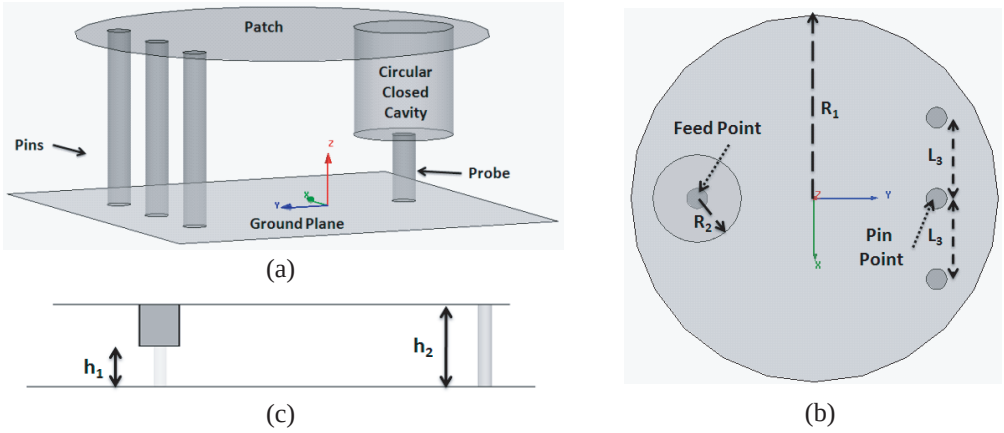

Figure 1: Definition of parameters used in the design of proposed antenna. (a) 3D view; (b) Top view; (c) Side view.

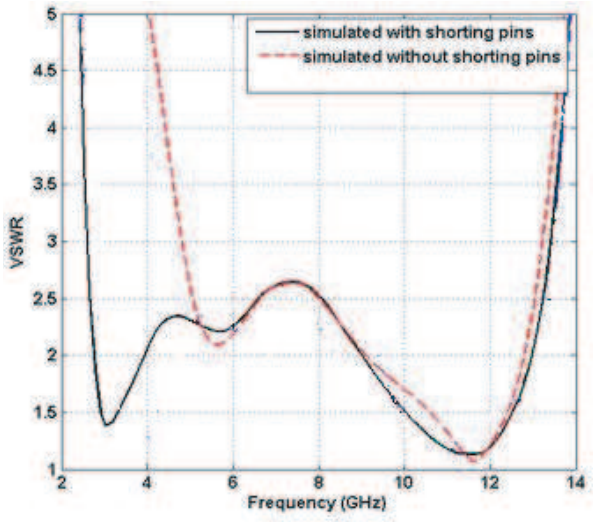

Figure 2: Computer Simulation values of VSWR for Antenna 1 with and without shorting pins.

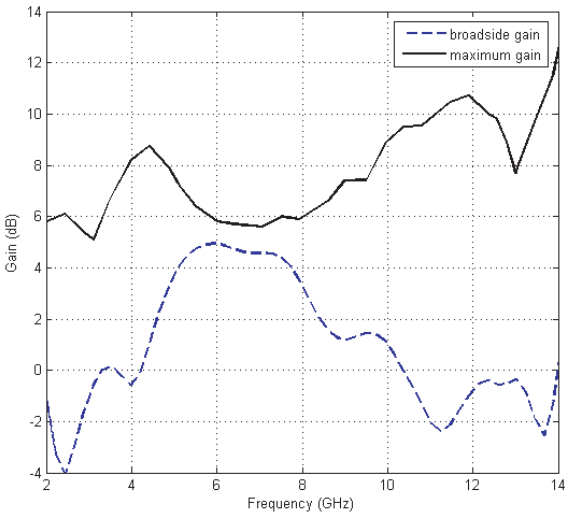

Figure 3: Simulated gain of Antenna 1.

Table 1: Dimensions of Antenna 1, 2 and 3 (units in mm).

Parameters	**Antenna 1**	**Antenna 2**	**Antenna 3**
$\mathbf{R_1}$	12.5	42	19
$\mathbf{R_2}$	3	8	4.5
$\mathbf{L_3}$	5.5	15	7
$\mathbf{h_1}$	4	5.6	5
$\mathbf{h_2}$	10.5	30	18
Pin point	(0, 8.3)	(0, 33.8)	(0, 13.3)
Feed point	(0, −8)	(0, −27.3)	(0, −11.3)

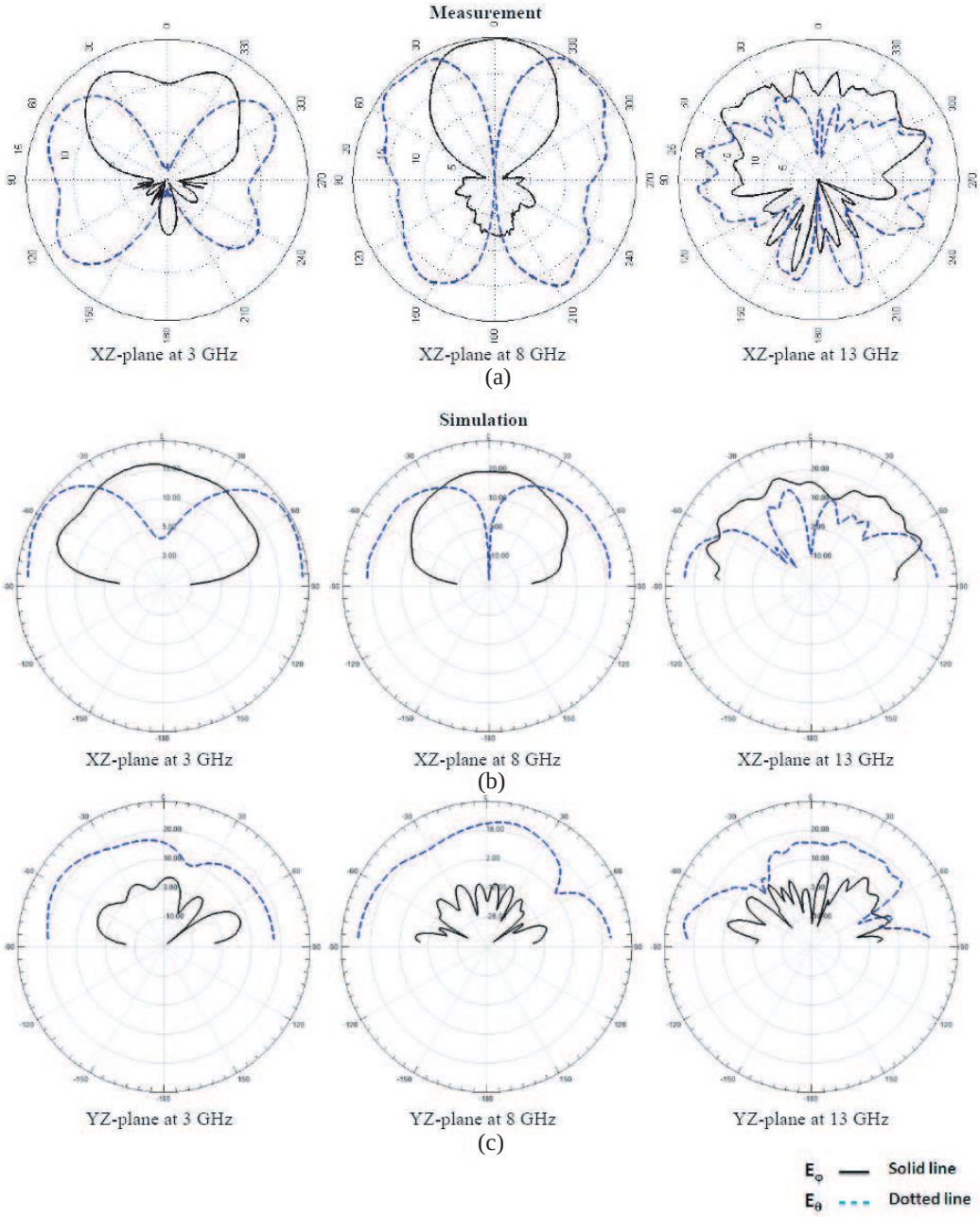

Figure 4: Computer simulation of radiation patterns of Antenna 1 with shorting pins.

Table 2: Design data of Antenna 1, 2, and 3.

	Antenna 1	Antenna 2	Antenna 3
Frequency bandwidth with shorting pins	2.6–13.2 GHz (134.2%)	0.8–3.6 GHz (127.3%)	1.7–7.1 GHz (122.7%)
Frequency bandwidth without shorting pins	5–13 GHz (89%)	1.5–3.5 GHz (80%)	3.2–7.1 GHz (76%)
size	$\pi * 0.091\lambda_{f\,\min}$ $*(0.108\lambda_{f\,\min})^2$	$\pi * 0.08\lambda_{f\,\min}$ $*(0.112\lambda_{f\,\min})^2$	$\pi * 0.102\lambda_{f\,\min}$ $*(0.107\lambda_{f\,\min})^2$

3. DESIGN

A parametric investigation of the proposed antenna structure is made for its various geometrical dimensions as denoted in Fig. 1. The antennas 1, 2 and 3 as shown in Table 1 have different parameters. The simulation results are obtained by HFSS version 12.

The optimum value of diameter of shorting pins is found to be equal to 0.7 mm. With the installation of shorting pins, the radius of the circular patch is equal to $0.108\lambda_{f\,\min}$ at the lower end of the frequency band, namely 2.6 GHz. The air substrate height is $h_2 = 0.091\lambda_{f\,\min}$ and the length of thinner probe of feed is $h_1 = 0.034\lambda_{f\,\min}$. The computer simulation results of SWR versus frequency for the antennas with and without shorting pins are drawn in Fig. 2. The relative bandwidth (defined with SWR ≤ 2.5) of antenna 1 with and without shorting pins are 134.2% and 89%.

The gain of antenna 1 with shorting pins is computed by simulation and is drawn in Fig. 3, Its radiation patterns are drawn at Fig. 4 for frequencies 3, 8 and 13 GHz in the XZ and YZ planes (as defined in Fig. 1). Observe that the radiation patterns are relatively stable across the 3–13 GHz frequency band, which is about 130%.

In order to show the degree of miniaturization of the proposed antenna 1, we compare its performance with that of the square patch microstrip antenna reported in [8], having the size

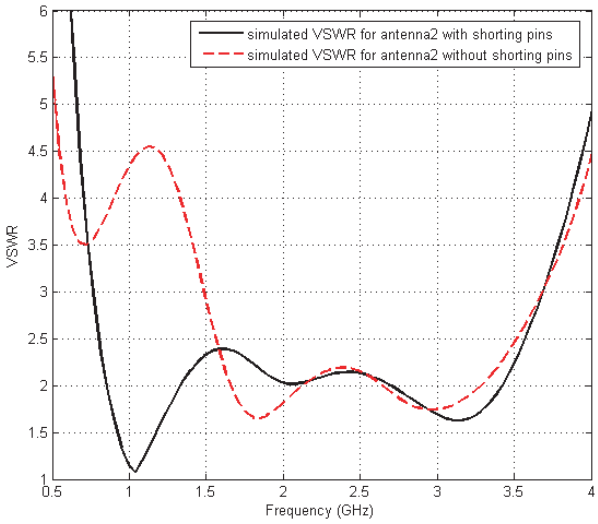

Figure 5: Simulated VSWRs of Antenna 2 with and without shorting pins.

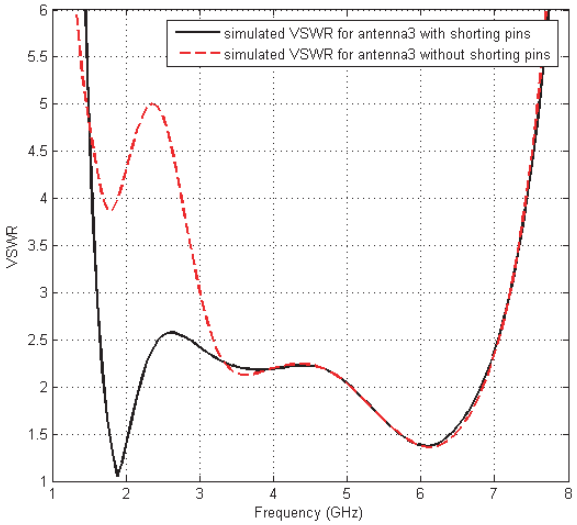

Figure 6: Simulated and measured VSWRs of Antenna 3 with and without shorting pins.

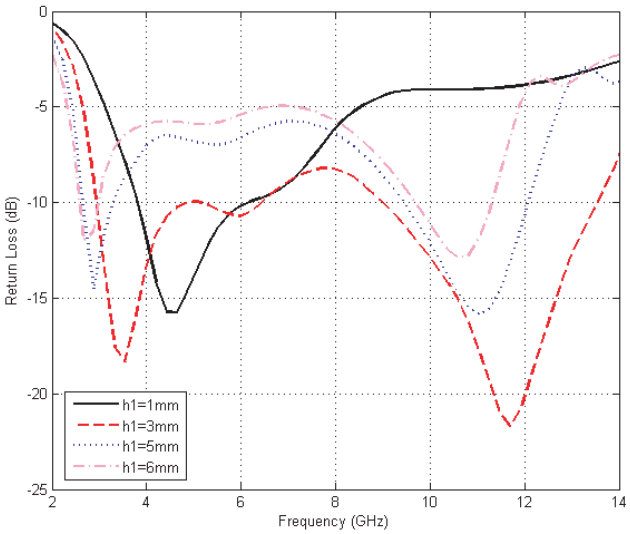

Figure 7: Return losses for different lengths of probe.

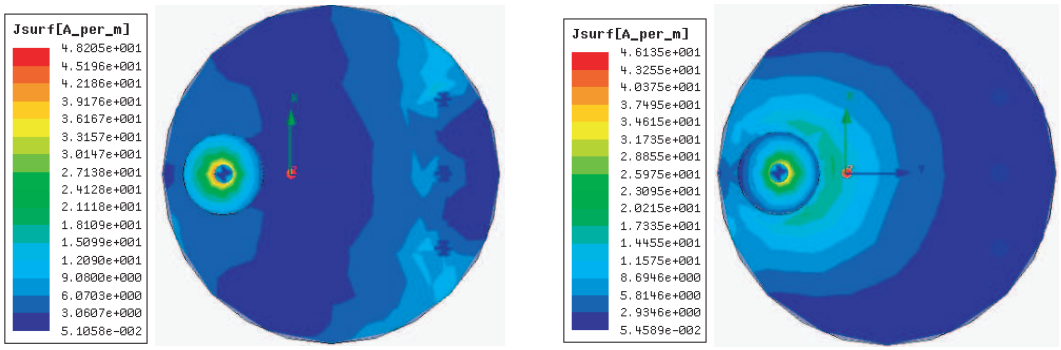

(a) (b)

Figure 8: Distribution of current on our proposed antenna (antenna 1) at different frequencies. (a) Current plot at 2.6 GHz; (b) Current plot at 13.2 GHz.

$0.198\lambda_{f\,\min} * 0.198\lambda_{f\,\min} * 0.093\lambda_{f\,\min}$.

Its relative bandwidth (SWR ≤ 2.5) is 73.8% in the frequency band 3.96-8.59GHz. Consequently, our proposed antenna 1 with shorting pins has 60.4% increase of frequency bandwidth and 9% reduction of size.

The dimensions of antennas 2 and 3 are also given in Table 1. The standing wave ratios (SWR) of antennas 2 and 3 with and without shorting pins are drawn in Figs. 5 and 6, respectively. The frequency bandwidths and relative bandwidths of antennas 1, 2 and 3 are given in Table 2. Observe that the relative bandwidths are better than 120% and 70% for antennas with and without shorting pins, respectively. Therefore, the proposed feeding structure may be used for any microstrip antenna, in order to enhance its frequency bandwidth.

The return losses of antenna 1 with shorting pins for various values of length h_1 (of the first section of feed probe) are drawn versus frequency in Fig. 7. Observe that as the length h_1 increases, the inductance of feed probe increases, its impedance matching deteriorates and the bandwidth worsens. The relative lengths of h_1 and h_2 (namely h_1/h_2) is a critical measure of impedance matching of the feed probe. The optimum values of h_1 and h_2 for antenna 1 are equal to 4 mm and 10.5 mm, respectively.

The current distributions on the patch of antenna 1 with shorting pins are drawn in Fig. 8 at the limits of 2.6–13.2 GHz frequency band.

4. CONCLUSION

In this paper, a novel coaxial probe feed is proposed for a circular metallic plate antenna suspended by shorting pins over a ground plate, which serves for its miniaturization and wideband characteristics for ultra wideband applications. By increasing the height of the plate above the ground plane, the antenna bandwidth increases considerably. The radiation patterns are also stable over the UWB bandwidth. Further innovations on the proposed antenna structure could be envisaged to achieve extended characteristics.

REFERENCES

1. Skrivervik, A. K., J.-F. Zurcher, O. Staub, and J. R. Mosig, "PCS antenna design: The challenge of miniaturization," *IEEE Antennas and Propagation Magazine*, Vol. 43, 12–27, August 2001.
2. Wei, L.-A., "Applications of ultra wideband," M.S., The University of Texas at Arlington, December 2006.
3. Kula, J. S., D. Psychoudakis, W.-J. Liao, C.-C. Chen, J. L. Volakis, and J. W. Halloran, "Patch-antenna miniaturization using recently available ceramic substrates," *IEEE Antennas and Propagation Mag.*, Vol. 48, No. 6, December 2006.
4. Schaubert, D. H., D. M. Pozar, and A. Adrian, "Effect of microstrip antenna substrate thickness and permittivity: Comparison of theories and experiment," *IEEE Trans. Antennas Propag.*, Vol. 37, 677–682, June 1989.

Design of UHF RFID Passive Tag Antenna Pasted on a Large Metal Structure

Shih-Chung Tuan[1], **Hsi-Tseng Chou**[2], **Kuo-Lun Hung**[2], **and Jen-Chung Chu**[2]

[1]Dept. of Communication Eng., Oriental Institute of Technology, Pan-Chiao, Taiwan
[2]Dept. of Communication Eng., Yuan Ze University, Chung-Li 320, Taiwan

Abstract— In this paper we present a new design of patch-type antenna using a loop circuit located inside the antenna structure to excite the antenna, which has potential to resolve the problem arising from the situation when the antenna is pasted on a large metal ground. The problem of large metal structures to the RFID tag antenna arises because most of the RFID uses electrical dipole-type antennas. In this case, the presence of large metal structure will short the antenna and reduce the radiation field strength. The proposed antenna structure is a magnetic type. The proposed design concept intends to optimize the field distribution within the substrate between the patch and ground, and therefore may reduce significantly the antenna size. Experimental study showed that the antenna may be used to enhance the reading range to be more than 3 meters.

1. INTRODUCTION

RFID is a kind of automatic identification system using electromagnetic (EM) wave as means for electronic information transmission, and using a reflected modulation as a main communication method to achieve the objective of speedy and accurate data acquisition. Therefore, the usability and universality of RFID system at UHF band have been increased in many different application fields in all countries such as automatic automobile identification management, highway tolling, and monitoring systems. Other applications include the tracking and management of goods in the warehouse. The operational principles of RFID are illustrated in Figure 1. In this study we introduce research, analysis and improvement methods to improve the malfunction of RFID tag antennas caused by the situation when it is pasted on the surface of a large mental structure with a less than 1 mm distance to the metal surface. Consider the applications of warehouse management system for large container yards as an illustration example. The RFID system can be used as the main tool for a real time monitoring and inquiry of the traffic, locations of entry/exit and storage of containers. Therefore we know that unmanned RFID wireless tag system has become one of the key methods with the most potential for warehouse management. However, this application of metal object management will face a problem when electronic tag of RFID is place on large metal materials (such as containers). The destructive interference from the environment to the system performance of RFID will affect the accuracy and distance of RFID reading. The solution provided by this study can help the system to achieve a longer reading distance by improving the antenna performance. Therefore, this study not only has academic significance, but also provides a solution to meet the requirements of practical applications.

In particular, this paper presents a new antenna design that can be pasted on the surface of a large mental object based on the implementation of microstrip-type antenna structure. In order to reduce the antenna size, a new feeding structure that employs a loop circuit located within the antenna structure is proposed. Numerical and experimental studies have been performed and have shown that the new antenna design may significantly enhance the RFID reading distance.

2. THE PROBLEM OF RFID TAG ATTACHED TO A LARGE METAL OBJECT

This application will face a common problem arising from a fact that a large metal object usually has a rather large radar cross section (RCS) [1–3] and results in significant interferences to the reading of the tag. The problem of radar cross section (RCS) area, σ, of metal object to the RFID tag antenna has been revealed and can be found in [1–3]. In various applications, the installation of tag antenna on metal objects with the micro-strip line approach will cause the malfunction of micro-strip antenna because its RCS is very small due to the interference from the radar cross section effect of large metal object. The electronic license plate is an example for this. The second issue is that the RFID tag antenna is usually made of metal. When it is attached to metal object at a low operating frequency of 900 MHz band, a short circuit might occur if the distance between

top and bottom metal surfaces is less than 1 mm, and this will lead to a significant degradation of RFID performance. In this study we employed a tag IC produced by TI (Texas Instruments) with the model number RI-UHF-STRAP-08 and operating frequency at 860 MHZ–960 MHz. Factors affecting the reading range of RFID system can be divided into two aspects, i.e., forward radio link and backscatter radio link [4, 5]. However, the fully established connection is essential regardless of forward radio link or backscatter radio link. Therefore it is desired to maximize the system transmission distance.

3. THE DESIGN AND SIMULATION OF RFID TAG ATTACHED TO METAL OBJECTS

In this paper we consider the large metal object as a part of antenna and propose a new antenna design to achieve the design requirement of maximum reading distance over 3 meters. In the study we utilize a simulation tool of HFSS to design a horizontally polarized antenna. The main antenna design concept is to use a loop circuit as an excitation to the micro-strip antenna as illustrated in Figure 2. A "loop" circuit is referred because two short pins have been employed to connect the feeding line and the top surface of microstrip patch. The feeding microstrip circuit is formed in a meanderline shape which allows one to reduce the size of microstrip patch. This way the original micro-strip antenna design can operate normally, and the communication performance and read range can be enhanced by including metal substrate as part of the antenna design as shown in Figure 2.

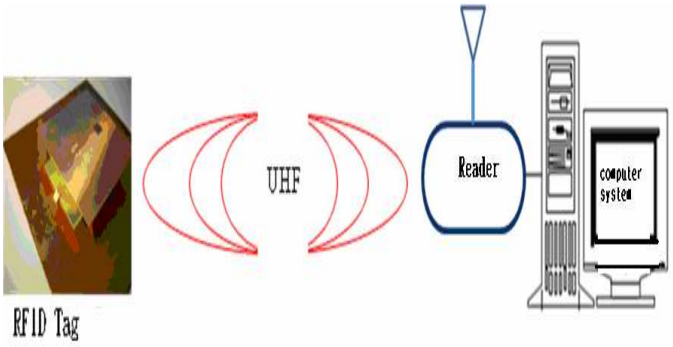

Figure 1: Reflected modulation UHF RFID system.

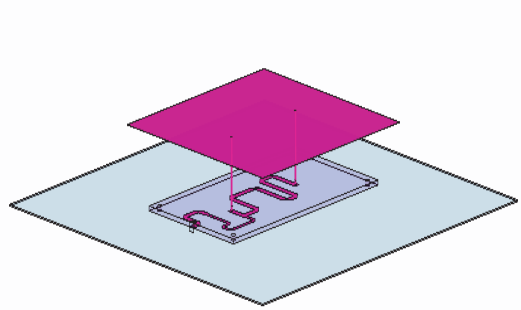

Figure 2: Including metal substrate as part of the antenna design.

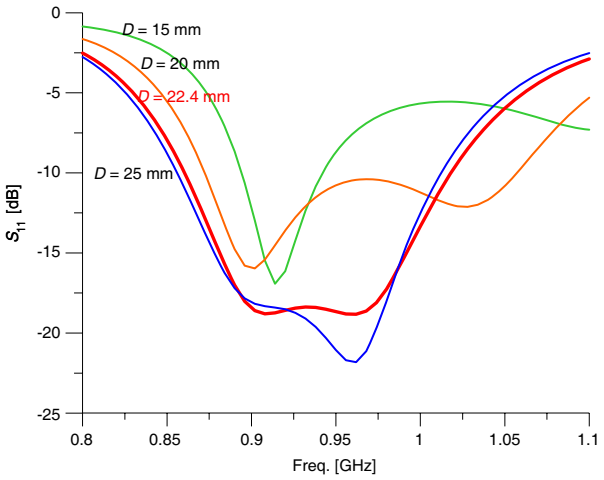

Figure 3: Four different heights at 15/20/22.4/25 mm by design of vertical heights on the left and right sides of loop antenna at 915 MHz.

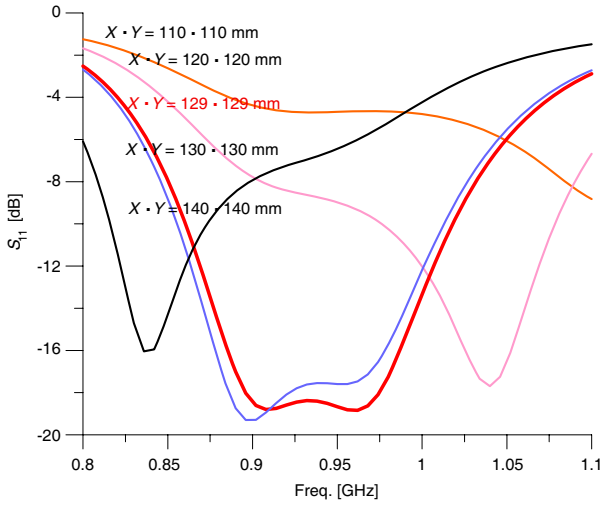

Figure 4: Dimension of radiation metal plate vs. antenna efficiency.

4. ANALYSIS OF DISTANCE AND PERFORMANCE OF LOOP-EXCITED ANTENNAS

The basic theory for loop circuit design is based on its need of $\lambda/2$ to produce a pair of magnetic currents for same polarization in the design of patch antenna. We may change the range of main operating frequency by changing the length of loop circuit. In the current design, the center frequency is at 915 MHz. To understand the characteristics of the antenna design, one varies the height of the patch measured from the ground by 15/20/22.4/25 mm, where the variations of reflection coefficients are shown in Figure 3. In this case, it is observed that a large value of height will increase the bandwidth of operational frequency.

Secondly, one examines the effects of the patch size to the antenna performance. A characteristic study is shown in Figure 4 where the reflection coefficients of the antenna with respect to various patch sizes are shown. In the end from Figures 4 and 5 we conclude that the dimension of 129 × 129 mm will lead to the optimal working frequency performance and pattern size and direction. This is as shown in Figures 4 and 5. The loop circuit with center frequency at 915 MHz is designed on the FR4 PCB board with the dimension of 1.2 × 80 × 136 mm as shown in Figure 6. The micro-strip antenna of PCB board will be facing downward directly to the large copper ground (0.05 thickness × 240 width × 240 length mm) with vertical distance between them at 0.6 mm. The vertical loop conductors on both sides of loop antenna are connected to radiation copper plate (0.05 thickness × 129 width × 129 length mm) above loop antenna by using tinned copper wire (0.1 width × 0.65 thickness × 22.4 length mm) to construct the complete loop antenna structure. The working bandwidth of original design of TAG antenna is 850 MHz–930 MHz with center frequency as 915 MHz. The measured 3D pattern with center frequency of 0.915 GHz shown in Figure 7 indicates that the maximum energy occurs vertically above the antenna, The further confirmation of results of co-polarization and cross-polarization at XZ plane or YZ plan as shown in the curve Figures 8 and 9 indicate that the polarization with the maximum performance all occurs at 0 degree of every plane, and the cross-polarization with the maximum performance occurs at 45 degrees of every plane. Therefore we know that this TAG antenna is capable of complete communication of data transmission with RFID reader along the Z axis perpendicular to antenna according to design requirement without being affected by large metal substrate. The signal transmitted from RFID reader can also be sent to IC chip with the most complete fashion.

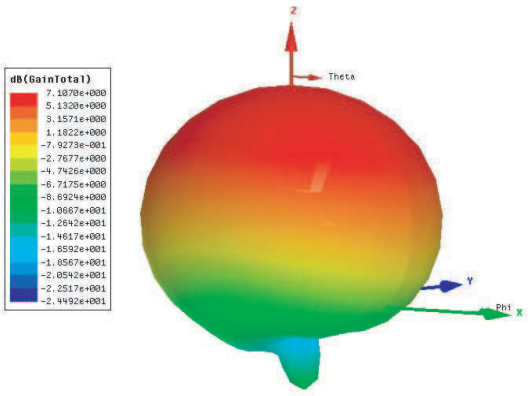

Figure 5: 3D radiation pattern with dimension of radiation metal plate (129 mm × 129 mm).

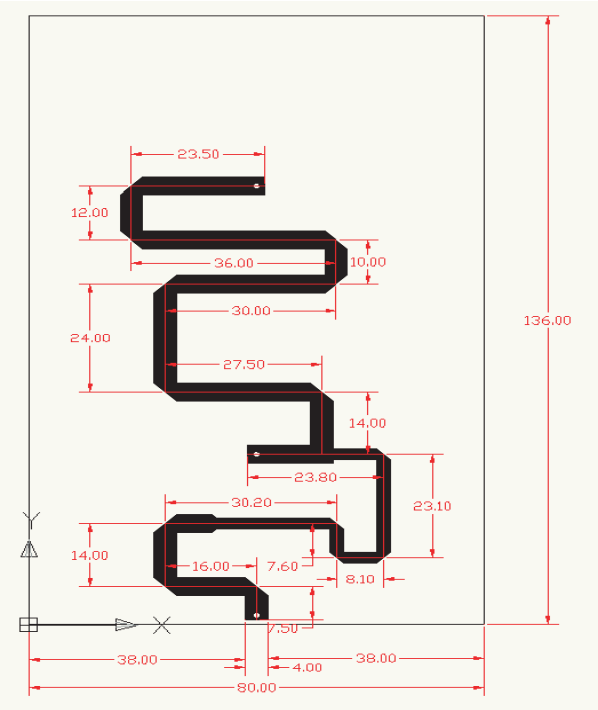

Figure 6: Micro-strip antenna beneath the FR4 PCB board.

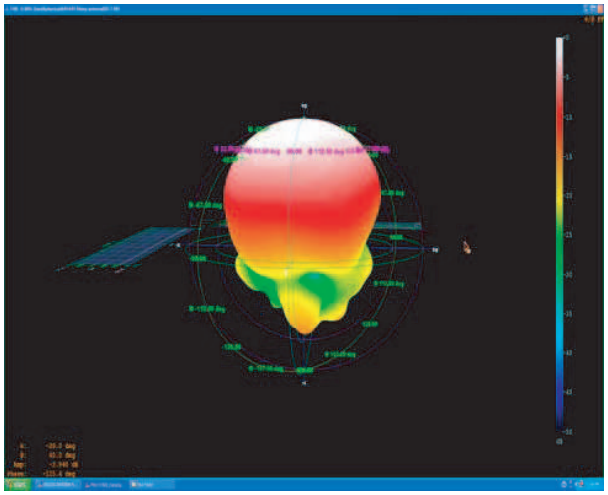

Figure 7: 3D radiation pattern with center frequency 915 MHz.

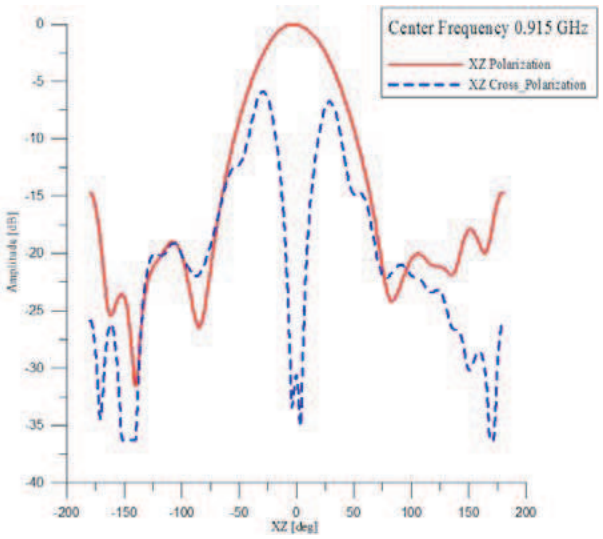

Figure 8: Co-polarized and cross-polarized pattern at XZ plane with 915 MHz.

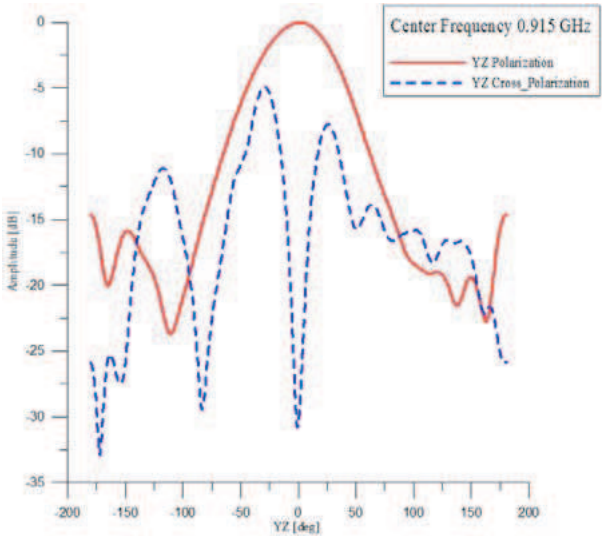

Figure 9: Co-polarized and cross-polarized pattern at YZ plane with 915 MHz.

5. USING RFID READER TO MEASURE THE READ DISTANCE AND ANGLE OF TAG ANTENNA

The designed antenna is examined in the test of reading range by using the ALIEN ALR-9800 RFID reader available in the market as the main testing system equipment which has the same range of working frequency at 900 MHz–928 MHz band. Experiment has shown that at a reading range of 4.8 meters straightly away from the reader the amount of recognizable data is 1180 items/second, which is acceptable in a practical application. This is the farthest reading range this antenna has achieved. We also examined the situation when the antenna's boresite does not point directly to the antenna. We have observed that at an angle of within 40 degrees, the reading range is roughly 4.6 meters away from reader.

6. CONCLUSIONS

In this paper a new antenna design is presented, which has been shown to improve the RFID system performance significantly. In particular, our study shows that the antenna can be placed on a large metal substrate and can indeed achieve the working performance without the need to use additional medium (such as absorbers) between Tag and metal plate as an insulator. The main concept of design is to add a loop circuit inside the original micro-strip antenna, which can change the field distribution within the substrates of microstrip-type antenna, and therefore change the magnetic currents existed on the slots formed by the patch and ground such that the malfunctioning antenna

placed too close to metal plate can now operate normally. The overall isolation and reading distance are enhanced. From simulation results we know that the combination of metal object and original antenna will surely affect the energy reception and frequency variation. By appropriately modifying the performance of the auxiliary loop circuit, the corresponding center frequency can be obtained. The proper impedance can also be obtained to match the metal.

REFERENCES

1. Nikitin, P. V. and K. V. Seshagiri Rao, "Theory and measurement of backscattering from RFID tags," *IEEE Antennas and Propagation Magazine*, Vol. 48, No. 6, 212–218, December 2006.
2. Lu, C.-S., "Characteristic investigation on the UHF passive RFID tag design when it is pasted on a large metal body," Master Thesis, Department of Communications Engineering, Yuan-Ze University, 2009.
3. Seshagiri Rao, K. V., P. V. Nikitin, and S. F. Lam, "Antenna design for UHF RFID tags: A review and a practical application," *IEEE Transactions on Antennas and Propagation*, Vol. 53, No. 12, 3870–3876, December 2005.
4. Wen, S.-K., "Read range of passive RFID systems and impact of tag antenna curving on RFID," Master Thesis, Department of Communications Engineering, Yuan-Ze University, 2008.
5. Nikitin, P. V., K. V. S. Rao, S. F. Lam, V. Pillai, R. Martinez, and H. Heinrich, "Power reflection coefficient analysis for complex impedances in RFID tag design," *IEEE Transactions on Microwave Theory and Techniques*, Vol. 53, No. 9, 2721–2725, Dec. 2006.

A Low Profile Printed Tri-band Antenna Using Multi-band Artificial Magnetic Conductor Ground Plane

Fuguo Zhu[1], **Steven Gao**[1], **and Jiadong Xu**[2]

[1]Surrey Space Centre, University of Surrey, Guildford, GU2 7XH, Surrey, UK
[2]School of Electronics and Information, Northwestern Polytechnical University, Xi'an 710072, China

Abstract— This letter presents the design, implementation and measurement results of a low profile tri-band wire antenna. The height of the whole antenna is 4.8 mm, almost $\lambda/23$ at the lowest frequency. An artificial magnetic conductor (AMC) is integrated with the antenna. This leads to a low profile antenna which can achieve multi-band operations and have a unidirectional radiation pattern. The AMC exhibits a characteristic of in-phase reflection in two frequency regions. To prove the concept, a prototype tri-band antenna with this AMC is designed, fabricated and measured. The results will be useful for applications in portable devices which require a compact antenna for multiple wireless systems.

1. INTRODUCTION

Low profile printed dipole and slot antenna elements are widely used on ground-based, vehicular, airborne, and ship-board applications [1]. The implementation of printed wire antenna with a metallic ground plane can achieve a unidirectional beam, while return loss of antenna would deteriorate sharply when operating very close to a ground plane. Therefore, printed wire antennas should be separated far from the ground plane which results in a large size of antenna system and makes it difficult for applications in portable devices where a compact low-profile antenna is required.

To overcome this problem, AMC is utilized to make the wire antenna compact and more directional with its in phase reflection property. The reflection phase of an AMC surface varies continuously from 180° to −180° versus frequency and it is stated that, the reflection phase range of $90° \pm 45°$ allows a low profile wire antenna to obtain good return loss [2]. And various low profile wire antennas have emerged. An EBG surface is used a ground plane for a curl antenna to realize a low-profile design as well as a circularly polarized pattern [3]. To replace the above curl antenna, a designed artificial ground plane consisted of a thin grounded slab loaded with periodic rectangular patches is used as the ground plane for the dipole and a low profile circularly polarized antenna is achieved [4]. Besides, both voltage standing wave ratio (VSWR) and gain of a broadband spiral antenna can be improved due to the enhanced bandwidth artificial magnetic ground [5].

However, for our best knowledge, low profile multi-band wire antenna with multiband AMC has not been investigated yet. This letter presents the design, implementation and measurement results of a low profile tri-band wire antenna by using a multiband AMC based on [7]. The reflection phase changes from 180° to −180° versus frequency in two frequency regions. Compared to the antenna with metal ground and free space, the proposed antenna has good impedance matching and unidirectional patterns.

2. CONFIGURATION OF LOW PROFILE MULTIBAND WIRE ANTENNA

Figure 1 shows the structure of the proposed low profile multiband wire antenna with three layers. The top layer is the wire antenna which has multi arms to resonate at multi-frequencies [6], and the width of the wire is 1.5 mm. The bottom layer is AMC structure and the middle layer is air. Metal is printed on FR4 with dielectric constant 4.4 and thickness 1.6 mm. Ansoft HFSS 12 with setting of two pairs of master-slavery boundary and one Floquet port is used to simulate and optimize the reflection phase of AMC [7]. This AMC has a valuable advantage of easy-tuning. The whole antenna is investigated via parametric study and the optimized dimensions are shown in Figure 1. In order to verify the design, an antenna prototype is fabricated and shown in Figure 2.

3. SIMULATED AND MEASURED RESULTS

The simulated results in Figure 3 show that, the designed antenna resonates at three frequencies: $f_1 = 2.62$ GHz, $f_2 = 4.63$ GHz, $f_3 = 5.61$ GHz. And Figure 3 also shows the measured return loss: $f_1 = 2.62$ GHz, $f_2 = 4.66$ GHz, and $f_3 = 5.80$ GHz. The measured results agree very well with the simulated results, though there is a little discrepancy in the bandwidth of the third frequency at

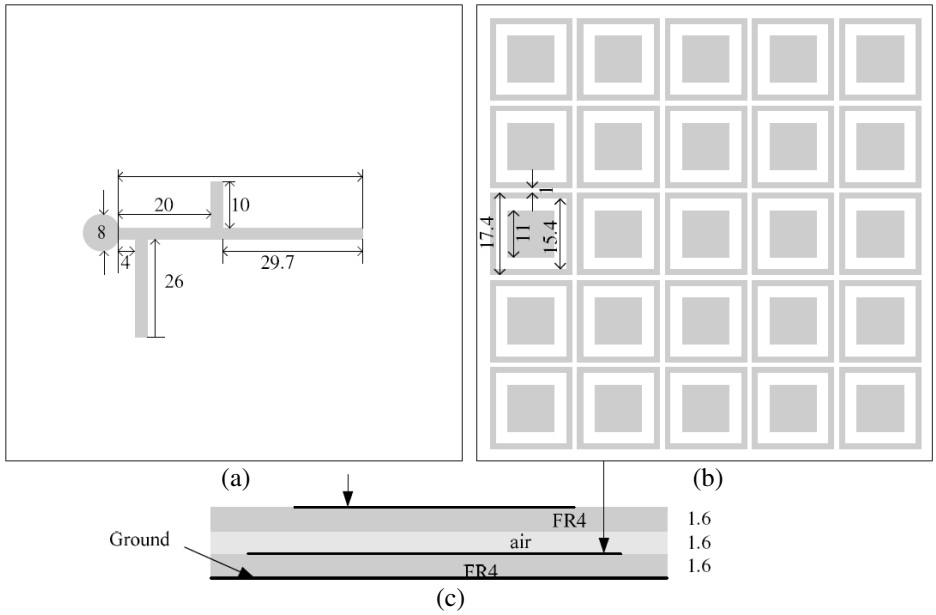

Figure 1: Configuration of the low profile multiband wire antenna (unit: mm). (a) wire antenna, (b) AMC structure, (c) Three layers.

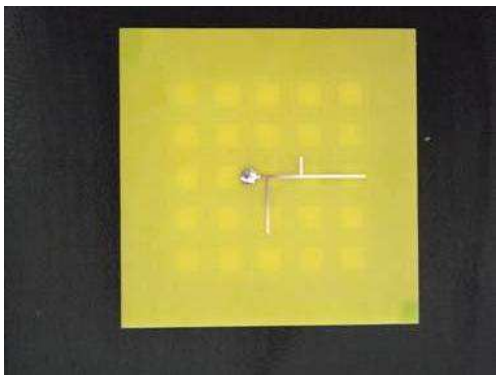

Figure 2: Photo of fabricated antenna prototype.

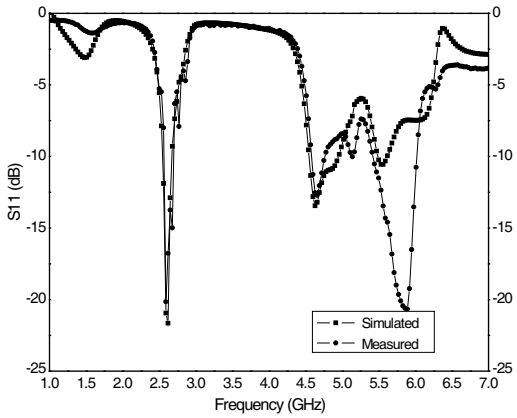

Figure 3: Simulated and measured reflection coefficient.

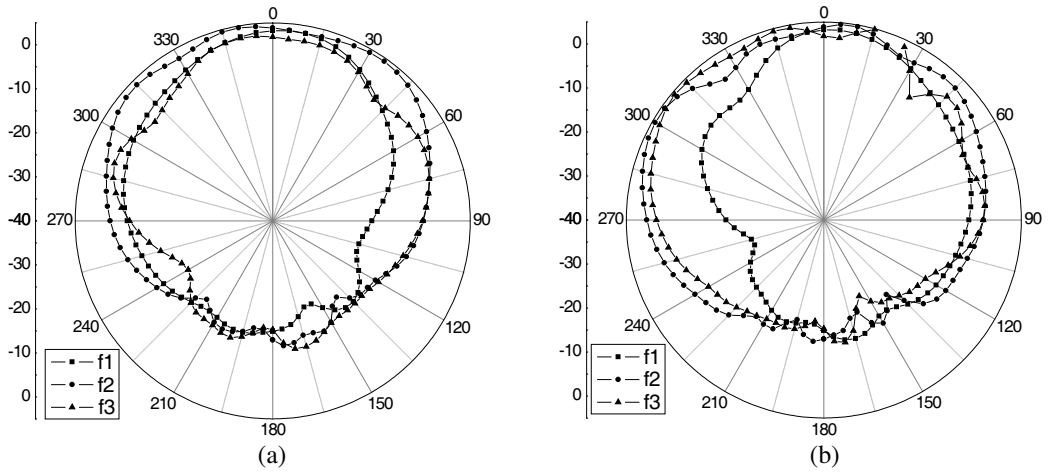

Figure 4: Simulated radiation patterns at different frequencies in (a) E plane and (b) H plane.

−10 dB. Hence, the printed multi-band wire antenna has a good return loss when integrated with AMC.

Simulated far field patterns of wire antenna in *xoz* and *yoz* plane are depicted in Figure 4 and the gain of the antenna almost reaches 3 dB at three frequencies. Besides, the beam angle is wide. The directivity is much better than that in the free space.

4. CONCLUSION

A low profile printed tri-band antenna combined of a printed wire antenna and a designed multiband AMC ground plane is proposed in this paper. The antenna resonates at three frequencies due to multiple arms and the AMC ground plane consists of periodic square patch and square ring patch. Due to the distinct effect of artificial ground plane-reflection phase varies from 180° to −180° versus frequency in two frequency regions, the low profile antenna reaches the objective of good impedance matching and the directivity is better than that of free space and PEC ground plane. Furthermore, a prototype is made and tested. The measured results verify the antenna concept. Therefore, the antenna can be utilized in portable devices.

REFERENCES

1. Bell, J. M. and M. F. Iskander, "A low-profile archimedean spiral antenna using an EBG ground plane," *IEEE Antennas Wireless Propag. Lett.*, Vol. 3, 223–226, 2004.
2. Yang, F. and Y. Rahmat-Samii, "Reflection phase characterization of the EBG ground plane for low profile wire antenna applications," *IEEE Trans. Antennas Propag.*, Vol. 51, 2691–2703, 2003.
3. Yang, F. and Y. Rahmat-Samii, "A low-profile circularly polarized curl antenna over an electromagnetic bandgap (EBG) surface," *Microw. Opt. Tech. Lett.*, Vol. 31, 264–267, 2001.
4. Yang, F. and Y. Rahmat-Samii, "A low profile single dipole antenna radiating circularly polarized waves," *IEEE Trans. Antennas Propag.*, Vol. 53, 3083–3086, 2005.
5. Yousefi, L., B. Mohajer-Iravani, and O. M. Ramahi, "Enhanced bandwidth artificial magnetic ground plane for low-profile antennas," *IEEE Antennas Wireless Propag. Lett.*, Vol. 6, 289–292, 2007.
6. Tefiku, F. and C. A. Grimes, "Design of broadband and dualband antennas comprised of series-fed printed strip dipole pairs," *IEEE Trans. Antennas Propag.*, Vol. 48, 2000.
7. Luo, X. F., P. T. Teo, A. Qing, and C. K. Lee, "Design of double-square-loop frequency-selective surfaces using differential evolution strategy coupled with equivalent-circuit model," *Microw. Opt. Tech. Lett.*, Vol. 44, 159–162, 2005.

A Wide Bandwidth Rectangular Dielectric Resonator Antenna for LTE 4G Handset Front-end

I-Tseng Tang, Simon C. Li, Ding-Bing Lin, C. H. Syu, and Bo-Yuo Chen
Graduate Institute of Communication Engineering, National University of Tainan, Taiwan

Abstract— A new 2.6 GHz CMOS LTE 4G handset receiver front-end with a wideband rectangular dielectric resonator antenna are proposed. The antenna provides an impedance bandwidth of 95% for VSWR ≤ 2.5. A monopole antenna conformed standard ($2.05 \sim 5.8$ GHz) characteristics including return loss and radiation patterns were analyzed and discussed. LTE 4G handset receiver front-end using merged folded cascoded (MFC) scheme demonstrate a 13.7 dB gain, low noise figure of 5.6 dB, and IIP3 at -1.67 dBm with 1.97 mA bias current from a 1.0-V power supply.

1. INTRODUCTION

LTE (Long Term Evolution) is the next generation for mobile wireless communications. Higher date rate of 100 Mbit/s in downlink and 50 Mbit/s in uplink by FDD and TDD in the OFDM (Orthogonal Frequency Division Multiplexing) platform with simple direct conversion architecture are major advantages of LTE over the current mobile technology. OFDM, a spectrum-sharing method different than that of previous generations, provides flexible and efficient use of different carrier bandwidths along with tolerance to noise and multipath interference. LTE phones will have to be backwards-compatible with GSM and 3G CDMA. networks. Therefore, LTE have more stringent requirement of linearity and noise level than previous mobile network standards. Design of LTE RF front-end in the 2.6 GHz frequency band becomes crucial need of 4G cellular phone.

Multiple-Input, Multiple-Output (MIMO) antenna designs can increase the bit-rate using spatial multiplexing, which is basically gluing several antennas together. Recently, the dielectric resonator antenna has been extensively studied owing to its numerous advantages such as high radiation efficiency, low weight, and miniature size. The shapes of DRAs are various and different, such as hemispherical, cylindrical and rectangular. DRAs can be excited by different feeding method, such as coaxial feed, microstrip line and co-planar lines. The DRAs can be completed low profile due to high dielectric permittivity of the materials.

In this paper, we propose a new 2.6 GHz CMOS LTE 4G handset receiver front-end with a wideband rectangular dielectric resonator antenna.

2. LTE 4G FRONT-END DESIGN

2.1. Antenna Design

A wideband rectangular dielectric resonator antenna suitable for 2.6 GHz CMOS LTE 4G handset receiver front-end is shown in Fig. 1. Fig. 1 shows the geometry and configuration of the proposed antenna. The proposed antenna is to fabricate on a low-cast FR-4 substrate with dielectric constant $\varepsilon_r = 4.4$, loss $\tan\delta = 0.02$, and thickness $h = 0.8$ mm. A rectangular dielectric resonator is inserted a substrate with a size of $43 \times 30\,\text{mm}^2$. The dimension of dielectric resonator is $31 \times 21 \times 5.08\,\text{mm}^3$ with a permittivity of $\varepsilon_r = 9.8$.

The dielectric resonator antenna is excited by a 50 Ω microstrip feed line. In order to an impedance matching, the monopole is connected to the feed connector to achieve enhanced input impedance matching over the preferred bandwidth. Besides, setting a stub beside the dielectric resonator can be improved the impedance matching. Just like the method of step impedance matching. Fig. 2 shows the effects of the dielectric resonator with and without side patch.

2.2. LTE 4G Front-end Design

A 2.6 GHz CMOS LTE receiver front-end using merged folded cascoded (MFC) circuit scheme [3] is proposed as shown in Fig. 3. In order to achieve low power consumption, the dc current path from the power supply to the LNA is removed. Instead, a mixer is stacked above the LNA and a large bypass capacitor between the LNA and the mixer is inserted, and hence a reliable ac ground is ensured. In this merged scheme, the LNA operates by only reusing the dc bias current of the mixer without any additional power consumption. However, if a LNA merged with a single-balanced mixer vertically there may not be much voltage headroom since many transistors would be stacked

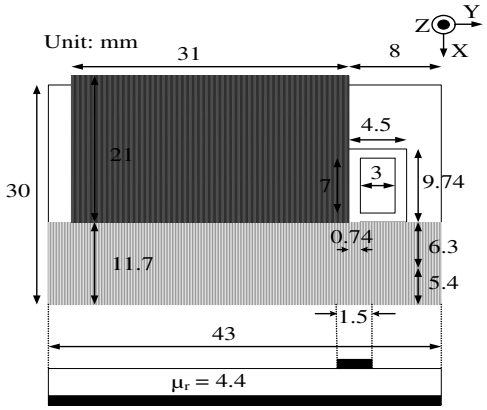

Figure 1: Geometry and configuration of the proposed antenna.

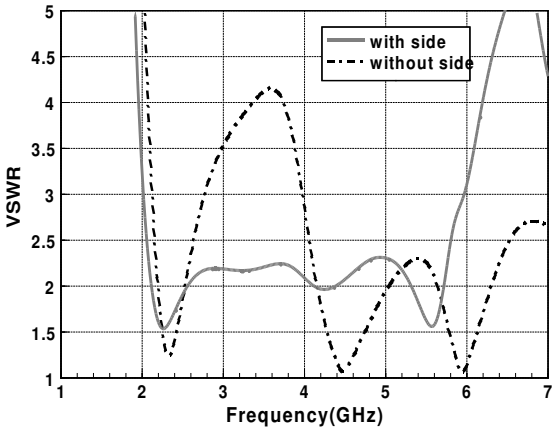

Figure 2: Effects of the dielectric resonator with and without side stub.

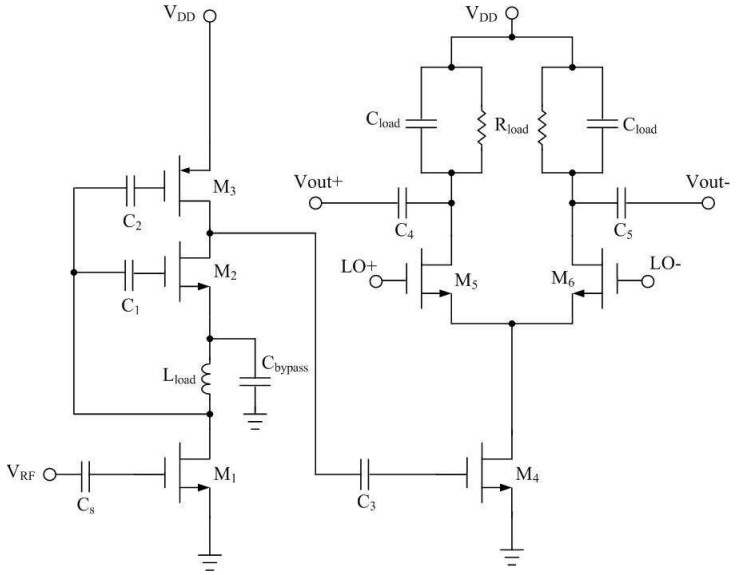

Figure 3: Merged folded-cascoded (MFC) LTE 4G handset front-end.

between VDD to ground. To prevent RF performance degradation caused by the absence of the conventional LNA stage, both a LNA and a mixer are merged in the proposed front-end. A merged folded-cascoded mixer instead of a single-balanced mixer in the MFC LTE 4G handset front-end is shown in Fig. 3.

In addition, an inverter-type transconductance stage instead of a single nMOS transistor is utilized to enhance the gain of the mixer. Therefore, a better RF performance compared to those of a cascaded LNA and mixer with this merge of the LNA and mixer with the inverter-type transconductance stage is achieved. This low power scheme consumes no more than the amount of power used in the merged LNA and mixer, as it reuses the dc bias current. This merged LNA and mixer provide a forward gain of 15.3 dB and a noise figure of 5.5 dB under a 0.61 mW dc power shown in Fig. 4.

Noise figure of the proposed front-end can be substantially improved by the large gain of merged LNA. As merged LNA sufficiently suppresses white and flicker noises modulated by the mixer. Besides, a folded-cascode mixer is inherently less affected by flicker noise. In direct-conversion receivers, flicker noise is the dominant noise source since the down-converted RF signal at the mixer output is noticeably corrupted by flicker noise. Consequently it becomes a demanding task to reduce flicker noise for a low-power mixer design. In a fully differential mixer, the output signal is only affected by flicker noise generated in the switching stage. The noise figures of mixer switching stage at various intermediate frequencies are plotted in Fig. 5. The conversion gain and IIP3 of the

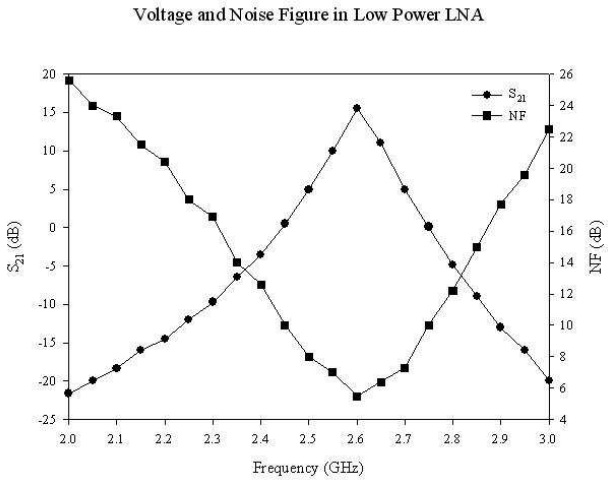

Figure 4: Voltage gain and noise figure of merged LNA and mixer.

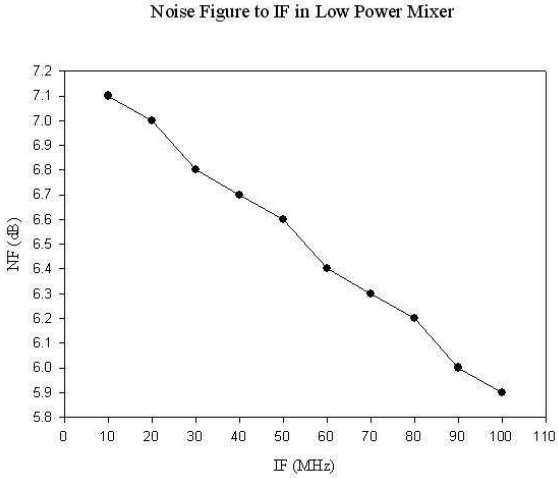

Figure 5: Noise figure to IF in the mixer switching stage.

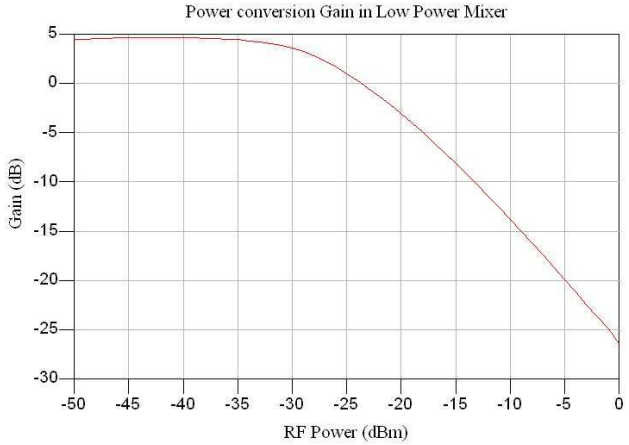

Figure 6: Conversion gain of the mixer switching stage.

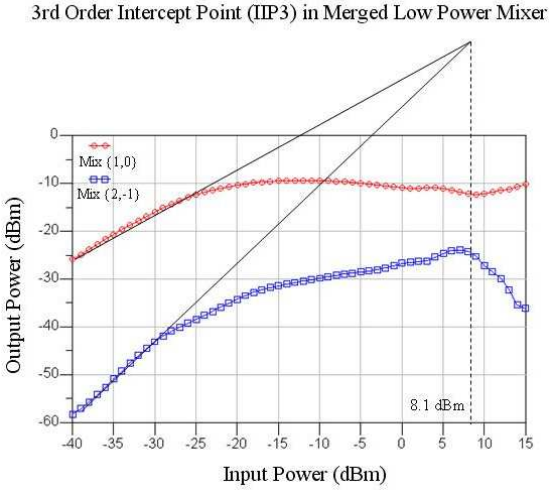

Figure 7: IIP3 of the mixer switching stage.

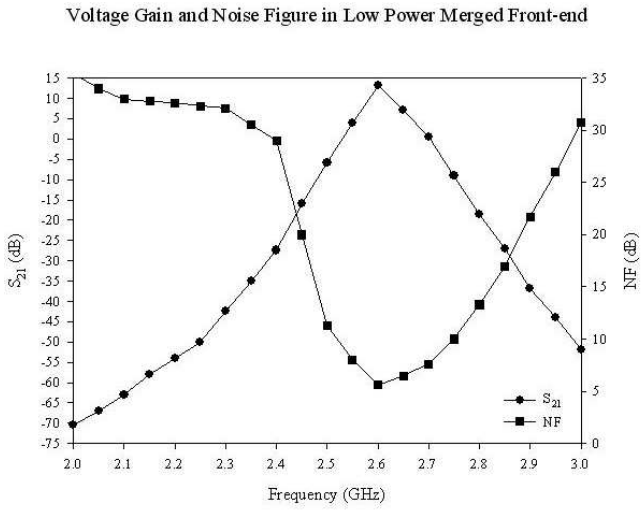

Figure 8: S_{21} and noise figure of MFC LTE 4G handset front-end.

Table 1: Summary of MFC receiver front-end for LTE 4G handset.

LTE Front-End Characteristics	This work	
	2.6 GHz	unit
Supply	1	V
Forward Gain	13.7	dB
Conversion Gain	5.0	dB
$P_{\text{in}-1\,\text{dB}}$	−24.5	dBm
IIP3	−1.67	dBm
Isolation (RF Port)	−27.2	dB
Isolation (LO Port)	−26.4	dB
Isolation (IF Port)	−13.0	dB
Noise Figure	5.6	dB
Power Consumption	1.97	mW

Table 2: Major performance comparisons with previous works.

RF front-end Performance	[4]	[5]	[6]	This work
Frequency [GHz]	2.44	0.9	0.9	2.6
Supply Voltage [V]	1.8	1.8	1.8	1
Voltage Gain [dB]	21.4	15	10	13.7
IIP3 [dBm]	−18	1.5	−5	−1.67
Noise Figure [dB]	13.9	4	3.6	5.6
Power Consumption [mW]	6.4	4.32	3.6	1.97

mixer switching stage is 5 dB and 8.1 dBm as indicated in Figs. 6 and 7, taking only 1.3 mA from a 1.0-V power supply.

In Fig. 8, MFC receiver front-end achieves a forward gain S_{21} of 13.7 dB and a noise figure of 5.6 dB at 100 MHz with 1.97 mA bias current from a 1-V power supply. In order to reduce power consumption, the dc current path from the power supply to the LNA is replaced by a stacked mixer transconductance stage. In this scheme, the LNA operates by only reusing the dc bias current of the stacked mixer. Voltage gain and noise figure of MFC front-end are shown in Fig. 4. The performances of merged folded-cascoded (MFC) front-end for 4G LTE handset are summarized in Table 1. Table 2 lists major performance comparisons with previous works.

3. CONCLUSION

A 2.6-GHz fully integrated CMOS receiver front-end using merged folded-cascoded circuit scheme and a wideband rectangular dielectric resonator antenna are proposed and demonstrated. The antenna provides an impedance bandwidth of 95% for VSWR $\leq$ 2.5. A monopole antenna conformed standard (2.05 $\sim$ 5.8 GHz) characteristics. The proposed front-end improves noise figure and conversion gain by employing a vertically merged LNA and folded-cascoded mixer. The fully integrated 2.4-GHz receiver front-end is fabricated using 0.18 µm CMOS technology, and a voltage gain of 13.7 dB with a noise figure of 5.6 dB is achieved with 1.97 mW power consumption.

ACKNOWLEDGMENT

Authors would appreciate the financial support from National Science Council of Taiwan, NSC 99-2221-E-024-019.

REFERENCES

1. Sulaiman, M. I. and S. K. Khamas, "A singly fed rectangular dielectric resonator antenna with a wideband circular polarization," *IEEE Antennas and Wireless Propagation Letters*, Vol. 9, 2010.

2. Liang, X.-L. and T. A. Denidni, "Cross-T-shaped dielectric resonator antenna for wideband applications," *Electronics Letters*, Vol. 44, No. 20, 2008.
3. Jarvinen, J. A. M., et al., "2.4-GHz receiver for sensor applications," *IEEE J. Solid-State Circuits*, Vol. 40, No. 7, 1426–1433, Jul. 2005.
4. Semiconductor, T., "TQ9203-low current RFIC down converter," *Wireless Communication Products*, 1995.
5. Oh, N. J., S. G. Lee, and J. H. Ko, "A CMOS 868/915 MHz direct conversion ZigBee single-chip radio," *IEEE Commun. Mag.*, Vol. 43, No. 12, 100–109, Dec. 2005.
6. Kwon, I., "A single-chip CMOS transceiver for UHF mobile RFIC reader," *IEEE J. Solid-State Circuits*, Vol. 43, No. 3, 729–738, Mar. 2008.

Design of Elliptical Microstrip Patch Antenna Using ANN

Amit Agrawal, D. Vakula, and N. V. S. N. Sarma
National Institute of Technology, Warangal, India

Abstract— In this paper a novel technique is proposed to design Elliptical microstrip patch antenna using Artificial Neural Networks (ANN) for circular polarization. ANN model is developed to calculate the antenna dimensions for the given resonant frequency, aspect ratio, dielectric constant and height of substrate. ANN is designed using Radial basis function neural network architecture. The results obtained by RBF network are compared with the results of IE3d simulation. The network showed high success rate.

1. INTRODUCTION

Microstrip patch antenna is used for high-performance spacecraft, aircraft, missile and satellite applications, where size, weight, cost, performance, ease of installation, and aerodynamic profile are constraints. These patch antennas are low-profile, conformable to planar and non-planar surfaces, simple and inexpensive to manufacture using modern printed circuit technology. They are also mechanically robust when mounted on rigid surfaces and compatible with MMIC designs. When a particular patch shape and excited mode are selected they are very versatile in terms of resonant frequency, polarization, radiation pattern, and impedance.

In this work Elliptical microstrip patch antennas (EMSA) are the ones under consideration as their geometry presents greater potentials for a variety of electrically small low-profile antenna applications. The elliptical shape has several advantages like providing larger flexibility in the design, more degrees of freedom compared to the circular geometry and circular polarization is achieved with single feed. Elliptical patch geometry is perhaps least analyzed regular shape geometry due to involvement of Mathieu's and modified Mathieu's function in mathematical analysis. The involvement of these functions makes mathematics of elliptical patch geometries extremely difficult. There are various methods available for the calculation of resonant frequency for elliptical patch antenna. These methods obtain resonant frequency for even (f^e) and odd (f^o) modes as the function of input variables, which are the height of the dielectric substrate (h), dielectric constant (ε_r), and antenna dimensions (the major and the minor axis) [2, 3]. But reverse calculation of the antenna dimensions from the inputs like frequencies (f^e, f^o), height (h) and dielectric constant (ε_r) is not available in the literature. In this paper, the antenna dimensions are determined by using Artificial Neural Networks.

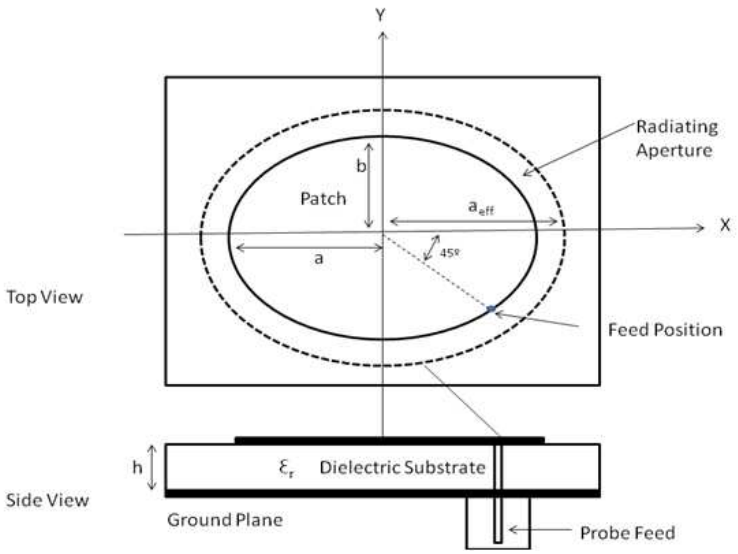

Figure 1: Elliptical microstrip patch antenna for circular polarization.

ANN design aims at utmost simplicity and self-organization. In the present paper radial basis function neural network (RBFNN) are used. The RBFNN architecture is similar to a general feed-forward Back Propagation (FFBP) network. The RBFNN is one of the approaches which show a great promise in this sort of problems because of its faster learning capacity.

2. THEORY

Elliptical patch antenna is shown in Fig. 1, where a is the semi major axis, b is the semi minor axis and a_{eff} is the effective semi-major axis. The feed position is located along the 45° line between the major and minor axis of the elliptical patch. The radiated fields cause two modes that are perpendicular to each other and have equal amplitude, but are 90° out of phase. An elliptical patch antenna with optimum dimensions acts as a Circular Polarized wave radiator [2].

The patch is excited by a coaxial probe extending through the ground plane and contacting the patch as is shown in Fig. 1. The empirical formulas for calculation of dual resonance frequency using approximated Mathieu function [1–3] are listed below.

$$a_{eff} = a\left[1+\frac{2h}{\pi\varepsilon_r a}\left\{\ln\left(\frac{a}{2h}\right)+(1.41\varepsilon_r+1.77)+\frac{h}{a}(0.268\varepsilon_r+1.65)\right\}\right]^{1/2} \quad (1)$$

$$f_{11}^{e,o} = \frac{15}{\pi e a_{eff}}\sqrt{\frac{q_{11}^{e,o}}{\varepsilon_r}} \quad (2)$$

$$q_{11}^{e} = -0.0049e+3.7888e^2-0.7278e^3+2.314e^4 \quad (3)$$

$$q_{11}^{o} = -0.0063e+3.8316e^2-1.1351e^3+5.2229e^4 \quad (4)$$

where

a — Semi-major axis,
h — Height of dielectric substrate,
ε_r — Permittivity of dielectric substrate,
a_{eff} — Effective semi-major axis,
e — Eccentricity of elliptical patch,
$f_{11}^{e,o}$ — Dual-Resonance frequency,
$q_{11}^{e,o}$ — Approximated Mathieu function of the dominant ($TM_{11}^{e,o}$) mode.

3. ANN MODELING

RBFNN has three layers of neurons, namely input, hidden and output, which are fully interconnected as shown in Fig. 2. The first layer is composed of input nodes. The number of nodes, $n$is equal to the dimension of input vector $X = (x_1, x_2, \ldots, x_n)$. The second layer is a hidden layer composed of multivariate Gaussian nonlinear units that are connected directly to all of the input layer nodes. Each neuron in the hidden layer operates as the Gaussian transfer function [4].

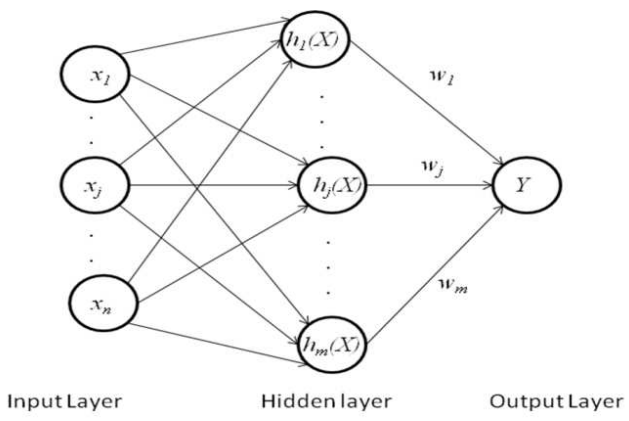

Figure 2: RBF network structure.

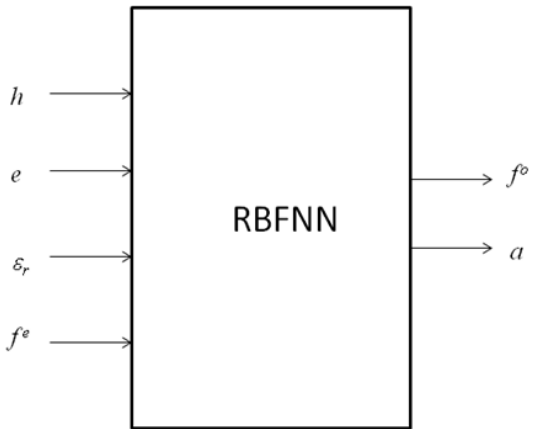

Figure 3: RBFNN model for EMSA.

In order to design RBFNN, network weights are to be found. Finding the RBF weights is called network training. The RBFNN has to be trained with the input $P = (X_1, X_2, \ldots, X_N)$ data and the targets $T = (t_1, t_2, \ldots, t_N)$. By using set of input-output pairs, called training set, the network parameters are optimized in order to fit the network targets to the given inputs. After training, the RBF network can be used with data whose underlying statistics is similar to that of the training set, known as testing set. A trained neural network can be used for high-level design, providing fast and accurate answers to the task it has learned.

In this paper RBFNN is built to obtain antenna dimensions from the function of input variables, which are resonant frequency (f^e), the height of the dielectric substrate (h), dielectric constants of the dielectric material (ε_r) and the eccentricity of elliptical patch (e) as shown in Fig. 3.

4. RESULTS AND ANALYSIS

For the purpose of training and testing, data set is generated by using Equations (1) to (4) mentioned in above theory section. Here data set is generated for two different h values (0.3175 cm and 0.1575 cm) and the eccentricity of elliptical patch is taken as constant value (0.2178) for the purpose of generating circular polarization (i.e., aspect ratio $(b/a) = 0.976$) [2]. Frequency ranges from 1 to 3 GHz. Network topology design contains 4 input nodes and 2 output nodes. ANN models are trained by 75 data sets and tested for 25 data sets and the maximum epochs are 75. Some of the results are shown in tabular form below.

Table 1: For input parameter $-h = 0.3175$ cm, $e = 0.2178$ and $\varepsilon_r = 2.48$.

Input parameter	Targeted Results using equations (1 to 4)		RBFNN Results		% Error	
f^e (GHz)	f^o (GHz)	a (cm)	f^o (GHz)	a (cm)	f^o	a
1.0011	1.0126	5.4192	1.0126	5.4192	0	0
1.4937	1.5108	3.5202	1.5108	3.5202	0	0
1.9989	2.0218	2.5505	2.0218	2.5505	0	0
2.4939	2.5224	1.9848	2.5224	1.9849	0	0.005
2.9075	2.9408	1.6616	2.9421	1.6609	0.044	0.042

Table 2: For input parameter $-h = 0.1575$ cm, $e = 0.2178$ and $\varepsilon_r = 2.48$.

Input Parameter	Targeted Results using equations (1 to 4)		RBFNN Results		% Error	
f^e (GHz)	f^o (GHz)	a (cm)	f^o (GHz)	a (cm)	f^o	a
1.0202	1.0319	5.5000	1.0320	5.4998	0.010	0.004
1.4990	1.5162	3.6818	1.5162	3.6819	0	0.003
2.0015	2.0244	2.7121	2.0244	2.7121	0	0
2.4898	2.5183	2.1465	2.5183	2.1465	0	0
2.9544	2.9883	1.7828	2.9883	1.7827	0	0.006

Table 3: For $e = 0.2178$ and $\varepsilon_r = 2.48$ simulation and RBFNN results are compared.

Input Parameters		Simulation Results Using IE3d		RBFNN Results		% Error	
h (cm)	a (cm)	f^e (GHz)	f^o (GHz)	f^e (GHz)	f^o (GHz)	f^e	f^o
0.3175	5.4192	1.0000	1.0072	1.0011	1.0126	0.110	0.536
0.3157	3.5202	1.5130	1.5130	1.4937	1.5108	1.275	0.145
0.1575	2.7121	1.9970	2.0110	2.0015	2.0244	0.450	0.666
0.1575	2.1465	2.5048	2.5252	2.4898	2.5183	0.598	0.273
0.1575	1.7828	2.9896	2.9896	2.9544	2.9883	1.177	0.043

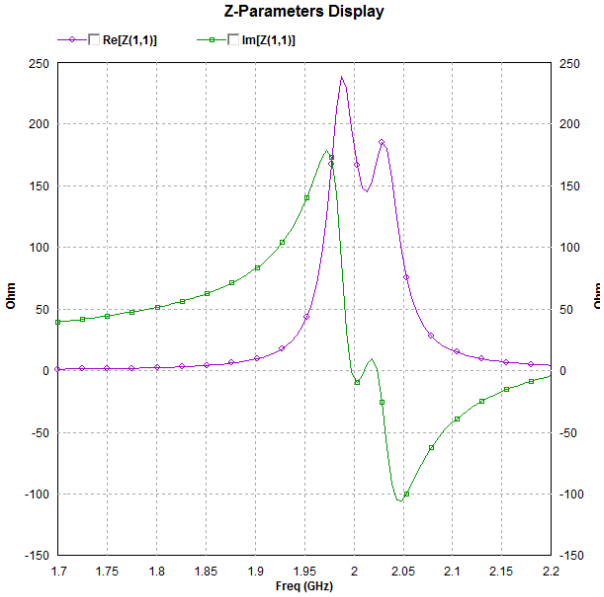

Figure 4: Impedance variation.

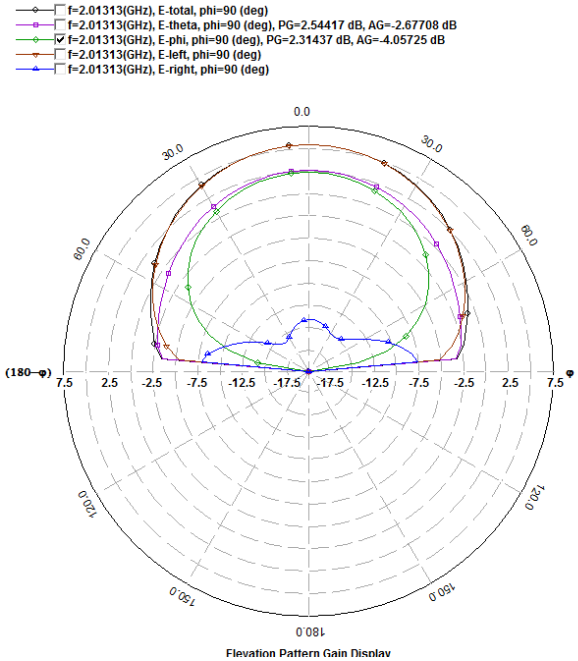

Figure 5: Radiation pattern.

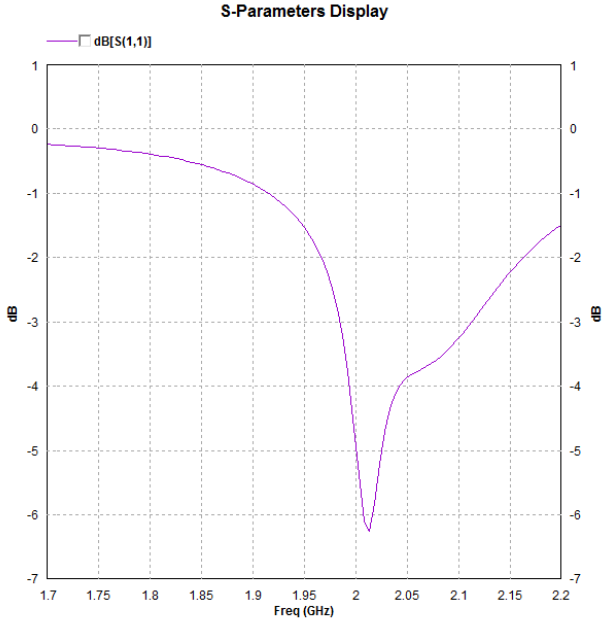

Figure 6: Return loss curve.

Table 1 shows the % error in f^o and a when the inputs to RBFNN are $h = 0.1575\,\text{cm}$, $e = 0.2178$, $\varepsilon_r = 2.48$ and f^e is varying in between 1 to 3 GHz. Table 2 shows the % error in f^o and a when the inputs to RBFNN are $h = 0.3175\,\text{cm}$, $e = 0.2178$, $\varepsilon_r = 2.48$ and f^e is varying between 1 to 3 GHz. Some of the results from Table 1 and Table 2 are compared with IE3d simulation results in Table 3.

For the cases shown in Table 3 impedance variation, return loss, and radiation pattern are simulated using IE3d. A good circular polarization, return loss, and Z parameter curves are observed for all test results. For one of the sample case ($h = 0.1575\,\text{cm}$, $e = 0.2178$, $\varepsilon_r = 2.48$ and $a = 2.7121\,\text{cm}$) the variation of impedance is shown in Fig. 4. The radiation pattern is plotted in Fig. 5. The return loss is indicated in Fig. 6 which shows a loss of $-6.2519\,\text{dB}$ at the frequency 2.013 GHz.

5. CONCLUSION

The results obtained by using RBFNN for elliptical microstrip patch antennas are in good agreement with available targeted results. The proposed network requires less training time and is more accurate in prediction. Using these RBFNN models, various possible dimensions can be obtained to achieve high bandwidth and single feed circular polarization. ANN models are simple, easy to apply and very useful for antenna engineers to predict both patch dimensions and resonant frequency.

REFERENCES

1. Kumprasert, N., "Theoretical study of dual-resonant frequency and circular polarization of elliptical microstrip antennas," *IEEE AP-S International Symposium*, Vol. 2, 1015–1020, July 2000.
2. Long, S. A., L. C. shen, D. H. Schaubert, and F. G. Farrar, "An experimental study of the circular-polarized elliptical printed-circuit antenna," *IEEE Trans. Antennas Propag.*, Vol. 29, No. 1, 95–99, January 1981.
3. Mythili, P. and A. Das, "Simple approach to determine resonant frequencies of microstrip antennas," *IEE Proc. — Microw. Antennas Propag.*, Vol. 145, No. 2, 159–162, April 1998.
4. Zhang, L., B. Soong, A. T. Ho, and J. Ong, "Using RBF algorithm for landcover or clutter classification for mobile planning," *VTC Proceedings IEEE*, Vol. 1, 465–467, May 2000.
5. Mishra, A., G. B. Janvale, B. V. Pawar, and P. M. Patil, "The design of circular microstrip patch antenna by using Quasi-Newtoon algorithm of ANN," *J. Electromagnatic Analysis & Application*, Vol. 2, 444–449, July 2010.

GPS Antenna Design and Measurement

Kuo-Liang Wu[1], **Jwo-Shiun Sun**[1], **Y. D. Chen**[2], **and Guan-Yu Chen**[1]

[1]Department of Electronic Engineering, National Taipei University of Technology, Taiwan
[2]Antenna and EMC Laboratory, HTC Corporation, Taiwan

Abstract— This paper accomplished a GPS band for meander inverted-F monopole antenna structure and easy applied mobile cellular phone application. A meander line antenna has several meander line sections so as to shorten the length from the corresponding monopole antenna in this design. In high performance meander line antenna for GPS and A-GPA applications, where size, profile, and performance are of major considerations, shorter length of antenna are desirable. The measured and simulated data including return loss, antenna gain and radiation patterns are presented.

1. INTRODUCTION

GPS as a satellite-based positioning system operated by the United States Department of Defense was officially put into operation in 1995. Using the difference in the radio signal propagation times of at least three of the 24 GPS satellites, a GPS receiver can accurately determine its position worldwide to within a few meters. Signals for civil use are transmitted at a frequency of 1575.42 MHz and bands. The general GPS functions of PDA support the assisted functionality in 2.5/3G wireless networks. Traditional antennas such as monopoles, dipoles and patches are not suitable to meet the requirements of modern wireless communication and highly demanding mobile GPS systems. As a result, there is the need for alternative approaches to small antenna and high performance design. This paper describes a miniaturized meander shorting monopole for integration in modern GPS wireless systems.

2. ANTENNA DESIGN

The resonance mode of a shorting meander wire antenna (Figure 1) covers the GPS communication bandwidth of 1571.42–1579.42 MHz. The simple wire tuning expansion are introduced to confine the resonance mode region and to facilitate the frequency modes and impedance match expansion easily for antenna and wireless system integration design. This paper proposes meander shorting monopole antenna design for single-band GPS wireless communications, especially for PDA and Smart mobile phones. The single-frequency design for mobile handset mainly utilizes meander line to excite radiation mode. By tuning the dimensions of meander line, the VSWR ratio of the antenna's resonance frequency can be achieved to 2, which makes it very promising for GPS and A-GPS operations.

3. MEASUREMENTS

The design requirements for GPS antenna is combined into multiple objective goals, such as simplicity of the antenna geometry, radiation pattern, return loss (Figure 2), antenna impedance (Figure 3) and polarizations. This design in general to a mobile communication apparatus and global positioning system antenna, and more particularly to a mobile communication system, which utilizes a small-scale metal for the GPS antenna design. In this paper, the experiment setup has done [1, 2]. The phase of the two field components is measured relative to the signal generator, and a double ridge horn serves as a source antenna. Equations (1) and (2) may be expan [3, 4] to give simple expressions that can be inserted into data logging software to provide a direct conversion from dual linear to RHCP and LHCP at each measurement angle.

$$E_{RHCP} = \frac{1}{\sqrt{2}}(E_H + jE_V) \tag{1}$$

$$E_{LHCP} = \frac{1}{\sqrt{2}}(E_H + jE_V) \tag{2}$$

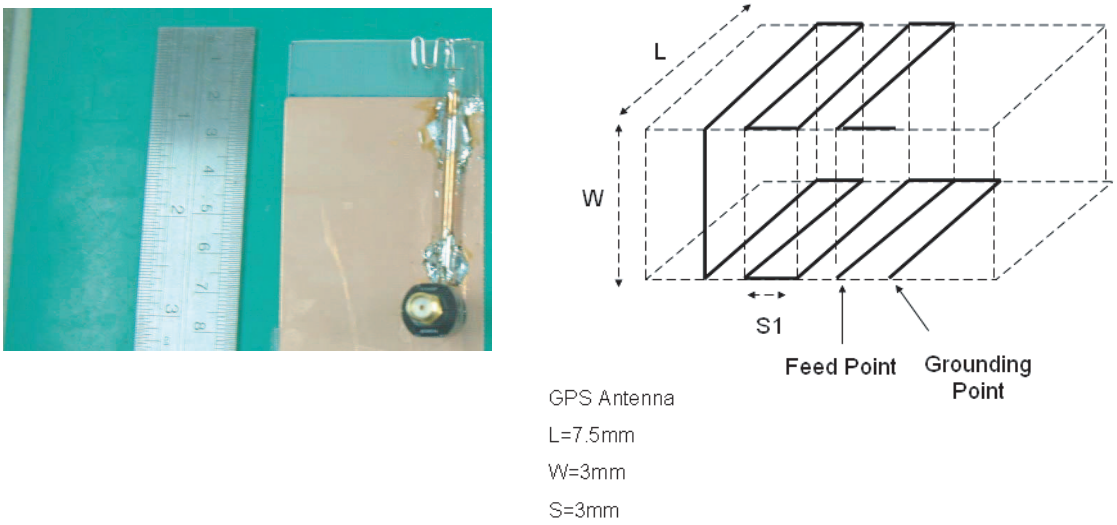

Figure 1: The proposed GPS antenna.

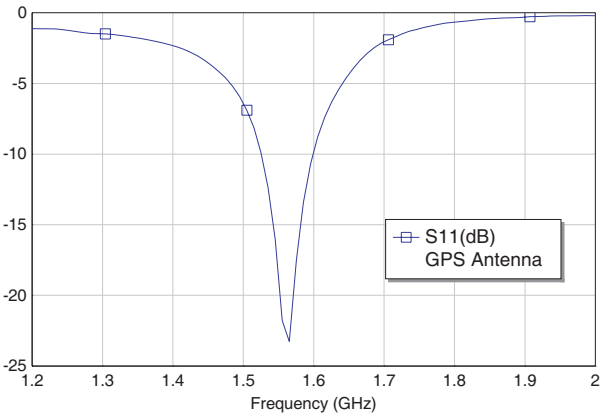

Figure 2: The measured GPS antenna of S_{11}.

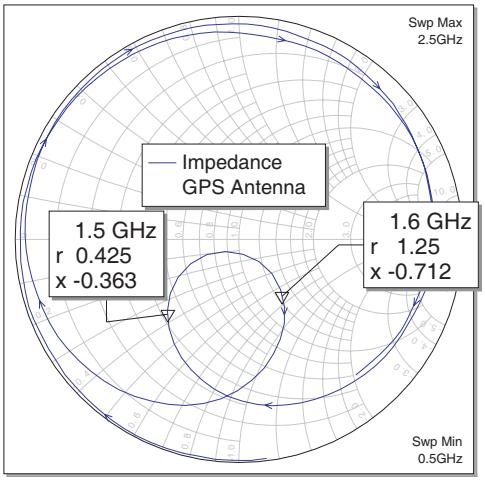

Figure 3: The measured GPS antenna of impedance.

4. RESULTS

This article describes a low profile, compact, meander loaded monopole antenna with single feed. A shorting type monopole is used to enhance the impedance matching. This provides a low radiation resistance within the GPS band. Shorting meander inverted-F monopole antenna leads to a middle gain. In addition, the meander loading also permits the antenna's height and to be reduced antenna size. This antenna also offers a characteristic of high radiation efficiency. Antenna bandwidth (1.52 GHz to 1.6 GHz) was experimentally obtained for a return loss −10 dB. In well known antenna design techniques a matching structure is typically employed to provide matching between the antenna and the GPS circuitry for efficient transfer of energy.

5. CONCLUSIONS

In this paper, a compact and low profile internal meander wire monopole antenna for single band has been proposed. This antenna was designed and measured. A good agreement between measurement and analysis has been obtained. The proposed antenna shows a suitable operating bandwidth and it easy to cover the GPS for location wireless operation and operation of a mobile handset phone, co-design, co-integration, GPS OTA [5–7] and application operations.

ACKNOWLEDGMENT

The authors acknowledge the Antenna and EMC Department of HTC, Taiwan for sport the wireless technique and measurement environment.

REFERENCES

1. Chen, G. Y., J. S. Sun, S. Y. Huang, Y. D. Chen, C. H. Lin, and J. Y. Yang, "Mobile handset measurement for wireless system networking," *2006 China-Japan Joint Microwave Conference (2006 CJMW)*, 698–701, Chengdu, China, Aug. 2006
2. Chen, G. Y., J. S. Sun, and Y. D. Chen, "The 3D far-field antenna measurement technology for radiation efficiency, mean effective gain and diversity antenna operation," *2006 The 7th International Symposium on Antennas, Propagation, and EM Theory (2006 ISAPE)*, 42–45, Guilin, China, Oct. 2006.
3. Kraus, J. D. and R. J. Marhefka, *Antennas for all applications*, McGraw-Hill, 2002.
4. Toh, B. Y., R. Cahill, and V. F. Fusco, "Understanding and measuring circular polarization," *IEEE Transactions on Education*, Vol. 46, No. 3, 313–318, Aug. 2003.
5. Chen, G. Y., J. S. Sun, K. Chang, and Y. D. Chen, "Antenna pattern measurement," *PIERS Proceedings*, 331–333, Beijing, China, Mar. 23–27, 2009.
6. Chen, G. Y., J. S. Sun, C. H. Lin, K. K. Tiong, and Y. D. Chen, "Small antenna measurement facilities," *PIERS Proceedings*, 157–158, Hangzhou, China, Mar. 24–28, 2008.
7. Chen, G. Y., C. H. Lin, J. S. Sun, K. K. Tiong, and Y. D. Chen, "3D far-field antenna scanning technique apply to radiation efficiency and mean effective gain measurement," *IEEE TENCON 2007*, 113, Taipei, Taiwan, Oct. 2007.

A Novel Fractal Patch Antenna for UWB Applications

Xue-Yong Zhang, **Shao-Bin Liu**, **Chun-Zao Li**, **Bo-Rui Bian**, **and Xiang-Kun Kong**
College of Electronic and Information Engineering
Nanjing University of Aeronautics and Astronautics, Nanjing 210016, China

Abstract— A novel fractal antenna is proposed for ultra-wideband (UWB) systems. We introduce a three-stage Sierpinski fractal geometry as the radiating element. The proposed antenna has compact dimension of 15 mm × 20 mm × 1.6 mm. The designed antenna has a wide bandwidth of more than 8.6 GHz (2.5–11.1 GHz) for a return loss of less than 10 dB. Also, the proposed antenna gives bidirectional pattern in the E plane and omni directional radiation pattern in the H plane over its whole frequency band of interest. In the paper, some parametric studies on the effect of the antenna on return loss are also done. So, the proposed antenna is considered a good candidate for UWB applications.

1. INTRODUCTION

Ultra-wideband (UWB) communications systems have been investigated and developed over the last few years. The FCC first approved rules for the commercial use of UWB in February 2002. By April of that year, the FCC gave formal approval for the unlicensed use of the technology between 3.1 and 10.6 GHz. The technology promises high-speed transmission rate for short-range, lower power consumption, simpler hardware configuration in communication applications such as RFID devices, sensor networks, radars and location tracking. Although antenna designers have study the technology a lot in recent years, they have remained one of the highest researches challenges for improving their performance. Nowadays, several UWB antennas have been designed for PCMCIA cards in laptop computers for spatial diversity which were so large that they can't be used. Therefore, in order to solve this key issue in UWB antenna design, the size of antennas should be reduced. Consequently recent UWB antenna development tends to focus on miniaturized size, working at the frequency band of UWB systems. Fractal geometry has been proved as an alternative design method to design miniature antennas.

In this paper, we propose a microstrip patch antenna embedded with a Sierpinski fractal geometry, which exhibits a large size reduction. The size reduction is achieved by increasing the electrical length of the antennas. In other words, the surface current is redirected so that it has to take a longer path length on the microstrip patch. By using this concept, higher fractal iteration is implemented on the patch antenna to further increment its surface currents path length. A three-stage Sierpinski fractal geometry is introduced as a radiating element. The patch is fed by a microstrip feed line, and this novel antenna has a good matching to 50 ohms at the frequency of UWB systems. Besides having good electrical behavior at the frequency band of 3.1–10.6 GHz, the new antenna achieves the purpose of miniaturization. The results show that a new design method provides sufficient antenna performances such as wide impedance bandwidth and omnidirectional radiation pattern.

2. ANTENNA DESIGN AND GEOMETRY

We consider the design of a novel UWB antenna. The structure of the antenna is shown in Fig. 1, It is printed on a 1.6 mm-thick substrate, dielectric $er = 4.4$ with the size of $W \times L = (15 \times 20)\,\mathrm{mm}^2$, the radiating element consists of a three-stage Sierpinski fractal geometrythe side lengths of the triangles $t_1 = 8\,\mathrm{mm}$, $t_2 = 5.89\,\mathrm{mm}$, $t_3 = 2.43\,\mathrm{mm}$, $t_4 = 1.47\,\mathrm{mm}$. The antenna is fed by a microstrip line for a 50 ohms characteristic impedance of the feedline, the width of the feedline $w_1 = 0.75\,\mathrm{mm}$, $w_2 = 3.00\,\mathrm{mm}$, the length of feedline $f = 5.40\,\mathrm{mm}$.

The finite length ground plane W has an area of $W \times H = (15 \times 5.3)\,\mathrm{mm}^2$. The wide bandwidth and wide impedance matching with reduced size of the antenna is achieved due to resultant of different magnetic currents of the structure.

3. RESULTS AND ANALYSIS

The optimal parameter values of the antenna are listed in part II. The simulated return loss of the proposed antenna is shown in Fig. 2, which clearly indicates that the impedance bandwidth of the

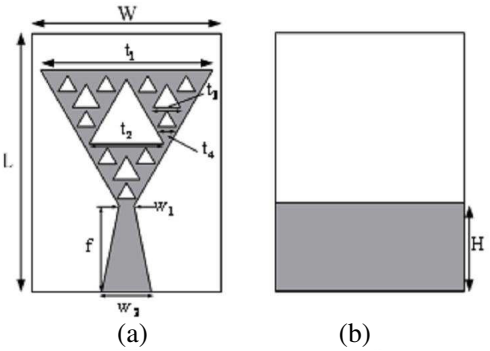

Figure 1: Top and bottom layer view of the UWB antenna: (a) front side view; (b) rear side view.

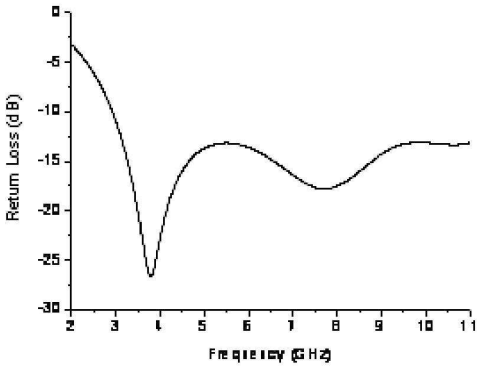

Figure 2: Simulated return loss of the proposed UWB antenna.

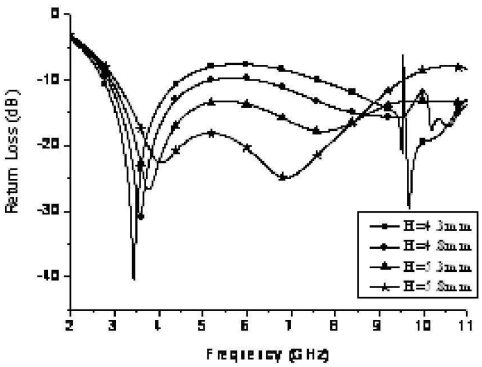

Figure 3: Simulated return loss for different height of ground plan.

antenna covers the frequency range of 3.1 GHz–10.6 GHz for return loss less than 10 dB. The ultra wideband is due to multiple resonances introduced by the three-stage Sierpinski geometry.

A further analysis is carried out to determine the effect of antenna parameters on the input matched bandwidth. The antenna parameters studied are those most likely to be modified in the case of integrating the antenna with other multilayer devices.

The parametric analysis of the antenna is carried out by varying one parameter and keeping other parameters constant. Fig. 2 displays the simulated return loss for different height of ground plane ($H = 4.3$, 5.8, 5.3 and 5.8 mm). The responses clearly illustrate that as the height of ground plane increases, the impedance matching becomes poorer at the higher frequencies and slight shift in resonant frequency takes place. If the height value is decreased, the response over the frequency range of 5 GHz–7 GHz becomes poorer. Hence, it is concluded that the height of ground plane is one of the parameters that affects the impedance matching. It is also found that the optimal value for this case is 5.3 mm.

The width and length of the feedline are also important parameters to control the resistive part of the antenna impedance. Fig. 4 depicts the effect of bandwidth for different length of the feedline ($f = 3.4$ mm, 4.4 mm, 5.4 mm and 6.4 mm), which discloses the profiles of the impedance matching. It is observed that the input match is sensitive to change the length of feedline, especially at higher frequencies. The optimal value for this case is 5.4 mm.

Figure 5 shows the simulated return loss varying by the width of feedline, which is more susceptible parameters for the input impedance. It is found that as the parameter w_2 increases, although we have better impedence match at low frequency, the return loss get worse over the frequency range of 5 GHz–7 GHz. After optimization, the width for the optimized design is 3.0 mm.

From the spectrum of impedance performance, it can be seen that there are two resonances around the frequencies at 4 and 8 GHz. These resonances correspond to the different modes of field distribution and play important roles on the explanation of the radiation patterns. The electric field distributions of these resonant modes are then simulated and the correspondent radiation patterns are investigated at 4 GHz, 8 GHz and 10 GHz, as shown in Fig. 6. From an overall view of

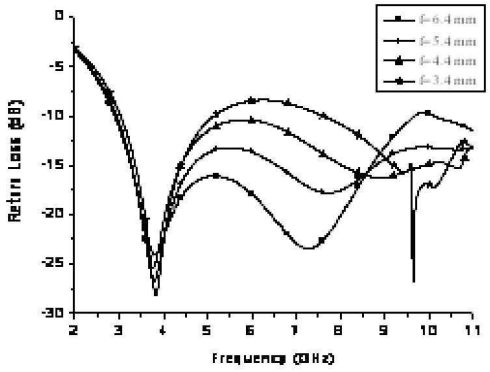

Figure 4: Simulated return loss for different length of the feedline.

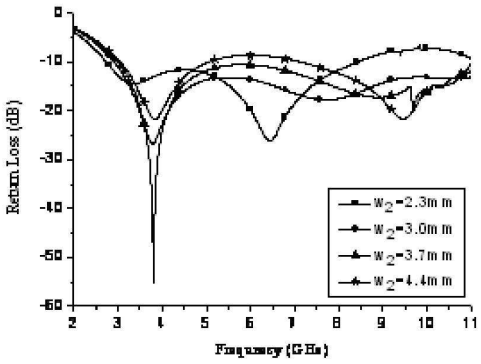

Figure 5: Simulated return loss of the width of feedline.

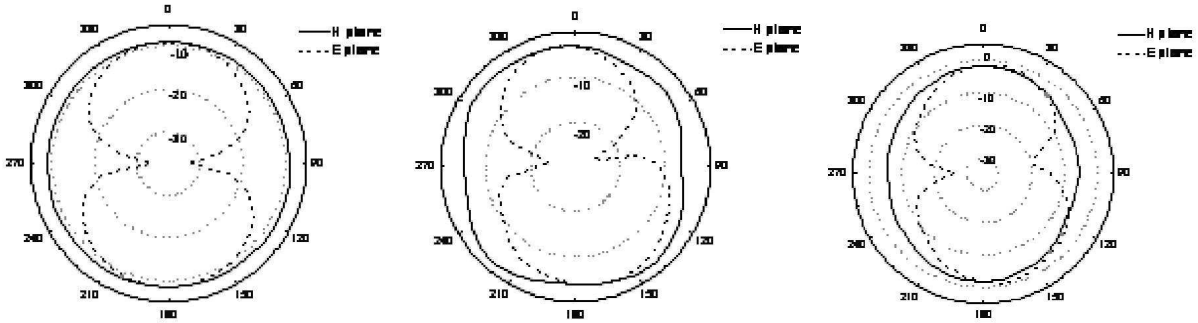

(a) (b) (c)

Figure 6: Simulated radiation patterns for the proposed antenna at: (a) 4 GHz; (b) 8 GHz; (c) 10 GHz.

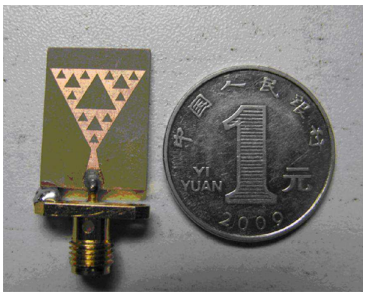

Figure 7: The picture of the proposed antenna.

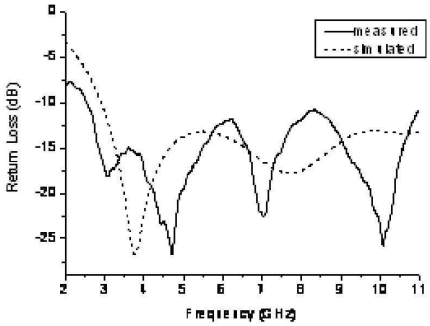

Figure 8: The simulated and measured return loss for the proposed antenna.

these radiation patterns, the antenna behaves quite similarly to the typical printed monopoles. The E-plane patterns are bidirectional, and the H-plane patterns are almost omnidirectional. However, the H-plane pattrens become more directive in the higher band. This is because the finite ground plane radiates more electromagnetic waves at higher frequencies so as to deteriorate the radiation patterns more significantly.

Figure 7 shows the photo of a UWB antenna. In the measurement, a 50 ohms SMA is connected to the end of the feeding strip and grounded to the edge of the ground plane. The performance of the proposed antenna is measured using the Agilent N5230A network analyzer. Fig. 8 shows the simulated and measured return loss of the proposed antenna. It is noticed that the return loss is less than 10dB at the frequency of 3.1–10.6 GHz, which meets the requirements of UWB technology.

4. CONCLUSION

A novel monopole antenna was designed for ultra wideband operation. The proposed antenna has compact dimension of 15 mm × 20 mm × 1.6 mm, In order to cover the required bandwidth from 3.1 to 10.6 GHz, the antenna is constructed using a three-stage Sierpinski fractal as the radiating patch. The measured 10 dB return loss bandwidth of the proposed antenna ranged from 2.5 to 11.1 GHz. The antenna had nearly omni-directional radiation patterns over the entire UWB frequency band. Also In the proposed paper, some parametric studies on the effect of the antenna on return loss are done. One can conclude that the designed antenna could be used for a variety of wireless services.

ACKNOWLEDGMENT

This work was supported in part by the supports from the Chinese Natural Science Foundation (Grant No. 60971122), in part by the Aviation Science Foundation (Key project 2009ZA52008) and in part by the Open Research Program in China's State Key Laboratory of Millimeter Waves (Grant No. K201103).

REFERENCES

1. Jones, E., "Measured angle-diversity performance of the wire-grid lens antenna," *IEEE Trans. Antennas Propagat.*, 484–486, May 1967.
2. Wong, K. L., S. W. Su, and Y. L. Kuo, "A printed ultra-wideband diversity monopole antenna," *Microwave Opt. Techno. Lett.*, Vol. 38, No. 4, 257–259, 2002.
3. Ammann, M. J. and Z. N. Chen, "Wideband monopole antenna formulti-band wireless systems," *IEEE Antennas Propag. Mag.*, Vol. 45, No. 2, 146–150, Apr. 2003.
4. Bao, X. L. and M. J. Ammann, "Printed UWB antenna with coupledslotted element for notch-frequency function," *Int. J. Antennas Propagat.*, Vol. 2008, 1–7, 2008.
5. Ding, Y., G.-M. Wang, and J.-G. Liang, "Compact band-notched ultrawidebandprinted antenna," *Microw. Opt. Technol. Lett.*, Vol. 49, 2686–2689, Nov. 2007.
6. Puente, C., J. Romeu, R. Pous, and C. Cardama, "On the behavior of the Sierpinski multiband antenna," *IEEE Trans. Antennas Propagat.*, Vol. 46, 517–524, Apr. 1998.
7. Anguera, J., C. Puente, and C. Borja, "A procedure to design stacked microstrip patch antenna based on a simple network model," *Microw. Opt. Technol. Lett.*, Vol. 30, No. 3, 149–151, Aug. 2001.
8. Ooi, B.-L., "A modified contour integral analysis for Sierpinski fractal carpet antennas with and without electromagnetic band gap ground plane," *IEEE Trans. Antennas Propagat.*, Vol. 52, 1286–1293, May 2004.
9. Song, C. T. P., P. S. Hall, and H. Ghafouri-Shiraz, "Perturbed sierpinski multiband fractal antenna with improved feeding technique," *IEEE Trans. Antennas Propagat.*, Vol. 51, 1011–1017, May 2003.
10. Behdad, N. and K. Sarabandi, "A wideband bi-semicircular slot antenna," *Proc. Dig. 2004 IEEE Antennas and Propagation Society*, 1903–1906, Jun. 2004.
11. Wi, S. H., Y. S. Lee, and J. G. Yook, "Wideband microstrip patch antenna with U-shaped parasitic elements," *IEEE Trans. Antennas Propagat.*, Vol. 55, No. 4, 1196–1199, Apr. 2007.

WLAN Antenna Design and Measurement

Chien-Pang Chou[1], **Jwo-Shiun Sun**[1], **Y. D. Chen**[2], **and Guan-Yu Chen**[1]

[1]Department of Electronic Engineering, National Taipei University of Technology, Taiwan
[2]Antenna and EMC Laboratory, HTC Corporation, Taiwan

Abstract— A high performance monopole antenna (Figure 1) fabricated using a folded wire line with loading effect as radiator is presented. A prototype of the proposed monopole antenna with a compact area size of 19.5 mm × 6 mm is implemented, and the multi-band WLAN antenna shows a wide operating bandwidth of about 560 MHz and 3550 MHz for low band and high band, bandwidth, making it easy to cover the IEEE 802.11a, IEEE 802.11b, IEEE 802.11g and IEEE 802.11n (MIMO) bands for wireless communication and future 4G wireless operation of a mobile VoIP/VoWLAN handset phone.

1. INTRODUCTION

The Institute of Electrical and Electronics Engineers (IEEE) has defined the most important characteristics of wireless LAN in the 802.11a, 802.11b, 802.11g and 802.11n group of standards of wireless network communication. Data is transmitted predominantly in the radio frequency range 2.4 GHz and 5 GHz. In this implement, the study mainly focuses on the current trends in development of compact and low profile multi-media PDA and smart mobile phone and provides a wideband monopole antenna design suitable for application in wireless LAN communicating system in the near future. By utilizing the monopole antenna structure, the proposed antenna design is easy to be embedded into the mobile phone co-integration operation. Some antenna structures [1] to satisfy specific bandwidth specifications for modern wireless LAN communication systems such as IEEE 802.11a (5.15–5.35 GHz and 5.47–5.825 GHz), IEEE 802.11b (2.4–2.485 GHz), IEEE 802.11g (2.4–2.485 GHz) and IEEE 802.11n (2.4–2.485 GHz, 5.15–5.35 GHz and 5.47–5.825 GHz) have been implemented and developed. Antennas [2, 3] that can be easily integrated on the RF circuit board and module of a wireless device for wireless consumer electronics operations has been reported recently. In this implement, the study mainly focuses on the current trends in development of compact and low profile Wi-Fi PDA and smart mobile phone and provides a wideband monopole antenna design suitable for application in wireless LAN communicating system in the near future. In this design, the innovative monopole antenna for single fed to excite dual radiator path is presented. These proposed antennas can find applications in wireless LAN IEEE 802.11a/b/g/n and VoIP/WiFi wireless systems application. The design of a dual wideband monopole antenna with dual path of folded wire and loading radiator with applications for wireless VoIP and VoWLAN uses is investigated. With the broadside radiations, the proposed dual wideband monopole antenna carries a stable gain variation in the 2.4–2.5 GHz and 5–6 GHz bands, respectively.

2. ANTENNA DESIGN

An internal small antenna usually suffers from degradation in performance of narrow bandwidth and radiation efficiency. In this experiment, we design [4–7] and fabricate a dual broadband interior type wire monopole with a high performance radiation pattern over a design operation band using dual path, as shown in Figure 1. It has a measured return loss bandwidth (referenced −6 dB) about 560 MHz with center frequency at 2.35 GHz (2.02–2.56 GHz) and 3500 MHz with center frequency at 5.42 GHz (4.525–8.095 GHz), as shown in Figure 2. With the rapid growth of mobile Wi-Fi technique, wireless communication devices are more mini-size and had multi-band wireless functions. In this paper, the dual wideband monopole antenna has several advantages over conventional monopole-like antenna and planar antenna for mobile handsets. The small compact and low profile antenna radiator structure such as the wire monopole antenna with loading that can be mounted on the portable equipment are becoming very attractive for the VoIP and VoWLAN communications application. In this design, we designed a novel compact internal wire monopole antenna with loading effect for multi-band operation covering the IEEE 802.11a/b/g/n and Bluetooth co-existed bands and applications. In this design, multi-band monopole antenna for Wireless LAN antenna device applications is proposed. This kind of folded wire monopole antenna co-design can overcome the narrow bandwidth problem that happens to the conventional patch antenna; in

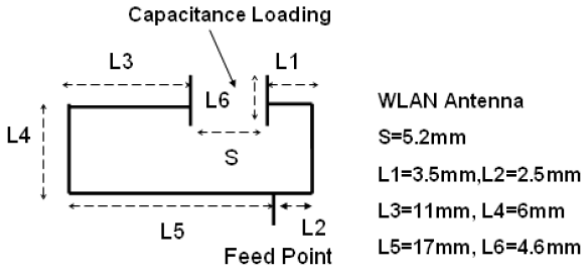

Figure 1: Dual wideband monopole antenna with capacitance-loading.

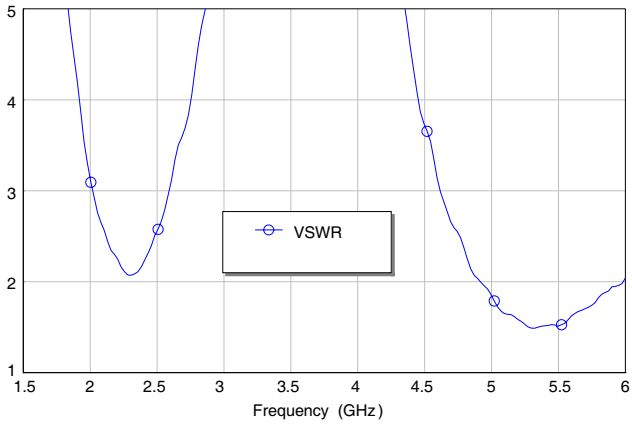

Figure 2: Measured data of VSWR.

practical application, when electronic components are placed very close to the conventional antenna, large degradation of the antenna performance will occur. In the proposed wire antennas, by adding a low-Q resonator factor as a wideband radiator design, antenna coupling between the low band and high band radiator can be improved and enhanced antenna bandwidth. We present an innovative wire monopole antenna suitable for application as an internal antenna co-integration on mobile PDA handheld. The proposed dual monopole antenna is designed on a practical PCB size (100 mm × 60 mm), which serves as a support for the monopole, and has a radiator compact size of 19.5 mm × 6 mm. The proposed wire monopole is formed by two wire line. This long folder wire line radiator has a total length of about $(L3 + L4 + L5 + L6/2)$, which excited low band antenna bandwidth of the wire monopole antenna. The short metal patch radiator has a total length of about $(L1 + L2 + L4 + L6/2)$, which excited high band antenna bandwidth of monopole antenna. With the finite dimensions of the folded wire monopole antenna in this design, the total length of the effective radiator wire path of the antenna is close to one quarter wavelength at free space of the center frequency of low band and high band, the low band resonant frequency of the long wire radiator occurs at about 2350 MHz center frequency and high band resonant frequency of the short wire radiator occurs at about 5420 MHz center frequency. In addition, by fine-tuning the length of the wire length of the long and short radiator, the antenna resonant frequency of the bandwidth can be effectively controlled, but antenna multi-coupling effect for multi-interference by long folded wire so the antenna resonant frequency has affected with each other.

3. RESULTS

A 50 Ω semi-rigid RF cable is used to feed the monopole folded wire antenna with loading effect, and is co-design and co-testing on the same PCB board. The feeding network is a wideband 50 Ω low loss RF cable as probe. The PCB material is metal conductor and dielectric substrate with the thickness 1 mm and relative permittivity 4.6. The dual wideband impedance bandwidth is easily to apply practical PDA handset for VoIP/Wi-Fi application and wireless system integration and easily to fine tuning the antenna and RF circuit matching interface. The operating bandwidths of the proposed antennas can cover the 2.4/5.2/5.8 GHz WLAN bands, and the antenna gain is about larger than 2–3 dBi in the 2.4 GHz and 5 GHz full bands; respectively. Besides, they can also

Table 1: Measured gain data.

Frequency (MHz)	2400	2440	2480	2500	5000
Gain (dBi)	2.6	2.9	2.8	2.9	3.8
Frequency (MHz)	5200	5400	5600	5800	6000
Gain (dBi)	3.9	3.6	3.8	3.7	3.9

generate the good radiation patterns in the azimuth plane and good antenna performance has been obtained. Based on the antenna measurement system [8–10] and coordinates for H-plane, $E1$-plane and $E2$-plane. The measured data as shown in Table 1.

4. CONCLUSIONS

In this paper, a compact and low profile internal folded wire monopole antenna with loading effect for multi-bands has been proposed. This antenna was designed and measured. A good agreement between measurement and analysis has been obtained. The proposed antenna shows a wider operating bandwidth and it easy to cover the IEEE 802.11a, IEEE 802.11b, IEEE 802.11g and IEEE 802.11n bands for wireless communication and 4G wireless multimedia operations of a mobile handset phone, co-design, co-integration and application.

ACKNOWLEDGMENT

The authors acknowledge the Antenna and EMC Department of HTC, Taiwan for sport the wireless technique and measurement environment.

REFERENCES

1. Wong, K. L., *Planar Antennas for Wireless Communication*, John Wiley & Sons, Inc., 2003.
2. Balanis, C. A., *Antenna Theory*, John Wiley & Sons, Inc., 1997.
3. Kraus, J. D. and R. J. Marhefka, *Antennas for All Applications*, McGraw-Hill, 2002.
4. Chou, C. P., G. Y. Chen, J. S. Sun, and Y. D. Chen, "Wideband WLAN antenna design for PDA operation," *The 8th WSEAS International Conference on Applied Electromagnetics, Wireless and Optical Communications (ELECTRO'10)*, 29–32, Penang, Malaysia, Mar. 23–25, 2010.
5. Lo, C. M., K. L. Wu, J. S. Sun, and G. Y. Chen, "Helical antenna design and measurement for cellular phone operation," *The 10th WSEAS International Conference on Applied Informatics and Communications (AIC'10)*, 181–184, Taipei, Taiwan, Aug. 2010.
6. Lin, C. H., K. K. Tiong, J. S. Sun, Y. D. Chen, and G. Y. Chen, "A compact internal planar antenna with a capacitive tuner for 3G and 4G mobile phone application," *The 10th WSEAS International Conference on Applied Informatics and Communications (AIC'10)*, 185–187, Taipei, Taiwan, Aug. 2010.
7. Wen, S. H., K. L. Wu, J. S. Sun, and G. Y. Chen, "Novel Wi-Fi antenna design and measurement," *The 10th WSEAS International Conference on Applied Informatics and Communications (AIC'10)*, 99–102, Taipei, Taiwan, Aug. 2010.
8. Chen, G.-Y., J.-S. Sun, K. Chang, and Y. D. Chen, "Antenna pattern measurement," *PIERS Proceedings*, 331–333, Beijing, China, Mar. 23–27, 2009.
9. Chen, G.-Y., J.-S. Sun, C.-H. Lin, K.-K. Tiong, and Y. D. Chen, "Small antenna measurement facilities," *PIERS Proceedings*, 157–158, Hangzhou, China, 2008.
10. Chen, G. Y., C. H. Lin, J. S. Sun, K. K. Tiong, and Y. D. Chen, "3D far-field antenna scanning technique apply to radiation efficiency and mean effective gain measurement," *IEEE TENCON 2007*, 113, Taipei, Taiwan, Oct. 2007.

Cellular Antenna Design and Measurement

Chien-Pang Chou[1], **Y. D. Chen**[2], **Jwo-Shiun Sun**[1], **and Guan-Yu Chen**[1]

[1]Department of Electronic Engineering, National Taipei University of Technology, Taiwan
[2]Antenna and EMC Laboratory, HTC Corporation, Taiwan

Abstract— A high performance monopole antenna is designed. A prototype of the proposed monopole antenna with a compact area size is implemented, and the antenna shows a wide operating bandwidth for low band and high band bandwidth, making it easy to cover the GSM, EDGE, CDMA, CDMA 2000, W-CDMA and UMTS band for wireless communication and 2.5G/3G dual mode operation of a mobile handset phone.

1. INTRODUCTION

Mobile antenna that can be easily integrated on the RF circuit board and module of a wireless device for wireless consumer electronics operations has been reported recently. Some antenna structures [1, 2] to satisfy specific bandwidth specifications for modern wireless cellular communication systems such as GSM (824–894 MHz), EGSM (880–960 MHz), DCS (1710–1880 MHz), PCS (1850–1990 MHz), CDMA Cellular (824–894 MHz) and CDMA PCS (1750–1990 MHz) have been implemented and developed. Mobile communications have progressed very speedily and many mobile terminals are required small dimensions and compact size then to meet the miniaturization requirement and are very capable quality for satisfying concerns of antenna design. In this paper, monopole antenna analysis [3, 4] and design in practical PDA handset size for experiment is implemented. Frequency characteristics and antenna input impedance optimized with various design parameters are analyzed and measured. Designed internal monopole antenna on the handset is simulated and measured. And the internal monopole antenna attached on the handset is tested for far-field antenna anechoic chamber. And a result of the external monopole antenna bandwidth is referenced −6 dB return loss and bandwidth cover 922–1010 MHz and 1560–2360 MHz, respectively. So the internal folded wire and metal path monopole antenna has a wider antenna bandwidth in comparison with traditional external monopole antenna. The proposed antenna, therefore, has advantages to meet wider bandwidth requirements, easy fabrication, matching tuning, and radiation pattern control by wire and metal patch radiator.

2. ANTENNA DESIGN

In this paper, the folded wire and metal patch co-design monopole antenna has several advantages over conventional monopole-like antenna and planar antenna for mobile handsets. In this antenna design, the wire and metal patch monopole antenna must consider radiator, antenna input impedance and radiation polarization for specific absorption rate issue. In this design, we designed a novel compact internal monopole antenna for multi-band operation covering the GSM, DEGE, CDMA, CDMA 2000, W-CDMA and UMTS bands and application. We present an innovative monopole antenna (Fig. 1) suitable for application as an internal antenna in a 2.5G and 3G mobile handset. The proposed dual path monopole antenna (Figure 1) co-design is designed on a practical PCB size (100 mm × 60 mm), which serves as a support for the monopole, and has a radiator compact size of 40 mm × 10 mm × 10 mm. The proposed monopole is formed by two folded wire line and metal patch. This long folded wire line radiator has a total length, which excited low

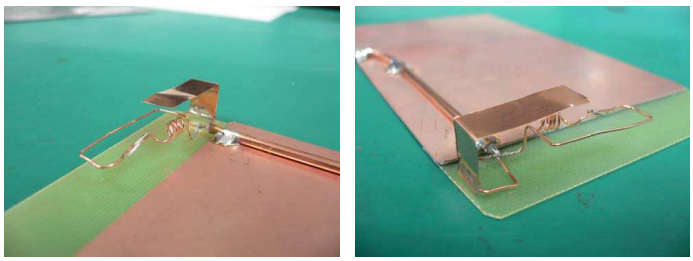

Figure 1: Dual wideband monopole antenna design.

band antenna bandwidth of the wire monopole antenna. The short metal patch with wire line radiator has a length, which excited high band antenna bandwidth of the monopole antenna. With the finite dimensions of the folded wire monopole antenna in this design, the total length of the effective radiator wire path of the antenna is close to one quarter wavelength at free space of the center frequency of low band and high band, the low band resonant frequency of the long wire radiator occurs at about 960 MHz center frequency and high band resonant frequency of the short wire radiator occurs at about 1980 Hz center frequency.

3. RESULTS

Figure 2 shows the VSWR data of the proposed antenna structure. We used PCB (100 mm × 60 mm) for practical PDA phone size. A 50 semi-rigid RF cable is used to feed the monopole antenna, and is co-design and co-testing on the same PCB board. The feeding network is a wideband 50 Ω low loss RF cable as probe. The PCB material is metal conductor and dielectric substrate with the thickness 1 mm and relative permittivity 4.6. The main radiator part of the wire antenna is to approach ground plane spacing about 5 mm. These two wider resonant frequencies of wire and patch monopole antenna, has a wider antenna impedance bandwidth, thereby making it possible that the resonant frequencies of the antenna be tuned to occur, respectively, at bandwidth (reference VSWR = 3) about 922–1010 MHz and 1560–2360 MHz. The dual wideband radiator in this monopole antenna structure, the operating impedance bandwidth for the further wireless

Table 1: Measured antenna directivity, gain, and efficiency.

Frequency (MHz)	800	850	900	950
Directivity (dBi)	3.41	3.83	3.31	4.26
Gain (dBi)	−2.38	−2.25	−1.21	0.12
Efficiency (dB)	−5.79	−6.08	−4.52	−4.14
Efficiency (%)	26.38	24.64	35.33	38.59

Frequency (MHz)	1000	1500	1600	1700
Directivity (dBi)	3.51	5.35	4.06	4.32
Gain (dBi)	1.28	4.02	3.59	3.88
Efficiency (dB)	−2.23	−1.33	−0.47	−0.44
Efficiency (%)	59.89	73.56	89.74	90.3

Frequency (MHz)	1750	1800	1850	1900
Directivity (dBi)	4.37	4.66	4.32	4.5
Gain (dBi)	4.46	4.61	4.55	4.98
Efficiency (dB)	0.09	−0.05	0.23	0.48
Efficiency (%)	102.19	98.87	105.42	111.64

Frequency (MHz)	1950	2000	2150	2200
Directivity (dBi)	4.14	4.3	4.54	4.57
Gain (dBi)	4.37	3.35	4.32	3.22
Efficiency (dB)	0.23	−0.95	−0.22	−1.35
Efficiency (%)	105.49	80.35	95.09	73.23

Frequency (MHz)	825	925	2300	
Directivity (dBi)	3.06	3.61	4.38	
Gain (dBi)	−2.38	−0.99	3.1	
Efficiency (dB)	−5.44	−4.6	−1.28	
Efficiency (%)	28.6	34.66	74.51	

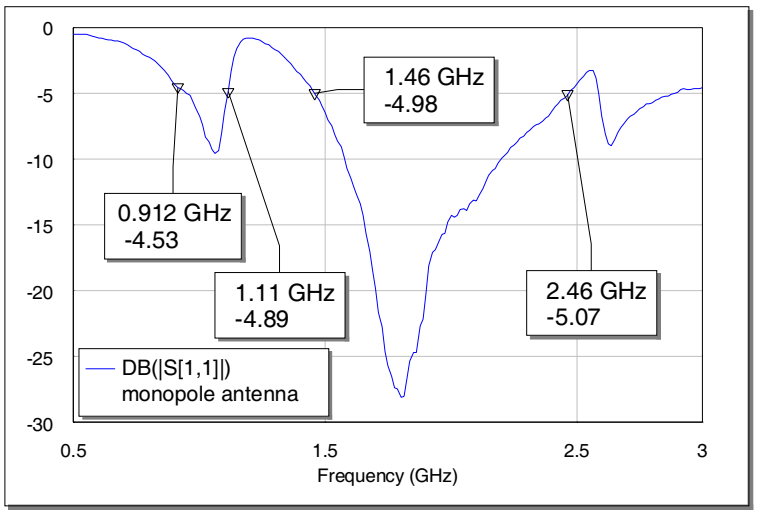

Figure 2: Measured data of return loss.

communication bands can be obtained. Besides, it can also generate the good radiation patterns in the azimuth plane and good antenna performance has been obtained. Based on the measurement coordinates [5–7] for H-plane, E_1-plane and E_2-plane. The measured 3D antenna data, as shown in Table 1.

4. CONCLUSION

In this paper, a compact and low profile internal monopole antenna for multi-bands has been proposed. This antenna was designed and measured. A good agreement between measurement and analysis has been obtained. The proposed antenna shows a wider operating bandwidth and it easy to cover the GSM, EDGE, CDMA, CDMA 2000, W-CDMA and UMTS band for wireless communication and 2.5G/3G dual mode operation of a mobile handset phone, co-design, co-integration and application.

ACKNOWLEDGMENT

The authors acknowledge the Antenna and EMC Department of HTC, Taiwan for sport the wireless technique and measurement environment.

REFERENCES

1. Wong, K. L., *Planar Antennas for Wireless Communication*, John Wiley & Sons, Inc, 2003.
2. Zurchur, J. F. and F. Gardiol, *Broadband Patch Antennas*, Artech House, 1995.
3. Kraus, J. D. and R. J. Marhefka, *Antennas for All Applications*, McGraw-Hill, 2002.
4. Johnson, R. C. and H. Jasik, *Antenna Engineering Handbook*, McGraw-Hill, Inc., 1961.
5. Chen, G. Y., J. S. Sun, K. Chang, and Y. D. Chen, "Antenna pattern measurement," *PIERS Proceedings*, 331–333, Beijing, China, Mar. 23–27, 2009.
6. Chen, G. Y., J. S. Sun, C. H. Lin, K. K. Tiong, and Y. D. Chen, "Small antenna measurement facilities," *PIERS Proceedings*, 157–158, Hangzhou, China, Mar. 24–28, 2008.
7. Chen, G. Y., C. H. Lin, J. S. Sun, K. K. Tiong, and Y. D. Chen, "3D far-field antenna scanning technique apply to radiation efficiency and mean effective gain measurement," *IEEE TENCON 2007*, 113, Taipei, Taiwan, Oct. 2007.

Investigating the Effect of Nonlinearity on Adaptive Arrays

Cheng-Nan Hu
Communication Research Center (CRC), Oriental Institute of Technology
No. 58, Sec. 2, Sihchuan Rd, Ban-Ciao City, Taipei County, Taiwan, R.O.C.

Abstract— With witness the 4G wireless evolution, one can experience the technology competition between *Mobile WiMAX* and *LTE (Long Term Evolution)*. One of the enabling technologies to the focused issue, "Convergence and Competition on the Way toward 4G", from the wireless communication prospects by various viewpoints of the contributing authors [1, 2], is the "Beam forming architecture" to support space-division multiple access (SDMA) [3]. This approach enables multiple users within the same radio cell to be accommodated on the same frequency and time slot. The beam forming technologies are used to modify its time, frequency, and spatial response by using internal feedback for controlling the amplitude/phase weighting of the adaptive array [4]. However, realizing the beam-forming techniques poses high linearity demands on RF/IF up-/down-conversion chain because the inter-modulation products (IMPs) due to nonlinear distortion will degrade the radiation pattern, resulting in the poor signal quality. This study modeling the multi-modulated input signals for multi-carrier power amplifier (MCPA) at up-/down-conversion chain is introduced. The nonlinearity effects of the MCPAs on an 8-element adaptive array are investigated to assess the radiation pattern deviation due to the phantom lobes [5] generated by IMPs at MCPA.

1. THEORETICAL ANALYSIS

Figure 1 illustrates a system diagram of the adaptive array. In receiving, the incoming signal/interference from direction (θ_0, ϕ_0)/(θ_j, ϕ_j) received by a dx-spaced N-element antenna array is amplified, down-converted, and transformed the base-band signal from analog to digital format, individually. Followed by the embedded processor the received signal pulse trains is used to compute the optimum adaptive weighting vector ($\bar{W}_{opt}$) for forming the radiation pattern with antenna gain enhancement at signal direction (θ_0, ϕ_0) whereas, with noise reduction by synthesizing nulls at interference directions (θ_j, ϕ_j) such that signal-to-noise ratio (SNR) can be increased to improve the quality of received signal. In transmitting, the adaptive weighting vector ($\bar{W}_{opt}$) can be used to generate multiple radiation patterns to keep good signal quality on radio-link between base-station (BS) and mobile-stations (MSs) and, meanwhile, to synthesize nulls on direction of the other un-linking mobiles. Consequently, the influence of the so called "co-channel interference" can be minimized. Such a closed-loop feedback accomplishing by adaptive processor enables the filtering overlapping signals in space domain spectrally and temperately from multiple mobile units. The analysis of the nonlinear distortion involved in RF/IF up-/down-conversion chain is very complex and parametric dependent issue. Since the amount of the harmonic higher-order products is mostly contributed by MCPA, this study focuses on modeling the nonlinearity effects of the amplifiers on array performance to multi-users applications. The input signal to MCPA at i'th antenna element on SDMA system (Figure 1) can be expressed by consisting of M phase modulated carriers with amplitude A_m and phase ϕ_{m} given by

$$s_i(t) = \sum_{k=1}^{M} A_k \exp[j((\omega_c + \omega_i)t + \phi_k(t))], \tag{1}$$

where ω_c is the carrier frequency and ω_i is the offset from the carrier frequency of user i. Assume that the amplifier is memoryless, i.e., the AM/PM and AM/AM conversion curves are not functions of frequency. In this sense, we assume that the signal is narrowband. Upon the multi-modulated carriers input signal (1) applying to MCPAs (Figure 1) in conjunction with array antennas, it turns out that the IMPs at each MCPA's output signals must be separately calculated to investigate the non-linearity effects on antenna radiation performance. To efficiently calculate this, Shimbo [6] proposed the method by fitting the AM/AM and AM/PM characteristic to a Bessel series expansion such that the output signal of MCPA at n'th antenna element can be written as

$$y_n(t) = \sum_{l_1=-\infty}^{\infty} \sum_{l_2=-\infty}^{\infty} \cdots \sum_{l_M=-\infty}^{\infty} \left[M_n(l_1, l_2, \ldots, l_M; t) \left\{ \exp\left(j\omega_c t + j \sum_{k=1}^{M} l_k(\omega_k t + \varphi_{nk}(t) \right) \right\} \right], \tag{2}$$

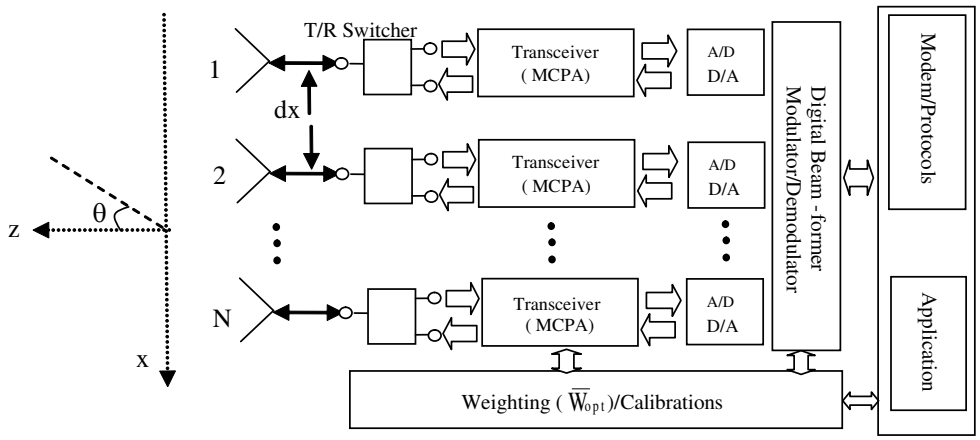

Figure 1: Functional block diagram of an adaptive antenna array for MIMO systems.

where φ_{nk} is the sum of the information-bearing phase of signal k at antenna n. Eq. (2) describes the signals at the fundamental frequency and those generated by nonlinearity, e.g., harmonics, spurious of all frequencies, and all order of IMPs. To restrict the sum only to the fundamental and third order IMPs in the first zone of the output, some constrains have to be considered as discussed in [7]. The function, $M_n(l_1, l_2, \ldots, l_M; t)$ is a complex valued function referred as the *Shimbo Amplitude Function* (SAF), which gives the complex baseband amplitude of the signal component in the output signal corresponding to the set of in indices $\{l_k\}_{k=1}^{M}$. In general, the ASF function calculation is expressed by the Bessel function series expansion of the non-linearity $g(\cdot)e^{jf(\cdot)}$, yielding a simple and useful expression of the complex function $M_n(l_1, l_2, \ldots, l_M; t)$ denoted as

$$M_n(l_1, l_2, \ldots, l_M; t) \cong \sum_{p=1}^{P} b_p \prod_{k=1}^{M} J_{lk}(\alpha s A_k), \tag{3}$$

where the coefficients of α, b_{p} in a Bessel series expansion for n'th antenna element can be obtained by solving

$$\{\alpha, b_1, b_2, \ldots, b_P\} \cong \arg \min_{\alpha, b_1, \ldots b_P} \left\{ \left| g(A)e^{jf(A)} - \sum_{p=1}^{P} b_p J_1(\alpha p A) \right| \right\}, \tag{4}$$

where $g(A)/f(A)$ is the amplitude/phase of the output signals corresponding to the normalized amplitude (A) of the input signal. $g(A)/f(A)$ can be the measured or simulated data fitted by limiter model [8]. Thus, utilizing the computed sub-carriers and it corresponding output amplitude approximated by (3), one can calculate the output signal distortion due to AM/AM and AM/PM conversion of the MCPA, which will alter adaptive weighting vector, resulting in radiation pattern deviation. At element n, the distorted weight of user i applied to a signal on frequency $\omega_c + \omega_i$ is denoted as $\tilde{\varepsilon}_{ni}$:

$$\tilde{\varepsilon}_{ni} = \frac{1}{\rho_i} \left[\sum_{l_1, l_2, \ldots, l_M = -\infty}^{\infty} M_n(l_1, l_2, \ldots, l_M; t) \left\{ \exp\left(j \sum_{k=1}^{M} l_k(\omega_k t + \varphi_{nk}(t)) - j\omega_i t \right) \right\} \right], \tag{5}$$

where the constrain to come out the signal component in indices $\{l_i\}_{i=1}^{M}$ must be fulfilled to assure outputs on frequency $\omega_c + \omega_i$ only. In (5), the gain factor ρ_i is used to compensate the path loss between MSs and BS to maintain a proper transmitter/receiver dynamic ranging. In this study, ρ_i is obtained by taking mean value of all of input signal levels to operate at 1 dB gain compression point. With the computed distorted weight coefficient (5), one can assess the adaptive array pattern deviation.

2. NUMERICAL RESULTS

To simplify the analysis, a single stage amplifier using Motorola device (MRF9742) incorporating the effect of bond-wire inductance and bounding-pad capacitance in Motorola MOSFET Root model

is utilized to characterize the amplifiers nonlinear behavior. Large signal analysis techniques to a power amplifier includes: a sequence of HB analysis with time-varying phasors; the conventional Single Envelope Transient (SET); and enhanced Multi Envelop Transient. Figure 2(a) illustrates the schematic of the single-stage power amplifier for nonlinearities analysis using *Agilent Advance Design System 2009 (ADS09)*. Applying the *ADS09* Simulator, the simulated amplitude/phase of the output power level against input power level ranging from −20 dBm to 30 dBm is plotted in Figures 2(b)/(c), showing the (AM/AM)/(AM/PM) conversion under large signal operation and illustrating the 1 dB gain compression at input power level of 16.5 dBm. Also, in Figures 2(b)/(c), the simulated data is fitted by using Cann's limiter model (solid-line with squares) with $\rho = 4.2$; $\kappa_a = 12$; $\kappa_\varphi = 0.5$ and Shimbo model (solid-line) for nonlinear characteristic of the amplifier (MRF9742). Considering an input multicarrier signals consisting of three modulated subcarriers are equal spaced ($\delta\omega$), so that ω_1, $\omega_1 + \delta\omega = \omega_2$, and $\omega_1 + 2\delta\omega = \omega_3$, one can obtain the subcarriers and its corresponding output signals approximated by ASF (3&4) as plotted in Figures 2(b)/(c) (solid-line with circles/triangles for $\omega_{\rm i} = \omega_{1\&3}/\omega_2$). To investigate the impact of the nonlinearity distortion on adaptive array pattern, a $\lambda/2$-spaced eight-element uniform linear array (ULA) is studied using the MMSE algorithm [9]. The case of the numerical study consists of one desired signal, located at (0°, 0°), and three interference, located at (20°, 0°), (40°, 0°), and (60°, 0°) respectively. To investigate the nonlinearity effect on adaptive radiation pattern, the simulated far-field patterns with/without including the IMPs generated by MCPAs are plotted in Figure 3 for comparison, showing the antenna gain reducing by 0.22 dB and the sidelobe level increasing by 9.43/10.10/9.16 dB corresponding to θ of 20°/40°/60°.

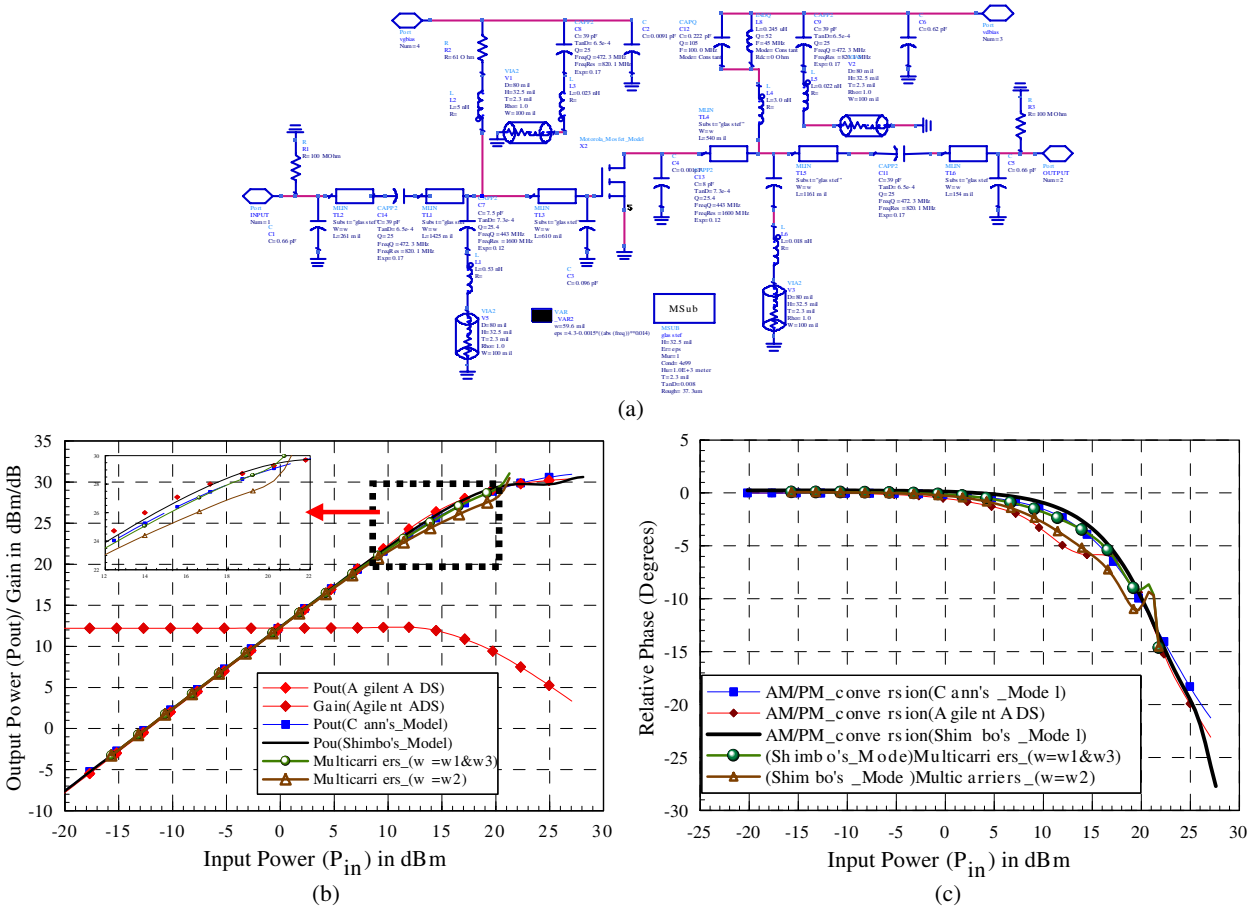

Figure 2: (a) The schematic of the amplifier (Motorola PA MRF9742) for nonlinearities analysis using *Agilent ADS2009 Simulator*, (b)/(c) the simulated amplitude/phase of the output power/Gain against the input power level for comparsion, including the Agilent ADS simulated results (dashed-line with diamonds), the data fitted by Cann's model (solid-line with squares) with $\rho = 4.2$; $\kappa_{\rm a} = 12$; $\kappa_\varphi = 0.5$; $\rho = 4.2$; the data fitted by Shimbo's model (solid-line), and the Shimbo's result with three modulated subcarriers (solid-line with circles/triangles for $\omega_{\rm i} = \omega_{1\&3}/\omega_2$).

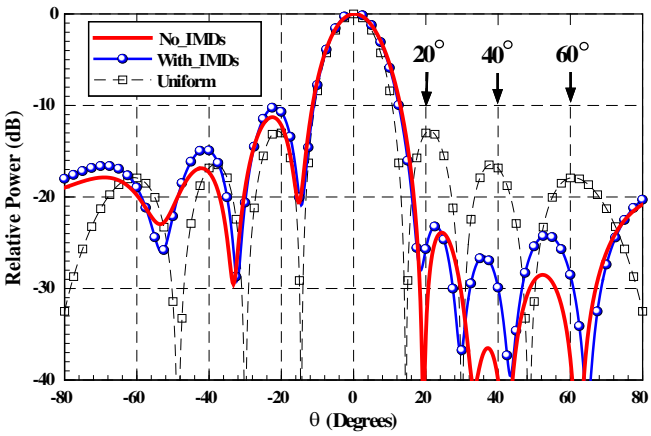

Figure 3: Simulated far-field patterns with uniform distribution (dashed-line with squares) and MMSE adaptive algorithm with/without considering the nonlinearity distortion (solid-line/solid-line with circles) for comparison.

3. CONCLUSSIONS

For multi-carrier communication, the Shimbo's model is used to assess the effect of nonlinearity on the radiation pattern, showing the pattern deviated by shifting nulls at interference directions. Subsequently, the capability of the noise power suppression is degraded.

REFERENCES

1. Tsoulos, G., M. Beach, and J. McGeehan, "Wireless personal communications for the 21th century: european technological advances in adaptive antennas," *IEEE Communication Magazine*, Vol. 35, No. 9, 102–109, Sep. 1997.
2. Parkvall, S., A. Furuskar, and E. Dahlman, "Evolution of LTE toward IMT-advanced," *IEEE Communication Magazine*, Vol. 49, No. 2, 84–91, Feb. 2011.
3. Park, C. S., Y.-P. E. Wang, G. Jongren, and D. Hammarwall, "Evolution of uplink MIMO for LTE-advanced," *IEEE Communication Magazine*, Vol. 49, No. 2, 112–121, Feb. 2011.
4. Tyler, N., B. Allen, and H. Aghvami, "Adaptive antennas: the calibration problem," *IEEE Communication Magazine*, Vol. 42, No. 12, 114–122, Dec. 2004.
5. Laperle, C., T. Lo, J. Litva, and R. Turner, "Modeling of nonlinearity and their effects on digital beamforming," *IEEE AP-S*, Vol. 1, No. 20–24, 124–127, Seattle, USA, Aug. 1994.
6. Shimbo, O., "Effects of intermodulation, AM-PM conversion, and additive noise in multicarrier TWT systems," *Proceedings of IEEE*, Vol. 59, No. 2, 230–238, 1971.
7. Schneider, W. K. W., "Efficient simulation of multicarrier digital communication systems in nonlinear channel environments," *IEEE Journal on Selected Areas in Communications*, Vol. 11, 328–339, 1993.
8. Cann, A. J., "Nonlinearity model with variable knee sharpness," *IEEE Trans. On Aerospace and Electronic System*, Vol. 16, 874–878, 1980.
9. Huang, Z. and C. A. Balanis, "BER of adaptive array in AWGN channel," *IEEE Trans. Ant. Propa.*, Vol. 56, No. 7, 2089–2097, 2008.

A Differential Multi-band CMOS Low Noise Amplifier with Gain Flatness Performance and Bandwidth Enhancement

San-Fu Wang[1], **Jan-Ou Wu**[2], **Hua-Pin Chen**[1], **and Yang-Hsin Fan**[3]

[1]Department of Electronic Engineering, Ming Chi University of Technology
Taipei 243, Taiwan, R.O.C.
[2]Department of Electronic Engineering, De Lin Institute of Technology
Tucheng, Taipei, Taiwan, R.O.C.
[3]Department of Computer Science and Information Engineering
National Taitung University, Taitung, Taiwan, R.O.C.

Abstract— In this paper, a differential multi-band CMOS low noise amplifier (LNA) is proposed that is operated within a range of 1300 MHz $\sim$ 3000 MHz with input matching capacitor switching and gain flatness enhancement technique. Traditional multiband LNAs have poor performances on gain flatness performance. Therefore, we propose a new multiband LNA which obtain good gain flatness performance by integrating the characteristics of the transistor transconductance and LC resonant load. The new LNA can also achieve a tunable frequency at different matching capacitance conditions.

1. INTRODUCTION

Traditional narrow-band LNA can reject unwanted signals, image signals and interferences of the receiver, but it can't meet the required of multi-standard function or wide-band solution. Therefore, the multi-band LNA has a high selectivity and sensitivity is needed [1]. Traditional multi-band LNA architectures utilize the separate LNAs in parallel to cover each operating frequency [2, 3]. This type of receiver needs integration several narrow-band LNAs, so it usually can yield implementations with a large area and great power consumption. Nowadays, most multi-band LNAs uses source inductive degeneration technique to provide real input impedance and signal gain at a specific frequency [4–6]. However, the wireless communication market is moving towards the integration of different standards, even the source inductive degeneration amplifier is the most popular matching method in the design of multi-band LNA, the operating bandwidth of the source inductive degeneration technique multi-band LNA is still not enough.

For those reasons, the CMOS differential multi-band LNA which can improve the multi-band input matching, wide-band interference rejection and maximum gain flatness performance is proposed.

2. THE PROPOSED CIRCUIT

The difficulty in designing a multi-band LNA comes from the fact that it has to provide different functions. So, to design a multi-band LNA, it must satisfy different operating bandwidths at different standards. In order to meet the trends of increasingly standards in a receiver system, the operation bandwidths and gain flatness performance of the multi-band LNA must be improved. Therefore, the multi-band LNA which can satisfy the requests at the same time has been proposed in Fig. 1. And the analysis of this circuit is shown as follows.

2.1. Bandwidth Enhancement

Nowadays, most multi-band LNAs are also based on the narrow-band topology. However, the conventional narrow-band LNAs has poor performance on improving S_{11} offset for input matching components process variation and multi-standard support, because it is difficult to change the inductances and capacitances of input matching network, especially for the inductance of chip inductor which is not easy to be adjusted by digital or analog control. Therefore, the multi-band LNA is usually implemented with wide-band input matching, and the source inductive degeneration amplifier [6] is the most popular matching method in the design of multi-band LNA. It employs an inductor in series with the source of the MOS to generate a real resistance at the input of the LNA. So, the source inductive degeneration technique needs input matched inductors L_g, L_d, and capacitor C_d (in Fig. 1), and the input impedance of the source inductive degeneration amplifier

Z_{in} can be derived as

$$Z_{in} = j\omega(L_g + L_d) + \frac{1}{j\omega(C_{gs}, M_{n1} + C_d)} + \frac{gmM_{n1}L_d}{(C_{gs}, M_{n1} + C_d)} \tag{1}$$

where ω is the operation frequency, C_{gs}, M_{n1} are the gate-source capacitances of the input transistors M_{n1}, gm, M_{n1} is the transistor trans-conductance of M_{n1}.

To match the input impedance for maximum power transfer, Z_{in} must be matched to R_s. So, the value $j\omega(L_g + L_d)$ and $\frac{1}{j\omega(C_{gs}, M_{n1}+C_d)}$ need to be cancel each other, and $\frac{gmM_{n1}L_d}{(C_{gs}, M_{n1}+C_d)}$ must be matched to R_s. Based on above illustrates, the operating bandwidth of the source inductive degeneration technique can be increased substantially by a switch capacitor C_d. For example, when the LNA is operated in high frequency mode, the value $j\omega(L_g + L_d)$ and $\frac{1}{j\omega(C_{gs}, M_{n1}+C_d)}$ will be cancel each other with smaller C_d. On the contrary, the LNA is operated in low frequency mode, the value $j\omega(L_g + L_d)$ and $\frac{1}{j\omega(C_{gs}, M_{n1}+C_d)}$ will be cancel each other with large C_d.

Through the above design, the proposed multi-band LNA will have a wider operating bandwidth.

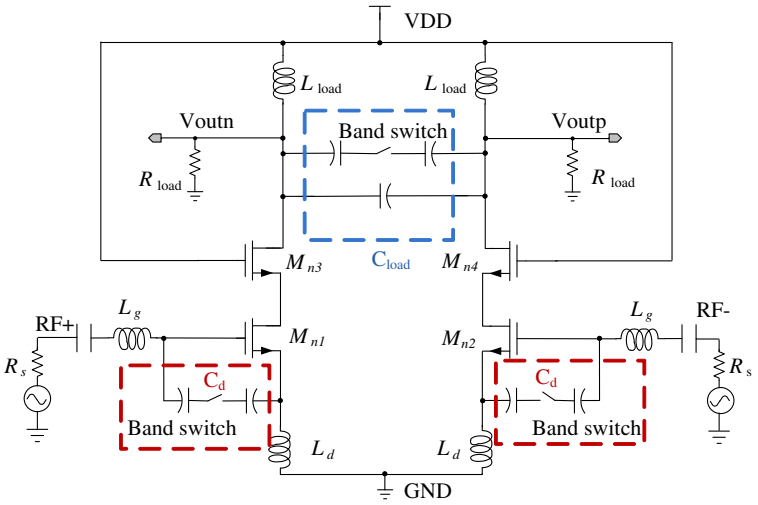

Figure 1: Different multi-band LNA.

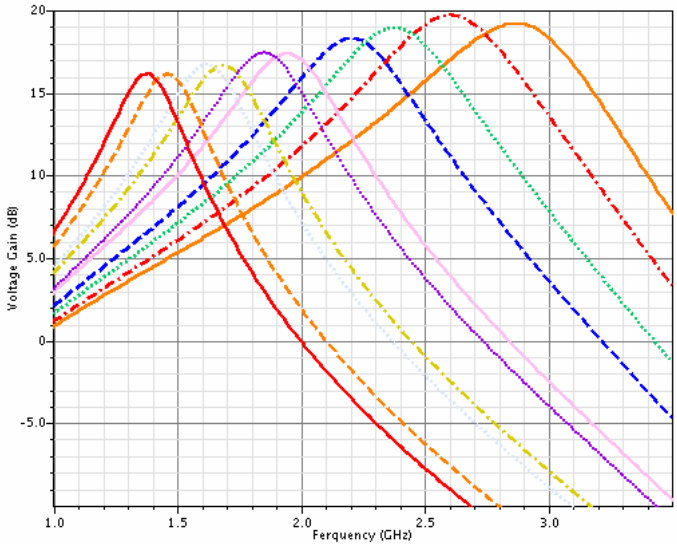

Figure 2: Simulation the voltage gain of proposed multi-band LNA.

2.2. Gain Flatness Improvement

The source inductive degeneration amplifier has a poor gain flatness performance, it is because the gain of the source inductive degeneration amplifier is determined by the trans-conductance of the input transistor [7, 8] and output load. However, the trans-conductance of the input transistor would degeneration by input degeneration inductor. Therefore, the gain flatness performance enhanced achieved by trade-off in degeneration inductances and LC tank inductances.

Based on the above principle, the proposed multi-band LNA can achieve the requirement of wider bandwidth and better gain flatness performance.

3. SIMULATION RESULTS

We simulated the multi-band LNA with Cadence's EDA-Spectre RF using TSMC 0.18-µm RF CMOS process. The following figures give us the results respectively. Figs. 2 to 5 show the results for different functions that verify the circuit functions in Fig. 1.

Figure 2 shows the simulation result of voltage gain, and it is operated in the range from 1350 MHz $\sim$ 3000 MHz, and the gain of high frequency mode is higher than low frequency mode. The voltage gain of the LNA which is better than 16 dB in the range from 1350 MHz $\sim$ 3000 MHz, and the maximum gain variable is less than 3.7 dB. It has satisfied gain flatness at multi-standards application.

Figures 3 to 5 illustrated the simulation results for the input reflection coefficient, noise figure and 1-dB compression point in Fig. 1. Fig. 3 shows the simulation result of S_{11} that verifies the circuit input impedance in Fig. 1, it shows the simulation result of S_{11} parameter which is smaller than -11.6 dB at the wanted switching mode, so the input impedance matching is close to 50 ohm

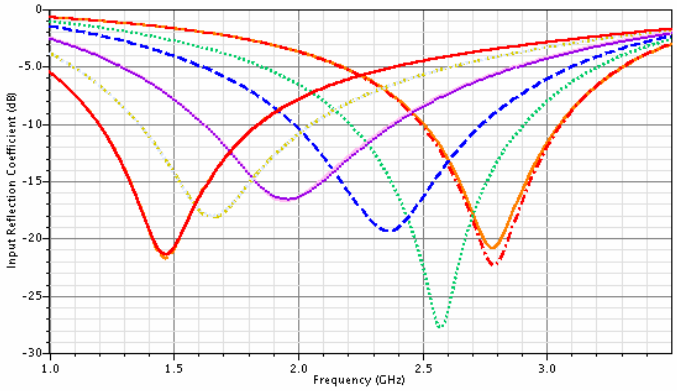

Figure 3: Simulation the input reflection coefficient of proposed multi-band LNA.

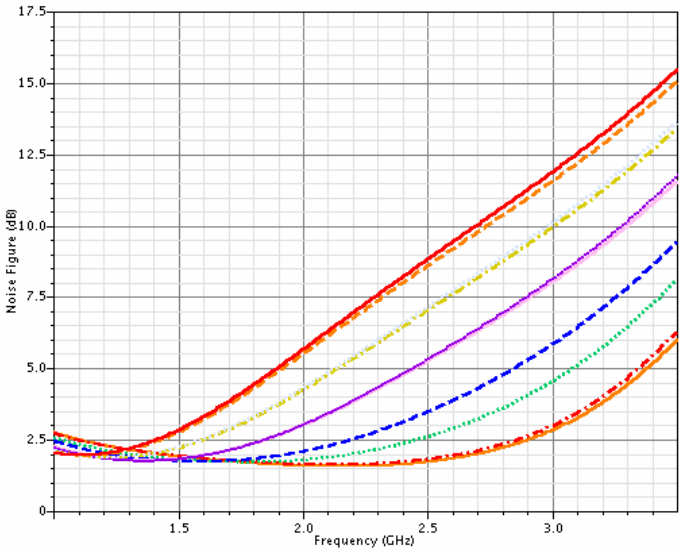

Figure 4: Simulation the noise figure of proposed multi-band LNA.

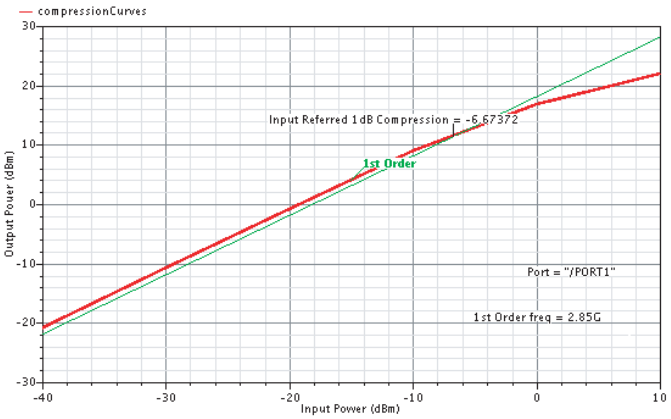

Figure 5: Simulation the 1-dB compression point of proposed multi-band LNA.

Table 1: CMOS differential multi-band LNA with 2.4 G interference rejection.

Specification	Simulation		
Operation Frequency(GHz)	1.35	2.25	3
S_{11} (dB)	−15.65	−18	−11.6
Voltage gain (dB)	16	17.1	18.17
NF (dB)	2.3	2.57	2.8
P_1 dB (dBm)	−0.5	−3.6	−5.66
Power Dissipation (mW, without interference rejection)	17.49	17.49	17.49

between 1350 MHz and 3000 MHz. Fig. 4 shows the simulation noise figure of the entire LNA, and the noise figure is below 2.6 dB over the bandwidth. To check the linear requirement, a 1-dB compression point (P_1 dB) performance of the LNA is −6.7 dB at 2850 MHz operation frequency, and the simulation result is shown in Fig. 5. A summary of the proposed multi-band LNA's characteristics is given in Table 1.

4. CONCLUSION

This paper has discussed the performance of the multi-band LNA. The architecture of the multi-band LNA using the source inductive degeneration, switching capacitance and LC tank load is proposed in order to achieve a multi-band and small gain variation LNA for multi-standard applications. The noise figure is less than 2.8 dB at operating frequencies of 1350 MHz ∼ 3000 MHz.

ACKNOWLEDGMENT

The author would like to thank the Chip Implementation Center of Taiwan, R.O.C. for project support.

REFERENCES

1. Hashemi, H. and A. Hajimiri, "Concurrent multiband low-noise amplifiers-theory, design, and applications," *IEEE Transactions on Microwave Theory and Techniques*, Vol. 50, No. 1, 288–301, Jan. 2002.
2. Hwang, M.-W., M. Ahn, S. Beck, J.-C. Lee, S. Hong, S. Lee, S. Jeong, S. Lim, H. Cho, Y.-J. Kim, I.-C. Hwang, and J. Kim, "A multi-mode multi-band CMOS direct-conversion mobile-TV tuner for DVB-H/T and T-DMB/DAB applications," *Proc. of IEEE Symposium on VLSI Circuits*, 94–95, Jun. 2008.
3. Wu, S. and B. Razavi, "A 900-MHz/1.8-GHz CMOS receiver for dual-band applications," *IEEE Journal of Solid-State Circuits*, Vol. 33, No. 12, 2178–2185, Dec. 1998.
4. Martins, M. A., J. R. Fernandes, and M. M. Silva, "Multi-band combined LNA and mixer," *Proc. IEEE International Symposium on Circuits and System*, 920–923, May 2008.

5. Martins, M. A., J. R. Fernandes, and M. M. Silva, "Techniques for Dual-Band LNA design using cascode switching and inductor magnetic coupling," *Proc. IEEE International Symposium on Circuits and System*, 1449–1452, May 2007.
6. Boric-Lubecke, O., J. Lin, A. Verma, I. Lo, and V. M. Lubecke, "Multiband 0.25 µm CMOS Base Station Chips for Indirect and Direct Conversion Receivers," *IEEE Transactions on Circuits and Systems I*, Vol. 55, No. 7, 2106–2115, Aug. 2008.
7. Li, Q. and Y. P. Zhang, "A 1.5-V 2–9.6-GHz inductorless low-noise amplifier in 0.13-µm CMOS," *IEEE Transactions on Microwave Theory and Techniques*, Vol. 55, No. 10, 2015–2023, Oct. 2007.
8. Gatta, F., E. Sacchi, F. Svelto, P. Vilmercati, and R. Casrello, "A 2-dB noise figure 900-MHz differential CMOS LNA," *IEEE Journal of Solid-State Circuits*, Vol. 36, No. 10, 1441–1452, Oct. 2001.

Performance Analysis in Using Repeaters with Coordination among Base Stations for LTE-A Systems

Hsien-Wei Tseng[1], **Yang-Han Lee**[2], **Ming-Hsueh Chuang**[3], **Wei Chien**[4], **Chih-Yuan Lo**[2], **and Yu-De Liao**[1]

[1]Computer and Communication Engineering, De Lin Institute of Technology, Taiwan, R.O.C.
[2]Electrical Engineering, Tamkang University, Taiwan, R.O.C.
[3]Electronic Engineering, National Taiwan University of Science and Technology, Taiwan, R.O.C.
[4]Electronic Engineering Department, De Lin Institute of Technology, Taiwan, R.O.C.

Abstract— LTE-A technique will play an important role in the next generation wireless communications due to it has the advantages of high transmission rate and wide communication bandwidth especially it also provides high quality throughput when the user is moving in high velocity. The system performance and parameters characteristics resulting from utilizing LTE-A technique will be provided to the system designers valuable references in their development of future IMT-Advanced wireless communication systems. When the system bandwidth becomes wider the system utilization performance will be varied widely and may become inefficiency when the number of users served in the system coverage areas varies and the communication environments change. It could adopt the coordination technique among base stations to effectively utilize the system resources and to reduce the possible interferences among signals in their transmissions.

In this paper it considers of how to utilize repeaters in the base station coverage areas to optimize the spectral efficiency of the base station in its backbone transmission. It utilizes repeaters to improve the indoor signal transmission quality when the users in the indoor environment could not receive the signal transmitted from the outdoor base stations.

1. INTRODUCTION

As the emergence of new wireless communication technologies the demand for network applications becomes diversified and the request for service quality is also correspondingly increased; the network has become an indispensible apparatus in human life. It then incurs the issue of how to properly utilize and apply the network resource anytime and anywhere. Early generations of wireless mobile communication system are unable to meet the current users requirements that the network service providers need to expand their system bandwidth through new wireless technology development and meanwhile to expand their wireless networks coverage range. The new interface standard proposed by Third Generation Partnership Project (3GPP) and IEEE 802.16m all contains the advantages of high transmission data rate, broad bandwidth and wide coverage area; and it comes to the problem of how to select or set the optimum system parameters for the new development systems in practical operations. As shown in Figure 1, a user is located in the coverage area of many base stations. After the user is inter-connected by many base stations through the implementation of the coordination operation among base stations, the user's receiving gain can be increased and also its interference can be reduced by implementing the techniques such as Coordinated Multi-input Multi-output (Co-MIMO) and Coordinated Multiplexing (CoMP) [1–3]. In this paper it will analyze the probable bandwidth occupied by the base station when users are interconnected by many base stations and then to determine the proper situation to implement the coordination scheme among base stations to improve the system performance. When base station 1 (BS1) and base station 2 (BS2) use different carrier frequencies, the user equipment (UE) or the user can base on the magnitudes of each base station's signal to noise ratio to determine which link has better receiving signal quality; on the other hand when both stations use the same carrier frequency the UE will have enhancement in its received signal strength by using proper combining technique.

2. CHANNEL MODEL

Channel fading plays an important role in the wireless communication; when a signal transmits through the channel it will encounter various interferences such as the multipath effect when the signal transmits through the buildings, forests and terrains. The multipath effect will enhance or fade the transmitted signal to make it is impossible at the receiver terminal to accurately determine the transmitted signal but by using statistical consideration. The channel model in wireless

communication is derived through analysis and simulation of the channel statistical characteristics and modified through empirical measurements; many channel models have been proposed [4–9]. Summarily the received signal strength at the base station/mobile station can be estimated from the following equation:

$$P\,(\text{dBm}) = P_t + G_t + G_r - PL \tag{1}$$

P_t: Transmitting power of base station/mobile station (dBm); G_t: Antenna gain of mobile station/base station (dBi); G_r: Antenna gain of base station/mobile station (dBi); PL is the path loss in dB and has value as shown in the following Equation (3) as recommended by 3GPP Release 9.

In the communication environment when a signal transmits from outdoor to indoor, as shown in Figure 2, its path loss model is also provided in 3GPP Release 9 document [10]. It is realized that when the user is located inside the building it has a high probability that the user could not receive the transmitted signal due to the high path loss due to signal penetration. As shown in Figure 3 is the resulting path loss when the distance between the base station and the building is around 500 m, it has around 20 dB penetration loss when the signal passes through the building. With this additional loss the system performance will be unable to meet its minimum requirement and we will then consider using repeaters to improve the received indoor signal quality and also to analyze how the system performance has been upgraded when repeaters are implemented.

$$PL_{\text{urban-micro}} = 40\log 10(d) + 7.8 - 18\log 10(h_{BS}) - 18\log 10(h_{UT}) + 2\log 10(f_c) \tag{2}$$

$$PL\,[\text{dB}] = PL_b + PL_{tw} + PL_{in} \tag{3}$$

$$PL_b = PL_{B1}(d_{out} + d_{in}) \tag{4}$$

$$P_{tw} = 14 + 15(1 - \cos(\theta))^2 \tag{5}$$

$$PL_{in} = 0.5 d_{in} \tag{6}$$

$3\,\text{m} < d_{out} + d_{in} < 1,000\,\text{m}$, $0\,\text{m} < d_{in} < 25\,\text{m}$, $h_{BS} = 10\,\text{m}$, $h_{UT} = 3(n_{FL} - 1) + 1.5\,\text{m}$, $n_{FL} = 1$, $\theta = 45°$. PL_b: Basic path-loss; PL_{tw}: Loss through wall; PL_{in}: Loss inside; n_{FL}: Number of

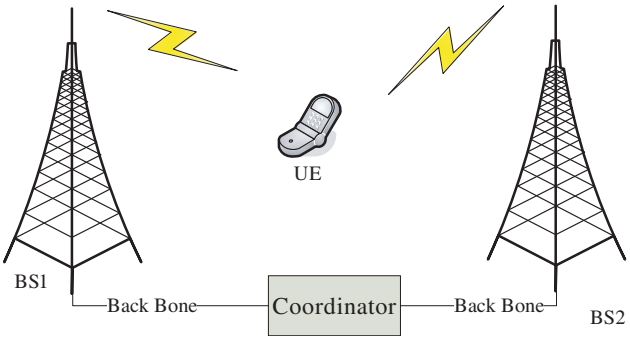

Figure 1: UE is covered in multiple base stations.

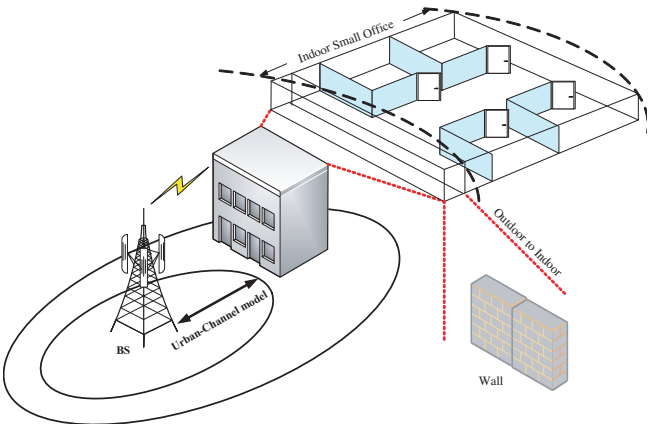

Figure 2: The near real scene.

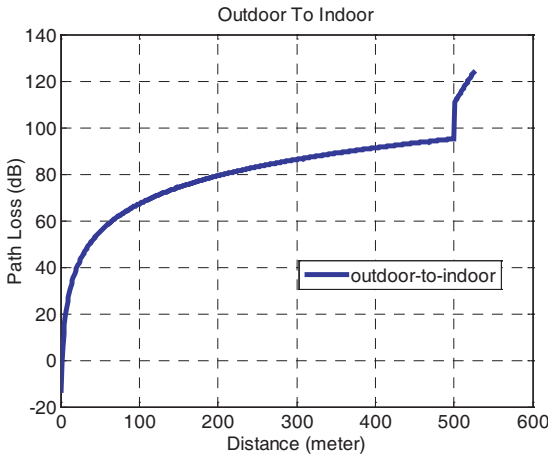

Figure 3: The near real scene path loss.

floor; P_{LB1}: The path loss model for urban- micro; d_{out}: Distance from BS to the wall next to UE location; d_{in}: Perpendicular distance from to UE; θ: Angle between LOS to the wall and a unit vector normal to the wall.

3. SYSTEM SIMULATION PARAMETERS

In this section we perform the system performance simulation of LTE system and it also makes comparison and analysis of the system performances when it has or without coordination scheme implemented. The system simulation parameters are listed in Table 1. The System Simulation Functional Block Diagram is as shown in Figure 4.

4. ANALYSIS WHEN CERTAIN BS-IMPLEMENTED APPARATUS ARE INDOOR INSTALLED

4.1. Analysis of Repeaters

When indoor users are unable to receive outdoor base station signals some buildings are usually installed repeaters to improve their receiving signal qualities as shown in Figure 5.

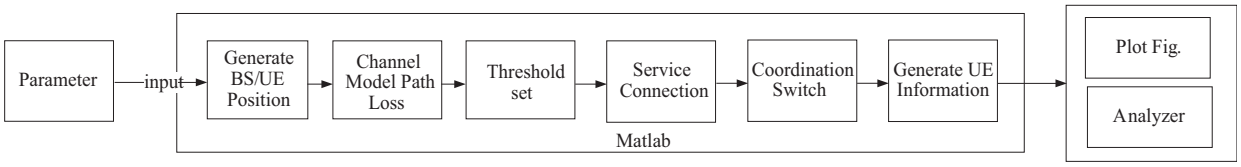

Figure 4: System simulation functional block diagram.

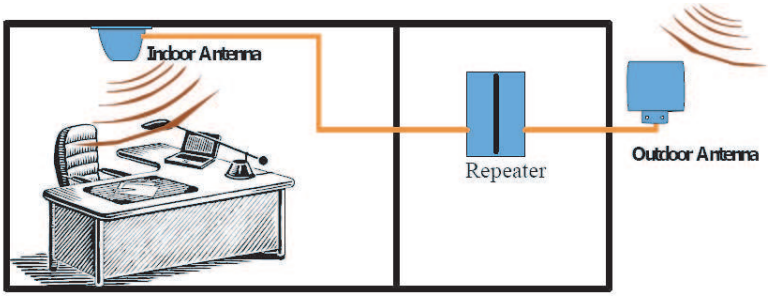

Max. Output Power	+20dBm
Linear Gain	80 dB
Noise Figure	5dB
Sync. Signal Detection Level	≧-90dBm

Figure 5: The set up of a repeater and its parameters [11].

Table 1: LTE parameter.

Duplex Mode	FDD
Carrier Frequency	2 GHz
Bandwidth	10 MHz
Code Rate	1/3
AMC	QPSK, 16-QAM, 64QAM
BS Power	1 W
BS antenna gain	17 dBi
UE antenna gain	0 dBi
UE Power	200 mW
BS Height	35 m
UE Height	1.5 m

Table 2: Users service quality and bandwidth occupancy when repeaters are installed.

With Repeater									
	MS Number	10		30		50		80	
BS No.		DL	UL	DL	UL	DL	UL	DL	UL
BS 1	connect	3.6	3.6	15.5	15.5	25	25	31.7	40.6
BS 2	connect	5.5	5.5	16	16	25.2	25.9	33.6	43.9
BS 3	connect	4.9	4.9	14.9	14.9	24	24	31	36.6
BS 1	Mbps	0.6912		2.976		4.8		6.656	
BS 2	Mbps	1.056		3.072		4.8832		7.1104	
BS 3	Mbps	0.9408		2.868		4.608		6.3104	
Total	Mbps	2.688		8.9088		14.2912		20.0768	
	MS Number	100		120		150		200	
BS No.		DL	UL	DL	UL	DL	UL	DL	UL
BS 1	connect	32.6	47.9	32.4	56.5	31.9	63.8	31.6	63.5
BS 2	connect	33.4	52.3	33	59.9	34.2	66.4	32.2	64.9
BS 3	connect	32.5	47	32.4	59.2	31.9	63.9	30.7	61.8
BS 1	Mbps	7.2384		7.7632		8.1664		8.1088	
BS 2	Mbps	7.6224		8.0576		8.6272		8.2752	
BS 3	Mbps	7.168		7.936		8.1728		7.8848	
Total	Mbps	22.0288		23.7568		24.9664		24.2688	
Without Repeater									
	MS Number	10		30		50		80	
BS No.		DL	UL	DL	UL	DL	UL	DL	UL
BS 1	connect	5.1	5.1	12.8	12.8	22.6	22.6	31.6	36.7
BS 2	connect	4	4	13.7	13.7	23.7	23.7	32.1	36.7
BS 3	connect	3.9	3.9	12.4	12.4	19.4	19.4	29.9	32.8
Indoor	connect	1.3	1.3	3.9	3.9	6.1	6.1	8.5	8.5
BS 1	Mbps	0.9792		2.4576		4.3392		6.3936	
BS 2	Mbps	0.768		2.6304		4.5504		6.4576	
BS 3	Mbps	0.7488		2.3808		3.7248		5.9264	
Total	Mbps	2.496		7.4688		12.6144		18.7776	
	MS Number	100		120		150		200	
BS No.		DL	UL	DL	UL	DL	UL	DL	UL
BS 1	connect	33.4	42	31.7	53.6	32.3	62.4	32.9	65.6
BS 2	connect	32.9	47.4	32	55.9	33.2	63.9	34.1	67.1
BS 3	connect	32.5	39.2	32.2	50.3	31.6	59.2	32.3	63.7
Indoor	connect	12	12	12.5	12.5	18.3	18.3	21.4	21.4
BS 1	Mbps	6.9632		7.488		8.128		8.4096	
BS 2	Mbps	7.2448		7.6736		8.3392		8.6592	
BS 3	Mbps	6.6688		7.3408		7.8336		8.2112	
Total	Mbps	20.8768		22.5024		24.3008		25.28	

4.2. System Performance Analysis with Coordination Scheme Implemented and Repeaters Are Installed Coordination

As shown in Figure 6 is the environment when repeaters are installed due to the indoor users could not receive the signal transmitted from outdoor base station transmitted signal. When 50 buildings (houses) are considered and their averages are taken after 10 simulation trials the users

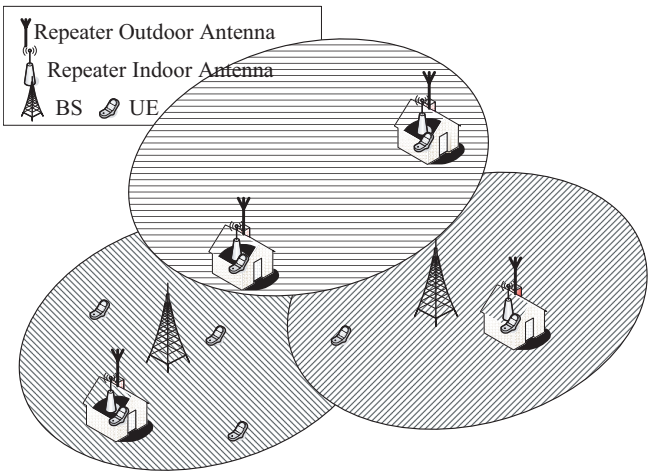

Figure 6: The environment with coordination scheme implemented and repeaters installed.

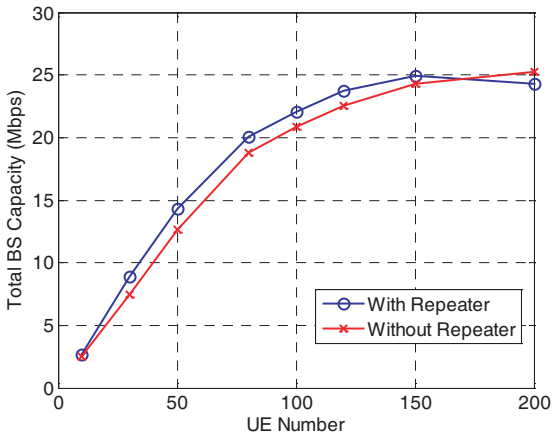

Figure 7: Total BS capacity with and without repeaters installed.

service performance and bandwidth occupancy in coordination environment are shown in Figure 6. The users' service performance and the BS throughput statistics are listed in Table 2.

The total base stations capacity of integrating three base stations with and without repeaters implemented is shown in Figure 7. It appears that it generates higher BS capacity when repeaters are implemented in the system.

5. CONCLUSION

When system bandwidth becomes wider in next generation communication systems the users density in the base stations coverage areas may be varied depending on the communication schedule, communication environment etc. When the spectrum efficiency becomes worse it could possibly increase the spectrum efficiency and improve the user's signal quality when coordination scheme is implemented. In the outdoor to indoor signal transmission it showed in this paper from simulation results that the spectrum utilization of the base station had greatly improved when repeaters are implemented comparing with without using repeaters.

ACKNOWLEDGMENT

This study is partially support from the National Science Council, R.O.C. under contracts NSC 99-2219-E-009-014, NSC 97-2221-E-032-027-MY3.

REFERENCES

1. Liu, G., J. Zhang, D. Jiang, L. Lei, Q. Wang, and F. Qin, "Downlink interference coordination and mitigation for future LTE-advanced system," *Asia-Pacific Conference on Communications, APCC 2009*, 225–229, 2009.
2. Rahman, M., H. Yanikomeroglu, and W. Wong, "Interference avoidance with dynamic intercell coordination for downlink LTE system," *IEEE Wireless Communications and Networking Conference, WCNC 2009*, 1–6, 2009.
3. Brueck, S., J. Giese, L. Zhao, and A. Dekorsy, "On MAC layer throughput enhancements in LTE-A by downlink macro diversity," *IEEE International Conference on Communications Workshops, ICC Workshops 2009*, 1–5, 2009.
4. "IEEE 802.16m Evaluation Methodology Document (EMD)", *IEEE 02.16m-08/004r5*, Jan. 2009
5. Srinivasan, R., J. Zhuang, L. Jalloul, R. Novak, and J. Park, "IEEE 802.16m Evaluation Methodology Document," *IEEE 802.16 Broadband Wireless Access Working Group, 80216m-08_003r7(SDD)*, Jan. 15, 2009.
6. Erceg, V., K. V. S. Hari, M. S. Smith, D. S. Baum, and P. Soma, "Channel models for fixed wireless applications," *IEEE 802.16 Broadband Wireless Access Working Group, C802.16.3c-01/29r4*, Jun. 2003.

7. Molisch, A. F., H. Asplund, R. Heddergott, M. Steinbauer, and T. Zwick, "The COST259 directional channel model — I. Overview and methodology," *IEEE Trans. Wireless Communcation*, Vol. 5, 3421–3433, 2006.
8. Steinbauer, M., A. F. Molisch, and E. Bonek, "The double-directional radio channel," *IEEE Antennas and Propagation Magazine*, 51–63, Aug. 2001.
9. Foschini, G. J. and M. J. Gans, "On limits of wireless communications in a fading environment when using multiple antennas," *Wireless Personal Communications*, Vol. 6, 311–335, Feb. 1998.
10. Rel.9 3GPP TR 36.814, "Further advancements for E-UTRA physical layer aspects," Mar. 2010.
11. Coiler, WiMAX Band Selective Repeater-BR-2600, http://www.coiler.com.tw.

Approximate Outage Probability Expressions for Evaluating Cooperative Communications

Chengkun Sun, Takashi Kodama, and Hua-An Zhao
Department of Computer Science and Electrical Engineering, Kumamoto University, Japan

Abstract— Cooperative communication systems have emerged as a significant concept to improve reliability and throughput in wireless systems. Some existing cooperative diversity protocol are shown to increase the diversity order, allowing single-antenna nodes to cooperate and achieve performance like a real MIMO system. In this paper, we focus on improving the precision of analysis of Amplify-and-Forward (AF), Decode-and-Forward (DF) in terms of outage probability. Especially, we derive some approximate expressions of outage probability for these three relaying protocols. The approximate expressions are proved to be better than some existing ones, in other words our approximations are much closer to the truth value. In our research, we use the outage probabilities calculated by Monte Carlo Method (MCM) as the reference for the reason that they are the nearest to the truth value. We show analytically and experimentally that our expressions are better than some existing approximate expressions in low Signal to Noise Ratios (SNR) as well. The simulation results and our analysis can prove the accuracy and concision of the expressions. Besides, the approximate expressions are useful to the analysis of outage probability when we investigate the performance of relaying protocols.

1. INTRODUCTION

Cooperative diversity, originally proposed in [1, 2], is a significant concept which has induced many different cooperative diversity protocols. The high reliability and throughput of some efficient protocols such as AF, DF, etc has been proved in [3], and J. Nicholas Laneman et al. develop performance characterizations in terms of outage events and associated outage probabilities which measure robustness of the transmissions to fading, focusing on the high SNR regime. Especially, the asymptotic (in SNR) analysis of outage probability emphasize the achievable diversity order. Moreover, the outage probability analysis is useful to evaluating the performance of cooperative diversity protocols, or rather we have to care about the outage probability of protocols when we aim to improve the reliability.

As far as we know, a set of concise expressions parameterized by SNR and spectral efficiency R are supplied in [3] and used to the analysis of outage behavior. But they cannot be used as low-SNR approximations for the reason that they focus only on high SNR regime. In this paper we derive new approximate expressions of outage probability of AF and DF, and it is also proved that our results are more accurate than those high-SNR approximations. In addition, the simulations by using our newly derived approximate expressions is better than MCM in terms of time complexity.

2. SYSTEM MODEL

We consider a system with a source terminal S, a relay terminal R and a destination terminal D, and moreover, each terminal has only one antenna. In our model for the wireless channel, narrow-band transmissions suffer the effects of frequency nonselective fading and additive noise. Our analysis of outage probability mainly focuses on the case of slow fading, to capture scenarios in which delay constraints are on the order of the channel coherence time. In this paper we utilize channel state information (CSI) at the receivers only while some previous works employs CSI at the transmitters in order to exploit coherent transmission. In addition, half-duplex transmission is employed to overcome the interference between transmitted and received signals. Thus, to ensure half-duplex operation, we divide each channel into orthogonal subchannels. Figure 1 shows our channel allocation for an example time-division approach with two terminals.

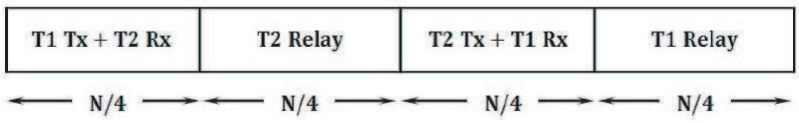

Figure 1: Time-division channel allocations for orthogonal cooperative diversity.

2.1. Channel Model

Under the above orthogonality constrains, we can now conveniently, and without loss of generality, characterize our channel models using a time-division notation. Due to the symmetry of the channel allocations, we focus on the message of "source" terminal T_1, which potentially employs terminal T_2 as a "relay" terminal. We utilize a baseband-equivalent, discrete-time channel model for the continuous-time channel, and we consider N consecutive uses of the channel, where N is large. Moreover, we model the channels between terminals as Rayleigh flat fading with additive white Gaussian noise. Fading remains constant during one time slot, i.e., during the time required to transmit one block of data from the source to the destination.

Then we review the mathematical description on the basis of the above assumption. For direct transmission, the channel is modeled as

$$y_d[n] = h_{sd}x_s[n] + z_d[n] \tag{1}$$

where $x_s[n]$ is the source transmitted signal, and $y_d[n]$ is the destination received signal and $n = 1, \ldots, N/2$.

For cooperative diversity, the channel is modeled during the first half on the block as

$$y_r[n] = h_{sr}x_s[n] + z_r[n], \tag{2}$$

$$y_d[n] = h_{sd}x_s[n] + z_d[n] \tag{3}$$

for $n = 1, \ldots, N/4$, where $x_s[n]$ is the S transmitted signal and $y_r[n]$ and $y_d[n]$ are the R and D received signals, respectively. For the second half of the block, we model the received signal as

$$y_d[n] = h_{rd}x_r[n] + z_d[n] \tag{4}$$

for $n = N/4 + 1, \ldots, N/2$, where $x_r[n]$ is the relay transmitted signal and $y_d[n]$ is the destination received signal. In (1)–(4), h_{ij} captures the effects of path-loss, shadowing, and frequency nonselective fading, and $z_j[n]$ captures the effects of receiver noise and other forms of interference in the system, where $i \in \{s, r\}$ and $j \in \{r, d\}$. We consider the scenario in which the fading coefficients are known to the appropriate receivers, but not known to the transmitters. More specifically h_{ij} are zero-mean, circularly symmetric complex Gaussian random variables, so that $|h_{ij}|^2$ are exponentially distributed with mean σ_{ij}^2. Furthermore, we model $z_j[n]$ as zero-mean mutually independent, circularly symmetric, complex Gaussian random sequences with variance N_0.

2.2. Review of AF, DF Protocols

Fixed relaying protocol is a kind of fundamental cooperative diversity protocol among all the relaying protocols. Under this mode the relay terminal always forwards the message it received from the source terminal in the preceding time slot. Furthermore, this scheme includes Amplify-and-Forward and Decode-and-Forward. As for AF, the relay transmits a scaled version of its received noisy signal while under the DF protocol the relay fully decodes, re-encodes and retransmits the source message. Therefore, the appropriate channel model for AF or Df is (2)–(4). For AF protocol, the source terminal transmits its information as $x_s[n]$, say, for $n = 1, \ldots, N/4$. During this interval, the relay processes $y_r[n]$, and relays the information by transmitting

$$x_r[n] = \beta y_r[n - N/4] \tag{5}$$

for $n = N/4 + 1, \ldots, N/2$. To remain within its power constraint (with high probability), an amplifying relay must use gain

$$\beta \leq \sqrt{\frac{P}{|h_{sr}|^2 P + N_0}} \tag{6}$$

where we allow the amplifier gain to depend upon the fading coefficient h_{sr} between the source terminal and relay terminal. And P is the average signal energy over one symbol period received at the relay terminal. Moreover, in this paper we assume that P of source or relay is constant.

For DF protocol, during the interval the relay terminal processes $y_r[n]$ by decoding as estimate $\hat{x}_s[n]$ of the source transmitted signal. The relay terminal transmits the signal

$$x_r[n] = \hat{x}_s[n - N/4] \tag{7}$$

for $n = N/4 + 1, \ldots, N/2$.

3. OUTAGE PROBABILITY

In this section, we make an improvement on the low-complexity approximate expressions of outage probability of AF and DF. Although some concise approximations of outage probability for all kinds of cooperative diversity protocols have been derived, those expressions are not precise enough when the SNR approaches zero. In other words, these high-SNR approximations apply to the analysis of diversity order or outage behavior, focusing on high-SNR regime. Therefore, we derive some more exact expressions than the former ones in order to make the analysis of outage probability more accurate.

First of all we will briefly review the concept of outage event and outage probability. As a function of the fading coefficients viewed as random variables, the maximum average mutual information for a protocol is a random variable denoted by I. For a target rate (or spectral efficiency) R, $I < R$ denotes the outage event, and $Pr[I < R]$ denotes the outage probability.

3.1. Amplify-and-Forward

The AF protocol produces an equivalent one-input, two-output complex Gaussian noise channel with different noise levels in the outputs. The maximum average mutual information between the input and the two outputs, achieved by i.i.d. complex Gaussian inputs, is given by [3, 4]

$$I_{AF} = \frac{1}{2}\log\left(1 + SNR|h_{sd}|^2 + f\left(SNR|h_{sr}|^2, SNR|h_{rd}|^2\right)\right). \tag{8}$$

For Rayleigh fading, i.e., $|h_{ij}|^2$ independent and exponentially distributed with parameters σ_{ij}^{-2} the high-SNR behavior is approximated as

$$p_{AF}^{out} := Pr[I_{AF} < R] \approx \left(\frac{1}{2\sigma_{sd}^2}\frac{\sigma_{sr}^2 + \sigma_{rd}^2}{\sigma_{sr}^2\sigma_{rd}^2}\right)\left(\frac{2^{2R}-1}{SNR}\right)^2. \tag{9}$$

In [5], an asymptotic approximation is obtained as follows

$$p_{AF}^{out} \approx Pr\left[SNR|h_{sd}|^2 + SNR\frac{\sigma_{sr}^2}{\sigma_{sr}^2 + \sigma_{rd}^2}|h_{rd}|^2 < 2^{2R} - 1\right] \tag{10}$$

by utilizing the result of Fact 1 in Appendix and Taylor's Theorem, we get the approximate expression as follows.

$$p_{AF}^{out} \approx \left(\frac{1}{2\sigma_{sd}^2}\frac{\sigma_{sr}^2 + \sigma_{rd}^2}{\sigma_{sr}^2\sigma_{rd}^2}\right)\left(\frac{2^{2R}-1}{SNR}\right)^2\left(1 - \frac{1}{3}\left(2^{2R}-1\right)\left(\frac{1}{SNR\sigma_{sd}^2} + \frac{\sigma_{sr}^2}{\left(\sigma_{sr}^2 SNR + \sigma_{rd}^2 SNR\right)\sigma_{rd}^2}\right)\right), \tag{11}$$

the results of simulation show that (11) is better than (10) when SNR approaches to zero.

3.2. Decode-and-Forward

The maximum average mutual information for repetition-coded DF can be readily shown to be

$$I_{DF} = \frac{1}{2}\min\left\{\log\left(1 + SNR|h_{sr}|^2\right), \log\left(1 + SNR|h_{sd}|^2 + SNR|h_{rd}|^2\right)\right\}. \tag{12}$$

For Rayleigh fading, the outage probability for repetition-coded DF can be calculated according to

$$\begin{aligned} p_{DF}^{out} :&= Pr[I_{DF} < R] \\ &= Pr\left[|h_{sr}|^2 < \frac{2^{2R}-1}{SNR}\right] + Pr\left[|h_{sr}|^2 \geq \frac{2^{2R}-1}{SNR}\right] Pr\left[|h_{sd}|^2 + |h_{rd}|^2 < \frac{2^{2R}-1}{SNR}\right], \end{aligned} \tag{13}$$

as $SNR \to \infty$, by using the results of Fact 1 in Appendix and Taylor's Theorem we conduct that

$$p_{DF}^{out} \approx \frac{1}{\sigma_{sr}^2}\frac{2^{2R}-1}{SNR}. \tag{14}$$

However, for the purpose of improving the accuracy we calculate the exact value by

$$p_{DF}^{out} = 1 - e^{-(2^{2R}-1)/(\sigma_{sr}^2 SNR)} + e^{-(2^{2R}-1)/(\sigma_{sr}^2 SNR)} p_{SD+RD}^{out}, \tag{15}$$

$$p_{SD+RD}^{out} = \begin{cases} 1 - \left(1 + \frac{2^{2R}-1}{SNR\sigma_{sd}^2}\right) e^{-(2^{2R}-1)/(SNR\sigma_{sd}^2)} & \sigma_{sd}^2 = \sigma_{rd}^2 \\ 1 - \frac{\sigma_{rd}^2}{\sigma_{rd}^2-\sigma_{sd}^2} e^{-(2^{2R}-1)/(SNR\sigma_{sd}^2)} - \frac{\sigma_{sd}^2}{(\sigma_{sd}^2-\sigma_{rd}^2)} e^{-(2^{2R}-1)/(SNR\sigma_{sd}^2)} & \sigma_{sd}^2 \neq \sigma_{rd}^2. \end{cases} \tag{16}$$

In previous works formula (9) and (14) are derived and used to evaluate the diversity order

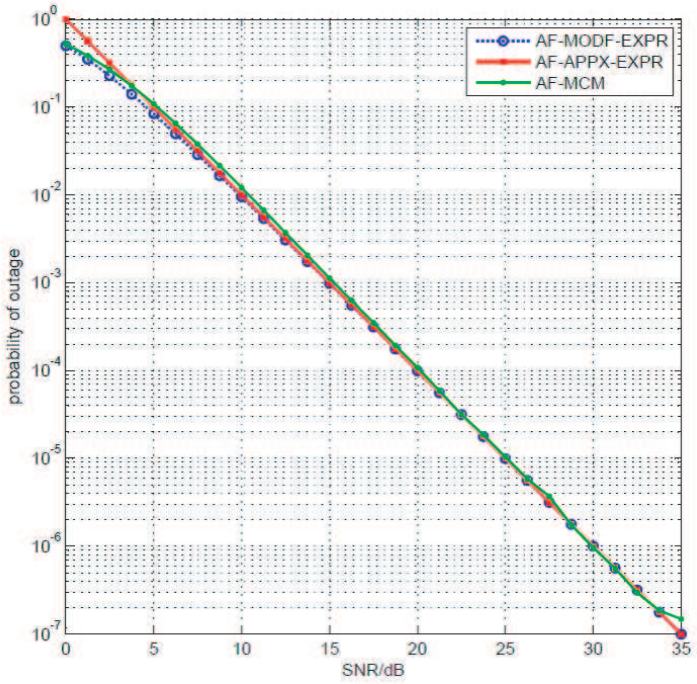

Figure 2: Outage probability of AF protocol.

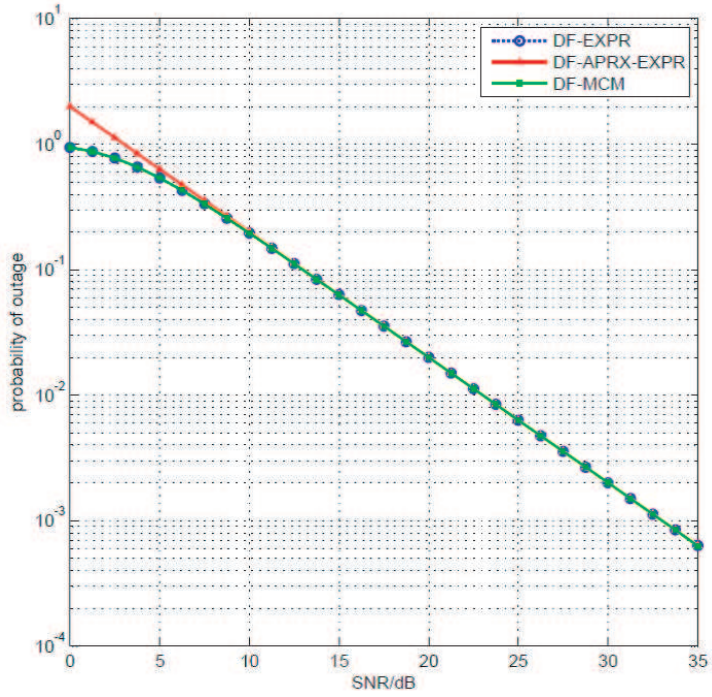

Figure 3: Outage probability of DF protocol.

through proper parameterization. In this paper, we aim to improve the accuracy of analysis by utilizing the formula (11) and (15).

4. SIMULATION RESULTS

In this section we make a comparison between the high-SNR approximations and our newly derived expressions. In the simulations, we use the result calculated by MCM as the baseline performance for the reason that it is more closer than the others. Furthermore, we specialize all of the results to the case of statistically symmetric networks, e.g., $\sigma_{ij}^2 = 1$ without loss of generality.

Figure 2 is the result of outage probability of AF protocol while Figure 3 is the one of DF protocol, both of the target transmission rates are set by $R = 0.5\,\text{bit/s/Hz}$. Figure 2 shows that our expression is better than previous one when SNR is less than 2.5 dB. And we can draw the similar conclusion from Figure 3 as well, moreover, the error rate of our expression is almost zero.

5. CONCLUSION

Our simulation results prove that formula (11) and (15) are better than previous high-SNR approximate expressions in terms of accuracy when we make an analysis of outage probability of AF and DF protocols especially when the SNR approaches to zero. Another point is that our results can be used to some other cooperative diversity protocols that are compounded from AF and DF protocols. But as we can see that these modified expressions do not apply to the analysis of diversity order. All in all they are useful to evaluating the performance of relaying protocols in terms of outage probability.

6. APPENDIX

Fact 1: Let $w = u + v$, where u and v are independent exponential random variables with parameters λ_u and λ_v, respectively. Then the cumulative distribution function (CDF)

$$P_w(\omega) = \begin{cases} 1 - (1 + \lambda\omega)e^{-\lambda\omega} & \lambda_u = \lambda_v = \lambda \\ 1 - \left[\left(\frac{\lambda_v}{\lambda_v - \lambda_u}\right) e^{-\lambda_u\omega} + \left(\frac{\lambda_u}{\lambda_u - \lambda_v}\right) e^{-\lambda_v\omega}\right] & \lambda_u \neq \lambda_v. \end{cases} \tag{17}$$

can be represented by (17).

REFERENCES

1. Sendonaris, A., E. Erkip, and B. Aazhang, "User cooperation diversity, Part I: System description," *IEEE Trans. Commun.*, Vol. 51, 1927–1938, Nov. 2003.
2. Sendonaris, A., E. Erkip, and B. Aazhang, "User cooperation diversity, Part II: Implementation aspects and performance analysis," *IEEE Trans. Commun.*, Vol. 51, 1939–1948, Nov. 2003.
3. Laneman, J. N., D. N. C. Tse, and G. W. Wornell, "Cooperative diversity in wireless networks: Efficient protocols and outage behavior," *IEEE Trans. Inform. Theory*, Vol. 50, No. 12, 3062–3080, Dec. 2004.
4. Telatar, İ. E., "Capacity of multi-antenna Gaussian channels," *Europ. Trans. Telecommun.*, Vol. 10, 585–596, Nov.–Dec. 1999.
5. Zhou, C., "The study of cooperative diversity protocols in wireless communication," [M]. Ph.D. dissertation, NUPT, China, 26–42, Mar. 2010.
6. Zimmermann, E., P. Herhold, and G. Fettweis, "On the performance of cooperative diversity protocols in paractical wireless systems," *2003 IEEE 58th Vehicular Technology Conference, VTC 2003-Fall*, Vol. 4, 2212–2216, Otc. 2003.

Improvement of Source Stirring to Field Uniformity in Reverberation Chamber

Shuang Li[1], **Jianguo Wang**[1, 2], **Haiyan Xie**[1], **and Xicheng Lu**[1]

[1]Northwest Institute of Nuclear Technology, P. O. Box 69-12, Xi'an 710024, China
[2]School of Electronic and Information Engineering, Xi'an Jiaotong University, Xi'an 710049, China

Abstract— Current highpower microwave (HPM) sources generate very short pulses. The durations of such pulses are much less than the characteristic time of mechanical movement in the traditional reverberation chambers (RCs). Thus it is not suitable to use mechanical stirring to research the HPM effect on the subsystems such as electronic or electric equipments in the RC However, the way of source stirring, without mechanical tuning equipments, is feasible to stir the field distribution in the RC by changing the positions of the sources. This article mainly studies the influence of source stirring on the field distribution in RC under short HPM pulse excitation. Firstly, the source's position is proved to be an important factor that may affect the field distribution. Then the focus is on the effects of moving the sources consecutively on the characteristics of the electromagnetic field. As a statistical process, the main attention is paid to the maximums and the standard deviations of the electric field strength. The results show that it is capable to stir the field and enhance the homogeneity of field distribution with source stirring. Therefore, the method of source stirring can improve the field uniformity effectively and it is valid to make a homogenous electromagnetic field environment for HPM effect tests.

1. INTRODUCTION

The high-power microwave (HPM) technology develops fast in recent years. It threatens not only the military equipments but also the civil infrastructures [1–3]. So it is important to have the HPM effect tests on the equipments. Traditionally, the HPM effect tests on the whole systems can be carried out in the open area test site and the anechoic chamber. The conventional techniques are effective and straightforward. However, they cost much and the experiment processes are complex. Moreover, the response of the whole system has a strong relationship with the subsystems in it. The electromagnetic environment around the subsystems is very complex. The HPM can enter the cavities through apertures, slots and so on. And the interaction between the HPM and the subsystems in the cavity can affect the whole system destructively. Thus it is essential to have the HPM effect tests on the subsystems. While, the conventional test methods could hardly simulate the complex electromagnetic environment around the subsystems. Then it is greatly difficult to take the HPM effect tests on the subsystems.

As a new test equipment for the electromagnetic measurement, the reverberation chamber (RC) can provide a statistically homogeneous and isotropic field [4]. With the ability of simulating the complex electromagnetic environment, it has an important influence on the research of HPM effect in the complex resonators. The research of RC develops rapidly in the last twenty years. Professor Hill worked on the research of basic theory of RC. He presented the plane wave integral representation in the RC study and brought the RC technology into the electromagnetic compatibility (EMC) measurement [5, 6]. Prof. Crawford and his colleagues performed a series of experiments on the design of configuration and the evaluation of performances in the RC [7]. Recently, more and more new design ideas are appeared too. Y. Huang developed the way of source stirring into the RC firstly. The technique gets rid of the limit of mechanical stirrers successfully and provides a new approach to realize the uniform field in RC [8]. However the research of the RC now is mostly based on the continuous wave excitation and little attention is paid to the characteristics of the RC with pulse excitation. Through both theoretical analysis and numerical results, this article focuses on the field characteristics of RC with short HPM pulse excitation and the feasibility of the source stirring in the improvement of the field uniformity in such RCs.

2. THEORETICAL ANALYSE

2.1. The Mode Theory in Ideal Resonators

As an electrically large and enclosed resonator in nature, the RC could be taken as a three-dimensional resonator with source in it, which is shown in the Fig. 1(a). The rectangle resonator is made of the ideal conductor and the excitation source I_0 is placed at the position (x_0, y_0, z_0).

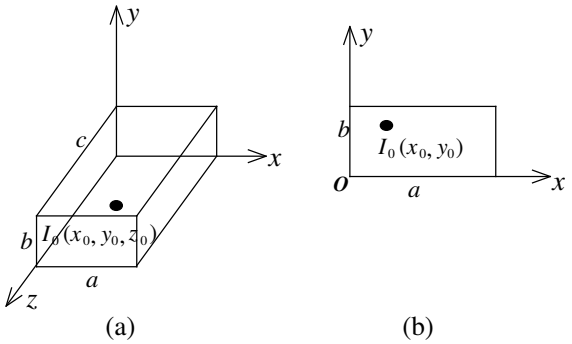

Figure 1: The models of three-dimensional and two-dimensional cavities, (a) three-dimensional, (b) two-dimensional.

In order to acquire the forms of the electromagnetic field distribution in that cavity, it is essential to take the corresponding dyadic Green's function into account. The questions can be represented as [8]

$$E = \frac{1}{j\omega\varepsilon} \int \bar{\bar{G}} \cdot I_0(x_0, y_0, z_0) dV', \tag{1}$$

where $\bar{\bar{G}}$ is the dyadic Green's function and V' denotes the area for the integral.

It is very complex to solve the function (1) above. Therefore, the two-dimensional cavity is considered to simplify the problem. A simplified two-dimensional ideal rectangular cavity is shown in Fig. 1(b) and $I_0(x_0, y_0)$ is the source in it. The electric field in the cavity is expressed as [9]

$$E_z = \frac{4j\omega\mu_0 I_0}{ab} \sum_{m=1}^{\infty} \sum_{n=1}^{\infty} \frac{\sin(m\pi x_0/a) \sin(m\pi x/a) \sin(n\pi y_0/b) \sin(n\pi y/b)}{k^2 - (m\pi/a)^2 - (n\pi/b)^2}, \tag{2}$$

where a and b are the dimensions of the cavity and m and n are mode indices. ω is the angular frequency and μ_0 is the magnetic permeability constant

The frequency of the mode f_{mn} in the cavity is given by

$$f_{mn} = \frac{c_0}{2} \sqrt{\left(\frac{m}{a}\right)^2 + \left(\frac{n}{b}\right)^2}, \tag{3}$$

where c_0 is the velocity of light in the free space.

Based on the Equation (2), the electric field distributions in the cavity are determined by the following two parts: (i) The shape and dimensions of the cavity, expressed by the parameters of a and b; (ii) the characteristics of the excitation source, including the position (x_0, y_0), the frequency and so on. The RC can be disturbed by changing either the boundaries or the excitation parameters. The source stirring method is based on (ii). When the working frequency, dimensions, and boundary conditions of the cavity are fixed, the energy distribution among the modes is determined by excitation source [10]. So changing the positions of the source continuously will stir the energy distribution among different modes and consequently the electromagnetic field can be well stirred.

2.2. The Statistical Method for the Uniformity

The main advantage of the RC is its ability to provide a uniform electromagnetic environment. But it does not mean that the field strength in the chamber are all equal at any time. The uniformity here is just a statistical concept actually. And the statistics is employed to describe the characteristics of the field.

According to the international standard of IEC 61000-4-21 [11], there are eight probes at the corners in the test volume to detect the field strength in the chamber. When the source comes to an individual location in one stirring period, the probes are used to record the maximums of the three rectangular components of the electric field strength respectively. The maximum is marked as $E_{\xi \max i}$ $(\xi = x, y, z)$ and the suffix i indicates the i-th location in an entirely stirring cycle. At last, all the recorded values should be normalized by the input power in one period.

The average values of the electric field along the three coordinates individually and the combined average values of the three components are:

$$\langle E_\xi \rangle = \frac{1}{N} \sum_{i=1}^{N} E_{\xi \max i} (\xi = x, y, z) \tag{4}$$

and

$$\langle E_{xyz} \rangle = \frac{1}{3N} \sum_{\xi=\{x,y,z\}} \sum_{i=1}^{N} E_{\xi \max i}, \tag{5}$$

where N expresses the number of measurement points and it is equal to eight here, which is the number of the probes.

And then the standard deviations of the field strength are

$$\sigma_\xi = \sqrt{\frac{\sum\limits_{i=1}^{N} (E_{\xi \max i} - \langle E_\xi \rangle)^2}{N-1}}, \quad (\xi = x, y, z) \tag{6}$$

and

$$\sigma_{xyz} = \sqrt{\frac{\sum\limits_{\xi=\{x,y,z\}} \sum\limits_{i=1}^{N} (E_{\xi \max i} - \langle E_{xyz} \rangle)^2}{3N-1}}. \tag{7}$$

The corresponding deviations expressed in terms of dB relative to the mean values are given by

$$\sigma_\xi|_{\mathrm{dB}} = 20 \log \frac{\sigma_\xi + \langle E_\xi \rangle}{\langle E_\xi \rangle} \quad (\xi = x, y, z) \tag{8}$$

and

$$\sigma_{xyz}|_{\mathrm{dB}} = 20 \log \frac{\sigma_{xyz} + \langle E_{xyz} \rangle}{\langle E_{xyz} \rangle}. \tag{9}$$

3. THE NUMERICAL MODEL

This research aims at the field characteristics in the RC with HPM pulse excitation. While, the transient field in the RC changes rapidly with time and it is hard to reach the steady state [12]. Moreover, main attention here is paid to the study of the HPM effect on the EUT. So it is not appropriate to take the method of mechanical stirring in such RCs and the way of source stirring, avoiding the mechanical equipments, is feasible to stir the field distribution in the RC. Therefore it can successfully be applied in the RC with HPM excitation. The study primarily focuses on the impact of source stirring on the field distribution by changing the positions of the source continuously.

The dimensions of the model are $0.46\,\mathrm{m} \times 0.59\,\mathrm{m} \times 0.62\,\mathrm{m}$ and the material is chosen as the perfect electronic conductor. The structure of the chamber is shown in Fig. 2. The source is placed at the corner of the chamber and at least a quarter wavelength far away from the walls. It transmits toward the z-direction. There are some metallic diffusers randomly on one wall of the chamber in order to spread the reflected waves into many directions [13]. The distances of the test volume to the walls are not less than a quarter wavelength of the lowest useful frequency.

The chamber is excited by the following rectangle pulse

$$F = \sin\left(2\pi \times 3.0 \times 10^9 \times t\right) \times u(t), \quad u(t) = \begin{cases} 1, & 0 < t \le 10\,\mathrm{ns} \\ 0, & t > 10\,\mathrm{ns} \end{cases}. \tag{10}$$

By simulating a three-dimensional chamber with the use of the finite difference time domain (FDTD) codes, the work compares the transient response of electric field in each model first of all. Then the characteristics of the field in the frequency domain are analyzed through the statistical calculation of the electric field's maximums and standard deviations.

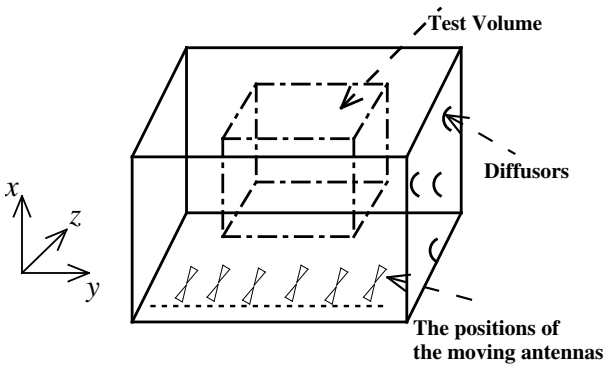

Figure 2: The source stirring model.

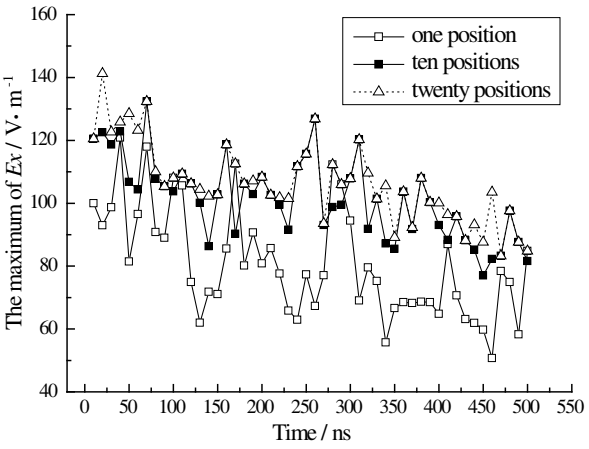

Figure 3: The characteristics of the x-component of the electric field in the time domain.

4. THE SIMULATION RESULTS

4.1. The Results in the Time Domain

In order to realize the source stirring, the source moves at several separate locations in a stirring period. One, ten and twenty positions are selected for the comparison. The statistical characteristics of the transient field, which are represented by the x-component of the electric field, are shown in Fig. 3.

As can be seen in Fig. 3, the maximum values of field strength are different with different stirring steps. And the more the stirring steps are, the higher the maximum will be obtained. This is mainly owing to that the source transmits at a few positions and there are more mode components at the electric field points. So the fields are disturbed with the source's removes and may reach a higher peak value. On the contrary to the mechanical stirring, the source stirring could be achieved by the electronic operations in practice, which means the avoidance of the mechanical equipments and a larger areas for test. What's more, the maximum of electric field can reach a higher value with stirring the source. Thus this method is feasible in the RC with short pulse excitation and is available for the HPM effect tests in RC.

4.2. The Results in the Frequency Domain

The results in frequency during the three stirring processes are displayed in Table 1 below.

Table 1: The maximums of the components of the electric field in the three stirring process.

$E_{\xi\,\max}$	one position	ten positions	twenty positions
$E_{x\,\max}/\left(\mathrm{V}\cdot\mathrm{m}^{-1}\right)$	2997.685	4448.631	4448.631
$E_{y\,\max}/\left(\mathrm{V}\cdot\mathrm{m}^{-1}\right)$	2327.056	2734.444	3090.118
$E_{z\,\max}/\left(\mathrm{V}\cdot\mathrm{m}^{-1}\right)$	2438.539	2726.439	3860.343

In the twenty positions stirring course, the maximum of the field reaches as high as 6.7 kV/m with an input power of 1-Watt averagely. This field environment is completely competent for the HPM effect tests under given frequencies. Moreover, the peak values increase with the increment of the stirring steps. Thus it is able to afford a higher field strength with the same input power and gets rid of the requirement of the power amplifier. It could be seen in the Table 1 that the maximums of the $E_{x\,\max}$ in the ten-positions and twenty-positions cases are equal. This is due to that the moving positions in the two unconcerned processes have a certain superposition and fortunately the source at this superposition exactly excites the maximum of the $E_{x\,\max}$. What's more, the x-components of the field strength are the largest among the three components during all the three stirring processes. This is related with the shape of the resonator. Obviously, the length along the x-direction is the shortest of the resonator and the electric field in the chamber are the compounds of all the direct and reflected electromagnetic waves. As a result, there are more reflected waves along the x-direction correspondingly and the amplitudes of the field are larger consequently.

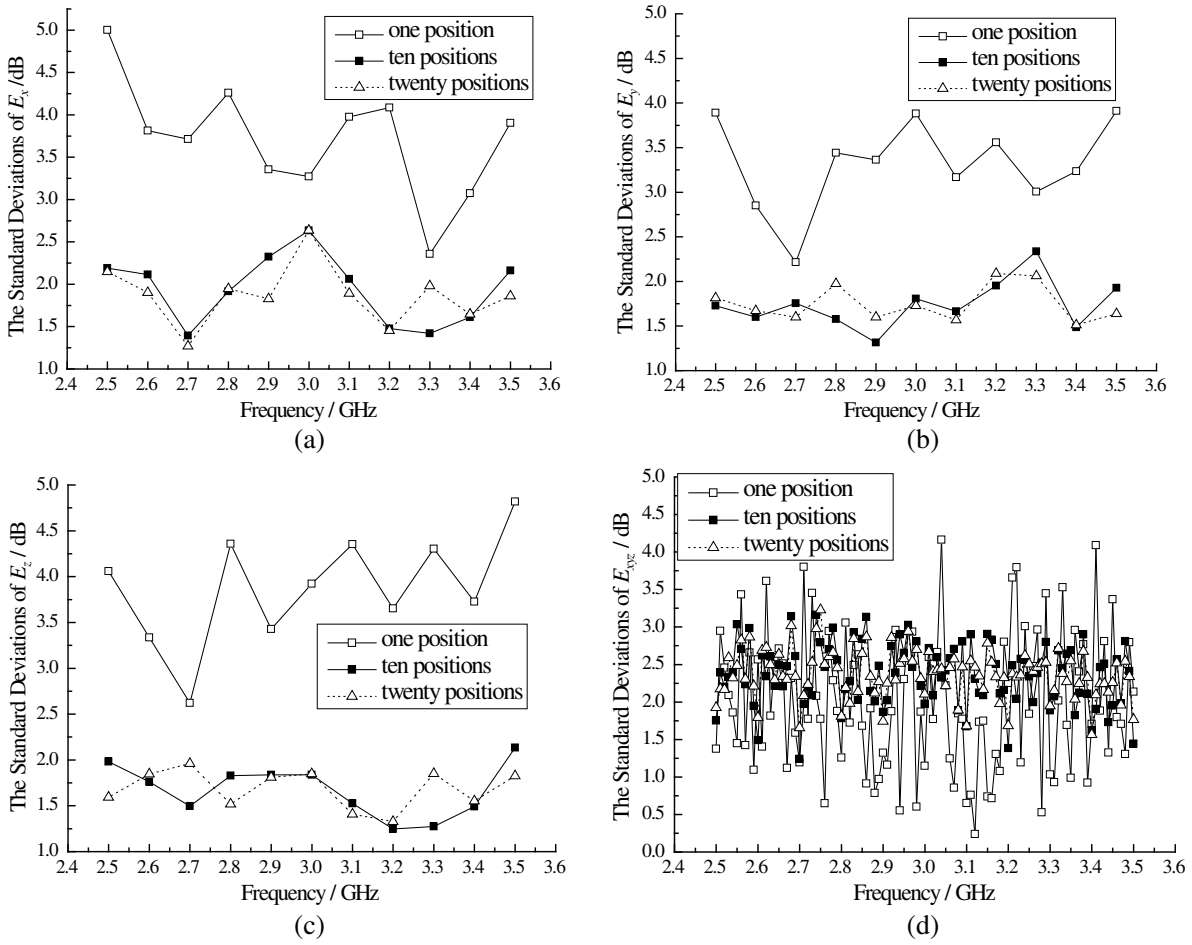

Figure 4: The standard deviations of the field strengths in different stirring ways, (a) the x-component, (b) the y-component, (c) the z-component, (d) the combined of xyz components.

The strengths of the points in the chamber change greatly with the movement of the source and it is essential to take a statistical analysis of the field strengths in a whole stirring period to explain the uniformity of the field. According to the statistical method mentioned above, the field uniformity in the three stirring ways are exhibited as in Fig. 4.

As can be seen in the Figs. 4(a), (b) and (c), the standard deviations of the three components in the one position case are very high and the curves shake strongly. It indicates that the field strength of the points differ from each other. So this stirring way is not possible to offer a uniform environment and is not suitable for the HPM effect tests in the RC. In contrast to that, the standard deviations under the ten and twenty positions cases get smaller and the homogeneity of the fields are well improved. Furthermore, the standard deviations are all less than 3 dB after the stirring, which accord with IEC 61000-4-21. The results of the combined deviations are similar. As shown in Fig. 4(d), the deviations under ten and twenty positions are smaller than that under one position and they are mostly less than 3 dB which means an improvement of the field uniformity in all the three directions. Theoretically the more positions the source move, the more uniform the field will be obtained. And this is fully proved in Fig. 4(d), where the deviation results under twenty positions are smaller than those under ten positions in the main. Thereby extending the working region of the source is useful to stir the field well and effective to improve the uniformity.

5. CONCLUSIONS

By changing the positions of the sources continuously, the article studies the impact of the source stirring method on the characteristics of the field in the RC under HPM excitation. Firstly, the influence of the source's position on the field distribution is analyzed theoretically. And then the statistical results including the maximums and the standard deviations of the field strength in a complete stirring period are compared. The results demonstrate that the source stirring method

is appropriate in RC excited by HPM pulses and it could stir the field distribution effectively. Moreover, it is capable to improve the uniformity of the field. So the source stirring is powerful to make a homogeneous field environment and is significant for the research of HPM effect test in the RC.

REFERENCES

1. Benford, J., J. Swegle, and E. Schamiloglu, *High Power Microwaves*, 2nd Edition, CRC Press, New York, 2007.
2. Baker, R. J. and E. Schamiloglu, *High-power Microwave Sources and Technologies*, Tsinghua University Press, Beijing, 2004.
3. Backstrom, M. G. and K. G. Lovestrand, "Susceptibility of electronic systems to high-power microwaves: Summary of test experience with coherent OFDR," *IEEE Transactions on Electromagnetic Compatibility*, Vol. 46, No. 3, 396–403, Aug. 2004.
4. Corona, P., J. Ladbury, and G. Latmiral, "Reverberation chamber research-then and now: A review of early work and comparison with current understanding," *IEEE Transactions on Electromagnetic Compatibility*, Vol. 44, No. 1, 87–94, Feb. 2002.
5. Hill, D. A., "Plane wave integral representation for fields in reverberation chambers," *IEEE Transactions on Electromagnetic Compatibility*, Vol. 40, No. 3, 209–217, Aug. 1998.
6. Hill, D. A., "Electromagnetic theory of reverberation chamber," National Institute of Standards and Technology, TN 1506, Dec. 1998.
7. Crawford, M. L. and G. H. Koepke, "Design, evaluation, and use of a reverberation chamber for performing electromagnetic susceptibility/vulnerability measurements," National Bureau of Standards, TN 1092, Apr. 1986.
8. Huang, Y. and D. J. Edwards, "A novel reverberating chamber: The source-stirred chamber," *8th International Conference on Electromagnetic Compatibility*, 120–124, Oxford, UK, 1992.
9. Shen, Y. M. and Y. G. Gao, "Research about source-stirred reverberation chamber and electromagnetic interference measuring receiver in the field of electromagnetic compatibility tests," Ph.D. Thesis, 60–70, Beijing University of Posts and Telecommunications, Beijing, 2006.
10. Ding, J. J., "Theory, measurement and design of reverberation chamber," Beijing Jiao Tong University, Beijing, China, Aug. 2005.
11. Electromagnetic compatibility (EMC), Part 4-21: Testing and measurement techniques-reverberation chamber test methods. International Electromagnetical Commission, IEC SC77B-CISPR/A JWGREV, Geneva, Switzerland, Aug. 2003.
12. Rothenhaeusler, M., "High power microwave testing in a reverberation chamber," *Proc. 39th European Microwave Conf.*, 295–298, Rome, Italy, Sep. 2009.
13. Petrisch, M. and A. J. Schwab, "Investigation of the field uniformity of a mode-stirred chamber using diffusers based on acoustic theory," *IEEE Transactions on Electromagnetic Compatibility*, Vol. 41, No. 4, 446–451, Nov. 1999.

Notebook EMI Noise Analysis and WLAN TIS Performance Improvement with Periodic Structure

Han-Nien Lin[1], **Ming-Cheng Chung**[1], **and Ming-Shan Lin**[2]

[1]Department of Communications Engineering, Feng-Chia University
100 Wen-Hua Rd., Taichung 40724, Taiwan, R.O.C.
[2]Section of EMC, Bureau of Standards, Metrology & Inspection
M.O.E.A., Taipei, Taiwan, R.O.C.

Abstract— Cloud computation and always-connected Internet gains the most industrial attention for the past few years. Meanwhile, with the development of IC technologies advancing toward higher operating frequenciesand the trend of miniaturization on wireless communication products, the circuits and components are placed much closer than ever before. The system with highly integrated high-speed digital circuits and multi-radio modules are now facing the challenge from performance degradation by even more complicated platform EMI noisy environment. The EM noises emitted by unintentionally radiated interference sources may severely impact the receiving performance of antenna, and thus result in the severe performance degradation of wireless communications. Therefore, we have investigated and analyzed the EMI noise characteristics of commonly embedded digital devices for further high performance wireless communications design. Since the CAMERA or CMOS camera module is most adopted to the popular mobile devices like cellular phone or Netbook, we hence focus on EMI analysis of the built-in camera module by application of IEC 61967-3 method. To improve the wireless communication TIS performance onnotebook computer, we first investigated the EMI noise from the built-in camera module and analyzed the impact of various camera modes on performance with throughputmeasurement. We then utilized the near-field EM surface scanner to detect the EMI sources on notebook and locate themajor noise sources around antenna area with 2-D hot-spot distribution plot. Finally, we designed and implemented periodic structures for isolationon the notebook computer to effectively suppress noise source-antenna coupling and improve the receiving sensitivity of wireless communication system.

1. INTRODUCTION

Due to the miniaturization of a variety of wireless communications products, the layout and trace routing of circuits and components become much denser than ever before. Meanwhile, with the development of IC technologies advancing toward nano-meter processing and higher operating frequencies in recent years, the systems of highly integrated high-speed digital circuits and multi-radio modules are now facing the challenge from performance degradation by more complicated electromagnetic noisy environment. The EM noises emitted by unintentionally radiated interference sources will severely impact the receiving performance of antenna, and thus result in the severe performance degradation of wireless communications platform. The causes for throughput or coverage reduction due to degradation of wireless system could result from conducted or radiated EMI noises from nearby digital components.This study is to further RF sensitivity analysis for components and devices on laptop computer. To utilize the near-field EM scanner to detect the EMI sources on laptop, we can locate the major noise sources in 2D hot-spot distribution graph. Therefore, we have investigated and analyzed the noise effect of co-existing high-speed digital devices and multi-radios platform for further high-sensitivity wireless communications design. From the emission levels and locations of the noisy components, we can figure out their impact on throughput and receiving sensitivity of wireless communication and find the solution to improve performance.

2. THE IMPACT OF CAMERA MODULE ON WIRELESS PERFORMANCE

The common interference noise sources on integrated highspeeddigital wireless communication product nowadaysinclude: CPU, LCD panel [1], Memory, digital components [2], high-speed I/O interconnect, wires and cables [3], etc. Theabove mentioned noises are usually coupled to nearby sensitivedevices through radiation, conduction, or crosstalk. Theresulted EMI problem will further degrade the systemsensitivity and performance for wireless communications.The purpose of this study is first to measure the noise leveland the related spectra at the antenna port, and then follow IEC61967-3 surface scan method utilizing near-fieldelectromagnetic measuring system equipped

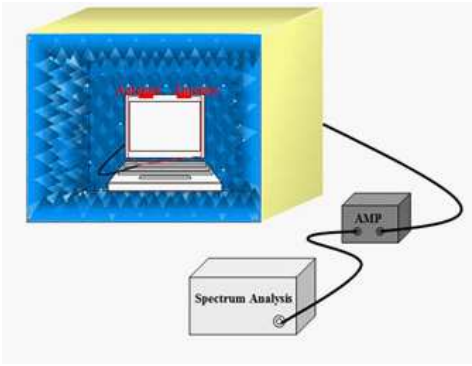

Figure 1: Setup for noise level measurement.

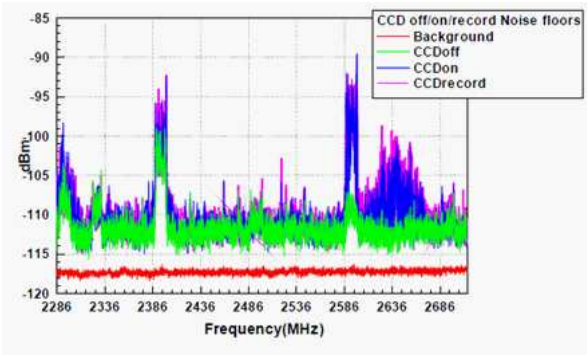

Figure 2: Noise level for different Camera operation mode.

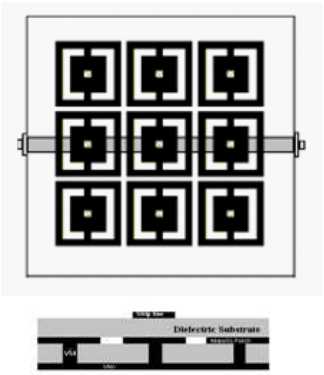

Figure 3: Schematic of periodic structure.

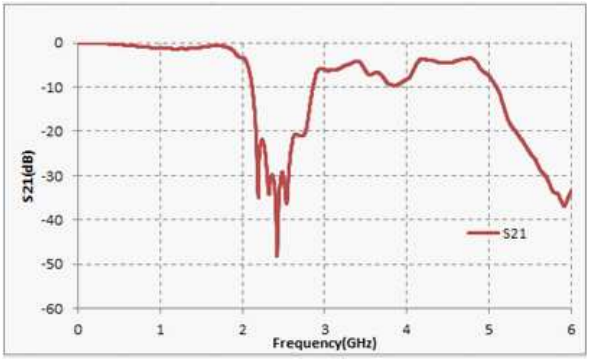

Figure 4: Simulated transmission coefficient of periodic structure.

with visualinterface to locate the noise source with field strength ofemitted noise by color-enhanced pattern. Because a variety of digital components exist inside laptopcomputer, we focus on Camera module that is equipped in allcomputers and usually placed in the proximity of antennas. Toinvestigate the effect of various Camera operation modes, (such as off, standby, and RECORD mode) on noise level atthe antenna port, we first arranged the test setup as laptopnormally working and scanned the ambient noise. Afteractivating the Camera module for testing mode, we measuredthe noise spectrum at antenna port to find out the interferencefrequencies and located the noise source(s) from 2D hot-spotfield distribution obtained by near-field electromagneticmeasuring system.

The platform noise under investigation is analyzed bynoise floor measurement system. The complete PNS (platform noise measuring system) is composed of shieldedbox, pre-amplifier, spectrum analyzer, and EUT (Laptopcomputer). The noise level measuring system and setup forfrequency domain is shown in Fig. 2. Variation of noise level for Camera module at differentoperation mode is shown in Fig. 2. We can observe thesignificant variation of noise level in 2386∼2416 MHz, 2586∼2600 MHz frequency range when Camera is activated and operated atRecord mode. Since the crystal oscillation of Camera is 48 MHz, we can conclude that its 50th and 54th harmonics justfall at 2400 MHz and 2592 MHz, the most significant noiselevel frequencies, respectively. Therefore, the receivingsensitivity and thus the communications performance in 2.4 GHz band are degraded by the activation of Camera functions.

3. ANALYSIS OF EBG STRUCTURE DESIGN

From Bragg condition [4]. The stop-band and center frequency of EBG structure presented in this paper is around 2.4 GHz for WLAN system. When FR4 substrate (ε_r = 4.4 and thickness 16 mm) is used in this design, The dimension and EBG structure investigated in this paper are 3×3 Unit cellsas shown in Fig. 3. The resulted transmission characteristic is shown in Fig. 4, where the bandwidth of stop-band is around 600 MHz (2.1∼2.7 GHz) to meet −20 dB attenuation specification.

4. RESULTS OF SURFACE-SCANNING MEASUREMENT

We can easily find out the interference frequenciesgenerated by camera module form the result of noise levelmeasurement. We then utilize the near-field surface scanner tofurther locate the area with higher noise level. We also place the EBG structure between the antennas and Camera module for further analysisThe scannedarea for camera module is illustrated as shown in Fig. 6. However, since the total scanned area is quite large for datastorage, we divide it into three parts and measure the noiselevel individually. From the scanned result of antenna part shown in Fig. 7, wefind that the hot-spot and thus the noise level is higher forcamera module operated in RECORD mode than disabledmode. We can also find that the scanned result shown in Fig. 8 reveals higher noise level around 2400 MHz forcamera module operated in RECORD mode than disabledmode. The results for overlap area of antenna and cameramodule during OFF and RECORD mode are shown in Figs. 9 and 10 respectively. It shows that the camera moduleoperating in RECORD mode will result in strongerinterference to antenna due to stronger near-field coupling. After placedEBG structure in the overlap the near-field coupling significantly reduced. From the scanned result of camera module part shown in Fig. 11, we find that the hot-spot and thus the noise level is higherfor camera module operated in different operation mode.Because the magnetic probe was aligned in parallel withconnector of Camera module, the more significant noise levelwas observed around the connector when Camera wasactivated in RECORD mode. From the result shown in Fig. 12, we

Figure 5: Setup of PNS measuring system.

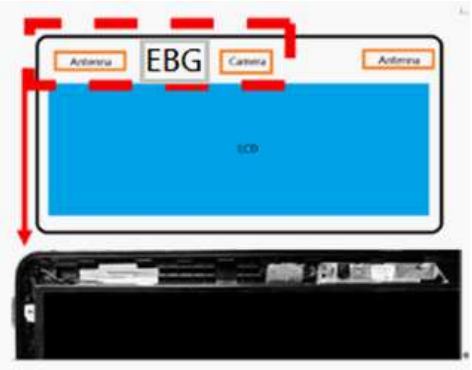

Figure 6: Physical Camera under test.

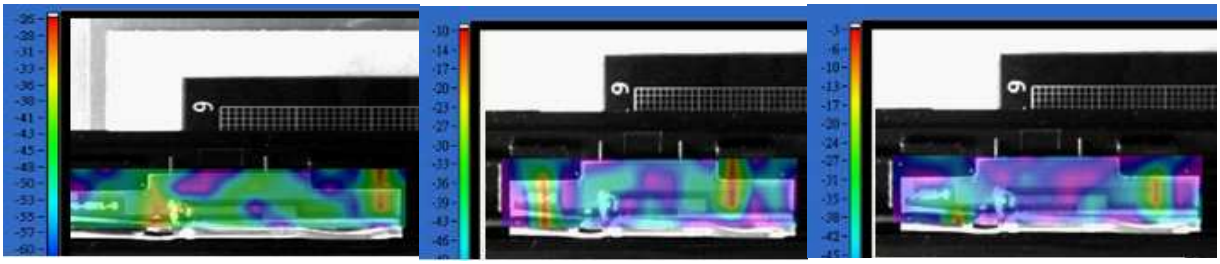

(a) (b) (c)

Figure 7: 2D Hot-spot scanned resultfrom antenna zone. (a) Disabled mode. (b) RECORD mode. (c) RECORD mode with EBG.

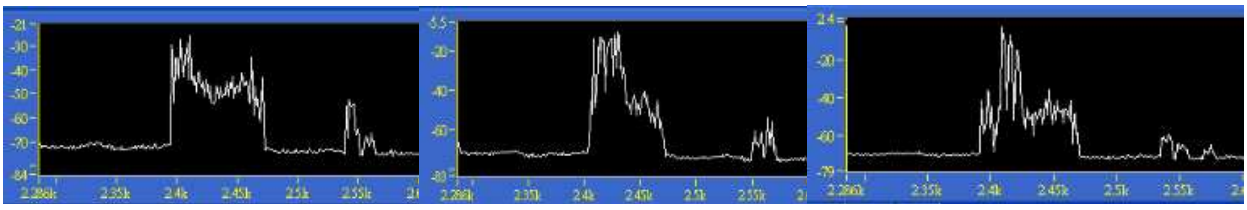

(a) (b) (c)

Figure 8: Corresponding spectrum of surface scanning noise from antenna zone. (a) Disabled mode. (b) RECORD mode. (c) RECORD mode with EBG.

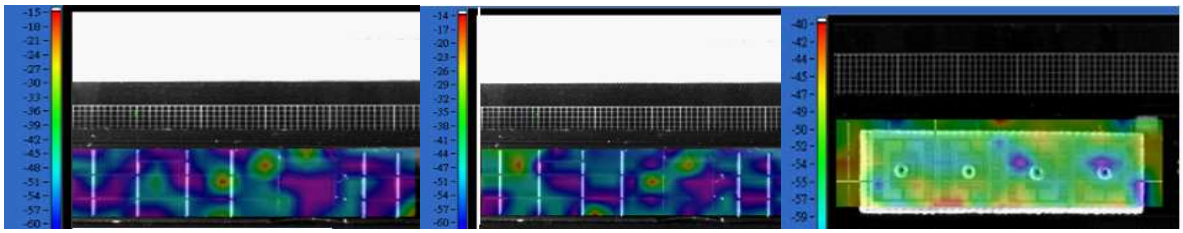

(a) (b) (c)

Figure 9: 2D Hot-spot resultscannedfrom overlap area. (a) Disabled mode. (b) RECORD mode. (c) RECORD mode with EBG.

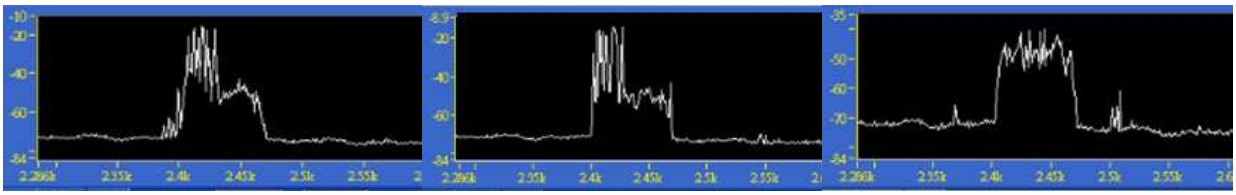

(a) (b) (c)

Figure 10: Corresponding noise spectrum from surface scanning onoverlapped area. (a) Disabled mode. (b) RECORD mode. (c) RECORD mode with EBG.

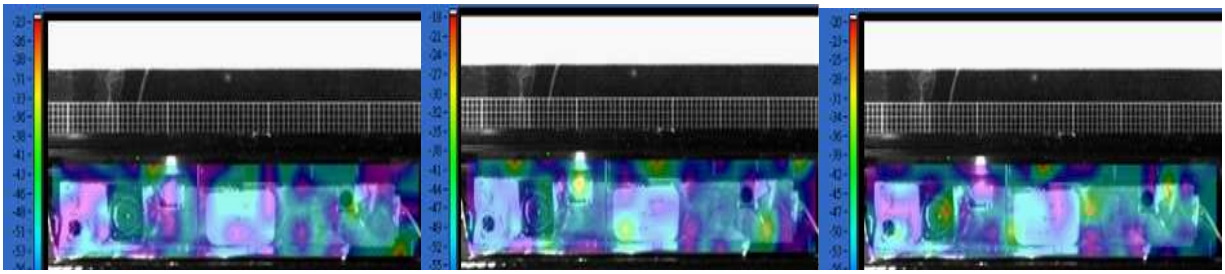

(a) (b) (c)

Figure 11: 2D Hot-spot result scanned from Camera zone. (a) Disabled mode. (b) RECORD mode. (c) RECORD mode with EBG.

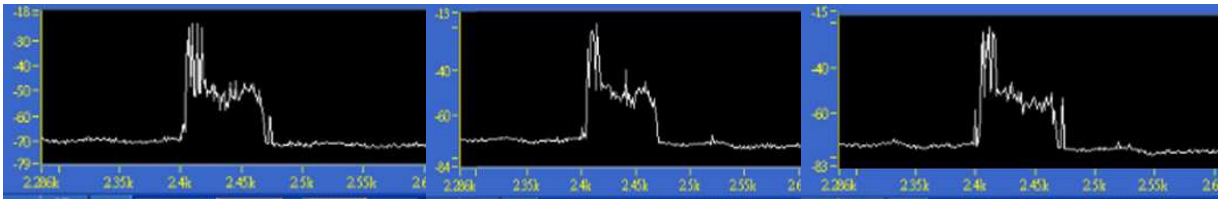

(a) (b) (c)

Figure 12: Corresponding noise spectrum from surface scanning on Camera zone. (a) Disabled mode. (b) RECORD mode. (c) RECORD mode with EBG.

can identify the frequency band interfered by the Cameraoperating in different function mode. Since the crystaloscillation of Camera is 48 MHz, we can find that its 50th harmonics just falls at 2400 MHz and has significant impact onnoise level at antenna port.

5. CONCLUSION

To utilize the near-field surface scanner, we can obtain the distribution for those commonly found noise sources. Finally, we designed and implemented periodic structures for isolation on the notebook computer to effectively suppress noise source-antenna coupling and improve the receiving sensitivity of wireless communication system We can further find the optimal orientation and location of component to improve overall communications performance.

ACKNOWLEDGMENT

The authors would like to thank funding from NSC (NationalScience Council). The original research work presented in this paper was made possible in part by the NSC under Contract No. NSC 99-2221-E-035 -013, grant from NSC Taiwan.

REFERENCES

1. Ranganathan, S., D. G. Beetner, R. Wiese, and T. H. Hubing, "An expert system architecture to detect system-level automotiveemc problems,".
2. Lee, S.-K. J.-M. Lim, K.-S. Lee, O.-S. Choi, B.-W. Lee, D.-W. Kim, M. Hayakawa, and Y. Kami, "The solutions of LCD panel (T-Con) EMI noise for wireless integration," *IEEE International Symposium on Electromagnetic Compatibility, 2007. EMC 2007*, 1–4, July 9–13, 2007.
3. Ko, C.-W., Y.-S. Hong, W.-J. Jin, J.-S. Shim, D.-W. Kim, J.-B. Lee, J.-H. Choi, M.-H. Yoo, and J.-T. Kong, "EMI analysis of the LCD panel considering the display driver IC operations," *IEEE 14th Topical Meeting on Electrical Performance of Electronic Packaging*, 225–228, October 24–26, 2005.
4. Caloz, C. and T. Itoh, *Electromagnetic Metamaterials: Theory and Design*, Wiley-Interscience, New Jersey, 2006.

Grey Relational Clustering Applied to FPGA System Routing with Minimal Wire Length and Delay

Jan-Ou Wu[1], **Yang-Hsin Fan**[2], **and San-Fu Wang**[3]

[1]Department of Electronic Engineering, De Lin Institute of Technology, Tu-Cheng, Taipei, Taiwan, R.O.C.
[2]Department of Computer Science and Information Engineering, National Taitung University
Taitung, Taiwan, R.O.C.
[3]Department of Electronic Engineering, Ming Chi University of Technology
Taipei, Taiwan,, Taiwan, R.O.C.

Abstract— This paper proposes *grey relational clustering to hierarchical routing* (GRCHR) to solve physical routing problems for *field programmable gate array* (FPGA). The study comprises of four stages to achieve routed timing constraints with minimal wire length and delay. In the first stage, the predominant method exploits the *grey relational clustering of hierarchical* (GRCH) approach that consists of grey relational analysis theory and *grey local topology modification* (GLTM) technology to satisfy the demanding placement requirements. In the second stage, the global routing strategy applies line-probe hightower and matching-based segmentation technology to attain a set of shorter nets and wires for routing regions. In the third stage, the detail routing scheme adopts dogleg router algorithm to decrease routing track number in routing channel and assigns the connection block and switch block in channel routing. Furthermore, we compute Elmore delay model to obtain minimal delay within the assigned routing regions. Finally, the effectiveness of the proposed approach is demonstrated by assessing a case for four sinks example. The evaluation of MCNC benchmarks via *versatile place and route* (VPR) tool for verification will be assessed in the future work.

1. INTRODUCTION

Field programmable gate array (FPGA) is a popular platform while develops electronic products by application specific integrated circuit (ASIC). The advantages include fast verification and time-to-market issue. Moreover, advance FPGA provides embedded multiple processors that can be used to design embedded system. It can fast to simulate and verify complex digital circuit. Therefore, the trend for developing consumer electronics, computer, communicating products and control system of car is toward FPGA system.

The placement and route for FPGA is a significant problem due to the capacity of FPGA is greatly increment to hundreds or thousands of million design elements. In 1998, Kusse and Rabaey [1] discuss energy efficient issue that divides functionalities into specific area. They stated up to 65% power consumption is waste on routing issue. Therefore, commercial companies such as Actel [2], Altera [3] and Xilinx [4] aim at placement and route algorithm and tools.

Shahookar and Mazumder [5] discuss the architecture of FPGA that consists of *configurable logic block* (CLB), programmable interconnect area, I/O blocks and I/O pads. The CLB is used to implement logic functionalities. The placement of CLBs are variant that depends on all CLBs being routed successfully. Programmable interconnect area consists of connection box and switch block. The connection box is designed for connect logic blocks with vertical and horizontal channel. The switch box is used to route for CLBS. These two boxes are significant factors for routing successfully. I/O blocks and I/O pads communicating signal to external blocks.

2. GREY RELATIONAL ANALYSIS

The grey system was developed by Deng [6] in 1989 to solve uncertain system problems. Equations (1)–(5) are typically applied in grey relational analysis when analyzing the grey relational effect. First, assign data into initial arrays in Equation (1) that is presented as $X_i(k)$. Second, calculate the grey relational coefficients of a reference point $X_i(k)$ to other points $X_j(k)$ via Equation (2). Third, $\Delta_{ij}(k)$ is the difference between the reference point $X_i(k)$ to other points $X_j(k)$ in Equation (3). Δmin and Δmax are the minimum and maximum differences among $\Delta_{ij}(k)$,

respectively that is shown in Equations (4) and (5).

$$\begin{aligned} X_1(k) &= (x_1(1), x_1(2), \ldots\ldots, x_1(k)) \\ X_2(k) &= (x_2(1), x_2(2), \ldots\ldots, x_2(k)) \\ X_3(k) &= (x_3(1), x_3(2), \ldots\ldots, x_3(k)) \\ X_n(k) &= (x_n(1), x_n(2), \ldots\ldots, x_n(k)) \end{aligned} \tag{1}$$

$$\gamma(X_i(k), X_j(k)) = \frac{\Delta\min + \zeta \cdot \Delta\max}{\Delta_{ij}(k) + \zeta \cdot \Delta\max} \tag{2}$$

$$\Delta_{ij}(k) = |X_i(k) - X_j(k)| \tag{3}$$

$$\Delta\min = \forall \overset{\min}{j} \in i, \forall \overset{\min}{k} |X_i(k) - X_j(k)| \tag{4}$$

$$\Delta\max = \forall \overset{\max}{j} \in i, \forall \overset{\max}{k} |X_i(k) - X_j(k)| \tag{5}$$

3. GREY RELATIONAL CLUSTERING OF HIERARCHICAL FPGA

This study proposed *grey relational clustering of hierarchical* (GRCH) approach to solve routing problem. Figure 1 demonstrates the design flow of grey relational clustering placement The GRCH adopts grey relational analysis theory and *grey local topology modification* (GLTM) technology to determine the location of placement. The procedures of is describes as following. First, the values of grey relational degree for each node are computed via grey relational analysis. Second, the best node of candidate is decided via the maximum of grey relational analysis. Third, the nodes connect to best node is constructed as a new parent node namely S. The S and the other two nodes are calculated their values of grey relational degree and then assemble grandfather node U. The U and the other nodes are analysis and then constructed to the father of grandfather node namely V. These procedures are iterated until the topology tree with minimal wire is build.

The global routing is performed after GLTM is assembled in GRCH procedure. It consists of a set of steps. First, The CLBs and I/Os inside FPGA are placed to $N \times N$ matrix. The locations are determined via space filling curves [7] that are exhibited in Figure 2. Second, we adopt line-probe hightower algorithm [8] to find out minimal wire of global routing. Third, we record individual wire information that consists of vertical and horizontal paths. The 3 dimension data structure is used to save information. For example, i={start column(row), end column(row), channels of route}. Four, we use match and merge strategy [9] to route.

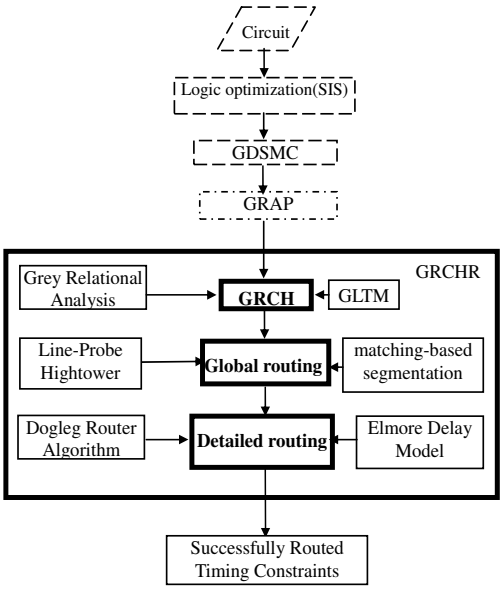

Figure 1: Grey relational clustering placement design flow.

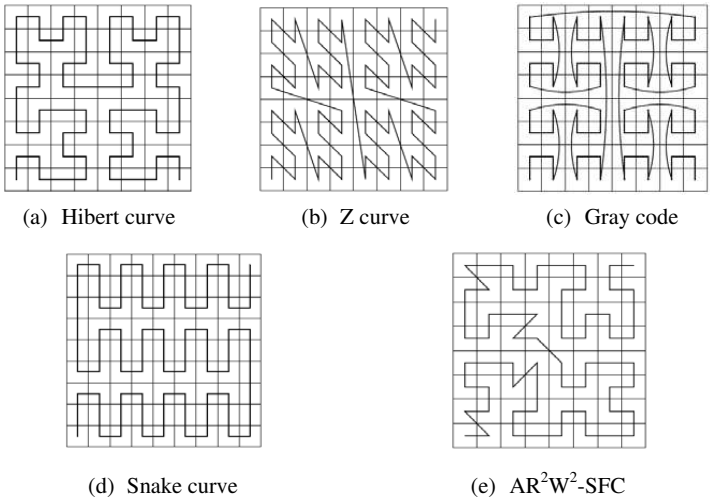

Figure 2: FPGA placement methods.

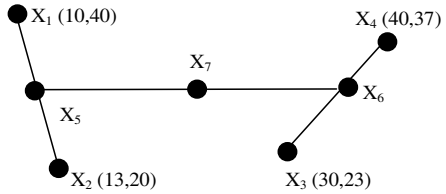

Figure 3: Parent node of constructing tree for four sinks placement.

Table 1: Wire length of constructing tree for 4 sinks.

Topological tree & Total wire length							
a0	5538.85 µm	b0	5531.41 µm	c0	6471.67 µm	GLTM	5206.38 µm
a1	8153.12 µm	b1	6282.70 µm	c1	6811.41 µm		
a2	7601.62 µm	b2	7280.49 µm	c2	7504.09 µm		
a3	**5206.38 µm**	b3	7442.00 µm	c3	6131.82 µm		
a4	5509.91 µm	b4	6089.78 µm	c4	7765.09 µm		

Switch block and connection block are considered in detail routing. The effect factors include the balance of segments length and the number of track is minimal. Therefore, we use dogleg router algorithm [10] to reduce the number of tracks. However, Szymanski [11] stated that the channel density should be the minimal if the number of tracks and doglegs are minimal. Therefore, it becomes a *non-deterministic polynomial l* (NP) complete problem.

An example is shown in Figure 3 for four sinks placement. if the coordination of four sinks are X_1(10,40) X_2(13,20), X_3(30,23) and X_4(40,37). The parent node is constructed as X_7 Suppose the fabrication process is 0.18 µm [12]. The units of resistance and capacity is 0.075Ω and 0.118 fF. Next, we compute the wire length via RC Elmore [13] and LTM [14]. The number of 15 wire lengths is individually calculated that is illustrated in Table 1. Columns 1, 3 and 5 in Table 1 show the name for 15 wire length. However, if the number of 15 wires length is separately computed via GLTM. The candidate of minimal wire length is a3 that is displayed in column 1 in Table 1.

4. CONCLUSIONS

Grey relational clustering to hierarchical routing approach is used to solve placement and routing problem of FPGA. We proposed GLTM to achieve minimal wire length. In global routing stage, we apply line-probe hightower to obtain minimal wire for global route. Moreover, we adopt matching-based segmentation technology to attain a set of shorter nets and wires for routing regions. In detail routing, we achieve minimal tracks and channel density and delay timing constraint. Finally, the proposed obtain a minimal wire and delay result for placement and route in FPGA.

REFERENCES

1. Kusse, E. and J. M. Rabaey, "Low-energy embedded FPGA structures," *Proceedings of the International Symposium on Low Power Electronics and Design*, 155–160, Aug. 1998.
2. Actel Inc., Axcelerator family FPGA, 2004.
3. Altera Corporation, *Stratix II Device Handbook*, Vol. 1, Jul. 2004.
4. *Electronics Weekly*, 12, ABI/INFORM Trade & Industry, Feb. 25, 2004.
5. Shahookar, K. and P. Mazumder, "VLSI cell placement techniques," *ACM Computing Surveys*, Vol. 23, No. 2, 143–220, 1991.
6. Deng, J., "Introduction to grey system theroy," *The Journal of Grey System*, Vol. 1, No. 1, 1–24, 1989.
7. Asano, T., D. Ranjan, T. Roos, E. Welzl, and P. Widmayer, "Space filling curves and their use in the design of geometric data structures," *Theortical Computer Science — Special Issue: Latin American Theoretical Informatics*, No. 1, Vol. 181, Jul. 1997.
8. Hightower, D. W., "A solution to the line routing problem on a continous plane," *Proceeding of 6th Design Automation Workshop*, 1969.
9. Lin, J.-M., S.-R. Pan, and Y.-W. Chang, "Graph matching-based algorithms for array-based fpga segmentation design and routing," *IEEE/ACM International Conference on Computer-aided Design*, 1998.
10. Deutsch, D. N., "A dogleg channel router," *Proceeding of 13 th ACM/IEEE Design Automation Conference*, 425–433, 1976.
11. Szymanski, T. G., "Dogleg channel routing is NP-complete," *IEEE Transactions on Computer-Aided Design*, Vol. 4, 31–41, 1985.
12. Sarkar, P. and C. K. Koh, "Routability-driven repeater block planning for interconnect-centric floorplanning," *IEEE Trans. CAD of Integrated Circuits and Systems*, Vol. 20, No. 5, 660–671, 2001.
13. Email, W. C., "The transient response of damped linear networks," *J. Appl. Phys.*, Vol. 19, 55–63, 1948.
14. Saaied, H., D. Al-Khalili, and A. J. Al-Khalili, "Area minimization of clock distribution networks using local topology modification," *IEEE International Systems-on-Chip (SOC) Conf.*, 227–230, 2003.

Design of Reaction Cavity for a Microwave-assisted Synthesis System

Myungsik Kim, **Jongmin Kim**, **and Kwangsoo Kim**
Sogang University, Republix of Korea

Abstract— This paper focuses on the microwave assisted synthesis system for the automatic preparation system of positron emission tomography (PET) radiopharmaceuticals. Recently, many microwave assisted chemical synthesis system has been developed, since the system has several advantages such as the reaction acceleration, the enhanced physicochemical properties, and so on. However, most systems are the microwave generation part and the reaction part all-in one then it is hard to apply to the already developed systems, specially, the radio-labeling applications in the limited space of a hot-cell. For the problem, we developed a stand-alone reaction cavity, which is connected to the power controllable magnetron using flexible cable. The cavity is a doughnut-shape and an electric field is radiated through the middle windows of the center hole, to which a vial is inserted. The cavity is simulated using HFSS and the resonance properties are measured using Agilent E8357A network analyzer. The experiment results using a vial with radius of 22 mm and height of 38 mm, which is used in the preparation system, show that the water in the vial is heated stably.

1. INTRODUCTION

PET is a nuclear medicine imaging technique that produces a three-dimensional image of the physiology and chemistry of the body by scanning gamma ray emitted from small amount of radioactive molecules. A metabolism in certain tissues such as cancer tissue, brain and heart activities, and so on can be efficiently mapped using the PET. However, the high cost to produce the radiopharmaceuticals is a bar to use PET widely. In order to cut the cost, it is very important to reduce the time as well as increasing radiochemical yield in preparation of the radiopharmaceuticals, since the half-life of the used radionuclides is very short. For example, the half-life of fluorine-18 (F-18), which is widely used in PET, is about 110 minutes. In the radiopharmaceuticals synthesis procedures, the heating process to remove solvent which contain radionuclides take times over several tens minutes. However, it is almost impossible to reduce the time by controlling the heating temperature of an electric heater used in the current system, since the radionuclides is crystalized and adhered to the vial's inner surface easily. For the problem, a considerable number of studies have been performed on microwave assisted synthesis technique [1–3].

Different from the current heating system by the heat conduction, the microwave based heating technique has several advantages. Dielectric molecules such as water in a material are vibrated by the microwave then the material is heated uniformly and very fast. Thus, many microwave assisted synthesis systems are developed to accelerate the chemical reaction. However, many systems are microwave generation part and reaction part all-in one then it is hard to install to pre-developed systems without changing its layout. Also, since the material is heated inside a large cavity, which randomly reflect the microwaves, the microwave field intensity inside the sample is affected by the shape and positions of vials. Specifically, since radiopharmaceuticals synthesis system is generally placed in lead-shielded hot-cell, the microwave synthesis system should be designed considering the restrict available space in the hot-cell.

For the problem, we developed stand-alone microwave synthesis system as the first step. The prototype microwave reactor is feeded through flexible coaxial cable then the microwave generation part can be placed outside the hot-cell. The reactor is designed as donut-shape and the vial can be inserted to center hole. In order to apply energy stably, transmitted microwave is radiated through ring-shape window at the middle of center hole. The experiment result of heating water inside vial according to various microwave output show that the developed system works very well.

This paper is organized as follows. In Section 2, we briefly describe the developed microwave based heating system and its components and the stand-alone prototype microwave reactor and its test results. The experimental results of heating water are shown in the Section 3. Finally, conclusions are drawn in Section 4.

2. OVERVIEW OF DEVELOPED SYSTEM

Figure 1 shows a simple diagram of the developed system. The system is composed of three parts: a generated microwave power controllable magnetron, a waveguide-coaxial transition unit, and a microwave reactor. The power source to the magnetron is divided as high volt transformer (HVT) and low volt transformer(LVT). Therefore, the microwave output power from the magnetron is varied by controlling the high voltage to the anode while fixing the low voltage to the filament of the magnetron. The radiated microwave from the antenna probe of the magnetron is transmitted

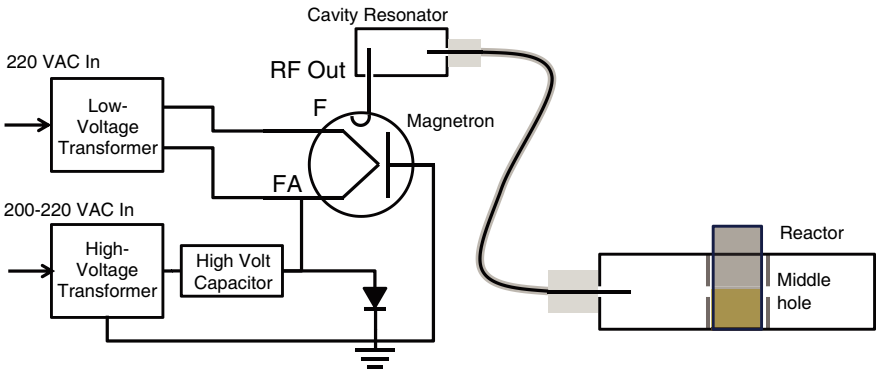

Figure 1: Diagram of the developed system.

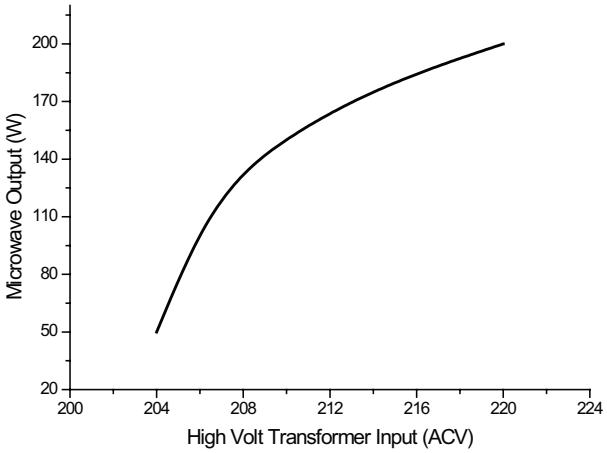

Figure 2: Microwave output power according to the input AC voltage to HVT.

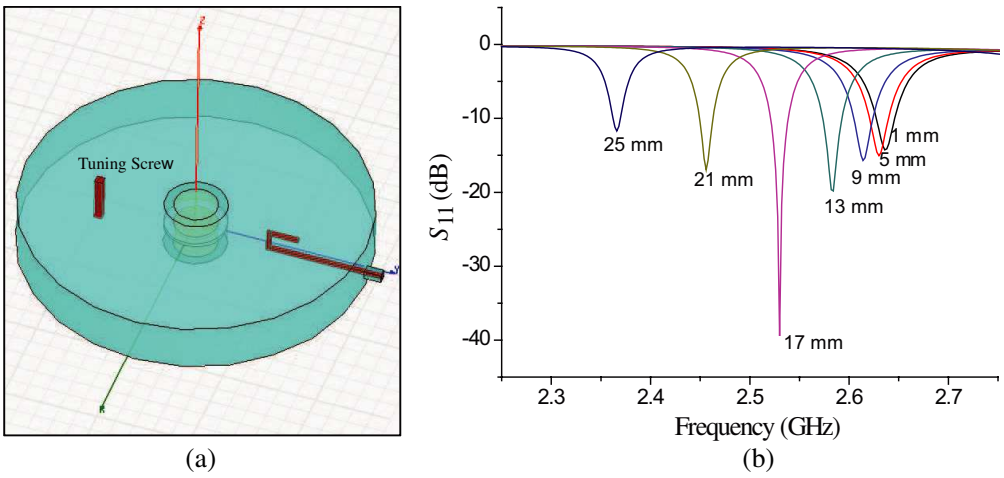

Figure 3: (a) Design of the microwave reactor. (b) Simulation results about the change of the reflection coefficient according to the length of tuning screw.

to microwave reactor through a coaxial cable, of which the end is male N-type connector, using a waveguide-coaxial transition unit. The unit is sized of Ø62 × 54 mm and antenna probe of the magnetron is inserted to center hole of lower side. The radiated microwave is transmitted to monopole antenna with the length of 32 mm installed to upper side, which is connected to the coaxial cable. Fig. 2 shows the microwave output according to the input AC voltage to the HVT measured by an Agilent U2001A USB power meter with 40 dB attenuator. When the AC voltage input is over 204 V, the microwave is generated and raised to 200 W about 220 V input.

2.1. Microwave Reactor

The microwave generated from magnetron is transmitted to microwave reactor through flexible coaxial cable. Fig. 3 shows the design of the prototype microwave reactor and its simulation results of the reflection coefficient. The reactor is donut-shape sized of 182 mm × 26 mm with Ø23 mm center hole. The hole size is determined considering the size of the used vial in the radiopharmaceuticals synthesis system for PET. Microwave from magnetron is fed through the hooked probe inside the resonant cavity as shown in the left of Fig. 3. A vial filled with a solution is inserted into the center hole and heated by the microwave radiated through 2 mm ring shaped window at the middle of the center hole. In order to tune the resonance frequency of the reactor, a tuning screw is installed on the opposite direction of upper side from the microwave feeding probe. The simulation results using HFSS electromagnetic field simulator are shown in the right of Fig. 3. The reactor is designed as about 2.7 GHz cavity and tuned to 2.45 GHz by expanding the tuning screw length. As shown in the figure, the reflection coefficient is −17 dB with resonance frequency of 2.45 GHz when the length of the tuning screw is 21 mm.

Figure 4 shows the snapshot of the developed reactor and its test result measured using Agilent E8357A network analyzer. The outer size of the reactor is □195 × 34 mm with 23 mm center hole.

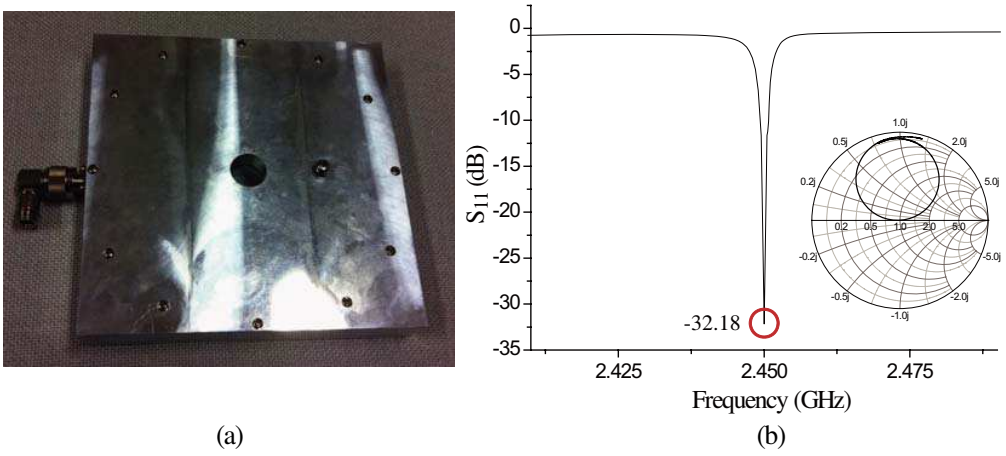

Figure 4: (a) Snapshot of the developed reactor. (b) Test result about the reflection coefficient.

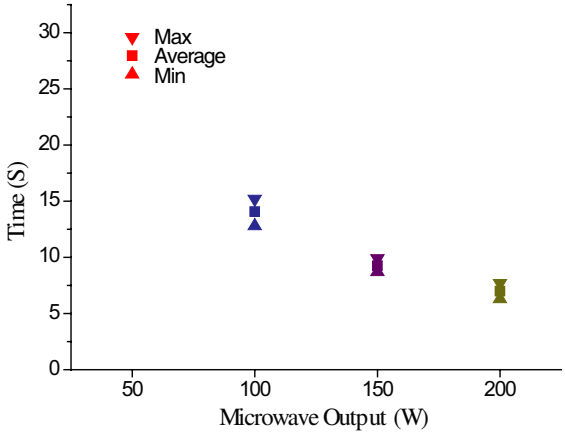

Figure 5: Water heating performance test according to various the microwave outputs.

N-type connector is connected to the hooked probe for microwave feeding. The reflection coefficient of the reactor with smith chart are shown in the right of Fig. 4. The S_{11} is around -32 dB with the resonance frequency of 2.45 GHz.

3. EXPERIMENTAL RESULTS

In order to verify the validity of the developed system, we performed experiments of water heating. 5 ml water is bottled in the 22 mm $\times$ 38 mm vial and heated from 25 degrees to 65 degrees using the developed microwave reactor. 10 trials are performed with various microwave outputs of 50, 100, 150, and 200 W. Fig. 5 shows the statistics of the time taken to heat the water. In the figure, the squares show the average and the triangles and the inverted triangles are the minimums and maximums of each trial. When the microwave is 50 W, it takes about 28 seconds to heat the water and the time is decreased by raising the microwave output power then about 7 seconds are taken with the microwave output of 200 W. The results prove that the system can heat the solution in a vial very stably.

4. CONCLUSION

The improvement of the heating process is very important to reduce cost to prepare the radiopharmaceuticals in the automated propagation system for using PET widely. For the problem, a microwave assisted synthesis system is developed in this paper. To cope with the limited space to install the heating system such as hot-cell, a stand-alone type system is developed. A microwave reactor is separated and the microwave is transmitted to the reactor through a flexible cable from a power controllable magnetron. As the first step, we design a donut-shaped microwave reactor and perform water heating test under various microwave outputs. The experiment results show that the system can heat the water very stably. Our major contributions can be summarized as: 1) the stand-alone type microwave heating system is developed, 2) efficient microwave reactor is designed. Our future effort includes the development of compact reaction cavity to use in various fields and feed-back controller for automated solution heating.

ACKNOWLEDGMENT

The research was supported by the Converging Research Center Program through the Ministry of Education, Science and Technology (2011K000706)

REFERENCES

1. Hayes, B. L., "Recent advances in microwave-assisted synthesis," *Aldrichimica ACTA*, Vol. 37, 66–77, 2004.
2. Lidstrom, P., J. Tierney, B. Wathey, and W. Jacob., "Microwave assisted organic synthesis — A review," *Tetrahedron*, Vol. 57, No. 51, 9225–9283, 2001.
3. Stone-Elander, S. and N. Elander, "Microwave applications in radiolabelling with short-lived positron-emitting radionuclides," *Journal of Labelled Compounds and Radiopharmaceuticals*, Vol. 45, No. 9, 715–746, 2002.

Simulations and Analysis of the Corner Geometry and Its Influence on the Electromagnetic Behavior of Components and Structures: Comments on GTEM and Other Microwave Guided Structures Designs

H. X. Araújo and L. C. Kretly
University of Campinas, Brazil

Abstract— In this paper, it is shown the electromagnetic influence of the rounded corners which arises on the mechanical manufacturing process. Normally, microwave devices and resonant cavities are designed on the EM simulator with sharp corners. However, with this consideration, some response and behaviors are neglected.

Concerning the differences between sharp and rounded corners, the investigation was carried out for a GTEM — Gigahertz Transverse Electromagnetic Chamber, specifically the APEX (the exciter sector) and a horn antenna. An EM simulator, based on the Finite Element method (FEM) was employed with very accurate models to identify the influence of the rounded corners on the propagation regime. To be sure that the simulation tool is doing a refined numerical solution, a close up of the meshing at the corner was verified. The simulated results show that the numerical analysis is compatible with the analytical solution for electrostatic fields presented in several works. Also, they show a non-negligible sensitivity of S_{11} parameter when comparison between sharp and rounded corners are done.

1. INTRODUCTION

The electromagnetic analytical treatment of corner geometry on electronic circuits, RF systems or microwaves components is normally neglected and sharp corner is a constant geometry that empires on the simulation work and design procedure. This fact arises from the simplicity of analysis of the sharp geometry compared to the rounded ones and the computational cost required. In large dimensions, this approximation is acceptable, but it is inaccurate in the region of the corners and these singularities impact the performance of the implemented structure or device. Generally, in the literature the corner is analyzed on the electrostatic regime and not on the propagation one.

In [1] is proposed a numerical method to approximate the electric scalar potential based on observations, where the solutions are influenced by changes of the curvature radius.

Thus, based on the differences between sharp and round corners, some studies and investigation were done to verify the impact of this mismatch on a GTEM — Gigahertz Transverse Electromagnetic Chamber, specifically the APEX (the exciter sector) and a horn antenna. An EM simulator — CST Studio (but not limited to), based on the Finite Element method (FEM) was employed with very accurate models to identify the influence of the rounded corners on the propagation regime.

Although the classical works on rounded corners [2, 3] were focused on high power and strong electric fields, the analysis presented here shows clearly that even for low power excitation and in high frequency range, there is a noticeable field disturbance on the pattern.

2. GTEM CHAMBER ANALYSIS

Based on a transverse electromagnetic cell (TEM), which is basically a planar expanded transmission line operating in the TEM mode to simulate a free space planar wave, the concept of a gigahertz transverse electromagnetic chamber (GTEM) was inspired [4]. Normally, the electromagnetic compatibility analysis using the TEM cell is limited in 1 GHz [5], which in some applications is a problem. Thus, the great advantage of the GTEM chamber is its capability to measure EMC/EMS/EMI from some megahertz up to 18 GHz of devices that are physically small and compacts, especially electronic components and antennas [6].

At low frequencies only the TEM mode propagates on the chamber. However, with the increase of the operational frequency, TE and TM modes can be excited inside the chamber. The minimum frequency is calculated from the first lower resonant of the higher modes, which depends on the size and shape of the chamber. The main advantage of the GTEM cell is the small size and low cost, and further it is not necessary any additional external shielding.

There are some known ways to build a GTEM chamber, such as casting the metal sheet or through the solder of two or more folded metallic sheet. Therefore, depending on the fabrication (casting or folding the metal sheet) the corners are completely different. In Figs. 1 and 2, are shown the construct structure.

As the metallic sheets were folded, a radius of curvature with the dimensions of the sheet thickness was imposed. This physical imposing sometimes causes a large divergence between the simulated and experimental results, especially at higher frequencies. As the fabricated apex showed in Fig. 2 was made from mm range thickness brass sheet, the radius of curvature is also on this range. Thus, comparing the return loss between the apex designed with sharp corners and rounded ones, a subtle difference on the behavior can be observed for the low and medium frequencies but a large deviation for high frequency as can be seen in Fig. 3.

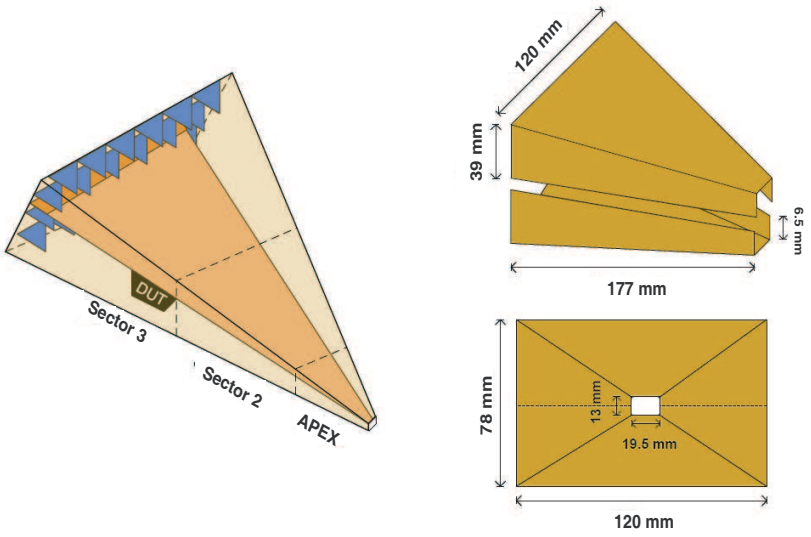

Figure 1: (a) GTEM chamber; (b) APEX details.

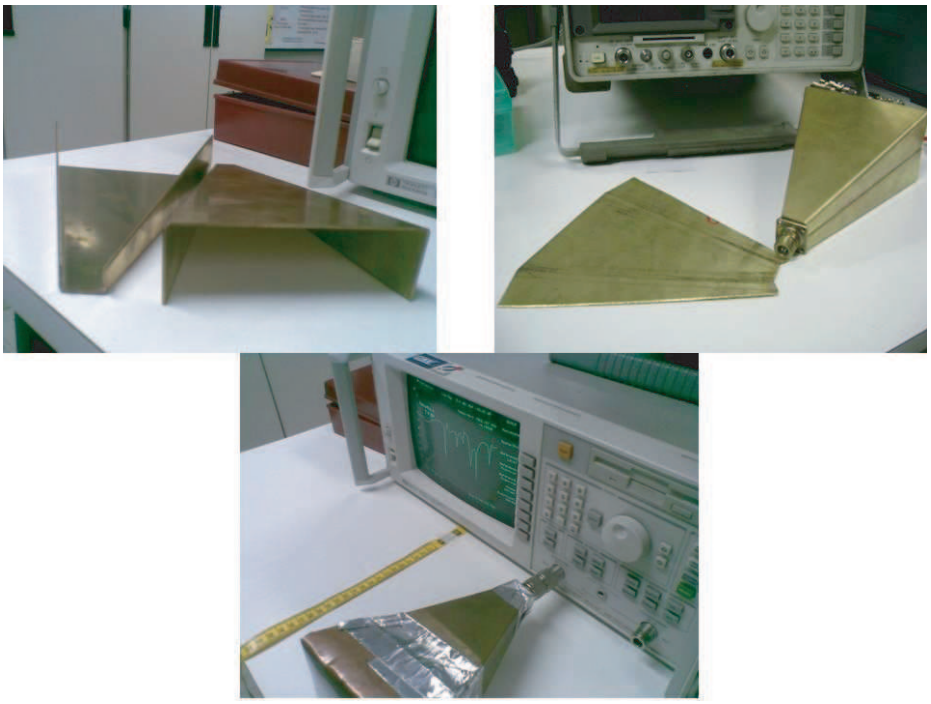

Figure 2: Fabricated APEX with rounded corners.

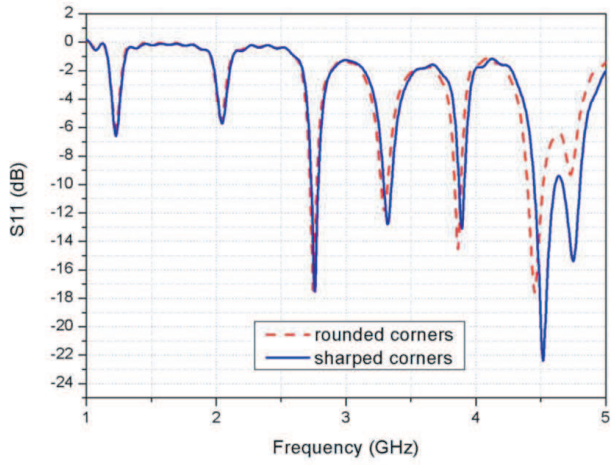

Figure 3: S_{11} parameter for the APEX of a GTEM cell.

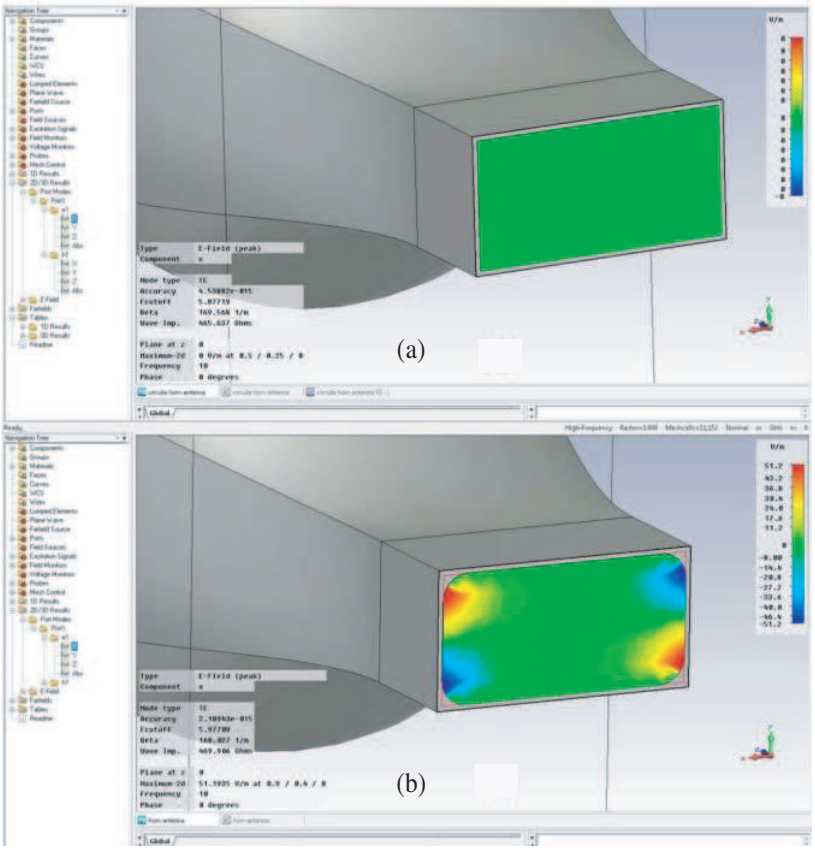

Figure 4: E_x field distribution on: (a) circular horn antenna with sharp corners; and (b) with rounded corners.

3. CIRCULAR HORN ANTENNA SIMULATION

Horns are versatile microwave antennas, easy to design and built with predictable performance. In the literature, several works deals with the design and characterization of this antenna, making known it's behavior and response. However, there are no studies that show the influence of the manufacturing process and its consequences on the final device performance. Normally, the designer cares only with the boundary conditions and the material characteristics, neglecting the ways that the device will be fabricate. In this context, this work compares the response of a broadband circular horn antenna, designed with sharp and rounded corners, as shown in Fig. 4. As mentioned before, the influence of the corners shape on the behavior of device increases as soon as the frequency is increased.

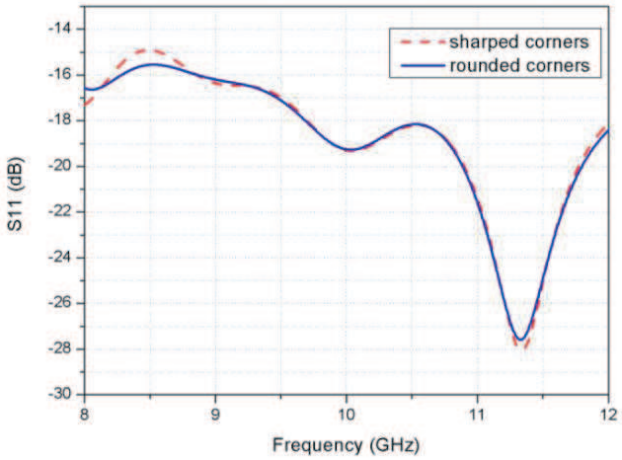

Figure 5: S_{11} parameter for circular horn antenna.

Although the S_{11} parameter (return loss) of the rounded corners, showed in Fig. 5 denotes a subtle deviation compared to the sharp ones, it must emphasized that this is a particular result for this specific device which is a broadband antenna.

4. CONCLUSIONS

In this work the analysis of the differences between EM structures using sharp and rounded corners were done. This study is necessary to increase the precision of the usual methodology which simplifies the assumption of sharp corners instead of rounded ones. The common assumption of sharp corners implies in solutions that are not very consistent with the reality, especially at high frequencies. In large dimensions, this approximation is acceptable, but it is inaccurate in the region of the corners and these singularities impact the performance of the implemented structure or device. As a rule of thumb every designed device must be simulated to take care of the impact of the fabrication process on the geometry and on the microwave propagation characteristics.

In general, for large microwave devices the concerns about fabrication process that affects the geometry is not too restrictive. However, simulation and calculation must be emphasized when micro devices are designed using for example MEMS technology or other fabrication process for subminiature components. To be sure that the simulation tool is doing a refined numerical solution the designer must carefully refine the meshing.

REFERENCES

1. Krähenbühl, L., F. Buret, R. Perrusel, D. Voyer, P. Dular, V. Péron, and C. Poignard, "Treatment of rounded and sharp corners in the numerical modeling of 2D electrostatic fields," *MOMAG*, Vila Velha, Brazil, August 2010.
2. Matthaei, G. L., L. Young, and E. M. T. Jones, *Microwave Filter, Impedance-Matching Networks, and Coupling Structures*, Artech House, New Jersey, 1980.
3. Cohn, S. B., "Rounded corners in microwave high-power filters and other components," *IRE Transaction on Microwave Theory and Technique*, 389–397, 1961.
4. Konigstein, D. and D. Hansen, "A new family of TEM-cells with enlarged bandwidth and optimized working volume," *Proceedings of the 7th International Zurich Symposium on Electromagnetic Compatibility*, 127–130, Zurich, March 1987.
5. "Electromagnetic Compatibility (EMC) — Part 4: Testing and Measurement Techniques — Section 3: Radiated, Radio-Frequency, Electromagnetic Field Immunity Test," International Standard CEI/IEC 1000-4-3, Geneva, Feb. 1995.
6. Montrose, M. I. and E. M. Nakauchi, *Testing for EMC Compliance*, Wiley Interscience, New York, 2004.

Flat-topped Field Correlations in Extremely Strong Turbulence

Yahya Baykal
Electronic and Communication Engineering Department, Çankaya University
Öğretmenler Cad. No. 14, Yüzüncüyıl, Balgat 06530, Ankara, Turkey

Abstract— In extremely strong turbulent horizontal atmospheric optical links, field correlations of flat-topped Gaussian incidence are evaluated. Field correlations are represented versus the diagonal distance at the receiver plane, for variations in the number of beams forming the flat-topped structure, receiver points, source sizes, link lengths, structure constants and the wavelengths. Our results in extremely strong turbulence are compared to their free space counterparts which only reflect the diffraction patterns at the receiver plane. The effects of the inner scale of turbulence on the field correlations in extremely strong turbulence are examined in detail and it is observed that the size of the inner scale in extremely strong turbulence can considerably influence the field correlations of flat-topped beams.

1. INTRODUCTION

Flat-topped beams, whose incident field profiles are described by different formulations [1–3] are applied to weakly turbulent media to find the average intensity [4, 5] and intensity fluctuations [6–9]. It is found that [6] under certain source parameters, flat-topped beams can provide advantage in short distance atmospheric optical telecommunication systems. In the backbone telecommunications infrastructure, it is important to be able to use atmospheric optical links in very long distance links where the atmosphere assumes extremely strong turbulence. Fante [10] and Wang and Plonus [11] applied extremely turbulent atmosphere statistics to find the received intensity fluctuations. We have recently found the field correlations of flat-topped Gaussian beams in weakly turbulent short atmospheric optical links [12]. In the current paper we extend our work in [12] to evaluate the field correlations when the atmosphere experiences extremely strong turbulence. We intend to apply our results in heterodyne detection in very long horizontal atmospheric optical links which can possibly be used in telecommunications backbone infrastructure.

2. FORMULATION

The field correlations at two different points $\mathbf{p}$ and $\mathbf{p}+\mathbf{r}$ in a plane located at horizontal link distance L from the source is found as [12]

$$\langle u(\mathbf{p})u*(\mathbf{p}+\mathbf{r})\rangle = \int_{-\infty}^{\infty}\int_{-\infty}^{\infty}\mathbf{d}^2\mathbf{s}_1 \int_{-\infty}^{\infty}\int_{-\infty}^{\infty}\mathbf{d}^2\mathbf{s}_2\frac{u(\mathbf{s}_1)u*(\mathbf{s}_2)}{(\lambda L)^2}\exp\left[\frac{i\pi}{\lambda L}\left(|\mathbf{s}_1-\mathbf{p}|^2-|\mathbf{s}_2-(\mathbf{p}+\mathbf{r})|^2\right)\right]\Gamma_2^m(\mathbf{s}_2-\mathbf{s}_2,\mathbf{r}), \quad (1)$$

where $u(\mathbf{s_i})$, $\mathbf{i}=1,2$ and $u(\mathbf{p},L)$ are respectively the source field at the transverse source point $\mathbf{s}=(s_x,s_y)$ and the received field at the transverse receiver point $\mathbf{p}=(p_x,p_y)$, $\Gamma_2^m(\mathbf{s_2}-\mathbf{s_2},\mathbf{r})$ is the second order medium coherence function, λ is the wave length, $*$ is the complex conjugate. Here $|\mathbf{r}|=\sqrt{r_x^2+r_y^2}$ is defined as the diagonal distance from the point $\mathbf{p}=(p_x,p_y)$. For flat-topped Gaussian beam incidence, the incident field is given by $u(\mathbf{s})=\sum_{\ell=1}^{N}(-1)^{\ell-1}(N-1)![\ell!(N-\ell)!]\exp(-0.5\ell|\mathbf{s}|^2/\alpha_s^2)$ where ! denotes the factorial, N is the total number of Gaussian beams forming the flat-topped Gaussian profile and α_s is the Gaussian source size [3]. For extremely strong turbulence, the second order medium coherence function is given by [10, 11] $\Gamma_2^m(\mathbf{s_2}-\mathbf{s_2},\mathbf{r})=\exp[-\rho_e^{-2}(|\mathbf{s_1}-\mathbf{s_2}|^2+|\mathbf{s_1}-\mathbf{s_2}|\cdot|\mathbf{r}|+|\mathbf{r}|^2)]$ where $\rho_e=1.36C_n^{-1}k^{-1}L^{-1/2}\ell_0^{1/6}$ is the coherence length of the medium in extremely strong turbulence, ℓ_0 is the inner scale of turbulence, C_n^2 is the structure constant, "$\cdot$" is the dot product. Employing $u(\mathbf{s})$ and $\Gamma_2^m(\mathbf{s_2}-\mathbf{s_2},\mathbf{r})$ in Eq. (1), solving the integrals, we obtain a similar structure of formulation as in [12] except ρ_e, then we find the field correlations of flat-topped

Gaussian beams in extremely strong turbulence as

$$\langle u(\mathbf{p})\, u*(\mathbf{p}+\mathbf{r})\rangle = 0.25k^2L^{-2}\sum_{\ell=1}^{N}\sum_{\ell_1=1}^{N}(AB)^{-1}(-1)^{\ell+\ell_1-2}\left[(N-1)!\right]^2\left[\ell!\,(N-\ell)!\right]\left[\ell_1!\,(N-\ell_1)!\right]$$
$$\times\exp\left[\left(\frac{1}{4A}+\frac{1}{8A^2B\rho_e^2}\right)\left(E_x^2+E_y^2\right)\right]\exp\left[\frac{1}{2AB\rho_e^2}\left(E_xF_x+E_yF_y\right)+\frac{F_x^2+F_y^2}{4B}\right], \quad (2)$$

where $k=2\pi/\lambda$ is the wave number, $A=-\frac{ik}{2L}+\frac{\sqrt{\ell}}{2\alpha_s}+\frac{1}{\rho_e^2}$, $B=\frac{ik}{2L}+\frac{\sqrt{\ell_1}}{2\alpha_s}+\frac{1}{\rho_e^2}-\frac{1}{A\rho_e^4}$, $E_x=-\frac{ikp_x}{L}+\frac{r_x}{\rho_e^2}$, $E_y=-\frac{ikp_y}{L}+\frac{r_y}{\rho_e^2}$, $F_x=\frac{ik}{L}(p_x+r_x)-\frac{r_x}{\rho_e^2}$, $F_y=\frac{ik}{L}(p_y+r_y)-\frac{r_y}{\rho_e^2}$.

3. RESULTS

In this section, results obtained by taking the absolute value of Eq. (2) are represented. The vertical axes are thus $|\langle u(\mathbf{p})u*(\mathbf{p}+\mathbf{r})\rangle|$ which are abbreviated in the figure captions as AFC (Absolute Field Correlation). Unless otherwise stated, all plots are for flat-topped Gaussian beams at $\lambda=1.55\,\mu$m and for $p_x=p_y=0$. The systematic followed in providing Figures 1–16 is that in all the plots, absolute value of the field correlations are drawn versus the diagonal distance from the point $\mathbf{p}=(p_x,p_y)$. Variations of the absolute value of the field correlations are exhibited against the variations of parameters N, (p_x,p_y), α_s, L, C_n^2 and λ. Grouping of the Figures are made such that in the set of figures for the parameters N, (p_x,p_y), α_s and L, the first, the second and the third Figures represent the variations of smaller ℓ_0 value, larger ℓ_0 value and in no turbulence, respectively. For example Figures 1, 2 and 3 show the absolute value of the field correlations for variations of N when $\ell_0=1\,$mm, $\ell_0=5\,$mm and $C_n^2=0$, respectively. In the grouping of the Figures for the parameters C_n^2 and λ, the first and the second Figures represent the variations of smaller ℓ_0 value and larger ℓ_0 value, respectively and no plots are provided in no turbulence. From Figures 1–16, it is observed that in extremely strong turbulence, at a constant diagonal distance,

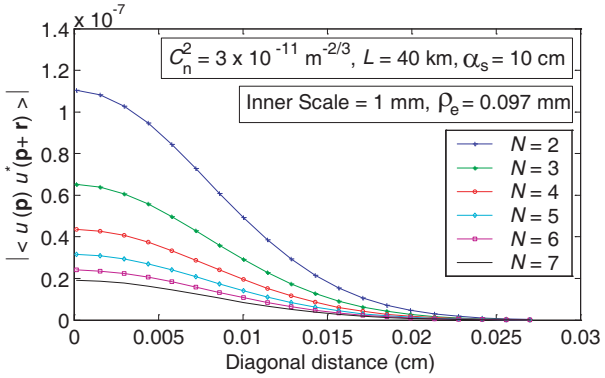

Figure 1: AFC for various N when $\ell_0=1\,$mm.

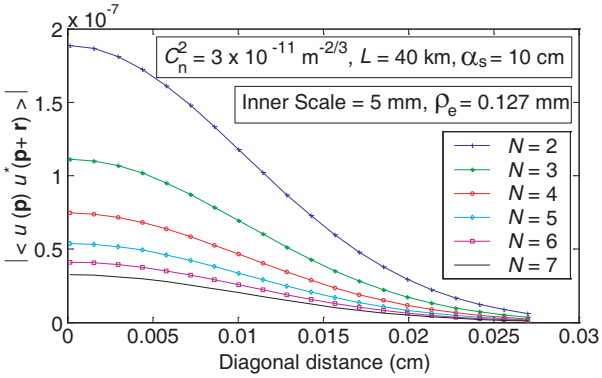

Figure 2: AFC for various N when $\ell_0=5\,$mm.

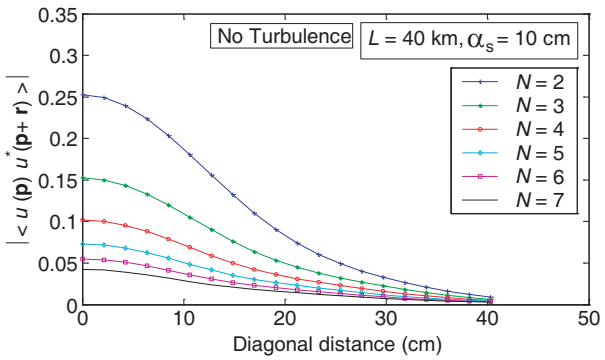

Figure 3: AFC for various N in no turbulence.

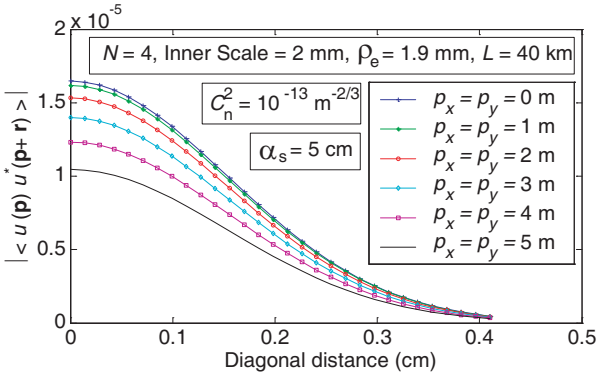

Figure 4: AFC for various p_x, p_y when $\ell_0=2\,$mm.

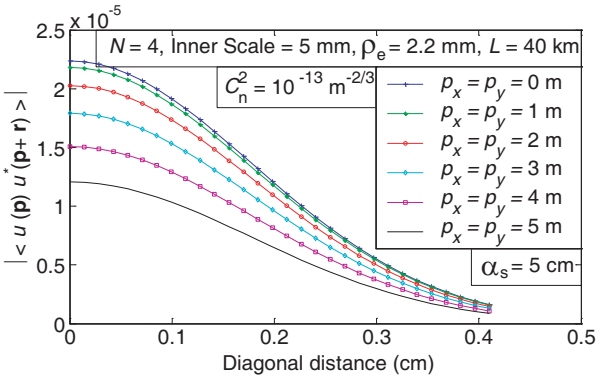

Figure 5: AFC for various p_x, p_y when $\ell_0 = 5\,\mathrm{mm}$.

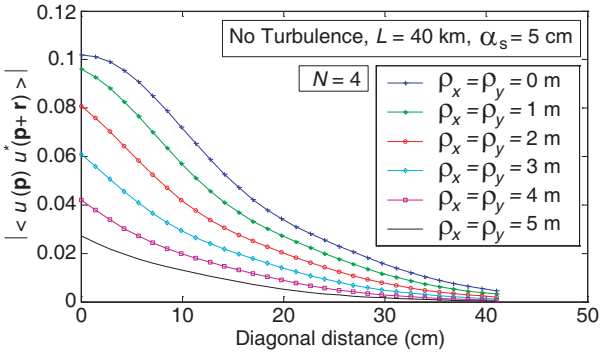

Figure 6: AFC for various p_x, p_y in no turbulence.

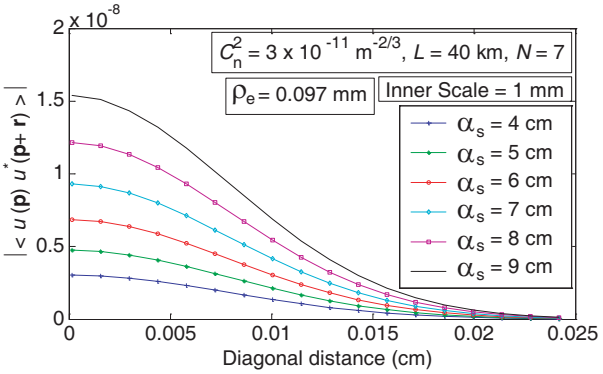

Figure 7: AFC for various α_s when $\ell_0 = 1\,\mathrm{mm}$.

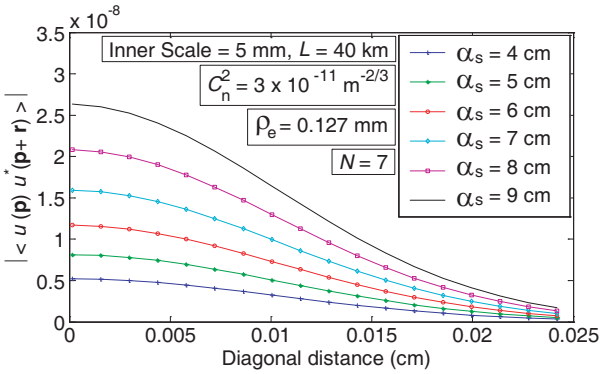

Figure 8: AFC for various α_s when $\ell_0 = 5\,\mathrm{mm}$.

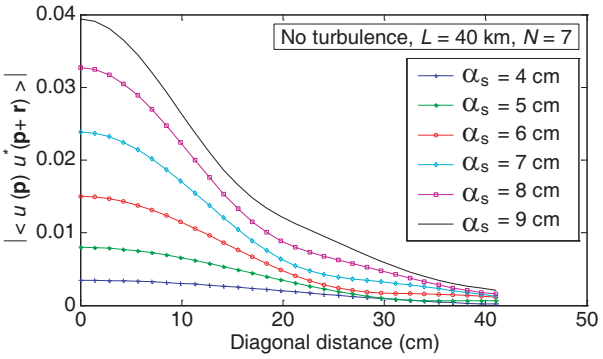

Figure 9: AFC for various α_s in no turbulence.

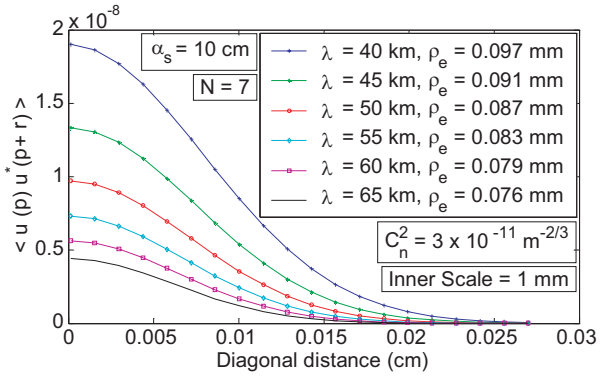

Figure 10: AFC for various L when $\ell_0 = 1\,\mathrm{mm}$.

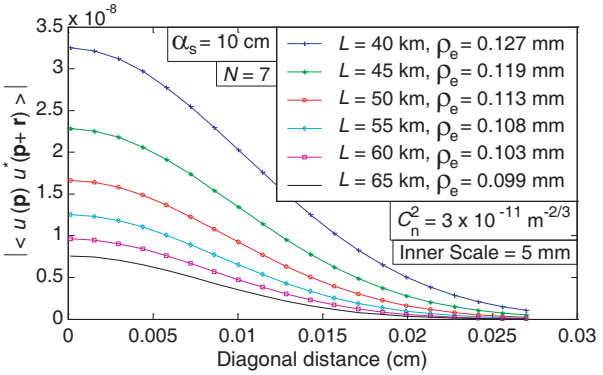

Figure 11: AFC for various L when $\ell_0 = 5\,\mathrm{mm}$.

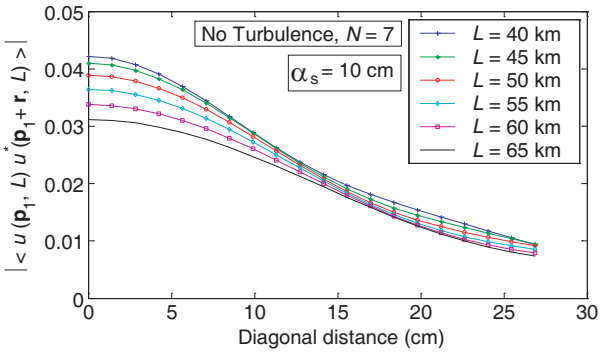

Figure 12: AFC for various L in no turbulence.

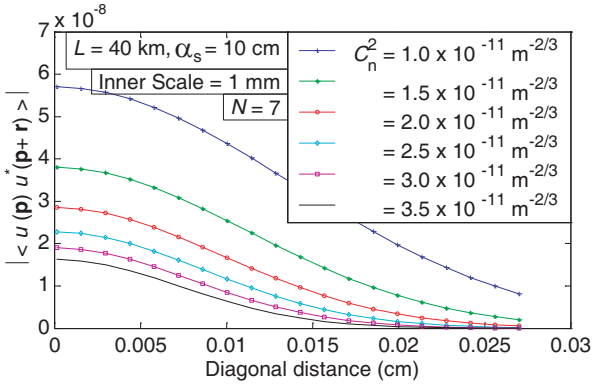

Figure 13: AFC for various C_n^2 when $\ell_0 = 1\,\text{mm}$.

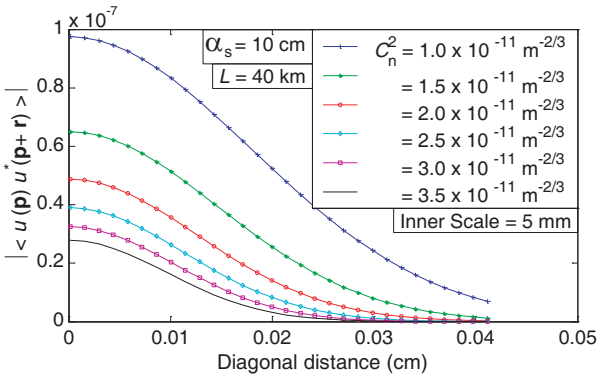

Figure 14: AFC for various C_n^2 when $\ell_0 = 5\,\text{mm}$.

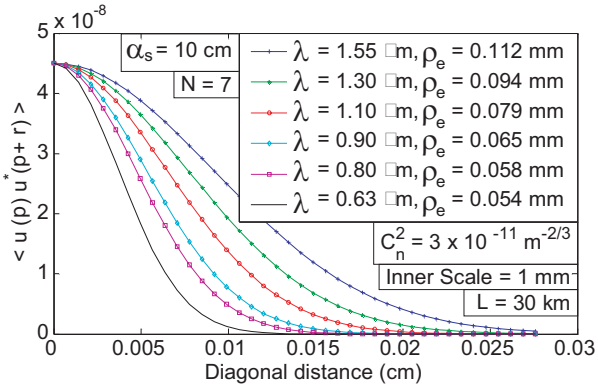

Figure 15: AFC for various λ when $\ell_0 = 1\,\text{mm}$.

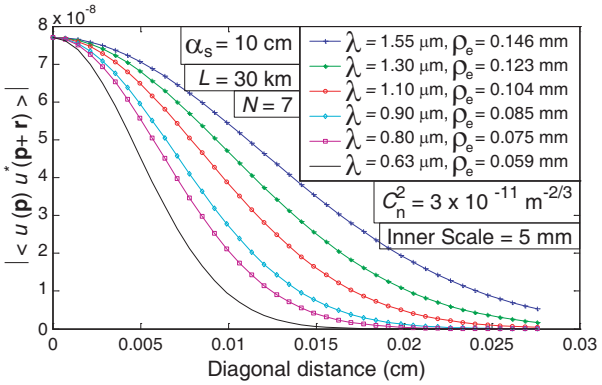

Figure 16: AFC for various λ when $\ell_0 = 5\,\text{mm}$.

smaller N, $(p_x^2 + p_y^2)^{1/2}$, L and C_n^2 and larger α_s and λ yield larger AFC. Being valid under all parameter range, as the inner scale becomes larger, AFCs become larger, and when the diagonal distance is sufficiently large, AFCs will approach to zero. Additionally, no turbulence values of AFCs are incomparably larger than the corresponding values in extremely strong turbulence.

4. CONCLUSION

The absolute values of the field correlations of flat-topped Gaussian beams evaluated in extremely strong turbulence have very small magnitude, especially when the inner scale of turbulence is small. For larger inner scales, the absolute value of field correlations can attain several order of magnitudes higher as compared to the magnitudes obtained for smaller inner scales. However, whatever the inner scale is, the flat-topped Gaussian absolute field correlations in the absence of turbulence, yield extremely larger values when compared to their counterparts in the presence of extremely strong turbulence. Our results can find application in very long distance atmospheric optics links to be potentially used in telecommunications backbone systems.

REFERENCES

1. Gori, F., "Flattened Gaussian beams," *Opt. Commun.*, Vol. 107, No. 5–6, 335–341, 1994.
2. Li, Y., "New expressions for flat-topped light beams," *Opt. Commun.*, Vol. 206, No. 4–6, 225–234, 2002.
3. Li, Y., "Light beams with flat-topped profiles," *Opt. Lett.*, Vol. 27, No. 12, 1007–1009, 2002.
4. Eyyuboğlu, H. T., Ç. Arpali, and Y. Baykal, "Flat topped beams and their characteristics in turbulent media," *Opt. Express*, Vol. 14, No. 10, 4196–4207, 2006.
5. Arpali, Ç., C. Yazıcıoğlu, H. T. Eyyuboğlu, S. A. Arpali, and Y. Baykal, "Simulator for general-type beam propagation in turbulent atmosphere," *Opt. Express*, Vol. 14, No. 20, 8918–8928, 2006.
6. Baykal, Y. and H. T. Eyyuboğlu, "Scintillation index of flat-topped-Gaussian beams," *Appl. Opt.*, Vol. 45, No. 16, 3793–3797, 2006.

7. Baykal, Y. and H. T. Eyyuboğlu, "Scintillations of incoherent flat-topped Gaussian source field in turbulence," *Appl. Opt.*, Vol. 46, No. 22, 5044–5050, 2007.
8. Cowan, D. C., J. Recolons, L. C. Andrews, and C. Y. Young, "Propagation of flattened Gaussian beams in the atmosphere: A comparison of theory with a computer simulation model," *Proceedings of SPIE*, 62150B, Orlando, Kissimmee, FL, USA, April 2006.
9. Baykal, Y., H. T. Eyyuboğlu, and Y. Cai, "Scintillations of partially coherent multiple Gaussian beams in turbulence," *Appl. Opt.*, Vol. 48, No. 9, 1943–1954, 2009.
10. Fante, R. L., "Intensity scintillations of an EM wave in extremely strong turbulence," *IEEE Trans. Antenn. Prop.*, Vol. 23, No. 2, 266–268, 1977.
11. Wang, S. C. H., M. A. Plonus, and C. F. Ouyang, "Irradiance scintillations of a partially coherent source in extremely strong turbulence," *Appl. Opt.*, Vol. 18, No. 8, 1133–1135, 1979.
12. Baykal, Y., "Field correlations of flat-topped Gaussian and annular beams in turbulence," *Opt. Lasers Eng.*, Vol. 49, No. 5, 647–651, 2011.

A Three-zone Ternary Phase Superresolving Diffractive Optical Element

Yaoju Zhang, Chaolong Fang, and Xianjie Wang
College of Physic and Electronic Information Engineering, Wenzhou University
Wenzhou 325035, Zhejiang, China

Abstract— Based on the vector diffraction theory, a three-zone ternary phase diffractive optical element is designed to improve the resolution of near-field optical storage systems with a solid immersion lens (SIL). When the designed three-zone ternary phase diffractive optical element is inserted in the near-filed SIL optical recording system, the focused spot size decreases 21%, and at the same time the side-lobes intensity is limited within 10%. However, the spot intensity descends merely 20%. Compared with the existing three-zone binary diffractive optical element, under the condition of the identical central spot intensity, the designed diffractive optical element has better superresolving effect.

1. INTRODUCTION

Solid immersion lens (SIL) technology is considered as a feasible scheme to achieve high-density optical data storage [1], which can be divided into two categories: one is the hemispheric SIL [2] and the other is the super-hemispheric SIL [3]. The difference between the near-field SIL optical storage system and the traditional far-field optical storage system is that a SIL is placed in the proximity to geometry focus of the objective lens, and a high recording density for optical storage can be achieved by recording evanescent field from the SIL. In order to improve the recording density further, many methods was presented, such as two-photon volumetric storage [4], holographic storage [5] and optical recording using surface plasmons in gold nanorods [6]. However, considering technologies, costs and many other factors, it's difficult for them to enter the market. Recently, some interests have been paid to the method of super-resolving diffractive optical elements (DOEs) [7–13], due to that such DOEs (especially the phase-only DOEs) are cheap and easy to be fabricated in practice.

When some DOEs are inserted in near-field SIL optical recording systems, however, the intensity of the focused spot isn't high enough [7] and/or the side-lobe intensity isn't kept at a low level on the condition of achieving high optical resolution [8, 9]. Through two-zone amplitude DOEs can improve the resolution of low numerical apeture (NA) systems with a SIL [10], they are invalid for high-NA SIL systems because the intensity of the central spot is very small in this case [11]. Two-zone phase DOEs can increase the resolution of high-NA SIL systems, but the sidelobe intensity is quite large [8, 12]. In 2004, Liu et al. demonstrated that the five-zone amplitude DOE can improve the focal depth of near-field optical solid immersion lens optical storage system, but the side-lobe intensity isn't also suppressed [10]. The three-zone amplitude [7] and binary phase DOEs [12] can increase the focal depth and decrease the sidelobe intensity of near-field SIL optical storage systems, but the intensity of the central spot is quite small. The continuous phase DOE can achieve high density data storage with a high central spot intensity, but it's difficult to be fabricated [13]. In designing DOEs to increase the resolution of near-field SIL systems, three aspects must be considered: (1) the DOEs must be easily fabricated in practic, (2) the recording spot has a small side-lobe intensity; (3) the intensity reduction of the focused spot must be as small as possible. To attain this aim, we design a three-zone ternary phase (TTPF) diffractive optical element to optimize the optical field distributions of a near-field SIL optical storage in this paper. The designed TTPF DOE can improve the resolution by 21%, while the central intensity of the focused spot is dropped by merely 20%. Compared with the three-zone binary phase-only (TBPF) DOE, the resolution is remarkably improved with the three-zone ternary phase-only DOE.

2. VECTOR DIFFRACTIVE FORMULA

The schematic diagram of near-field optical storage system with a DOE is shown in Fig. 1. A hemispheric SIL is placed behind an objective lens (L) with a high NA whose focus is on the bottom surface of the SIL, and the DOE (F) is placed before the objective lens. Supposing that the system is illuminated by a unite-amplitude x-polarized beam, the transmitted field distribution near the focus of the SIL, according to the procedure which is similar to that of Török et al. [14], is given by:

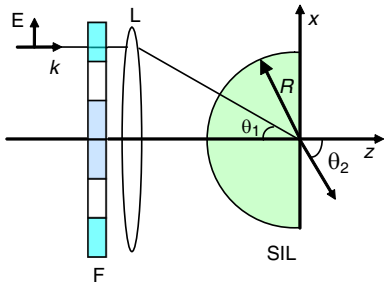

Figure 1: The schematic diagram of near-field optical storage system with a SIL and a DOE.

$$\begin{pmatrix} E_x \\ E_y \\ E_y \end{pmatrix} = \begin{pmatrix} I_0(u,v) + I_2(u,v)\cos 2\varphi \\ I_2(u,v)\sin 2\varphi \\ -2iI_1(u,v)\cos\varphi \end{pmatrix}, \tag{1}$$

where φ is the angle between the direction of the observation and the polarization direction of the incident field, and (r, φ, z) are the cylindrical coordinates in image space. The ordinate origin lies in the geometric focus O, and the axial and transverse optical coordinates is $u = n_2 k_0 z \sin^2\theta_{1m}$, $v = n_1 k_0 r \sin\theta_{1m}$ respectively, n_1, n_2 is the refractive index of the SIL and the air, k_0 is the wavenumber in vacuum and θ_{1m} is the maximum of the convergence semi-angle of the objective lens. In the formula (1), I_n are integrals over the effective aperture of the system, and they are given by:

$$I_n = \int_0^{\theta_{1m}} A_{nx} J_n\left(\frac{v\sin\theta_1}{\sin\theta_{1m}}\right) \exp\left(\frac{iu\cos\theta_2}{\sin^2\theta_{1m}}\right) d\theta_1, \tag{2}$$

where

$$\begin{aligned} A_{0x} &= P(\theta_1)\sqrt{\cos\theta_1}\sin\theta_1(t_s + t_p\cos\theta_2) \\ A_{1x} &= P(\theta_1)\sqrt{\cos\theta_1}\sin\theta_1 t_p \sin\theta_2 \\ A_{2x} &= P(\theta_1)\sqrt{\cos\theta_1}\sin\theta_1(t_s - t_p\cos\theta_2) \\ \theta_2 &= \arcsin(n\sin\theta_1) \end{aligned}. \tag{3}$$

In the formula (3) and (4), J_n is the Bessel function of the first kind of order n; t_s and t_p are the Fresnel coefficients at the interface between the SIL and the air; $P(\theta_1)$ is a transmittance function, which describes the effect of placing a circular symmetric pupil DOE in front of the objective lens.

3. DESIGN OF TTP-DOE

The DOEs have a ability to improve the resolution or the focal depth, moreover the phase DOEs are easy and low-cost for fabrication, so the TTP-DOE is designed for decreasing the spot size. Its transmittance function is given by:

$$P(\theta_1) = \begin{cases} e^{i\delta_1} & 0 < \theta_1 < \varepsilon\,\theta_{1m} \\ 1 & \varepsilon\,\theta_{1m} < \theta_1 < \eta\,\theta_{1m} \\ e^{i\delta_2} & \eta\,\theta_{1m} < \theta_1 < \theta_{1m} \end{cases}, \tag{4}$$

where ε and η are the boundary parameters of the TTP-DOE; δ_1, δ_2 are the phase transmittance factors; θ_{1m} is the maximum of the semi-convergence angle of the objective lens.

In order to characterize quantitatively lateral image pattern, we use three parameters (G, S and M). The spot size G gives a measure of the resolution, which is defined as the ratio between the HWHMs (half-width at half-maxima) of spots. The intensity of the focused spot S gives a measure of the image brightness, which is defined as the ratio between the intensities of central peak with and without the DOE. M is defined as the maximum side-lobe intensity and measured with respect to the focused spot. Due to that the structural parameters play an important role [10–18], for example, the TBPF of the appropriate structural parameters can extend the depth by 60%, we should find the appropriate structural parameters to optimize the transmitted field distribution. In such case, for achieving the minimum focused spots, the TTPF can be designed by the following optimizing procedure:

$$\begin{aligned} &\text{Minimize} \quad G(\varepsilon, \eta, \delta_1, \delta_2) \\ &\text{Subject to} \quad \begin{cases} M(\varepsilon, \eta, \delta_1, \delta_2) \le M_0 \\ S(\varepsilon, \eta, \delta_1, \delta_2) \le S_0 \end{cases}, \end{aligned} \tag{5}$$

where M_0 and S_0 is the desired side-lobe intensity and the central spot intensity.

In the design process, we suppose $n_1 = 2$, $n_2 = 1$, $\theta_{1m} = 65°$ and $M_0 = 0.1$, $S = 0.8$. When the spot size G is 0.79, the structural parameters of the TTPF are obtained as ($\delta_1 = -72.1°$, $\delta_2 = -40.4°$, $\varepsilon = 0.25$, $\eta = 0.543$) through solving the nonlinear Equation (5) by the MATLAB optimization Toolbox. As comparison, we presented the resolution of the three-zone binary phase (TBPF) DOE with the structural parameter ($\delta = 65.5°$, $\varepsilon = 0.232$, $\eta = 0.504$), which are obtained through using the same method and constrained condition above. It is shown from the Fig. 2 that the intensity distributions ($I = |E_x|^2 + |E_y|^2 + |E_z|^2$) with the TTPF DOE, the TBPF DOE and without any DOEs (NF) are described by the solid curve, dashed curve and doted curve respectively. The intensity distribution is normalized to the maximum intensity of itself. From the figure, we can see that the scheme with the TTPF DOE inserted in the optical data storage system is very feasible since the HWHM is decreased by 21% in the x-direction and by 14% in the y-direction, while the intensity of the focused spot is reduced by only 20% and the side-lobe intensity is limited within a very low level, compared with the case without any DOEs. However, for the TBPF, it isn't more remarkable for reducing the spot size under the same constrained condition.

For a good understanding of the TTPF DOE, we also establish the constrained condition for the TBPF DOE as follows: We suppose that the spot size of the TTPF-DOE is equal to that of the TBPF DOE, the side-lobe intensity $M_0 \le 0.1$, when the maximum value of the central spot intensity is 0.62, the structural parameters of the TBPF is obtained as ($\delta = 103.9°$; $\varepsilon = 0.442$; $\eta = 0.544$).

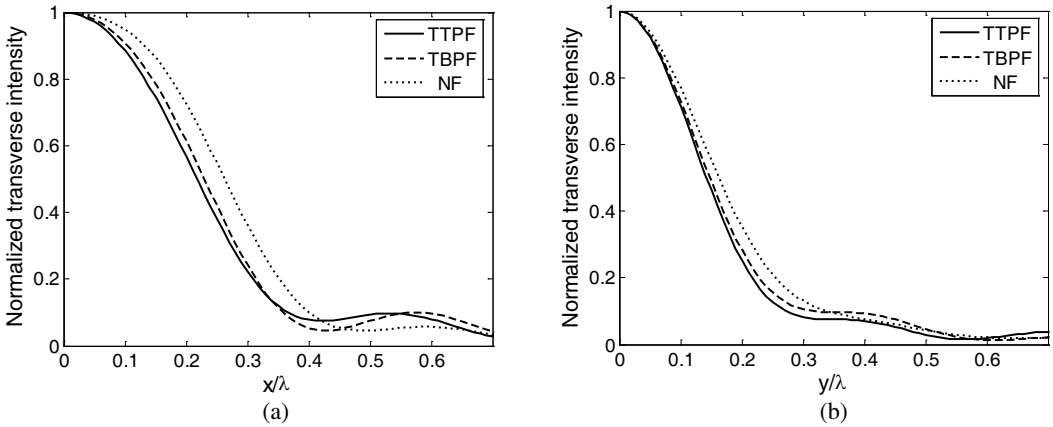

Figure 2: The intensity distributions in the x direction (a) and y direction (b) where $n_1 = 2$, $n_2 = 1$, and $\theta_{1m} = 65°$. The structure parameters of the TTPF and the TBPF are ($\delta_1 = -72.1°$; $\delta_2 = -40.4°$; $\varepsilon = 0.25$; $\eta = 0.543$) and ($\delta = 65.5°$; $\varepsilon = 0.232$; $\eta = 0.504$), respectively.

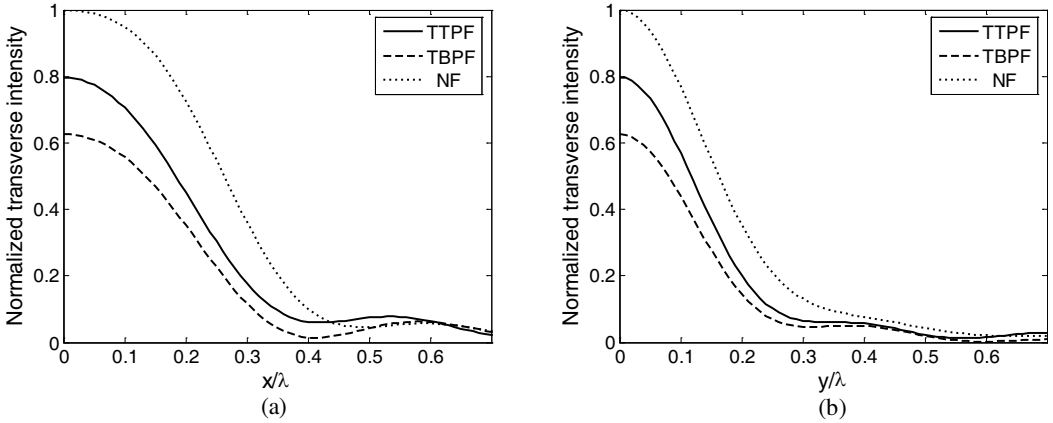

Figure 3: The intensity distributions in the x direction (a), and in the y direction (b) where $n_1 = 2$, $n_2 = 1$, and $\theta_{1m} = 65°$. The structure parameters of the TTPF and the TBPF are ($\delta_1 = -72.1°$; $\delta_2 = -40.4°$; $\varepsilon = 0.25$; $\eta = 0.543$) and ($\delta = 103.9°$; $\varepsilon = 0.442$; $\eta = 0.544$), respectively.

In Fig. 3, the intensity distributions are shown on the focused plane with the TTPF, the TBPF and the NF, which is normalized to the maximum intensity of the NF. We can see from the figure that the intensity of the focused spot with the TBPF DOE decreases to 62% approximately. The result is shown that the intensity of the focused spot with the TTP DOE is obviously higher than the case with the TBPF DOE while their spot sizes are kept the same.

4. CONCLUSIONS

In summary, a TTP-DOE is designed to improve the resolution of a near-field SIL optical storage system. The design is based on the vector diffraction theory and the optimizing toolbox in Matlab is used. In design, we limit the sidelobe intensity quite low ($M < 0.1$) and the intensity of the focused spot is quite high ($S > 0.8$). These constrained conditions can satisfy the requirements of some actual near-field SIL optical storage. Under these constrained conditions, the obtained structure parameters of the three-zone phase DOE are $\delta_1 = -72.1°$; $\delta_2 = -40.4°$; $\varepsilon = 0.25$; $\eta = 0.543$. The resolution of the system is improved by 21% in the x-direction using the designed TTPF DOE, which is larger than that using the TBPF DOE. When the same resolution is kept, the intensity of the focused spot with the designed TTPF DOE is larger than that with the TBPF DOE whose structure parameters are obtained by the similar optimizing method.

ACKNOWLEDGMENT

This work was supported by the National Natural Science Foundation of China under contract 61078023.

REFERENCES

1. Milster, T. D., "Near-field optics: A new tool for data storage," *Proceedings of the IEEE*, Vol. 88, No. 9, 1480–1490, 2000.
2. Mansfield, S. M., W. R. Studenmund, G. S. Kino, and K. Osato, "High-numerical-aperture lens system for optical storage," *Opt. Lett.*, Vol. 18, No. 4, 305–307, 1993.
3. Terris, B. D., H. J. Mamin, D. Rugar, G. S. Kino, and W. R. Studenmund. "Near-field optical data storage using a solid immersion lens," *Appl. Phys. Lett.*, Vol. 65, No. 4, 388–390, 1994.
4. Hu, Y., Z. Zhang, Y. Chen, Q. Zhang, and W. Huang, "Two-photon-induced polarization-multiplexed and multilevel storage in photoisomeric copolymer film," *Opt. Lett.*, Vol. 35, No. 1, 46–48, 2010.
5. Lee, S, Y. C. Jeong, J. Lee, and J. K. Park, "Multifunctional photoreactive inorganic cages for three-dimensional holographic data storage," *Opt. Lett.*, Vol. 34, No. 20, 3095–3097, 2009.
6. Zijlstra P., J. W. M. Chon, and M. Gu, "Five-dimensional optical recording mediated by surface plasmons in gold nanorods," *Nature*, Vol. 459, 410–413, 2009.
7. Zhang, Y., "A new three-zone amplitude-only DOE for increasing the focal depth of near-field solid immersion lens systems," *J. Mod. Opt.*, Vol. 53, No. 13, 1919–1925, 2006.
8. Lu, Y., J. Xie, and M. Hai. "Binary pure-phase DOE optimized the optical distribution of solid immersion lens," *Opt. Commun.*, Vol. 215, No. 4–6, 251–255. 2003.
9. Liu, C. and S.-H. Park, "Numerical analysis of an annular-aperture solid immersion lens," *Opt. Lett.*, Vol. 29, No. 15, 1742–1744, 2004.
10. Lu, Y., J. Zhang, H. Ming, and P. Wang. "Increase the storage density of solid immersion lens system by high-pass angular spectrum filter method," *Opt. Commun.*, Vol. 203, No. 1–2, 87–92, 2000.
11. Zhang, Y, C. Zheng, and Y. Zou. "Focal-field distribution of the solid immersion lens system with an annular DOE," *Optik.*, Vol. 115, No. 6, 277–280, 2004.
12. Zhang, Y., H. Xiao, and C. Zheng, "Diffractive super-resolution elements applied to near-field optical data storage with solid immersion lens," *New J. Phys.*, Vol. 6, 75, 2004.
13. Zhang, Y., "Three-zone phase-only DOE increasing the focal depth of optical storage systems with a solid immersion lens," *Appl. Phys. B*, Vol. 86, No. 1, 97–103, 2007.
14. Ye, X. and Y. Zhang, "Optimizing the optical field distribution of solid immersion lens system by a continuous phase DOE," *Opt. Lett. Chin.*, Vol. 5, No. 6, 318–321, 2007.
15. Török, P., P. Varga, Z. Laczik, and G. R. Booker, "Electromagnetic diffraction of light focused through a planar interface between materials of mis-matched refractive indices: structure of the electromagnetic field," *Opt. Soc. Am. A*, Vol. 12, No. 2, 325–332, 1995.

Degree of Polarization of Random Electromagnetic Vortex Beams in Atmospheric Turbulence

Jinhong Li[1], **Meiling Duan**[2], **Yamei Luo**[3], **and Jilin Wei**[1]

[1]Department of Physics, Taiyuan University of Science and Technology, Taiyuan 030024, China
[2]Department of Physics, North University of China, Taiyuan 030051, China
[3]Department of Biomedical Engineering, Luzhou Medical College, Luzhou 646000, China

Abstract— Using the extended Huygens-Fresnel principle and the quadratic approximation of the phase structure function, and taking the random electromagnetic Gaussian Schell-model (GSM) vortex beams as a typical example of random electromagnetic vortex beams, the analytical expressions for the cross-spectral density matrix of random electromagnetic GSM vortex beams with topological charge $m = +1$ propagating through atmospheric turbulence are derived, and used to study the degree of polarization of random electromagnetic GSM vortex beams in atmospheric turbulence and to compare the results of random electromagnetic GSM vortex-free beams. The influence of vortex and atmospheric turbulence on the degree of polarization is analyzed. The validity of our results is interpreted physically.

1. INTRODUCTION

The laser beam propagation through atmospheric turbulence is of considerable importance in connection with laser communications, optical radar, satellite remote sensing, and distance measuring etc. for a long time [1, 2]. Over the past several years there has been substantial interest in studying the random electromagnetic beams, because of its importance in the theories of coherence and polarization of light [3–16]. The degree of polarization of random electromagnetic beams propagating through free space [7, 11], turbulent atmosphere [4, 6, 12], fractional Fourier transform optical systems [3], misaligned optical systems [8], optical fibers [5], and Gaussian cavity [9] have also been extensively studied. All the above studies are limited to the random electromagnetic vortex-free beams. Recently, Gbur and Tyson analyzed the propagation of scalar vortex beams through weak-to-strong atmospheric turbulence and topological charge conservation by using multiple phase screen simulation, and showed that the topological charge could be used as an information carrier in optical communications [17]. Thus, an interesting question arises: what will happen for the degree of polarization of random electromagnetic vortex beams in atmospheric turbulence?

The purpose of the present paper is to study the changes in the degree of polarization of random electromagnetic vortex beams through atmospheric turbulence. In Section 2, the analytical expressions for the cross-spectral density matrix of random electromagnetic Gaussian Schell-model (GSM) vortex beams propagating through atmospheric turbulence are derived. Changes in the on-axis and transverse degree of polarization of random electromagnetic GSM vortex beams in atmospheric turbulence and comparison with those of random electromagnetic GSM vortex-free beams are illustrated by numerical calculation examples in Section 3. Section 4 concludes the main results obtained in this paper.

2. THEORETICAL FORMULATION

The cross-spectral density matrix of random electromagnetic beams at the source plane is expressed as [18]

$$\overleftrightarrow{W}(\mathbf{s}_1,\, \mathbf{s}_2,\, 0, \omega) = \begin{bmatrix} W_{xx}(\mathbf{s}_1,\, \mathbf{s}_2,\, 0, \omega) & W_{xy}(\mathbf{s}_1,\, \mathbf{s}_2,\, 0, \omega) \\ W_{yx}(\mathbf{s}_1,\, \mathbf{s}_2,\, 0, \omega) & W_{yy}(\mathbf{s}_1,\, \mathbf{s}_2,\, 0, \omega) \end{bmatrix}, \tag{1}$$

where

$$W_{ij}(\mathbf{s}_1,\, \mathbf{s}_2,\, 0, \omega) = \langle E_i^*(\mathbf{s}_1,\ 0, \omega) E_j(\mathbf{s}_2,\ 0, \omega) \rangle\,, \quad (i, j = x, y \text{ unless otherwise stated}) \tag{2}$$

In Eq. (2), quantities E_x and E_y represent the realizations of the Cartesian electric-field components, $\mathbf{s}_l = (s_{lx},\, s_{ly})$ $(l = 1,\, 2)$ is the two-dimensional position vector at the source plane $z = 0$. The * and $<>$ stand for the complex conjugate and ensemble average, respectively. ω is the frequency and omitted later for brevity.

The elements $W_{ij}(s_1, s_2, 0)$ of the cross-spectral density matrix of random electromagnetic GSM vortex beams at the source plane are expressed as [19]

$$\begin{aligned} W_{ij}(\mathbf{s}_1, \mathbf{s}_2, 0) &= A_i A_j B_{ij} \left[s_{1x}s_{2x} + s_{1y}s_{2y} + i\mathrm{sgn}(m)s_{1x}s_{2y} - i\mathrm{sgn}(m)s_{2x}s_{1y}\right]^{|m|} \\ &\quad \times \exp\left[-\left(s_1^2 + s_2^2\right)\right]/w_0^2 \exp\left[-\left(\mathbf{s}_1 - \mathbf{s}_2\right)^2/(2\sigma_{ij}^2)\right], \end{aligned} \tag{3}$$

where A_i is the amplitude of the electric field-vector component E_i, B_{ij} are correlation coefficients between two components E_i and E_j of the electric field-vector at the points s_1 and s_2 in the source plane, σ_{ij} is related to the spatial correlation length, w_0 is the waist width, $\mathrm{sgn}(m)$ denotes the sign function, m specifies the topological charge, and in the following we take $m = +1$. For $m = 0$ Eq. (3) reduces to those of random electromagnetic GSM vortex-free beams.

In accordance with the extended Huygens-Fresnel principle [2], the elements $W_{ij}(\rho_1, \rho_2, z)$ of the cross-spectral density matrix of random electromagnetic GSM vortex beams propagating through atmospheric turbulence are given by

$$\begin{aligned} W_{ij}(\rho_1, \rho_2, z) &= (k/2\pi z)^2 \iint d^2\rho_1 \iint d^2\rho_2 W_{ij}(\mathbf{s}_1, \mathbf{s}_2, 0) \\ &\quad \times \exp\{-ik/2L[(\rho_1 - \mathbf{s}_1)^2 - (\rho_2 - \mathbf{s}_2)^2]\}\langle \exp[\psi^*(\rho_1, \mathbf{s}_1) + \psi(\rho_2, \mathbf{s}_2)]\rangle, \end{aligned} \tag{4}$$

where $\rho_l \equiv (\rho_{lx}, \rho_{ly})$ is the position vector at the z plane, k is the wave number related to the wave length λ by $k = 2\pi/\lambda$, and $\psi(\rho, \mathbf{s})$ represents the random part of the complex phase of a spherical wave due to the turbulence, and can be written as [20]

$$\langle \exp[\psi^*(\rho_1, \mathbf{s}_1) + \psi(\rho_2, \mathbf{s}_2)]\rangle \cong \exp\{-1/\rho_0^2[(\mathbf{s}_1 - \mathbf{s}_2)^2 + (\mathbf{s}_1 - \mathbf{s}_2)(\rho_1 - \rho_2) + (\rho_1 - \rho_2)^2]\}, \tag{5}$$

where $\rho_0 = (0.545C_n^2k^2z)^{-3/5}$ denotes the spatial coherence radius of a spherical wave propagating through turbulence, C_n^2 is the refraction index structure constant describing the strength of atmospheric turbulence.

Tedious but straightforward integral calculations lead to the analytical expressions for the elements of the cross-spectral density matrix of random electromagnetic GSM vortex beams in turbulence which is given by

$$\begin{aligned} W_{ij}(\rho, z) &= A_i A_j B_{ij} \left\{ \frac{k^2 \bar{b}_x \bar{b}_y (\bar{d}_x^2 + \bar{d}_y^2 + c)}{4z^2 a_{ij} c^3} \exp\left(\frac{\bar{d}_x^2 + \bar{d}_y^2}{c}\right) - \frac{k^2 w_0^2 (\bar{g}_x^2 + \bar{g}_y^2 + f)}{32 z^2 f^3} \exp\left(\frac{\bar{g}_x^2 + \bar{g}_y^2}{f}\right) \right. \\ &\quad \left. -i\left[\frac{k^2 w_0 \bar{b}_x \bar{d}_x \bar{g}_y}{4z^2\sqrt{2a_{ij}c^3 f^3}} \exp\left(\frac{\bar{d}_x^2}{c} + \frac{\bar{g}_y^2}{f}\right) - \frac{k^2 w_0 \bar{b}_y \bar{d}_y \bar{g}_x}{4z^2\sqrt{2a_{ij}c^3 f^3}} \exp\left(\frac{\bar{d}_y^2}{c} + \frac{\bar{g}_x^2}{f}\right)\right]\right\}, \end{aligned} \tag{6a}$$

where

$$\bar{b}_i = exp[-k^2/(4a_{ij}z^2)\rho_i^2)], \quad \bar{d}_i = (k^2\rho_i)/(4a_{ij}z^2), \quad \bar{g}_i = (ik\rho_i)/(2z). \quad (i = x, y) \tag{6b}$$

The spectral degree of polarization [21] of random electromagnetic GSM vortex beams propagating through atmospheric turbulence are given by

$$P(\rho, \mathbf{z}) = \sqrt{1 - \frac{4\mathrm{Det}\vec{\vec{W}}(\rho, \mathbf{z})}{[\mathrm{Tr}\vec{\vec{W}}(\rho, \mathbf{z})]^2}}, \tag{7}$$

where Det and Tr stand for the determinant and the trace. Eqs. (6) and (7) describe the changes in spectral degree of polarization of random electromagnetic GSM vortex beams propagating through turbulence, which depend on the correlation length σ_{ij}, waist width w_0, wave length λ, structure constant C_n^2, and propagation distance z.

3. NUMERICAL CALCULATIONS AND ANALYSES

Figure 1 gives the on-axis degree of polarization $P$of random electromagnetic GSM vortex-free beams (a) and random electromagnetic GSM vortex beams (b) in atmospheric turbulence versus the propagation distance z for different values of correlation length σ_{yy}. The calculation parameters are $\lambda = 1.06\,\mu\text{m}$, $A_x = A_y = 2$, $B_{xx} = B_{yy} = 1$, $B_{xy} = 0.2\exp(i\pi/6)$, $B_{yx} = 0.2\exp(-i\pi/6)$, $w_0 = 3\,\text{cm}$, $\sigma_{xx} = 1.5\,\text{cm}$, $\sigma_{xy} = \sigma_{yx} = 2\,\text{cm}$, $C_n^2 = 10^{-14}\,\text{m}^{-2/3}$. As can be seen, the on-axis degree of polarization of random electromagnetic GSM vortex-free beams changes non-monotonously with increasing z(a), and there exists a maximums for P. From Fig. 1(b), it is seen that the changes in the on-axis degree of polarization of random electromagnetic GSM vortex beams with increasing propagation distances $z$depend on the correlation length σ_{yy}, P has a maximum and a minimum when $\sigma_{yy} = 1$ and $2\,\text{cm}$. However, for the case of $\sigma_{yy} = 1.5\,\text{cm}$, the P has a maximum. For

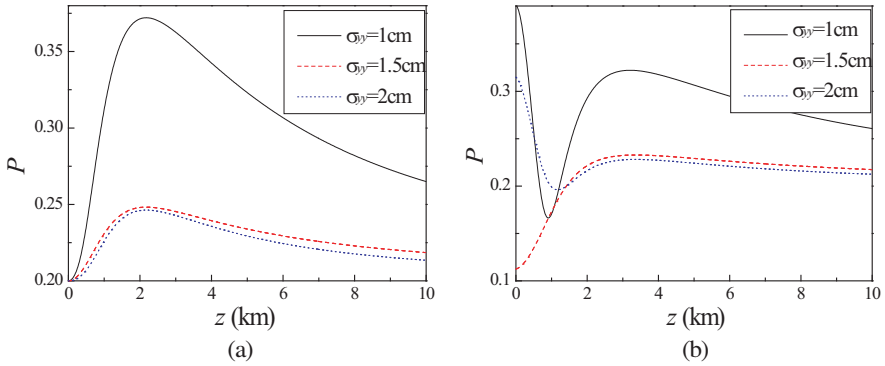

Figure 1: (Color online) On-axis degree of polarization P of random electromagnetic GSM vortex-free (a) and vortex (b) beams in atmospheric turbulence versus the propagation distance z for different values of correlation length σ_{yy}.

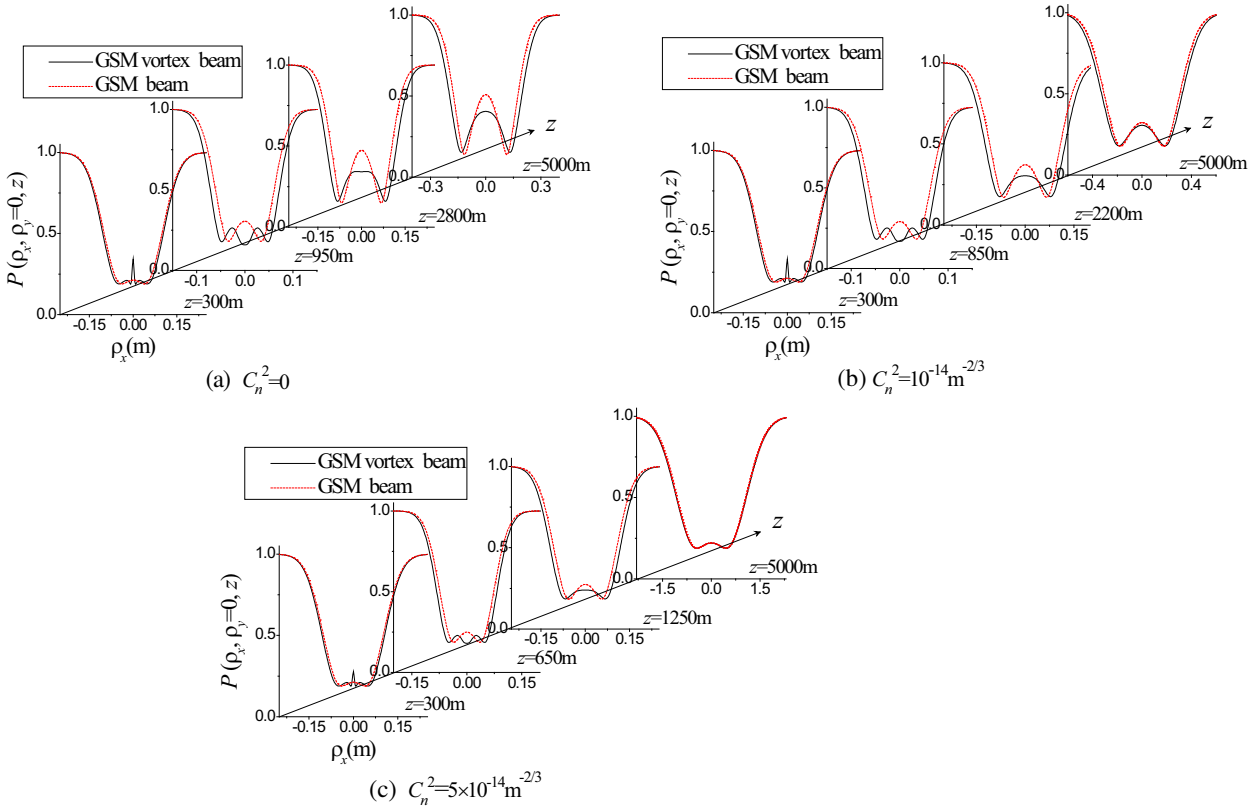

Figure 2: (Color online) Evolution of degree of polarization of random electromagnetic GSM vortex beam (—) and random electromagnetic GSM vortex-free beam (· · ·) for different values of the structure constant C_n^2.

the case of $\sigma_{yy} = 1\,\mathrm{cm}$, letting $\partial P/\partial z = 0$ results in $z = 991\,\mathrm{m}$, $3210\,\mathrm{m}$ and $\partial^2 s_1/\partial z^2|_{z=991\,\mathrm{m}} > 0$, $\partial^2 s_1/\partial z^2|_{z=3210\,\mathrm{m}} < 0$, which means that P have a maximum and a minimum. The physical explanation of $\sigma_{yy} = 2\,\mathrm{cm}$ is similar to $\sigma_{yy} = 1\,\mathrm{cm}$ in Fig. 1(b). A comparison of Fig. 1(a) with Fig. 1(b) shows the influence of vortex on the changes in the on-axis degree of polarization of random electromagnetic beams.

Figures 2(a)–(c) give the evolution of the transverse degree of polarization P of random electromagnetic GSM vortex beam (solid curves) and random electromagnetic GSM vortex-free beam (dotted curves) for different values of C_n^2. $\sigma_{yy} = 1\,\mathrm{cm}$ and the other calculation parameters are the same as those in Fig. 1. From Figs. 2(a)–(c), we see that the spatial profiles of transverse degree of polarization of random electromagnetic GSM vortex beam (solid curves) undergo several stages of evolution, the larger the structure constant C_n^2 is, the shorter the evolution distance becomes. For example, for $C_n^2 = 0$, 10^{-14} and $5 \times 10^{-14}\ \mathrm{m}^{-2/3}$ the propagation distance for the presence of a two peaks three valleys profile of the transverse degree of polarization is $z = 950$, 850 and 650 m, respectively. Therefore, an increase of the structure constant C_n^2 accelerates the evolution process of the transverse degree of polarization. From Figs. 2(a)–(c), it is seen that the spatial profiles of transverse degree of polarization of random electromagnetic GSM vortex-free beams (dotted curves) remain unchanged upon propagation. A comparison of solid curves with dotted curves shows that because of the existence of the vortex, the evolution process of transverse degree of polarization of random electromagnetic GSM vortex beams in atmospheric turbulence are different from those of random electromagnetic GSM vortex-free beams.

4. CONCLUSIONS

In this paper, based on the extended Huygens-Fresnel principle, the analytical expressions for the cross-spectral density matrix of random electromagnetic GSM vortex beams propagating through atmospheric turbulence have been derived, and the changes in degree of polarization of random electromagnetic GSM vortex beams in atmospheric turbulence have been studied and compared with those of random electromagnetic GSM vortex-free beams. It has been shown that the vortex affects the evolution behavior of degree of polarization in atmospheric turbulence. For example, the spatial profiles of transverse degree of polarization of random electromagnetic GSM vortex beams undergo several stages of evolution upon propagation, but this is not the case for random electromagnetic GSM vortex-free beams. An increase of the C_n^2 speeds up the evolution process of the degree of polarization of random electromagnetic GSM vortex beams. The results obtained are useful for studying the changes in the degree of polarization of other types of random electromagnetic vortex beams in atmospheric turbulence and for their controlling.

ACKNOWLEDGMENT

This work was supported by the Doctoral Scientific Research Starting Foundation of Taiyuan University of Science and Technology (No. 20102016), the Natural Science Foundation of Luzhou Medical College, and the Doctoral Scientific Research Starting Foundation of North University of China.

REFERENCES

1. Strohbehn, J. W., *Laser Beam Propagation in the Atmosphere*, Springer-Verlag, New York, 1978.
2. Andrews, L. C. and R. L. Phillips, *Laser Beam Propagation through Random Media*, SPIE Press, Bellingham, 1998.
3. Cai, Y., D. Ge, and Q. Lin, "Fractional Fourier transform for partially coherent and partially polarized Gaussian-Schell model beams," *J. Opt. A: Pure Appl. Opt.*, Vol. 5, 453–459, 2003.
4. Eyyuboglu, H. T., Y. Baykal, and Y. Cai, "Degree of polarization for partially coherent general beams in turbulent atmosphere," *Appl. Phys. B*, Vol. 89, 91–97, 2007.
5. Huang, W., S. A. Ponomarenko, M. Cada, and G. P. Agrawal, "Polarization changes of partially coherent pulses propagating in optical fibers," *J. Opt. Soc. Am. A*, Vol. 24, 3063–3068, 2007.
6. Cai, Y., O. Korotkova, H. T.Eyyuboglu, and Y. Baykal, "Active laser radar systems with stochastic electromagnetic beams in turbulent atmosphere," *Opt. Express*, 16, 15834–15846, 2008.
7. Korotkova, O., T. D. Visser, and E. Wolf, "Polarization properties of stochastic electromagnetic beams," *Opt. Commun.*, Vol. 281, 515–520, 2008.

8. Du, X. and D. Zhao, "Changes in the polarization and coherence of a random electromagnetic beam propagating through a misaligned optical system," *J. Opt. Soc. Am. A*, Vol. 25, 773–779, 2008.
9. Yao, M., Y. Cai, H. T. Eyyuboglu, Y. Baykal, and O. Korotkova, "Evolution of the degree of polarization of an electromagnetic Gaussian Schell-model beam in a Gaussian cavity," *Opt. Lett.*, Vol. 33, 2266–2268, 2008.
10. Zhao, C., Y. Cai, and O. Korotkova, "Radiation force of scalar and electromagnetic twisted Gaussian Schell-model beams," *Opt. Express*, Vol. 17, 21472–21487, 2009.
11. Sahin, S., O. Korotkova, G. Zhang, and J. Pu, "Free-space propagation of the spectral degree of cross-polarization of stochastic electromagnetic beams," *J. Opt. A: Pure Appl. Opt.*, Vol. 11, 085703, 2009.
12. Pu, J. and O. Korotkova, "Propagation of the degree of cross-polarization of a stochastic electromagnetic beam through the turbulent atmosphere," *Opt. Commun.*, Vol. 282, 1691–1698, 2009.
13. Zhu, S., Y. Cai, and O. Korotkova, "Propagation factor of a stochastic electromagnetic Gaussian Schell-model beam," *Opt. Express*, Vol. 18, 12587–12598, 2010.
14. Zhu, S. and Y. Cai, "M2-factor of a stochastic electromagnetic beam in a Gaussian cavity," *Opt. Express*, Vol. 18, 27567–27581, 2010.
15. Yao, M., Y. Cai, O. Korotkova, Q. Lin, and Z. Wang, "Spatio-temporal coupling of random electromagnetic pulses interacting with reflecting gratings," *Opt. Express*, Vol. 18, 22503–22514, 2010.
16. Wu, G. and Y. Cai, "Modulation of spectral intensity, polarization and coherence of a stochastic electromagnetic beam," *Opt. Express*, Vol. 19, 8700–8714, 2011.
17. Gbur, G. and R. K. Tyson, "Vortex beam propagation through atmospheric turbulence and topological charge conservation," *J. Opt. Soc. Am. A*, Vol. 25, 225–230, 2008.
18. Wolf, E., *Introduction to the Theory of Coherence and Polarization of Light*, Cambridge University Press, Cambridge, 2007.
19. Maleev, I. D., D. M. Palacios, A. S. Marathay, and G. A. Swartzlander, "Spatial correlation vortices in partially coherent light: Theory," *J. Opt. Soc. Am. B*, Vol. 21, 1895–1900, 2004.
20. Wang, S. C. H. and M. A. Plonus, "Optical beam propagation for a partially coherent source in the turbulent atmosphere," *J. Opt. Soc. Am.*, Vol. 69, 1297–1304, 1979.
21. Mandel, L. and E. Wolf, *Optical Coherence and Quantum Optics*, Cambridge University Press, Cambridge, 1995.

Design and Simulation of Optical Planar Chiral Metamaterial

Fang-Qing Yang, Jie Li, and Jian-Feng Dong
Institute of Optical Fiber Communication and Network Technology
Ningbo University, Ningbo 315211, China

Abstract— The twisted double-layer metallic wires and twisted conjugated gammadion planar chiral metamaterials working in near-infrared frequency region have been designed and optimized. The simulated results show that the larger circular dichroism, exceptionally strong optical activity and the negative refractive index of the chiral metamaterials can be realized. The negative refractive index is due to a large chiral parameter which does not require simultaneously negative permittivity and negative permeability.

1. INTRODUCTION

Recently, a new route to realize negative refractive index due to a large chiral parameter in the chiral media has been proposed [1, 2]. The chiral media are composed of particles that cannot be superimposed on their mirror images. Their important electromagnetic properties are the optical activity and circular dichroism [3–8]. In the isotropic chiral media, the constitutive relations are expressed as: $\begin{pmatrix} \mathbf{D} \\ \mathbf{B} \end{pmatrix} = \begin{pmatrix} \varepsilon\varepsilon_0 & -i\kappa/c \\ i\kappa/c & \mu\mu_0 \end{pmatrix} \begin{pmatrix} \mathbf{E} \\ \mathbf{H} \end{pmatrix}$, where ε and μ are the relative permittivity and permeability of the chiral media, ε_0 and μ_0 are the permittivity and permeability of vacuum, κ is the chiral parameter, and c is the speed of light. In the chiral media, the eigenwaves are the right-handed circularly polarized (RCP, +) wave and left-handed circularly polarized (LCP, −) wave. The index of refractive for RCP (n_+) and LCP (n_-) is given by $n_\pm = (n \pm \kappa)$, where $n = \sqrt{\mu\varepsilon}$. When the absolute of κ is large enough, either n_+ or n_- becomes negative.

Several chiral structures with large chiral parameters have been investigated, such as cross-wire [3, 4], twisted rosettes [5, 6], twisted metallic foil [7, 8] and conjugated gammadion [9]. In this paper, we present two chiral structures: twisted double-layer metallic wires and twisted conjugated gammadion. These chiral structures have larger circular dichroism and exceptionally stronger optical activity, and the negative refractive indices of the right-handed circularly polarized (RCP) and left-handed circularly polarized (LCP) waves can be realized at the near-infrared frequency region.

2. STRUCTURE PARAMETERS

The chiral metamaterials we studied are composed of gold metallic material separated by a dielectric layer, and each unit cell of structure is shown in Figure 1. For twisted double-layer metallic wires (Figure 1(a)), the lower four wires form a unit and each wires rotates 0°, 90°, 180°, 270° respectively for the requirement of four-fold symmetry, the upper layer is rotated $\delta = 60°$ counterclockwise. For twisted conjugated gammadion (Figure 1(b)), the upper gammadion is rotated α degree clockwise and the other α degree counterclockwise, $\alpha = 10°$. It is necessary to notice that the angle δ and α are chosen after optimized. These structures are periodic, and the periodic boundary conditions are applied to the x and y directions in numerical simulations. We use a finite-element frequency-domain approach for simulations.

3. SIMULATION RESULTS AND DISCUSSION

In order to study the transmission behavior of the twisted double-layer metallic wires, we simulated the transmission spectra for the RCP (T_{++}) and LCP (T_{--}) waves, as shown in Figure 2(a). There are obvious differences between the transmissions of RCP and LCP waves around the resonances. Around the lower resonant frequency of 245 THz, the transmission of LCP wave is 13–14 dB lower than that of the RCP wave. While around the higher resonant frequency of 270 THz, the transmission of RCP wave is 12–13 dB lower than that of the LCP wave. Using the standard definitions, we can calculated the polarization azimuth rotation angle, $\theta = \frac{1}{2}[\arg(T_{++}) - \arg(T_{--})]$. Around the two resonant frequencies, the polarization azimuth rotation angles θ reach their maximum values (Figure 2(c)). The maximum θ arrived about 140°. Figure 2(b) shows transmission spectra of twisted conjugated gammadion for the LCP (T_{--}) and RCP (T_{++}) waves. Around the lower resonant frequency, the transmission of RCP wave is higher than that of LCP wave; while around

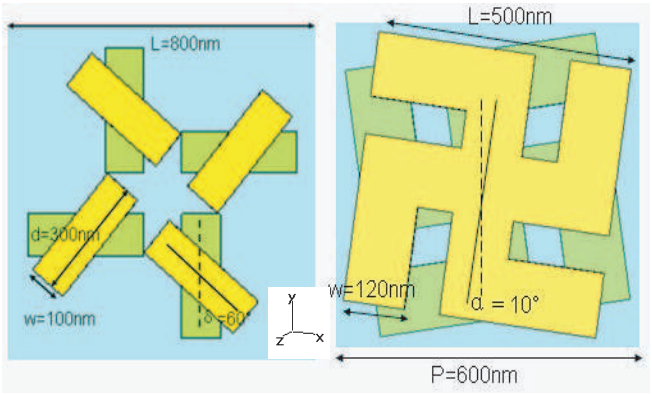

Figure 1: (a) Schematics and geometry parameters of one unit cell of twisted double-layer metallic wires and (b) twisted conjugated gammadion. The thickness of twisted double-layer metallic wires and dielectric layer are $t = 50\,\text{nm}$, $h = 40\,\text{nm}$, respectively. The every layer thickness of twisted conjugated gammadion and dielectric layer are 60 nm.

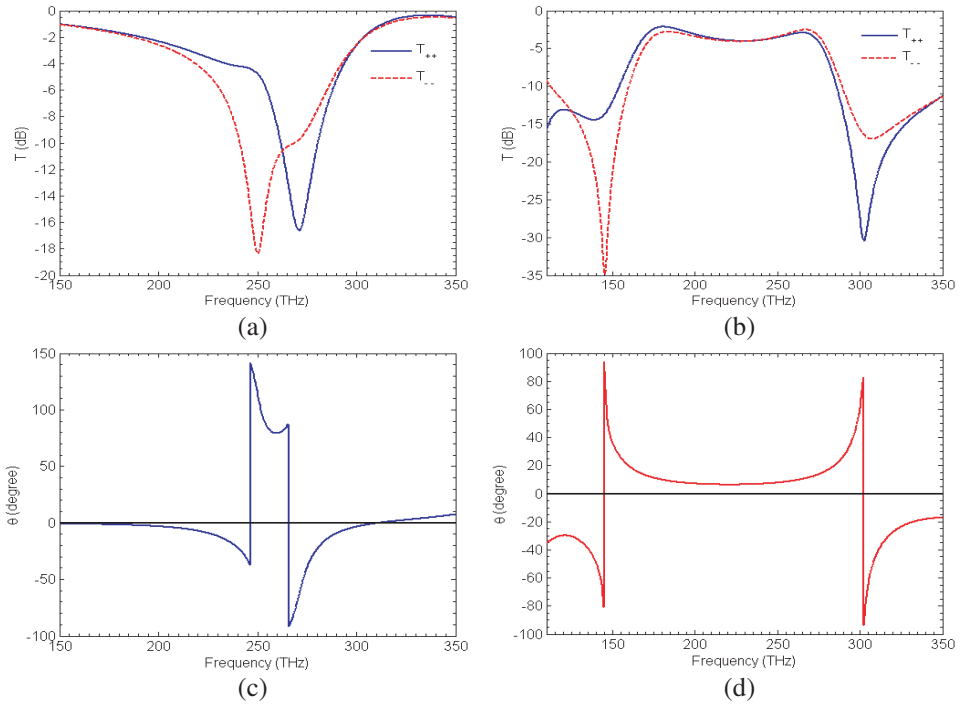

Figure 2: The transmission spectra for LCP (T_{--}) and RCP (T_{++}) waves and the polarization azimuth rotation angle θ. (a) and (c) for twisted double-layer metallic wires; (b) and (d) for twisted conjugated gammadion.

the higher resonance frequency, the transmission of RCP wave is lower than that of LCP wave. In Figure 2(d), at the two resonant frequencies, the polarization azimuth rotation angles θ reach their maximum value, θ reaches 95° at 145 THz, and is up to −95° at 300 THz.

Figures 3(a) and (b) present the circular dichroism, $\Delta = |T_{++}| - |T_{--}|$ and ellipticity angle, $\eta = \frac{1}{2}\arcsin(\frac{|T_{++}|^2-|T_{--}|^2}{|T_{++}|^2+|T_{--}|^2})$ for twisted conjugated gammadion. Around the two resonances, the circular dichroisms reach their maximum value. Especially, in the middle of the two resonances regions, the ellipticity angle $\eta = 0$, which corresponds to a pure optical activity effect, i.e., for the linear polarization incident wave, the transmitted wave will still be linear polarization but with a rotated angle θ. For twisted conjugated gammadion, we gain a polarization rotation angle of 10° at 240 THz, this rotation angle for a total structure thickness of just 180 nm can be translated into strong optical activity (55,000°/mm).

Figure 4 shows the effective parameters n, n_+, n_-, κ, ε and μ for twisted double-layer metallic wires and twisted conjugated gammadion. For twisted double-layer metallic wires, around the

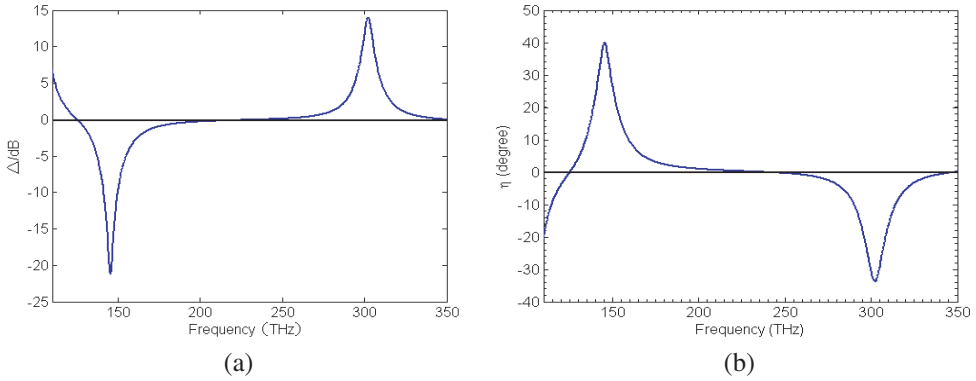

Figure 3: The (a) circular dichroism and (b) ellipticity angle η for twisted conjugated gammadion.

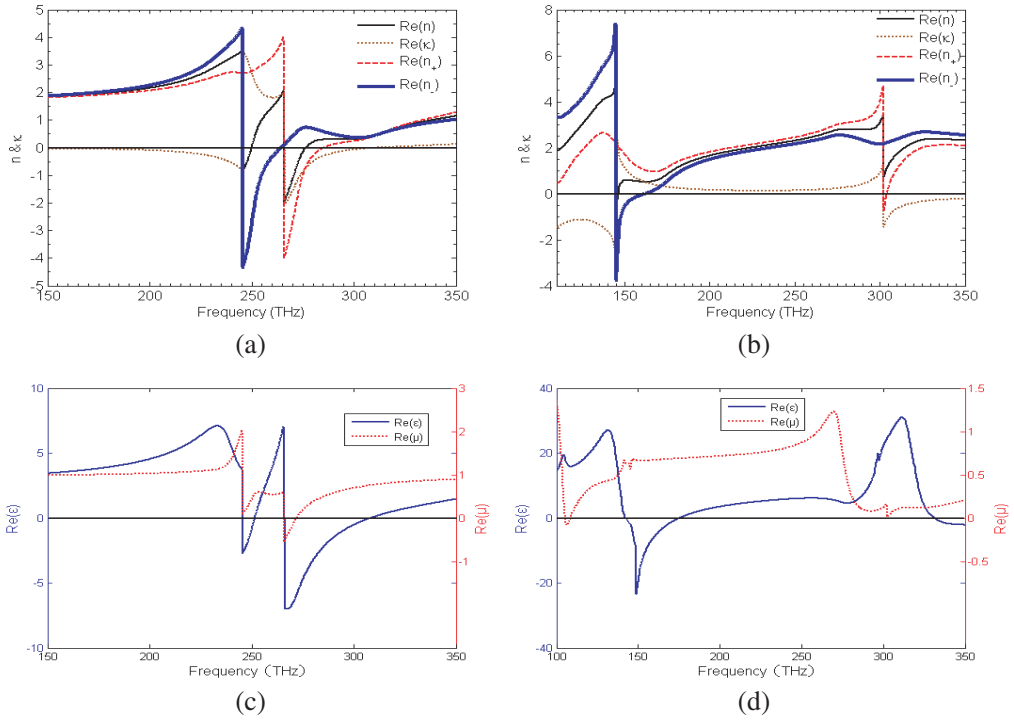

Figure 4: The refractive index (n), refractive index for RCP (n_+) and LCP (n_-), chiral parameter κ, permittivity and permeability. (a) and (c) for twisted double-layer metallic wires; (b) and (d) for twisted conjugated gammadion.

two resonances, the chiral parameter reaches their maximum values (Figure 4(a)). Due to the relation of $n_\pm = n \pm \kappa$, the large chiral parameter can lead the refractive index of LCP (n_-) and RCP (n_+) waves to negative at the resonant frequencies of 145 THz and 270 THz, respectively. In Figure 4(c), it is clear that Re(μ) is positive throughout the entire frequency range (except the small range around 270 THz), while Re(ε) is negative around the two resonances. For twisted conjugated gammadion structure, obviously, n is positive through the entire frequency from 110 THz to 350 THz. However, the refractive index of LCP (n_-) is negative between 145 THz and 165THz, and the refractive index of RCP (n_+) is negative between 300 THz and 305 THz, their maximum negative refractive index can reach -4 and -0.8, respectively (Figure 4(b)). Figure 4(d) shows the real parts of the relative permittivity ε and permeability μ, there is no overlap region of negative Re(ε) and Re(μ). For the traditional metamaterials, this will not result in negative index. It is clear that the negative index of LCP (RCP) wave is actually attributed to the relatively small n and large chiral parameter κ.

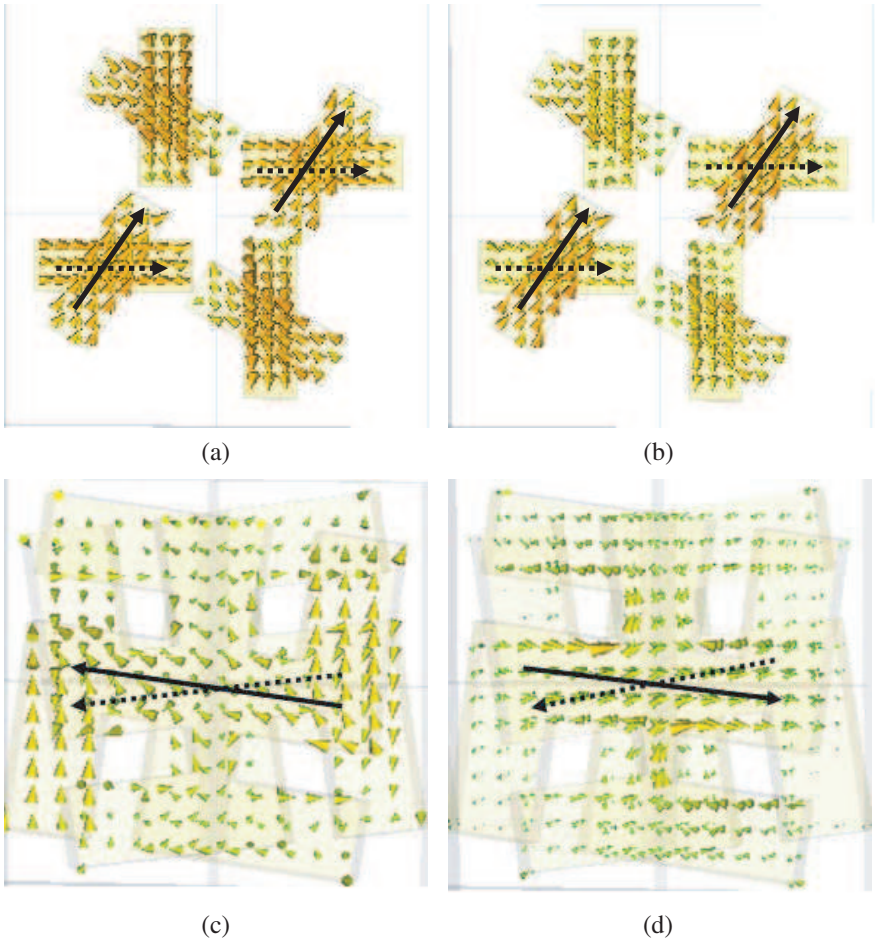

Figure 5: The current distribution at (a) 245 THz and (b) 270 THz for twisted double-layer metallic wires and at (c) 145 THz and (d) 300 THz for twisted conjugated gammadion. (Real and dashed lines correspond to the direction of currents for upper and lower layers, respectively).

In order to understand the mechanism of the resonant behavior, the currents density distribution for twisted double-layer metallic wires and twisted conjugated gammadion is shown in Figure 5. For twisted double-layer metallic wires, at the lower and higher frequency resonance, both the currents on the upper and lower layer are parallel (Figures 5(a) and (b)), the entire structure is similar to an electric-dipole, so both of the resonants are electric resonants. However, for twisted conjugated gammadion, at the lower frequency resonance, the currents on the upper and lower layer are parallel (Figure 5(c)), the entire structure is similar to an electric-dipole, so the resonant is electric resonant. In contrast, at the higher frequency resonance, the current flowing on the top and bottom layer is antiparallel (Figure 5(d)), the entire structure is similar to a magnetic-dipole, the resonant is magnetic resonant.

4. CONCLUSION

In this paper, we proposed two chiral metamaterials: twisted double-layer metallic wires and twisted conjugated gammadion. The simulation results show that the larger circular dichroism and exceptionally strong optical activity are found at the resonant frequency regions for these two structures. Especially at ellipticity angle $\eta = 0$ for twisted conjugated gammadion, the rotated angles is about 10°, the rotated angle for a total metamaterials thickness of just 180 nm ($55{,}000^\circ$/mm), which is larger than the value reported in references [4]. The refractive index, chirality parameter, relative permeability and permittivity are retrieved from simulated transmissions and reflections. It is actually that negative refractive index originates from large chiral parameters of these structures.

ACKNOWLEDGMENT

This work is supported by the National Natural Science Foundation of China (61078060), the Natural Science Foundation of Zhejiang Province, China (Y1091139), Ningbo Optoelectronic Materials

and Devices Creative Team (2009B21007), and is partially sponsored by K. C. Wong Magna Fund in Ningbo University.

REFERENCES

1. Pendry, J. B., "A chiral route to negative refraction," *Science*, Vol. 306, 1353–1355, 2004.
2. Tretyakov, S., A. Sihvola, and L. Jylha, "Backward-wave regime and negative refraction in chiral composites," *Photonics Nanostruct. Fundam. Appl.*, Vol. 3, No. 2–3, 107–115, 2005.
3. Zhou, J., J. Dong, B. Wang, T. Koschny, M. Kafesaki, and C. M. Soukoulis, "Negative refractive index due to chirality," *Phys. Rev. B*, Vol. 79, No. 12, 121104 (R), 2009.
4. Decker, M., M. Ruther, C. E. Kriegler, J. Zhou, C. M. Soukoulis, S. Linden, and M. Wegener, "Strong optical activity from twisted-cross photonic metamaterials," *Opt. Lett.*, Vol. 34, No. 16, 2501–2503, 2009.
5. Plum, E., V. A. Fedotov, A. S. Schwanecke, N. I. Zheludev, and Y. Chen, "Giant optical gyrotropy due to electromagnetic coupling," *Appl. Phys. Lett.*, Vol. 90, No. 22, 223113, 2007.
6. Plum, E., J. Zhou, J. Dong, V. A. Fedotov, T. Koschny, C. M. Soukoulis, and N. I. Zheludev, "Metamaterial with negative index due to chirality," *Phys. Rev. B*, Vol. 79, No. 3, 035407, 2009.
7. Wu, Z., B. Q. Zeng, and S. Zhong, "A double-layer chiral metamaterial with negative index," *Journal of Electromagnetic Waves and Applications*, Vol. 24, No. 7, 983–992, 2010.
8. Ye, Y. and S. He, "90° polarization rotator using a bilayered chiral metamaterial with giant optical activity," *Appl. Phys. Lett.*, Vol. 96, No. 20, 203501, 2010.
9. Zhao, R., L. Zhang, J. Zhou, T. Koschny, and C. M. Soukoulis, "Conjugated gammadion chiral metamaterial with uniaxial optical activity and negative refractive index," *Phys. Rev. B*, Vol. 83, 035105, 2010.

Achieving All-optical Diode through Non-symmetrical Nonlinear Cavity and the Effect of Photon Tunneling

Yong-Feng Gao[1], **Yun-Tuan Fang**[2], **and Ming Zhou**[3]

[1]School of Mechanical Engineering, Jiangsu University, Zhenjiang, Jiangsu 212013, China
[2]Department of Physics, Zhenjiang Watercraft College, Zhenjiang, Jiangsu 212003, China
[3]Center for Photon Fabrication Science and Technology
Jiangsu University, Zhenjiang, Jiangsu 212013, China

Abstract— Basing on the effect of photon tunneling, we have studied the transmission properties of a non-symmetrical nonliear cavity through transfer matrix method. It is found that a unidirectional diode-like transmission occurs with this structure. For the same incident frequency and incident intensity, while light is at switch-up status for left incidence, the light is at switch-down status for right incidence.

1. INTRODUCTION

Among the driving forces in the study of nonlinear optics in waveguiding structures is the possibility of constructing fast, efficient devices for use in all optical computation or in the routing of signals for telecommunications. Photonic cavities that strongly confine light are finding applications in many areas of physics and engineering, including coherent electron–photon interactions [1], ultra-small filters [2, 3], low-threshold lasers [4], photonic chips [5], nonlinear optics [6] and quantum information processing [7].

As we have known, total internal reflection occurs when light comes from an optically denser material to another material at incidence angles greater than the critical angular determined by the ratio of the refractive indexes of the two materials. Although no energy is transferred into the second medium, there exist electromagnetic fields that decay exponentially away from the interface. The decaying fields are called evanescent waves. When a third medium with sufficiently large refractive index is placed behind a thin slab of the second material, photons can tunnel through the second medium into the third. This phenomenon, called photon tunneling, radiation tunneling, or frustrated total reflection [7–9], has been known for a long time and has found applications in attenuated total reflectance spectroscopy [10] and scanning photon tunneling microscopy [11]. In this paper, we design a photonic cavity based on the effect of photon tunneling. This photonic cavity has a high Q value with an ultra-compact structure. If the above mentioned photonic cavity is composed of nonlinear material with a non-symmetrical structure, an all-optical diode, a device that transmits light of a given frequency and intensity in only one direction is also achieved. The theoretical and experimental feasibility of all-optical diodes in a variety of geometries has been investigated. Dowling et al. [12, 13] proposed a diode in a Bragg structure composed of alternate stacks of linear and Kerr nonlinear media. Mingaleev and Kivshar [14] investigated the feasibility of an all-optical diode in a Kerr nonlinear photonic crystal waveguiding structure using optical bistability. The nonreciprocal transmission behavior based on asymmetric nonlinear absorption was studied numerically and verified experimentally in 2007 [15]. Ref. [16] investigated nonlinear transmission in a layered structure consisting of a slab of positive index material (PIM) with Kerr-type nonlinearity and a sub-wavelength layer of linear NIM material sandwiched between semi-infinite linear dielectrics. Unidirectional diode-like transmission with enhanced operational range is demonstrated. In Ref. [16], the incidence angle is less than the angle of total internal reflection, thus the light transmits through the whole structure in a propagation mode. In addition, the detailed mechanism of all-optical diode behavior is not given and the incident angle is limited in a small range in Ref. [16]. Very recently, Ref. [17] investigated the feasibility of constructing compact and highly efficient all-optical diodes based on light tunneling mechanism in heterostructures. However, we believe that our present diode proposal has some significant advantages over these other proposals, notably because it is based on an ultra-simple structure and ordinary materials that is easily obtained.

2. STRUCTURE MODEL AND TRANSMISSION MECHANISM

The structure model is shown in Fig. 1. A cavity layer B is placed within two air layers A and A' with different thicknesses, which forms an non-symmetrical ABA' structure. The ABA' structure is

placed within two prisms (indicated by C) with $n_c = 3.4$ ($\varepsilon_c = n_c^2$, $\mu_c = 1$) that are used to couple light into and out the ABA'structure. The cavity layer is chosen as nonlinear material with Kerr nonlinearity. Its refraction index is written as $n_B = n_1 + n_2|E|^2$, where n_2 is nonlinear coefficient. All the light is normally incident on the surface of one prism and transmits out from the surface of the other prism. Thus the incidence angular from the prism to the interface of layer A is equal to an interior angle α of the prism as indicated in Fig. 1(a). Because of $n_C > n_A$, there is an angle $\alpha_0 = \arcsin(1/3.4) = 0.2985\,\text{rad}$ corresponding to a critical angle. When $\alpha > \alpha_0$, there is a total internal reflection on the interface of the first layer A and the light field within the first layers A exponentially decreases. In general, evanescent wave cannot propagate. However, if the thickness of layer A is much narrow, the evanescent field will be coupled into layer B. According to geometrical optics, the light coupled into the cavity undergoes a total internal reflection on both interfaces of the cavity. If the wavelength of incident light satisfies some conditions, an optical resonance in a form of standing wave [18] within the layer B will occur, which leads to an effect of photon tunneling.

3. TRANSMISSION SPECTRA AND FIELD DISTRIBUTION FOR LINEAR CASE

We firstly consider low intensity incidence, thus the nonlinear effect of layer B can be neglected ($n_B = 2.4$). The transmission spectra of the structure ABA' are obtained through the traditional transfer matrix method [18] for $\alpha = 0.4\,\text{rad}$, $d_A = 2500\,\text{nm}$, $d_B = 1000\,\text{nm}$ and $d_{A'} = 2000\,\text{nm}$, where d_A, d_B and $d_{A'}$ are the thicknesses of layers A, B and A', respectively. In calculations, we use two opposite incident directions. One is from the left prism C and out from the right prism C, the other is reversed. The results show that the transmission spectra are just the same for both incident directions. There are a series of discrete narrow transmission peaks within wide and deep

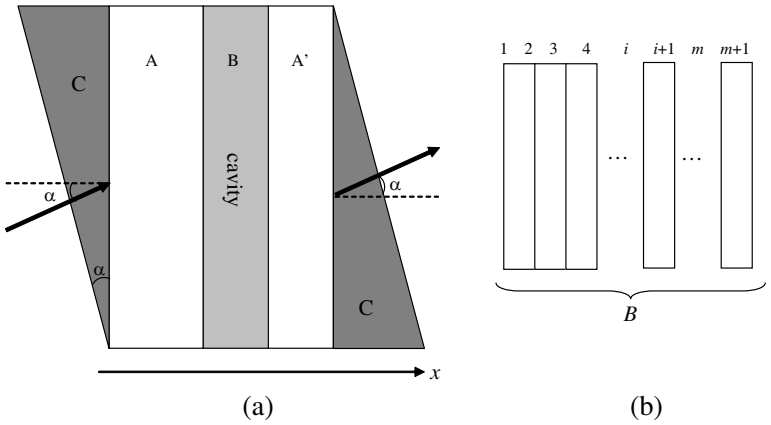

Figure 1: The structure model.

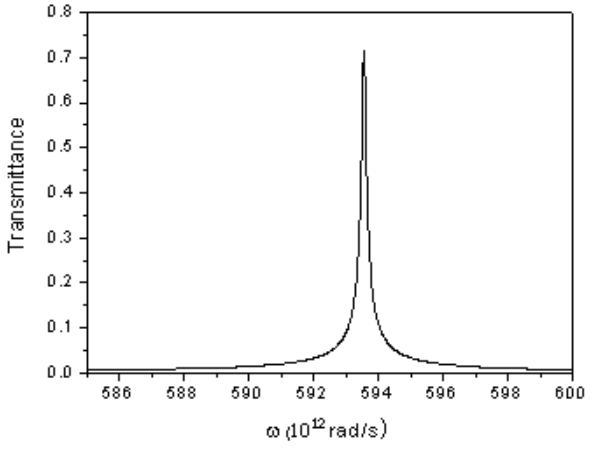

Figure 2: The transmission spectra for both incident directions.

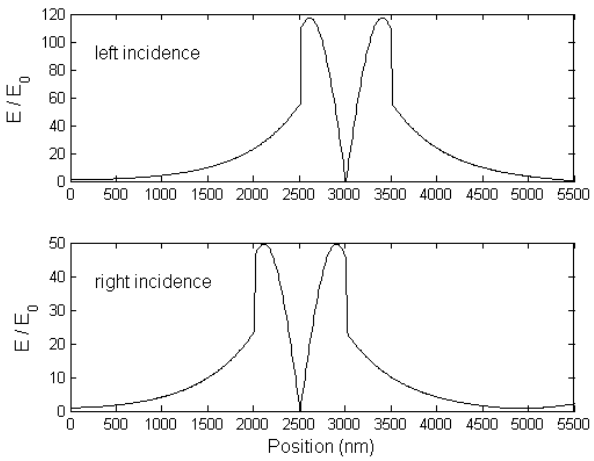

Figure 3: The distribution of relative electric field intensity within the whole structure for both incident directions.

background of band gap. Due to the non-symmetrical structure, the transmittance is a little less than 1. For the limit of figure size, only one peak positioned at $\omega = 593.55 \times 10^{12}$ rad/s is given in Fig. 2. Although the transmission spectra are exactly the same for both incident directions, the distribution of field is different. Fig. 3 shows the distribution of relative electric field intensity within the whole structure for both incident directions, where E_0 is the incident electric field intensity. It is clear that the field intensity within layer B for left incidence is more two times of that for right incidence. It is the difference of field intensity within layer B for two incident directions that make it possible to construct all-optical diode device.

4. NONRECIPROCAL TRANSMISSION BEHAVIORS FOR NONLINEAR CASE

In this section, we consider the transmission properties basing on the nonlinear effect of layer B. When light intensity increases, n_B will accordingly increase due to the nonliearity. Thus the resonant frequency will shift to low frequency and cross the incident frequency. When the resonant frequency and incident frequency overlap, a resonance within layer B and a behavior of optical bistablity will occur. Especially, as mentioned in above section, the filed intensity within layer B is different for two opposite incident directions, thus the nonliear effect for two incident directions is different. Therefore, the bistability with spatially nonreciprocal character is expected.

In order to verify the above analysis, we study the dependence of output on input of the sandwich structure ABA' at an incident angle through the transfer matrix method [15]. In the calculations, medium C is regarded as matrix material and its shape is irrespective to the results. Because the refraction index of layer B is dependent on the localized field intensity due to the nonlinearity, the traditional transfer matrix method must be modified. In the modified method layer B is divided m sublayers. The two interfaces of the ith sublayer are labeled as i and $i+1$, which is shown in Fig. 1(b). If m is large enough, the field intensity within each sublayer can be looked as the same and each sublayer has the same refraction index. In addition, we deduce the input intensity reversibly from the output intensity. For oblique incidence the tangential components of the electric field and magnetic field on the two interfaces of the ith sublayer are related by the eigen matrix T_i, which is written as

$$\begin{bmatrix} E_i \\ H_i \end{bmatrix} = \begin{bmatrix} \cos\beta_i & -\frac{i}{p_i}\sin\beta_i \\ -ip_i\sin\beta_i & \cos\beta_i \end{bmatrix} \begin{bmatrix} E_{i+1} \\ H_{i+1} \end{bmatrix} = T_i \begin{bmatrix} E_{i+1} \\ H_{i+1} \end{bmatrix} \tag{1}$$

where $\beta_i = \omega/cn_ih_i\cos\theta$, $p_i = \sqrt{\varepsilon_i}/\sqrt{\mu_i}\cos\theta$ for TE waves and $p_i = \sqrt{\varepsilon_i}/(\sqrt{\mu_i}\cos\theta)$ for TM waves. $\omega, c, n_i, h_i, \theta$ are incident angular frequency, light velocity in free space, refraction index, thickness of the ith sublayer and the incident angle, respectively. If the electric field on the interface of $i+1$ is known, the field intensity and refraction index for the ith sublayer are obtained through Eq. (1). Thus the electric field on the interface of i is known, and the field intensity and refraction index for the $i-1$th sublayer are obtained. Through m times circulation, the electric field on the two interfaces of the whole layer B are related by the eigen matrix T_B, which is shown as

$$\begin{bmatrix} E_1 \\ H_1 \end{bmatrix} = T_1T_2\ldots T_i\ldots T_m \begin{bmatrix} E_{m+1} \\ H_{m+1} \end{bmatrix} = T_B \begin{bmatrix} E_{m+1} \\ H_{m+1} \end{bmatrix} \tag{2}$$

Therefore, the eigen matrix for whole structure of ABA' is

$$T = T_AT_BT_A = \begin{bmatrix} T_{11} & T_{12} \\ T_{21} & T_{22} \end{bmatrix} \tag{3}$$

If the structure is placed at C background material, the transmittance for TE waves is obtained from the absolute value of t as

$$t = \frac{E_{out}}{E_{in}} = \frac{2}{T_{11} + T_{12}p_0 + T_{21}/p_0 + T_{22}} \quad \left(p_0 = \sqrt{\frac{\varepsilon_0}{\mu_0}}n_c\cos\theta_i\right) \tag{4}$$

Given a value of output intensity, the input intensity can be deduced through Eqs. (1)–(4). Thus the dependence of input on output is obtained.

We choose the incident frequency $\omega = 592.5 \times 10^{12}$ rad/s that is at a little distance away from the peak frequencies in the left direction. The nonlinear coefficient for layer B is chosen $n_2 = 3.5 \times 10^{-10}$. Fig. 4 shows the dependence of output intensity on input intensity and the

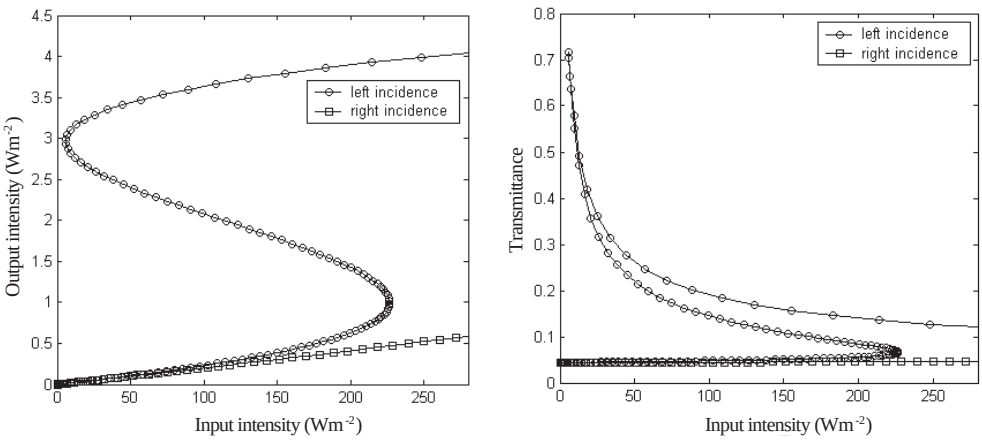

Figure 4: The dependence of output intensity on input intensity and the dependence of transmittance on input intensity.

dependence of transmittance on input intensity. As is seen, the bistability behavior firstly occurs for left incidence. Both the threshold values of $5.84\,\mathrm{Wm}^{-2}$ and $226.5\,\mathrm{Wm}^{-2}$ are very small. As light transforms from switch-down to switch-up, for the same incident intensity of $226.5\,\mathrm{Wm}^{-2}$, the light is still at switch-down for right incidence. For incident intensity of $226.5\,\mathrm{Wm}^{-2}$, the transmittance $T = 0.15$ with left incidence, while $T = 0.05$ with right incidence for the same incident intensity. The transmission contrast is $C = (T_{left} - T_{right})/(T_{left} - T_{right}) = 50\%$. The relatively low value of transmission contrast is the main drawback of our design.

5. CONCLUSION

In this paper, we have studied the linear and nonlinear transmission properties of a non-symmetrical cavity. The cavity is made of an ordinary dielectric material layer within two air layers with different thicknesses. In the linear case, although the transmission spectra are the same for both incident directions, the field distributions are different due to the non-symmetrical property of structure. In the nonlinear case, an unidirectional diode-like transmission occurs. For a special incident frequency, while light is at switch-up status for left incidence, the light is at switch-down status for right incidence. Due to its ultra-simple structure and easily obtained materials, our design may be found applications in future photonic device.

ACKNOWLEDGMENT

The authors acknowledge the financial support from the National Natural Science Foundation of China (grant 50975129), from the A Project Funded by the Priority Academic Program Development of Jiangsu Higher Education Institutions (PAPD), and from the Senior Talent Foundation of Jiangsu University (07JDG074).

REFERENCES

1. Khitrova, G., H. M. Gibbs, F. Jahnke, M. Kira, and S. W. Koch, "Nonlinear optics of normal-modecoupling semiconductor microcavities," *Rev. Mod. Phys.*, Vol. 71, No. 5, 1591–1639, 1999.
2. Noda, S., A. Chutinan, and M. Imada, "Trapping and emission of photons by a single defect in a photonic bandgap structure," *Nature*, Vol. 407, 608–610, 2000.
3. Song, B. S., S. Noda, and T. Asano, "Photonic devices based on in-plane hetero photonic crystals," *Science*, Vol. 300, 1537, 2003.
4. Painter, O., R. K. Lee, A. Scherer, A. Yariv, J. D. O'brien, P. D. Dapkus, and I. Kim, "Two-dimensional photonic band-gap defect mode laser," *Science*, Vol. 284, No. 5421, 1819–1821, 1999.
5. Noda, S., K. Tomoda, N. Yamamoto and A. Chutinan, "Full three-dimensional photonic bandgap crystals at near-infrared wavelengths," *Science*, Vol. 289, No. 5479, 604–606, 2000.
6. Spillane, S. M., T. J. Kippenberg, and K. J. Vahala, "Ultralow-threshold Raman laser using a spherical dielectric microcavity," *Nature*, Vol. 415, 621–623, 2002.

7. Zhang, Z. M. and C. J. Fu, "Unusual photon tunneling in the presence of a layer with a negative refractive index," *Appl. Phys. Lett.*, Vol. 80, No. 6, 1097–1099, 2002.
8. Pendry, J. B., "Radiative exchange of heat between nanostructures," *J. Phys.: Condens. Matter*, Vol. 11, 6621–6633, 1999.
9. Yeh, P., *Optical Waves in Layered Media*, Wiley, New York, 1988.
10. Griffiths, P. R. and J. A. de Haseth, *Fourier Transform Infrared Spectroscopy*, Wiley, New York, 1986.
11. Reddick, R. C., R. J. Warmack, D. W. Chilcott, S. L. Sharp, and T. L. Ferrell, "Photon scanning tunneling microscopy," *Rev. Sci. Instrum.*, Vol. 61, No. 12, 3669–3677, 1999.
12. Scalora, M., J. P. Dowling, C. M. Bowden, and M. J. Bloemer, "The photonic band edge optical diode," *Appl. Phys.*, Vol. 76, No. 4, 2023–2026, 1994.
13. Tocci, M. D., M. J. Bloemer, M. Scalora, J. P. Dowling, and C. M. Bowden, "Thin-film nonlinear optical diode," *Appl. Phys. Lett.*, Vol. 66, No. 18, 2324–2326, 1995.
14. Mingaleev, S. F. and Y. S. Kivshar, "Nonlinear transmission and light localization in photonic-crystal waveguides," *J. Opt. Soc. Am. B*, Vol. 19, No. 9, 2241–2249, 2002.
15. Philip, R., M. Anija, C. S. Yelleswarapu, and D. V. G. L. N. Rao, "Passive all-optical diode using asymmetric nonlinear absorption," *Appl. Phys. Lett.*, Vol. 91, No. 41, 141118/3, 2007.
16. Litchinitser, N. M., I. R. Gabitov, A. I. Maimistov, and V. M. Shalaev, "Effect of an optical negative index thin film on optical bistability," *Opt. Lett.*, Vol. 32, No. 2, 151–153, 2007.
17. Xue, C. H., H. T. Jiang, and H. Chen, "Highly efficient all-optical diode action based on light-tunneling heterostructures," *Opt. Express*, Vol. 18, No. 7, 7479–7487, 2010.
18. Born, M. and E. Wolf, *Principles of Optics*, 7th Edition, Cambridge U. Press, 1999.

Magneto-optical Photonic Band-gap Structures with Optimized Characteristics

Othman Sidek, Muhammad Hassan Bin Afzal, and Shahid Kabir
Collaborative μ-Electronic Design Excellence Centre (CEDEC)
Universiti Sains Malaysia, Malaysia

Abstract— Magneto optical photonic band-gap structures (MO-PBG) consist of cyclic dielectric structures in such a way that they have a strong impact on the transmission of electromagnetic waves. They act similar to the way that the sporadic prospective in semiconductor crystals affects the electron movement by defining permitted and prohibited electronic energy bands. This paper investigates the properties of MO-PBG structures, which hold recurrent interior regions of high and low dielectric constants in such a way that transmission through this specific type of structure definitely depends on the wavelength. This paper also provides a thorough review of different types of MO-PBG structures. These structures are simulated and their characteristics and results compared with related reference values. Finally, a front-end program is introduced, which will help users to understand, measure and evaluate the different characteristics of these structures in order to select the most suitable structure with optimized characteristics for further applications.

1. INTRODUCTION

The basic concept of magneto-optical photonic band-gap structures have been researched, studied and experimented in one form or another for more than a hundred years, but the defined term "MO-PBG Structure" was first introduced and applied by the scientists Eli Yablonovitch and Sajeev John in 1987. Both of them published two ground-breaking papers on this specific topic in the same year [1–3]. Since then, these extraordinary structures have been used in a diverse range of applications, such as reflective coatings, boosting the overall performance of light-emitting diodes (LEDs) and providing exceedingly reflective mirrors in certain laser cavities for enhanced performance. Basically, magneto optical photonic band-gap structures (MO-PBG) consist of cyclic dielectric structures placed in such a way that they have a strong impact on the transmission of electromagnetic waves. They act similar to the way that the sporadic prospective in semiconductor crystals affects electron movement by defining permitted and prohibited electronic energy bands. To transmit signals in material engineering, semiconductor crystals are typically used to control and guide the performance of electrons. In a similar fashion, scientists tried to discover how to appropriately utilize the flow of light or photons through media and obtain the highest output. The results of this quest have introduced the basic concept behind photonic band-gap materials, also known as photonic crystal materials.

Magneto-optical PBG structures play quite a significant role in industrial fields in modern civilization, as they are an integral part of many modern devices, such as optical isolators, magneto optical recording devices, electro-optical tunable filters, and many more. This paper investigates the properties of MO-PBG structures, which maintain recurrent interior regions of high and low dielectric constants in such a way that transmission through this specific type of structure definitely depends on the wavelength. Finally, a front-end program is introduced, which will help users to understand, measure and evaluate the different characteristics of these structures in order to select the most suitable structure with optimized characteristics for further applications.

2. MAGNETO-OPTICAL PHOTONIC BANDGAP STRUCTURES

In general, photonic band-gap structures are special types of frequency bands in the shape of periodic structures, where incident light is energetically reflected. There are various types of periodic structures currently available, such as film stacks, fiber brag grating and photonic crystals [4]. These typical MO-PBG structures can be separated into three classes according to their structural shape: 1-dimensional, 2-dimensional, and 3-dimensional. Figure 1 presents the three different types of MO-PBG structures, where the different colors represent different materials with different dielectric constants.

Magneto-optic fiber brag grating is basically an enhanced and modified version of an MO-PBG structure with higher efficiency. In this particular structure also, one of the principle characteristics,

such as the polarization-mode conversion of light inside the optical fibers, is totally based on magneto-optical effects. Figure 2 represents the mode of propagation of no less than four dissimilar guided light beams inside the magneto-optic fiber brag grating (MFBG) structure [7].

These special types of MO-PBG structures tend to produce a large amount of Faraday Effect and Kerr effect as well, because of their minimal thickness. Due to these effects, the overall efficiency of these structures often tends to decrease considerably [5, 6]. To solve these types of problems, a certain amount of defects is usually applied. Well constructed structures could also help overcome these problems and achieve the ideal 45° Faraday rotation for enhanced performance. In the case of the Faraday Effect, light is transmitted throughout the magnetized material and reflected back from the magneto optical substance. There are various methods of manufacturing MO-PBG structures using different methods to enhance one specific property in order to facilitate a specific application; one example of the latest types of MO-PBG structure is the quasi-periodic photonic crystal (QPC) based on the Thue-Morse sequence [8].

3. SIMULATION OF MO-PBG STRUCTURES

The primary focus of this project is to study and explore the different transmission properties of multi-layer thin films of MO-PBG structures, as well as dielectric materials. The reason behind this is to examine how different layer-stacking procedures could affect the various properties of MO-PBG structures, such as transmittance, rotation degree, thickness etc. The most widely used material is Bismuth-substituted Yttrium-Iron Garnet (Bi-YIG). The dielectric layer is usually formed from Silicon dioxide (SIO_2). Examples of a multi-layered structure are illustrated in Figure 3 [9, 13].

In this study, the letter M is used to represent the magneto-optical layer and the letter G is used to represent the dielectric layer. The structure of a multi-layer film is constructed such that the periodicity of the layers is always symmetric about the centre of the film. Figure 4 illustrates a simple basic structure of MO-PBG with periodically situated dielectric layers in the centre.

According to Sakaguchi and Sugimoto, several MO-BPG structures with different types of stacking systems can be analyzed. There are generally three types of MO-BPG structures: single-layer, double-layer and triple-layer. Although more layers can be stacked into MO-PBG structures, periodicity can still be maintained at the centre of the films [10].

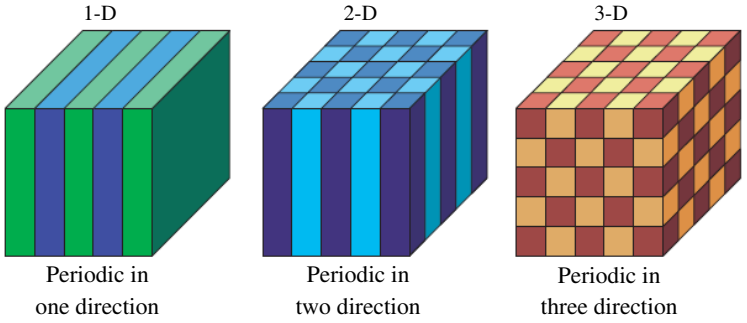

Figure 1: Typical examples of different 1-D, 2-D and 3-D mo-pbg structures.

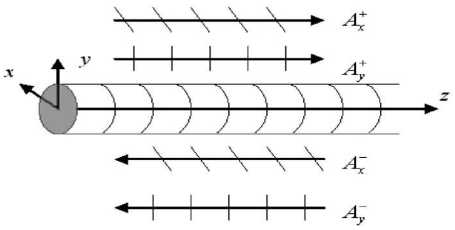

Figure 2: Mode of propagation of linearly polarized light beams in MFBG structures.

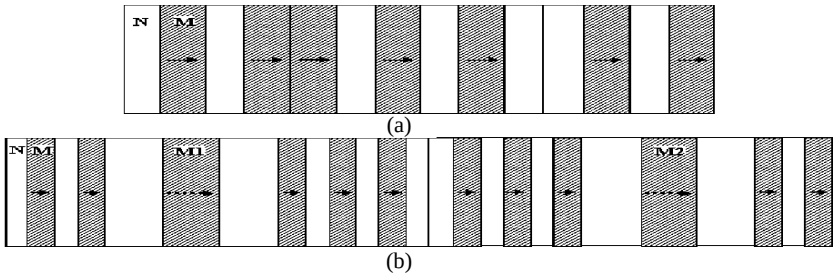

Figure 3: Two examples of a multi-layered structure, where both (a) and (b) have different sequences.

G	M	M	G	G	M	G	M

Figure 4: A simple basic structure representing a double-layer GMMG structure.

Table 1: Arrangement of different mo-pbg structures.

Structure Type	**Structure Properties**	
	Name of the Structures	**Arrangement of Structures**
Single-Stack Layers	GM	[GM]n [MG]n
	MG	[MG]n [GM]n
	G2	[GM]n [2G] [MG]n
	M2	[MG]n [2M] [GM]n
Double-Stack Layers	GMMG	[GM]n [MG]n . [MG]n [GM]n
	MGGM	[MG]n [GM]n . [GM]n [MG]n
	G2M2	[GM]n [2G] [MG]n . [MG]n [2M] [GM]n
	M2G2	[MG]n [2M] [GM]n . [GM]n [2G] [MG]n
Triple-Stack layers	GMMG3	[GM]n [MG]n . [MG]n [GM]n . [GM]n [MG]n
	MGGM3	[MG]n [GM]n . [GM]n [MG]n . [MG]n [GM]n
	G2M23	[GM]n [2G] [MG]n . [MG]n [2M] [GM]n . [GM]n [2G] [MG]n
	M2G23	[MG]n [2M] [GM]n . [GM]n [2G] [MG]n . [MG]n [2M] [GM]n

4. DIFFERENT TYPES OF MO-PBG STRUCTURES

Transmission properties for multiple stacks of basic structures do not affect the rotation properties; nevertheless, all available MO-PBG structures are explained in Table 1, just to clarify the possibility of improving the transmittance without any deterioration in rotation. These MO-PBG structures are divided into three groups based on their stacking layers [10]. Here, n is the number of discrete repetitions of the stacking layers. Theoretically, the multiple stack layer structure shows considerable enhancement in both rotation and transmittance. Nevertheless, a higher number of stacks also generally imply increased structural thickness. Consequently, attempts have been made to generate miniature structures that are suitable for many of the modern optical applications. Most applications necessitate that the thickness of the structures usually be kept at less than 20 µm [10].

5. PROBLEMS IN DESIGNING MO-PBG STRUCTURES

In general, there are two types of problems that arise while manufacturing MO-PBG structures. Firstly, the overall transmission efficiency decreases significantly for lower degrees of Faraday rotation. Ideally, the degree of Faraday rotation should be 45°; three to four defects can be introduced into these structures to improve the overall transmission quality. The second problem occurs when there is a significant increase in the thickness of these structures that goes over 40 nm; this is when the defects are introduced to improve the transmission efficiency. To overcome these problems, it is necessary to determine some middle ground where both the structural thickness and the degree of Faraday rotation are made to compromise in order to provide an enhanced performance. A basic front-end program is designed to facilitate the observation, study and evaluation of the various characteristics of MO-PBG structures to find the optimal type of structure to employ in practical applications such as in various fiber optic sensor based SHM applications and many others in related areas [11–13].

6. FRONT-END PROGRAM TO EVALUATE AND OPTIMIZE MO-PBG STRUCTURES

One of the objectives of this study is to design a front-end program or user interface and to simulate the codes for the different types of MO-PBG structures, so that when a user inputs certain parameters, it can generate outputs that inform the user about the different layers of MO-PBG structures and their detailed properties, such as changes in the degree of rotation, and variations in transmittance, as well as in thickness. The primary target of the front-end program is to generate all the available MO-PBG structures with different layers and to illustrate their properties. The front-end program is designed to help a general user acquire an in-depth understanding about

various types of MO-PBG structures, their distinctive features, and characteristics. Using this information, a user can easily evaluate and decide which type of structure would be optimal for application in different circumstances. This front-end program was designed through the use of the following programs:

- Microsoft Net Work. Net 2.0
- Programming language C# (C Sharp)
- Third party Control DevExpress

A general user, however, is only required to have Visual Studio 2008 — express edition, and DevExpress (Developers Express) software to run this front-end program and to access its different features. Figure 5 presents a screenshot of a typical application of this front-end program or user interface for the graphical representation of rotation angle vs. thickness for a single-layer structure.

7. RESULTS & DISCUSSION

In order to develop the front-end program and to simulate the codes, experimental work was carried out throughout the study, and the program was modified accordingly so that it could generate the corresponding values for the different types of MO-PBG structures and their various layer stacks. The outputs of the program were compared with the results found in the literature of previous studies, such as the research work by Sakaguchi and Sugimoto [10].

The resulting properties and characteristics of the different structures produced through the experimental work in this study correspond very well with the results found in the literature [10]. It can be seen from Figure 5 that the front-end program developed is very user-friendly, and provides a comprehensive evaluation of the different MO-PBG structures based on the user's inputs. Some of the significant characteristics of MO-PBG structures that have been observed throughout the experimental period are the following:

- As the repetition number (n) increases, the degree of rotation also increases. Regarding the output characteristics of different structures and their layer formation, some of them share the same values, such as GM and G2, MG and M2, GMMG and MGGM, as well as G2M2 and M2G2. But three stack layers possess different characteristics compared to the other structures, and thus contain characteristics that are unique from the others.
- The degree of rotation largely depends on the number of layers of the structure. When the structure's thickness is small, it produces a large degree of rotation, but the transmittance decreases significantly.
- It has been found that multiple stacks of the basic structures pick up transmittance without any decline in the degree of rotation. Therefore, a rotation of close to 45°, which is essential for applications such as isolators, is achievable at a transmittance of around 0.8 (the optical loss is less than 1 dB). In this specific case, it is possible to obtain a multilayer Faraday rotator applicable to isolators by optimizing the periodic structures.

Figure 5: Screenshot of the front-end program application producing a graph of rotation angle vs. thickness for a single-layer GM structure.

8. CONCLUSION

MO-PBG structures are widely employed in numerous industrial applications with a great deal of success. However, these structures need to be properly designed and their properties need to be optimized based on the characteristics needed for a particular application. This study provides an in-depth view of the concept behind MO-PBG structures and the diverse characteristics of these structures, particularly since they can consist of various types of stacking layers. A front-end program is then developed through experimentation based on the various types of MO-PBG structures described in previous research. The program provides the user with information about all the available MO-PBG structures with different layers, along with their distinctive features, properties and characteristics. Using this information, a user can easily evaluate and decide which type of structure would be optimal for application in different circumstances. Furthermore, a user can also determine what effects changing certain parameters can have on the structure in order to optimize a structure for a particular application. The resulting properties and characteristics of the different structures produced through the experimental work in this study correspond very well with the results found in the literature.

REFERENCES

1. Bykov, V. P., "Spontaneous emission in a periodic structure," *Soviet Physics JETP*, Vol. 35, 269–273, 1972.
2. Yablonovich, E., "Inhibited spontaneous emission in solid-state physics and electronics," *Physical Review Letters*, Vol. 58, 2059–2062, 1987.
3. John, S., "Strong localization of photons in certain disordered dielectric superlattices," *Physical Review Letters*, Vol. 58, 2486–2489, 1987.
4. Levy, M., H. C. Yang, M. J. Steel, and J. Fujita, "Flat-top response in one-dimensional magnetic photonic bandgap structures with faraday rotation enhancement," *Journal of Lightwave Technology*, Vol. 19, No. 12, 2001.
5. John, D. J., G. J. Steven, N. W. Joshua, and D. M. Robert, *Photonic Crystals: Molding the Flow of Light*, Princeton University Press, New Jersey, 2008.
6. Vukovic, A., P. Sewell, and T. M. Benson, "Analysis of 3-D diffraction effects and oblique incidence in magneto-optic photonic bandgap structures," *Journal of Lightwave Technology*, Vol. 24, No. 7, 2006.
7. Wu, B. J., X. Liu, and K. Qiu, "Characteristics of magneto-optic fiber Bragg gratings for use in optical signal processing," *Optical Fiber Technology*, Vol. 15, 165–171, 2009.
8. Grigoriev, V. V. and F. Biancalana, "Bistability and stationary gap solitons in quasiperiodic photonic crystals based on thue-morse sequence," *Photonics and Nanostructures — Fundamentals and Applications*, Vol. 8, 285–290, 2010.
9. Belotelov, V. I. and A. K. Zvezdin, "Magneto-optical properties of photonic crystals," *Journal of the Optical Society of America B*, Vol. 22, No. 1, 2005.
10. Sakaguchi, S. and N. Sugimoto, "Multi-layer films composed of periodic magneto-optical and dielectric layers for use as Faraday rotators," *Optical Communication*, Vol. 162, No. 1–3, 64–70, 1999.
11. Sidek, O., M. H. B. Afzal, and S. Kabir, "Determining the effect of faraday-rotation and optimum rotation angle in different types of magneto-optical PBG structures," *PIERS Proceedings*, 799–802, Marrakesh, Morocco, March 20–23, 2011.
12. Yablonovitch, E., "One-way road for light," *Nature*, Vol. 461, 744–745, 2009.
13. Afzal, M. H. B., O. Sidek, and S. Kabir, "Fiber optic sensor-based concrete structural health monitoring," *Proceedings of Saudi International Electronics, Communications and Photonics Conference Riyadh*, Saudi Arabia, April 23–26, 2011.

Velocity Curl and Theorems in Electromagnetic Fields

Zi-Hua Weng
School of Physics and Mechanical & Electrical Engineering
Xiamen University, Xiamen 361005, China

Abstract— The paper discusses the influences of the velocity curl and field strength on some conservation laws and the theorems in the electromagnetic and gravitational fields. With the algebra of quaternions, the theorem of linear momentum, the conservation of linear momentum, the theorem of angular momentum, and the conservation of angular momentum can be deduced from the quaternion definitions of the physical quantities. The study claims that the gravitational strength and electromagnetic strength will impact the conservation laws and theorems directly. Meanwhile the velocity curl has an effect on these conservation laws and theorems also.

1. INTRODUCTION

The concept of the linear momentum was originated by some great scientists. The linear momentum of the particle and the conservation of linear momentum were first introduced by R. Descartes in 1644. Further the concept of the linear momentum extended from the particle to the gravitational field and electromagnetic field, and covered the quantum mechanics [1]. The angular momentum is an important concept in the physics with numerous applications. The concept of the angular momentum includes that in the gravitational field and electromagnetic field. In the classical theories the linear momentum is impacted by the velocity, the mass, and the force etc. While the angular momentum is influenced by the velocity, the angular velocity, the mass, the torque, the force, and the field strength etc. in the gravitational field and the electromagnetic field.

The algebra of quaternions [2] can be used to describe the conservation laws and the theorems in the electromagnetic field and the gravitational field. In terms of the features of octonions [3], we can obtain the theorem of linear momentum, the conservation of linear momentum, the theorem of angular momentum, and the conservation of angular momentum in the gravitational field and electromagnetic field [4]. It is found that the velocity, the velocity curl, the field potential, and the field strength have the influences on the conservation laws and the theorems in the gravitational and electromagnetic fields.

2. GRAVITATIONAL FIELD

The theorems in the gravitational field [5] can be described by the algebra of quaternions, and impacted by the gravitational potential, the velocity, and the force etc.

In the quaternion space, the coordinate is the r_i, with the basis vector $\mathbb{E}_g = (\mathbf{i}_0, \mathbf{i}_1, \mathbf{i}_2, \mathbf{i}_3)$. The radius vector is $\mathbb{R}_g = \Sigma(r_i \mathbf{i}_i)$, the velocity is $\mathbb{V}_g = v_0 \Diamond \circ \mathbb{R}_g = v_0(1+\delta) + \Sigma(v_j \mathbf{i}_j)$, and the velocity curl is $\mathbb{U}_g = \Diamond \circ \mathbb{V}_g = \Sigma(u_i \mathbf{i}_i)$. Herein the $\circ$ is the quaternion multiplication. $\mathbf{i}_0 = 1$; $r_0 = v_0 t$; v_0 is the speed of light, and t is the time. $\Diamond = \Sigma(\mathbf{i}_i \partial_i)$; $\partial_i = \partial / \partial r_i$; $i = 0, 1, 2, 3$. $\delta = -\nabla \cdot \Sigma r_j \mathbf{i}_j$.

The gravitational potential is $\mathbb{A}_g = \Sigma(a_i \mathbf{i}_i)$, and can be defined from the quaternion quantity $\mathbb{X}_g$, that is, $\mathbb{A}_g = \Diamond \circ \mathbb{X}_g$. And the gravitational strength is $\mathbb{B}_g = \Diamond \circ \mathbb{A}_g = \Sigma(b_i \mathbf{i}_i)$, which includes two parts, $\mathbf{g}/v_0 = \partial_0 \mathbf{a} + \nabla a_0$, and $\mathbf{b} = \nabla \times \mathbf{a}$. And that the gauge equation is selected as $b_0 = 0$. Herein $\mathbf{a} = \Sigma(a_j \mathbf{i}_j)$; $\nabla = \Sigma(\mathbf{i}_j \partial_j)$; $j = 1, 2, 3$.

The radius vector $\mathbb{R}_g$ and the quaternion $\mathbb{X}_g = \Sigma(x_i \mathbf{i}_i)$ can be combined together to become the compounding radius vector $\bar{\mathbb{R}}_g = \mathbb{R}_g + k_{rx} \mathbb{X}_g$, and the compounding quantity $\bar{\mathbb{X}}_g = \mathbb{X}_g + K_{rx} \mathbb{R}_g$. The related space is called as the quaternion compounding space, which is one kind of function space. In this compounding space, the coordinate is $\bar{r}_i = r_i + k_{rx} x_i$ for the basis vector $\mathbf{i}_i$, and the radius vector is $\bar{\mathbb{R}}_g = \Sigma(\mathbf{i}_i \bar{r}_i)$. We gain the compounding velocity $\bar{\mathbb{V}}_g = v_0 \Diamond \circ \bar{\mathbb{R}}_g = \mathbb{V}_g + v_0 k_{rx} \mathbb{A}_g$, the compounding velocity curl $\bar{\mathbb{U}}_g = \Diamond \circ \bar{\mathbb{V}}_g = \mathbb{U}_g + v_0 k_{rx} \mathbb{B}_g$, the compounding gravitational potential $\bar{\mathbb{A}}_g = \Diamond \circ \bar{\mathbb{X}}_g = \mathbb{A}_g + K_{rx} \mathbb{V}_g / v_0$, and the compounding gravitational strength $\bar{\mathbb{B}}_g = \Diamond \circ \bar{\mathbb{A}}_g = \mathbb{B}_g + K_{rx} \mathbb{U}_g / v_0$. Herein $k_{rx} = 1/v_0$ and $K_{rx} = 1/k_{rx}$ are the coefficients.

The compounding source $\bar{\mathbb{S}}$ of the gravitational field in the quaternion compounding space covers the linear momentum density $\bar{\mathbb{S}}_g = m(\bar{\mathbb{V}}_g + v_0 \delta)$, and can be defined as,

$$\mu \bar{\mathbb{S}} = -(\bar{\mathbb{B}}_g / v_0 + \Diamond)^* \circ \bar{\mathbb{B}}_g = \mu_g \bar{\mathbb{S}}_g - \bar{\mathbb{B}}_g^* \circ \bar{\mathbb{B}}_g / v_0, \tag{1}$$

where m is the mass density; $*$ denotes the quaternion conjugate; μ is the constant, and μ_g is the gravitational constant; $\bar{\mathbb{B}}_g^* \circ \bar{\mathbb{B}}_g/(2\mu_g)$ is the field energy density.

From the $\bar{\mathbb{R}}_g$ and $\bar{\mathbb{P}}_g = \mu\bar{\mathbb{S}}/\mu_g$, the compounding angular momentum density is defined as $\bar{\mathbb{L}}_g = \bar{\mathbb{R}}_g \circ \bar{\mathbb{P}}_g$. The compounding torque-energy density $\bar{\mathbb{W}}_g$ can be defined from the above compounding angular momentum density $\bar{\mathbb{L}}_g = \Sigma(\bar{l}_i\mathbf{i}_i)$,

$$\bar{\mathbb{W}}_g = v_0(\bar{\mathbb{B}}_g/v_0 + \Diamond)^* \circ \bar{\mathbb{L}}_g, \tag{2}$$

where the compounding torque-energy includes the potential energy, the kinetic energy, the torque, and the work etc. in the gravitational field. The $\bar{\mathbb{S}}$ is the extension of the $\bar{\mathbb{S}}_g$.

From the above compounding torque-energy density $\bar{\mathbb{W}}_g$, the compounding force-power density is defined as, $\bar{\mathbb{N}}_g = v_0(\bar{\mathbb{B}}_g/v_0 + \Diamond)^* \circ \bar{\mathbb{W}}_g$. While the $\bar{\mathbb{N}}_g$ is the function of the force density and the power density in the gravitational field. And the compounding force density is $-\Sigma(\mathbf{i}_j\bar{n}_j)/(2v_0)$, with the $\Sigma(\mathbf{i}_j\bar{n}_j)$ being the vectorial part of the $\bar{\mathbb{N}}_g$. As an especial and simple case, one part $\bar{\mathbb{F}}_g$ of the compounding force-power density $\bar{\mathbb{N}}_g$ can be defined from the $\bar{\mathbb{P}}_g$,

$$\bar{\mathbb{F}}_g = v_0(\bar{\mathbb{B}}_g/v_0 + \Diamond)^* \circ \bar{\mathbb{P}}_g, \tag{3}$$

where the $\bar{\mathbb{F}}_g$ includes the inertial force density and gravitational force density etc.

2.1. Theorem of Linear Momentum

In the quaternion compounding space, the compounding linear momentum density is $\bar{\mathbb{P}}_g = \Sigma(\bar{p}_i\mathbf{i}_i)$. By Eq. (3), the part force density $\bar{\mathbb{F}}_g$ is,

$$\bar{\mathbb{F}}_g = \bar{f}_0 + \Sigma(\bar{f}_j\mathbf{i}_j), \tag{4}$$

where $\bar{p}_0 = \widehat{m}\bar{v}_0$, $\bar{p}_j = m\bar{v}_j$. m and $\widehat{m}$ are the inertial and gravitational mass densities respectively.

The vectorial part $\bar{\mathbf{f}}$ of part force density $\bar{\mathbb{F}}_g$ can be decomposed from the above,

$$\bar{\mathbf{f}} = \Sigma(\bar{f}_j\mathbf{i}_j) = v_0\partial_0\bar{\mathbf{p}} + \bar{p}_0\bar{\mathbf{h}}^* + \bar{\mathbf{h}}^* \times \bar{\mathbf{p}} + v_0\nabla^*\bar{p}_0 + v_0\nabla^* \times \bar{\mathbf{p}}, \tag{5}$$

where $\bar{\mathbf{h}} = \Sigma(\bar{b}_j\mathbf{i}_j)$, $\bar{\mathbf{p}} = \Sigma(\bar{p}_j\mathbf{i}_j)$.

The above can be rewritten as follows,

$$\bar{\mathbf{f}} = \partial\bar{\mathbf{p}}/\partial t + \bar{\mathbf{F}}, \tag{6}$$

where $\bar{\mathbf{F}} = \bar{p}_0\bar{\mathbf{h}}^* + \bar{\mathbf{h}}^* \times \bar{\mathbf{p}} + v_0\nabla^*\bar{p}_0 + v_0\nabla^* \times \bar{\mathbf{p}}$. In some cases, there may exist the $\bar{\mathbf{f}} = 0$.

In case the time t is one single independent variable, the $\partial\bar{\mathbf{p}}/\partial t$ will become the $d\bar{\mathbf{p}}/dt$. Therefore we obtain the theorem of linear momentum,

$$(\bar{\mathbf{f}} - \bar{\mathbf{F}})dt = d(m\bar{\mathbf{v}}),$$

where the $\bar{\mathbf{v}} = \Sigma(\bar{v}_j\mathbf{i}_j)$ is the vectorial part of the compounding velocity $\mathbb{V}_g$.

Further there is the conservation of linear momentum from the above if $(\bar{\mathbf{f}} - \bar{\mathbf{F}}) = 0$,

$$d(m\bar{\mathbf{v}}) = 0. \tag{7}$$

The above means the force density $(\bar{\mathbf{f}} - \bar{\mathbf{F}})$ covers the gravitational force density etc., but does not include the inertial force density according to Eq. (6). And the theorem of linear momentum is only one of simple cases of Eq. (5), and is impacted by the velocity $\mathbf{v}$ and vectorial potential $\mathbf{a}$, although the influence of $\mathbf{a}$ may be quite tiny. So is the case for the conservation of linear momentum.

2.2. Theorem of Angular Momentum

The vectorial part $\bar{\mathbf{w}}$ of torque-energy density $\bar{\mathbb{W}}_g$ can be decomposed from Eq. (2),

$$\bar{\mathbf{w}} = \Sigma(\bar{w}_j\mathbf{i}_j) = v_0\partial_0\bar{\mathbf{l}} + (\bar{\mathbf{h}} + v_0\nabla)\bar{l}_0 + (\bar{\mathbf{h}} + v_0\nabla) \times \bar{\mathbf{l}}. \tag{8}$$

The above can be rewritten as follows,

$$\bar{\mathbf{w}} = \partial\bar{\mathbf{l}}/\partial t + \bar{\mathbf{W}}, \tag{9}$$

Table 1: The octonion multiplication table.

	1	$\mathbf{i}_1$	$\mathbf{i}_2$	$\mathbf{i}_3$	$\mathbf{I}_0$	$\mathbf{I}_1$	$\mathbf{I}_2$	$\mathbf{I}_3$
1	1	$\mathbf{i}_1$	$\mathbf{i}_2$	$\mathbf{i}_3$	$\mathbf{I}_0$	$\mathbf{I}_1$	$\mathbf{I}_2$	$\mathbf{I}_3$
$\mathbf{i}_1$	$\mathbf{i}_1$	-1	$\mathbf{i}_3$	$-\mathbf{i}_2$	$\mathbf{I}_1$	$-\mathbf{I}_0$	$-\mathbf{I}_3$	$\mathbf{I}_2$
$\mathbf{i}_2$	$\mathbf{i}_2$	$-\mathbf{i}_3$	-1	$\mathbf{i}_1$	$\mathbf{I}_2$	$\mathbf{I}_3$	$-\mathbf{I}_0$	$-\mathbf{I}_1$
$\mathbf{i}_3$	$\mathbf{i}_3$	$\mathbf{i}_2$	$-\mathbf{i}_1$	-1	$\mathbf{I}_3$	$-\mathbf{I}_2$	$\mathbf{I}_1$	$-\mathbf{I}_0$
$\mathbf{I}_0$	$\mathbf{I}_0$	$-\mathbf{I}_1$	$-\mathbf{I}_2$	$-\mathbf{I}_3$	-1	$\mathbf{i}_1$	$\mathbf{i}_2$	$\mathbf{i}_3$
$\mathbf{I}_1$	$\mathbf{I}_1$	$\mathbf{I}_0$	$-\mathbf{I}_3$	$\mathbf{I}_2$	$-\mathbf{i}_1$	-1	$-\mathbf{i}_3$	$\mathbf{i}_2$
$\mathbf{I}_2$	$\mathbf{I}_2$	$\mathbf{I}_3$	$\mathbf{I}_0$	$-\mathbf{I}_1$	$-\mathbf{i}_2$	$\mathbf{i}_3$	-1	$-\mathbf{i}_1$
$\mathbf{I}_3$	$\mathbf{I}_3$	$-\mathbf{I}_2$	$\mathbf{I}_1$	$\mathbf{I}_0$	$-\mathbf{i}_3$	$-\mathbf{i}_2$	$\mathbf{i}_1$	-1

where $\bar{\mathbf{l}} = \Sigma(\bar{l}_j \mathbf{i}_j)$; $\bar{\mathbf{W}} = (\bar{\mathbf{h}} + v_0\nabla)\bar{l}_0 + (\bar{\mathbf{h}} + v_0\nabla) \times \bar{\mathbf{l}}$; Sometimes there may exist $\bar{\mathbf{w}} = 0$.

When the time t is only one independent variable, the $\partial\bar{\mathbf{l}}/\partial t$ will be reduced to the $d\bar{\mathbf{l}}/dt$. And we obtain the theorem of angular momentum,

$$(\bar{\mathbf{w}} - \bar{\mathbf{W}})dt = d\bar{\mathbf{l}},$$

and if the $(\bar{\mathbf{w}} - \bar{\mathbf{W}}) = 0$, the conservation of angular momentum can be reduced to

$$d\bar{\mathbf{l}} = 0. \tag{10}$$

The above means the torque density $(\bar{\mathbf{w}} - \bar{\mathbf{W}})$ covers the term $\bar{\mathbf{h}} \times \bar{\mathbf{l}}$ etc., but does not include the term $\partial\bar{\mathbf{l}}/\partial t$ from Eq. (8). As one simple case of Eq. (7), the theorem of angular momentum is impacted by the velocity $\mathbb{V}_g$, the gravitational potential $\mathbb{A}_g$, the quaternion $\mathbb{X}_g$, the radius vector $\mathbb{R}_g$, the gravitational strength $\mathbf{h}$, and the vectorial part of the velocity curl $\mathbb{U}_g$ etc. And so is the situation for the conservation of angular momentum in the gravitational field.

3. GRAVITATIONAL AND ELECTROMAGNETIC FIELDS

The gravitational field and electromagnetic field both can be illustrated by the quaternion, and their quaternion spaces will be combined together to become the octonion space [6]. In other words, the characteristics of gravitational field and electromagnetic field can be described with the octonion space simultaneously. In the quaternion space for the electromagnetic field, the basis vector is $\mathbb{E}_e = (\mathbf{I}_0, \mathbf{I}_1, \mathbf{I}_2, \mathbf{I}_3)$, the radius vector is $\mathbb{R}_e = (R_0, R_1, R_2, R_3)$, and the velocity is $\mathbb{V}_e = (V_0, V_1, V_2, V_3)$. The $\mathbb{E}_e$ is independent of the $\mathbb{E}_g$, with $\mathbb{E}_e = \mathbb{E}_g \circ \mathbf{I}_0$. Both of them can be combined together to become the basis vector $\mathbb{E}$ of the octonion space, that is, $\mathbb{E} = (\mathbf{i}_0, \mathbf{i}_1, \mathbf{i}_2, \mathbf{i}_3, \mathbf{I}_0, \mathbf{I}_1, \mathbf{I}_2, \mathbf{I}_3)$.

In the octonion space, the octonion radius vector is $\mathbb{R} = \Sigma(\mathbf{i}_i r_i + k_{eg}\mathbf{I}_i R_i)$, the octonion velocity is $\mathbb{V} = v_0 \Diamond \circ \mathbb{R} = \Sigma(v_0^\delta + \mathbf{i}_j v_j + k_{eg}\mathbf{I}_i V_i)$, and the octonion velocity curl is $\mathbb{U} = \Diamond \circ \mathbb{V} = \Sigma(\mathbf{i}_i u_i + k_{eg}\mathbf{I}_i U_i)$. The gravitational potential $\mathbb{A}_g$ and the electromagnetic potential $\mathbb{A}_e = \Sigma(\mathbf{I}_i A_i)$ are combined together to become the octonion potential, $\mathbb{A} = \Diamond \circ \mathbb{X} = \mathbb{A}_g + k_{eg}\mathbb{A}_e$, which can be defined from the octonion quantity $\mathbb{X} = \mathbb{X}_g + k_{eg}\mathbb{X}_e$. The octonion strength, $\mathbb{B} = \Diamond \circ \mathbb{A} = \mathbb{B}_g + k_{eg}\mathbb{B}_e$, consists of the gravitational strength $\mathbb{B}_g$ and the electromagnetic strength $\mathbb{B}_e$. The electromagnetic strength $\mathbb{B}_e$ involves two components, $\mathbf{E}/v_0 = \partial_0\mathbf{A} + \nabla \circ \mathbf{A}_0$, and $\mathbf{B} = \nabla \times \mathbf{A}$. The gauge equations are $b_0 = 0$ and $B_0 = 0$. Herein the symbol $\circ$ denotes the octonion multiplication. k_{eg} and k_{rx} are the coefficients for the dimensional homogeneity. $\mathbb{X}_e = \Sigma(X_i\mathbf{I}_i)$. $v_0^\delta = v_0(1+\delta)$.

The radius vector $\mathbb{R}$ and octonion $\mathbb{X}$ in the octonion space can be combined together to become the compounding radius vector $\bar{\mathbb{R}} = \mathbb{R} + k_{rx}\mathbb{X}$, and the compounding quantity $\bar{\mathbb{X}} = \mathbb{X} + K_{rx}\mathbb{R}$. The related space is called as the octonion compounding space, which is one kind of function space also. Similarly we obtain the compounding field potential $\bar{\mathbb{A}} = \Diamond \circ \bar{\mathbb{X}} = \mathbb{A} + K_{rx}\mathbb{V}/v_0$, the compounding field strength $\bar{\mathbb{B}} = \Diamond \circ \bar{\mathbb{A}} = \mathbb{B} + K_{rx}\mathbb{U}/v_0$, the compounding velocity $\bar{\mathbb{V}} = \mathbb{V} + v_0 k_{rx}\mathbb{A}$, and the compounding velocity curl $\bar{\mathbb{U}} = \mathbb{U} + v_0 k_{rx}\mathbb{B}$.

In the coordinate system of the octonion compounding space, the coordinate is $(\bar{r}_i + k_{eg}\bar{R}_i\mathbf{I}_0)$ for the basis vector $\mathbf{i}_i$, and the radius vector is $\bar{\mathbb{R}} = \Sigma\left\{\mathbf{i}_i \circ (\bar{r}_i + k_{eg}\bar{R}_i\mathbf{I}_0)\right\}$. In this compounding space, the compounding source $\bar{\mathbb{S}}$ involves the linear momentum density $\bar{\mathbb{S}}_g$, and the electric current density $\bar{\mathbb{S}}_e = q\bar{\mathbb{V}}_e$. While the latter is the field source of the electromagnetic field. The compounding

source $\bar{\mathbb{S}}$ satisfies,

$$\mu\bar{\mathbb{S}} = -(\bar{\mathbb{B}}/v_0 + \Diamond)^* \circ \bar{\mathbb{B}} = \mu_g\bar{\mathbb{S}}_g + k_{eg}\mu_e\bar{\mathbb{S}}_e - \bar{\mathbb{B}}^* \circ \bar{\mathbb{B}}/v_0, \tag{11}$$

where $k_{eg}^2 = \mu_g/\mu_e$; q is the electric charge density; μ_e is the electromagnetic constant; $*$ denotes the conjugate of octonion. $\bar{\mathbb{B}}^* \circ \bar{\mathbb{B}}/\mu_g = \bar{\mathbb{B}}_g^* \circ \bar{\mathbb{B}}_g/\mu_g + \bar{\mathbb{B}}_e^* \circ \bar{\mathbb{B}}_e/\mu_e$ is the field energy density.

The compounding angular momentum density is $\bar{\mathbb{L}} = \bar{\mathbb{R}} \circ \bar{\mathbb{P}}$ in the compounding space. And the compounding torque-energy density $\bar{\mathbb{W}}$ is defined from the compounding strength $\bar{\mathbb{B}}$ and the compounding angular momentum density $\bar{\mathbb{L}}$,

$$\bar{\mathbb{W}} = v_0(\bar{\mathbb{B}}/v_0 + \Diamond) \circ \bar{\mathbb{L}}, \tag{12}$$

where the compounding torque-energy includes the potential energy, the kinetic energy, the torque, and the work etc. in the gravitational and the electromagnetic fields. $\bar{\mathbb{P}} = \mu\bar{\mathbb{S}}/\mu_g$.

We can define the compounding force-power density $\bar{\mathbb{N}} = v_0(\bar{\mathbb{B}}/v_0 + \Diamond)^* \circ \bar{\mathbb{W}}$ from the compounding torque-energy density $\bar{\mathbb{W}}$. The force-power density includes the force density and power density in the gravitational field and the electromagnetic field. The part $\bar{\mathbb{F}}$ of the compounding force-power density $\bar{\mathbb{N}}$ is defined from the compounding linear momentum density $\bar{\mathbb{P}} = \mu\bar{\mathbb{S}}/\mu_g$,

$$\bar{\mathbb{F}} = v_0(\bar{\mathbb{B}}/v_0 + \Diamond)^* \circ \bar{\mathbb{P}}, \tag{13}$$

where the part force density includes that of the gravitational force, Lorentz force [7], inertial force, and the interacting force between electromagnetic strength with magnetic moment etc.

3.1. Theorem of Linear Momentum

The compounding linear momentum density is $\bar{\mathbb{P}} = \bar{p}_0 + \Sigma(\bar{p}_j\mathbf{i}_j) + \Sigma(\bar{P}_i\mathbf{I}_i)$ in the compounding octonion space. And the m and $\widehat{m}$ are the inertial and gravitational mass densities respectively; $\bar{p}_0 = \widehat{m}\bar{v}_0$; $\bar{p}_j = m\bar{v}_j$; $\bar{P}_i = M\bar{V}_i$; $M = k_{eg}\mu_e q/\mu_g$.

By Eq. (13), the part compounding force density $\bar{\mathbb{F}}$ is,

$$\bar{\mathbb{F}} = \bar{f}_0 + \Sigma(\bar{f}_j\mathbf{i}_j) + \Sigma(\bar{F}_i\mathbf{I}_i). \tag{14}$$

The vectorial part $\bar{\mathbf{f}}$ of part force density $\bar{\mathbb{F}}$ can be decomposed from the above,

$$\bar{\mathbf{f}} = \Sigma(\bar{f}_j\mathbf{i}_j) + \Sigma(\bar{F}_i\mathbf{I}_i), \tag{15}$$

and then the above can be rewritten as follows,

$$\bar{\mathbf{f}} = \partial\bar{\mathbf{z}}/\partial t + \bar{\mathbf{F}}, \tag{16}$$

where $\bar{\mathbf{F}} = \left\{\Sigma(\bar{f}_j\mathbf{i}_j) - \partial\bar{\mathbf{z}}/\partial t\right\} + \Sigma(\bar{F}_i\mathbf{I}_i)$, which is the extension of Eq. (6). $\bar{\mathbf{z}} = \Sigma(m\bar{v}_j)\mathbf{i}_j$.

When the time t is only one independent variable, the $\partial\bar{\mathbf{z}}/\partial t$ will become $d\bar{\mathbf{z}}/dt$. Therefore we obtain the theorem of linear momentum in the octonion compounding space,

$$(\bar{\mathbf{f}} - \bar{\mathbf{F}})dt = d\bar{\mathbf{z}},$$

further if the $(\bar{\mathbf{f}} - \bar{\mathbf{F}}) = 0$, the conservation of linear momentum is derived from the above,

$$d\bar{\mathbf{z}} = 0. \tag{17}$$

The above means the $(\bar{\mathbf{f}} - \bar{\mathbf{F}})$ covers the gravity density and Lorentz force density etc., but does not include the inertial force density from Eq. (16). The theorem of linear momentum is only one simple case of Eq. (15), and is influenced by the velocity $\mathbf{v}$ and vectorial potential $\mathbf{a}$ etc. So is the case for the conservation of linear momentum in the gravitational and electromagnetic fields.

3.2. Theorem of Angular Momentum

In the octonion space, from the angular momentum density, $\bar{\mathbb{L}} = \Sigma(\bar{l}_i\mathbf{i}_i) + \Sigma(\bar{L}_i\mathbf{I}_i)$, we have the torque-energy density in Eq. (12),

$$\bar{\mathbb{W}} = \Sigma(\bar{w}_i\mathbf{i}_i) + \Sigma(\bar{W}_i\mathbf{I}_i). \tag{18}$$

The vectorial part $\bar{\mathbf{w}}$ of torque-energy density $\bar{\mathbb{W}}$ can be decomposed from the above,

$$\bar{\mathbf{w}} = \Sigma(\bar{w}_j\mathbf{i}_j) + \Sigma(\bar{W}_i\mathbf{I}_i), \tag{19}$$

and that the above can be rewritten as follows,

$$\bar{\mathbf{w}} = \partial\bar{\mathbf{j}}/\partial t + \bar{\mathbf{W}}, \tag{20}$$

where $\bar{\mathbf{W}} = \left\{\Sigma(\bar{w}_j\mathbf{i}_j) - \partial\bar{\mathbf{j}}/\partial t\right\} + \Sigma(\bar{W}_i\mathbf{I}_i)$. $\bar{\mathbf{h}} = \Sigma(\bar{b}_j\mathbf{i}_j)$; $\bar{\mathbf{j}} = \Sigma(\bar{l}_j\mathbf{i}_j)$.

When the time t is one single independent variable, the $\partial\bar{\mathbf{j}}/\partial t$ can be simplified to the $d\bar{\mathbf{j}}/dt$. And we obtain the theorem of angular momentum in the octonion compounding space,

$$(\bar{\mathbf{w}} - \bar{\mathbf{W}})dt = d\bar{\mathbf{j}},$$

and that the conservation of angular momentum can be gained if $(\bar{\mathbf{w}} - \bar{\mathbf{W}}) = 0$,

$$d\bar{\mathbf{j}} = 0. \tag{21}$$

The above means that the torque density $(\bar{\mathbf{w}} - \bar{\mathbf{W}})$ covers the terms $\bar{\mathbf{h}} \times \bar{\mathbf{j}}$ etc., but does not include the term $\partial\bar{\mathbf{j}}/\partial t$ from Eq. (20). And the theorem of angular momentum is one simple case of Eq. (19), and is influenced by the radius vector $\mathbb{R}$, the velocity $\mathbb{V}$, the velocity curl $\mathbb{U}$, the octonion quantity $\mathbb{X}$, the field potential $\mathbb{A}$, and the field strength $\mathbb{B}$ etc. So is the situation for the conservation of angular momentum in the gravitational and electromagnetic fields.

4. CONCLUSIONS

In the quaternion spaces, we obtain the theorem of linear momentum and the conservation of linear momentum from the definition of force. Similarly there are the theorem of angular momentum and the conservation of angular momentum too. And it is found that the gravitational strength has an influence on the conservation laws and the theorems regarding the linear momentum.

In the octonion compounding spaces, we obtain the related conservation laws and the theorems similarly, and find the velocity curl, the field potential, and the field strength have the influence on the conservation laws and the theorems relevant to the linear momentum and angular momentum in the electromagnetic field and gravitational field.

It should be noted that the study for the conservation laws and theorems of physical quantities examined only some simple cases in the electromagnetic field and gravitational field. Despite its preliminary features, this study can clearly indicate the above conservation laws and the theorems are only some simple inferences due to the low velocity curl and weak strength in the electromagnetic field and the gravitational field. For the future studies, the research will concentrate on only some predictions about the conservation laws and the theorems with the high velocity curl and the strong strength in the electromagnetic and gravitational fields.

ACKNOWLEDGMENT

This project was supported partially by the National Natural Science Foundation of China under grant number 60677039.

REFERENCES

1. Dirac, P. A. M., *The Principles of Quantum Mechanics*, 4th Edition, Oxford University Press, Oxford, 1958.
2. Hamilton, W. R., *Elements of Quaternions*, Longmans, Green & Co., London, 1866.
3. Cayley, A., *The Collected Mathematical Papers of Arthur Cayley*, The Cambridge University Press, Cambridge, 1889.
4. Maxwell, J. C., *A Treatise on Electricity and Magnetism*, Dover Publications Inc., New York, 1954.
5. Newton, I., *The Mathematical Principles of Natural Philosophy*, trans. A. Motte, Dawsons of Pall Mall, London, 1968.
6. Weng, Z.-H., "Velocity curl and spin in electromagnetic fields," *PIERS Proceedings*, 352–356, Marrakesh, Morocco, March 20–23, 2011.
7. Lorentz, H. A., *The Theory of Electrons*, Dover Publications Inc., New York, 1952.

Surface Soil Moisture Retrieval from the Temporal Evolution of Surface Temperature for Bare Surface

Wei Zhao[1, 2, 3] **and Zhao-Liang Li**[1, 2]

[1]State Key Laboratory of Resources and Environment Information System
Institute of Geographical Sciences and Natural Resources Research, CAS, Beijing 100101, China
[2]LSIIT, UdS, CNRS, Bld Sebastien Brant, BP10413, 67412 Illkirch, France
[3]Graduate University of Chinese Academy of Sciences, Beijing 100049, China

Abstract— Land surface soil moisture (SSM) has an important role for groundwater recharge, agriculture, soil chemistry, and climate forecasting. Many recent scientific research efforts have aimed toward a predictive-understanding of SSM over space and time based on the instantaneous observations of land surface temperature (LST). However, the information provided by the temporal variation of LST has been less considered or discussed. The present study aims to find the relationship between the temporal variation of LST and SSM and then to propose a method for retrieving SSM from geostationary satellite data. Due to the absence of the accurate SSM measurements at large scale, NOAH land surface model (LSM) is used to provide the temporal evolution of the LST under different soil types and SSM conditions for cloud free days and bare soil surfaces. Two empirical models (linear and second-degree polynomial forms) are proposed to estimate SSM using the two LST temporal variables TN (the LST rising rate normalized by the difference in the net surface shortwave radiation during the mid-morning) and t_d (the time at which the daily maximum temperature occurs). The root mean square errors (RMSE) of the SSM retrieved using the linear and second-degree models with simulated data are found to be $0.03\,\mathrm{m}^3/\mathrm{m}^3$ and $0.024\,\mathrm{m}^3/\mathrm{m}^3$ respectively. The results show that the coefficients except for the constant term in both models are independent of the atmospheric conditions and soil types, but the constant term varies with atmospheric forcing data. This study indicates that the SSM of bare soil surfaces can be estimated with high accuracy if the constant term is obtained or estimated accurately.

1. INTRODUCTION

Land surface soil moisture (SSM) has critical importance on the physical processes governing energy and water exchanges at the land-atmosphere boundary. Soil moisture controls the extent to which plants can exploit sunlight in the photosynthesis and the effectiveness with which agriculture, forestry and freshwater resources can be developed [1]. Therefore, it plays an important role for groundwater recharge, agriculture, soil chemistry, and climate forecasting.

Because of the spatial and temporal heterogeneity of SSM due to the variation of the soil properties, topography and vegetation cover, SSM field measurements can not provide accurate regional SSM, and remote sensing, particularly thermal infrared remote sensing, becomes an effective way to estimate SSM in regional scale. For bare surfaces, land surface temperature (LST) observed by the thermal infrared sensors is greatly influenced by the SSM through changing the thermal properties of the surface soil. The surface soil thermal inertia (TI), one of the soil thermal properties, has been found to be highly related with SSM although the relationship varies with soil types [2, 3]. On the basis of the surface albedo and the difference between daytime and nighttime LST, apparent thermal inertia (ATI) considered as an approximation of TI was defined and used to retrieve SSM [4]. However, the relationship between TI or ATI and SSM is not unique and varies with soil type and atmospheric condition, and most of the studies are based on instantaneous observation realized by the polar satellites (NOAA, MODIS). A few studies are concerned with SSM estimation from the temporal variation of LST provided by the geostationary satellites (GOES, METEOSAT). Wetzel et al. [5, 6] conducted a preliminary study on the estimation of SSM from the temporal variations of LST and demonstrated that the mid-morning differential of the LST with respect to the absorbed solar radiation is optimally sensitive to the SSM. On the basis of the aforementioned studies, Zhao and Li [7] performed a systematic sensitivity study about the influence of environmental factors including SSM, albedo, soil physical and atmospheric parameters on the LST and its temporal variation. The results indicated that the two LST temporal variables TN (the LST rising rate normalized by the difference in the net surface shortwave radiation during 1.5 h and 4.5 h after sunrise in the mid-morning) and t_d (the time at which the daily maximum

temperature occurs) are highly related to SSM. A simple linear model was proposed to estimate SSM using TN and t_d. It has been proved that this linear model gives a larger relative error of SSM under extremely dry condition, and all the coefficients of the proposed model are highly related to atmospheric conditions.

In the present study, following the work of Zhao and Li [7], an improved method will be proposed to retrieve SSM using TN and t_d with the coefficients independent of the atmospheric conditions. Because there is no accurate SSM measurements at large scale, NOAH land surface model (LSM) is used to simulate the temporal evolution of the LST under different soil types and SSM conditions for cloud free days and bare soil surfaces. A description of NOAH LSM and atmospheric forcing data are described in Section 2. The methodology is presented in Section 3. Section 4 shows the results. Conclusions are provided in Section 5.

2. NOAH LSM AND ATMOSPERIC FORCING DATA

2.1. NOAH LSM

Due to the lack of SSM in the pixel scale of geostationary satellites, NOAH LSM was selected in this study to simulate the diurnal evolution of the LST under different soil types and soil moisture contents for bare surfaces, and to provide the LST temporal information and SSM for model development.

NOAH LSM is a stand-alone, 1-D column model which can be executed in either coupled or uncoupled mode, and it can be used to execute single-site or regional land-surface simulations. The key input to the model includes land-use (vegetation) type, soil texture and slope. The secondary input parameters can be specified as function of the above three primary parameters. Atmospheric forcing data are needed to drive the model.

As the LST responds to the SSM at depths of 4–5 cm, the soil layer is modified and separated into six layers with a depth of 5, 10, 15, 30, 40 and 100 cm. The soil moisture of the first layer represents the SSM. In addition, surface albedo parameterization in the biosphere-atmosphere transfer scheme is adopted in the model to simulate the surface albedo as function of the SSM and soil color.

2.2. Forcing Data

AmeriFlux (http://public.ornl.gov/ameriflux/index.html) level 2 half-hourly data at Santa Rita Mesquite Savanna site in 2007 were used as the atmospheric forcing data to drive NOAH LSM. Because of the semiarid climate at this site, there are enough clear days to run NOAH LSM, and eight cloud free days in 2007 (Day of year: DOY 74, 105, 107, 150, 171, 246, 269 and 284) were selected to represent different meteorological conditions

3. METHODOLOGY

As the simple linear model proposed by Zhao and Li [7] has been proved to be inaccurate for extremely dry condition, in addition, the coefficients in the model are atmosphere dependent, to increase the SSM retrieved accuracy and make the model more general (ideally independent of atmospheric condition), an improved linear model and a second-degree polynomial model are proposed to estimate the SSM using the two variables TN and t_d both derived from the daily evolution of LST [7]. The forms of these two models are:

$$\text{Model 1:} \quad SSM = a_0 + a_1\left(\frac{TN}{0.05}\right) + a_2\left(t_d - 12\right) \tag{1}$$

$$\text{Model 2:} \quad SSM = b_0 + b_1\left(\frac{TN}{0.05}\right) + b_2\left(\frac{TN}{0.05}\right)^2 + b_3\left(\frac{TN}{0.05}\right)\cdot(t_d - 12) + b_4(t_d - 12) + b_5\left(t_d - 12\right)^2 \tag{2}$$

in which TN in K*m2/W, td in h and SSM in m^3/m^3.

4. RESULTS

To derive the TN and t_d for SSM estimation, NOAH LSM simulation should be conducted firstly. As indicated in Figure 1, different simulations were conducted for 12 different soil types in NOAH LSM with various SSM (ranging from its minimum value to its maximum value) on the eight cloud free days under bare soil surface condition. Diurnal evolution of LST, net surface shortwave radiation (NSSR) and SSM were generated by NOAH LSM. TN and t_d were calculated from the simulated diurnal evolution of LST and NSSR [7]. Regression was then performed with Model 1

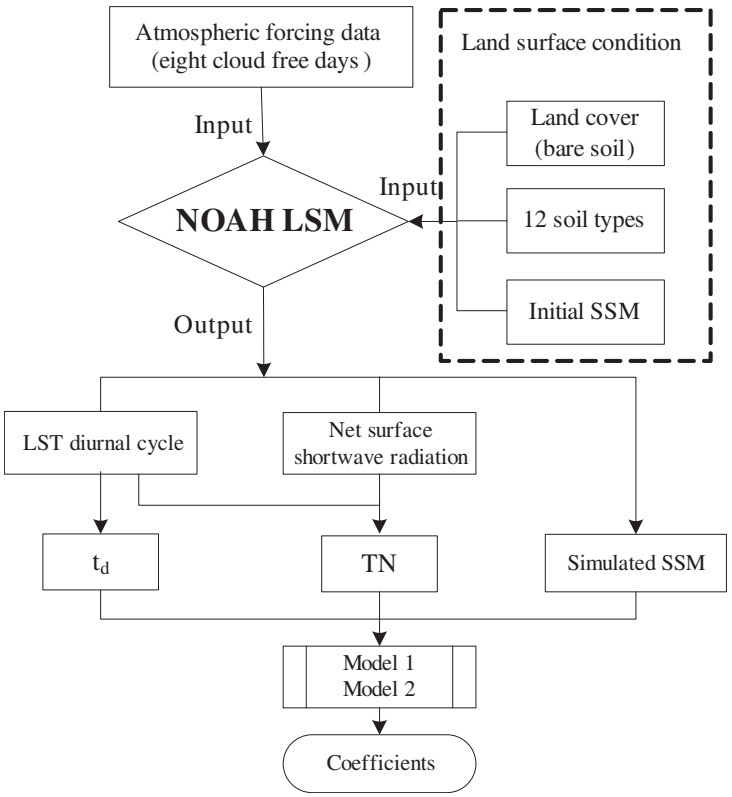

Figure 1: Scheme for retrieving the coefficients of Models 1 and 2 (Equations (1) and (2)) with NOAH LSM simulation for bare soils.

Table 1: Coefficients and RMSE of SSM estimation using Model 1 and Model 2.

DOY	**Model 1 (Equation (1))**				**Model 2 (Equation (2))**						
	a_0	a_1	a_2	RMSE	b_0	b_1	b_2	b_3	b_4	b_5	RMSE
74	1.663	−0.954	−0.357	0.029	−0.411	−1.874	0.633	−0.089	2.459	−0.78	0.012
105	1.394	−0.877	−0.32	0.026	−0.084	−1.125	0.325	−0.171	1.869	−0.713	0.013
107	2.052	−1.061	−0.557	0.017	1.476	−2.676	0.497	0.503	0.57	−0.372	0.011
150	2.043	−0.979	−0.536	0.030	1.886	−4.182	1.307	0.472	1.201	−0.591	0.014
171	2.066	−0.997	−0.57	0.024	0.318	−2.566	0.902	0.048	2.021	−0.713	0.013
246	2.296	−1.256	−0.655	0.018	−3.956	1.02	−0.123	−1.093	5.165	−1.351	0.011
269	1.644	−0.836	−0.42	0.028	−3.359	1.407	−0.246	−1.101	4.575	−1.253	0.017
284	1.301	−0.826	−0.265	0.034	−1.621	0.058	−0.086	−0.485	3.201	−1.031	0.012

and Model 2 using TN and t_d against the actual SSM for each day, and the coefficients of both models were retrieved finally.

As shown in Table 1, both models can retrieve SSM with RMSEs within $0.035\,\mathrm{m}^3/\mathrm{m}^3$ for a given day and the soil texture shows little impact on the estimating results. For Model 1, the total root mean squared error (RMSE) of the SSM for the eight days is $0.026\,\mathrm{m}^3/\mathrm{m}^3$, but the points are a little dispersive for extreme dry condition. While compared with Model 1, the result of Model 2 is much better with RMSE = $0.013\,\mathrm{m}^3/\mathrm{m}^3$and the estimated SSM is very close to actual SSM, and all the points lay on the $1:1$ line as displayed in Figure 2. However, it is clear that the coefficients a_0–a_2 in Model 1 and b_0–b_5 in Model 2 vary everyday, indicating that they are highly depend on the atmospheric forcing data (see Table 1).

To find the relationship of the coefficients in both models, the correlation analysis was conducted, and the results are listed in Table 2. As shown in this table, the absolute values of the correlation coefficients were all above 0.75. The coefficients a_0–a_2 in Model 1 and b_0–b_5 in Model 2 were highly correlated with each other, indicating that the contribution of TN and t_d to the SSM variation are strongly related.

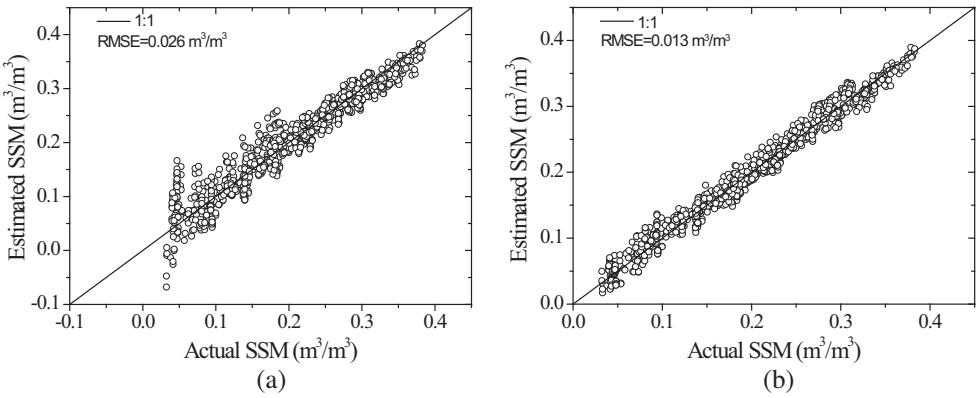

Figure 2: Scatter plot of actual SSM and SSM estimated using (a) Model 1 and (b) Model 2 for the eight cloud free days.

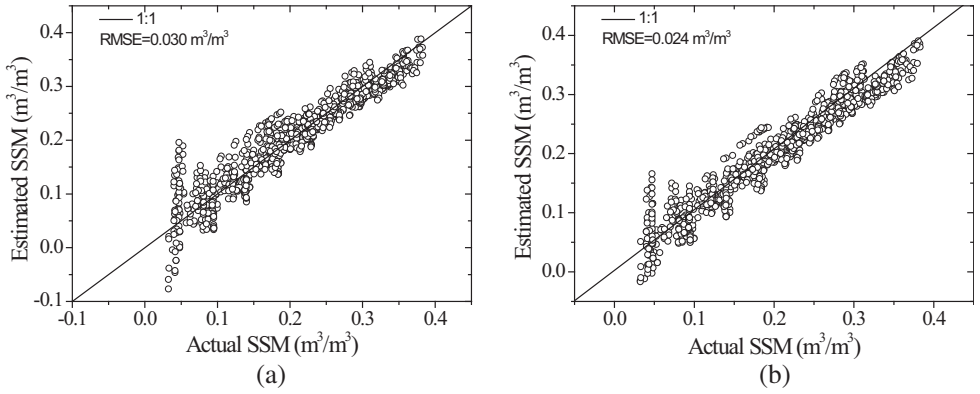

Figure 3: Scatter plot of the actual SSM and SSM estimated using (a) Model 1 and (b) Model 2 with coefficients in Table 3.

Table 2: Correlation coefficient in Model 1 (left) and Model 2 (right).

	a_0	a_1	a_2
a_0	1		
a_1	−0.871	1	
a_2	−0.987	0.851	1

	b_0	b_1	b_2	b_3	b_4	b_5
b_0	1					
b_1	−0.959	1				
b_2	0.862	−0.962	1			
b_3	0.991	−0.961	0.852	1		
b_4	−0.984	−0.900	−0.765	−0.978	1	
b_5	0.971	−0.895	0.758	0.975	−0.993	1

To transfer the variation of a_1–a_2 and b_1–b_5 on atmospheric condition to the constant term a_0 and b_0 respectively, and to make a_1–a_2 and b_1–b_5 independent of the atmospheric conditions, a linear mixed model (random intercept method) was applied to the whole dataset [8]. In this model, the variables of the same day were grouped into the same group, there are therefore eight groups for the whole data. Comparison of the SSM estimated by the random intercept method with the actual SSM is depicted in Figure 3. The RMSE of SSM is $0.03\,m^3/m^3$ and $0.024\,m^3/m^3$ respectively. Although the RMSEs are a bit larger than those obtained for each single day and the points are more dispersive in extremely dry conditions, the number of coefficients related to atmospheric condition in Models 1 and 2 is reduced to only one (a_0 and b_0 respectively) and other. coefficients a_1–a_2, b_1–b_5 are constant and independent of atmospheric conditions (Table 3). Consequently, SSM can be estimated accurately provided that the constant values of α_0, β_0 are known or estimated for each day according to the atmospheric conditions.

In order to understand the interrelationship between the constant terms and the atmospheric parameters, correlation analysis was also conducted for a_0 and b_0 against the atmospheric parameters including maximum and minimum air temperature, daily average air temperature, daily average

Table 3: Values of the coefficients a_1–a_2, b_1–b_5 in Models 1 and 2.

Model 1	a_1	a_2			
	−0.915	−0.416			
Model 2	b_1	b_2	b_3	b_4	b_5
	−0.972	0.227	−0.195	1.027	−0.376

wind speed, average air temperature in the morning and average wind speed in the morning. However, there was no obvious simple connection for a_0 and b_0 with these atmospheric parameters. Further research is still needed to find the inherent connection between them.

5. CONCLUSION

Two empirical models (linear and second-degree polynomial forms) were proposed to estimate SSM for bare soil surfaces with the two LST temporal variables TN (the LST rising rate normalized by the difference in the net surface shortwave radiation during the mid-morning) and t_d (the time at which the daily maximum temperature occurs). Data simulated by NOAH LSM for different soil types and atmospheric conditions were used to establish these two models, and the results indicated that both of them are able to capture the variation of SSM with high accuracy for a given atmospheric condition. However, the coefficients are dependent of the atmospheric conditions. In order to reduce the number of the coefficients related to the atmospheric conditions, a simple linear mixed model (random intercept method) was applied and the results indicated that the coefficients a_1–a_2, b_1–b_5 in Models 1 and 2 are independent of the atmospheric conditions and only the constants α_0, β_0 vary with the atmospheric forcing data. The RMSEs of the retrieved SSM are within $0.03\,m^3/m^3$ and the results showed that SSM can be retrieved well provided that the value of the constant term α_0, β_0 is available or estimated. However, further study is still needed to understand the inherent relationship between the constant terms and atmospheric forcing data.

ACKNOWLEDGMENT

This work has been partially supported by the European Commission (Call FP7-ENV-2007-1 Grant nr. 212921) as part of the CEOP-AEGIS project (http://www.ceop-aegis.org/) coordinated by the University of Strasbourg, by the National Natural Science Foundation of China under Grant 40971199, by China International Science and Technology Cooperation project (0819).

REFERENCES

1. Henderson-sellers, A., "Soil moisture: A critical focus for global change studies," *Global and Planetary Change*, Vol. 13, 3–9, 1996.
2. Idso, S. B., R. D. Jackson, R. J. Reginato, B. A. Kimball, and F. S. Nakayama, "The dependence of bare soil albedo on soil water content," *Journal of Applied Meteorology*, Vol. 14, 109–113, 1975.
3. Schmugge, T. J., B. Blanchard, A. Anderson, and J. Wang, "Soil moisture sensing with aircraft observations of the diurnal range of surface temperature," *Journal of the American Water Resources Association*, Vol. 14, No. 1, 169–178, 1978.
4. Verstraeten, W. W., F. Veroustraete, C. J. Van Der Sande, I. Grootaers, and J. Feyen, "Soil moisture retrieval using thermal inertia, determined with visible and thermal spaceborne data, validated for European forests," *Remote Sensing of Environment*, Vol. 101, 299–314, 2006.
5. Wetzel, P. J., D. Atlas, and R. H. Woodward, "Determining soil moisture from geosynchronous satellite infrared data: A feasibility study," *Journal of Climate and Applied Meteorology*, Vol. 23, 375–391, 1984.
6. Wetzel, P. J. and R. H. Woodward, "Soil moisture estimation using GOES-VISSR infrared data: A case study with a simple statistical method," *Journal of Climate and Applied Meteorology*, Vol. 26, 107–117, 1987.
7. Zhao, W. and Z.-L. Li, "Sensitivity study of soil moisture on the temporal evolution of surface temperature over bare surfaces," *International Journal of Remote Sensing*, 2011, in press.
8. Bryk, A. S. and S. W. Raudenbush, *Hierarchical Linear Models: Applications and Data Analysis Methods*, Sage, Newbury Park, CA, 1992.

Sideband Level Suppression Improvement via Splitting Pulses in Time Modulated Arrays under Static Fundamental Radiation

E. Aksoy and E. Afacan
Department of Electrical & Electronics Engineering
Gazi University, Maltepe, Ankara, Turkey

Abstract— In this work, an idea which can be used for minimisation of sideband level (SBL) of a time-modulated array (TMA) is presented. The idea is based on splitting pulses while the total switch-on durations remain constant which provides an additional degree of freedom in design and it is shown that lower SBL can be achieved under static fundamental radiation. Also it is shown with an example that the general opinion that maximum level of sideband radiation occurs in first sideband is not always true.

1. INTRODUCTION

After introduction of time modulation concept [1] and first application of time-modulated antenna array to synthesize ultra-low sidelobes [1] Yang et al. brought back scientific communities' attention to this topic via publishing a study [3] about supressing the sideband level with differential evolution (DE) algorithm in 2002. From this time on, several researches have been realized about to suppress or control the sideband radiation which is caused by periodic switching and to shape the fundamental pattern to satisfy desired specifications [4–10].

First pulse shifting research appeared in [6] to steer the main beam of first harmonic, then it has been followed by [9] and [10]. Since the starting instants of a pulse appears in array factor as a phase term it can be used for SBL suppression as well as steering the harmonic frequencies as reported in [9]. It is also possible to steer the harmonic beams and to control the SBL at the same time by dividing a known distribution by a factor $K > 1$ and progressively distributing this new coefficients like progressive phase shifting (which can be considered as shifting the pulses) [10].

One common point of all these harmonic radiation control methods except [4] and [9] is that there exists a single pulse in one period. First pulse splitting approach appears in [4] with binary optimization of closing predefined parts of totally on-state array (or opening some parts of a fully off-state array). In a recent publication [9], this condition appears in a different way of shifting the pulses. When a pulse shifted in a rotational manner some pulses appears as seperated in one period and both of these approaches are aimed to suppress the sideband level of harmonic frequencies. Also it must be noted that a powerful formulation which gives the total power associated to the harmonic radiations of a TMLA and a formal formulation of TMLAs may be found in [11].

In this paper, it is aimed to illustrate that the seperated pulses may produce lower SBL's than shifted ones and also it is shown with an example that the common opinion that maximum sideband level occurs in first harmonic frequency does not always hold true.

2. BRIEF THEORY

Consider an N element linear array is placed on positive z-axis and each element of this array is swithed by a switching device and suppose that there are Q_n pulses with different durations and beginning times in each modulating period of corresponding array element, so that the most general form of modulating function caused by switching may be defined as:

$$U_n(t) = \begin{cases} 1, & \tau_n^{2q} < t \leq \tau_n^{2q+1} \\ 0, & \text{otherwise} \end{cases} \tag{1}$$

where $\forall q \in \mathbb{N}$, $q \leq Q_n - 1$ and $0 \leq \tau_n^0 < \tau_n^1 < \tau_n^2 \cdots < \tau_n^{2q+1} \leq T_p$. Here T_p is the modulating period and τ represents the rise and fall instants of a pulse where τ_n^{2q} represents the starting instant of a pulse. Under these conditions the general array factor term of a TMLA becomes [7]:

$$F(\theta) = \sum_{m=-\infty}^{\infty} \sum_{\langle n \rangle} I_n C_n^m e^{j\beta_n} e^{jkd_n \cos(\theta)}, \tag{2}$$

where C_n^m represents the complex Fourier coefficients and by letting $\gamma_n^q = \left(\tau_n^{2q+1} - \tau_n^{2q}\right)/T_p$ which represents the duration of a pulse and $w_p T_p = 2\pi$, these coefficients may be written as:

$$C_n^m = \begin{cases} \sum_{q=0}^{Q_n-1} \gamma_n^q, & m = 0 \\ \dfrac{1}{\pi m} \sum_{q=0}^{Q_n-1} \sin\left(m\pi\gamma_n^q\right) e^{-jmw_p\tau_n^{2q}} e^{-jm\pi\gamma_n^q}, & |m| > 0. \end{cases} \tag{3}$$

From Eq. (3) it is clear that C_n^0 is the summation of each pulse in one modulation period of the corresponding array element which means that the known fundamental radiations may be synthesized by keeping this summation equal to the corresponding static distribution coefficients such as Taylor or Chebyshev etc.

It is also clear that and also reported in [6, 9, 10] that starting instants appear as phase terms in array factor and provide an additional control on electronic scanning or SBL suppression.

3. NUMERICAL EXAMPLES AND DISCUSSION

In this section a set of numerical examples are given in two subsections to show the harmonic minimisation capability of the proposed idea and capability of independent minimisation of each harmonic frequency. To make fair comparisons, a 16 element −30 dB Chebyshev array is considered as in [5] and [9] and for simplicity each seperable pulse is divided into two pulses and switch-on instants of first pulses are selected as the beginning of each modulation period. Looking from this perspective there will be two independent variables; first pulse duration and the distance between first pulse and the second pulse in one period. From this perspective, by setting the optimization vector as $\vec{v} = \left\{\vec{\tau_n^0}, \vec{\delta_n}\right\}$ where τ_n^0 and δ_n represent the first pulse duration and distance between first pulse and second one, respectively, following cost function is minimized:

$$\Psi\left(\vec{v}\right) = \max\left\langle H\left\{\Lambda_m\left(\vec{v}\right) - \Lambda_{ref}\left(\vec{v}\right)\right\}\Lambda_m\left(\vec{v}\right)\right\rangle, \quad m = 1, \ldots, K \tag{4}$$

where $\Lambda_m\left(\vec{v}\right) = \max\left\{SBL_m\right\}$, Λ_{ref} a predefined sideband level and $H\left\{\cdot\right\}$ is Heaviside unit step function. In Eq. (4) m represents the harmonic number and for full control of harmonic frequencies K must be taken as $K \to \infty$ however $K = 5$ seems to be enough for −22 dB threshold. Since we are dealing with a known distribution it is not necessary to control the fundamental radiation.

3.1. Suppression Capability

In [5] and [9] it is shown that under static fundamental radiation a SBL minimisation method or control can be made by varying the starting instants of pulses and a −19.5 dB SBL is achieved in [9] via a method called pulse shifting which is approximately 7 dB better than achieved in [5]. If the same conditions (i.e., −30 dB Chebyshev array) are considered and switching sequence is

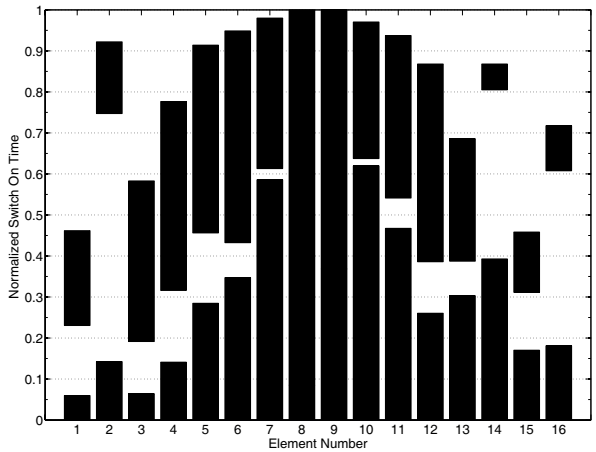

Figure 1: On-off time sequence of 16 element −30 dB Chebyshev pattern optimized to reduce SBLs.

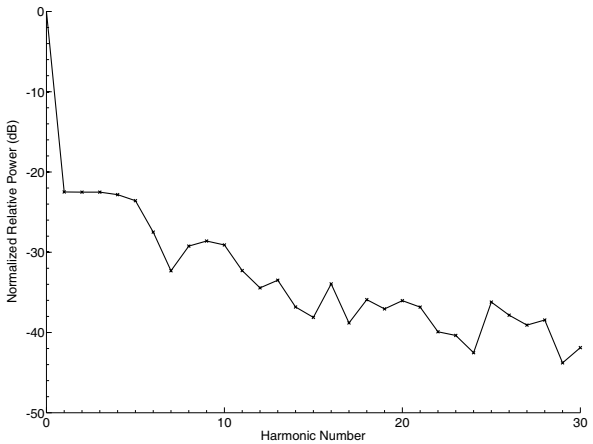

Figure 2: Sidebands caused by switching according to Fig. 1.

optimized via pulse splitting using *DE/best/1/bin* as described and used in [12] with algorithm parameters of population size $P = 50$, crossover probability $Cr = 0.6$ and mutation factor $F = 0.6$, the resultant switching scheme is given in Fig. 1. Moreover, maximum SBL of first 30 harmonics and the radiation pattern related to Fig. 1 are given in Fig. 2 and Fig. 3, respectively.

As it can be seen from Fig. 2 and Fig. 3 SBLs can be lowered to a value ($\approx -22.51\,\mathrm{dB}$) below $-19.5\,\mathrm{dB}$ which is found in [9] by splitting pulses.

3.2. Independent Control of Each Harmonic

It is known from published works that there exist methods for total minimisation of radiation in harmonic frequencies directly or indirect ways (i.e., [9]), however the disadvantage of the sideband radiations can not be considered as only a power loss. It is shown in recently published papers [6, 10] that it is possible to communicate over these frequencies, this brings the possibility of misusing these radiations, for example gathering information and espionage issues in military applications. Suppose that there is a scenario in which supressing the only first or second harmonic (or any combination) independently is necessary (e.g., communication over fundamental radiation and second harmonic but not over the others). This case requires enough power transmission in second harmonic to establish a communication and the suppression of other harmonics to prevent data transmission on related frequencies. If the same scenario described in Section 3.1 is considered and optimization process is performed under same conditions, resultant switching scheme is given in Fig. 4 and corresponding sideband levels and radiation patterns are given in Fig. 5 and Fig. 6 respectively.

As it can be seen from Fig. 5 suppression of the first sideband and others without minimizing the second one is achievable. This result provides independent control of each harmonic. There exists

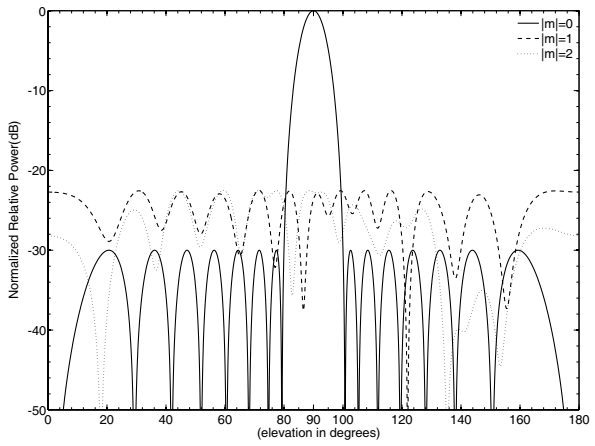

Figure 3: Radiation patterns related to Fig. 1.

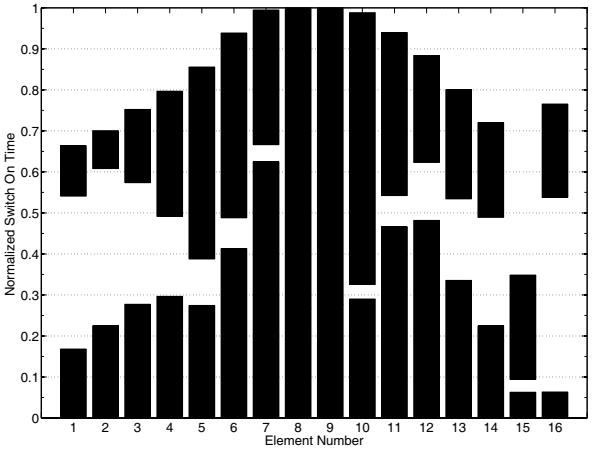

Figure 4: On-off time sequence of 16 element $-30\,\mathrm{dB}$ Chebyshev pattern optimized to reduce first sideband.

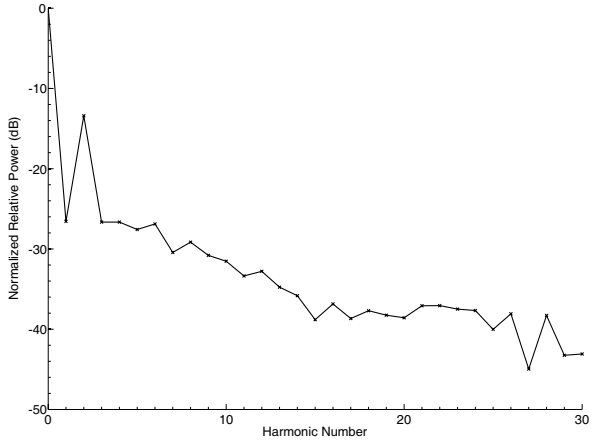

Figure 5: Sidebands caused by switching according to Fig. 4.

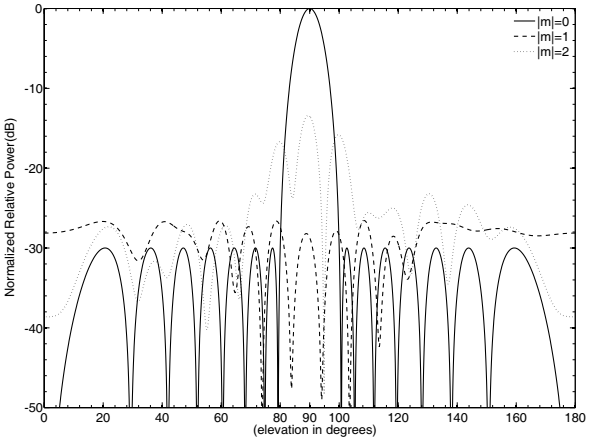

Figure 6: Radiation patterns related to Fig. 4.

a general opinion that suppressing the first sideband is enough to minimize the other harmonics (indirect harmonic minimisation), however this generalization does not hold true if there exist more than one pulse in each period. Additionally, as shown in Fig. 5 this seperation process brings an additional freedom to separately control each harmonic frequency.

4. CONCLUSION

In this study, an idea about controlling the maximum level of harmonic radiations via splitting pulses while the total switch-on durations are constant is presented. Two different examples are given to illustrate the effectiveness of this approach. This approach provides an additional degree of freedom in design and it is shown with first example that SBL suppression capability seems to be better than other published works. Also splitting pulses provides an independent control of each harmonic frequency. Finally, it is illustrated that first sideband level is not always greater than other harmonics.

REFERENCES

1. Shanks, H. E. and R. W. Bickmore, "Four-dimensional electromagnetic radiators," *Canad. J. Phys.*, Vol. 37, 263–275, 1959.
2. Kummer, W. H., A. T. Villeneuve, T. S. Fong, and F. G. Terrio, "Ultra-low sidelobes from time-modulated arrays," *IEEE Trans. Antennas Propag.*, Vol. 11, No. 6, 633–639, 1963.
3. Yang, S., Y. B. Gan, and A. Qing, "Sideband suppression in time-modulated linear arrays by the differential evolution algorithm," *IEEE Antennas Wirel. Propag. Lett.*, Vol. 1, 173–175, 2002.
4. Yang, S., Y. B. Gan, A. Qing, and P. K. Tan, "Design of a uniform amplitude time modulated linear array with optimized time sequences," *IEEE Trans. Antennas Propag.*, Vol. 53, No. 7, 2337–2339, 2005.
5. Tennant, A. and B. Chambers, "Control of the harmonic radiation patterns of time-modulated antenna arrays," *Proc. IEEE AP-S Int. Symp.*, S. Diego, California, USA, July 5–12, 2008.
6. Li, G., S. Yang, Y. Chen, and Z. Nie, "A novel electronic beam steering technique in time modulated antenna arrays," *Progress In Electromagnetics Research*, Vol. 97, 391–405, 2009.
7. Aksoy, E. and E. Afacan, "Thinned nonuniform amplitude time modulated linear arrays," *IEEE Antennas Wirel. Propag. Lett.*, Vol. 9, 514–517, 2010.
8. Poli, L., P. Rocca, L. Manica, and A. Massa, "Handling sideband radiations in time modulated arrays through particle swarm optimization," *IEEE Trans. Antennas Propag.*, Vol. 58, No. 4, 1408–1411, 2010.
9. Poli, L., P. Rocca, L. Manica, and A. Massa, "Pattern synthesis in time-modulated linear arrays through pulse shifting," *IET Microw. Antennas Propag.*, Vol. 4, No. 9, 1157–1164, 2010.
10. Tong, Y. and A. Tennant, "Simultaneous control of sidelobe level and harmonic beam steering in time-modulated linear arrays," *Electronics Letters*, Vol. 46, No. 3, 201–202, 2010.
11. Brégains, J. C., G. Franceschetti, and F. Ares, "Signal radiation and power losses of time-modulated arrays," *IEEE Trans. Antennas Propag.*, Vol. 56, No. 6, 1799–1804, 2008.
12. Aksoy, E. and E. Afacan, "Planar antenna pattern nulling using differential evolution algorithm," *Int. J. Electron. Commun.*, Vol. 63, 116–122, 2009.

Generalized Representation of Sideband Radiation Power Calculation in Arbitrarily Distributed Time-modulated Planar and Linear Arrays

E. Aksoy and E. Afacan
Department of Electrical & Electronics Engineering, Gazi University, Maltepe, Ankara, Turkey

Abstract— In this study, grid independent general representation of formulation of sideband radiation (SR) power calculation in time-modulated planar and linear arrays is aimed. It is shown that both distinct formulations can be written in one form which provides an expectation about conformal case.

1. INTRODUCTION

Recently a useful formulation which gives the total radiated power associated with the harmonic frequencies of a TMLA is published by Brégains et al. [1]. After this work, Poli et al. applied this same idea to rectangular grid planar arrays [2]. Both of these formulations provide calculation simplicity when the harmonic radiation is concerned but they are still in distinct forms.

In this study, generalization of the formulation originally given in [2] which is constructed on the idea given in [1] to a grid independent form for linear cases is aimed while trying to keep the original notation as much as possible.

2. FORMULATION

Consider a planar array consisting of total N elements whose elements are on the x-y plane but not on a canonical grid. The array factor of this array may be written as

$$AF\left(\theta,\phi,t\right)=e^{j\omega_0 t}\sum_{\langle n\rangle}I_n g_n\left(t\right)e^{jkx_n\sin\theta\cos\phi}e^{jky_n\sin\theta\sin\phi}, \tag{1}$$

where x_n and y_n represent apsis and ordinate values in standard Cartesian coordinate system of corresponding element, respectively. k is the wave number and I_n represents the element excitations. $g_n\left(t\right)$ is a periodic function. Since $g_n\left(t\right)$ is periodic it can be expanded to Fourier Series which is:

$$g_n\left(t\right)=\sum_{h=-\infty}^{\infty}G_{nh}e^{jh\omega_p t}, \tag{2}$$

where

$$G_{nh}=\frac{1}{T_p}\int_{-T_p/2}^{T_p/2}g_n\left(t\right)e^{-jh\omega_p t}dt. \tag{3}$$

As in [2] it is also assumed that:

$$g_n\left(t\right)=\begin{cases}1, & 0<|t|\leq\frac{\tilde{t}_n}{2}\\ 0, & \text{otherwise}\end{cases}. \tag{4}$$

According to [1] and [2] the total power radiated on harmonics is given by:

$$P_{SR}=\frac{1}{2}\int_0^{2\pi}\int_0^{\pi}\sum_{\substack{h=-\infty\\ h\neq 0}}^{\infty}\left|\mu_h\left(\theta,\phi\right)\right|^2\sin\theta d\theta d\phi \tag{5}$$

where $\mu_h\left(\theta,\phi\right)$ for planar arrays can be written as:

$$\mu_h\left(\theta,\phi\right)=\sum_{\langle n\rangle}I_n e^{jkx_n\sin\theta\cos\phi}e^{jky_n\sin\theta\sin\phi} \tag{6}$$

From relation $\left|\mu_h\left(\theta,\phi\right)\right|^2=\mu_h\left(\theta,\phi\right)\mu_h^*\left(\theta,\phi\right)$, $\left|\mu_h\left(\theta,\phi\right)\right|^2$ becomes:

$$|\mu_h(\theta,\phi)|^2 = \sum_{\langle n\rangle} I_n e^{jkx_n \sin\theta\cos\phi} e^{jky_n \sin\theta\sin\phi} \left(\sum_{\langle n\rangle} I_n e^{jkx_n \sin\theta\cos\phi} e^{jky_n \sin\theta\sin\phi}\right)^*$$
$$|\mu_h(\theta,\phi)|^2 = \sum_{\langle n\rangle} (|I_n| G_{nh})^2 + \sum_{\substack{m,n=0 \\ m\neq n}}^{N-1} \Re\{I_m I_n^*\} G_{nh} G_{mh} e^{jk(x_m-x_n)\sin\theta\cos\phi} e^{jk(y_m-y_n)\sin\theta\sin\phi} \quad (7)$$

where $\Re\{\cdot\}$ represents the real part of a complex number, so that P_{SR} becomes:

$$P_{SR} = \frac{1}{2}\left[F_1(\theta,\phi) + F_2(\theta,\phi)\right] \quad (8)$$

where

$$F_1(\theta,\phi) = \sum_{\substack{h=-\infty \\ h\neq 0}}^{\infty} \sum_{\langle n\rangle} (|I_n| G_{nh})^2 \int_0^{2\pi}\int_0^{\pi} \sin\theta d\theta d\phi \quad (9)$$

and

$$F_2(\theta,\phi) = \sum_{\substack{h=-\infty \\ h\neq 0}}^{\infty} \sum_{\substack{m,n=0 \\ m\neq n}}^{N-1} \Re\{I_m I_n^*\} G_{nh} G_{mh} \int_0^{2\pi}\int_0^{\pi} e^{jk(x_m-x_n)\sin\theta\cos\phi} e^{jk(y_m-y_n)\sin\theta\sin\phi} \sin\theta d\theta d\phi. \quad (10)$$

Since Eq. (4) produces real results for G_{nh},G_{mh} and from [1], the infinite summation of $G_{nh}G_{mh}$ becomes:

$$\sum_{\substack{h=-\infty \\ h\neq 0}}^{\infty} G_{nh} G_{mh} = \tau_{mn_{MinVal}} - \tau_m \tau_n, \quad (11)$$

so that $F_1(\theta,\phi)$ reduces to:

$$F_1(\theta,\phi) = 4\pi \sum_{\langle n\rangle} |I_n|^2 \left[\tau_n (1-\tau_n)\right]. \quad (12)$$

For $F_2(\theta,\phi)$ the integral inside summation must be solved. To do this (like in [2]) by using:

$$a\cos(x) + b\sin(x) = \sqrt{a^2+b^2} cos\left(x - \tan^{-1}\left(\frac{b}{a}\right)\right), \quad (13)$$

complex exponentials in integrals becomes:

$$F_\theta = e^{jk\sin\theta\sqrt{(x_m-x_n)^2+(y_m-y_n)^2}\cos\left(\phi-\tan^{-1}\left(\frac{y_m-y_n}{x_m-x_n}\right)\right)}. \quad (14)$$

So integrals in Eq. (10) may be written as:

$$F_\theta = \int_0^{\pi}\left[\int_0^{2\pi} e^{jk\sin\theta\sqrt{(x_m-x_n)^2+(y_m-y_n)^2}\cos\left(\phi-\tan^{-1}\left(\frac{y_m-y_n}{x_m-x_n}\right)\right)} d\phi\right]\sin\theta d\theta$$
$$= \int_0^{\pi} 2\pi J_0\left(k\sin\theta\sqrt{(x_m-x_n)^2+(y_m-y_n)^2}\right)\sin\theta d\theta. \quad (15)$$

Letting $\sqrt{(x_m-x_n)^2+(y_m-y_n)^2} = C$ Eq. (15) may be written as:

$$2\pi\int_{-\pi/2}^{\pi/2} J_0(kC\cos\theta)\cos\theta d\theta = 2\pi\int_{-\pi/2}^{0} J_0(kC\cos\theta)\cos\theta d\theta + 2\pi\int_0^{\pi/2} J_0(kC\cos\theta)\cos\theta d\theta \quad (16)$$

By letting $\theta = -\theta$ and since $J_0(x)$ is even Eq. (16) reduces to:

$$2\pi \int_{-\pi/2}^{\pi/2} J_0(kC\cos\theta)\cos\theta d\theta = 4\pi \int_0^{\pi/2} J_0(kC\cos\theta)\cos\theta d\theta. \tag{17}$$

Again by letting $u = \pi/2 - \theta$ Eq. (17) becomes

$$2\pi \int_0^{\pi} J_0(kC\sin\theta)\sin\theta d\theta = 2\pi \int_{-\pi/2}^{\pi/2} J_0(kC\cos\theta)\cos\theta d\theta = 4\pi \int_0^{\pi/2} J_0(kC\sin\theta)\sin\theta d\theta. \tag{18}$$

Using the relation [3]

$$J_{\mu+v+1}(z) = \frac{z^{v+1}}{2^v\Gamma(v+1)} \int_0^{\pi/2} J_\mu(z\sin\theta)\sin^{\mu+1}\theta\cos^{2v+1}\theta d\theta, \tag{19}$$

and by letting $\mu = 0$ and $v = -1/2$ Eq. (17) reduces to:

$$4\pi \int_0^{\pi/2} J_0(kC\sin\theta)\sin\theta d\theta = 4\pi \frac{J_{1/2}(kC)\,\Gamma\left(\frac{1}{2}\right)}{\sqrt{2kC}} = 4\pi j_0(kC) = 4\pi \frac{\sin(kC)}{kC}. \tag{20}$$

Substituting Eq. (20) and Eq. (11) into Eq. (10) $F_2(\theta,\phi)$ becomes:

$$F_2(\theta,\phi) = 4\pi \sum_{\substack{m,n=0 \\ m\neq n}}^{N-1} \Re\{I_m I_n^*\}\left[\tau_{mn_{MinVal}} - \tau_m\tau_n\right] \frac{\sin\left(k\sqrt{(x_m-x_n)^2+(y_m-y_n)^2}\right)}{k\sqrt{(x_m-x_n)^2+(y_m-y_n)^2}}. \tag{21}$$

Combining Eq. (12) and Eq. (21) P_{SR} becomes:

$$\begin{aligned} P_{SR} = {} & 2\pi \sum_{\langle n\rangle} |I_n|^2 \left[\tau_n(1-\tau_n)\right] \\ & + 2\pi \sum_{\substack{m,n=0 \\ m\neq n}}^{N-1} |I_m||I_n| \cos(\beta_m-\beta_n)[\tau_{mn_{MinVal}} - \tau_m\tau_n] \frac{\sin\left(k\sqrt{(x_m-x_n)^2+(y_m-y_n)^2}\right)}{k\sqrt{(x_m-x_n)^2+(y_m-y_n)^2}}. \end{aligned} \tag{22}$$

Integrating Eq. (30) in [1] gives the same result for linear arrays (note that the domain of second summation is not the same with the case given here).

$$P_{SR} = 2\pi \sum_{\langle n\rangle} |I_n|^2 \left[\tau_n(1-\tau_n)\right] + 2\pi \sum_{\substack{m,n=0 \\ m\neq n}}^{N-1} |I_m I_n| \cos(\beta_m-\beta_n)\left[\tau_{mn_{MinVal}} - \tau_m\tau_n\right] \frac{\sin(k(z_m-z_n))}{k(z_m-z_n)} \tag{23}$$

It can be easily seen from Eq. (22) and Eq. (23) that both equations are in the same form and can be represented as one equation. Both $\sqrt{(x_m-x_n)^2+(y_m-y_n)^2}$ and $(z_m-z_n) = \sqrt{(z_m-z_n)^2}$ gives the Euclidian distance and $\beta_m - \beta_n$ gives the phase difference between distinct elements in standard Cartesian coordinate system and can be represented as d_{mn} and Δ_{mn}^{β}, respectively. So that both formulations may be written in one form which is:

$$P_{SR} = 2\pi \sum_{\langle n\rangle} |I_n|^2 \left[\tau_n(1-\tau_n)\right] + 2\pi \sum_{\substack{m,n=0 \\ m\neq n}}^{N-1} |I_m||I_n| \cos\left(\Delta_{mn}^{\beta}\right)\left[\tau_{mn_{MinVal}} - \tau_m\tau_n\right] \frac{\sin(kd_{mn})}{kd_{mn}}. \tag{24}$$

It must be noted that these formulations are valid if there exist only one pulse per period which are symmetric around $t = 0$. If there exist more than one pulse in each period Eq. (24) must be extended to a new general form and if relative positions of pulses are not symmetric around $t = 0$ total loss seems to be not equal to the symmetric cases.

3. CONCLUSION

In this paper a general representation of total power loss calculation for planar and linear arrays and some comments about power loss calculations are presented. It is shown that both distinct formulations given in published works can be combined and written in one form. This form also provides an expectation about the conformal case.

REFERENCES

1. Brégains, J. C., J. Fondevila-Gómez, G. Franceschetti, and F. Ares, "Signal radiation and power losses of time-modulated arrays," *IEEE Trans. Antennas Propag.*, Vol. 56, No. 6, 1799–1804, 2008.
2. Poli, L., P. Rocca, L. Manica, and A. Massa, "Time modulated planar arrays — Analysis and optimisation of the sideband radiations," *IET Microw. Antennas Propag.*, Vol. 4, No. 9, 1165–1171, 2010.
3. Watson, G. N., "A treatise on the theory of Bessel functions," Cambridge University Press, London, 1922.

Synthesis of Pencil-beam Patterns with Time-modulated Concentric Circular Ring Antenna Arrays

L. Zheng, S. Yang, Q. Zhu, and Z. Nie
School of Electronic Engineering, University of Electronic Science and Technology of China (UESTC)
Chengdu 611731, China

Abstract— In this paper, a method for the synthesis of pencil beam patterns from time modulated circular ring antenna arrays is presented. The time modulation approach is applied to the uniformly excited concentric circular ring array (CCRA) to suppress the sidelobe level with fixed beamwidth. Based on the proposed method, some numerical examples are compared with the published results of the conventional concentric circular ring arrays. Numerical results show the achievable performance of time modulation in successfully synthesizing low sidelobe patterns even if the amplitude excitations are uniform.

1. INTRODUCTION

Circular antenna arrays that have several advantages over other type of array antenna configurations, such as the all-azimuth scan capability and invariant beam pattern in every ϕ-cut, thus finding considerable interest in various applications including sonar, radar, and mobile and commercial satellite communications systems [1–4]. Concentric circular ring array (CCRA) that contains many concentric circular rings of different radii and number of elements have several advantages, including the flexibility in array pattern synthesis and design both in narrowband and broadband beamforming applications [1]. Previous studies on array pattern synthesis of CCRA were mainly focused on controlling the sidelobe level (SLL) in the array pattern [1–6] or optimizing the synthesized array pattern [5, 7]. Uniformly excited and equally spaced antenna arrays have high directivity but they usually suffer from higher SLLs. To reduce the SLLs further, the array can be made aperiodic by nonuniformly spacing the rings and the elements with all excitation amplitudes keeping uniform [3, 4]. Another possible solution to reduce the higher SLLs is to use an equally spaced or optimized spaced array with amplitude weighting the elements [2, 7]. The search algorithms, such as simulated annealing (SA) [3], genetic algorithms (GAs) [4] and particle swarm optimization (PSO) [7], have also been used in the process of low sidelobe array pattern synthesis.

In this work, the time modulation approach [8, 9] based on the DE algorithm [10] is applied to the uniformly excited CCRA for sidelobe reduction. This technique proceeds by time weighing the rings in the array with each ring controlled by a high speed and periodic-working RF switch, while all elements in an individual ring are weighted in time intervals by the same value and the weight values of different rings are optimized by the DE algorithm. Due to the additional degree of design freedom-time, the SLL can be further reduced as compared to the published results in [4], while keeping the amplitude excitations uniform.

2. THEORETICAL ANALYSIS

The arrangement of elements in planar circular arrays may contain multiple concentric circular rings, with different radius or number of elements, thus giving rise to different radiation patterns. Fig. 1 shows the configuration of M concentric circular ring arrays [1, 2] in x-y plane. The mth ring has a radius r_m and a number of elements N_m, where $m = 1, 2, \ldots, M$. The linear distance between the adjacent elements on the mth circle ring is d_m. All the elements of the CCRA are uniformly excited.

If a plane wave of frequency f_0 is incident at an angle (θ, ϕ) with respect to the spherical coordinate system of the array, the array factor of the output signal for the CCRA with a single element at the center is given by

$$E(\theta, \phi, t) = \left\{ 1 + \sum_{m=1}^{M} \sum_{n=1}^{N_m} I_m e^{jkr_m \sin\theta \cos(\phi - \phi_{mn})} \right\} e^{j2\pi f_0 t} \tag{1}$$

where $k = 2\pi/\lambda$ is the wave number and I_m are the excitation amplitude of elements on mth circular ring (where $I_m = 1$ throughout this study for the uniformly excited elements).

Now, all the elements on a circle are controlled by a same high speed RF switch, which can be used to maintain the invariant beam pattern in every ϕ-cut. The operational time intervals for each different ring vary from circle to circle, except that the single element at the center is always illuminated. The periodic switch-on time function $U_m(t)$ $(m = 1, 2, \ldots, M)$ for each switch can be expressed in the form of

$$U_m(t) = \begin{cases} 1, & 0 \le t \le \tau_m \\ 0, & \text{otherwise} \end{cases} \tag{2}$$

where τ_m $(0 \le \tau_m \le T_p)$ in (2) is the switch-on time interval of each ring array elements in each modulation period T_p and the time modulation frequency is $F_p = 1/T_p$. Substituting (2) into (1) and decomposing it into Fourier series with different frequency components $f_0 + p \cdot F_p$ $(p = 0, \pm 1, \pm 2, \ldots, \pm\infty)$, then the far-field pattern (1) is given by

$$\begin{aligned} E(\theta, \phi, t) &= \left\{ 1 + \sum_{m=1}^{M} \sum_{n=1}^{N_m} I_m U_m(t) e^{jkr_m \sin\theta \cos(\phi - \phi_{mn})} \right\} e^{j2\pi f_0 t} \\ &= \sum_{p=-\infty}^{\infty} \left\{ 1 + \sum_{m=1}^{M} \sum_{n=1}^{N_m} i_{pm} e^{jkr_m \sin\theta \cos(\phi - \phi_{mn})} \right\} e^{j2\pi (f_0 + mF_p)t} \end{aligned} \tag{3}$$

The complex amplitude i_{pm} is given by

$$i_{pm} = \frac{I_m \cdot \tau_m}{T_p} \cdot \frac{\sin(\pi p \tau_m \cdot F_p)}{\pi p \tau_m \cdot F_p} \cdot e^{-j\pi p \tau_m \cdot F_p} \tag{4}$$

At the center frequency $(p = 0)$, the amplitude of the Fourier component i_{0m} can be simplified as

$$i_{0m} = I_m \cdot \tau_m / T_p \tag{5}$$

Thus, the radiation patterns of sideband components (harmonic frequency components $f_0 + p \cdot F_p$, $p \ne 0$) and the center frequency f_0 can be written by (6) and (7), respectively.

$$|E_m(\theta, \phi)| = \left| 1 + \sum_{m=1}^{M} \sum_{n=1}^{N_m} i_{pm} e^{jkr_m \sin\theta \cos(\phi - \phi_{mn})} \right| \tag{6}$$

$$|E_0(\theta, \phi)| = \left| 1 + \sum_{m=1}^{M} \sum_{n=1}^{N_m} I_m \cdot \tau_m / T_p e^{jkr_m \sin\theta \cos(\phi - \phi_{mn})} \right| \tag{7}$$

According to (7), it is observed that though all the elements of the CCRA are uniformly excited, there is an additional factor τ_m/T_p which can be applied to synthesize the desired pencil beam patterns with lower SLLs. The DE algorithm [10] is used to optimize the switch-on time intervals

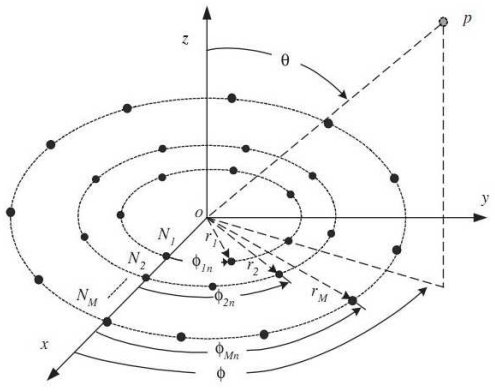

Figure 1: Diagram of a concentric circular ring array (CCRA).

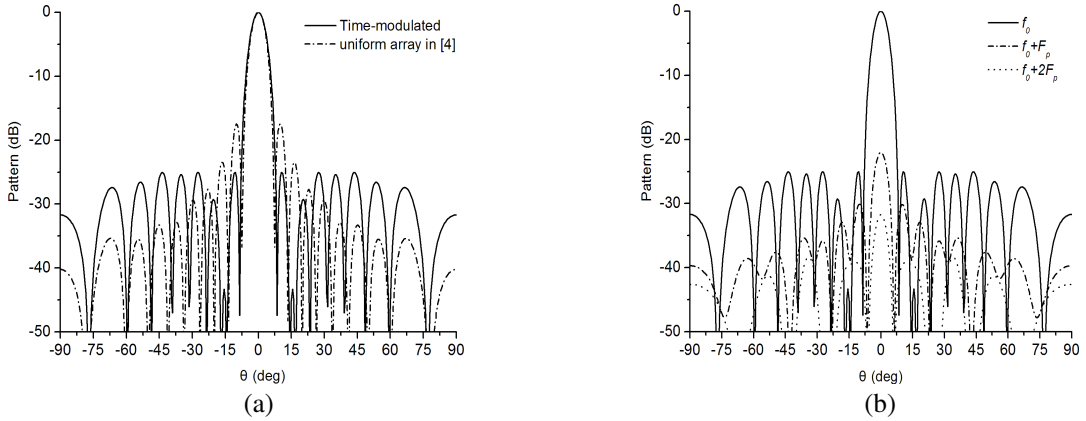

Figure 2: (a) Radiation patterns of the time-modulated CCRA (solid curve) and the conventional uniform CCRA (dash-dot line) in $\phi = 0$ plane. (b) Radiation patterns of the time-modulated CCRA at the center frequency f_0 and the first two sideband frequencies $f_0 + F_p$, $f_0 + 2F_p$ in $\phi = 0$ plane.

Table 1: Optimum switch-on time intervals of the time-modulated CCRA.

Ring no.	1	2	3	4	5	6	7	8	9
Number of elements	6	12	18	25	31	37	43	50	56
$\tau_m(us)$	0.9964	0.9998	1.0000	0.9958	0.9465	0.9154	0.4926	0.0606	0.9507

with the optimization parameter vector $v = \{\tau_m\}$. The fitness function to be minimized is to obtain the desired pencil beam pattern with minimum SLL and sideband level (SBL) is given by

$$f^{(n)}(v) = w_1 \cdot \mathrm{SLL}^{(n)}_{\max}(v)\,|_{f_0} + w_2 \cdot \mathrm{SBL}^{(n)}_{\max}(v)\,|_{f_0+F_p} + w_3 \cdot |\mathrm{FNBW}_o - \mathrm{FNBW}_d|\, H(T) \qquad (8)$$

where n denotes the nth generation evolution generations, $\mathrm{SLL}_{\max}$ and $\mathrm{SBL}_{\max}$ are the maximum SLL at the center frequency and the maximum sideband level (SBL) at the first sideband frequency, FNBW_o and FNBW_d are obtained and desired value of first null beamwidth respectively, and $w_1 \sim w_3$ are the weighting factors of each term to emphasize the different contributions to the cost function.

3. NUMERICAL RESULTS

Firstly, a planar uniform array of nine concentric circular rings is considered [4]. In this example, the uniform array has equal element spacing and amplitude weighting for each element. The radius of each ring of the array antenna is made equal to $0.5\lambda m$, where m is the ring number counted from the innermost ring 1. The total number of isotropic elements including the central element in such an array is 279. Elements are equi-spaced on a common circle with the spacing between elements is approximately $\lambda/2$. And, the obtained pattern is shown in [4] Fig. 2(b), it has a directivity of 29.35 dB, a peak sidelobe level of -17.4 dB, a first null beamwidth of 14.8 degree and is symmetric in ϕ.

Problem is now to find the optimal set of switch-on time intervals distribution that will generate a pencil beam pattern in the vertical plane with minimum SLL while keeping the desired first null beamwidth unchanged. Typical DE simulation parameters [10] are set as follows: the population size $N_{POP} = 5N_{PAR}$, the mutation factor $\beta = 0.6$, and the crossover probability $P_{cross} = 0.9$. Obtained results and its comparison to the uniformly excited array [4] are shown in Fig. 2. Fig. 2(a) shows that the SLL of the time-modulated CCRA is -25.0 dB, which is 7.6 dB lower than that of the result in [4]. Fig. 2(b) illustrates the normalized radiation patterns at f_0 and the first two sideband frequencies $f_0 + F_p$, $f_0 + 2F_p$, and the SBL is suppressed to below -22.0 dB. Although, only the pattern of $\phi = 0$ plane is presented, the array pattern is symmetric in ϕ for its uniform excitation and elements spacing. Numerical results show the achievable performance of the approach in improving the SLL, which is more powerful than the amplitude weighing method [6], even if the amplitude excitations are uniform in this example. Table 1 shows the corresponding optimized switch-on time intervals and the number of elements in each circular ring.

Secondly, the spacing between the adjacent elements of the above uniform CCRA were optimized with optimal element number N_m in each ring. The detailed results obtained from this array

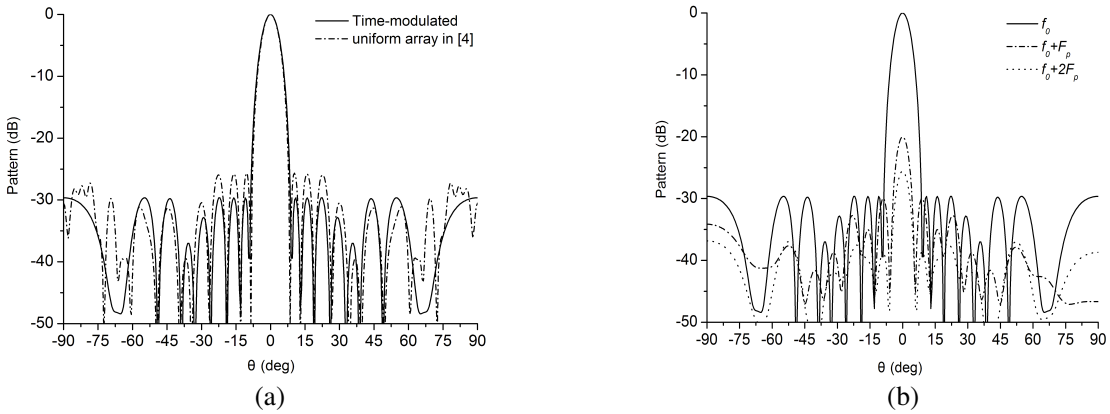

Figure 3: (a) Radiation patterns of the time-modulated CCRA (solid curve) and the conventional uniform CCRA (dash-dot line) in $\phi = 0$ plane. (b) Radiation patterns of the time-modulated CCRA at the center frequency f_0 and the first two sideband frequencies $f_0 + F_p$, $f_0 + 2F_p$ in $\phi = 0$ plane.

distribution are shown in [4], where the array has 183 elements arranged as shown in Fig. 2(g) [4] and the directivity is 28.5 dB and the maximum SLL is −25.58 dB. When the time modulation is introduced as stated in the former example, the SLL was further suppressed to −29.57 dB with the SBL below −20.0 dB. The results are shown in Fig. 3.

4. CONCLUSIONS

This paper presents a pattern synthesis approach for the synthesis of multiple concentric circular ring antenna arrays. It can generate a pencil beam pattern in the vertical plane with reduced SLL, while keeping the first null beamwidth the same as that of a uniformly excited CCRA. Numerical results show the excellent sidelobe control capability for pencil beam pattern synthesis by using the time modulation technique. As compared to the amplitude weighing method, the difficulty of the amplitude control is instead of controlling the switch-on time intervals,which can be more precisely and more rapidly realized. The proposed method is very simple and can be applied to the design of time modulated antenna arrays with other geometrical configurations.

ACKNOWLEDGMENT

This work was supported in part by the Natural Science Foundation of China under Grant No. 60971-030 and in part by the 111 project of China (Grant No. B07046).

REFERENCES

1. Dessouky, M. I., H. A. Sharshar, and Y. A. Albagory, "Efficient sidelobe reduction technique for small-sized concentric circular arrays," *Progress In Electromagnetics Research*, Vol. 65, 187–200, 2006.
2. Dessouky, M. I., H. A. Sharshar, and Y. A. Albagory, "Optimum normalized-gaussian tapering window for side lobe reduction in uniform concentric circular arrays," *Progress In Electromagnetics Research*, Vol. 69, 35–46, 2007.
3. Vicente-Lozano, M., F. Ares-Pena, and E. Moreno, "Pencil-beam pattern synthesis with a uniformly excited multi-ring planar antenna," *IEEE Antennas and Prpagation Magazine*, Vol. 42, No. 6, 70–74, 2000.
4. Haupt, R. L., "Optimized element spacing for low sidelobe concentric ring arrays," *IEEE Trans. Antennas Propagation*, Vol. 56, No. 1, 266–268, 2008.
5. EI-Kamchouchi, H., "Ultra-low-sidelobe-level concentric-ring-array pattern synthesis using Bessel neural networks [antenna designer's notebook]," *IEEE Antennas and Prpagation Magazine*, Vol. 52, No. 4, 102–105, 2010.
6. Chatterjee, A., G. K. Mahanti, and A. Chakraborty, "Synthesis of pencil beam pattern with a multiple concentric circular ring array antenna with minimum side lobe level and fixed first null beamwidth," *Proceedings of International Conference on Electronic Computer Technology (ICECT)*, 71–74, Kuala Lumpur, Singapore, May 2010.

7. Yunhong, L., K. C. Ho, and C. Kwan, "3-D array pattern synthesis with frequency invariant property for concentric ring," *IEEE Trans. Signal Processing*, Vol. 54, No. 2, 780–784, 2006.
8. Fondevila, J., J. C. Brégains, F. Ares, and E. Moreno, "Optimizing uniformly excited linear arrays through time modulation," *IEEE Antennas Wireless Propagat. Lett.*, Vol. 3, 298–301, 2004.
9. Yang, S., Y. B. Gan, and A. Qing, "Antenna array pattern nulling using a differential evolution algorithm," *Int. J. RF Microwave Computer-Aided Eng.*, Vol. 14, 57–63, January 2004.
10. Yang, S., Y. B. Gan, A. Qing, and P. K. Tan, "Design of a uniform amplitude time modulated linear array with optimized time sequences," *IEEE Trans. Antennas Propagat.*, Vol. 53, No. 7, 2337–2339, July 2005.
11. Yang, S., Y. B. Gan, and A. Qing, "Sideband suppression in time-modulated linear arrays by the differential evolution algorithm," *IEEE Antennas Wireless Propagat. Lett.*, Vol. 1, 173–175, 2002.

Sideband Suppression with Sub-sectional Optimized Time Steps in Time Modulated Linear Arrays

Q. Zhu, **S. Yang**, **L. Zheng**, **and Z. Nie**
School of Electronic Engineering, University of Electronic Science and Technology of China (UESTC)
Chengdu 611731, China

Abstract— This paper presents a novel approach to suppress sideband levels in time modulated linear arrays (TMLAs). The approach is based on the dividing of the time modulation period T_p into several subsections, and the "switch-on" and "switch-off" time in each subsection is optimized by the differential evolution (DE) algorithm. As compared to previous approach, the new approach has more flexibility and can be used to reduce sideband levels significantly. Numerical results of using the approach to suppress sideband levels in the case of uniform and non-uniform excitations are given.

1. INTRODUCTION

Time modulated antenna arrays can be used to realize low/ultra-low sidelobe with very low excitation dynamic-range ratios, even in the case of uniform excitations by using an additional degree of freedom — time [1]. However, the inherent characteristic of time modulated arrays is that there are many sideband signals spaced at multiples of the modulation frequency. To improve the efficiency of low/ultra-low sidelobe time modulation antenna arrays, the sideband levels (SBL) need to be suppressed as low as possible [2].

In 2002, S. Yang et al. proposed an approach based on the differential evolution (DE) algorithm to suppress the SBL in time modulated linear arrays (TMLAs) [2]. In 2004, J. Fondevila et al. minimized the SBL in uniformly excited TMLAs via the simulated annealing (SA) technique [3]. In 2010, L. Poli et al. handled sideband radiations in TMLAs through particle swarm optimization (PSO) [4]. S. Pal et al. proposed a multi-objective optimization approach for the design of TMLAs with low SLL and SBL [5]. In 2005, a uniformly excited TMLA with both suppressed sidelobe and sideband was designed and the array utilized time sequences optimized by the binary genetic algorithm (GA) [6]. The approach was based on the so called binary optimized time sequences (BOTS). In 2009, L. Poli et al. proposed a pattern synthesis approach and controlled the SBL in TMLAs through pulse shifting [7]. In 2010, a method for the problem of array thinning in TMLAs was proposed to suppress the SLL and SBL in [8].

In this paper, a novel type of time modulation scheme — sub-sectional optimized time steps (SOTS) in TMLAs is proposed for the suppression of SBL and SLL simultaneously. The approach is based on the division of the time modulation period T_p into several subsections, and the "switch-on" and "switch-off" time in each subsection is optimized via the differential evolution (DE) algorithm. A few numerical results are presented to demonstrate the effectiveness of the proposed approach.

2. THEORY

For simplicity, a half wavelength spaced TMLA of $2N$ isotropic elements is considered. The array is symmetric in both geometry and "on-off" time with respect to the array center. The time modulation period of the TMLA is T_p, and the modulation frequency is $f_p = 1/T_p$. If a plane wave with the center frequency f_0 is incident at the angel θ measured from broadside, the array factor can be given by

$$E(\theta, t) = e^{j2\pi f_0 t} \cdot \sum_{k=1}^{N} A_k \cdot U_k(t) \cdot 2\cos\left(\left(k - \frac{1}{2}\right)\pi \cdot \sin\theta\right) \tag{1}$$

where A_k is the time-independent static excitation amplitude for the kth element, $U_k(t)$ represents corresponding periodic "on-off" time function. For different time modulation schemes, $U_k(t)$ has different expression.

If the modulation frequency f_p is much lower than the center frequency f_0, (1) can be decomposed into Fourier series with different frequency components separated by f_p. Thus (1) can be written

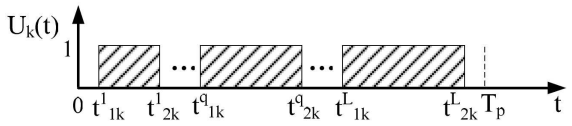

Figure 1: SOTS time modulation scheme.

by

$$E(\theta,t)=\sum_{m=-\infty}^{+\infty}\left[e^{j2\pi(f_0+m\cdot f_p)t}\sum_{k=1}^{N}a_{mk}\cdot 2\cos\left(\left(k-\frac{1}{2}\right)\pi\cdot\sin\theta\right)\right] \tag{2}$$

where m ($m=0,\pm1,\pm2,\ldots,\pm\infty$) denotes the order of sidebands, a_{mk} represents the complex excitation for the kth element at the mth sideband and is given by

$$a_{mk}=\frac{1}{T_p}\int_0^{T_p}A_k\cdot U_k(t)e^{-j2\pi mf_pt}\cdot dt \tag{3}$$

The time modulation scheme with sub-sectional optimized time steps (SOTS) is shown in Fig. 1. The modulation period T_p is divided into L subsections. In each subsection, the "switched-on" time t^q_{1k} ($q=1,2,3\ldots,L$) and "switch-off" time t^q_{2k} is optimized by DE. $U_k(t)$ are given by

$$U_k(t)=\begin{cases}1 & t^q_{1k}\le t\le t^q_{2k}\\ 0 & \text{others}\end{cases},\quad q=1,2\cdots L \tag{4}$$

then a_{mk} can be given by

$$a_{mk}=A_k\cdot\sum_{q=1}^{L}\frac{t^q_{2k}-t^q_{1k}}{T_p}\sin c(\pi mf_p(t^q_{2k}-t^q_{1k}))e^{-j\pi mf_p(t^q_{2k}+t^q_{1k})} \tag{5}$$

when m=0, a_{0k} can be used to synthesize low/ultra-low SLL pattern at f_0.

In order to suppress SBL while realizing low/ultra-low SLL, the DE algorithm is selected as the global optimization method. The static excitation amplitudes, the switch-on times and switch-off times in each subsection constitute the optimization parameter vector $v=\{A_k,t^1_{1k},t^1_{2k},t^2_{1k},t^2_{2k}\ldots t^L_{1k},t^L_{2k}\}$, and the cost function is given by

$$\begin{aligned}f^{(n)}(\mathbf{v}) \;=\; & w_1\cdot(SLL^{(n)}(\mathbf{v})-SLL_d)\,|_{f_0}+w_2\cdot(SBL^{(n)}_{\max}(\mathbf{v})-SBL_d)\,|_{f_0+m\cdot f_p}\\ & +w_3\cdot\sum_{k=1}^{N}\sum_{q=1}^{L}(t^q_{2k}-t^q_{1k})+w_4\cdot\sum_{k=1}^{N}\sum_{q=1}^{L-1}(t^{q+1}_{1k}-t^q_{2k})\end{aligned} \tag{6}$$

where the superscript n is the number of evolution generations, $SLL^{(n)}$ and SLL_d denote the calculated and desired maximum sidelobe level at f_0, $SBL^{(n)}_{\max}$ and SBL_d denote the calculated and desired maximum sideband level at the selected m sideband frequencies, t^q_{2k} and t^q_{1k} represent the "switch-on" time and "switch-off" time, w_1, w_2 ,w_3 and w_4 are the corresponding weighting factors for each term, which are given by

$$\begin{aligned}w_1&=\begin{cases}0 & SLL^{(n)}\le SLL_d\\ 1 & \text{others}\end{cases},\qquad w_2=\begin{cases}0 & SBL^{(n)}_{\max}\le SBL_d\\ 1 & \text{others}\end{cases},\\ w_3&=\begin{cases}0 & t^q_{2k}-t^q_{1k}=0\text{ or }\ge 0.04\\ 100 & \text{others}\end{cases},\ w_4=\begin{cases}0 & t^{q+1}_{1k}-t^q_{2k}=0\text{ or }\ge 0.04\\ 100 & \text{others}\end{cases}\end{aligned} \tag{7}$$

3. NUMERICAL RESULTS

In the first case, a 16-element TMLA with uniform amplitude distribution is considered, namely, $A_k=1$. A -30 dB SLL pattern is selected as the target pattern at f_0. For comparing the feasibility of the SOTS scheme with previous approaches, TMLAs with pulse shifting and BOTS are considered firstly. Fig. 2 and Fig. 3 show the normalized far field patterns at the center frequency and the

first two sideband frequencies with pulse shifting and BOTS schemes. As can be seen, the SLLs are both about −30 dB and the SBLs are about −21 dB and −22 dB, respectively.

For the TMLA with pulse shifting, the phase of the complex excitation can be adjusted in $[-2\pi, 0]$ arbitrarily. For the TMLA with BOTS, the SBL is almost −22 dB, which is shown in Fig. 3. To further suppress the SBL, the code length L must be increased. However, this will increase the implementation error of the RF switches [6] and is thus not recommended.

Next, a uniformly excited 16-element TMLA with SOTS is considered, and L is set as 5. The array is symmetric, and 80 variables need to be optimized. A −30 dB SLL pattern is selected as the target pattern at f_0. Fig. 4 shows the far field pattern of a uniformly excited 16-element TMLA with SOTS at f_0,$f_0 + f_p$ and $f_0 + 2f_p$. The SLL and maximum SBL are about −30.00 dB and −27.5 dB, respectively. By comparing Fig. 4 with Fig. 2 and Fig. 3, it is observed that the SBL of TMLA with SOTS is about 6.5 dB and 5.5 dB lower than that in Fig. 2 and Fig. 3 respectively. Fig. 5 shows the corresponding SBLs at the first 25 sideband frequencies. The "on-off" time distributions are compiled and plotted in Fig. 6. Since the array is symmetric in its excitation, only half of the "on-off" time distributions are given.

In the second case, a non-uniform amplitude 16-element TMLA is considered. In conventional antenna arrays, the excitation amplitude ratio of a −30 dB SLL Taylor $\bar{n}$ distribution ($\bar{n} = 4$) is about 1:0.25. Now a −40 dB SLL pattern is selected as the target pattern in TMLAs with $1 : 0.25$ static excitation amplitude ratio. For TMLAs with pulse shifting and BOTS, the SBLs are −36.5 dB and −24.5 dB respectively. For the TMLA with SOTS, the SBLs are all almost below −39.5 dB. Fig. 7 shows the 3-D space and frequency response plot of the TMLA with SOTS scheme.

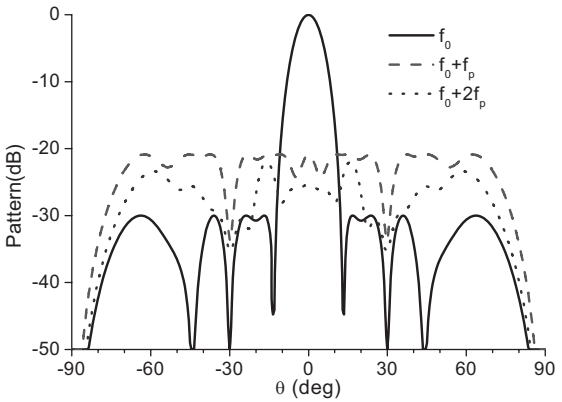

Figure 2: Normalized pattern of the 16-element uniform amplitude TMLA with pulse shifting.

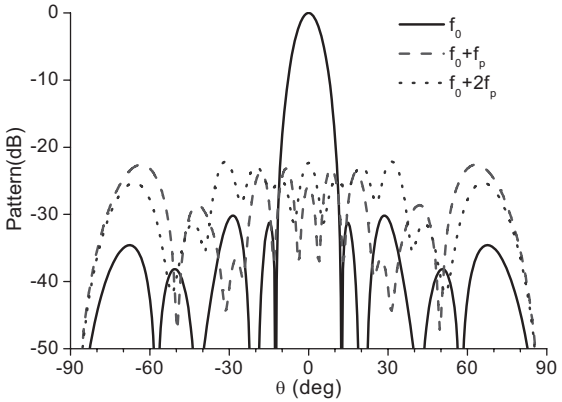

Figure 3: Normalized pattern of the 16-element uniform amplitude TMLA with BOTS time scheme.

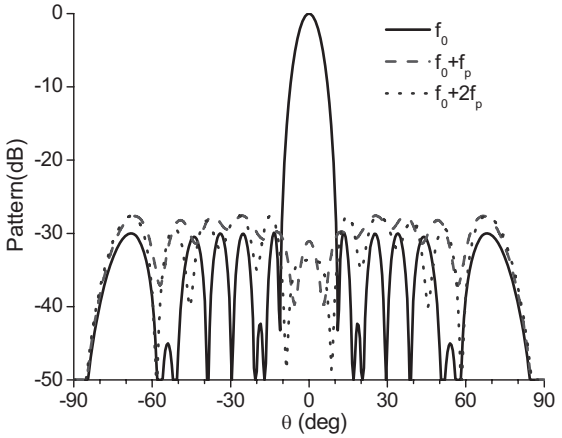

Figure 4: Normalized pattern of the 16-element uniform amplitude TMLA with SOTS time scheme.

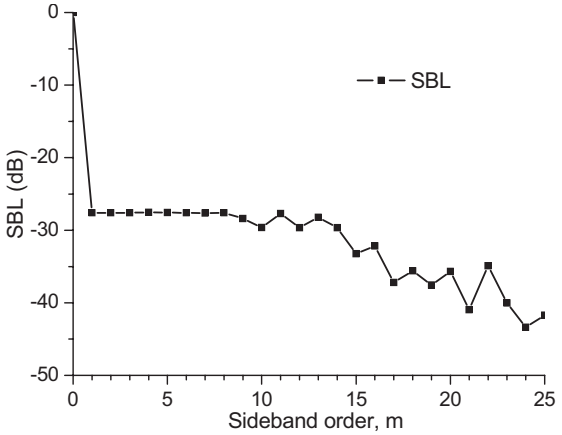

Figure 5: Normalized SBLs at the first 25 sidebands of the16-element uniform amplitude TMLA with SOTS time scheme.

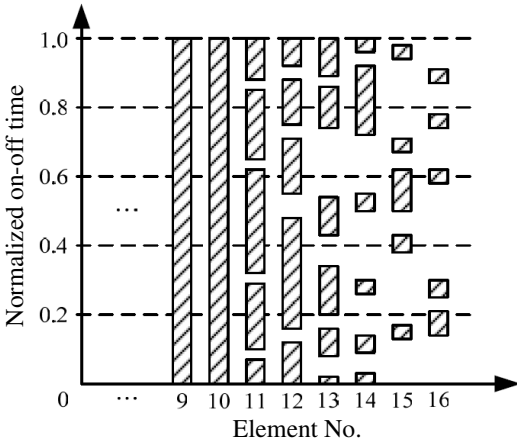

Figure 6: Normalized on-off time of the 16-element uniform amplitude TMLA with SOTS time scheme.

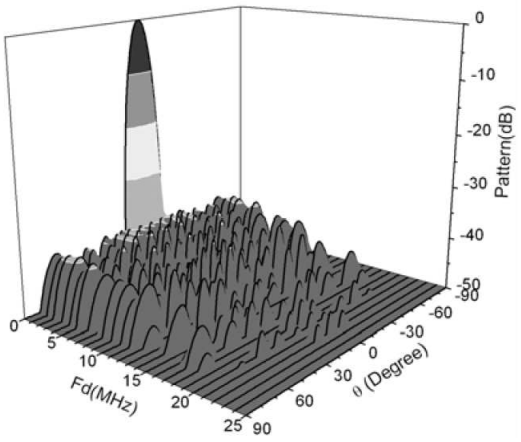

Figure 7: Space and frequency response plot of the 16-element non-uniform amplitude TMLA with SOST time scheme.

4. CONCLUSIONS

This paper proposed a new type of time modulation scheme to suppress the SBL while designing low/ultra-low SLL TMLAs. The time modulation period is divided into several time steps, and the "switch-on" and "switch-off" time in each time step is optimized via the differential evolution (DE) algorithm. The SBL can be suppressed to less than −27.5 dB while maintaining a −30 dB SLL for a 16-element TMLA with uniform amplitude excitations. When designing a −40 dB SLL 16-element TMLA with 1 : 0.25 static excitation amplitude ratio, the SBL can be suppressed to less than −39.5 dB. Based on the numerical results, it is found that the TMLAs with SOTS have the lowest SBL. The study show that the proposed SOTS time scheme is more robust for the synthesis of low/ultra-low SLL patterns with suppressed SBL than previous approaches such as pulse shifting and binary optimized time sequences in TMLAs.

ACKNOWLEDGMENT

This work was supported by the Natural Science Foundation of China under Grant No. 60971030, and partially supported by the 111 project of China under Grant No. B07046.

REFERENCES

1. Yang, S., Y. B. Gan, and P. K. Tan, "Comparative study of low sidelobe time modulated linear arrays with different time schemes," *Journal of Electromagnetic Waves and Applications*, Vol. 18, No. 11, 1443–1458, 2004.
2. Yang, S., Y. B. Gan, and A. Qing, "Sideband suppression in time-modulated linear arrays by the differential evolution algorithm," *IEEE Antennas Wireless Propagat. Lett.*, Vol. 1, 173–175, 2002.
3. Fondevila, J., J. C. Bregains, F. Ares, and E. Moreno, "Optimizing uniformly excited linear arrays through time modulation," *IEEE Antennas Wireless Propagat. Lett.*, Vol. 3, 298–301, 2004.
4. Poli, L., P. Rocca, L. Manica, A. Massa, "Handling sideband radiations in time-modulated arrays through particle swarm optimization," *IEEE Trans. Antennas Propagat.*, Vol. 58, No. 4, 1408–1411, April 2010.
5. Pal, S., S. Das, and A. Basak, "Design of time-modulated linear arrays with a multi-objective optimization approach," *Progress In Electromagnetics Research B*, Vol. 23, 83–107, 2010.
6. Yang, S., Y. B. Gan, A. Qing, and P. K. Tan, "Design of a uniform amplitude time modulated linear array with optimized time sequences," *IEEE Trans. Antennas Propagat.*, Vol. 53, No. 7, 2337–2339, July 2005.
7. Poli, L., P. Rocca, L. Manica, and A. Massa, "Pattern synthesis in time-modulated linear arrays through pulse shifting," *IET Microw. Antennas Propag.*, Vol. 4, No. 9, 1157–1164, 2010.
8. Aksoy, E. and E. Afacan, "Thinned nonuniform amplitude time-modulated linear arrays," *IEEE Antennas Wireless Propagat. Lett.*, Vol. 9, 514–517, 2010.

A Fast 3D System for AR Film Thickness Measurement of Single Crystalline Silicon Solar Cells

H. N. Yen and H. C. Wang
Department of Electronic Engineering, St. John's University, Taiwan

Abstract— For increasing marketing competence, silicon solar cell manufacturers have adopted optical inspection techniques in production lines to perform product classification and statistical process analysis. The product classification is based on overall photoelectric conversion efficiency of the solar cell itself. Two factors directly influence the overall photoelectric conversion efficiency of the solar cell, i.e., composed materials and anti-reflection (AR) film coating on substrate. Since film thickness variation of the AR layer will induce color change on the surface of solar cell, a cost-effective three dimensional (3D) system is proposed to perform fast AR film thickness measurement of single silicon crystalline solar cells.

The proposed system first uses a color CCD to capture the red-green-blue color image of inspected single silicon crystalline solar cell, and transforms it to hue-saturation-lightness image format. And then the area and boundary of different hue-value images are calculated and sorted with the image thresholding and label operation. Besides, with the corresponding measurement procedure on specified hue-value regions of using a precise height measurement instrument, such as the wavelength scanning profiler, the regression equation between the hue value and AR film thickness is obtained, and then implemented into the proposed 3D system to perform large area scanning AR film thickness measurement of single silicon crystalline solar cells. Compared to the optical ellipsometry, the measurement speed of the proposed system is fast. It take only 0.1 seconds to finish the AR film thickness measurement of a 12.5 cm × 12.5 cm solar-cell image, and the measurement accuracy can reach 3 nm.

1. INTRODUCTION

The continuing decrease of the energy sources has made solar energy technology one of the fastest developing techniques today. The solar energy is generally now used by crystalline silicon solar cell [1]. In recent years, more and more solar-cell manufacturers adopt automatic vision inspection techniques in production lines to perform product classification and statistical process control (SPC) in time. Product classification can provide more commercial selections for solar-cell wholesalers, and then increase the product profits. Moreover, overall photoelectric conversion efficiency of the solar cells can be enhanced with SPC analysis.

To increase the overall photoelectric conversion efficiency is always the key issue for solar-cell manufacturers [2]. For silicon solar-cell manufacturers, the effort they can do in increasing the overall photoelectric conversion efficiency is to reduce internal defects and reflection loss as possible.

There will be 30 $\sim$ 35% reflection loss if the solar cell has not processed with antireflection coating (AR). Currently, the AR layer of commercial silicon solar cell is coated mostly with single-layer transparent film of Si3N4. Thickness variation of such transparent film will induce color change on solar-cell surface, and the more light color indicates the thicker AR layer.

Since the uniformity of AR directly influences the overall photoelectric conversion efficiency of the solar cell itself [3], it is necessary to measure film thickness in time during manufacturing process. Traditionally, the thickness of transparent thin film is measured by Ellipsometry. However, the measurement speed of using Ellipsometry is too slow to meet requirement of on-line inspection, and the implementation cost of Ellipsometry is expensive. Because the film thickness variation of AR will induce the color change on the solar-cell surface, this paper proposes an area scanning system based on color vision technique to perform fast measurement of AR film thickness of single crystalline silicon solar cells.

2. METHOD

This study applies color image processing technique to develop a computer vision system for measuring AR film thickness. The proposed system uses a ring-type LED as a front lighting source. A color CCD camera is first used to capture the color image and transfer to personal computer. And then using image processing techniques and statistical skill, such as image thresholding label operation and regression analysis, to perform AR film thickness measurement of the single crystalline silicon solar cell.

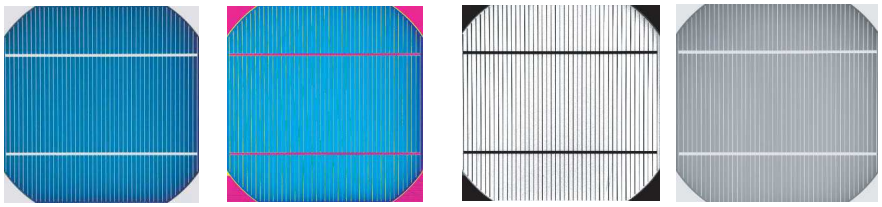

(a) (b) (c) (d)

Figure 1: HSL image of the inspected solar cell. (a) Original image. (b) Hue image. (c) Saturation image. (d) Lightness image.

2.1. Color Transform and Quantization

The captured red-green-blue (RGB) image is transformed to hue-saturation-lightness (HSL) image, as shown as Fig. 1, and the color transform equations are described as Eqs. (1)–(3)

$$H = \begin{cases} 0^\circ, & \text{if } \max = \min \\ \left(60^\circ \times \dfrac{g-b}{\max - \min} + 360^\circ\right) \bmod 360^\circ, & \text{if } \max = r \\ 60^\circ \times \dfrac{b-r}{\max - \min} + 120^\circ, & \text{if } \max = g \\ 60^\circ \times \dfrac{r-g}{\max - \min} + 240^\circ, & \text{if } \max = b \end{cases} \tag{1}$$

$$S = \begin{cases} 0 & \text{if } \max = 0 \\ \dfrac{\max - \min}{\max} = 1 - \dfrac{\min}{\max}, & \text{otherwise} \end{cases} \tag{2}$$

$$L = \frac{1}{2}(\max + \min) \tag{3}$$

Figure 1(a) shows the original image of an inspected solar cell, and Figs. 1(b)–(d) show the corresponding hue, saturation and value images. For an HSL image of a single crystalline silicon solar cell, the color information is decided with the hue image. Generally, the color in hue image is represented by a ring of 360 degree1. In this study, the color in hue image is transformed to 0–255 color level for the convenience of calculation.

After the hue image is extracted from HSL image, it was first processed by median filtering to remove optical noise, and then was quantized for the purpose of clustering different hue value area and enhancing image processing speed. Double threshold-value technique [4] was used to perform image segmentation of the quantized hue image in this study. Collocated with four connectivity method, the proposed system can perform area labeling [5] for each specified hue-value region and display color distribution of the inspected solar cell.

2.2. Regression Relationship between AR Film Thickness and Hue Value

After obtaining the whole hue-value data of the inspected solar cell, the proposed system first uses a high accuracy optical thin film thickness measurement instrument to measure the corresponding film thickness values on different hue-value regions And then the specified hue values and their corresponding thickness data are sorted and put into regression equation to establish the relationship formula. In this study, quadratic regression equation was used to obtain the relationship formula between AR film thickness and hue vale. The quadratic regression equation is described as Eq. (4), in which X and Y represent hue value and measured thickness data, respectively. Finally, the formula is implemented into the proposed system for automatically performing AR film thickness measurement.

$$Y = AX^2 + BX + C \tag{4}$$

3. EXPERIMENT RESULTS

The hardware implementation of the proposed system is as shown as Fig. 2. The color CCD and the collocated lens are used to capture color image of the inspected silicon solar cell. The ring light source is used to provide uniform lighting. The program developed by us was implemented to the personal computer to perform specified image processing such as color image format transformation, image thresholding and area labeling.

In this study, three pieces of commercial single crystalline silicon solar cells were used as the training samples to acquire the regression formula between AR film thickness and hue color level. The three sample solar cells are from the same manufacturing process and have the same size of 12.5 cm × 12.5 cm These samples were put on the table successively at training stage, as shown as Fig. 2, and processed with the color format transformation and quantization procedure abovementioned.

Twelve specified hue-value regions from the three sample solar cells were measured by an optical thin film thickness measurement instrument of 5 nm accuracy. These specified hue values and their corresponding thickness data are sorted as Table 1.

With the data regression process, the coefficients of Eq. (4) can be acquired to build the relationship formula between AR film thickness and hue vale as Eq. (5).

$$Y = 0.01529X^2 + (-9.182)X + 2103 \tag{5}$$

In this research, another single crystalline silicon solar cell was used to test the measurement performance of the proposed system. The test sample solar cell was processed with the proposed system, and the processing time for an image of 768 × 768 pixels is less than 0.1 second on an Intel Core2 2.4-GHz personal computer (PC). The 3D surface profile of the AR layer of test sample solar cell is displayed as Fig. 3, in which the film thickness within the non-transparent busbar area is set to zero.

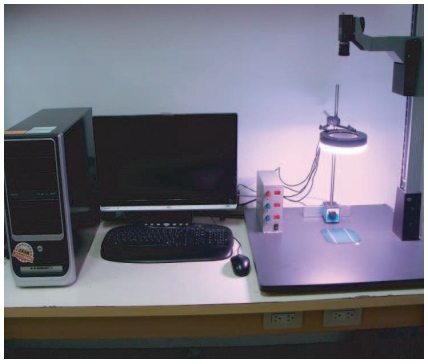

Figure 2: The hardware implementation of the proposed system.

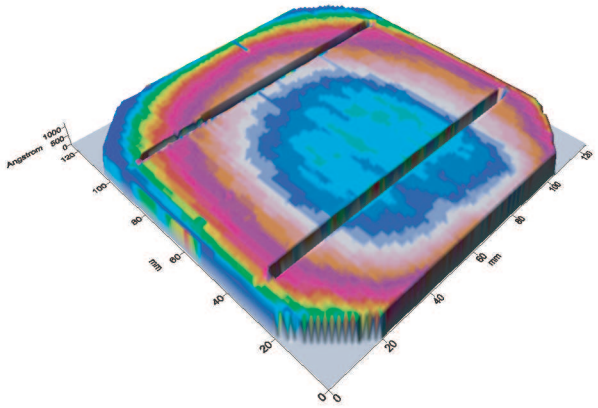

Figure 3: 3D surface profile of the AR layer of test sample solar cell.

Table 1: The specified hue values and their corresponding thickness data measured with an optical thin film measurement instrument of 5 nm accuracy.

Hue value	137	138	139	140	141	142	145	147	148	150	153	154
Thickness value measured with an optical film thickness measurement instrument (Å)	1,141	1,112	1,111	1,109	1,108	1,107	1,095	1,064	1,079	1,069	1,056	1,051

Table 2: Comparisons of accuracy between the proposed system and an thin film thickness measurement instrument of 5 nm accuracy.

Color level of hue value	Thickness value measured with the proposed system (Å)	Thickness value measured with an film thickness measurement instrument (Å)	Accuracy (Å)
164	1,008	1,022	−14
138	1,127	1,153	−26
149	1,074	1,050	24
163	1,012	999	13
139	1,122	1,111	11
155	1,047	1,042	5

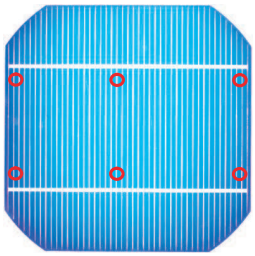

Figure 4: Six specified hue-value region measured by the proposed system and an optical thin film thickness measurement instrument of 5 nm accuracy.

The test sample solar cell was also measured six specified hue-value region, as shown as six red circles in Fig. 4, with an optical thin film thickness measurement instrument of 5 nm accuracy for measurement accuracy comparison The comparisons of accuracy between the proposed system and the optical thin film thickness measurement instrument are sorted as Table 2.

4. CONCLUSIONS

In this paper, a 3D measurement system for AR film thickness measurement of single silicon crystalline solar cells is presented. The proposed system integrates color image processing techniques and regression skill to perform fast 3D measurement of solar-cell AR film in an area. This area-measuring approach can speed up the thickness measurement of AR films. Experiments from real sample single silicon crystalline solar cells have shown that the 3D profiling and film thickness are efficient and effective with the proposed system. Compared to the optical ellipsometry, the measurement speed of the proposed system is fast. It takes only 0.1 seconds to finish the AR film thickness measurement of a 12.5 cm × 12.5 cm solar-cell image, and the measurement accuracy can reach 3 nm.

REFERENCES

1. Szlufcik, J., S. Sivoththaman, J. F. Nus, R. P. Mertens, and R. V. Overstraeten, "Low-cost industrial technologies of crystalline silicon solar cells," *Proceedings of the IEEE*, Vol. 85, No. 5, 711–730, May 1997.
2. Rath, J. K., "Low temperature polycrystalline silicon a review on deposition, physical properties and solar cell applications," *Solar Energy Materials & Solar Cells*, Vol. 76, 431–487, 2003.
3. King, D. L., B. R. Hansen, and D. J. Aiken, "New methods for measuring performance of monolithic multi-junction solar cells," *IEEE Conf.*, 1197–1201, Sandia National Laboratories, Albuquerque, NM, 2000.
4. Chen, Q., Q. S. Sun, P. A. Heng, and D. S. Xia, "A double-threshold image binarization method based on edge detector," *Pattern Recognition*, Vol. 41, 1254–1267, 2008.
5. Leitner, R., H. Mairer, and A. Kercek, "Real-time classification of polymers with NIR spectral imaging and blob analysis," *Real-Time Image.*, Vol. 9, 245–251, 2003.

Multimodality Imaging of Digital Holographic Microscopy

Xin-Ji Lai[1], **Yu-Chih Lin**[1], **Han-Yen Tu**[2], **and Chau-Jern Cheng**[1]

[1]Institute of Electro-Optical Science and Technology, National Taiwan Normal University
Taipei 11677, Taiwan
[2]Department of Electrical Engineering, Chinese Culture University, Taipei 11114, Taiwan

Abstract— We propose and demonstrate a multimodality imaging technique of digital holographic microscopy for measuring the complex wavefronts and the state of polarization going through the specimen. The incident light with two orthogonal polarization states is used for obtained the polarization encoded digital hologram of the specimen. The Jones vector representation of the specimen can be synthesized and determined by calculating the relative amplitude and phase of the orthogonal polarization states of the transmitted waves. In the preliminary experiments, the multimodality imaging approach was validated by examining the polarization states of a twisted nematic liquid crystal spatial light modulator.

1. INTRODUCTION

The digital holographic microscopy (DHM) has been widely investigated and has great potential applications, such as measuring whole wavefronts of a specimen, because it can quantitatively assess all information in a complex wavefronts derived from a digital hologram [1–5]. In contrast to traditional microscopy techniques like confocal laser scanning microscopy, atomic force microscope and scanning electron microscope, digital holographic microscopy permits a non-destructive, non-invasive and low energy penetration measurement with full-field information of the specimen, and can directly observe the multimodality images of the specimen with single hologram acquisition. Furthermore, not only the amplitude and phase information including the refractive index [2, 3] or topography image can be quantitatively measured and analyzed from the reconstructed image of the digital hologram, but also the state of polarization through the specimen can be determined by using the two orthogonal polarizations through the specimen from different detection ports for generating the polarization-encoded digital holograms [4]. Hence, a rapid full-field measurement and direct observation of the whole wavefronts of specimen including amplitude, phase and polarization can be executed to perform multimodality imaging. In this study, we employed a twisted nematic liquid crystal spatial light modulator (TN-LC SLM) to validate the multimodality imaging of digital holographic microscopy [5].

2. PRINCIPLE

Digital holographic microscopy can simultaneously record full-field information through optical interference and the complex wavefront information (amplitude and phase) can quantitative analyzed by numerical calculation. For improving the capability and applications of the digital holographic microscopy, we propose a multimodality imaging technique for detecting the polarization state through the specimen by using two-port digital holographic microscopy. The system configuration for digital hologram recording and reconstruction is illustrated in Fig. 1. According to Fig. 1, the specimen is put in the object plane $U_O(x, y)$ and is magnified by an objective lens into an intermediate image $U_i(\xi, \eta)$. From the Fresnel-Kirchhoff diffraction formulation [6], the diffracted object

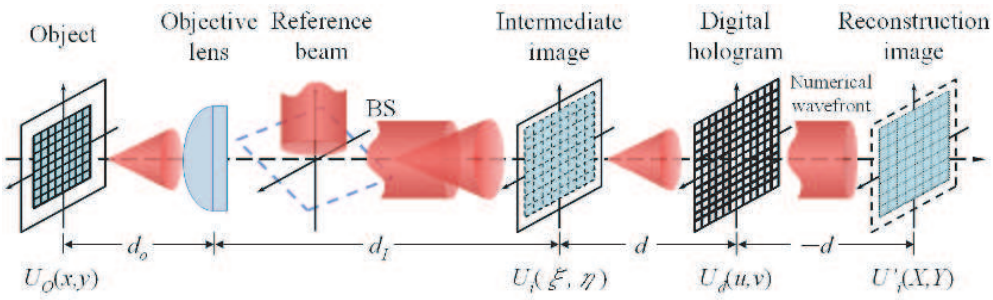

Figure 1: Conceptual diagram of the digital holographic microscopy for multimodality imaging.

wave propagating from the intermediate image in the hologram plane $U_d(u,v)$ can be represented as follows:

$$U_d(u,v) = \frac{e^{j\frac{2\pi d}{\lambda}}}{j\lambda d} e^{j\frac{k}{2d}(u^2+v^2)} \iint \left[U_i(\xi,\eta) e^{j\frac{k}{2d}(\xi^2+\eta^2)} e^{-j\frac{2\pi}{\lambda d}(\xi u+\eta v)}\right] d\xi d\eta, \tag{1}$$

where d is the propagation distance between intermediate image and hologram plane and k is the wave number. As in optical holographic recording, the object wave is interfered with a reference wave, and the holographic intensity pattern is recorded by a complementary metal-oxide-semiconductor (CMOS) image sensor. The off-axis reconstruction method, which is inserted a spatial filtering mask at the Fourier spectrum, is used to eliminate the zero-order and conjugate terms. Then, the filtered digital hologram can be numerically back- propagated to the intermediate image plane for image reconstruction. Thus, the complex wavefront $U_i'(X,Y)$ with the polarization states in the reconstruction plane can be represented by Jones formalism as follows:

$$U_i'(X,Y) = \begin{bmatrix} A_x(X,Y)\exp[i\Phi_x(X,Y)] \\ A_y(X,Y)\exp[i\Phi_y(X,Y)] \end{bmatrix}, \tag{2}$$

where A_x and A_y represent the amplitude components, and Φ_x and Φ_y are the phase components of each polarization states. Then, the azimuth angle ψ between amplitude transmittance A_x and A_y can be calculated as follows:

$$\tan\psi = \frac{A_y(X,Y)}{A_x(X,Y)}. \tag{3}$$

The phase shift δ between x- and y-components of the transmitted wave going through the specimen can be represented as

$$\delta = \Phi_y(X,Y) - \Phi_x(X,Y). \tag{4}$$

The inclination angle can also be calculated by the phase shift and azimuth angle as follows:

$$\tan 2\phi = \tan 2\psi \cos\delta. \tag{5}$$

Finally, the relative amplitude and phase components of the Jones vector obtained from Eqs. (2)–(5) can described the polarization states of the transmitted wave going through the specimen.

3. EXPERIMENTS

The experimental setup of digital holographic microscopy for multimodality imaging is illustrated in Fig. 2. This configuration is based on modified Mach-Zehnder interferometer with two orthogonal polarization ports. The coherent light source is a laser diode with a wavelength of 658 nm and the laser beam is spatially filtered and expanded into a collimated beam with uniform plane wavefront. Then, the expanded beam going through the beam splitter (BS_1) was divided into object and

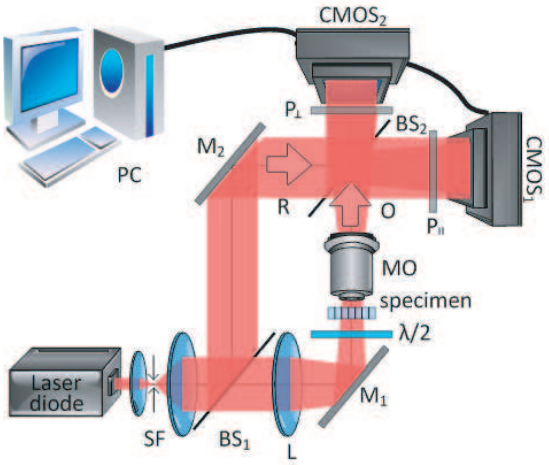

Figure 2: Experimental setup of the multi-modality imaging of digital holographic microscope system.

reference waves, wherein a 20× microscope objective with numerical aperture (N.A.) 0.4 was used in the object arm to magnify the twisted nematic liquid crystal cells of the spatial light modulator. To obtain a specific polarization state of incidence, a half wave plate ($\lambda/2$) was used to select suitable polarization state of the object beam. Then the resultant object wave was combined with the reference beam through the beam splitter (BS_2). Two polarizers with the parallel ($P_{\parallel}$) and perpendicular ($P_{\perp}$) polarization were employed in front of $CMOS_1$ and $CMOS_2$ image sensors, respectively to measuring the birefringence of the specimen. The chip size of CMOS sensor is 1/2" and the number of pixels is $1280\,(H) \times 1024\,(V)$ with pixel size $5.2\,\mu m^2$, which can be operated at 25 frames per second (fps) for capturing the hologram patterns. The numerical reconstruction was performed in a personal computer. From the diffraction limit criterion, we can also obtain a lateral resolution of about 1 µm at 658 nm with NA = 0.4. Also, the axial resolution can be estimated down to 6 nm. In the experiments, we measured the polarization states of twisted nematic liquid crystal spatial light modulator with different voltages of applied gray level, which can be used to modulate the amplitude transmittance and phase retardation of the liquid crystal cells.

4. RESULTS AND DISCUSSION

The experimental results are illustrated in Fig. 3, which describes the amplitude transmittance and phase distribution at input gray level 255 and 0. Figs. 3(a)–3(b) and 3(c)–3(d) are the amplitude and phase distribution through the perpendicular and parallel polarization state, respectively. Figs. 3(e) and 3(f) represent the azimuth angle ψ and phase shift δ, which are calculated from Eqs. (3) and (4). Then the Jones vector of the liquid crystal cell operated at the gray level 255 and 0, respectively, can also be obtained as

$$J_{gray=255}\,(\psi,\delta) = \begin{bmatrix} 0.17 \\ 0.98 + 0.07i \end{bmatrix} \quad \text{and} \quad J_{gray=0}\,(\psi,\delta) = \begin{bmatrix} 0.99 \\ 0.05 + 0.05i \end{bmatrix}.$$

Further, the polarization state of the liquid crystal cell in different gray level can also be obtained by the DHM system as shown in Fig. 4. The experimental results in Figs. 4(a) and 4(b) (inside

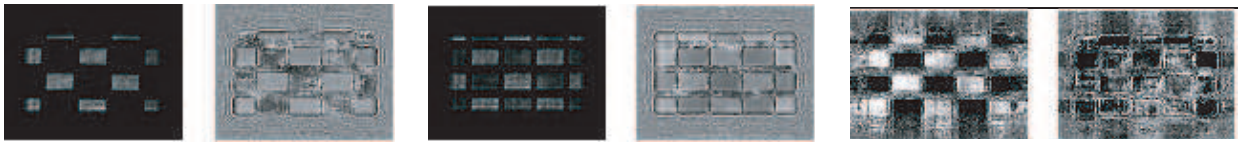

(a) (b) (c) (d) (e) (f)

Figure 3: Reconstruction images of liquid crystal cells by multimodality DHM: (a) amplitude distribution A_x, (b) phase distribution Φ_x, (c) amplitude distribution A_y, (d) phase distribution Φ_y, (e) azimuth angle ψ and (f) phase shift δ.

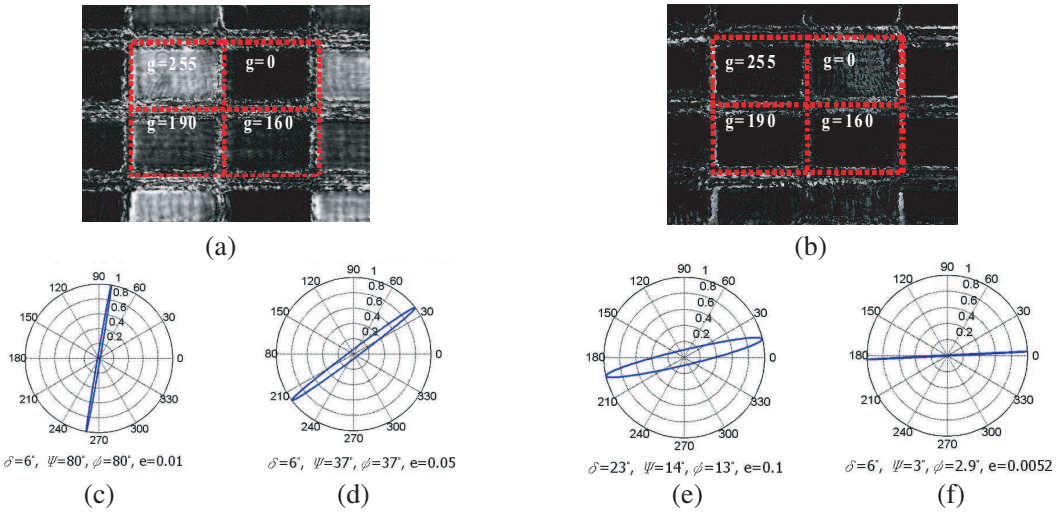

(a) (b) (c) (d) (e) (f)

Figure 4: Polarization state of the TN-LC SLM of different input gray level (a) phase shift δ, (b) azimuth angle ψ, (c) $g = 255$, (d) $g = 190$, (e) $g = 160$ and (f) $g = 0$.

the red dotted grid) indicate the polarization state with different azimuth angles and the phase shifts as shown in Figs. 4(c) to 4(f), which the polarization ellipses of the liquid crystal cell in gray level 255, 190, 160, and 0 were verified. The inclination angle ϕ and the ellipticity e can also be obtained from Fig. 4. Then from these results, we can find that the polarization state of the liquid crystal cells will be rotated by 90 degree from gray level 255 to 0. The result of Fig. 4(e) was measured as an elliptic polarization. The experimental results measured by the multimodality digital holographic microscopy show that the whole wavefronts information (including amplitude, phase and polarization) can thus be measured simultaneously and quantitatively analyzed.

5. CONCLUSIONS

This work has proposed and experimentally demonstrated the multimodality imaging properties of digital holographic microscopy by use of two orthogonal polarizations for obtaining the entire optical field information. The complex fields (amplitude and phase) and the birefringence of the polarizing devices, such as liquid crystal spatial light modulator, can thus be measured and characterized by digital holographic microscopy. The multimodality imaging of digital holographic microscopy can measure not only the three-dimensional structure but also the birefringence of the specimen, and provide the potential functional studies and dynamic investigations in polarization optics and biological cells.

ACKNOWLEDGMENT

This work was financially supported in part by the National Science Council, Taiwan, R.O.C., under contract No. NSC-99-2221-E-003-010-MY3.

REFERENCES

1. Lin, Y.-C., C.-J. Cheng, and T.-C. Poon, "Optical sectioning with a low-coherence phase-shifting digital holographic microscope," *Appl. Opt.*, Vol. 50, No. 7, B25–B30, 2011.
2. Lin, Y.-C., Y.-T. Lee, X.-J. Lai, C.-J. Cheng, and H.-Y. Tu, "*In situ* mapping of light-induced refractive index gratings by digital holographic microscopy," *Jpn. J. Appl. Phys.*, Vol. 49, 102501-1–102501-7, 2010.
3. Lin, Y.-C. and C.-J. Cheng, "Determining the refractive index profile of micro-optical elements using transflective digital holographic microscopy," *J. Opt.*, Vol. 12, 115402-1–115402-5, 2010.
4. Colomb, T. and C. Depeursinge, "Polarization imaging by use of digital holography," *Appl. Opt.*, Vol. 41, 27–37, 2002.
5. Cheng, C. J., Y. C. Lin, M. L. Hsieh, and H. Y. Tu, "Complex modulation characterization of liquid crystal spatial light modulators by digital holographic microscopy," *Jpn. J. Appl. Phys.*, Vol. 47, 3527–3529, 2008.
6. Goodman, J. W., *Introduction to Fourier Optics*, 2nd Edition, McGraw-Hill, New York, 1996.